



---

# **A heuristic evaluation of the energy performance of a Vestas V52 wind turbine in a peri-urban environment**

---

Author:

Raymond Byrne (MSc)

Supervisors:

Prof. Neil Hewitt

Prof. Philip Griffiths

*A thesis submitted in fulfillment of the requirements  
for the degree of Doctor of Philosophy*

Centre for Sustainable Energy Technologies  
Belfast School of Architecture & the Built Environment

November 29, 2022

(I confirm that the word count is less than 100,000 words)



## Declaration of Authorship

I, Raymond Byrne, declare that this thesis titled, "*A heuristic evaluation of the energy performance of a Vestas V52 wind turbine in a peri-urban environment* " and the work presented in it are my own and has not been submitted for another degree at any other University or Institution. All external references and sources used are clearly acknowledged and properly identified within the contents.

**Signed:**

A handwritten signature in black ink that reads "Raymond Byrne". The script is cursive and fluid, with the first letters of the first and last names being capitalized and prominent.

**Date:** November 29, 2022





UNIVERSITY OF ULSTER

# Abstract

Faculty Of Computing, Eng. & Built Env.

Belfast School of Architecture & the Built Environment

Doctor of Philosophy

## **A heuristic evaluation of the energy performance of a Vestas V52 wind turbine in a peri-urban environment**

by Raymond Byrne

As wind energy continues to expand, new markets for distributed wind applications are expected, including behind-the-meter applications at industrial consumer sites in peri-urban areas. The presence of buildings in these areas can give rise to complex wind regimes that have not been widely studied in the context of medium and large-scale wind turbine deployment in these environments. This PhD examines the impacts of building obstacles on the wind resource and the subsequent impact on the energy performance of a large-scale Vestas V52 wind turbine operating in a peri-urban wind environment. The research is informed by long-term real-world turbine performance data, multilevel onsite LiDAR wind measurements and measurements from a dedicated local offsite met mast. A novel wind turbine electrical energy rose is developed to evaluate the energy predictions of a national mesoscale wind atlas as well as four widely used industry microscale wind flow model approaches. Wind shear, turbulence and gust characteristics are assessed against current wind turbine international design standards and in relation to the site morphological characteristics. A new low-cost morphological site pre-screening framework is developed, recommending wind measurement heights and flow model configurations to improve peri-urban wind turbine micro-siting. The research suggests that this framework could lead to a 10% increase in annual energy output compared to current IEA micro-siting recommendations. The addition of a peri-urban turbulence intensity design reference value of 25% to current IEC design standards is also suggested.



# Acknowledgements

Firstly, I wish to acknowledge and sincerely thank my supervisors, Professor Neil Hewitt and Professor Philip Griffiths, for their very valuable and continued guidance, support and encouragement throughout this PhD, including the four peer reviewed Journal publications that resulted.

I also wish to acknowledge the following:

- The Doctoral College at the University of Ulster, for its administrative support and its excellent in-class and online PhD training programmes
- My work colleague Dr. Paul MacArtain at Dundalk Institute of Technology, whose expertise in funding acquisition greatly helped secure the field measuring equipment and software used in this PhD. Also, for his assistance in equipment deployment on the ground
- My work colleague Mr. Gerry Reaburn (PhD Candidate) at Dundalk Institute of Technology, for his assistance in equipment deployment on the ground
- The Research Office and Human Resources Department at Dundalk Institute of Technology, for part funding the academic fees associated with this PhD
- Mr. Patrick Bishop, a local neighbouring land owner to Dundalk Institute of Technology, who facilitated the installation of a temporary wind met mast on his property and allowed regular access to the mast for number of months as part of this research
- Mr. Larry Staudt (Retired) formally of Dundalk Institute of Technology, for pioneering the installation the Vestas V52 wind turbine on the campus in 2005, that ultimately enabled this research to be carried out
- Dr. Davide Astolfi and Professor Francesco Castellani of the University of Perugia, Italy, for their collaboration in a small section of the work that resulted in an additional (5<sup>th</sup>) Journal publication as part of the collaborative international research efforts of IEA-Wind-Task 41-“Enabling Wind to Contribute to a Distributed Energy Future”
- For funding the wind LiDAR used in this research as part of the SPIRE2 project, the European Union’s INTERREG VA Programme (Grant No. INT-VA/049),

managed by the Special EU Programmes Body (SEUPB). The views and opinions expressed in this document do not necessarily reflect those of the European Commission or the Special EU Programmes Body (SEUPB)

# Contents

<b>Declaration of Authorship</b>	<b>iii</b>
<b>Abstract</b>	<b>v</b>
<b>Acknowledgements</b>	<b>vii</b>
<b>List of Figures</b>	<b>xxiv</b>
<b>List of Tables</b>	<b>xxiv</b>
<b>List of Abbreviations</b>	<b>xxv</b>
<b>1 Introduction</b>	<b>1</b>
1.1 General Introduction . . . . .	1
1.2 Outline of this PhD . . . . .	4
1.2.1 Thesis Layout . . . . .	5
1.3 Principal contributions of this research . . . . .	6
1.3.1 Peer reviewed Journal publications . . . . .	6
1.3.2 Conference proceedings . . . . .	7
1.3.3 Other partial contributions of this research . . . . .	7
<b>2 Literature Review</b>	<b>9</b>
2.1 Background . . . . .	9
2.2 Distributed wind challenges . . . . .	10
2.2.1 General challenges . . . . .	10
2.2.2 Urban wind challenges . . . . .	13
2.3 Distributed wind opportunities . . . . .	15
2.3.1 New innovations and niche markets . . . . .	15
2.3.2 Commercial scale behind-the-meter opportunities . . . . .	18
2.4 Distributed wind resource assessment . . . . .	19
2.4.1 Current wind resource assessment approaches . . . . .	21

2.4.2	Urban and peri-urban additional wind modelling complexities	25
2.5	Research gap identification	28
2.6	Aims of this PhD to help address the research gap	31
<b>3</b>	<b>Theoretical background</b>	<b>35</b>
3.1	Introduction	35
3.2	Overview of the atmosphere	35
3.2.1	Global circulation	35
3.2.2	Vertical profile of the ABL	40
3.2.3	Urban wind profiles	42
3.2.4	Thermal stability in the ABL	44
3.3	Modelling the atmosphere for wind energy	48
3.3.1	Global circulation and Mesoscale models	48
3.3.2	Microscale models	52
3.3.3	Linear flow model approaches	52
3.3.4	Orography	53
3.3.5	Obstacles	54
3.3.6	CFD flow approaches	57
3.3.7	Morphological approaches in urban environments	60
3.4	Wind statistics	64
3.4.1	Temporal wind speed	64
3.4.2	Wind power curves and AEP	66
3.4.3	Turbulence and gust factors	68
3.4.4	Wind shear and rotor equivalent wind speed	70
3.5	LiDAR Technology wind energy	72
3.5.1	Continuous wave (CW) LiDARs	73
3.5.2	Pulsed LiDAR	76
3.5.3	Some measurement limitations of LiDAR technologies	79
3.5.4	Choosing a LiDAR type for distributed wind applications	80
3.6	Chapter summary and justification of the research in this thesis	80
<b>4</b>	<b>SCADA data analysis and electrical energy rose development</b>	<b>85</b>
4.1	Objectives	85
4.2	Wind turbine description	86

4.2.1	Background to wind turbine installation . . . . .	86
4.2.2	Wind turbine technical overview . . . . .	88
4.2.3	Wind turbine SCADA system . . . . .	90
4.2.4	Gearbox replacement . . . . .	91
4.3	Site description . . . . .	93
4.4	Methods . . . . .	96
4.4.1	SCADA data quality assessment and wind turbine availability	96
4.4.2	Wind and power data analysis . . . . .	97
4.4.3	Electrical Energy Rose (EER) . . . . .	98
4.4.4	Gearbox aging and replacement comparison . . . . .	99
4.5	Results . . . . .	101
4.5.1	Data quality assessment . . . . .	101
4.5.2	Wind and power data analysis . . . . .	102
4.5.3	Inter-annual and seasonal energy analysis . . . . .	105
4.5.4	Seasonal and diurnal wind analysis . . . . .	108
4.5.5	Directional wind analysis . . . . .	110
4.5.6	Directional power curve and turbulence analysis . . . . .	114
4.5.7	EER and site feature analysis . . . . .	118
4.5.8	Impact of gearbox aging and replacement on wind turbine per- formance . . . . .	126
4.6	Discussion . . . . .	131
4.6.1	Obstacle impacts . . . . .	131
4.6.2	Gearbox replacement energy impact . . . . .	133
4.7	Conclusions and next steps . . . . .	133
5	<b>Assessment of mesoscale to microscale influences on wind turbine perfor- mance from the Irish wind atlas and onsite LiDAR wind measurements</b>	<b>135</b>
5.1	Objectives . . . . .	135
5.2	Overview of the remodelled Irish Wind Atlas . . . . .	137
5.3	Continuous Wave (CW) ZX (ZephIR) LiDAR . . . . .	141
5.3.1	Process of determining wind velocity . . . . .	142
5.3.2	Error handling in LiDAR system . . . . .	147
5.4	Methods . . . . .	148

5.4.1	Mesoscale assessment . . . . .	148
5.4.2	Microscale assessment method . . . . .	150
5.4.3	LiDAR data measurement . . . . .	152
5.5	Results . . . . .	154
5.5.1	Mesoscale . . . . .	154
5.5.2	Microscale . . . . .	157
5.5.3	Wind Atlas and SCADA directional wind and energy compar- isons . . . . .	159
5.5.4	Predicted AEP comparison of WT site with other local locations	165
5.5.5	Preliminary onsite LiDAR directional wind shear profiles . . .	166
5.5.6	Nacelle anemometer and LiDAR measured wind speeds . . . .	168
5.6	Discussion . . . . .	170
5.7	Conclusions and next steps . . . . .	171
<b>6</b>	<b>A comparison of four microscale wind flow models, coupled with onsite LiDAR wind measurements, in predicting the wind turbine EER</b>	<b>175</b>
6.1	Objectives . . . . .	175
6.2	Methods . . . . .	176
6.2.1	Site overview and measurement setup . . . . .	176
6.2.2	Linear flow model approaches . . . . .	180
6.2.3	WAsP-IBZ setup . . . . .	186
6.2.4	CFD flow model approaches . . . . .	190
6.2.5	WAsP CFD setup . . . . .	192
6.2.6	WindSim model setup . . . . .	193
6.2.7	Wind assessment and EER . . . . .	200
6.3	Results . . . . .	201
6.3.1	Wind turbine measured energy and model predictions . . . . .	205
6.3.2	Wind shear profiles . . . . .	216
6.4	Discussion . . . . .	224
6.5	Conclusions and next steps . . . . .	225
<b>7</b>	<b>Measured wind and morphological characteristics of the peri-urban envi- ronment and their impact on wind turbine performance</b>	<b>227</b>
7.1	Objectives . . . . .	227



7.2	Methods . . . . .	229
7.2.1	Measurement setup . . . . .	229
7.2.2	Morphological assessment of obstacle characteristics . . . . .	232
7.2.3	Energy assessment . . . . .	235
7.2.4	Turbulence and gust factors . . . . .	236
7.2.5	Wind shear and REWS . . . . .	238
7.2.6	Atmospheric Stability . . . . .	240
7.3	Results . . . . .	242
7.3.1	Obstacle morphological characteristics . . . . .	242
7.3.2	Energy comparison between mast and wind turbine locations . . . . .	254
7.3.3	Turbulence intensity and gust factor comparison between mast and wind turbine locations . . . . .	267
7.3.4	Wind shear across the rotor and REWS . . . . .	273
7.3.5	Atmospheric Stability . . . . .	278
7.4	Discussion . . . . .	282
7.5	Conclusions and next steps . . . . .	284
8	<b>Discussion and development of a site pre-screening framework for dis- tributed wind in peri-urban environments</b>	<b>287</b>
8.1	General discussion of findings . . . . .	287
8.2	A peri-urban site pre-screening framework . . . . .	297
8.3	Wind turbine design standard considerations . . . . .	300
8.4	Peri-urban wind measurement implementation experiences . . . . .	300
9	<b>Summary conclusions and future research needs</b>	<b>303</b>
	<b>Bibliography</b>	<b>307</b>
A	<b>Supplementary wind resource and modelling information</b>	<b>333</b>
A.1	Overview of the atmosphere . . . . .	333
A.1.1	Global circulation . . . . .	333
A.1.2	Vertical profile of the ABL . . . . .	338
A.1.3	Thermal stability in the ABL . . . . .	343
A.2	Modelling the atmosphere for wind energy . . . . .	346
A.2.1	Global circulation models . . . . .	347

A.2.2	Mesoscale models . . . . .	349
A.2.3	Thermal influences . . . . .	356
A.2.4	Microscale models . . . . .	358
A.2.5	Linear flow model approaches . . . . .	359
A.2.6	Orography . . . . .	360
A.2.7	Obstacles . . . . .	361
A.2.8	CFD flow approaches . . . . .	364
A.3	Some wind flow model comparison studies in the field . . . . .	367
A.4	Urban wind energy . . . . .	369
A.4.1	Urban vertical wind profiles . . . . .	369
A.4.2	Morphological approaches to determine surface roughness and displacement height . . . . .	376
<b>B</b>	<b>Nacelle anemometer and LiDAR comparisons</b>	<b>381</b>
B.1	Linear regressions between nacelle anemometer and LiDAR wind speeds . . . . .	381

## List of Figures

1.1	Layout of thesis . . . . .	6
3.1	Principal global wind circulation patterns . . . . .	36
3.2	Basic structure of the atmospheric boundary layer . . . . .	40
3.3	Surface roughness height, wind speed fluctuations and mean wind speed profile . . . . .	41
3.4	Schematic of sublayers within the UBL . . . . .	42
3.5	Schematic of sublayer wind speed profiles . . . . .	43
3.6	Schematic overviews of unstable and stable ABL . . . . .	45
3.7	Categories of modelling scales applicable to wind energy . . . . .	48
3.8	Downscaling from GCMs to RCMs . . . . .	49
3.9	General flow diagram in linear model assessment . . . . .	53
3.10	Flow around bluff obstacles . . . . .	55
3.11	Flow around multiple obstacles . . . . .	55
3.12	Percentage wind speed reduction in the wake of a two dimensional obstacle . . . . .	56
3.13	Time averaging of wind speed of a period $T$ . . . . .	58
3.14	Geometrical properties used in morphological definitions . . . . .	61
3.15	A representation of the relationship of $z_0$ and $d$ to the plan and frontal area density ratios . . . . .	63
3.16	Temporal wind speed representation over a period $T$ . . . . .	65
3.17	Rotor segments and wind measurement heights used to calculate rotor equivalent wind speed . . . . .	71
3.18	Basic principal of Doppler LiDAR operation . . . . .	73
3.19	CW LiDAR circular scanning patterns at different heights . . . . .	74
3.20	Example of beam focusing at two different focal points or distances . . . . .	75
3.21	Doppler beam swinging (DBS) concept . . . . .	77
3.22	Pulsed LiDAR operation . . . . .	78

3.23 Soft single beam focus for measuring at multiple heights simultaneously in pulsed LiDARs . . . . .	79
4.1 Vestas V52 wind turbine at DkIT . . . . .	88
4.2 Technical overview of Vestas V52 wind turbine . . . . .	89
4.3 Turbine nacelle mounted 2-D ultrasonic anemometer . . . . .	90
4.4 Wind turbine SCADA ground controller and user interface . . . . .	91
4.5 Wind turbine gearbox . . . . .	92
4.6 Wind turbine site at DkIT . . . . .	93
4.7 Topographic features up to 40 km from site . . . . .	94
4.8 Local obstacle features up to 1.5 km from site . . . . .	95
4.9 5-year wind speed distribution and power curve . . . . .	103
4.10 5-year wind turbulence intensity and coefficient of performance . . . .	105
4.11 8-year Inter-annual and seasonal energy performance . . . . .	107
4.12 5-year hub-height mean monthly and mean hourly wind speeds . . . .	109
4.13 5-year cumulative hourly energy output . . . . .	110
4.14 5-year wind roses . . . . .	111
4.15 72-sector seasonal wind roses . . . . .	112
4.16 72-sector directional wind power density . . . . .	114
4.17 Site and manufacture's power curve . . . . .	115
4.18 Directional power and turbulence intensity curves . . . . .	117
4.19 Wind turbine <i>EER</i> in 5° sectors . . . . .	118
4.20 Wind turbine <i>EER</i> overlaid at wind turbine location on local site plan .	119
4.21 Wind turbine hub height view looking 170° to 210° . . . . .	120
4.22 Wind turbine hub height view looking 150° to 170° . . . . .	121
4.23 Wind turbine hub height view looking 130° to 150° . . . . .	121
4.24 Wind turbine hub height view looking 95° to 130° . . . . .	122
4.25 Wind turbine hub height view looking 30° to 90° . . . . .	123
4.26 Wind turbine electrical energy rose overlaid on regional site plan . . .	124
4.27 Wind turbine hub height view looking 330° to 30° . . . . .	124
4.28 Wind turbine hub height view looking 220° to 290° . . . . .	125
4.29 Power curves — 2008, 2014, 2017–2018 and 2019 . . . . .	126
4.30 Relative bin-wise % differences in power curves . . . . .	127

4.31 Annual wind speed distributions for 2008, 2014 and 12 months in 2017-18 . . . . .	129
4.32 <i>AEP</i> variations compared to 2008 reference year . . . . .	131
5.1 ZX (ZephIR) LiDAR onsite . . . . .	141
5.2 An example of sensitivity focus distance of 20 m and 50 m . . . . .	142
5.3 Illustration of scanning beam . . . . .	143
5.4 Overview schematic of processing of back-scattered detected signal . .	144
5.5 Illustration of scanning beam . . . . .	146
5.6 Selected regional (top) and local (bottom) locations for wind atlas analysis . . . . .	149
5.7 Wind roses at 150 m a.g.l. for selected regional locations and at wind turbine site . . . . .	154
5.8 <i>WPD</i> comparison at 150 m a.g.l. between the four sites . . . . .	155
5.9 Wind roses at 60 m a.g.l. for selected local locations and at wind turbine site . . . . .	157
5.10 <i>WPD</i> at 60 m a.g.l. for selected local locations and at wind turbine site	158
5.11 Directional wind distributions predicted by the wind atlas and measured by the wind turbine SCADA system . . . . .	159
5.12 Wind turbine power curve . . . . .	162
5.13 Overlaid plots of the predicted wind turbine <i>AEP</i> and the measured <i>EER</i> on plan view . . . . .	163
5.14 Views from wind turbine nacelle at hub height showing some of the local obstacles . . . . .	164
5.15 Directional wind shear profiles from LiDAR measurements at wind turbine site . . . . .	166
5.16 Nacelle anemometer vs LiDAR measured wind speeds at hub-height .	169
6.1 LiDAR and met mast locations . . . . .	177
6.2 Measuring instruments . . . . .	178
6.3 Linear flow models . . . . .	183
6.4 Digital elevation map regional map and local area digitized surface roughness map . . . . .	188
6.5 Defining buildings as obstacles in WAsP . . . . .	189

6.6	Defining buildings as roughness elements in WAsP . . . . .	189
6.7	Local WAsP CFD tile setup on digital elevation map . . . . .	193
6.8	Overview of the WindSim tool modular approach to wind turbine micrositing . . . . .	194
6.9	WindSim digital elevation and surface roughness maps . . . . .	196
6.10	WindSim CFD grid set-up for buildings as roughness elements . . . .	197
6.11	Buildings as mesh blocking elements in WindSim . . . . .	199
6.12	WindSim CFD grid set-up for buildings as mesh blocking elements . .	199
6.13	Annual wind roses at multiple levels from LiDAR measurements . . .	202
6.14	Annual <i>WPD</i> at multiple levels from LiDAR measurements . . . . .	203
6.15	Log law fit to met mast measurements . . . . .	205
6.16	<i>EER</i> and directional energy distribution with wind speed . . . . .	207
6.17	Comparisons of model predicted <i>EERs</i> from multiple heights with the measured wind turbine <i>EER</i> (Downscaling) . . . . .	211
6.18	Comparisons of model predicted <i>EERs</i> from multiple heights with the measured wind turbine <i>EER</i> (Upscaling) . . . . .	212
6.19	Fitted log law profiles to LiDAR measured wind shear profiles 1 . . . .	218
6.20	Fitted log law profiles to LiDAR measured wind shear profiles 2 . . . .	219
6.21	Fitted log law profiles to LiDAR measured wind shear profiles 3 . . . .	220
6.22	Fitted log law profiles to LiDAR measured wind shear profiles 4 . . . .	221
6.23	Directional <i>WPD</i> profiles . . . . .	223
7.1	LiDAR and met mast locations . . . . .	229
7.2	Met mast installation setup . . . . .	231
7.3	16 sector divisions in 500 m segments in a 2 km radius as viewed from met mast and wind turbine locations . . . . .	233
7.4	Rotor segments and wind measurement heights used to calculate rotor equivalent wind speed . . . . .	239
7.5	Obstacle area-weighted heights viewed from met mast and wind turbine locations . . . . .	243
7.6	Obstacle maximum heights viewed from met mast and wind turbine locations . . . . .	244
7.7	Obstacle plan area fractions viewed from met mast and wind turbine locations . . . . .	246

7.8	Obstacle frontal area densities viewed from met mast and wind turbine locations . . . . .	247
7.9	7-year <i>EER</i> and selected directional power curve . . . . .	249
7.10	7-year directional power curve standard deviation and turbulence intensity . . . . .	250
7.11	Directional <i>WPD</i> at six heights . . . . .	254
7.12	7-month wind roses at met mast and wind turbine locations . . . . .	256
7.13	Mean hourly differences in wind speed and direction from south to north between the wind turbine and met mast . . . . .	258
7.14	7-month <i>EER</i> and directional energy comparisons between the met mast and wind turbine locations . . . . .	259
7.15	7-month <i>EER</i> and directional energy comparisons between the met mast and wind turbine locations for a bin centre clockwise rotation of $7.5^\circ$ . . . . .	262
7.16	7-month <i>EER</i> and directional energy comparisons between the met mast and wind turbine locations for a bin centre clockwise rotation of $15^\circ$ . . . . .	264
7.17	7-month <i>EER</i> and directional energy comparisons between the met mast and wind turbine locations for a bin centre clockwise rotation of $22.5^\circ$ . . . . .	266
7.18	Directional turbulence intensity at met mast and wind turbine locations . . . . .	268
7.19	Directional gust factors at met mast and wind turbine locations . . . . .	269
7.20	$90^{th}$ percentile turbulence intensity at various heights and suggested modification to IEC NTMs . . . . .	271
7.21	Directional vertical turbulence intensity at 60 m and omnidirectional $90^{th}$ percentile gust factors . . . . .	272
7.22	Fitted power law profiles to LiDAR measured directional wind profiles across the rotor disc ( $90^\circ$ , $157.5^\circ$ ) . . . . .	273
7.23	Fitted power law profiles to LiDAR measured directional wind profiles across the rotor disc ( $180^\circ$ , $202.5^\circ$ ) . . . . .	274
7.24	Fitted power law profiles to LiDAR measured directional wind profiles across the rotor disc ( $225^\circ$ , $247.5^\circ$ ) . . . . .	275

7.25 Fitted power law profiles to LiDAR measured directional wind profiles across the rotor disc ( $270^\circ$ , $315^\circ$ ) . . . . .	276
7.26 Directional wind shear exponent across the rotor and REWS comparison with shear and turbulence . . . . .	278
7.27 Richardson No. distribution characteristics (overall) and day time hours . . . . .	279
7.28 Richardson No. distribution characteristics night time and mean directional characteristics (overall) . . . . .	280
8.1 Outline flow diagram to site pre-screening . . . . .	297
A.1 Principal global wind circulation patterns . . . . .	333
A.2 Basic structure of the atmospheric boundary layer . . . . .	338
A.3 Surface roughness height, wind speed fluctuations and mean wind speed profile . . . . .	339
A.4 Turbulence scale length and friction velocity . . . . .	342
A.5 Schematic overviews of unstable and stable ABL . . . . .	344
A.6 Categories of modelling scales applicable to wind energy . . . . .	347
A.7 Downscaling from GCMs to RCMs . . . . .	348
A.8 Schematic of flow over the crest of a hill . . . . .	352
A.9 A simplified schematic of flow over a hill approximated by a wave number . . . . .	355
A.10 Schematic of mountain/valley flow . . . . .	357
A.11 Schematic sea breeze formation . . . . .	358
A.12 General flow diagram in linear model assessment . . . . .	359
A.13 Flow around bluff obstacles . . . . .	362
A.14 Flow around multiple obstacles . . . . .	362
A.15 Percentage wind speed reduction in the wake of a two dimensional obstacle . . . . .	363
A.16 Time averaging of wind speed of a period $T$ . . . . .	365
A.17 Simple schematic of IBL growth following a change in surface roughness	369
A.18 Basic schematic of UBL . . . . .	371
A.19 Schematic of sublayers within the UBL . . . . .	372
A.20 Schematic of sublayer wind speed profiles . . . . .	373



A.21 Schematic of vertical wind profiles over multiple roughness patches . . . . .	375
A.22 Geometrical properties used in morphological definitions . . . . .	377
A.23 A representation of the relationship of $z_0$ and $d$ to the plan and frontal area density ratios . . . . .	379
B.1 Directional linear regressions between nacelle anemometer and LiDAR wind speeds in north to southeast sectors . . . . .	381
B.2 Directional linear regressions between nacelle anemometer and LiDAR wind speeds in south to northwest sectors . . . . .	382



## List of Tables

1.1	IEC Wind turbine size classifications . . . . .	1
4.1	Regional site features . . . . .	94
4.2	Local site features . . . . .	95
4.3	Annual wind turbine availability and 10-minute data availability . . .	101
4.4	Yearly operational time fractions . . . . .	102
4.5	8-year mean monthly energy output values . . . . .	108
4.6	Power curve bin differences and K-S statistic tests, $\alpha = 0.05$ . . . . .	128
4.7	Wind resource parameters . . . . .	129
4.8	Energy parameters . . . . .	130
5.1	Orography complexity classification used in Irish Wind Atlas . . . . .	139
5.2	Site locations for wind atlas mesoscale and microscale analysis . . . . .	150
5.3	Directional wind speed distribution parameter values . . . . .	160
5.4	Difference in wind atlas predicted & measured . . . . .	161
5.5	Predicted and measured energy values . . . . .	162
5.6	<i>AEP</i> comparison at other local locations . . . . .	165
5.7	Linear regression between nacelle anemometer and LiDAR wind speeds . . . . .	169
6.1	Data acquisition details . . . . .	179
6.2	Surface roughness values for various terrain types . . . . .	184
6.3	WAsP-CFD Grid Setup – Obstacles as roughness elements . . . . .	193
6.4	WindSim Grid Setup – Obstacles as roughness elements . . . . .	198
6.5	WindSim Grid Setup – Obstacles as mesh blocking elements . . . . .	200
6.6	Directional <i>WPD</i> and (%) values w.r.t.to 200 m . . . . .	204
6.7	Annual mean wind speed predictions and (%) differences to the measured hub height annual mean wind speed . . . . .	206
6.8	<i>AEP</i> predictions and (%) differences compared with wind turbine <i>EER</i> . . . . .	208

6.9	Four worst case directional % discrepancies in predicted <i>EERs</i> at 60 m from each downscaling height . . . . .	214
6.10	Four worst case directional % discrepancies in predicted <i>EERs</i> at 60 m from each upscaling height . . . . .	215
7.1	Stability classes, (Newman and Klein, 2014) . . . . .	241
7.2	Sectoral description of energy, turbulence and morphological parameters (easterly to southerly sectors) . . . . .	251
7.3	Sectoral description of energy, turbulence and morphological parameters (westerly to northerly sectors) . . . . .	252
7.4	Met mast and SCADA data and K-S statistic tests, $\alpha = 0.05$ . . . . .	257
7.5	7-month directional energy comparison . . . . .	260
7.6	7-month directional energy comparison . . . . .	263
7.7	7-month directional energy comparison . . . . .	265
7.8	7-month directional energy comparison . . . . .	267
7.9	Stability class distributions . . . . .	281

## List of Abbreviations

<b>ABL</b>	<b>A</b> tomsphe <b>r</b> ic <b>B</b> oundary <b>L</b> ayer
<b>AEP</b>	<b>A</b> nnual <b>E</b> nergy <b>P</b> rediction
<b>ARPS</b>	<b>A</b> dvanced <b>R</b> egional <b>P</b> rediction <b>S</b> ystem
<b>AC</b>	<b>A</b> lternating <b>C</b> urrent
<b>a.s.l.</b>	<b>a</b> bove <b>s</b> ea <b>l</b> evel
<b>a.g.l.</b>	<b>a</b> bove <b>g</b> round <b>l</b> evel
<b>ADC</b>	<b>A</b> nalog to <b>D</b> igital <b>C</b> onverter
<b>BARRA</b>	<b>B</b> ureau of <b>M</b> eteorology <b>A</b> tomsphe <b>r</b> ic high-resolution <b>R</b> egional <b>R</b> eanalysis for <b>A</b> ustralia
<b>CERRA</b>	<b>C</b> opernicus <b>E</b> uropean <b>R</b> egional <b>R</b> e <b>A</b> nalysis
<b>CFD</b>	<b>C</b> omputational <b>F</b> luid <b>D</b> ynamics
<b>CL</b>	<b>C</b> anopy <b>L</b> ayer
<b>COAMPS</b>	<b>C</b> oupled <b>O</b> cean <b>A</b> tmosphe <b>r</b> e <b>M</b> esoscale <b>P</b> rediction <b>S</b> ystem
<b>COSMO</b>	<b>C</b> onsortium for <b>S</b> mall-scale <b>M</b> odeling
<b>CW</b>	<b>C</b> ontinuous <b>W</b> ave
<b>CREDIT</b>	<b>C</b> entre for <b>R</b> enewables & <b>E</b> nergy at <b>D</b> k <b>I</b> T
<b>DWEA</b>	<b>D</b> istributed <b>W</b> ind <b>E</b> nergy <b>A</b> ssociation (USA)
<b>DCCAE</b>	<b>D</b> epartment of <b>C</b> ommunications, <b>C</b> limate <b>A</b> ction & <b>E</b> nvironment (Ireland)
<b>DSM</b>	<b>D</b> emand <b>S</b> ide <b>M</b> anagement
<b>DOE</b>	<b>D</b> epartment of <b>E</b> nergy (USA)
<b>DWRA</b>	<b>D</b> istributed <b>W</b> ind <b>R</b> esource <b>A</b> ssessment
<b>DES</b>	<b>D</b> etached <b>E</b> ddy <b>S</b> imulation
<b>DTM</b>	<b>D</b> igital <b>T</b> errain <b>M</b> ap
<b>DBS</b>	<b>D</b> oppler <b>B</b> eam <b>S</b> winging
<b>DkIT</b>	<b>D</b> undalk <b>I</b> nstitute of <b>T</b> echnology
<b>DFIG</b>	<b>D</b> oubly-Fed <b>I</b> nduction <b>G</b> enerator
<b>DTED</b>	<b>D</b> igital <b>T</b> errain <b>E</b> levation <b>D</b> ataset

<b>DFT</b>	<b>D</b> igital <b>F</b> ourier <b>T</b> ransform
<b>DEM</b>	<b>D</b> igital <b>E</b> levation <b>M</b> ap
<b>EER</b>	<b>E</b> lectrical <b>E</b> nergy <b>R</b> ose
<b>ESMAP</b>	<b>E</b> nergy <b>S</b> ector <b>M</b> anagement <b>A</b> ssistance <b>P</b> rogram
<b>EAWA</b>	<b>E</b> uropean <b>A</b> ssociation of <b>W</b> ind <b>A</b> cademics
<b>ECMWF</b>	<b>E</b> uropean <b>C</b> entre for <b>M</b> edium- <b>R</b> ange <b>W</b> eather <b>F</b> orecasts
<b>EROS</b>	<b>E</b> arth <b>R</b> esources <b>O</b> bservation and <b>S</b> cience <b>C</b> enter
<b>EGM</b>	<b>E</b> arth <b>G</b> ravitational <b>M</b> odel
<b>FiT</b>	<b>F</b> eed- <b>i</b> n- <b>T</b> ariffs
<b>GCM</b>	<b>G</b> lobal <b>C</b> limate <b>M</b> odel
<b>GPA</b>	<b>G</b> roup <b>P</b> rocessing <b>A</b> pproach
<b>GPS</b>	<b>G</b> lobal <b>P</b> ositioning <b>S</b> ystem
<b>GCV</b>	<b>G</b> eneral <b>C</b> ollocated <b>V</b> elocity
<b>HRRR</b>	<b>H</b> igh <b>R</b> esolution <b>R</b> apid <b>R</b> efresh
<b>IRENA</b>	<b>I</b> nternational <b>R</b> enewable <b>E</b> nergy <b>A</b> ssociation
<b>I-SEM</b>	<b>I</b> ntegrated <b>S</b> ingle <b>E</b> lectricity <b>M</b> arket
<b>IEA</b>	<b>I</b> nternational <b>E</b> nergy <b>A</b> gency
<b>IEC</b>	<b>I</b> nternational <b>E</b> lectrotechnical <b>C</b> ommission
<b>ISL</b>	<b>I</b> nertial <b>S</b> ublayer
<b>JMA</b>	<b>J</b> apan <b>M</b> eteorological <b>A</b> gency
<b>LCOE</b>	<b>L</b> evelised <b>C</b> ost of <b>E</b> nergy
<b>LES</b>	<b>L</b> arge <b>E</b> ddy <b>S</b> imulation
<b>LiDAR</b>	<b>L</b> ight <b>D</b> etection <b>A</b> nd <b>R</b> anging
<b>LAM</b>	<b>L</b> imited <b>A</b> rea <b>M</b> odels
<b>LID</b>	<b>L</b> i <b>D</b> AR measurement location
<b>MCS</b>	<b>M</b> icrogeneration <b>C</b> ertificaton <b>S</b> cheme (UK)
<b>MC2</b>	<b>M</b> esoscale <b>C</b> ompressible <b>C</b> ommunity <b>M</b> odel
<b>MC</b>	<b>M</b> ass <b>C</b> onsistent
<b>M</b>	<b>M</b> et mast location
<b>NREL</b>	<b>N</b> ational <b>R</b> enewable <b>E</b> nergy <b>L</b> aboratory (USA)
<b>NYSERDA</b>	<b>N</b> ew <b>Y</b> ork <b>S</b> tate <b>E</b> nergy <b>R</b> esearch and <b>D</b> evelopment <b>A</b> uthority
<b>NWP</b>	<b>N</b> umerical <b>W</b> eather <b>P</b> rediction
<b>NTM</b>	<b>N</b> ormal <b>T</b> urbulence <b>M</b> odel

<b>NASA</b>	<b>National Aeronautics and Space Administration (USA)</b>
<b>NCEP</b>	<b>National Centres for Environmental Prediction</b>
<b>NOAA</b>	<b>National Oceanic and Atmospheric Administration</b>
<b>NARR</b>	<b>North American Regional Reanalysis</b>
<b>NIMA</b>	<b>National Imagery and Mapping Agency</b>
<b>NIST</b>	<b>National Institute for Standards and Technology</b>
<b>NTF</b>	<b>Nacelle Transfer Function</b>
<b>OEM</b>	<b>Original Equipment Manufacturer</b>
<b>PBL</b>	<b>Planetary Boundary Layer</b>
<b>QUICK</b>	<b>Quadratic Upstream Interpolation for Convective Kinematics</b>
<b>ROC</b>	<b>Renewable Energy Obligation Certificate</b>
<b>REAP</b>	<b>Rural Energy for America Program</b>
<b>RANS</b>	<b>Reynolds Averaged Navier Stoke's</b>
<b>RIX</b>	<b>Roughness Index</b>
<b>RSL</b>	<b>Roughness Sublayer</b>
<b>RCM</b>	<b>Regional Climate Models</b>
<b>RAMS</b>	<b>Atmospheric Modelling System</b>
<b>REWS</b>	<b>Rotor Equivalent Wind Speed</b>
<b>RIN</b>	<b>Relative Intensity Noise</b>
<b>RPM</b>	<b>Revolutions Per Minute</b>
<b>SCADA</b>	<b>Supervisory Control And Data Acquisition</b>
<b>SEUPB</b>	<b>Special EU Programmes Body</b>
<b>SEAI</b>	<b>Sustainable Energy Authority of Ireland</b>
<b>SRTM</b>	<b>Shuttle Radar Topography Mission</b>
<b>TAP</b>	<b>Technology Assistance Programmes (USA)</b>
<b>TKE</b>	<b>Turbulent Kinetic Energy</b>
<b>TL</b>	<b>Transition Layer</b>
<b>UBL</b>	<b>Urban Boundary Layer</b>
<b>UM</b>	<b>Unified Model</b>
<b>UTM</b>	<b>Universal Transverse Mercator</b>
<b>VAD</b>	<b>Velocity Azimuth-Display</b>
<b>VMP</b>	<b>Vestas Multi Processor</b>
<b>VMM</b>	<b>Virtual Met Mast</b>

<b>WAsP</b>	<b>Wind Atlas Application Program</b>
<b>WEI</b>	<b>Wind Energy Ireland</b>
<b>WIND</b>	<b>Wind Integration National Database (USA Toolkit)</b>
<b>WRF</b>	<b>Weather Research Forecast</b>
<b>WT</b>	<b>Wind Turbine location</b>
<b>WGS84</b>	<b>World Geodetic System 1984</b>
<b>WTR</b>	<b>Wind Turbine Rotor</b>
<b>WPD</b>	<b>Wind Power Density</b>
<b>WWPTO</b>	<b>Wind and Water Power Technologies Office</b>



## List of Symbols

(Regularly used symbols listed, others also defined within thesis)

$\vec{v}$	three dimensional wind velocity vector	m/s
$U(T)$	average horizontal wind speed in given time averaging period T	m/s
$T$	wind speed averaging time	s
$u'(t, T)$	longitudinal fluctuation in wind speed	m/s
$w'(t, T)$	vertical fluctuation in wind speed	m/s
$U_i$	normalized and averaged wind speed in bin $i$	m/s
$U_{REWS}$	rotor equivalent wind speed	m/s
$p(U)$	probability density function	
$c$	wind speed distribution scale factor	m/s
$k$	wind speed distribution shape factor	-
$\rho$	air density	kg/m <sup>3</sup>
$g$	acceleration due to gravity	m/s <sup>2</sup>
$z$	height of interest (e.g., wind turbine hub height)	m
$z_0$	surface roughness	m
$z_d$	zero-plane displacement height	m
$z_n$	wind measurements at height level number n	m
$T_n$	temperature measurement at height level number n	°C
$R$	rotor diameter	m
$P_i$	normalized and averaged power output in bin $i$	kW
$\delta_{i,j}$	Kronecker Delta function	-
$\nu_T$	kinematic eddy viscosity	m <sup>2</sup> /s
$u'_i u'_j$	Reynolds stresses	m <sup>2</sup> /s <sup>2</sup>
$I_U(t, T)$	horizontal turbulence intensity	-
$I_W(t, T)$	vertical turbulence intensity	-
$G_U(t, T)$	gust factor	-
$R_i$	Richardson number	-

$A_P$	total plan area of the buildings and obstacles	$\text{m}^2$
$A_T$	total plan area of region of interest	$\text{m}^2$
$A_f$	building frontal area	$\text{m}^2$
$A_p$	building plan area $\text{m}^2$	
$A_T$	total spatial area occupied by the buildings	$\text{m}^2$
$\lambda_P$	obstacle plan area fraction	-
$\lambda_f$	obstacle frontal area fraction	-
$h_{AW}$	plan area weighted building height	m
$h_{max}$	maximum building height	m
$h_m$	mean building height	m

# Chapter 1

## Introduction

### 1.1 General Introduction

The wind industry has grown rapidly in recent decades, consisting of large wind farm scale onshore and offshore industries that are primarily investor driven. Wind turbine sizes are currently classified by the International Electrotechnical Commission (IEC) based on rotor swept area that have associated approximate power ratings, Table 1.1.

**Table. 1.1.** IEC Wind turbine size classifications

<b>Classification</b>	<b>Rotor swept area (m<sup>2</sup>)</b>	<b>Power Rating (kW)</b>
Small-scale	$\leq 200$	$\sim 50$
Large-scale	$> 200$	$> 50$

With the ever increasing sizes in large-scale wind turbines in recent years to multi-MW power output ratings, a new classification of medium-scale wind turbine size between the small and large scales is being proposed by the Wind Technical Collaboration Programme (TCP) of International Energy Agency (IEA) in anticipation of the growth of distributed wind energy markets. This has yet to be finalised at the time of writing. Therefore, for the purposes of this research, in an Irish context, wind turbines with output power ratings from 50 kW to 500 kW are referred to as medium-scale wind turbines, based on the grid connection capacity categories for autoproducers (i.e. Category B (Non-Batch)<sup>1</sup>).

<sup>1</sup>ESBN, Ruleset for Enduring Connection Policy Stage 2 (ECP-2), August 2020

Distributed wind energy is broadly accepted to include single or a small number of small (0-50 kW), medium (50-500 kW) or large scale (> 500 kW) wind turbines with power ratings of up to  $\sim 2$  MW, deployed in individual or community owned projects as well as in behind the meter and off-grid applications. As wind energy continues to expand globally, new markets for distributed wind energy applications of interest to end-users/owners are anticipated. However, this sector of the wind energy market has had mixed success to date, primarily due to intermittent government incentives, technological challenges and competition with solar photovoltaic (PV) systems. With evolving new energy policies across the world such as the EU's Clean Energy Package, legal frameworks are being formed to enable consumers and communities to participate in energy generation as prosumers. These may accelerate new market opportunities in distributed wind. This is recognised by International Energy Agency through the formation of an collaborative wind energy Task, namely IEA Wind Task 41, which commenced in 2018 and aims to continue to 2022 and beyond. IEA Wind Task 41 focuses on enabling wind to contribute to a distributed energy future, particularly as electricity systems and grids evolve from centralised to distributed and the development of micro-grids in remote communities. Much of the research in the distributed wind space over the last two decades has been aimed at small scale wind systems with power ratings of less than 50 kW. This led to the development of a separate small scale wind turbine design standard by the International Electrotechnical Commission (IEC) that was adopted in the USA, UK, Denmark and Japan. Past government incentive programmes in small scale wind for consumers, such as the micro-generation scheme (MCS) in the UK were linked to compliance to parts or all of this standard. However, small scale wind systems still face a number of challenges, regarding performance, technological reliability and high capital costs, resulting in a continued sluggish market expansion. It is well known that the wind environment has a major influence on the viability of any wind energy project in terms energy output and turbine wear. As well as wind speed and direction; turbulence, shear, veer, inflow angle and atmospheric stability can have significant impacts on a wind turbine's performance. These factors are influenced by local microscale effects, such as obstacles and general surface roughness, and regional mesoscale features of the terrain. Accurate prediction of pre-construction

yield with the real-world post-construction yield of a wind project, at all scales, remains a challenge and an ongoing area of research. For investor driven wind farm developments, this can involve detailed wind flow modelling combined with comprehensive with measurement campaigns, both of which can be costly but justified and even necessary. In the small scale wind industry, detailed modelling and measurement campaigns are generally too cost prohibitive or are applied at various simplified levels of detail, which contribute to large discrepancies between energy predictions and the actual real-world performance of small scale wind turbines.

Another market opportunity within the distributed wind space is the deployment of more technological mature medium to large scale wind turbines in behind-the-meter applications (i.e., wind autoproduction), such as at large energy consuming industrial facilities. Specifically, facilities located at the edge towns near the rural to urban transition with low-rise industrial buildings i.e., semi or peri-urban areas, where the hub height of a medium to large scale turbine could be well above the heights of the buildings. Unlike typical onshore wind farm sites, the application of commercial scale behind-the meter wind tend to be single turbines at lower elevations in rural areas and in peri-urban areas (e.g., industrial estates) with a higher likelihood of being in vicinity of buildings. Obstacles, such as buildings, have not been a dominant feature of wind farms to date and therefore, limited research has been carried out on their impacts of energy performance in the context of wind farms. In the area of urban wind energy, much research has been carried out in the deployment of small scale wind turbines, particularly roof mounted systems, but these systems have had very little commercial success to date, primarily due to the very complex wind flow regimes around rooftops. In addition to building obstacles, parts of the regional terrain within 10s of km of a peri-urban location may be at higher elevations. These factors can result in complex wind flows with lower average annual wind speeds, unique wind speed distributions, high turbulence, high wind shear and highly directional wind flows at peri-urban sites. To date, there are few research publications in wind resource assessment, wind turbine micro-siting and real-world energy performance in peri-urban environments, specifically for the cases of medium to large scale wind turbines. This may be partially attributed to the lack of recorded long term, high-resolution time-series performance data for such projects being available in the public domain. Therefore, knowledge gaps exists for

these type of end-user/owner wind projects that fall in between the large scale and small scale wind industries in peri-urban wind environments where building obstacles are a significant feature. Such projects can involve high initial capital cost but may be limited in scale and budget for extensive onsite measurement and modelling campaigns that can be afforded to the large scale wind industry. At the same time, some degree of modelling and measurement is recommended to reduce risk in estimating expected energy predictions due to the complex wind regimes that may exist in peri-urban areas. There is also a question of how well current wind turbine design standards account for the turbulence in such environments with respect to mechanical fatigue loads and wear. The deployment of tall met masts at industrial peri-urban sites may be limited by ground spatial requirements and other onsite activities, leading to met mast installations with heights below the desired wind turbine hub height. In some cases, the installation of a met mast may be prevented altogether. This adds to the challenges in pre-construction energy prediction of actual post-construction energy performance. Recent advancements and the ease of deployment of light detection and ranging (LiDAR) technologies now give the opportunity to measure winds at multiple heights at such locations in the absence of met masts. Multiple height wind measurements could better inform wind flow models in energy predictions and assess wind shear and turbulence, leading to improvements in micro-siting medium and large scale wind turbines in peri-urban environments as well as informing industry wind turbine design standard revisions.

## **1.2 Outline of this PhD**

This PhD, “A heuristic evaluation of the energy performance of a Vestas V52 wind turbine in a peri-urban wind environment”, examines the impacts of building obstacle features on the wind resource and the subsequent impact on energy performance of an operating large scale Vestas V52 wind turbine in such an environment, through measurement and modelling. The research is informed by real-world turbine performance data, multilevel onsite LiDAR wind measurements and measurements from a local offsite met mast. Therefore, the research is "applied" in principal and outlined as follows:

- High resolution multi-annual time series data from the wind turbine supervisory control and data acquisition (SCADA) system is used to develop an novel electrical energy rose (EER) to assess the real-world directional energy performance with respect to the local peri-urban environment.
- A mesoscale analysis of the region is carried out with the remodelled Irish wind atlas to segregate the mesoscale influences of the region from the local microscale influences of the buildings in the vicinity of the wind turbine.
- High resolution time-series LiDAR wind data measurements, at multiple heights, onsite are used to drive four widely used microscale wind flow model approaches to assess their predictions with the EER of the wind turbine and to test model configurations and measurement heights that give the best results. LiDAR measured directional wind shear profiles are used to assess discrepancies in the model predictions with EER with respect of the local building obstacles.
- An alternative low cost approach, based on the morphological characteristics of the local environment, wind measurements from the onsite LiDAR and an offsite local rural met mast, is evaluated for the improvement of wind turbine micro-siting. In addition, measured wind turbulence and gust factors are assessed against current IEC wind turbine design standards for both large and small scale wind turbines. Suggested improvements to these standards are given for tower mounted wind turbines in peri-urban environments.
- Based on the overall findings, a framework is developed in peri-urban site pre-screening for deploying medium and large scale wind turbines in relation to, recommended measurement heights, flow model configurations and using a low-cost morphological approach to help with the siting of met masts and wind turbines.

### 1.2.1 Thesis Layout

A schematic layout of the thesis is outlined in Fig. 1.1. Based on the literature review and theoretical background chapters, four study chapters consider separate but interdependent factors of relevance for peri-urban wind turbine performance.

The learnings from the four study chapters are brought together to develop a framework for improving the deployment of medium and large scale wind turbines in peri-urban environments and suggestions for improving current prescribed IEC design standards with respect to turbulence and gust factors. The learnings are also used to further establish future research challenges and needs of distributed wind energy in peri-urban applications.

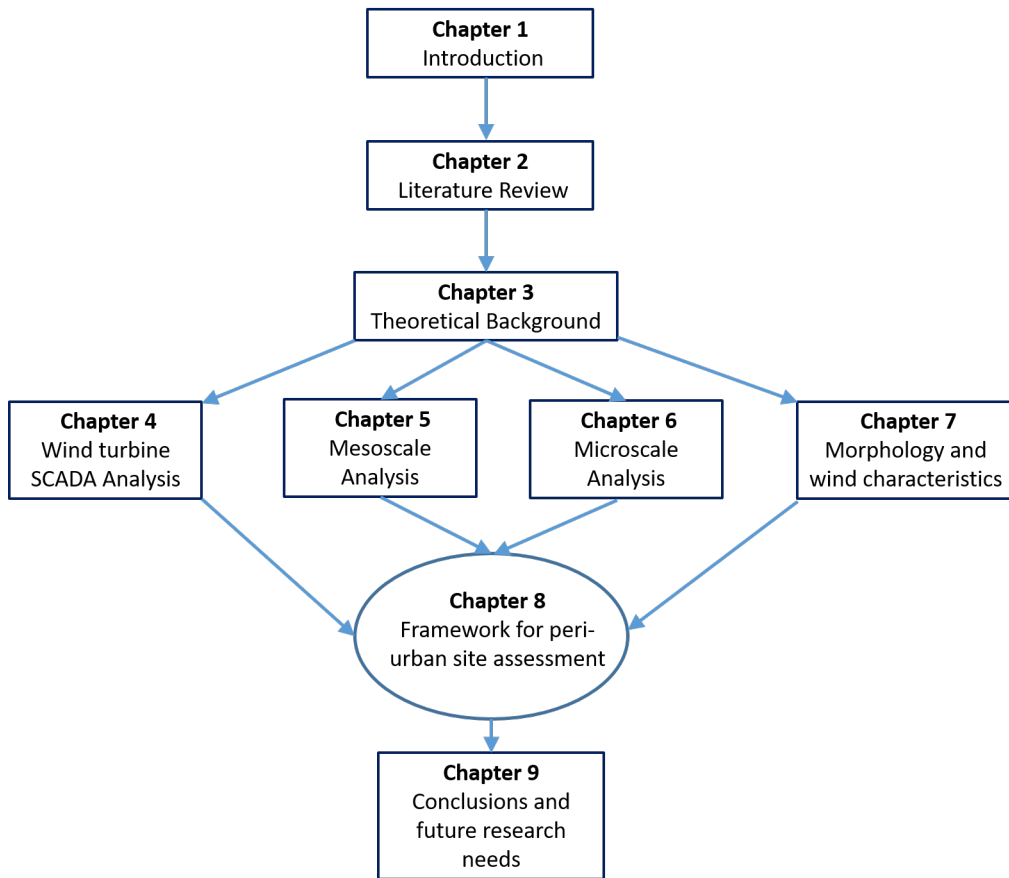


Fig. 1.1. Layout of thesis.

## 1.3 Principal contributions of this research

### 1.3.1 Peer reviewed Journal publications

1. Raymond Byrne, Neil J. Hewitt, Philip Griffiths, Paul MacArtain, *Observed site obstacle impacts on the energy performance of a large scale urban wind turbine using*



*an electrical energy rose*, Energy for Sustainable Development, Volume 43, 2018, Pages 23-37, ISSN 0973-0826, <https://doi.org/10.1016/j.esd.2017.12.002>

2. Raymond Byrne, Neil J. Hewitt, Philip Griffiths, Paul MacArtain, *An assessment of the mesoscale to microscale influences on wind turbine energy performance at a peri-urban coastal location from the Irish wind atlas and onsite LiDAR measurements*, Sustainable Energy Technologies and Assessments, Volume 36, 2019, 100537, ISSN 2213-1388, <https://doi.org/10.1016/j.seta.2019.100537>
3. Raymond Byrne, Neil J. Hewitt, Philip Griffiths, Paul MacArtain, *A comparison of four microscale wind flow models in predicting the real-world performance of a large-scale peri-urban wind turbine, using onsite LiDAR wind measurements*, Sustainable Energy Technologies and Assessments, Volume 46, 2021, 101323, ISSN 2213-1388, <https://doi.org/10.1016/j.seta.2021.101323>
4. Raymond Byrne, Neil J. Hewitt, Philip Griffiths, Paul MacArtain, *Measured wind and morphological characteristics of a peri-urban environment and their impact on the performance of an operational large-scale wind turbine*, Journal of Wind Engineering and Industrial Aerodynamics, Volume 212, 2021, 104592, ISSN 0167-6105, <https://doi.org/10.1016/j.jweia.2021.104592>

### 1.3.2 Conference proceedings

1. Raymond Byrne, Neil J. Hewitt, Philip Griffiths, Paul MacArtain, *A comparison of obstacle and surface roughness models in predicting the performance of an 850 kW wind autoproducer with onsite LiDAR measurements in a peri-urban area*, WESC 19: Cork, Ireland - June 17<sup>th</sup>-20<sup>th</sup> 2019
2. Raymond Byrne, *The energy performance of an 850 kW rated wind turbine in a peri-urban location in Ireland based on 10 years of operational data*, Wind Europe, Analysis of Operating Wind Farms 2016 (Poster)– Bilbao– 14<sup>th</sup>-15<sup>th</sup> April 2016

### 1.3.3 Other partial contributions of this research

IEA Wind Tasks 41 and 27 collaborations:

1. Byrne, Raymond; Astolfi, Davide; Castellani, Francesco; Hewitt, Neil J. 2020. *A Study of Wind Turbine Performance Decline with Age through Operation Data Analysis* Energies 13, no. 8: 2086. <https://doi.org/10.3390/en13082086>
2. Recommended Practice 19: *Micro-Siting Small Wing Turbines For Highly Turbulent Sites*, 2018, IEA Wind Task 27. <https://iea-wind.org/iea-publications/>

## Chapter 2

### Literature Review

#### 2.1 Background

The transition from fossil fuel based economies to decarbonised renewable energy based economies is a key goal of many countries. This has been driven by a number of factors such as greenhouse gas reduction targets, energy supply security and advances in wind energy science and technologies (Kulovesi and Oberthür, 2020). Wind energy is viewed as a major potential contributor to these transitions globally, particularly in jurisdictions that have abundant wind resources like Ireland (Gannon, 2018). Wind energy worldwide continues to grow year on year with a reported global installed capacity of up to 743 GW at the end of 2020, including 93 GW in 2020 alone (Lee and Zhao, 2021). This is up from the 60 GW of new capacity installed in 2019 (Lee and Zhao, 2020). The vast majority of this capacity is in onshore wind, however the offshore wind industry continues to expand. At the end of 2020, Europe had a total cumulative wind installed capacity of 220 GW installed, of which 25 GW is offshore (Komusanac et al., 2021). This is expected to grow to approximately 300 GW by 2025, including an extra 25 GW of offshore. To meet growing demand, wind turbine technologies have developed rapidly in recent years. Economies of scale aiming to reduce the levelised cost of energy (LCOE) has resulted in substantial increases in turbine sizes both physically and in power rating (Elia et al., 2020). Individual larger turbines can replace multiple smaller sized turbines which can reduce auxiliary infrastructural costs, such as civil works, while accessing a better wind resource using taller towers and larger rotors. The vast majority of new global installed wind capacity is made of large scale wind turbines while medium scale wind turbines found in older wind farms approaching end of life are now either being extended with major component upgrades or re-powered with fewer but larger wind

turbines. In addition, as onshore sites with the best wind resources are increasingly developed, the move to less windier sites has created the need for taller towers and larger rotor diameters to access the wind resource in an economically viable manner (Abdelilah et al., 2020). Separately, offshore wind turbines have increased dramatically in size the past decade with 10 MW rated wind turbines now coming to the market (Whitmarsh, 2018; Wiser and Bolinger, 2018). This industry has also been advanced by reducing costs in large wind turbine technology and is leading to an increasing move by turbine manufacturers towards offshore wind systems (Higgins and Foley, 2014; IRENA, 2020a). The industry is aiming for future turbine power ratings approaching 20 MW with rotor diameters well in excess of 200 m on floating offshore platforms.

## 2.2 Distributed wind challenges

### 2.2.1 General challenges

Although there is no, as of yet, formal international definition of distributed wind, it is broadly accepted to include single, or a small number, of small, medium to large scale wind turbines with power ratings of up to  $\sim 2$  MW, deployed in individual or community owned projects and off-grid systems (DWEA, 2015). It also can include behind-the-meter (or Autoproduction) applications where the electricity generated is consumed onsite and small privately owned wind farms. In contrast to the large scale, investor driven, wind industry, the distributed wind industry has not experienced the same rate of growth in recent years, primarily due to intermittent government incentives, technological challenges and competition with solar PV. (Nock and Baker, 2017; Foster et al., 2020). There is even some evidence of an increase in costs in the USA, though data is relatively sparse (Orrell et al., 2019). This raises a number of questions for the distributed wind industry in understanding why many of the technological advances and innovations that have improved the economic viability of large scale wind farm deployment have not emerged in the distributed wind sector and what additional research is required to further develop this industry. It is also viewed that distributed wind faces a number of its own unique challenges,

particularly with small scale technologies, such as in deployment methodologies, social acceptance strategies, wind resource assessment, optimum turbine siting and sizing, supply chain development, skilled personnel and consumer (or stakeholder) confidence in the technologies (Vilar, Xydis, and Nanaki, 2020). Unless these challenges are addressed, the attractiveness of the sector as a proposition for financial investment will remain low as is evident by the small number of small and medium scale wind turbine manufactures that operate in this space presently (Elshurafa et al., 2018; MacArtain, Byrne, and Hewitt, 2018; Panigrahi et al., 2020).

Wind turbines at all scales are broadly categorised by their rated power or rotor swept area. The International Electrotechnical Commission (IEC) categorise wind turbine designs into various design classes (IEC 61400-1, 2019). These classes define design standards based on the wind conditions a wind turbine is designed to operate in. These include wind speed and wind turbulence classes. The intention of the classes is have wind turbines designs that cover most operating wind environments. The values of wind speed and turbulence parameters are intended to represent a range of different site conditions but do not give a precise representation of any specific site. This will be discussed further in later chapters. The IEC defines a small scale wind turbine as having a rotor swept area of up to  $200 \text{ m}^2$  (16 m rotor diameter) which corresponds to a rated power of  $\sim 50 \text{ kW}$ . (IEC 61400-2, 2013). Small wind turbines at this scale is a separate industry to the large scale wind turbine industry, partially due to different (simpler) design approaches, manufacturing processes, end-users and IEC design definitions. Some countries deviate from this definition, for example, in the USA a small wind turbine is defined as have a rated power up to  $100 \text{ kW}$  (DOE, 2007). In Denmark a power rating of  $25 \text{ kW}$  has been used to define a small scale wind turbine, but also with different design and installation requirements for wind turbine rotor swept areas below  $5 \text{ m}^2$  ( $\sim 1 \text{ kW}$ ) and  $40 \text{ m}^2$  ( $\sim 8 \text{ kW}$ ) (Forsyth et al., 2015). The market for wind turbines rated below  $100 \text{ kW}$  has experienced continuous decline from 2012, due to incentives that have greatly diminished or disappeared altogether. According to the most recently published US distributed wind market report, covering distributed wind turbine installations from  $400 \text{ W}$  to  $\sim 2 \text{ MW}$ , the impacts of policies and consumer demands were not the same across all market sectors (Orrell et al., 2019). A noted challenge, from a consumer financing

perspective, were discrepancies between the prediction and actual energy performance, post installation. It also showed that of the capacity of 50.5 MW installed capacity in 2018, 47.4 MW came from wind turbines with power ratings above 1 MW, while 1.6 MW consisted of wind turbines rated between 100 kW and 1 MW. The remaining 1.5 MW comprised of wind turbines rated below 100 kW. (Foster et al., 2020) reported that experiences in the states of Iowa and New York showed that stable long term policies regarding financial incentives, zoning rules and administrative support, in combination with a good wind resource and high electricity prices can lead to market growth in distributed wind. In the UK, the distributed wind also has had mixed success to date. Following the introduction of the UK microgeneration scheme (MCS) in 2010, wind turbines of power ratings up to 50 kW could avail of generous feed-in-tariffs (FiTs) in the form of four renewable energy obligation certificates (ROCs) (RenewableUK, 2015). The market peaked in 2012, after which a policy review of FiTs and their subsequent reduction between 2015 and 2016 curbed growth in the market. FiTs finally ended in 2017 and the market demand for wind turbines up to 50 kW has effectively collapsed. Political instability, negative media commentary and planning requirements deemed inappropriate were also contributing factors (RenewableUK, 2014). Northern Ireland was a specific case where similar FiTs were afforded to wind turbines up to power ratings of 250 kW. The growth in single wind turbines up to 250 kW, in some cases at the grid extremities, created more than expected additional challenges for grid operators in relation to uncontrolled generation and power quality issues (Nock and Baker, 2017). The grid being small and not well interconnected, eventually led to prohibitive grid connection costs for single wind turbines of this size. In addition, the abolishment of FiTs in 2017 ended market growth (RenewableNI, 2021). An IEA Wind Task 27, dedicated to small wind turbine research, demonstrated that the power curve for a given small wind turbine system can vary between different consumer sites depending on wind turbulence and also be different its power curve measured at less turbulent accredited wind test sites (IEA Wind, 2018). It has also be shown that small wind design standards are currently limited in accounting for the higher turbulence that small wind turbines may experience in more complex environments outside of flat field locations (Evans et al., 2017).

### 2.2.2 Urban wind challenges

In recent years, the application of wind energy in urban areas has been gaining some interest primarily in the deployment of small scale wind turbines. Particular focus has been on the potential for micro and small scale wind systems (e.g., roof mounted systems) in city environments (KC, Whale, and Urmee, 2019). In some cases wind turbines are integrated into openings or between buildings (Abdulrahim Saeed, 2017). They are presented as attractive way for building and urban centres to generate electricity and offset carbon emissions. However, the built environment adds extra challenges in terms of the complex wind flows and low wind resource, planning, safety, liability building structural integrity, building comfort, noise, installation and maintenance. (Drew, Barlow, and Cockerill, 2013) investigated the potential energy yield for small wind turbines in the greater London area based on wind speed estimations and found less than 27% of the total city region has wind speeds above 4 m/s. However, the study was based on 1 km<sup>2</sup> grid resolution and assumed that turbulence impacts were negligible 5 m above the building. (Drew et al., 2015) followed this study with a techno-economic assessment of 33 small wind turbines using the UK's Energy Saving Trust wind speed estimator tool. It showed overestimates of wind speeds by up to 23% in some cases. However, at some high wind speed sites, wind speeds were underestimated, indicating that the tool could also potentially eliminate good locations for small wind turbines. (Emejeamara, Tomlin, and Millward-Hopkins, 2015) showed that urban rooftop environments experience high levels of gusts that contain significant energy at short temporal scales and suggest that small wind turbines designs with high response times and dynamic gust tracking algorithms could potentially double the energy capture. Further work in this area introduced a turbulence induced performance coefficient, for variable speed control of roof mounted vertical axis wind turbines, to better capture this energy (Emejeamara and Tomlin, 2020). (Ishugah et al., 2014) showed that high-rise buildings that are less obstructed by surrounding features may be more suitable locations for roof mounted small wind.

(Grieser, Sunak, and Madlener, 2015) studied the economics of small wind in urban areas for the case of Germany and concluded that only exposed areas with low building densities and wind speeds greater than 4 to 4.5 m/s were viable. (Sunderland and Conlon, 2010) showed significant variation in the energy performance of

a range of small wind turbine models using measured wind speeds at a Dublin city centre location compared with modelled predicted winds at the same location that used reference measurements made at Dublin airport 15 km away. Overestimates of 79% to 137% in energy predictions were found. (Heath, Walshe, and Watson, 2007) concluded in a study of building mounted wind turbines that the wind resource in urban areas is far from understood. This was due to urban wind flow profile characterisation being empirical based on wind tunnel experiments and simple regularly shaped obstacles, while the roughness characteristics of the urban surfaces and obstacles in real-world situations can vary drastically. Some field trial cases studies have shown that in many instances expected energy output fell well below what was obtained. In 2009, the a small wind field trial in Warwick, UK evaluated the energy performance of 26 roof mounted small wind turbines of a variety of sizes (Encraft, 2009). Measured wind speeds were 40% lower than model predicted wind speeds from the UK Numerical Objective Analysis Boundary Layer (NOABL) wind speed data base at 16 of the sites and the overall energy performance reported was very poor. However, the NOABL wind database is primarily based on surface met station wind observations and only considers general surface roughness at spatial scales above 1 km (DECC(UK), 2009). Therefore, it is difficult to get reliable estimates of wind speeds in urban areas because there is such variability in wind speed depending on the local building layout. Several studies of building mounted wind turbines at various locations in the USA were carried out by National Renewable energy Laboratory (NREL) (Fields et al., 2016). These showed that energy expectations were rarely met. It was also found that wind turbine mounting structures suitable for buildings added significant capital cost to the overall installation, even though the elimination of conventional electricity provided some offset of the cost. Not all buildings are suitable to mount wind turbines on in terms of shape structural properties, ease of access for safe installation and maintenance. However, some installations were deemed successful from the point of view of public relations and education. Overall, it was concluded that to optimise the chances of project success, clear and informed planning is required along with accurate wind resource assessment and wind characterisation such as turbulence and extreme wind directional changes. In addition, tools for accurate wind resources assessment around buildings are expensive and turbulence in these environments is not well understood, giving



rise to additional maintenance costs and a shortened lifetime expectancy. Current IEC design standards in wind turbine design and testing do not consider the high turbulence wind environments around building roofs. Therefore, current small scale wind turbines may operation outside of their design specifications, leading to safety risks and a reluctance by manufactures to install their products on buildings and give product warranties. A common conclusion of these studies is that low average wind speeds, high turbulence, low capacity factors, building mounting structural issues resulting in poor economics have hampered the development of urban small scale wind markets to date and that further research is required to optimise the locations of micro and small scale systems in urban environments. This has led to non-viable urban small scale wind energy projects resulting in low levels of financial investment in small scale wind technology development to date (Stathopoulos et al., [2018](#)).

## **2.3 Distributed wind opportunities**

### **2.3.1 New innovations and niche markets**

Despite the broad challenges, the new emerging policies, energy systems and enabling technologies are now giving new impetus for the continued development of distributed wind energy systems deployment across a broad range of markets globally. The EU Commission's new Clean Energy Package require member states to create legal frameworks to enable the development of community energy and energy prosumers by addressing market and regulatory barriers to participation in electricity markets (IRENA, [2020b](#)). Energy communities are now part of EU legislation based on two directives, namely, the Internal Electricity Market Directive [EU] 2019/944 and the Renewable Energy Directive [EU] 2018/2001 respectively (Milciuviene et al., [2019](#); Hall et al., [2020](#)). These directives ensure that community energy projects can participate in electricity markets in a proportional and non-discriminatory manner. Governments in countries like Ireland are designing policies for communities and citizens to become energy engaged as prosumers (DCCAE, [2019a](#)). According to an energy white paper Ireland's Transition to a Low Carbon

Energy Future 2015-2030 (DCCAE, 2019b), consumers and industry will be encouraged to become proactive energy users (i.e., prosumers), reducing energy demand and enabled/incentivised to participate actively in the electricity market via a range of local/onsite energy generation technologies. It is proposed in the 2021 Irish Climate Action Plan that 80% of electricity generation will come from renewable energy sources by 2030 (DECC, 2021). This has resulted in plans for new export tariffs for microgeneration systems up to 50 kW, planning rule extensions and the streamlining of the grid connection process for small scale renewable electricity systems up to 200 kW. Plans are also being developed for systems up to 1 MW. As electricity markets become more integrated (e.g., EU target model (Neuhoff, Wolter, and Schwenen, 2016)) and evolve from centralised grid systems towards smarter distributed grids, there may be additional market opportunities for the distributed wind industry, such as new generation capacity and the supply of grid services (Greenwood et al., 2017). Large energy users deploying behind-the-meter wind may also have the potential to trade electricity exports and provide various grid services if combined with other technologies such as energy storage and demand side management (DSM) (Ruth et al., 2019). Behind-the-meter wind also bring added benefits in given applications, such as reducing the carbon impact of the produced products of a business or industry.

New innovations in wind turbine control technologies and advances in electrical energy storage technologies are enabling variable wind energy to become more dispatchable and to provide grid support services (Aho et al., 2012; Apata and Oyedokun, 2020). This is broadening the market scope of distributed wind systems. Market potential projections in the USA show that the distributed wind market could exceed 20 GW by 2030, with the majority of installed capacity coming from large wind turbine technology installed in distributed applications (Gorroño-Albizu, Sperling, and Djørup, 2019; Lantz et al., 2016; Forsyth et al., 2017; Oteri et al., 2018). Some countries with limited transmission infrastructure may quickly reach integration limits for large central power generation and large scale renewable energy systems, indicating an expanding need for more distributed solutions. China, for example, has experienced severe curtailment of wind and solar generation due to the limitation of power transmission (Luo et al., 2015), while countries across

Africa and south-east Asia have limited transmission networks to support the deployment of large scale wind applications, leading to smaller scale deployments of more distributed technologies (IRENA, 2020b). Distributed wind can also play a role in off-grid and remote power supply systems in developing nations. In 2018 it was estimated that 900 million people globally ( $\sim 11\%$  of total world population) lacked access to electricity, down from 1.4 billion in 2010 (Bloomberg, 2020). According to the International Energy Agency (IEA), 580 million people in sub-Saharan regions alone lacked adequate to electricity in 2019 (IEA, 2020). (Ma et al., 2018) reports that 70% of Pacific Island communities experience energy poverty, while 60% of Russia's territory is not connected to centralised electricity (Ghani et al., 2019). Polar arctic communities, that currently use diesel at very high costs have potential to transition to renewable energy (Weis and Ilinca, 2010; Souba and Mendelson, 2018; Ringkjøb, Haugan, and Nybø, 2020). In addition, research base camps in the extreme climate of Antarctica could benefit from small scale renewable technologies (Tin et al., 2010). The IEA also identifies that approximately 34% of populations currently not served with electricity across the globe could be supplied by mini-grid solutions. These comprise of interconnected distributed generation and loads that can operate independently without the need for large utility grids (ESMAP, 2019). Realising these new potential opportunities for growth and expansion of a global distributed wind energy industry does not come without numerous challenges. Recognising this, the IEA commenced an international wind research Task in 2018 dedicated to distributed wind (Orrell and Baring-Gould, 2018). It focuses on enabling wind to contribute to a distributed energy future, particularly as electricity systems and grids evolve from centralised to distributed and the development of micro-grids in remote communities (Lantz et al., 2016; ESMAP, 2019). It aims to carry out research to help address some the barriers to unlocking markets for distributed wind. These include, developing clear technology and market definitions for distribution wind, assessing technology innovation needs, optimising deployment methodologies, research for future new and revisions of existing IEC standards, social acceptance strategies and added localised value beyond LOCE. It also aims to use relevant learnings from technology innovations in the large scale wind industry with respect to reducing LCOE. In addition, the Department of Energy (DOE) in the USA, through its Technology Assistance Programmes (TAP) is also supporting research and development

in distributed wind in the area of wind resource assessment (US DOE, 2020).

### 2.3.2 Commercial scale behind-the-meter opportunities

One market opportunity within the distributed wind sector is the deployment of medium to large scale wind turbines in behind-the-meter applications at commercial scale consumer sites, such as at large energy consuming industrial facilities, located in peri-urban areas (Hildreth and Kildegaard, 2009; Hanrahan et al., 2014; Ruth et al., 2019). It involves the generation of electricity using a medium or large scale wind turbine(s) for onsite consumption. The wind turbine is connected to the consumer side of the electricity meter, thereby offsetting the purchase of retail electricity from the grid, i.e., reducing electricity bills. Due to power (kW) mismatch with time of consumer demand and onsite generation, there will be times when a turbine produces too much power, in which case the resulting excess energy (kWh) is exported to the utility grid. At other times, when the wind turbine does not produce enough power, the resulting energy deficit is supplied by the utility grid. The economic advantage of behind-the-meter wind is that the unit of electricity (kWh) generated by the wind turbine that is consumed onsite is of a high value to the consumer, as it offsets electricity at the retail rate. Also, as a grid connection is already in place at consumer sites, the wind turbine grid connection costs and time to connection would likely be lower than a project requiring a new grid connection. Along with the general challenges facing distributed wind, outlined previously, additional challenges exist in the deployment of wind turbines in behind-the meter application operating as wind autoproducers. Firstly, turbine sizes suitable for many potential industrial users, in this market, is typically up to about 1 MW in size. Wind turbines of these power ratings are not widely manufactured as new products today, as newly available wind turbines have become larger. Secondly, to achieve best energy and economic performance, careful attention must be given to sizing a wind turbine to match the load power profile and energy demand at the given site. Electricity costs and local planning constraints are extra significant factors to be considered. Thirdly, behind-the-meter wind projects are also likely to be in areas closer to people and planning constraints may be more stringent in terms of setback distances from nearest neighbours/boundaries, shadow flicker and noise. Finally, assessment of the wind resource and the power performance characteristics of a given turbine at a

given site is of critical importance in siting, sizing and selection of a given turbine. Unlike small scale urban wind turbines and large scale rural wind farm projects, few studies exist on the performance of medium and large scale wind turbines in peri-urban and urban settings in relation to how pre-construction annual energy prediction(AEP) estimates compare with the real-world post-construction energy performance. Therefore, this last point is a principal focus of this research.

## 2.4 Distributed wind resource assessment

Technical details of the wind resource and its assessment in relation to distributed wind will be given in Chapter 3, however, an initial review is given here for the purposes of justifying the research gap identified later in this literature review. Few studies have been carried on medium to large scale wind turbines above power ratings of 50 kW but less than 2 MW in distributed wind applications. (Fields, Tennesand, and Baring-Gould, 2016) carried out an industry review on the current state of the industry in the USA regarding industrial practices employed in distributed wind resource assessment (DWRA). It was based on information gained through direct engagement with industry covering projects from 1 kW single turbine installations to multi MW community owned wind farms connected to electrical distribution systems. This review was part of the U.S. Department of Energy (DOE) Wind and Water Power Technologies Office (WWPTO) activities in distributed wind that focuses addressing reliability challenges of technology development, testing, certification and manufacturing. It highlighted the importance of accurate pre-construction DWRA and turbine suitability assessment for a given site and application in the optimisation of energy performance, subsequent LCOE and end-user confidence. A significant finding was that, due to the diversity of project sites and turbine sizes, there is little agreement on the accuracy of current DWRA methods with errors up to 250% between predicted energy performance and actual energy performance. This is the result of the variety of DWRA approaches of varying levels of complexity are being used in the distributed wind industry. These approaches range from the use of wind atlas data with varying temporal and spatial resolutions, combined with rules-of-thumb corrections to onsite measurements and

the use of various flow models at a given site. The review also showed that current DWRA processes largely exclude consideration of site-specific winds and turbine loading/suitability. Some of the challenges identified included, lack of robust methods for scaling wind data to lower hub heights, standardised guidelines for resource and siting assessment and lack of data availability and data incorporation. The principal conclusion of the review was that *“the distributed wind industry lacks representative atmospheric and turbine performance data to validate and benchmark existing methodologies for predicting project performance and site suitability”*. It also stressed the need of *“access to critical site information to facilitate atmospheric modelling, such as terrain, surface roughness, 3D buildings, and other surface features in a way that is affordable for the scale of distributed wind projects”*. Another investigation of a USA state funded programmes, namely the Rural Energy for America Program (REAP) and New York State Energy Research and Development Authority (NYSERDA), on 292 distributed projects found significant variation in performance and accuracy in performance prediction ranging from 62% to 134% (Tinnesand and Sethuraman, 2019). Significantly, these programmes required installers to have an approved level of training and the use of proven products. Therefore, this post installation investigation would be deemed to have been dealing with the current best-case state of the distributed wind industry in the USA. Another key finding was a broad spectrum of wind turbine rated power capacities, tower heights, system setups and deployments application. It concluded that DWRA improvements could reduce project costs by having tiered screening methodologies with different levels of complexity depending on site characteristics, project size and the accuracy requirements of owners or financiers. The study also concluded that any government incentives and supports should be linked to improved and consistent performance predictions and that sensitivity analysis to the priority of parameters required for best prediction accuracy requires more research to assess the impact on project economics. (Olsen and Preus, 2015) reported a number of case studies that had similar outcomes and concluded that the absence of resources specific to the distributed wind industry across all areas, such as wind resource assessment, product quality, training and information will inhibit future market expansion. The European Association of Wind Academics (EAWA) published research on the long term research challenges of wind energy (van et al., 2016). With respect to wind resource assessment, it was reported that

a complete understanding of the complexities of the wind resource in relation to wind energy applications, across all scales of deployment, has yet to be reached. Specifically, it was identified that *“as wind turbines are being installed more and more in complex terrain and offshore, the question is how to generalise an inflow classifications scheme so that many kinds of different locations can be well characterised”*. The study also stated that from a wind flow point of view, *“The inherent nonlinearity and chaos of fluid dynamics occur at all scales, from weather patterns relevant to wind power grid integration, to turbulence essential to dynamics turbine loads. The inability to calculate flows from first principles has made continued interaction between modelling and measurements indispensable. Although powerful computers now enable simulating turbulent wind conditions with increasing detail, precise results are not guaranteed.”* (Veers et al., 2019) reported in a review of the *“Grand challenges in the science of wind energy”* the need for *“an improved understanding of the physics of atmospheric flow in the zone of wind turbine or wind farm operation”*. The exact processes of how mesoscale influences, at scales from about 5 km to 100 km, interact with microscale influences, at scales down to 100 m remain poorly understood and is commonly referred to as the *“terra incognita”* (Wyngaard, 2004; Banta et al., 2018; Arthur et al., 2020). Therefore, for the distributed wind industry, consistent standardised approaches to wind resource and pre-construction energy assessment will be critical to the industry’s future success, particularly as more people with less experience in wind resource assessment enter the industry. In addition, the benefits of more standardised DWRA procedures combined with innovations in medium scale turbine design could greatly assist the distributed wind industry to follow a future trajectory of improving the LCOE in complex wind environments. New innovations in distributed wind turbine design, including taking learning from the large scale wind industry, could also improve the industry’s future outlook, such as enhanced controllability that enables a distributed wind turbine to be tuned to a site’s specific wind resource characteristics for high operational reliability and energy performance.

### 2.4.1 Current wind resource assessment approaches

It is well known that the wind environment has a major influence on the viability of any wind energy project in terms energy output (Jung and Schindler, 2020a;



Jung and Schindler, 2020b). The energy performance of any wind turbine is sensitive to a number of atmospheric parameters such as wind speed, wind direction, wind shear, wind veer, turbulence and air density (Wharton and Lundquist, 2010; Wagner et al., 2011; Bardal, Sætran, and Wangsness, 2015; Wallace, 2015; Rodrigo et al., 2018; Gualtieri, 2019). These parameters are influenced by local and regional features around the site (Manwell, McGowan, and Rogers, 2009). Site assessment procedures for wind turbines at rural based wind farms consider the impact of site physical features on the wind resource, at a range of spatial scales, such as orography, surface roughness and, in some cases, the impact of forests (Desmond, Watson, and Hancock, 2017).

Wind resource assessment for the prediction of annual energy yield for any given large scale wind project involves onsite wind measurements combined with various modelling approaches depending on the size and complexity of the site. There are a number of microscale modelling approaches that have varying degrees of accuracy, complexity and cost, ranging from linear flow, mass consistent (MC) to computational fluid dynamics (CFD). CFD models are of varying complexity, that solve equations for conservation of mass and momentum by solving the Navier-Stokes equations of fluid flow using turbulence closure techniques (Sanz Rodrigo et al., 2017). Diagnostic linear models linearize the Navier-Stokes equations and use wind statistics to parametrize the impact of site physical features on the wind resource (Zhang, 2015). Linear models are not computationally intensive. Early approaches that are still used today, especially in distributed wind projects, involve extrapolating data from nearby reference masts using linear microscale models such as Wind Atlas Application Program (WAsP) to estimate the *AEP* at the site of interest (Landberg et al., 2003; Petersen and Troen, 2012). WAsP is based on models for orographic height variations, terrain roughness and sheltering obstacles that were used in the development of the first European Wind Atlas (Troen and Lundtang Petersen, 1989). MC models solve the conservation of mass equations only and linearize the Navier-Stokes equation for the conservation of momentum and are reported to account for orographic effects better than linear models (Zhang, 2015). The most commonly used CFD models are based on the Reynolds Averaged Navier-Stokes (RANS) equations and Large Eddy Simulation (LES). RANS models parameterize all turbulent eddy scales and



resolve only the mean flow. LES models resolve time dependent but spatially averaged Navier-Stokes equations and requires very high computational power which is more costly (Cheng et al., 2003). LES explicitly resolves the largest turbulent eddies and filters out small scale turbulence eddies in the inertial subrange i.e. where turbulent kinetic energy in the fragmentation of large turbulent eddies is transferred to a cascade of ever decreasing smaller scale eddies that eventually dissipate. Therefore, LES is not commonly used in distributed wind project development, whereas linear and RANS approaches are more widely used. Detached Eddy Simulation (DES) is a combination of LES and RANS that uses LES only for regions of separated flow to reduce cost while keeping accuracy (Dadioti and Rees, 2017). The accuracy of CFD simulations are dependent on many variables such as the approach taken (e.g., RANS, LES, DES), initial conditions, boundary condition, mesh size, user experience and computation time (Franke et al., 2011). A practical limitation in combining nearby wind measurements with models for distributed wind projects is that nearby reference masts with data of sufficient quantity and quality of data may not always be available. An alternative approach is the use of numerical weather prediction (NWP) models that can estimate the wind resource over large regions. NWP models are increasingly being refined for wind resource assessment in the wind industry to give high-resolution wind climatology and wind data at regional mesoscale levels (Mann et al., 2017; Kalverla et al., 2018). This has been made possible with the availability of satellite weather observation data over years and decades. This data is reanalysed as hind casts to generate global spatial and temporal reanalysis data sets of a variety of meteorological parameters, including wind speed and direction at multiple heights in the atmosphere. Reanalysis data sets are provided by organisation such as such as the European Centre for Medium-Range Weather Forecasts (ECMWF), National Aeronautics and Space Administration, U.S.A. (NASA), National Centres for Environmental Prediction (NCEP), National Oceanic and Atmospheric Administration (NOAA) and Japan Meteorological Agency (JMA) for a range of time and spatial resolutions, in some cases down to 1-hour time resolution and 50 km spatial resolution (Kim, Kim, and Kang, 2018). Mesoscale modelling tools use reanalysis data as input to NWP models that downscale meteorological parameters from the global reanalysis data sets to horizontal resolutions of a few km to a few hundred km (Olsen et al., 2017). A range of mesoscale models are available such as

Weather Research Forecast (WRF), Advanced Regional Prediction System (ARPS), Atmospheric Modelling System (RAMS), Coupled Ocean Atmosphere Mesoscale Prediction System (COAMPS), High-Resolution Rapid Refresh (HRRR) and Unified Model (UM) of the UK met office. The downscaling processes use physical models of the atmosphere with sets of equations that model atmospheric processes and their interactions with regional features such as land masses and oceans down to small scales (Badger et al., 2014). Further downscaling of the data to microscale resolutions in the order of  $\sim 100$  m can then be carried out using statistical approaches with tools such as WAsP or with CFD simulation nested in the mesoscale model (Gasset, Landry, and Gagnon, 2012; Talbot, Bou-Zeid, and Smith, 2012; Rodrigo et al., 2018). The modelling approach to use depends on speed, cost and accuracy required in relation to the complexity of the wind project location and the wind project size. A summary comparison of the performance of a range of models in a variety of field studies is given in Appendix A. The studies show the site specific nature of the modelling approach use. More complex models do not always perform better, or even as good, as less complex models. There is also a high dependence of experience of the user and the choice and configuration of flow model should be based on reliable validation data.

In onshore wind farm developments, onsite wind measurements are highly recommended to validate models and is a requirement of investors to reduce financial risk. Typically wind measurements (speed and direction in the 2D horizontal plane) at multiple heights are along with other environmental parameters such as air pressure and ambient temperature are carried out and analysed (Bailey and McDonald, 1997; Roeth, 2010). The data is then processed to determine, wind speed distribution, wind power density (*WPD*) and *AEP*, wind shear and turbulence. However, many methods are not perfect and many challenges remain as outlined by the large scale wind industry (Veers et al., 2019), e.g., there still remains numerous questions on why the post-construction yields of some wind farms are not performing as was originally predicted. In some cases, post-construction yield analysis is carried out, particularly in cases of significant under performance. However, these occur primarily at the request of investors on a case-by-case basis, highlighting that there are currently no standardised methodologies in post-construction yield analysis. Therefore, improving pre-construction energy predictions with post-construction energy

performance, especially in complex natural terrain, remains an ongoing research effort in the wind farm industry involving advanced modelling techniques, across various temporal and spatial scales, and measurements using met masts and LiDAR technologies (Sanz Rodrigo et al., 2017). However, these advances can come with additional upfront project developments costs. In the distributed wind industry, the same issues will exist and may be exacerbated due to a higher likelihood of more complex wind flow regimes. These issues coupled with lower financial resources available, particularly for smaller distributed wind projects involving single wind turbines, may make accurate pre-construction energy predictions a very challenging prospect for this industry.

#### 2.4.2 Urban and peri-urban additional wind modelling complexities

Unlike wind farm sites where building obstacles have not typically been a dominant feature, peri-urban environments are likely to have a significant number of building obstacles in the vicinity of a prospective wind turbine location leading to complex wind flow regimes. Current IEA Wind recommendations for siting single small scale ( $\leq 50$  kW) wind turbines near obstacles state that the lowest point of the rotor swept area should have a height of at least twice the height of the obstacle within a distance of twenty times the height of the obstacle (IEA Wind, 2018). These recommendations are based on a number of earlier wind tunnel studies and empirical formulations on the impact of stand-alone obstacles, treated as two-dimensional obstacles, on wind flow (Counihan, Hunt, and Jackson, 1974; Wegley et al., 1980; Perera, 1981; Taylor and Salmon, 1993). Many of these studies were not originally for wind energy applications, but other research areas such as shelterbelts and pollution dispersion. However, they have been adopted for wind energy related flow models, such as the WAsP linear IBZ model and the IEC wind turbine performance testing standard (Mortensen, 2016; IEC 61400-12, 2019). Empirical obstacle models for wind energy have not undergone significant further development up to now, due to them not being significant features at wind farm sites. A more recent experimental study of wind flow in the wake of a solid, 3 m high and 30 m wide fence, treated as two-dimensional obstacle, was carried out by (Peña et al., 2016). It showed that wake effects of the fence were experienced vertically up to  $\sim 2.5$  times the height

of the fence and horizontally, downwind of the fence, to a distance  $\sim 11$  times the height of the fence. Standalone three-dimensional bluff bodies such as cuboid structures can have complex impacts on wind including flow detachment, separation cavities and recirculation zones in the wake, flow reattachment and vortex shedding (Peterka, Meroney, and Kothari, 1985). Complex recirculation zones that define the near wake can extend from 2 to 6 times the obstacle height downwind of the obstacle, while the far wake may extend to up to 18 times the obstacle height (Nieuwpoort, Gooden, and Prins, 2010; Vasilopoulos, Sarris, and Tsoutsanis, 2019). (Cheng et al., 2003) compared the RANS approach with LES for an array of cubes and concluded that RANS modelling gives significant uncertainties in the description of unsteady complex features such as separation zones, vortex shedding and recirculation zones. LES gives more accuracy but is more computational and cost intensive.

In real-world urban and peri-urban environments with many building obstacles, various complex flow regimes can form depending on building shapes and packing densities. Numerous studies of urban wind flows in cities show the complex nature of the wind characteristics in these environments. The urban atmospheric boundary layer or urban boundary layer (UBL) can grow up to 200 m at  $\sim 2$  km downwind in from the rural to urban interface, extending to 400 m over city centres (Best et al., 2008; Millward-Hopkins et al., 2013a). Within a UBL, local internal boundary layers can form depending on building heights, plan areas, and densities resulting in modified vertical wind speed profiles and increased turbulence (Mertens, 2006). Surface roughness elements (e.g., buildings) form the urban canopy layer (CL) that can adjust wind flow to give complex vertical wind speed profiles, including vertical displacement, speed up effects, flow separation and recirculation (Belcher, Jerram, and Hunt, 2003). The CL has a spatially averaged mean wind speed profile that increases exponentially with height up to heights similar to the building heights. Above the CL, a roughness sublayer (RSL) can extend from 2 to 5 times the local building heights with a spatially averaged mean wind speed profile that is logarithmic with height. Above the RSL, an inertial sublayer (ISL) is assumed to have logarithmic homogenous flow up to heights of 100 m to 200 m (Barlow, 2014). The actual heights of each sublayer is variable, depending on location. (Castro, 2017) showed that the exponential shape of the spatially-averaged mean wind speed profile within the CL may not always be the case, but the prediction of the roughness

length appropriate for the logarithmic profile above the CL does not critically depend on an exponential profile in the CL. Small wind turbine deployment in urban environments can find themselves located in the CL, or lower end of the RSL, where complex wind flows are challenging to harness. This a principal reason why urban small has not had much success to date. Flow modelling using CFD in the context of the urban wind energy has seen a focus on wind flow around different types of rooftops for wind energy exploitation (Herrmann-Priesnitz, Calderón-Muñoz, and Leboeuf, 2015; Toja-Silva et al., 2015; Wang et al., 2017). Large building obstacles can act like as bluff bodies where flow is dominated by large length scales and separation induced vortices.

Morphometric methods consider the geometric properties of a given area of interest. These methods use building heights, plan areas and windward frontal areas to determine the local scale aerodynamic roughness length  $z_0$ , the height where the mean wind velocity becomes zero due to surface roughness, and the zero-plane displacement  $z_d$ , the height where the wind velocity becomes zero due to building canopies (Macdonald, Griffiths, and Hall, 1998). However, determining values for  $z_0$  and  $z_d$  within urbanised areas remains challenging because of drastically varying roughness element heights and densities. (Kent et al., 2017) compared nine methods to determine local scale values for  $z_0$  and  $z_d$  at three sites (within 60 m of each other) in London, UK. The methods consisted of three anemometric observations at separate levels, six morphometric and one look-up table approach. The study showed that  $z_d$  varied between 5 and 45 m. There was better agreement between anemometric and morphometric when the height variation of roughness elements were taken into account implying that  $z_d$  is consistently greater than the local mean building height. The surface roughness  $z_0$  varied between 0.1 m and 5 m with values from morphometric methods consistently being 2 m to 3 m larger compared to anemometric estimates. None of morphometric methods consistently resembled the anemometric methods. The modelled plan area of the region measurements varied by up to a factor of three, depending upon the morphometric method used. These urban based studies highlight the complexities of the urban wind resource in relation to small wind, however, medium and large scale wind turbines in these areas may avoid the complexities of the CL and be influenced more by the RSL and ISL, but few studies exist in these cases.

## 2.5 Research gap identification

It is clear that accurate wind resource assessment is essential to assess the viability of a given project. The deployment of medium to large scale wind turbines in peri-urban locations, in terms of wind resource assessment and siting, lies somewhere between onshore wind farms and small scale wind turbines in complex urban locations. Like onshore wind farm projects, behind-the-meter projects can be financially viable but may be subject to more complex wind regimes. However, as mentioned previously, unlike typical onshore wind farm sites, behind-the-meter wind projects tend to be single turbines at lower elevations in rural areas (e.g., near agricultural farm buildings) or in peri-urban areas (e.g., industrial estates) with a higher likelihood of being in vicinity of man-made obstacles (e.g., buildings) and trees. In addition, parts of the regional terrain within 10s of km of the site may likely be at higher elevations than the turbine site itself. In relation to wind resource assessment this presents extra challenges in wind turbine siting in that many behind-the-meter sites may have complex wind flows that are heavily influenced by local obstacles, resulting in lower average annual wind average speeds, unique wind speed distributions, high turbulence, high wind shear and highly directional wind flows. To date, very few studies have been published on the pre- and post-construction energy performance of medium scale wind turbines operating behind the meter in peri-urban wind environments and the characteristics of the wind resource that affect an operating wind turbine's energy performance in the context of optimum turbine siting. (Staudt, 2006) published the economic performance of the 850 kW wind behind-the-meter wind turbine, used in this research, at Dundalk Institute of Technology (DkIT) on the east coast of Ireland. The predicted *AEP* value was 2 million kWh while actual metered energy output was 1.5 million kWh. (Cooney et al., 2017) using 1 year of performance data from 2008 for the same wind turbine showed the economics of the project was on a par with a typical wind farm developments due to the offsets in the purchase of retail electricity. However, the study also showed overestimates in predicted *AEPs* of  $\sim 25\%$  compared to measured annual energy output. (Liu, Han, and Lu, 2014) carried out an experimental study of the performance of a 100 kW rated Northwind 100 wind turbine located on the campus of Case Western Reserve University in Cleveland USA. The study analysed the power curve of the turbine

based on 3 months of wind and ambient temperature data. It focused on the effect of ambient temperature and resulting air density on power turbine power performance. They found a weak relationship between ambient temperature and power curve variations at that particular site. However, the study did not describe the site features or show, within the short time frame of data collection, a directional analysis of power performance. Therefore, the variation of power curve due to temperature alone is inconclusive. (Hildreth and Kildegaard, 2009) investigated the avoidance of demand charges using a behind-the-meter 1.65 MW wind turbine. The focus of the study was on the economic value of power kW demand reduction from a standing charge point of view, i.e., in addition to cost savings made as result of energy offset. Extrapolated wind speed data from a met mast to the hub height of the turbine, combined with the manufactures power curve was used to estimate the power production of the turbine. The study concluded that a potential extra 10% cost saving on demand charges was possible. The study assumed manufacture's power curve and assumed the simple power law in the wind data extrapolation from mast height to hub height. No site description nor its impact corresponding turbine energy performance was given. Unlike urban deployed small scale wind turbine projects, these medium and large scale turbine projects in urbanised environments did prove to be economically viable and showed the prospect to be optimised. Therefore, there exists a knowledge gap in understanding how well current modelling approaches predict the energy performance of more mature medium and large scale wind turbine technologies in peri-urban environments and the influence of the local building obstacle features that exist around them. It is also not well understood how well current IEC large (and small) wind turbine design standards (IEC 61400-1, 2019; IEC 61400-2, 2013) account for turbulence and gust factors in peri-urban environments with respect to medium and large scale wind turbines.

One practical challenge in addressing this gap in a peri-urban environment is that the un-obstructive deployment of tall met masts may be limited by ground spatial requirements such as the relatively large areas required for mast guy-wire installations and planning constraints, or it may be an operational inconvenience to normal business activities at the end-user site. This can lead met mast installations with shorter heights, below the desired wind turbine hub height at a project's pre-feasibility stage, or may even prevent the installation of a met mast altogether.



Combining these potential wind measurement limitations with the added complexity of wind flow regimes means that accurate pre-construction energy prediction of actual post-construction energy performance becomes a significant challenge. However, with the rapid growth in the large scale wind industry over the past decade combined and with advances in semiconductor, optic fibre and laser technology, remote sensing of wind flow based on light detection and ranging (LiDAR) technology now gives the opportunity to measure winds at multiple heights. Ease and speed of deployment, mobility and comprehensive wind measuring capability is making LiDAR technology more attractive to the wind industry today either as a supplement to wind met mast measurements or as a replacement technology to met masts. In basic terms, wind LiDARs operate by transmitting a laser beam of a well define wavelength in the infra-red (eye safe) region of the electromagnetic spectrum. The infra-red beam is back scattered by moving aerosols, that represent wind flow, and undergoes a Doppler shift in the process. The weak Doppler shifted back scattered beam is detected by the LiDAR and is mixed with the original transmitted beam to determine the frequency shift or beat frequency between the transmitted and received beam. It is from the beat frequency that the wind speed can be determined (Pitter, Slinger, and Michael, 2015). However, LiDAR technology specifically applied in wind resource assessment is relatively recent and the first commercial products were introduced in 2008 (Peña et al., 2015). Since then much validation work has been ongoing in order for the technology to gain broad acceptance in the wind industry which (Clifton, Elliott, and Courtney, 2013). It is now considered an approved measuring technology by IEC wind standards for power performance assessment of wind turbines at accredited wind test sites (IEC 61400-12, 2019). Two principal ground mounted vertical profiling LiDAR technologies for wind measurement application exist today. These are the a) continuous wave scanning LiDAR and b) pulsed LiDAR. They can make measurements at multiple heights as desired by the end-user. At a given height, both types of systems use backscattered optical measurements at multiple points around the horizontal plane of a conical scans. The backscattered signals are then digitally processed to determine a three-dimensional wind speed value at the given height. Therefore, LiDAR technology now offers the ability to make comprehensive wind measurements in peri-urban and urban environments for wind energy projects, overcoming potential any space, operational and



planning constraints associated with met masts. A LiDAR device is a key feature of this research and its use in a peri-urban environment for distributed wind assessment is a novel aspect. More details of the LiDAR used will be given in chapters 3 and 5.

## 2.6 Aims of this PhD to help address the research gap

The focus of this research is to assess and improve existing methods and procedures in micro-siting medium and large scale wind turbines for behind-the-meter wind applications at commercial scale sites. Commercial scale, in this case, refers to non-domestic sites such as factory or farm sites where the energy produced by a wind turbine is mostly consumed onsite. The research has an *applied* focus, using LiDAR technology combined with SCADA data from a large scale operating peri-urban wind turbine, data from an offsite rural met mast and industry flow models to help address the research gap. Specifically, to develop recommendations for deploying medium and large scale wind turbines in relation to onsite wind measurement heights, flow model configurations and to develop a low-cost alternative morphological approach to wind turbine (and met mast) micro-siting. Also, to assess from LiDAR measurements, turbulence and gust factors against current IEC wind turbine design standards for both large and small scale wind turbines and give suggestions for their improvements.

The first part of the research gives a theoretical background of the wind resource from the global scale, through mesoscale to microscale. A review of modelling approaches for each scale is given including, the production of wind atlases that are of low cost to end users. Emphasis is placed on microscale modelling in the environs of obstacles and buildings. A description of statistical wind characteristics and the principal operation of LiDAR technologies are also given.

The second part, investigates the multi-annual measured energy performance of an 850 kW Vestas V52 wind turbine with a hub height of 60 m and rotor diameter of 52 m, sited in a peri-urban area of low elevation in the vicinity of buildings. The wind turbine's long term 10-minute SCADA data is analysed to assess the energy performance of the turbine and to give insights into external site factors that

have influenced its performance over a multi-annual time frame. Part of the analysis involves the development of a novel electrical energy rose (*EER*), derived from the SCADA data, to assess the impact of external site factors on the wind turbine's energy performance.

The third part aims to distinguish regional mesoscale influences from local microscale influences on the *AEP* of wind turbine using the remodelled mesoscale Irish wind atlas. The technical details of the wind atlas and the LiDAR device used in this research is given. The wind atlas determination of directional wind power density at multiple locations up to  $\sim 40$  km away at a height of 150 m is used to assess mesoscale influences on a regional scale. An analysis of wind resource and modelled wind turbine predicted *EER* at the wind turbine site, at hub height, is compared to the actual wind turbine *EER* from measured SCADA data. LiDAR wind measurements at 120 m, 200 m and 300 m along with 150 m wind atlas data are used to assess wind flow far above local obstacles. The use of mesoscale based wind atlases for low cost site assessments along with insights and suggestions for wind energy planners in relation to mesoscale considerations are discussed.

The fourth part, compares four microscale modelling approaches, one linear and three RANS CFD, in the prediction of the *AEP* with the annual wind turbine *EER* over the same 1 year period. Two industry standard microscale modelling tools, namely WASP and WindSim are used to run the models. The four modelling approaches treat building obstacles in different manners. The four approaches are used predict the annual wind turbine *EER*, at the wind turbine hub-height, from downscaling or upscaling one year of onsite LiDAR wind measurements at multiple heights above and below the wind turbine hub height. The hub-height *EER* predictions over 16 directional sectors by each model are compared to the wind turbine *EER*. Directions with the biggest discrepancies between all four model and measurements are examined in relation to the local obstacles. In addition, measured directional wind shear profiles are compared to theoretical logarithmic profiles. The implications for the use of the models in peri-urban environments are discussed and suggestions are given for model configuration and input data measurement heights that give the best *EER* predictions.

The fifth part, is a wholly measurement based field study. A combination of multi-annual turbine SCADA data, 1 year of wind measurements from the onsite

LiDAR and wind measurements from an offsite rural met mast located 1.2 km away (less influenced by buildings) are analysed. The directional energy, wind turbulence, shear and gust factors are assessed in relation to the morphological properties of building obstacles in 16 directional sectors as viewed from both the wind turbine and met mast sites. The validity of current normal turbulence models (NTM), specified by IEC standards, for both small and large scale wind turbines are tested against the analysed data at both sites. Implications for large scale wind turbine micro-siting in peri-urban environments and future IEC design standard revisions are discussed. A new morphological approach to peri-urban wind turbine micro-siting is given and revisions to IEC standard normal wind turbulence models are suggested.

The final part of the thesis discusses the outcomes of the four studies in the general context of distributed wind in peri-urban wind environments and uses the learnings to develop a framework for pre-screening peri-urban sites for medium and large scale wind turbine deployment. Recommendations are given for placement and heights above buildings of onsite wind measurement sensors for best energy predictions with the use of microscale models. A simplified procedure for the morphological assessment of building in the vicinity of a wind turbine's location to indicate the lower bounds of minimum rotor tip height and lateral placement to take advantage of potential channelling of wind flow in more open directional sectors between buildings is given. The characteristics of turbulence and gust factors in the context of IEC standards development are discussed with the suggestion of a potential new peri-urban turbulence class. The concluding chapter summarises the main findings of the thesis and suggests future potential challenges and research needs of distributed wind energy in the peri-urban environment context.



## Chapter 3

### Theoretical background

#### 3.1 Introduction

The wind resource is highly complex and varies over a wide range of temporal and spatial scales. This chapter gives an overview of assessing and modelling the key atmospheric parameters relevant to wind energy resource assessment. Emphasis is given to mesoscale and microscale modelling techniques and to the characteristics of urban wind regimes. A more complete description of atmosphere in the context of wind energy can be found in Appendix A. An overview of wind statistics and the principals of LiDAR measurement technology is also given. The chapter ends with summary justifications of the modelling and measurement approaches that will be used in subsequent study chapters in the context of medium and large scale wind turbines in peri-urban environments.

#### 3.2 Overview of the atmosphere

##### 3.2.1 Global circulation

The origin of wind on the earth is the result of unequal heating by the sun of the earth's surface. Higher solar energy input in the lower latitudes compared to the higher latitudes result in thermally driven global wind circulation patterns that moves warmer air from equatorial regions towards the poles, Fig. 3.1. The earth's rotation and curvature gives rise to the Coriolis force that causes wind flow from the equator towards the poles to move eastwards and wind flow from the poles towards the equator to move westwards. The Coriolis force results in the formation of three principal global flow circulation cells, namely Hadley, Ferrel and Polar cells. These are

associated with well-known, latitude dependent, surface winds such as mid latitude westerlies and trade winds (Ahrens and Henson, 2017).

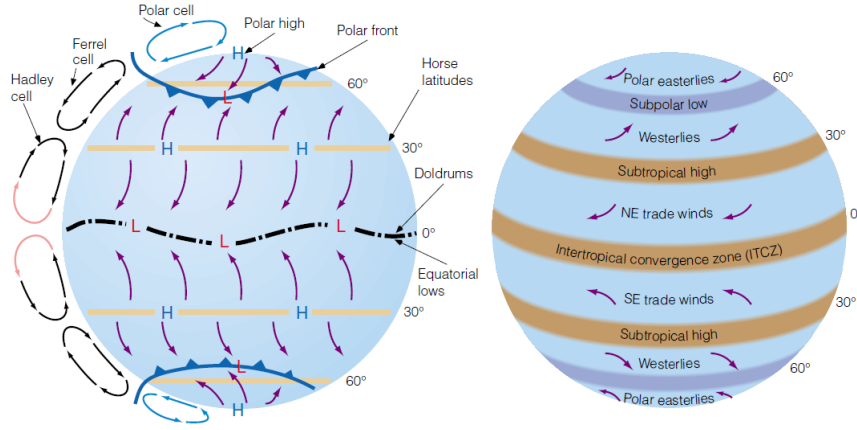


**Fig. 3.1.** Principal global wind circulation patterns (Ahrens and Henson, 2017).

The lower part of the earth's atmosphere where weather systems form is known as the troposphere. It contains  $\sim 80\%$  of the total mass of the atmosphere and varies in depth (height) from 6 km at the poles to 18 km at the equator with an average of  $\sim 10$  km in the mid latitudes. The atmospheric boundary layer (ABL), also known as the planetary boundary layer (PBL), is that part of the troposphere that is influenced by the earth's surface. The depth (height) of the ABL extends to  $\sim 2$  km. Interaction of the ABL with the earth's surface can modify global circulation patterns due to frictional stresses, orographic drag, ocean and coastal influences, heat energy and moisture exchange. This can create a wide variety of wind climates and wind conditions at numerous spatial and temporal scales, from thousands of km to sub-metre and inter-annual to sub-second respectively. The laws of conservation of mass, momentum and energy can fundamentally describe airflow in the ABL. As air is a viscous fluid, the conservations of mass and momentum can be described by the Navier Stokes differential equations of fluid flow, Eqs. (3.1) to (3.5) (Emeis, 2013).

$$\nabla \cdot (\rho \vec{v}) + \frac{\partial \rho}{\partial t} = 0 \quad (3.1)$$

$$\nabla \cdot \vec{v} = 0 \quad (3.2)$$

Where:

$\vec{v}$  - three dimensional wind velocity vector (m/s)  $\left[ \nabla = \left( \frac{\partial}{\partial x} + \frac{\partial}{\partial y} + \frac{\partial}{\partial z} \right) \right]$

$\rho$  - air density (kg/m<sup>3</sup>)

$$\frac{\partial u}{\partial t} + \vec{v} \nabla u + \frac{1}{\rho} \frac{\partial p}{\partial x} - f v + f^* w \mp v \frac{|\vec{v}|}{r} + F_x = 0 \quad (3.3)$$

$$\frac{\partial v}{\partial t} + \vec{v} \nabla v + \frac{1}{\rho} \frac{\partial p}{\partial y} + f u \pm u \frac{|\vec{v}|}{r} + F_y = 0 \quad (3.4)$$

$$\frac{\partial w}{\partial t} + \vec{v} \nabla w + \frac{1}{\rho} \frac{\partial p}{\partial z} - g - f u - f^* u + F_z = 0 \quad (3.5)$$

I      II      III      IV      V      VI      VII

Where:

$u$  - x component of the velocity vector (m/s)

$v$  - y component of the velocity vector (m/s)

$w$  - z component of the velocity vector (m/s)

$g$  - acceleration due to gravity (m/s<sup>2</sup>)

$f$  - horizontal Coriolis parameter  $2\Omega \sin(\Phi)$  (where  $\Omega$  is the angular rotation of the earth =  $7.3 \times 10^{-5}$  /s and  $\Phi$  is latitude in degrees)

$f^*$  - vertical Coriolis parameter  $2\Omega \cos(\Phi)$  (considered not be significant in wind energy)

$r$  - radius of curvature (of a pressure system) (m)

$F_{(x,y,z)}$  - three components of frictional and/or dissipative forces (N)

The terms of the moment equation I, II, III, IV, V, VI and VII are described below for reference in later sections.

**I** - an inertial term that describes the temporal variation of the wind components.

**II** - expresses the influence of local inertial interactions between the three wind velocity components on the wind flow vector (such as from advection).

**III** - pressure forces (e.g., between high and low pressure systems and hydrostatic pressure).

**IV** - gravitational force that acts only in the negative z direction.

**V** - Coriolis force due to the Earth's rotation.

**VI** - centrifugal force of curved motion around pressure systems (the upper sign applies to flows around low pressure systems, the lower sign to flows around high

pressure systems).

**VII** - frictional forces due to the turbulent viscosity (Reynolds stresses) of air and surface friction.

Each term can have a greater or smaller significance depending on the spatial and temporal scale of the atmospheric flow in question.

Air pressure is a measure of the air mass above a given location that is dependent on temperature. In the absence of strong vertical accelerations, pressure decreases with height described by the hydrostatic equation, Eq. (3.6).

$$\frac{\partial p}{\partial z} = -g\rho = -g\frac{p}{RT} \quad (3.6)$$

Where:

$R$  - universal gas constant ( $\text{JK}^{-1}\text{mol}^{-1}$ )

$T$  – absolute temperature (K)

The pressure gradient forces (III) are the principal driving forces in atmospheric flow. At large spatial scales (i.e., synoptic scales of  $\sim 1000$  km), when unequal heating occurs across the earth's surface, rising air in warm air masses creates lower surface air pressures. However, the rate of reduction in pressure with height is lower in warmer air masses compared to the cooler air masses. This gives rise to horizontal pressure gradients aloft which produces winds that blow from the high pressure area to the lower pressure area aloft to reduce the pressure gradients. This further reduces the pressure on the surface of the warmer air mass and surface air flows (wind) from the cold air mass that has higher surface pressure. All the other terms in the momentum equations just redistribute or dissipate the momentum created by the pressure gradient forces, i.e., the pressure gradients are the only driving forces. Above the ABL in the free stream wind, frictional forces (VII) are not significant. The Coriolis force (V), an “apparent” force, balances the pressure gradient forces (III) giving geostrophic winds that flow parallel to pressure isobars, Eqs. (3.7) and (3.8).

$$-\rho f u_g = \frac{\partial p}{\partial y} \quad (3.7)$$

$$\rho f v_g = \frac{\partial p}{\partial x} \quad (3.8)$$



Where:

$u_g$  and  $v_g$  are geostrophic wind components towards east and north respectively

In some instances the centrifugal forces (VI), also apparent forces, around pressures systems of high curvature must also be considered. As the tendency for flow is from high to low pressure, the centrifugal forces of high pressure systems create winds that add to the geostrophic winds, while the opposite is the case for low pressure systems. The resulting gradient winds are described by Eqs. (3.9) and (3.10) (Holton and Gregory, 2012).

$$-\rho f u = \frac{\partial p}{\partial y} \pm \rho u \frac{|\vec{v}|}{r} \quad (3.9)$$

$$\rho f v = \frac{\partial p}{\partial x} \mp \rho v \frac{|\vec{v}|}{r} \quad (3.10)$$

Below the free stream wind, i.e., in the ABL, drag forces (VII) due to surface roughness become increasingly significant the closer to the earth's surface. These have a deceleration effect the wind flow as the pressure gradient and frictional forces at the earth's surface come into balance. This causes a directional change in the wind flow from the geostrophic wind direction, that is parallel to pressure isobars, towards the direction of the pressure gradient forces (III) across the isobars. The interaction of flow with larger surface physical features such as mountain ranges, flat continental plains and coastal regions can alter large scale circulation patterns, creating smaller scale flow pattern on horizontal spatial scales from 10s to 1000s km, giving rise to regional or mesoscale wind climates. At the microscale level from single km down to sub-metre wind flow is further influence local terrain, surface roughness features, obstacles etc. Drag forces (VII) dominate at this scale and flow is normal to pressure isobars, i.e., in the direction of the pressure gradient.

### 3.2.2 Vertical profile of the ABL

The ABL over flat terrain is divided into three basic sub layers, Fig. 3.2.

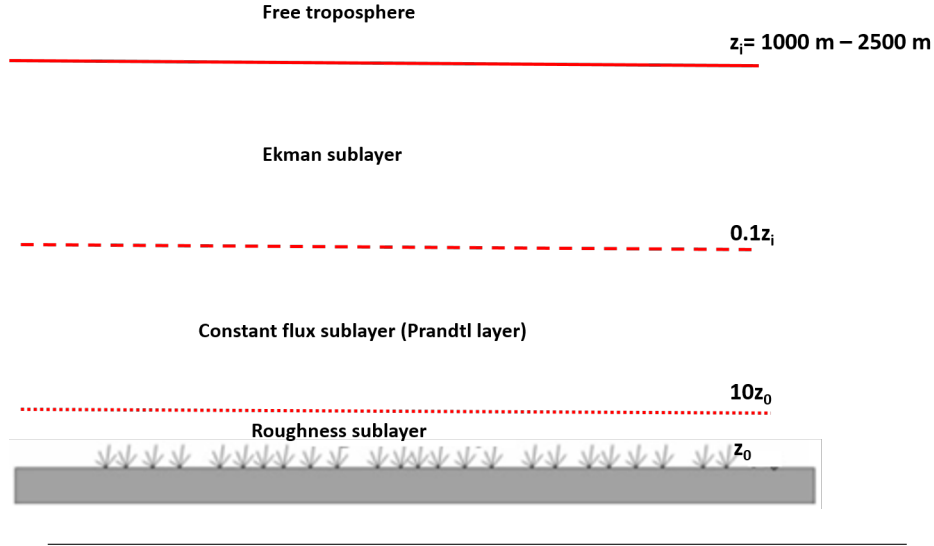


**Fig. 3.2.** Basic structure of the ABL (not to scale) - adapted from (Emeis, 2013).

At flat field locations, the RSL is just millimetres to a few centimetres high and is of little relevance to wind energy. The constant flux sub-layer (also known as surface boundary layer (SBL) or the Prandtl layer) is defined meteorologically as the region of the atmosphere where turbulent vertical fluxes of heat, momentum and moisture deviate less than 10% from surface values. It covers  $\sim$  the first 10% of the total ABL depth. In this layer, wind flow is heavily influenced by the roughness of the earth's surface due frictional forces giving rise to a variation of wind speed with height. Ground surface features such as vegetation and obstacles have a slowing effect on wind speed close to the ground and can increase turbulence in the flow. Wind shear represents the variation in the horizontal component of wind speed with height as a result of frictional influence (turbulent shear stress) of the earth's surface and the state of thermal stability of the ABL. The SBL extends up to  $\sim$  200 m and is where most onshore commercially operating wind turbine are situated today, i.e., rotor tip heights  $\sim$  100 m to 200 m. The Ekman layer is the third and uppermost layer that occupies approximately 90% of the ABL. In the Ekman layer the variation of wind speed with height decreases and gradually changes direction (wind veer) as the Coriolis force has an increasing influence on wind flow with increasing height. At the top of the Ekman layer, wind flow returns to geostrophic flow, entering the

free troposphere (or free atmosphere) where surface effects don't impact on wind flow and the Coriolis force and pressure forces dominate. As wind turbines become larger, their rotors may partially extend into the Ekman layer where the influence of the Coriolis effect needs to be considered, particularly with respect to the wind veer within the rotor swept area. However, this would be more of more concern for future large offshore wind turbines and not deemed to be a significant issue for distributed wind systems that are likely to remain operating in the Prandtl layer.

The wind speed at the surface reduces to zero at or near the surface at a height known aerodynamic roughness length  $z_0$  which is defined by the no-slip condition for viscous fluid flow, Fig. 3.3 (Nakayama and Boucher, 2000).  $z_0$  is an aerodynamic parameter that gives a measure of the height above a surface at which wind speed reduces to zero. It is a function of surface physical properties only and does not change with wind speed or atmospheric stability (see later) (Stull, 1988). Surface roughness lengths are used to categorise the roughness of various surface types (Manwell, McGowan, and Rogers, 2009).  $u'$  and  $w'_s$  represent turbulent the fluctuating wind speed about the mean wind speed in the horizontal direction and the vertical direction (at surface) respectively.

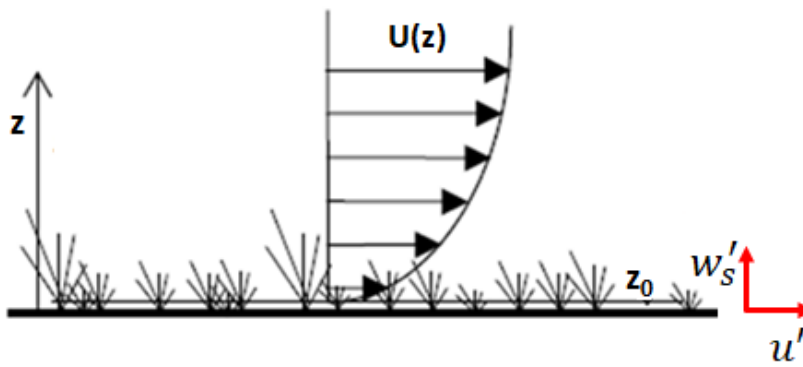


**Fig. 3.3.** Surface roughness height, wind speed fluctuations and mean wind speed profile (not to scale) - adapted from (Mertens, 2006).

The height and wind speed profile with height of the ABL is further complicated by the impact of thermal energy exchange between the earth's surface the ABL on turbulence. This can vary substantially on a diurnal basis depending on heat flux exchange (as result of solar irradiation) between the earth's surface at any given time and space. Heat flux is considered positive if it is directed from the atmosphere towards the ground (i.e., cooling the atmosphere), giving rise to a thermally stable atmosphere. A negative heat flux directed towards and heating the atmosphere results

in an unstable atmosphere. No net heat exchange give rise to a neutral atmosphere. This will be discussed further in Chapter 7.

### 3.2.3 Urban wind profiles

(Britter and Hanna, 2003; Millward-Hopkins, 2013; Barlow, 2014) suggest that a fully formed UBL can vary from 200 m in suburban areas to over 400 m dense in city centre environments, but that three sublayers within the UBL can form, Fig. 3.4. In descending order with height, these are the ISL, RSL and CL layers, as was discussed in the literature review.

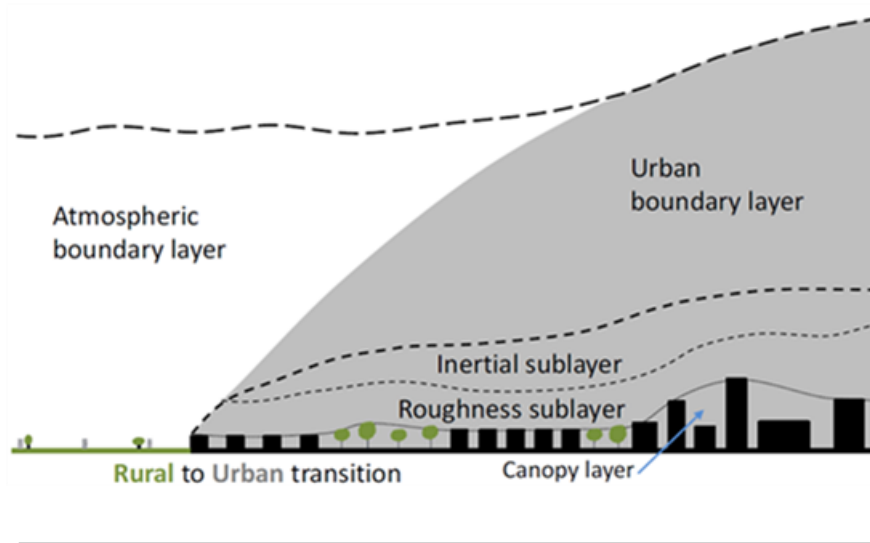
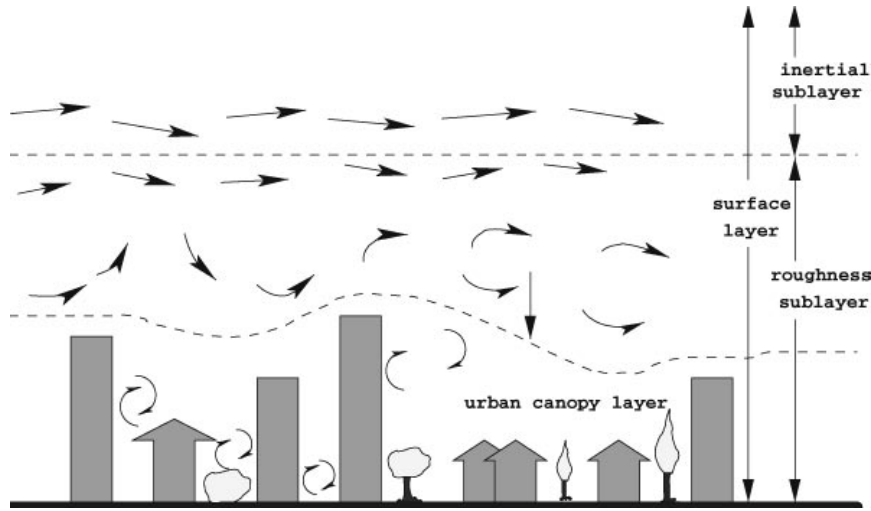


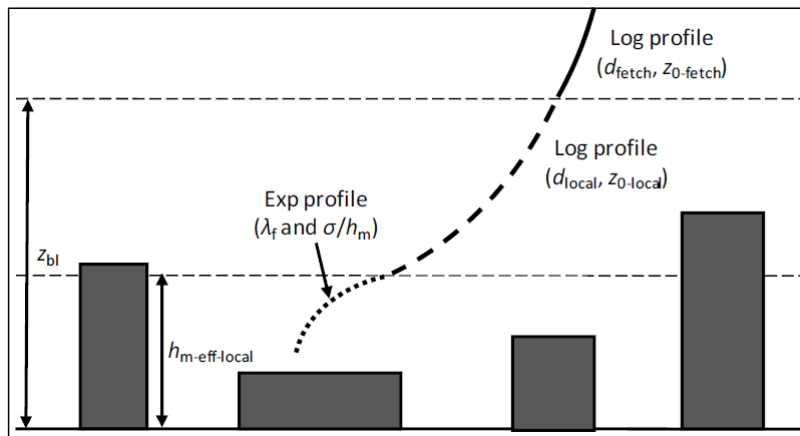
Fig. 3.4. Schematic of sublayers within the UBL (Millward-Hopkins, 2013).

The ISL is defined by a constant shear stress that gives homogeneous flow. It extends from  $\sim 100$  m to 200 m. This is a reason for UK Met Office approach using 200 m as a reference height for the UBL. Above the ISL wind speeds increase at a lower rate with height, i.e., reduced wind shear. The wind shear profile within the ISL can be described by the log law, assuming neutral stability at higher wind speeds. The profile depends on the broader region,  $\sim 1$  km, of surface roughness and displacement height, Fig. 3.5. The RSL has a higher level of spatial variation in the flow as it is more influenced by buildings. The RSL can extend from 2 to 5 times the height of the buildings (Barlow, 2014). The upper extent of the RSL is also referred to as the blending height (Grimmond and Oke, 1999). The average vertical wind speed profile can also be described as logarithmic and depends on the local surface roughness and displacement height. However, the high spatial deviations in wind speed can

lead to greater uncertainty in energy predictions from wind turbines in this layer. (Rooney, 2001; Britter and Hanna, 2003; Cheng et al., 2007; Millward-Hopkins et al., 2013c). Also, a limitation of ?? is that its prediction of the IBL height exceeds the upstream wind ISL with fetches greater than a few km (Best et al., 2008).



(a) Sublayers within UBL (Britter and Hanna, 2003)



(b) Schematic of sublayer wind speed profiles - adapted from (Millward-Hopkins et al., 2013b)

**Fig. 3.5.** Schematic of sublayer wind speed profiles.

The lowest layer, the CL, has a height in that is similar to the building heights up to  $\sim 25\%$  of the mean building height above the rooftops (Millward-Hopkins et al., 2013a). It consists of complex flow above, around and in between buildings. The flow complexities can include vortices, channelling and flow recirculation (Balogun et al., 2010; Theeuwes et al., 2019). Wind shear profiles are very difficult to predict in the CL. (Macdonald, 2000; Coceal and Belcher, 2004) suggest that that wind shear profiles can be approximated by exponential functions. When canopy forces are

in equilibrium, the stress divergence is equated with the drag force, ??, giving an exponential wind profile for  $u(z)$ . However, there are very high uncertainties in the profiles. The CL is very challenging for wind energy exploitation.

In real urban zones, to estimate logarithmic wind shear profiles, the aerodynamic parameters of the heterogeneous surfaces still have to be considered. The area considered should contain a sufficient number of buildings for surface homogeneity so that the bulk aerodynamic effects are meaningfully represented by  $z_0$  and  $d_0$ , but must not be overly large so that it does not contain a large mix of surface types, e.g., parks, industrial, residential etc. (Millward-Hopkins, 2013). In many studies, regions or surface roughness patches up to 1 km to 2 km are considered (Barlow, 2014; Allen et al., 2017). This is because up to a certain height (blending height), the influence of roughness patches of these sizes can affect wind flow such that individual IBLs can form for significant surface roughness changes from one patch to another, ??.

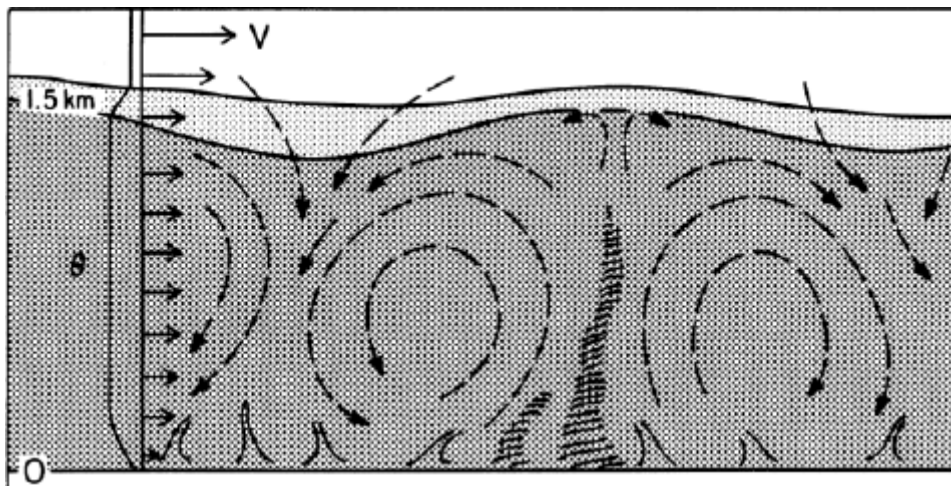
### 3.2.4 Thermal stability in the ABL

The height and wind speed profile with height of the ABL is further complicated by the impact of thermal energy exchange between the earth's surface the ABL on turbulence. This can vary substantially on a diurnal basis depending on heat flux exchange (as result of solar irradiation) between the earth's surface at any given time and space. The heat flux exchange can either be positive or negative depending on complex physical processes that are taking place at any given time, which is dependent on the electromagnetic properties of the earth's surface (e.g., absorptivity, reflectivity, and emissivity) at a given location. Heat flux is considered positive if it is directed from the atmosphere towards the ground (i.e., cooling the atmosphere) and negative if it is directed towards or heating the atmosphere. These give rise to three states of stability in the ABL (Wyngaard, 1990), which are:

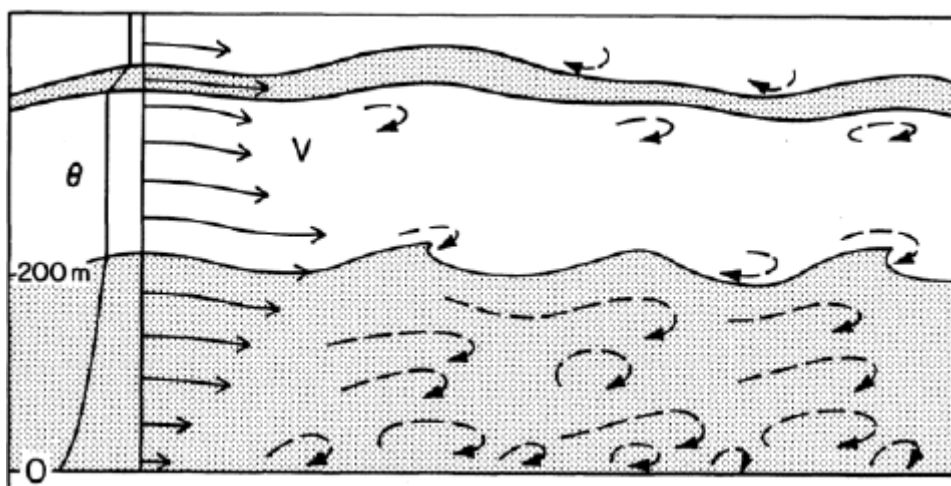
- *Unstable* - heat exchange is from the earth's surface to the atmosphere that usually occurs at time of high solar irradiance. This gives rise to warmer air of lower density on the bottom and cooler denser above and results in a convective boundary layer in which wind shear is reduced by turbulence mixing from vertical convective eddies, but turbulence is increased, Fig. 3.6(a).



- *Stable* - net heat exchange from the atmosphere to the earth's surface, i.e., the atmosphere is cooled from below, usually occurs at night. This give rise to a stable atmosphere where more dense cooler air is at the bottom under warmer air higher up. This suppresses convective eddies and thermally generated turbulence. High wind shear is feature of a stable atmosphere that can generate turbulence (mechanically) in horizontal wind flow, Fig. 3.6(b).
- *Neutral* - there no net heat exchange between the earth's surface and atmosphere, which usually occurs during periods of reduced solar irradiance, e.g., cloudy days or diffuse radiation. Neutral like conditions are more common at higher wind speeds.



(a) Unstable convective ABL



(b) Stable ABL

Fig. 3.6. Schematic overviews of unstable and stable ABL (Wyngaard, 1990).

In the context of wind energy, stability impacts on both wind shear and turbulence can give rise to added cyclical forces on wind turbine blades as they move round the rotor disc area. This has implications for the overall mechanical and structural design of a wind turbine system (including foundations, tower, nacelle and rotor). It also has implications for power performance as the wind turbine rotor disc is subjected to varying wind speed across the rotor disc.

Stability can be accounted for in the log law using a stability correction factor  $\psi$ , Eq. (3.11).

$$u(z) = \frac{u_*}{\kappa} \left( \ln \left( \frac{z-d}{z_0} \right) - \psi \left( \frac{z}{L} \right) \right) \quad (3.11)$$

$L$  is a length scale, known as the Obukuv length. It can be interpreted as the height above which turbulence production from buoyancy factors begins to dominate over production from mechanical wind shear, (Stull, 1988), and can be calculated from, Eq. (3.12).

$$L = \frac{-\bar{\theta}_v u_*^3}{\kappa g \left( \overline{w' \theta'_v} \right)_s} \quad (3.12)$$

Where:

$\bar{\theta}_v$  - virtual potential temperature (K) (it accounts for the effects of pressure and humidity)

$\overline{w' \theta'_v}$  - virtual potential heat flux (Km/s) (It includes both sensible and latent heat flux)

It should be noted that the virtual potential temperature used in this context is a per unit (kinematic) representation of heat energy, i.e., normalised to density and specific heat.

A positive  $L$  is a stable atmosphere,  $L = 0$  is neutral and a negative  $L$  is unstable. Based on meteorological field experiments, the following  $\psi$  relations have been formulated for the different stability conditions (Stull, 1988; Emeis, 2013). The unstable form of  $\psi$  is given by Eq. (3.13)

$$\psi \left( \frac{z}{L} \right) = 2 \ln \left( \frac{1+x}{2} \right) + \ln \left( \frac{1+x^2}{2} \right) - 2 \tan^{-1}(x) + \frac{\pi}{2} \quad (3.13)$$

Where:

$$x = \left( 1 - \frac{16z}{L} \right)^{\frac{1}{4}}$$



The stable form is given by Eq. (3.14).

$$\psi\left(\frac{z}{L}\right) = \begin{cases} -\frac{az}{L} & \text{for } 0 < \frac{z}{L} \leq 0.5 \\ -\frac{az}{L} + B\left(\frac{az}{L} - \frac{C}{D}\right)e^{-\left(\frac{BC}{D}\right)} - \frac{BC}{D} & \text{for } 0.5 < \frac{z}{L} \leq 7 \end{cases} \quad (3.14)$$

Where:

$a = 5$ ,  $A = 1$ ,  $B = 2/3$ ,  $C = 5$  and  $D = 0.35$

A practical implication in the determination of  $L$  using Eq. (3.12) requires the use of three dimensional ultrasonic anemometry with sample rates of at least 10 Hz in order to determine  $\overline{w'\theta'_v}$  and  $u_*$  as well as temperature sensors for  $\overline{\theta'_v}$ . An alternative method to determine atmospheric stability based on the Richardson number is described by Eq. (3.15).

$$R_i = \frac{\frac{g}{\theta} \frac{\partial \overline{\theta}}{\partial z}}{\left(\frac{\partial \overline{u}}{\partial z}\right)^2} \quad (3.15)$$

This can be approximated, Eq. (3.16), to a usable form for less costly measurement setups of temperatures and horizontal wind speeds, measured at two heights, on a met mast (Kelley, 2017). The measurement can be logged in 10-minute mean values.

$$R_i = \frac{g(T_2 - T_1)(z_2 - z_1)}{0.5((T_2 + T_1)(U_2 - U_1)^2)} \quad (3.16)$$

Where:

$z_1, z_2$  - two measurement heights (m)

$T_1, T_2$  - mean absolute temperature measurements at the two heights (K)

$U_1, U_2$  - horizontal mean wind speeds at the two heights (m/s)

In general,  $R_i < 0 \Rightarrow$  unstable;  $R_i = 0 \Rightarrow$  neutral;  $R_i > 0 \Rightarrow$  stable.

### 3.3 Modelling the atmosphere for wind energy

As air motion in atmosphere occurs on a wide range of spatial and temporal scales, it is computationally not possible at present to simulate wind flow at all scales simultaneously at high resolutions in a single modelling process. Therefore, modelling of the ABL for wind energy is divided into different categories of scale to solve the dynamic equations (Sanz Rodrigo et al., 2017). At each scale, the appropriate terms of Eqs. (3.3) to (3.5) are used and some may be simplified or ignored depending on their significance, Fig. 3.7.

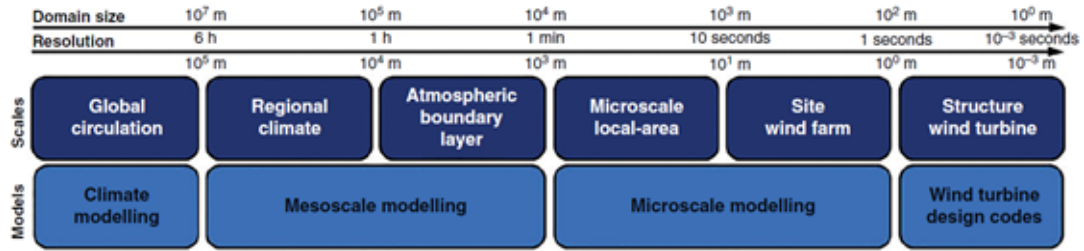


Fig. 3.7. Categories of modelling scales applicable to wind energy - adapted from (Sanz Rodrigo et al., 2017).

#### 3.3.1 Global circulation and Mesoscale models

Atmospheric global climate models (GCM) simulate large scale atmospheric motions and thermodynamic processes. They assimilate weather data observation from numerous surface observations stations around the globe and use numeric weather prediction models (NWP) to simulate the state of the atmosphere in three to six hour timeframes in a process termed “analysis”. They solve the sets of partial differential equations Eqs. (3.1) to (3.5) outlined in the previous section, along with equations of state (relating to density, pressure and temperature) and other process equations that describe the dynamic and thermodynamic processes in the earth’s atmosphere. The equations are discretised appropriate to the domain of interest, therefore not all scales of motions and processes are represented (Kniervel, 2006).

In GCMs, computational grid spatial resolutions are in the order of hundreds of km (Ambrizzi et al., 2019). In addition, historical surface data observations over a long term time period, e.g., years or decades, combined with the increasing volume of remote observation can be used by the NWP models to perform hind casts or reanalyses to generate long-term historical “reanalysis” data sets, which have now

an increasing significance in wind resource assessment (Kim, Kim, and Kang, 2018). These reanalysed data sets include of a variety of meteorological parameters, including wind speed and direction at multiple heights in the atmosphere. These have temporal scales in the order of hours with spatial scales of about 100 km, but in some cases down to one hour time resolution and 50 km spatial resolution. The choice of the horizontal and vertical grid structure and domain impacts the equation set and model performance. Current spatial scales implemented in GCM models, due to computational constraints, don't capture the effects of mesoscale features associated with associated with regional orography, such as mountains and coastal areas, i.e., spatial scales down the order of 10s of km. Therefore, limited area models (LAM) or regional climate models (RCM), also referred to as mesoscale models, are used to simulate the climate and weather forecasts at higher spatial and temporal resolutions (Ambrizzi et al., 2019).

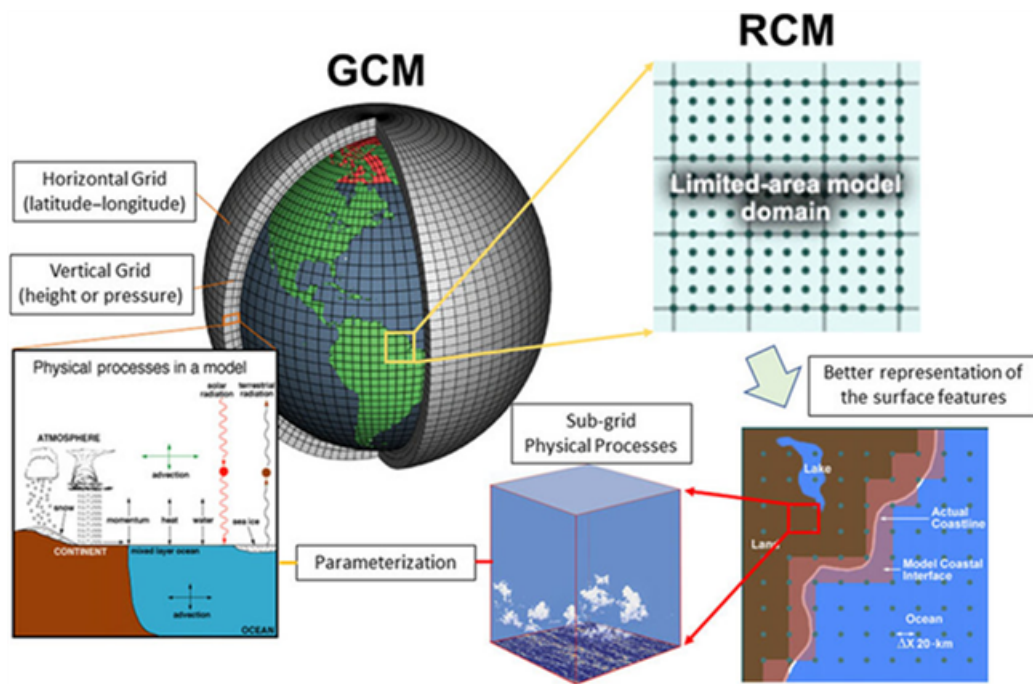


Fig. 3.8. Downscaling from GCMs to RCMs (Ambrizzi et al., 2019).

These regional or mesoscale models attempt to capture orographic features such as hills, valleys, and escarpments that can affect wind flow by channelling winds caused by deflection forces near a single feature. Such features include, single mountains, gaps between hills, narrow valleys and over a water body between two land-masses. Channelling usually results in an increase in wind speed however, wind

speed and directional changes depending on the size of the physical feature and scales of the winds involved. A number of thermally influenced flows, such as diurnal katabatic flows and gravity accelerated downslope winds in the lee of hills that can occur when strong thermally stable winds are forced over hills. Similarly, at locations near to large water bodies, such as coastal areas or near the shorelines of large lakes, the high heat capacity of water leads to uneven heating of the land and water surfaces that can result in thermally driven circulation of winds between the landmass and water body giving rise to land and sea breezes.

As well as surface roughness properties, large variations in elevation associated with hill and mountainous areas can introduce orographic drag. Orography refers to the elevation characteristics of the terrain. Depending on orographic complexity, the application of the wind speed profile laws in complex hilly and mountainous terrain is not always straight forward. One of the challenges with mesoscale models is a biased under estimations of wind speeds and accuracy of wind direction estimations due to unresolved complex and mountainous terrain effects (Standen et al., 2017). The shape, spatial scale and elevation variation can create a variety of mechanically influenced wind flows, such as speed up over crests of hills, gap and valley channelled flows between hills, flow blockage and flow steering. Orographic influences can span across the mesoscale to microscale ranges. Many linear downscaling flow models that assess orography and based on, or on some variation, of the Jackson-Hunt model that describes two dimensional wind flows over two dimensional low hills (Jackson and Hunt, 1975). In the Jackson-Hunt model, flow streamlines over hills are forced up and displaced by height variation of the terrain in the lower layer. Flow is divided into an inner layer where the perturbation shear stress and turbulence are significant and an inviscid outer layer where the perturbation diminishes and eventually vanishes with height.

Another approach is analysing the terrain shape causing the flow perturbation in terms of Fourier components and the equation are solved in Fourier space. Fourier transforms are used to independently calculate of velocity perturbations for each wavenumber vector. Inversion of the Fourier transforms gives the solutions for velocity perturbations in real space. A limitation of the approach is that it cannot account for flow separation effect and thus limits usage to terrain slopes of less than  $\sim 17^\circ$ . It has limitations in that the ratio of the height of the hill to its width must

be small. The UK Met Office UM, in mesoscale to microscale downscaling, employs orographic roughness parametrisation below reference height  $z_{ref}$ , that is characterised by a local orographic wave number  $k_w$  and a tuneable parameter  $a$ , (Howard and Clark, 2007). More details of the UK Met Office UM model will be given in Chapter 5 in describing the mesoscale remodelled Irish wind atlas, on which it is based. In this research, assessment of the mesoscale wind features in the region of the wind turbine site is made with the wind atlas and an evaluation of its energy prediction of the wind turbine compared to the actual wind turbine EER. This is to help inform the separate mesoscale influences with the microscale influences, particularly buildings, in shaping the measured *EER* of the wind turbine assessed in Chapter 4.

Thermal influences on wind climates can vary on seasonal and diurnal scales depending on location, broadly determined by atmospheric stability. In mountain/valley areas, heated rising air during the day can give relatively gently upslope winds from valley floors, known as anabatic winds. In the vicinity of large water bodies, such as the sea, during the day the land heats faster and air rises and reduces local air pressure at the surface. This results in wind flow from the sea to give a sea breeze. The sea breezes may be strongest in the afternoon when land is warmest and vertical turbulence circulation is strongest. The circulation reverses at night to give a land breeze from the land to the sea, but is not as strong, as the land can cool down faster. The strength of these winds may have seasonal peaks due to seasonal time lags in heating the water body.

NWP models at all scales are still far from perfect and have number of limitations, such as errors introduced in the discretisation process of the governing equations Eqs. (3.1) to (3.5), goodness of knowledge of initial conditions, boundary conditions and unresolved sub-grid processes that need to be parametrised. Another inherent limitation of current mesoscale modelling techniques for wind atlas generation is that the physical models of the atmosphere use don't fully account for the dynamical chaos of the atmospheric system (Sanz Rodrigo et al., 2017). It is intended that the next generation of mesoscale models for wind resource assessment will use probabilistic approaches based on ensemble predictions to help account for uncertainty of the physical models and imperfect observations of the atmosphere. However, these may still be limited by not being able to fully account for all sources

of error (Dörenkämper et al., 2020). This will require further research to improve the physical models along with higher resolution downscaling and calibration based on the past records of the ensemble errors.

### 3.3.2 Microscale models

Microscale models are used to assess local influences at a location of interest at smaller spatial scales in the order of 100s m to 10 s of km to optimise the siting of wind turbines for energy production. Microscale models consider influences of local orography and surface roughness at higher resolutions than mesoscale models as well as obstacles. Frictional forces (VII) in equations Eqs. (3.3) to (3.5) dominate at this scale and flow characteristics in the Prandtl layer is of most interest, particularly for distributed wind. Microscale models can consist of analytical or numerical flow models. They can be initialised from the outputs of mesoscale models, but can also be driven by local wind measurements, if available in sufficient quality and quantity, i.e., good quality measurement setup with records of a least one year of high-resolution wind measurements (e.g., 10-minute average data or higher resolutions). Both linear and CFD microscale modelling approaches are widely used in the wind industry. They have varying degrees of complexity, accuracy and cost depending on the site complexity and size a of wind project.

### 3.3.3 Linear flow model approaches

The Wind Atlas Application Program (WAsP) is a relatively common microscale modelling method used in the wind industry. Linear WAsP-IBZ is a diagnostic tool which calculates wind statistics by parametrising the influence of orography, roughness and obstacles (Topaloglu and Pehlivan, 2018). It was used in the development of the first European Wind Atlas (Troen and Lundtang Petersen, 1989). The general approach to linear flow models is outlined in Fig. 3.9. It requires measurements from a nearby measurement mast, preferably within 50 km of the wind turbine or wind farm location, and extrapolates it to the turbine hub height at the site of interest. At least one year of wind data from the reference masts at some reference measurement height is recommended (Landberg et al., 2003; Petersen and Troen, 2012).

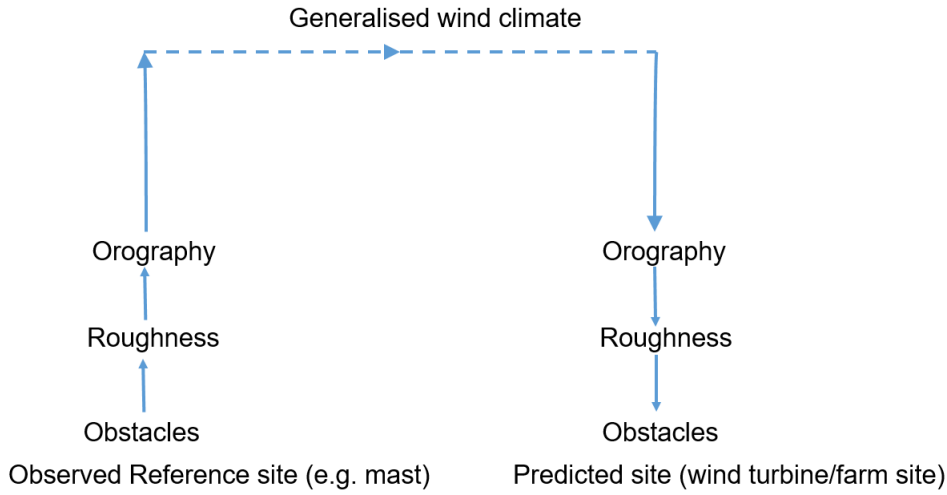


**Fig. 3.9.** General flow diagram in linear model assessment.

Assessments are carried out on local obstacles, surface roughness and orography at the reference mast location. Their impacts on wind speed and direction are accounted for in upscaling the met mast data to create a terrain independent generalised wind climate for the region. The generalised wind climate is describe by statistically binned wind speeds and directional sectors. It is assumed the generalised wind climate at the wind turbine location is the same as that at the reference met mast location. It is then downscaled at the wind turbine location to hub height accounting for local surfaces roughness, obstacles, orography and any neighbouring wind turbines. Wind turbine power curves are then combined with the modelled hub-height wind statistics data to predict and optimise wind turbine or wind farm *AEP*.

### 3.3.4 Orography

In the microscale modelling context, orography is modelled by linearization of the Naiver-Stokes equations, describing two-dimensional turbulent flow over low hills. The linear 'BZ-model' of (Troen and Lundtang Petersen, 1989), which is a wavenumber scaling technique based on Jackson-Hunt model referred to previously, is integrated (IBZ) into WAsP. It calculates the wind velocity perturbations in the boundary layer induced by orographic features. It uses a zooming mesh of high-resolution terrain height contour lines (20 m) close ( $\sim 1$  to 2 km radius from the centre of site location) to the site of interest with a lower resolution further away up to 5 km from

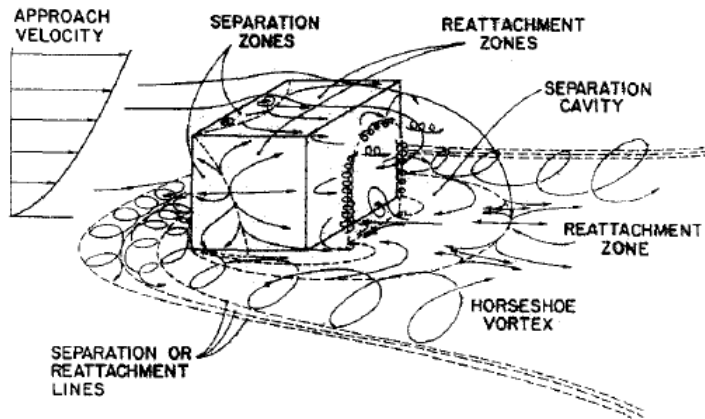


the site. It works best in terrain with slopes less than  $17^\circ$  and assumes steady state attached flow and neutral atmosphere stability. To improve the model in more complex terrain, (Mortensen and Petersen, 1998) applied a statistical correction based on a terrain's ruggedness index (RIX). The RIX value at given site is defined as the fractional extent of the surrounding terrain that is steeper than a certain critical slope and is a coarse measure of the extent of flow separation and bias of the model induced by terrain slopes. This technique uses a polar coordinate system, each radial line originating from the location of interest is divided into line segments by terrain height contour lines. The RIX value of the radius in question is the sum of the line segments representing slopes greater than a critical slope value divided by the entire radius. The overall RIX value for the site is the mean of the radius-wise RIX values. Attached flows are assumed when the overall RIX is close to zero. If  $RIX > 0$ , it is indicative that somewhere in the surrounding area the slopes are greater than  $0.3$  ( $17^\circ$ ) meaning the onset of flow separation. Accuracy can be improved by using at least two mast measuring locations on a site and establishing relationships using RIX differences ( $\Delta RIX$ ) between the measured (met mast) location and the wind turbine/farm site of interest. A regression analysis of WAsP-IBZ cross prediction error in wind speed from one mast to the other against  $\Delta RIX$  enables an empirical correction factor that is applied to the biased wind speed predictions in order to obtain the true wind speed at wind turbine hub height locations across a site. However, implementing multiple met masts increases costs.

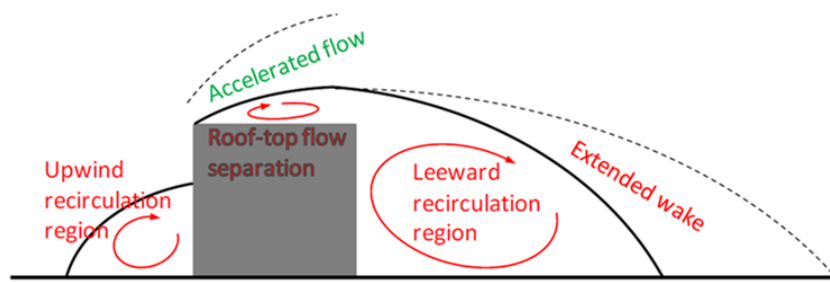
### 3.3.5 Obstacles

Surface obstacles in close proximity to the site of interest can have wake effects that can additionally perturb wind flow downwind of the obstacle. Fig. 3.10 show the complex wind flow around standalone three-dimensional cuboid structures that can consist of flow detachment, separation cavities and recirculation zones in the wake, flow reattachment and vortex shedding (Peterka, Meroney, and Kothari, 1985; Millward-Hopkins, 2013; Micallef and Van Bussel, 2018). As outlined in the literature review, complex recirculation zones that define the near wake can extend up to 2 to 6 times the obstacle height downwind of an obstacle, while the far wake may extend to up to 18 times the obstacle height. (Nieuwpoort, Gooden, and Prins, 2010; Vasilopoulos, Sarris, and Tsoutsanis, 2019).





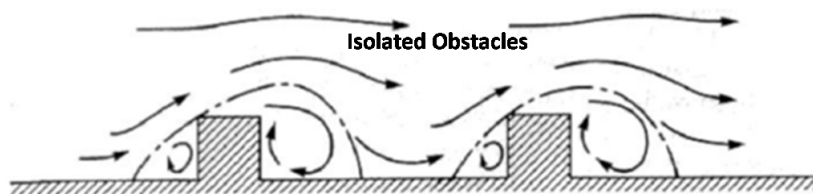
(a) Schematic of 3D flow



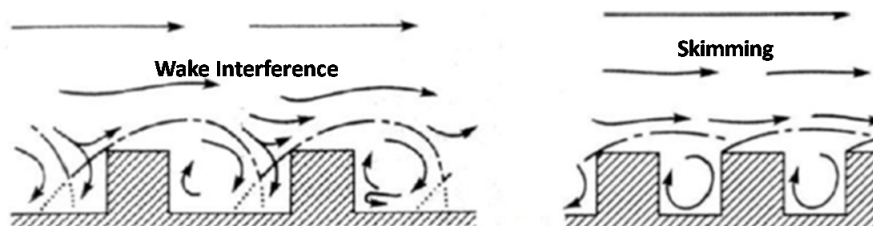
(b) Zones of flow in vertical plane

**Fig. 3.10.** Flow around bluff obstacles (Peterka, Meroney, and Kothari, 1985; Millward-Hopkins, 2013).

(Macdonald, Griffiths, and Hall, 1998) state that it is incorrect to apply the log law lower than twice the height of an obstacle. Some of the basic wind flow regimes are shown in Fig. 3.11 for different building densities (Grimmond and Oke, 1999).



(a) Isolated obstacles sufficiently spaced with no wake interference in the flow



(b) Closer spaced obstacles with wake interference to skimmed flow for high density

**Fig. 3.11.** Flow around multiple obstacles - adapted from (Grimmond and Oke, 1999).

The wakes of sufficiently spaced obstacles have little interference with each other. At closer proximities, wake interference can occur, while increasing spatial density leads to skimmed flow that results in uplift or displacement of the flow (Zajic et al., 2011). In WAsP-IBZ, for a given obstacle, if the turbine hub-height is less than 3 times the height of an obstacle and is less than 50 obstacle heights away from the obstacle then the obstacle is modelled by the WAsP-IBZ shelter model, otherwise it is treated as a surface roughness element. The WAsP-IBZ shelter model is based on a refined version a simple two dimensional obstacle of infinite length, derived from wind tunnel measurements by (Perera, 1981), Fig. 3.12. The fractional reduction in wind speed, downwind of the obstacle is described by Eqs. (3.17) to (3.19), (Troen and Lundtang Petersen, 1989; Peña et al., 2016).

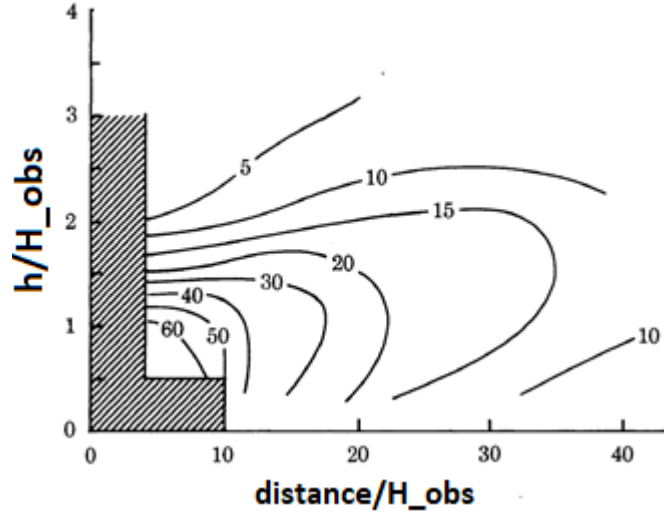


Fig. 3.12. Percentage wind speed reduction in the wake of a two dimensional obstacle - adapted from (Perera, 1981).

$$\frac{\Delta U_z}{U_h} = 9.75 \left( \frac{H}{h} \right)^{0.14} \frac{x}{h} (1 - P) \eta e^{(-0.67\eta^{1.5})} \quad (3.17)$$

$$\eta = \frac{H}{h} \left( K \frac{x}{h} \right)^{\frac{-1}{n+2}} \quad (3.18)$$

$$K = \frac{2\kappa^2}{\ln \frac{h}{z_0}} \quad (3.19)$$

Where:

$\Delta U_z$  – wind speed reduction at height  $z$  (m/s)

$U_h$  – free wind speed at obstacle height (m/s)

$U_z$  – wind speed at height of interest (m) (e.g., turbine hub height)

$P$  – porosity of obstacle (ratio of open area total area)

$h$  – obstacle height (m)

$x$  – distance downstream of obstacle (m)

$H$  – height of interest (m) (e.g., wind turbine hub height)

$z_0$  – surface roughness

$n$  – velocity profile exponent of  $\frac{1}{7}$

In the WAsP-IBZ shelter model, a zone of flow separation is considered to exist within a region defined by a straight line drawn from the top of the obstacle to the ground from 2 obstacle heights upwind of the obstacle to 5 obstacle heights downwind of the obstacle. The formula has limitations as it assumes normal non-skewed incident wind flow at the obstacle. Multiple obstacles are treated by considering the obstacle furthest away first and calculating the individual sheltering by all subsequent downstream obstacles towards the site of interest. If the zones of separation of very close obstacles overlap, then the relative sheltering is reduced by the fraction of the overlap.

### 3.3.6 CFD flow approaches

Numerical CFD models, commonly used in the wind industry are based on Reynolds averaged Navier Stokes (RANS) equations. In RANS CFD modelling wind speed is considered as fluctuations superimposed on time-averaged values, Fig. 3.13. This is represented by Eq. (3.20).

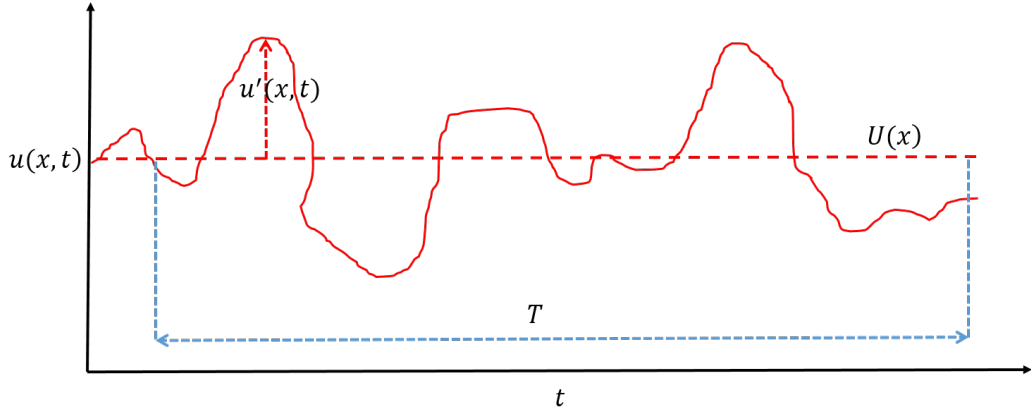


**Fig. 3.13.** Time averaging of wind speed of a period  $T$ .

$$u(x, t) = U(x) + u'(x, t) \quad (3.20)$$

Where:

$U(x)$ — time averaged mean wind speed (m/s)

$u'(x, t)$ — wind speed fluctuation about the mean (m/s)

This representation of wind speed is applied to the Navier Stokes equations Eqs. (3.1) to (3.5) to give the RANS representation that consists of the continuity Eq. (3.21), momentum Eq. (3.22) and turbulence models equations, Eqs. (3.23) to (3.27), for incompressible fluids without body forces (Cheng et al., 2003).

$$\frac{\partial U_i}{\partial x_i} = 0 \quad (3.21)$$

$$U_i \frac{\partial U_i}{\partial x_i} = -\frac{1}{\rho} \frac{\partial P}{\partial x_i} + \frac{\partial}{\partial x_j} \left( v \left( \frac{\partial U_i}{\partial x_j} + \frac{\partial U_j}{\partial x_i} \right) - \overline{u'_i u'_j} \right) \quad (3.22)$$

Where:

$U_i$  - time averaged mean wind speed (m/s)

$P$ — mean pressure (N/m<sup>2</sup>)

$\rho$  - air density (kg/m<sup>3</sup>)

$v$ — kinematic viscosity (m<sup>2</sup>/s)

$u'_i u'_j$  - Reynolds stresses (m<sup>2</sup>/s<sup>2</sup>)

To enable closure of the momentum equation, the Boussinesq linear isotropic eddy-viscosity hypotheses that gives a linear relationship between the Reynolds stresses and the mean velocity gradients is used, Eq. (3.23), (Toja-Silva et al., 2018). It assumes that variations in density does not effect the flow field (inertial term I in Eqs. (3.3) to (3.5)), apart from giving rise to buoyancy forces (term IV in Eq. (3.5)).

$$\overline{u'_i u'_j} = -v_T \left( \frac{\partial U_i}{\partial x_j} + \frac{\partial U_j}{\partial x_i} \right) + \frac{2}{3} k \delta_{i,j} \quad (3.23)$$

Where:

$k$  - turbulence kinetic energy ( $\text{m}^2/\text{s}^2$ )

$\delta_{i,j}$  - Kronecker Delta function

$v_T$  - kinematic eddy viscosity ( $\text{m}^2/\text{s}$ )

To solve Eq. (3.23) a statistical turbulence model is required. In this case, the standard  $k - \varepsilon$  turbulence model is used. The  $k - \varepsilon$  model uses two model transport equations that describes turbulence kinetic energy production  $k$  Eq. (3.24) and turbulence dissipation rate  $\varepsilon$  Eq. (3.25) .

$$\frac{\partial}{\partial x_i} (U_i k) = \frac{\partial}{\partial x_i} \left( \frac{v_T}{\sigma_k} \frac{\partial k}{\partial x_i} \right) + P_k - \varepsilon \quad (3.24)$$

$$\frac{\partial}{\partial x_i} (U_i \varepsilon) = \frac{\partial}{\partial x_i} \left( \frac{v_T}{\sigma_\varepsilon} \frac{\partial \varepsilon}{\partial x_i} \right) + c_{\varepsilon 1} \frac{\varepsilon}{k} P_k - c_{\varepsilon 2} \frac{\varepsilon^2}{k} \quad (3.25)$$

Where:

$c_{\varepsilon 1}, c_{\varepsilon 2}$  - constants

$\sigma_k, \sigma_\varepsilon$  - Prandtl number that connect the diffusivities of  $k$  and  $\varepsilon$  to the eddy viscosity

$P_k$  - the production of  $k$ , which is the product of the kinematic eddy viscosity and the modulus mean rate of strain tensor, Eq. (3.26).

$$P_k = v_T \left( \frac{\partial U_i}{\partial x_j} + \frac{\partial U_j}{\partial x_i} \right) \frac{\partial U_i}{\partial x_j} \quad (3.26)$$

$$v_T = c_\mu \frac{k^2}{\varepsilon} \quad (3.27)$$

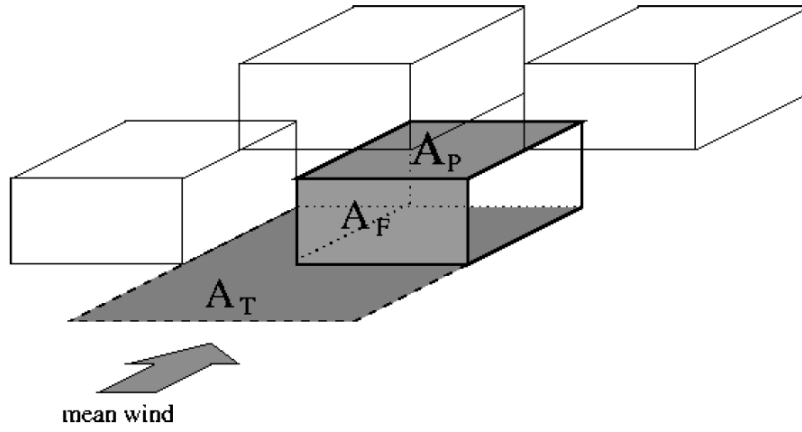
Where:

$c_\mu$  - a constant

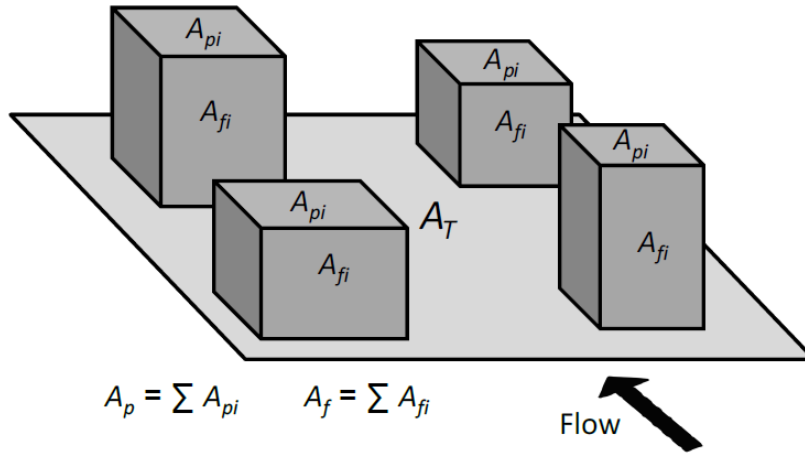
In Chapter 6, the WAsP linear model and three CFD RANS approaches, supplied with onsite LiDAR wind measurements, will be applied in the peri-urban environment and their energy predictions compared to the actual wind turbine energy performance.

### 3.3.7 Morphological approaches in urban environments

Morphological approaches consider geometric properties of buildings to determine surface roughness and displacement height in urban areas. (Macdonald, Griffiths, and Hall, 1998) reviewed morphological methods including those suggested in the European Wind Atlas, (Troen and Lundtang Petersen, 1989), and suggested an improved method to estimate surface roughness from obstacles described earlier by ???. It attempts to account for the non-linear increase in surface roughness length at high roughness densities. They account for peaks in the value of  $z_0$  vs building density and drag coefficients of isolated obstacles of different shapes and layouts. It also allows some calibration of the method with experiments to refine values for  $z_0$  and displacement height  $d$ . A number of experimental wind tunnel studies have attempted to relate morphological characteristics of urban environments to surface roughness and displacement heights using idealised arrays of cubes (Raupach, 1992; Bottema and Mestayer, 1998; Macdonald, Griffiths, and Hall, 1998; Duijm, 1999; Kastner-Klein and Rotach, 2004; Crago, Okello, and Jasinski, 2012; Böhm et al., 2013). The morphological parameters used are the *plan area fraction*,  $\lambda_p$ ; *frontal area fraction*,  $\lambda_f$ ; Eqs. (3.28) and (3.29), and the *mean building/obstacle height*,  $h_m$ .



(a) Geometrical properties of a single obstacle



(b) Geometrical properties of multiple obstacle

**Fig. 3.14.** Geometrical properties used in morphological definitions (Macdonald, Griffiths, and Hall, 1998; Grimmond and Oke, 1999).

$$\lambda_p = \frac{A_p}{A_T} \quad (3.28)$$

$$\lambda_f = \frac{A_f}{A_T} \quad (3.29)$$

Where:

$A_f$  - building frontal area ( $m^2$ )

$A_p$  - building plan area ( $m^2$ )

$A_T$  - total spatial area occupied by the buildings ( $m^2$ )

Assuming that surface drag is dominated by pressure exerted by buildings and that the ISL can be extended by a logarithmic profile, the ISL shear stress Eq. (3.30) and the surface drag Eq. (3.31) can be balanced to derive expressions for  $z_0$ ,  $h_m$  and  $d$  in terms of  $\lambda_p$  and  $\lambda_f$ , Eqs. (3.32) to (3.38).

$$F_D = \rho u_* A_T \quad (3.30)$$

$$F_D = 0.5\rho U_{hm}^2 C_D A_f \quad (3.31)$$

$$U(h_m) = \frac{u_*}{\kappa} \ln\left(\frac{h_m}{z_0}\right) \quad (3.32)$$

Where:

$h_m$  - mean building height (m)

Equating Eqs. (3.30) and (3.31) leads to gives relations of  $z_0$ ,  $h_m$  and  $d$  with morphological parameters  $\lambda_p$  and  $\lambda_f$ .

$$\rho u_* A_T = 0.5\rho \left(\frac{u_*}{\kappa} \ln\left(\frac{h_m}{z_0}\right)\right)^2 C_D A_f \quad (3.33)$$

$$\frac{z_0}{h_m} = e^{\left[-\left(0.5\frac{C_D}{\kappa^2}\lambda_f\right)^{-0.5}\right]} \quad (3.34)$$

When the displacement height  $d$  is included, equations Eq. (3.34) becomes Eq. (3.38).

$$\rho u_* A_T = 0.5\rho \left(\frac{u_*}{\kappa} \ln\left(\frac{h_m - d}{z_0}\right)\right)^2 C_D A_f \left(1 - \frac{d}{h_m}\right) \quad (3.35)$$

$$\frac{z_0}{h_m} = \left(1 - \frac{d}{h_m}\right) e^{\left[-\left(0.5\frac{C_D}{\kappa^2}\left(1 - \frac{d}{h_m}\right)\lambda_f\right)^{-0.5}\right]} \quad (3.36)$$

$$\frac{z_0}{h_m} = \left(1 - \frac{d}{h_m}\right) e^{\left[-\left(0.5\beta\frac{C_D}{\kappa^2}\left(1 - \frac{d}{h_m}\right)\lambda_f\right)^{-0.5}\right]} \quad (3.37)$$

(Macdonald, Griffiths, and Hall, 1998) give a relation between displacement height  $d$  and  $h_m$ , Eq. (3.38).

$$\frac{d}{h_m} = 1 + A^{-\lambda_p} (\lambda_p - 1) \quad (3.38)$$



Where:

$A$  - constant of 4.43 for staggered arrays of cubes and 3.59 for square arrays

(Grimmond and Oke, 1999) reviewed various studies that used morphological methods for application in real-world urban environments that use the geometric properties of building from GIS systems, i.e., the plan areas, frontal areas and spacing between buildings to create algorithms that determine  $z_0$  and  $d$ . The studies focused on a number of cities in North America. They concluded that morphological methods have the potential advantage that tall met towers are not required for measurement. However, because their empirical equations are derived from wind tunnel experiments, a challenge of application in real-world urban environments is the heterogeneous nature of building heights leading to a large scatter in the predicted values of  $z_0$  and  $d$ , illustrated by the grey areas shown in Fig. 3.15.

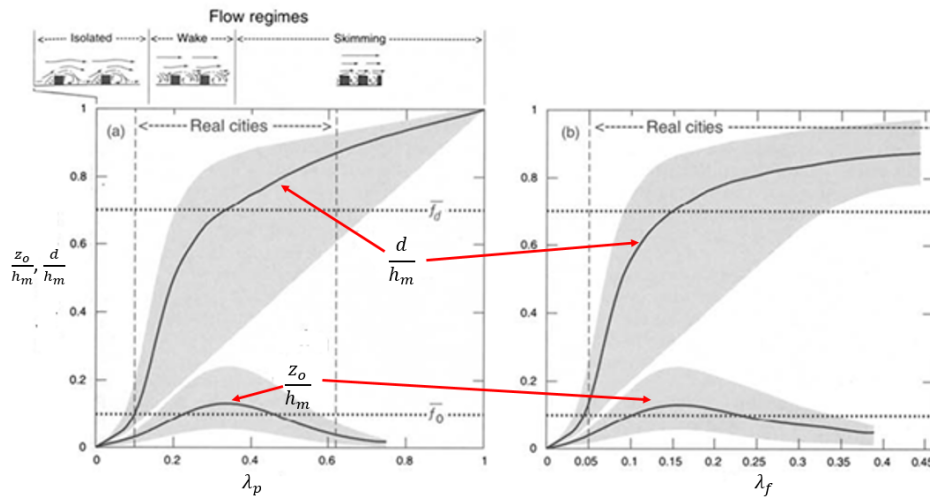


**Fig. 3.15.** A representation of the relationship of  $z_0$  and  $d$  to the plan and frontal area density ratios, (Grimmond and Oke, 1999).

It was also found that a number of the studies were carried out with a limited amount of high quality measurement data at the time resulting in poor agreement and therefore could not find a standard to which morphological algorithms could be tested. Another partial reason for poor agreement was due to necessary simplification of geometric description of the surface and the irreducible errors in the analysis of the available wind measurements over the inhomogeneous surfaces. More recent morphological studies that build on this work, in the context of small scale

wind deployment, showed that these approaches could work well down to the effective mean building heights, but that errors increase in environments with more heterogeneous environments. (Millward-Hopkins et al., 2011) showed that large uncertainties in defining building geometries gave up to 30% to 40% in wind speed predictions that can be even more exacerbated in energy predictions. This particularly was the case in the lower RSL near the CL where wind flow is very sensitive to building geometry. Other methods of urban wind resource assessment methods for small scale wind deployment have been proposed where the surface features of an urban environment described in the form of very complex topographic map that can be used as a compatible input to exiting mesoscale and microscale modelling tools (Simões and Estanqueiro, 2016). The method reduces computation time and is more user friendly. However, the methodology presented needs further characterization and calibration with measured data.

In Chapter 7, the directional morphological properties of the buildings about the wind turbine site and at an offsite met mast, outside the influence of buildings, will be described. These will be used assess their influences on the measured wind characteristics and the wind turbine performance. The results will help inform simplified procedure for a framework of micro siting medium and large scale wind turbines in peri-urban environments, described in Chapter 8.

## 3.4 Wind statistics

### 3.4.1 Temporal wind speed

Wind speed and wind direction are statistical in nature. Horizontal wind speed  $u(t)$ , sampled over given time period  $T$ , can be decomposed into an average value  $U(T)$  with a superimposed short-term fluctuation  $u'(t)$ , Fig. 3.16. If  $u(t)$  is taken a wind speed in the longitudinal  $x - direction$ , the  $v(t)$  and  $w(t)$  can be taken to be the wind speeds in the  $y - direction(lateral)$  and  $z - direction(vertical)$  respectively with similar decompositions into average and fluctuating components.

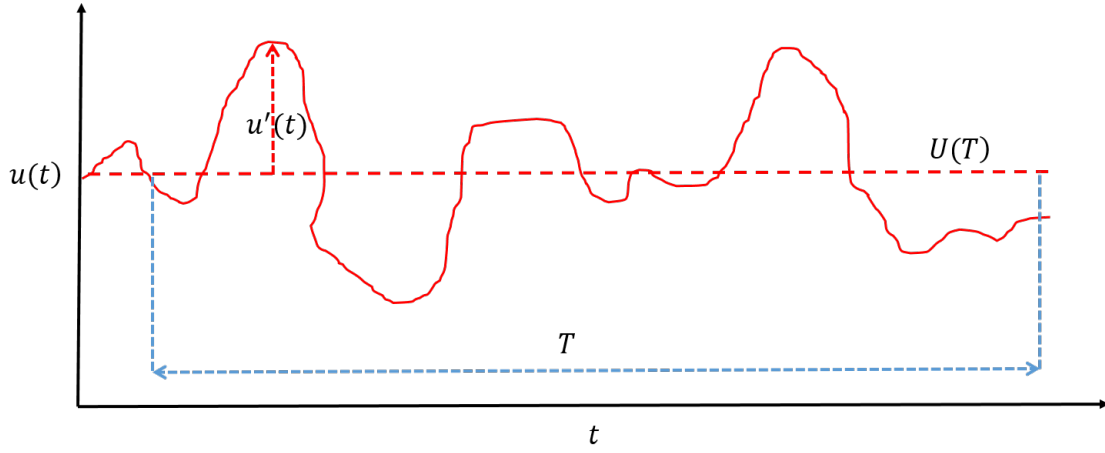


**Fig. 3.16.** Temporal wind speed representation over a period  $T$ .

Typically 2-D wind speed are measured with 1-second sampling rates averaged into 10-minute logged intervals. It is common practice to log the 10-minute average, minimum, maximum and standard deviation wind speeds (IEC 61400-12, 2019). Wind direction is also logged as 10-minute averages. The raw data is logged for at least a year (Roeth, 2010). The data is then quality checked and processed using a *method of bins*. This involves grouping 10-minute average wind data values into specific wind speed intervals (bins) and directional sectors from which frequency distributions of wind speed and direction over the full measurement period can be obtained. The wind speed bins usually have widths of 0.5 m/s and the frequency value of a given bin is taken to occur at mean wind speed value of the bin (close to bin centre). This in turn shows the proportion of time over the full measurement campaign that the wind speed had a given binned 10-minute average value. Similarly wind direction values are grouped into directional sectors commonly with interval widths of  $22.5^\circ$ , i.e., 16 sectors in  $360^\circ$ . The frequency of the wind speed bin data points that occur within each directional sector can be used to create a wind rose. The wind rose is a visual way of showing wind speed values and the proportion of time the wind blows with these values from each wind direction. Time series wind data can be characterised statistically by the well known Weibull distribution described by Eq. (3.39) (Manwell, McGowan, and Rogers, 2009).

$$p(U) = \left(\frac{k}{c}\right) \left(\frac{U}{c}\right)^{k-1} e^{-\left(\frac{U}{c}\right)^k} \quad (3.39)$$

Where:

$p(U)$  = probability density function

$U$  = mean wind speed (m/s)

$c$  = scale factor (m/s)

$k$  = shape factor (dimensionless)

The scale factor  $c$  and shape  $k$  can be determined from fitting a Weibull distribution to the measured wind speed distribution using the method of moments (Azad, Rasul, and Yusaf, 2014). The cumulative density function is described by Eq. (3.40).

$$F(U) = 1 - e^{\left[-\left(\frac{U}{c}\right)^k\right]} \quad (3.40)$$

### 3.4.2 Wind power curves and AEP

For a given Weibull probability density distribution the corresponding cumulative density function gives the portion or fraction of wind speed values that are below a given value of  $U$ , or to determine the proportion of wind speed values between two given wind speeds. Wind turbine power curves at accredited tests sites can be obtained using from binned wind speed Eq. (3.41) and power Eq. (3.42) data following (IEC 61400-12, 2019).

$$U_i = \frac{1}{N_i} \sum_{j=1}^{N_i} U_{n,i,j} \quad (3.41)$$

$$P_i = \frac{1}{N_i} \sum_{j=1}^{N_i} P_{n,i,m} \quad (3.42)$$

Where:

$U_i$  - normalized and averaged wind speed in bin  $i$

$U_{n,i,m}$  - normalized wind speed of data set  $m$  in bin  $i$

$P_i$  - normalized and averaged power output in bin  $i$

$P_{n,i,m}$  - normalized power output of data set  $m$  in bin  $i$

$N_i$  - number of 10-minute data sets in bin  $i$

The cumulative density function, Eq. (3.40) can be combined with a wind turbine power curve to estimate the AEP, Eq. (3.43).

$$AEP(kWh) = \sum_i^{N_i} \left\{ e^{-\left[\left(\frac{U_{i-1}}{c}\right)^k\right]} - e^{-\left[\left(\frac{U_i}{c}\right)^k\right]} \right\} P_i \left( \frac{U_{i-1} + U_i}{2} \right) N_h \quad (3.43)$$

Where:

$N_h$  = number of hours in the year

The directional  $AEP$  for a given directional sector bin “ $j$ ” is based on the fitted Weibull shape and scale factors of the wind speed distribution of the given direction, the time in given direction,  $N_h(j)$ , and the wind turbine power curve, Eq. (3.44).

$$AEP(j) = \sum_1^{N(j)_i} \left\{ e^{-\left[\left(\frac{U(j)_{i-1}}{c(j)}\right)^{k(j)}\right]} - e^{-\left[\left(\frac{U(j)_i}{c(j)}\right)^{k(j)}\right]} \right\} P_i \left( \frac{U(j)_{i-1} + U(j)_i}{2} \right) N_h(j) \quad (3.44)$$

Where:

$j = 360^\circ / \text{sector angular width}$

The total  $AEP$  is the sum the  $AEP$ s in each direction given by Eq. (3.45).

$$AEP = \sum_{j=1}^J AEP(j) \quad (3.45)$$

The  $WPD_{i,j}$  in a given directional sector Eq. (3.46) is time weighted by the number of data points in that sector to give the directional  $WPD_j$ , Eq. (3.47). The the total  $WPD_{tot}$  is the summation of  $WPD_j$  over all sectors by Eq. (3.47).

$$WPD_{i,j} = \frac{1}{2N_j} \sum_{n_i=1}^{n_i=N_{i,j}} \rho_{i,j} U_{i,j}^3 \quad (3.46)$$

Where:

$\rho_{i,j}$  - density of air  $kg/m^3$

$$WPD_j = WPD_{i,j} \frac{N_{i,j}}{N_{tot}} \quad (3.47)$$

$$WPD_{\text{tot}} = \sum_{j=1}^{N_j} WPD_j \quad (3.48)$$

Wind turbine SCADA systems monitor a variety of parameters including wind speed, wind direction, and power output. From this data a novel representation of real-world directional electrical energy output of an operating wind turbine developed in this research. This is referred to as an energy rose (*EER*). For a given directional sector  $j$  of width  $\Delta\theta_j$ , the electrical energy is expressed as summation of the product of mean logging interval power values  $P_{i,j}$  and the logging interval time period  $t_{i,j}$  (e.g. 10-minute), Eqs. (3.49) and (3.50).

$$E_j(\Delta\theta_j) = \sum_{i=1}^{N_{i,j}} P_{i,j}(\Delta\theta_j) \times t_{i,j} \quad (3.49)$$

$$EER_j = \sum_{j=1}^{N_j} E_j(\Delta\theta_j) \quad (3.50)$$

Where:

$N_{i,j}$  - number of points in data set  $i$  in directional sector  $j$

The use of the *EER* is described in Chapter 4 and is a key assessment parameter in subsequent chapters.

### 3.4.3 Turbulence and gust factors

Turbulence and gusts create dynamic fatigue and extreme static loads, than manifest themselves in turbine wear and failures. Using the parameters from Fig. 3.16, the horizontal turbulence intensity  $I_U$  is given by Eq. (3.51) (Wharton and Lundquist, 2012) .

$$I_U(t, T) = \frac{\sigma_u(t, T)}{U(T)} \quad (3.51)$$

The standard deviation  $\sigma_u(t, T)$  is given by root mean square of the variance, Eq. (3.52)

$$\sigma_U = \sqrt{u'^2(t, T)} \quad (3.52)$$

Similarly and vertical turbulence intensity  $I_W$  is described by Eq. (3.53)

$$I_W(t, T) = \frac{\sigma_w(t, T)}{U(T)} \quad (3.53)$$

$$\sigma_W = \sqrt{w'^2(t, T)} \quad (3.54)$$

Where:

$U(T)$  - average horizontal wind speed in given time averaging period  $T$

$u'(t, T)$  - longitudinal fluctuation in wind speed

$w'(t, T)$  - vertical fluctuation in wind speed

(Note! - Eqs. (3.51) and (3.52) specify turbulence intensity as fractions, whereas turbulence intensity specified as a percentage requires multiplication by 100.)

IEC 61400 design standards prescribe normal turbulence model (NTM) classifications for use in wind turbine design. NTMs are equations that give relationships between  $\sigma_U$  with  $U$  scaled by a reference turbulence intensity in the 15 m/s wind speed bin along with other constant scaling factors. NTMs are given for both small scale and large scale wind turbines. In the case of large scale wind turbines that conform to (IEC 61400-1, 2019), a characteristic value of the horizontal wind speed  $\sigma_U$  is given by Eq. (3.55).

$$\sigma_U = I_{ref} (0.75U_{hub} + b) \quad (3.55)$$

Where:

$U_{hub}$  - wind turbine hub height wind speed (m/s)

$I_{ref}$  - reference turbulence intensity (specified as a fraction)

$b$  - constant value of 5.6 m/s

$I_{ref}$  can have a range of values depending on the turbulence conditions a turbine is designed to operate in. An  $I_{ref}$  value of 0.18 represents the highest turbulence condition specified in the IEC standard in the 15 m/s wind speed bin. It is referred to as an A+ turbulence classification. For small wind turbines, conforming to (IEC 61400-2, 2013), the characteristic value of  $\sigma_U$  is given by Eq. (3.56).

$$\sigma_U = I_{ref} \frac{(15 + aV_{hub})}{(a + 1)} \quad (3.56)$$

Where:

$a$  - constant value of 2

As both  $I_U$  and  $I_W$  are variable with wind speed and relevant for fatigue load analysis in wind turbine design, curves of 90<sup>th</sup> percentile values are used to assess the IEC turbulence class in the case of  $I_U$ . IEC wind turbine design standards currently do not prescribe turbulence models for  $I_W$ . In Chapter 7, current IEC NTMs in this peri-urban environment will be assessed against the highest IEC NTM classifications and suggestions given for improved or new classes of NTMs for peri-urban environments for medium and large scale wind systems.  $I_W$  will also be assessed in terms of its significance relative to  $I_U$ .

Gusts can be significant in complex environments and can increase wind turbine wear, reducing longevity. The gust factor,  $G_U(t, T)$ , is defined as the ratio of the maximum 3-second gust  $\hat{u}(t, T)$  to the mean wind speed in a specified time period (e.g. 10-minute) Eq. (3.57) (Lombardo, 2021).

$$G_U(t, T) = \frac{\hat{u}(t, T)}{U(T)} \quad (3.57)$$

$G_U$  is specified as 1.4 in the IEC standards. In a similar way to  $I_U$ , the mean binned and 90<sup>th</sup> percentile values for  $G_U$  will also be assessed in Chapter 7.

#### 3.4.4 Wind shear and rotor equivalent wind speed

At locations with high wind shear or wind turbines with large rotors, the wind speed measured at the hub height alone may not adequately represent the wind flow incident on the rotor. The rotor equivalent wind speed (*REWS*) attempts to account for variation in the horizontal wind speed across the rotor swept area (or rotor disc). (Wagner et al., 2011; Wagner et al., 2014) developed a method to calculate the *REWS* for large wind turbine rotors from wind speed measurements at multiple heights across a rotor. This was aimed at wind turbines with large rotors (e.g., rotor diameters above 90 m) in rural locations, Fig. 3.17. Although the rotor diameters of wind turbines in distributed applications would likely be relatively small, complex wind



shear in peri-urban and urban environments may result in wind speed variation across the rotor disc. The *REWS* is determined from Eq. (3.58).

$$U_{REWS} = \left( \sum_{i=1}^n U_i^3 \frac{A_i}{A} \right)^{1/3} \quad (3.58)$$

Where:

$U_i$  – horizontal wind speed measured at a given height within the rotor swept area  $R$  - rotor diameter (m)

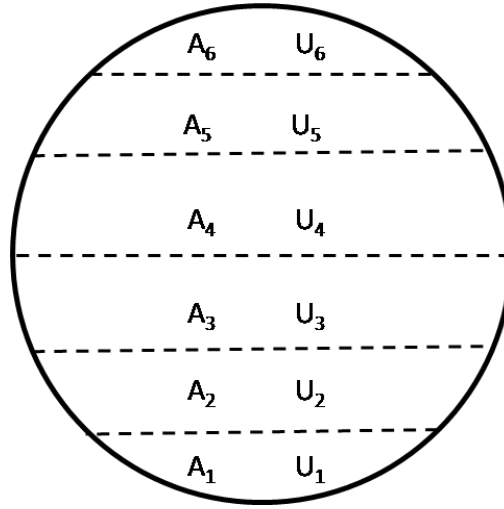


Fig. 3.17. Rotor segments and wind measurement heights used to calculate *REWS* - Adapted from (Wagner et al., 2011).

Turbulence also contains energy that can potentially be extracted depending on the wind speed at which it occurs and on the turbine rotor design. In terms of wind speed, the turbulent equivalent wind speed in general terms can be described by Eq. (3.59) (Wharton and Lundquist, 2012).

$$U_{I_u}(z) = \sqrt[3]{U(z) (1 + 3I_u^2)} \quad (3.59)$$

In Chapter 7, a comparison of directional hub-height wind speed  $U_{hub}$ , rotor equivalent wind speed  $U_{REWS}$ , hub height wind speed including turbulence  $U_{hub_{I_u}}$  and rotor equivalent wind speed including turbulence  $U_{REWS_{I_u}}$  are compared using LiDAR measurements. This is to assess if wind shear or turbulence has the bigger impact on wind speed deviation from the hub-height wind speed.

### 3.5 LiDAR Technology wind energy

Ground mounted LiDAR technologies can determine the wind velocity vector at multiple heights up to 300 m and has gained broad acceptance in the wind industry in recent years (Liu et al., 2019). The technology is anticipated to replace tall met masts, as wind turbines become larger. It has also gained approval in the IEC standard for measuring wind turbine power performance (IEC 61400-12, 2019). The technology has also been developed for forward measurements from the nacelle of wind turbines. This is where the LiDAR beam horizontally faces the oncoming wind flow. It can improve on wind information provided by nacelle anemometers and thereby improve wind turbine control. LiDAR technologies with measurement capabilities up to ranges of multiples of km, traditionally used in airport applications, are also becoming more prevalent in the wind industry for large wind farm wake studies and short term wind forecasting (Smith et al., 2014; Simley et al., 2018; Shimada et al., 2020). Two principal ground mounted LiDAR technologies for vertical wind profile measurements exist today. One is a continuous wave (CW) LiDAR that has a conical scan beam at a fixed elevation angle and uses a velocity azimuth-display (VAD) technique to determine the wind velocity. The second is pulsed LiDAR, which points the beam vertical, then tilts or swings the beam north, south, east and west, referred to as a Doppler beam swinging (DBS) technique. Both types are based on detection of Doppler shifted back-scattered beams. An infrared laser transmitter focuses a beam at the desired location (height) and the Doppler shifted back-scattered beam from the moving aerosols is detected Fig. 3.18. The detected optical beam is converted to an electrical signal that is digitally signal processed to determine the wind velocity.

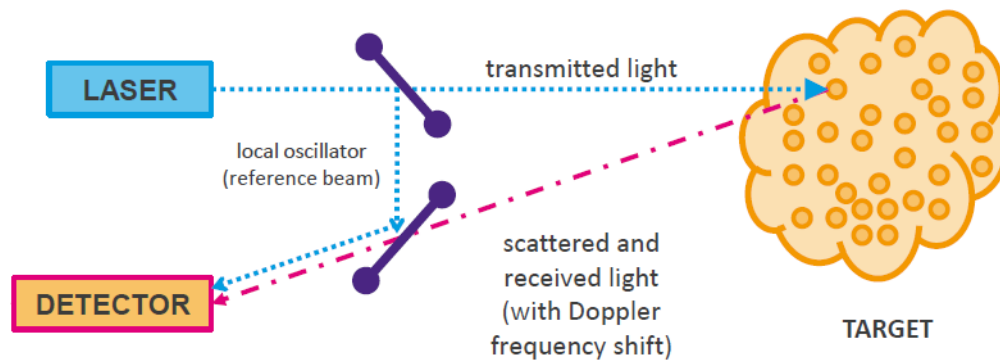
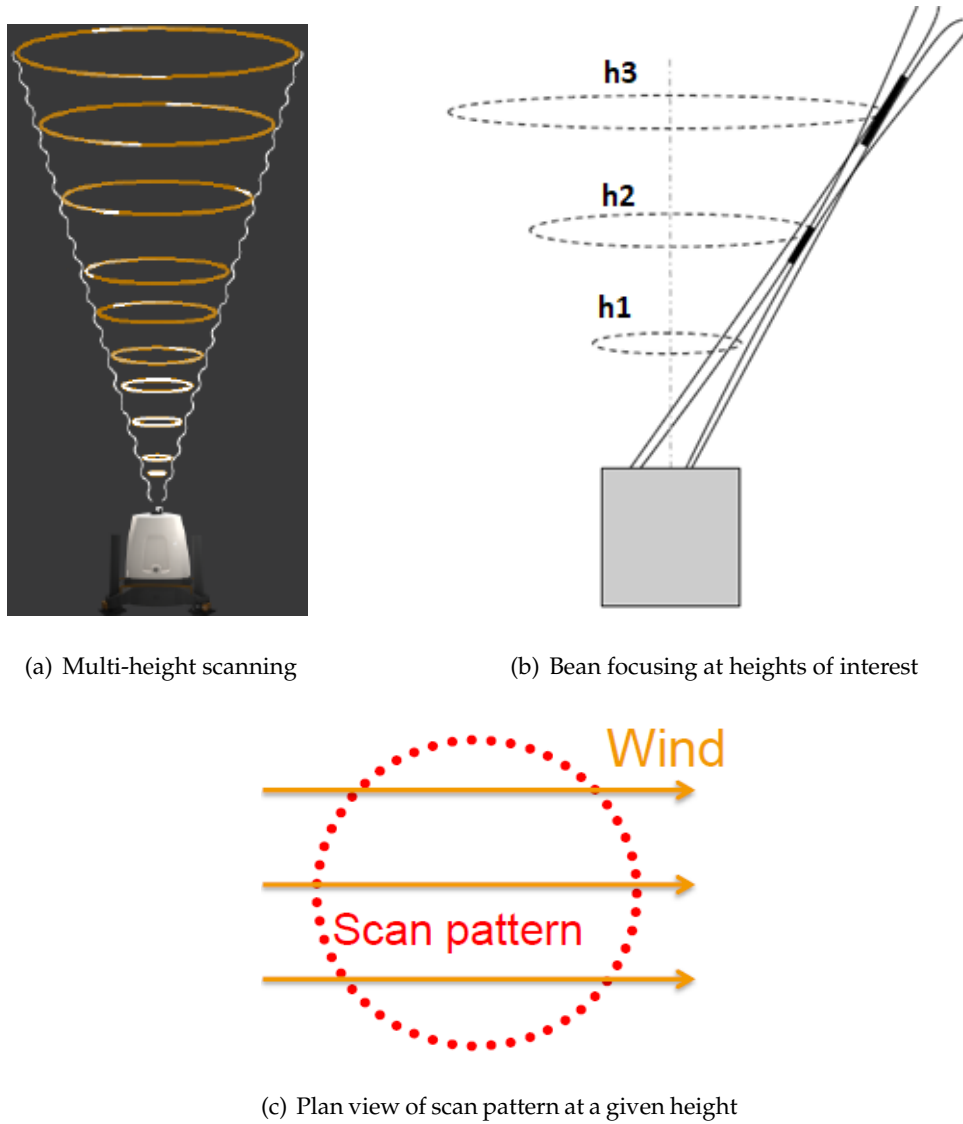


Fig. 3.18. Basic principal of Doppler LiDAR operation (Slinger and Harris, [2012](#)).

### 3.5.1 Continuous wave (CW) LiDARs

The CW LiDAR focuses a continuous transmitted laser beam via a telescope at given measurement height in a circular scan. The Doppler shifted back-scatter detected signal is processed to determine the three wind components. The CW LiDAR then adjusts its telescope to focus on the next measurement height.



**Fig. 3.19.** CW LiDAR circular scanning patterns at different heights - Adapted from (Pitter, Slinger, and Michael, 2015).

The beam or cone angle value  $\theta$  is a trade off between velocity resolution and atmosphere homogeneity. It has been demonstrated that best  $\theta$  values are between  $15^\circ$  and  $30^\circ$  (Peña et al., 2015). Even in complex terrain, in general wind non-homogeneous condition, no better estimation is obtained when reducing the cone angle. As the beam is focused at each height, the CW method has same sensitivity at each measurement height i.e. the probe volume is smaller at lower heights, Fig. 3.20. Therefore, it can performs better for turbulence and wind shear measurements that can be more prevalent at lower heights in the Prandtl layer. The returned signals for a period of time that corresponds to a specified segment of radial distance along the beam is called the range gate. The size of the range gate increases as the square of the distance. It is small at shorter distances but can become excessively large at

heights beyond 300 m.

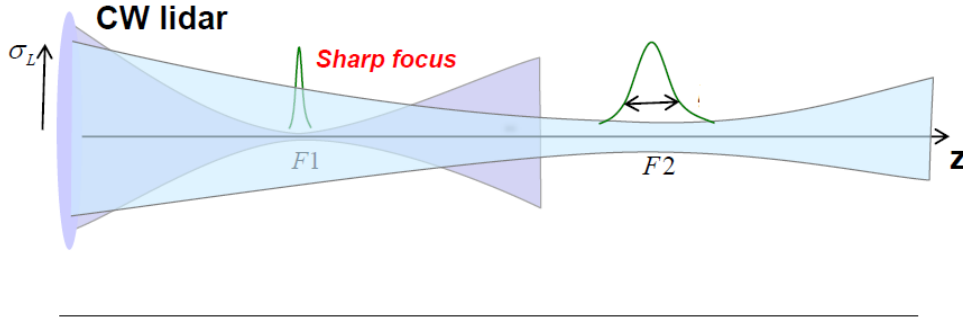


Fig. 3.20. Example of beam focusing at two different focal points or distances - Adapted from (Cariou, 2015).

In the case of the ZX (ZephIR) CW LiDAR, the beam or cone angle is set at  $30^\circ$  from the vertical axis. To determine the wind speed at a given height, the transmitted beam is focused and scans a circle at the given height in 1 second. There are 50 back-scattered signal points in each scan, i.e., 50 Hz (Pitter, Slinger, and Michael, 2015). The detected back-scattered beams are mixed with the local oscillator transmitted beam resulting in a beat frequency, i.e, the frequency difference between the transmitted and detected back-scattered beams. The electric field of the local oscillator  $e_{LO}(t)$  and a received back-scattered beam  $e_S(t)$  (t) can be described by Eqs. (3.60) and (3.61) respectively.

$$e_{LO}(t) = E_{LO} \cos(\omega_{LO}t) \quad (3.60)$$

$$e_S(t) = E_S \cos(\omega_S t) \quad (3.61)$$

The intensity  $i(t)$  of the fluctuating beam following mixing varies as described by Eqs. (3.62) and (3.63).

$$i_B(t) \propto [E_{LO} \cos(\omega_{LO}t) + E_S \cos(\omega_S t)]^2 \quad (3.62)$$

$$i_B(t) \propto [E_{LO}^2 + E_S^2] + 2E_{LO}E_S \cos(\omega_S - \omega_{LO})t \quad (3.63)$$

The constant term is filtered out leaving the fluctuating term due to the Doppler shift that varies at the beat frequency  $\delta f$ , Eq. (3.64).

$$\delta f = \frac{\omega_S - \omega_{LO}}{2\pi} \quad (3.64)$$

The line of sight velocity  $V_{LOS}$  can be determined from Eqs. (3.65) and (3.66).

$$\delta f = \frac{2V_{LOS}f}{c} = \frac{2V_{LOS}}{\lambda} \quad (3.65)$$

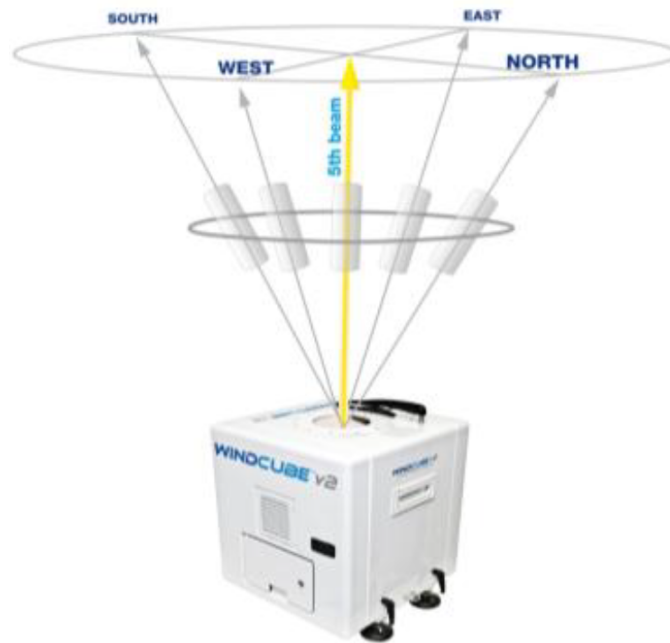
$$V_{LOS} = \frac{\delta f \lambda}{2} \quad (3.66)$$

The transmitted beam wave length is  $1.55 \mu\text{m}$  and maximum Doppler frequency is 50 MHz giving a maximum  $V_{LOS}$  of 38.8 m/s.  $V_{LOS}$  can then be used to give the three dimensional components of wind velocity, Eq. (3.67).

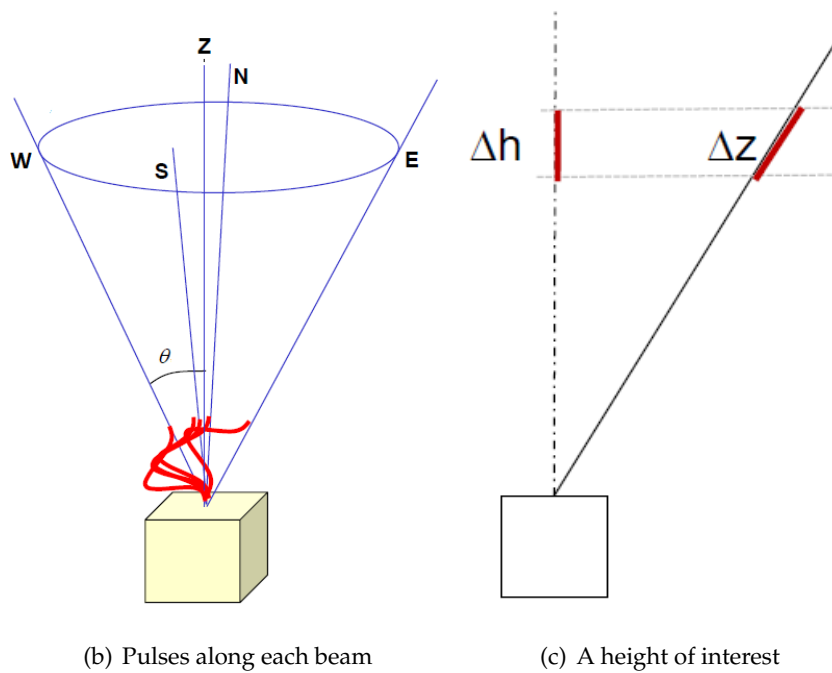
$$V_{LOS} = (u + v + w) \cdot \left( \frac{x + y + z}{\sqrt{x^2 + y^2 + z^2}} \right) \quad (3.67)$$

### 3.5.2 Pulsed LiDAR

In the case of pulsed LiDARs, the beam swings in 5 directions using the DBS technique, Fig. 3.21, (Cariou, 2015). Unlike a CW LiDAR, which determines the wind velocity at each height sequentially, the pulsed LiDAR determines the wind velocity simultaneously at each height, Fig. 3.22. Pulsed LiDARs sample wind flow at 2 to 4 Hz that contain wind speeds from all (up to 10) range gate measured simultaneously (Peña et al., 2015). For each beam direction, short pulses are transmitted at regularly spaced intervals. The time delay between an emitted pulse and the detection of its associated back-scattered signal determines the height of the measurements. The range gate length is always the same at any distance along the beam. The spatial resolution is independent of the measurement range, pulse width and the distance the pulse travels. A spectral analysis is computed on the backs-scattered signals contained within each gate to derive the radial velocities,  $V_r$  along the path of the each LiDAR beam. The radial velocities are used to determine the wind velocity vector at each height, Eqs. (3.68) to (3.71).



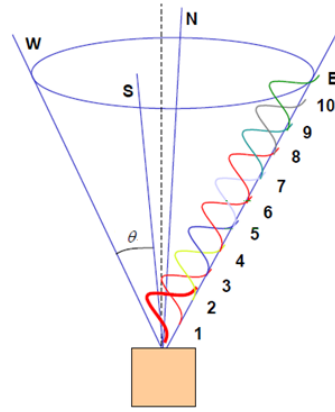
(a) WindCube LiDAR DBS



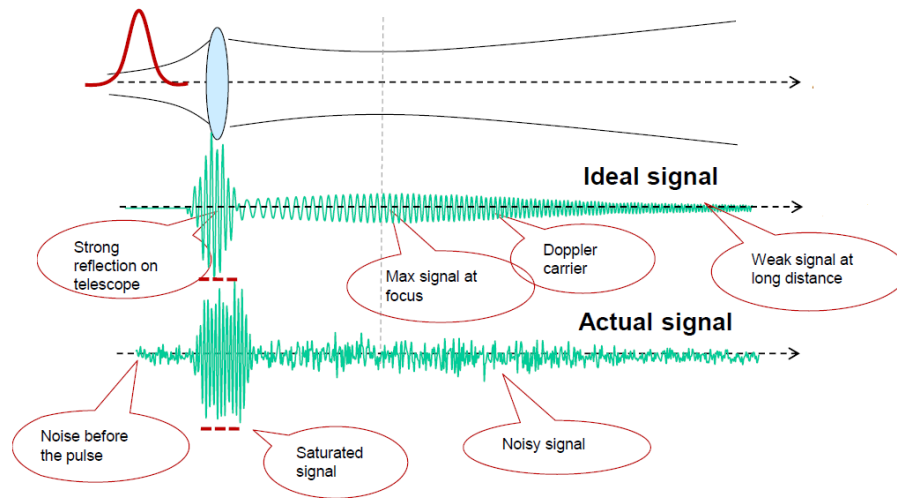
(b) Pulses along each beam

(c) A height of interest

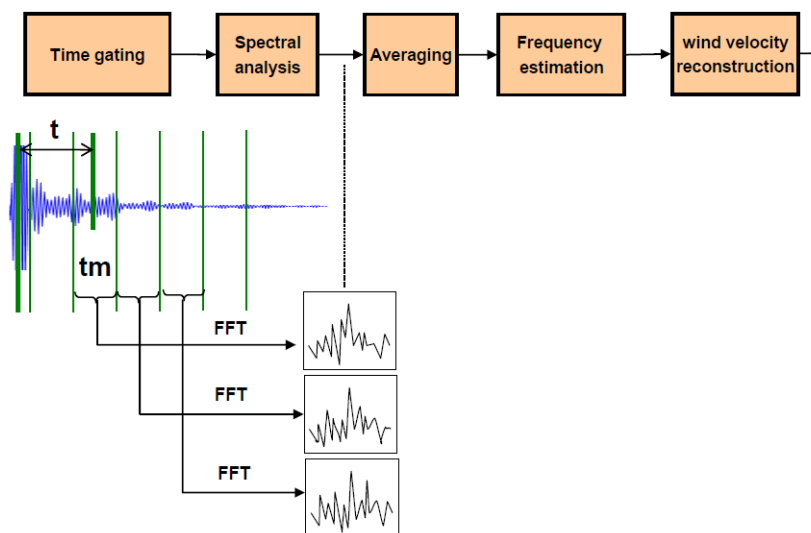
**Fig. 3.21.** Doppler beam swinging (DBS) concept - Adapted from (Cariou, 2015).



(a) Pulses along beam



(b) Pulse characteristics



(c) Signal processing

Fig. 3.22. Pulsed LiDAR operation - Adapted from (Cariou, 2015).



$$V = u + v + w \quad (3.68)$$

$$u = \frac{V_r 0 - V_r 180}{2 \sin \theta} \quad (3.69)$$

$$v = \frac{V_r 90 - V_r 270}{2 \sin \theta} \quad (3.70)$$

$$w = \frac{V_r 0 + V_r 180 + V_r 90 + V_r 270}{4 \cos \theta} \quad (3.71)$$

The beam of a pulsed LiDAR has a single soft focus allowing the simultaneous measurement at all heights for a given beam tilt. Its sensitivity is lower at lower heights compared to the CW approach, but may perform better at higher heights.

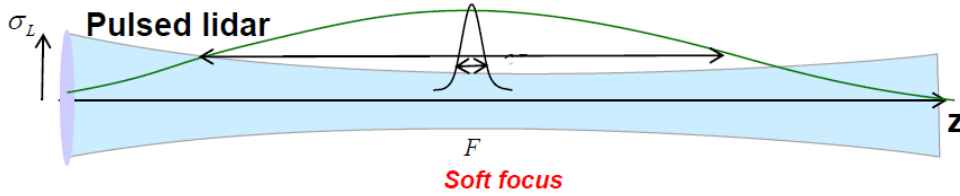


**Fig. 3.23.** Soft single beam focus for measuring at multiple heights simultaneously in pulsed LiDARs - Adapted from (Cariou, 2015).

### 3.5.3 Some measurement limitations of LiDAR technologies

LiDAR operation relies on the aerosol scattering with narrow Doppler broadening and therefore, requires the atmospheric regions of interest to have a sufficient amount of aerosols. Scattering from clear air molecules is not suitable because of Doppler broadening of more than a 1 GHz, which is not suitable for coherent detection. Doppler back scattered signal from low cloud, fog and rain can give invalid measurements. This data can be filtered out from the spectral analysis of the back-scattered signal, but it reduces the availability of valid wind data which may become significant in prolonged periods of windy and wet weather. In Polar regions where clear air in the atmosphere can be dry and aerosol free, back-scattered signals may be too weak to detect (Greco et al., 2020).

### 3.5.4 Choosing a LiDAR type for distributed wind applications

Comparing CW and pulsed LiDARs, there are some fundamental differences that need to be considered when choosing one over the other. CW LiDARs sample wind flow at 50 Hz, have high spatial resolution and fast data acquisition rates. CW LiDARs can measure winds to lower a height limit of 10 m a.g.l. The ever-increasing volume of the focused probe with distance limits it to heights beyond 300 m. Pulsed LiDARs have a lower acquisition rate, but then they measure wind speeds at multiple heights simultaneously that give it the potential to be more accurate at higher heights compared to CW LiDARs, but their resolution is limited by the deteriorating signal to noise ratios in measurements from far (high) distances. At lower heights they are limited to a minimum measurement height of 30 m a.g.l. In this research, a CW ZX (ZephIR) LiDAR has been chosen primarily for its ability to measure at lower measurement heights and its better capability to measure wind turbulence, which is more appropriate to distributed wind applications. More specific details of the CW ZX LiDAR will be given in Chapter 5.

## 3.6 Chapter summary and justification of the research in this thesis

This chapter has given an overview of the ABL along with wind resource modelling and measurement assessment techniques used in the wind industry. Specific attention has been given to mesoscale to microscale influences on wind flow for sites where obstacles are significant features, such as peri-urban and urban areas, based on the literature. In addition, *REWS* for wind turbine in complex wind shear regimes, turbulence intensity and gust factors have been defined. A new concept of an *EER* has been introduced to assess the post installation directional performance. An overview of two principal types of ground based vertical profiling LiDAR technologies has been given, including the pros and cons of both types and the reasons for selecting a CW LiDAR for this research. Due to the potential wide variety and complexity of wind regimes from flat to dense urban environments outlined in this chapter, the principal aim of this research is to improve the application of models

and wind measurements for the deployment of medium and large scale wind turbines in peri-urban environments that are within  $\sim 2$  km of the rural to urban interface. Therefore, the study chapters and the parts of the information outlined in this chapter that are used in them are outlined as follows:

- Chapter 4 analyses the multi-annual SCADA data of the operating data to give the base line real-world performance of the wind turbine in its peri-urban location. A description of the site and wind turbine system is given. This data analysis includes a data quality assessment to ensure that only valid data in normal turbine operation is considered. Information from Section 3.5 is used concerning power curve plots, turbulence intensity and the multi-annual seasonal and diurnal variations in wind speed and energy. The novel *EER* is created to show a high resolution directional profile of the electrical energy output. This *EER* overlaid on a local area 3-D map to give insights into the influence the local buildings from the directional shape of the *EER*. This leads on to Chapter 5, which considers the broader mesoscale influences on the shape of the wind turbine *EER*. As a separate additional point of interest, the real-world impact of gearbox replacement on energy performance is assessed.
- Chapter 5 focuses on the mesoscale influences on the shape of the *EER* using the remodelled mesoscale Irish Wind Atlas, which is based on the UK Met Office UM referred to in Section 3.3. Wind roses and *WPD* plots predicted by the Irish wind atlas are compared within the region and locally in the vicinity of the wind turbine location. Prediction of the wind turbine *AEP* from the mesoscale to microscale process of the wind atlas is compared to the actual wind turbine *EER* on a directional basis to help segregate the mesoscale and microscale influences on the *EER* shape. This is to give a clearer picture of the influences of the buildings as the wind atlas does not consider local buildings in detail. Preliminary onsite LiDAR onsite measurements are introduced to assess the directional wind shear to help give further insights of the directional discrepancies of the predicted *AEP* to the *EER*. More details on the production of the Irish wind atlas from UK Met Office UM and operation of the ZX CW LIDAR are also given in this Chapter.

- Chapter 6 assesses four microscale wind flow models, both linear and CFD models, described in Section 3.3, in predicting the *EER*. Both WAsP and Wind-Sim tools are used for the assessment. The models are coupled to onsite LiDAR wind measurements at multiple heights to see how well they perform, scaling from different heights and for different representations of building obstacles. The obstacle representations include the linear obstacle model, obstacles as roughness elements and as mesh blocking elements in the CFD models. Measured directional wind shear is compared to logarithmic profiles to assess for discrepancies and the existence of the urban sub-layers outlined in Section 3.4, particularly if the wind turbine rotor disc occupies more than one sub-layer. Learnings and recommendations of how best to utilise the models in peri-urban situations for best *AEP* predictions are given.
- Chapter 7 applies morphological methods described in Section 3.4 to develop and test a simplified procedure that relates the shape of the wind turbine *EER* with morphological descriptions of the local peri-urban environment within a 2 km radius of the wind turbine location. This captures the rural to urban interface. Measurements from an installed rural met mast, just outside the influence of the buildings, is used to generate an *EER* at its location. A morphological assessment around the met mast location is also carried out. The morphological assessments at both locations are compared in relation to their respective *EERs* to establish the values of the morphological parameters at and above which they become significant in influencing the energy performance of the wind turbine. An assessment of atmospheric stability is carried out based on the Richardson number, described in Section 3.2, using temperature measurements at the mast. The turbulence intensity and gust factors from measurements at both locations are compared against current IEC standard prescribed wind turbine design models outlined in Section 3.4. Modifications to the IEC models are suggested for peri-urban environments. In addition, LiDAR measurements across the rotor disc are used to determine the directional *REWS* and to assess whether wind shear or turbulence is dominant, and if *REWS* is significantly different to the hub-height wind speed for the relatively small 52 m rotor diameter.

- Chapter 8 considers all findings from Chapters 4, 5, 6 and 7 and discusses these in relation to the literature review and the new knowledge gained in this research. These are used to develop a low cost framework of recommendations for siting medium and large scale wind turbines, specifically for prospective peri-urban sites. This will include recommendation for site met masts, heights at which measurements should be taken, application of microscale flow models, morphological assessment and rotor disc height positioning above buildings. A discussion is given on IEC design standard improvements for medium and large scale wind turbines for peri-urban environments. The overall research and its findings is not intended to be an exhaustive representation of all possible approaches to optimum wind turbine siting in peri-urban environments, therefore limitations will be highlighted and suggestions made for future research that may be needed to continue to improve and evolve this area.
- Chapter 9 is the concluding chapter and broadly discusses the findings of the research in the context of distributed wind in peri-urban environments including the main improvements made, limitations of the findings, future challenges and research needs.



## Chapter 4

# SCADA data analysis and electrical energy rose development

### 4.1 Objectives

The objective of this chapter is to investigate the energy performance of an operating 850 kW Vestas V52 wind turbine sited at a peri-urban location of low elevation from wind turbine SCADA data measurements, on a multi-annual time frame. The location is Dundalk Institute of Technology (DkIT) in the Republic of Ireland, (53.983520°, -6.3913908°)<sup>1</sup>. The wind turbine SCADA system measures and logs a range of internal system operational and external wind and environmental parameters in 10-minute average values. The study includes investigations of the inter-annual, seasonal and diurnal energy characteristics of the wind resource and the electrical energy output. Particular focus is given to the directional variation of the electrical energy output with respect to the local built environment. This also includes directional power curves and turbulence intensity curves. As electrical energy output (kWh) is of most interest to end users of behind the meter wind systems, a novel electrical energy rose (*EER*) has been developed to illustrate the directional breakdown of the electrical energy produced, from the SCADA data. Insights into local site factors that have influenced its performance over the multi-annual time frame are given. In particular, the directional shape of the *EER* is overlaid on a satellite plan view map of the site and local surroundings to visually assess the shape of the *EER* with respect to the local buildings, e.g., if distinct or sharp changes in the *EER* align with any building features. Comparisons are made to current siting rules for single turbines in the vicinity of obstacles given the IEA Wind Task 27 guidelines referred to in the literature review. The results are also used to guide the research in

---

<sup>1</sup>Wind turbine location: <https://goo.gl/maps/ejhPDsoCvruNt4yP7>

subsequent chapters. In the later stages of this research, the thirteen year old gearbox in the wind turbine was replaced with a brand new one. An additional study was carried out to assess the impact of aging of the old gearbox on turbine energy performance. The key outcomes of this study is also included in this chapter.

This chapter is outlined as follows: Firstly, short descriptions of the wind turbine installation background, turbine technical aspects and SCADA system are given, along with a description of the wind turbine site and principal local building obstacles. Secondly, 9 years of 10-minute SCADA data is quality checked so that only years with the most complete sets of valid data are used. Thirdly, the wind resource and electricity production on inter-annual, monthly and hourly basis are assessed. Directional wind power density, turbulence intensity curves and wind turbine power curves and are also investigated. A novel 72 sector *EER* is produced and overlaid on a satellite plan. This is examined with respect to local buildings. Views from the turbine hub height in specific directions of interest are then used with the above information to give insights into the relative impact of site features on the wind turbine power curve, turbulence intensity, variations in directional wind power density and directional electrical energy performance. Fourthly, the results are discussed in the context of establishing initial site screening rules at the pre-feasibility stages of potential large-scale wind turbine installations in urbanised areas. This includes a comparison with current simple IEA siting rules and an outline some of the challenges of accurate wind resource assessment and energy assessment at complex sites in general. Finally, an additional short study examines the impact of gearbox aging on the wind turbine energy performance by comparing the changes energy output as a result of gearbox replacement in 2019. The motivation for the next chapter on the site mesoscale and LiDAR wind shear measurements is given based in the findings in this chapter.

## **4.2 Wind turbine description**

### **4.2.1 Background to wind turbine installation**

The Vestas V52 wind turbine at DkIT, Fig. 4.1, was installed as a behind-the-meter system in 2005. At the time it was the only known large-scale wind turbine on an educational campus anywhere in the world. The project was devised in 2002 by Larry



Staudt, the then director, of the Centre for Renewables & Energy at DkIT (CREDIT). In the period from 2003 to 2004, feasibility studies were carried out and planning permission obtained. This involved the assessment of the wind resource, campus electrical load demand, wind turbine sizing, ground works, noise, shadow flicker and visual impact. A comprehensive public consultation with local residents and businesses took place. This involved public information sessions and regular project updates. Planning permission was granted three months after application with no objections. Following a public tender process for the wind turbine, Vestas Wind Systems A/S was awarded the tender, being the only tender respondent at the time. A Vestas V52 wind turbine with a power rating of 850 kW, rotor diameter of 52 m and a tower height of 60 m was supplied. Grid connection was obtained under a grid connection rule derogation for parallel generators or autoproducers (behind-the-meter), that already have a site grid connection. The derogation was subject to a power export limit of 500 kW to the utility grid. This crucially avoided a longer grid connection application process associated with wind farms which, at the time, consisted of batches of wind farm application being processed in groups, referred the group processing approach (GPA). The GPA process depended on grid infrastructure development and was linked to applications for feed-in-tariffs (FiTs), which themselves had intermittent application periods known as Gates. These processes, along with planning permission, took from several years to up to a decade for many wind farms to progress from site assessment to construction and operation. The much shorter grid connection and planning permission times for the behind-the-meter wind turbine at DkIT enabled the turbine to be constructed in the summer of 2005, becoming operational in October 2005. The total capital cost was  $\sim$  €1270000. A capital equipment grant obtained from the Sustainable Energy Authority of Ireland (SEAI), under its research and development program at the time, covered  $\sim$  40% of the capital cost. For the first two years of operation, so as to avoid exceeding the 500 kW power export limit, the wind turbine was power limited to 700 kW as the campus base load demand was  $\sim$  200 kW. Subsequently, in the following  $\sim$  2 years, new buildings on campus were acquired and the base load exceeded 350 kW. This enabled the turbine to operate to its full rated power of 850 kW from  $\sim$  mid 2007 onwards. According to latest statistics from Wind Energy Ireland (WEI) of wind farms in the Republic of Ireland, there are almost 300 wind farms comprised of over 1800

wind turbines giving a total installed power capacity of just over 4000 MW (WEI, 2022). Of Within these total values, there are approximately 250 Vestas V52 wind turbines representing  $\sim 5\%$  of the total installed power capacity. This relatively low percentage is the result of the large sizes of wind turbines that have become available to wind farms developments in the past decade and the fact that the Vestas V52 wind turbine is no longer in production as a brand new model

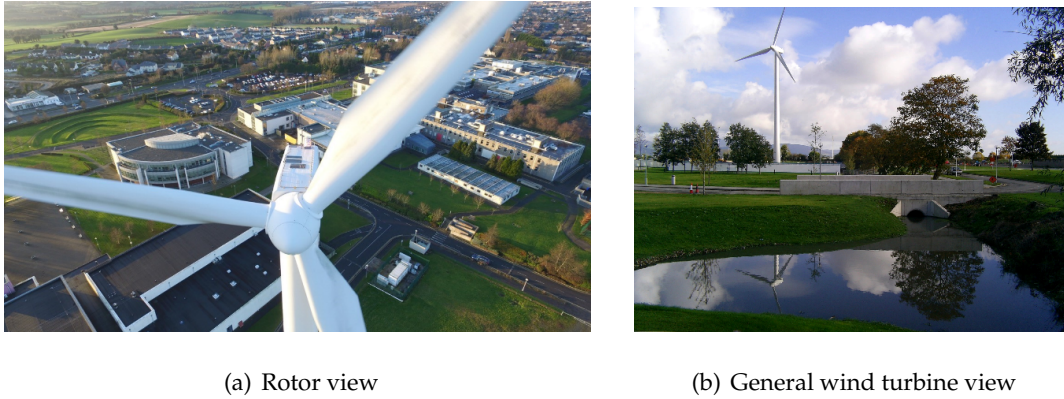


**Fig. 4.1.** Vestas V52 wind turbine at DkIT.

#### 4.2.2 Wind turbine technical overview

The 850 kW rated Vestas V52 wind turbine is a pitch regulated upwind turbine with active yaw and a three-blade rotor. The 26 m long blades are made of glass-fibre reinforced epoxy. Each blade consists of two blade shells which are bonded to a supporting beam. Steel thread inserts are glued into the blade and bolts connect the blade to the blade bearing. The blade bearing is a 4-point ball bearing bolted the rotor hub. The main shaft transmits the power through the gearbox to the electrical generator. The nominal, manufacturer specified, wind cut-in wind speed, when electricity starts to be produced occurs between 3 m/s and 4 m/s. Rated power occurs between 12 m/s and the cut-out wind speed of 25 m/s. The principal technical parts are shown in Fig. 4.2.

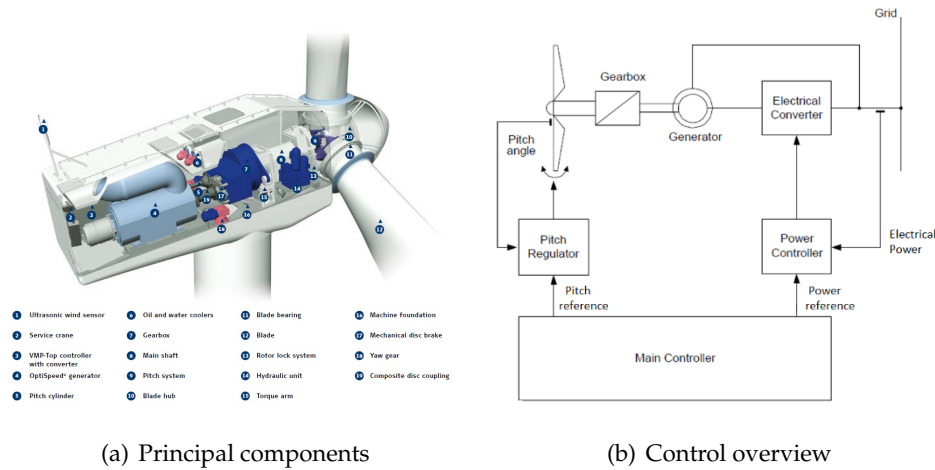


**Fig. 4.2.** Technical overview of Vestas V52 wind turbine - Adapted from Vestas user manual.

A hydraulic system with a single hydraulic pitch ram actively controls the pitch angle of all three blades simultaneously for maximising power capture or for aerodynamic braking, depending on operational conditions. The gearbox is a combined planetary and helical gearbox that steps up the main low-speed shaft rotational speed by a factor of 61.799 to the generator rotational speed at its high-speed shaft. The hydraulic system also supplies the necessary pressure for a parking disc brake on the high-speed shaft. The generator is an asynchronous 4-pole doubly-fed induction generator (DFIG) generator with wound rotor and slip rings. Its stator directly connects and synchronises to the utility grid when generator rotational speed conditions are correct. Alternating current (AC) of variable frequency can be injected into, or extracted from, the rotor of the generator via a back-to-back inverter system that is connected to the grid. It enables the rotor of the generator to physically rotate at a non-synchronous speed while the rotor electromagnetic fields remains synchronised to the stator fields, which are excited by the grid. This gives the wind turbine drivetrain, including the main rotor, semi-variable speed capability. Optimum wind turbine control is achieved using the Vestas OptiSpeed™ and OptiTip® control concepts that implement a number of control regimes for different wind speed ranges by selecting the optimal generator rotational speed and blade pitch angle for the given wind conditions. OptiTip™ control regulates the blade pitch angle at fixed generator revolutions per minute (RPM) while OptiSpeed™ controls the generator RPM at fixed blade pitch angle. Specifically, the following control regimes are implemented

for given wind speed ranges: fixed pitch, variable speed:  $< 3$  m/s; fixed speed, variable pitch: 3 m/s to 5 m/s; fixed pitch, variable speed: 5 m/s to 9 m/s; and fixed speed and variable pitch:  $> 9$  m/s. These control regimes help to maximise the rotor power coefficient below rated power and to reduce large torque spikes on the drive train from gusts. In normal turbine operation, the blade pitch angle is always below  $20^\circ$ . Wind turbine yawing with wind direction is achieved using two electrically driven yaw gears that rotate yaw pinions which are connected to a large toothed yaw ring. The yaw ring is coupled with claw bearings to a fixed slide ring bearing at the top of the tower. The wind turbine rotor can be paused aerodynamically by pitching the blades to full feather, i.e, a blade pitch angle of approximately  $86^\circ$  (Aerodynamically  $90^\circ$ ), and left idling without engaging the parking brake. In a fault condition or stop mode the blades are pitched to full feather and the parking/emergency disc brake on the high-speed shaft is engaged by the hydraulic system. All wind turbine functions are monitored and controlled by the Vestas Multi Processor (VMP) unit, that consists of a number microprocessor based control units, located inside the nacelle. It serves as a SCADA system that monitors and controls all wind turbine functions and the collection/logging of multiple data parameters. The turbine system is certified to all relevant IEC design standards.

#### 4.2.3 Wind turbine SCADA system



**Fig. 4.3.** Turbine nacelle mounted 2-D ultrasonic anemometer.



**Fig. 4.4.** Wind turbine SCADA ground controller and user interface.

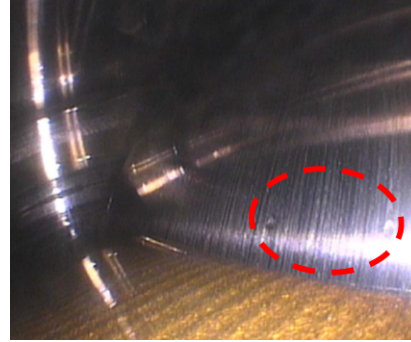
The following selected parameters of interest are logged by the wind turbine SCADA system in 10-minute average values: wind speed, wind speed standard deviation, absolute wind direction, relative wind direction, rotor (and generator) RPM, blade pitch angle, power output along with 10-minute minimum power output and maximum power output values. Wind speed and direction are measured by a nacelle mounted, Thies 2-D ultrasonic, anemometer, Fig. 4.3. It has a sampling rate of 20 ms from which the 10-minutes data averages are logged. The measurement resolutions are 0.1 m/s and  $1^\circ$  for wind speed and direction respectively. The SCADA system stores one month of 10-minute data internally. Therefore, each month of 10-minute data must be captured and stored externally in order to build up the long term multi-annual 10-minute time series data sets. This has been done since 2006, giving a unique data set for a wind turbine of this size in a peri-urban wind environment.

#### 4.2.4 Gearbox replacement

In July 2019, (during this PhD study) the gearbox, a Metso PLH-400V52 shown in Fig. 4.5, reached the end of life after thirteen years of operation. Based on a gearbox borescope inspection and oil sample tests, it was recommended by the service provider that the gearbox be replaced. Impact marks and indentation on planetary bearing roller were observed along with wear marks on teeth flanks. The oil sample test results showed an elevated copper particle count that was well in excess of the recommended limit.



(a) Metso PLH-400V52 planetary gearbox



(b) micro-pitting on high speed roller (top), impact marks on low speed roller (bottom)

**Fig. 4.5.** Wind turbine gearbox.

The replacement of the aged gearbox gave the opportunity to assess the impact on the energy output of its replacement with a brand new gearbox of the same model.



### 4.3 Site description

Dundalk town is located by the coast in the northeast of Ireland, Fig. 4.6. The DkIT campus is located at the southwest end of Dundalk town, near the transition from the rural to peri-urban environment.

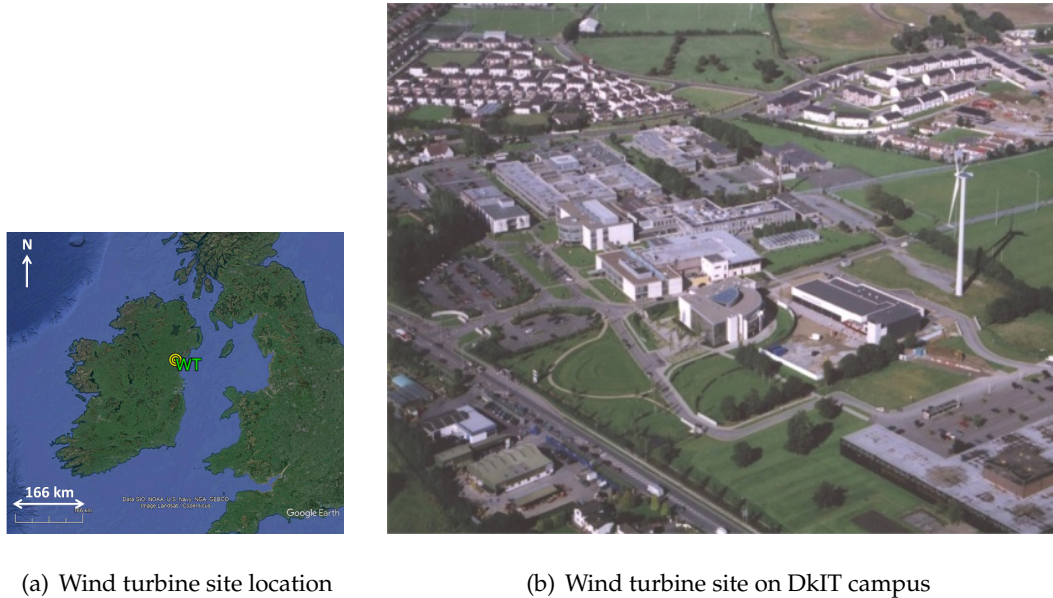


**Fig. 4.6.** Wind turbine site at DkIT.  
(GPS Co-ords:  $53.98352^\circ$ ,  $-6.391391^\circ$ )

The turbine location has an elevation of  $\sim 13$  m above sea level (a.s.l.). The surrounding rural terrain, within a 20 km radius of the wind turbine site, is low-lying rolling agricultural land. It has elevations below 50 m with sparsely dispersed shelterbelts approximately 3 m high. The coast of Dundalk bay is approximately 3 km to the east of the site. To the north and northeast, approximately 7.5 km to 20 km away, there are hills that range in elevation from 75 m to 563 m. The most significant elevated topographical features are identified in Fig. 4.7 and Table 4.1. With respect to the turbine location, nearby obstacle features consist of various types and density of buildings at various distances from the wind turbine in each direction, within  $\sim 1$  to 2 km radius of the wind turbine location. Fig. 4.8 shows a plan view of some of the principal local building obstacles around the turbine site. Table 4.2 lists the physical properties of the most significant buildings up to  $\sim 1.5$  km radius around the wind turbine.



**Fig. 4.7.** Topographic features up to 40 km from site.

**Table. 4.1.** Regional site features

Feature	Distance from wind turbine location (km)	Elevation (m)
A	7.5 - 15	75 - 563
B	13 - 18	10 - 540
C	17 - 40	0 - 663





**Fig. 4.8.** Local obstacle features up to 1.5 km from site. X is the wind turbine location.

**Table. 4.2.** Local site features

Obstacles	Description	Distance from turbine (m)	Height a.g.l. (m)	Cross sectional width - wind turbine view (m)
1	Industrial building	151 - 315	7	150
2	Tall hotel	335 - 420	47	70
3	Student apartments	241 - 312	13	90
4	Office blocks	520 - 670	8 - 13	420
5	Cluster of industrial buildings	550 - 1100	12	635
6	Campus building	80-330	11	240
7	Row of houses	487 - 728	7	320
8	Houses	225 - 650	7	600
9	Open field	0 - 450	0	350
10	Office blocks	520 - 670	8 - 13	420
11	Industrial buildings	770 - 1030	10	130

## 4.4 Methods

### 4.4.1 SCADA data quality assessment and wind turbine availability

All data is analysed using MATLAB®. A number of factors can impact upon quality and quantity of measured data available. These include turbine maintenance downtimes, turbine operational faults, grid outages, spurious data from sensor faults or sensor unavailability and data gaps due to communication network losses in external the data logging system. As a result, full years of complete data sets are not always captured. Therefore, the SCADA data is first checked for quality based on filtering within a range of valid data values that only include data where the wind turbine is in its normal mode of operation. A number of criteria are used to accept or reject 10-minute average data values based on the definition of an operational time fraction  $O$  used the (IEC 61400-12, 2019) wind turbine power performance standard, Eq. (4.1).

$$O = \frac{T_t - T_n - T_u - T_e}{T_t - T_n - T_e} \quad (4.1)$$

Where:

$T_t$  - total time period under consideration

$T_n$  - known time when turbine is non-operational (e.g., fault conditions or loss of grid)

$T_u$  - time when status of turbine is unknown (e.g., gaps in or loss of logged data)

$T_e$  - excluded time in the analysis (e.g., turbine servicing)

Wind turbine availability, Eq. (4.2) is the proportion of time the turbine is available to generate electricity over a given time period irrespective of wind conditions. Times of non-availability are only considered for internal faults of the turbine itself resulting in non-operation of the turbine. Faults due to the grid or downtimes due to scheduled maintenance are not considered as downtimes due to the turbine itself.

$$Availability(\%) = \frac{TurbineOK(hrs)}{GridOK(hrs) - ScheduledMaintenance(hrs)} \quad (4.2)$$

Filtering of invalid data is based on the status on blade pitch angle values as follows. In fault mode or in service mode the wind turbine rotor is paused with a fixed blade pitch angle of  $86^\circ$ . In normal operation, when the wind turbine rotor is spinning, the

pitch angle varies between  $-1^\circ$  and  $20^\circ$ . Therefore, all data coinciding with pitch angle data with values less than  $20^\circ$  is used to indicate normal turbine operation. Only years with  $O$  and availability greater than 90% are considered for further analysis to minimise seasonal bias in the analysis.

#### 4.4.2 Wind and power data analysis

With the high volume of data points in multi-annual 10-minute time series data, 16 sector and 72-sector wind roses are plotted along with a 72-sector  $WPD$  plot to give a high resolution picture of the directionality of the wind resource and wind power density at the site. Seasonal wind roses are also created along with plots of monthly and hourly average wind speeds. The directional wind power density  $WPD_{i,j}$ , Eq. (4.3), in wind speed bin  $i$  and directional sector  $j$ , defined in Chapter 3, is weighted by the number of data points  $N_{i,j}$  in that sector to give the directional  $WPD_j$ , Eq. (4.4). The total  $WPD_{tot}$  is the summation of  $WPD_{tot}$  over all sectors by Eq. (4.5).

$$WPD_{i,j} = \frac{1}{2N_j} \sum_{n_i=1}^{n_i=N_{i,j}} \rho_{i,j} U_{i,j}^3 \quad (4.3)$$

Where:

$\rho_{i,j}$  - density of air  $kg/m^3$

$$WPD_j = WPD_{i,j} \frac{N_{i,j}}{N_{tot}} \quad (4.4)$$

$$WPD_{tot} = \sum_{j=1}^{N_j} WPD_j \quad (4.5)$$

The turbulence intensity, Eq. (4.6), and power curves, Eqs. (4.7) and (4.8), are plotted for 8 directions, each covering sector widths of  $45^\circ$ , in order to assess the directional variation of these parameters in response to influences of local and regional obstacles on the wind regime.

$$I_U(t, T) = \frac{\sigma_u(t, T)}{U(T)} \quad (4.6)$$

Where:

$\sigma_U$  - the 10-minute horizontal wind speed standard deviation

Power curves are obtained using Eq. (4.7) and Eq. (4.8) for each directional sector following the IEC standard method (IEC 61400-12, 2019).

$$U_{i,j} = \frac{1}{N_{i,j}} \sum_{j=1}^{N_{i,j}} U_{i,j} \quad (4.7)$$

$$P_{i,j} = \frac{1}{N_{i,j}} \sum_{j=1}^{N_{i,j}} P_{i,j} \quad (4.8)$$

Where:

$U_{i,j}$  - normalized and averaged wind speed in bin  $i$  in direction sector  $j$

$P_{i,j}$  - normalized and averaged power output in bin  $i$  in direction sector  $j$

$N_{i,j}$  - number of 10-min data sets in bin  $i$  in direction sector  $j$

#### 4.4.3 Electrical Energy Rose (EER)

From a siting and obstacle impact perspective on electrical energy performance of most interest to the end-user, a novel approach of using an *EER* is used. It is generated from measured 10-minute average power and wind direction values to create a real-world 72-sector electrical EER plot that shows the electrical energy (kWh) output variation with the direction. The directional energy output from the turbine for a given directional sector width  $\Delta\theta_j$  can be expressed as summation of the product of average power  $P_j$  and time for each 10 minute time stamp  $t_{j,\theta}$  for the given directional sector width, Eqs. (4.9) and (4.10).

$$E_j(\Delta\theta_k) = \sum_{i=1}^{N_{i,j}} P_{i,j}(\Delta\theta_j) \times t_{i,j} \quad (4.9)$$

$$EER_j = \sum_{j=1}^{N_j} E_j(\Delta\theta_j) \quad (4.10)$$

Where:

$N_{i,j}$  - number of points in data set  $i$  in directional sector  $j$

The sector width of  $5^\circ$  gives a high resolution of the directional electrical energy output. The shape of the *EER* is used to give more distinct insights on how the turbine performs over a long (multi-annual) period in relation to the features in its surrounding environment. This is done by overlaying the *EER* plot on the site plans at regional and local scales indicated in Figs. 4.7 and 4.8 respectively in combination with the corresponding physical dimensional and distances data given in Tables 4.1 and 4.2 respectively.

#### 4.4.4 Gearbox aging and replacement comparison

The impact on power output and *AEP* due to variations in the power curve at different stages over the lifetime of the wind turbine are assessed. Power curves from individual years at staged periods over the gearbox operational life and after the gearbox replacement are compared. The years considered are 2008, 2014, 2017-18 with old gearbox and a 6-month period in 2019 with the new gearbox.

Firstly, a two-sample Kolmogorov–Smirnov (K–S) test is applied to the power curves in a bin-wise fashion to test if the power level changes are statistically significant i.e. if the power samples within each bin are coming from the same distribution. The K-S test is chosen as it is a powerful non-parametric method for comparing the empirical (cumulative) distribution functions of two samples (Arsenault, 2017). It quantifies the distance between the empirical distributions of both samples and can detect variance. It does not require both samples to have normal distributions, which is of its strengths. It applied to the power data using the MATLAB® *kstest2* function for a significance level  $\alpha$  of 0.05. Secondly, to assess the impact on *AEP*, the wind resource parameters using Eq. (4.11) for the wind years of 2008, 2017 and a 12-month period 2018-19 are assessed individually.

$$p(U) = \left(\frac{k}{c}\right) \left(\frac{U}{c}\right)^{k-1} e^{-\left(\frac{U}{c}\right)^k} \quad (4.11)$$

Where:

$p(U)$  = probability density function

$U$  = mean wind speed (m/s)

$c$  = scale factor (m/s)

$k = \text{shape factor (dimensionless)}$

The scale and shape factors are determined from the MATLAB® *fitdist* function that is based on the statistical method of moments. All power curves are combined with the wind resource parameters for each of the mentioned wind years separately to estimate the *AEP*, Eq. (4.12), for each wind year and power curve combination. This is done because the only way to estimate the difference in energy production, given two or more measured power curves, is weighting them against a reference wind speed distribution. 2008 is used as the reference baseline year as it has the most complete data set when the turbine was newest. The improvement in *AEP* from replacing the gearbox in 2019 is then examined using the 2019 power curve with the same wind years to investigate the potential contribution of the gearbox wear alone to energy performance degradation of the wind turbine.

$$AEP(kWh) = \sum_i^{N_i} \left\{ e^{-[(\frac{U_{i-1}}{c})^k]} - e^{-[(\frac{U_i}{c})^k]} \right\} P_i(\frac{U_{i-1} + U_i}{2}) N_h \quad (4.12)$$

Where:

$i$  - wind speed bin number

$U_i$  - mean wind speed in wind speed bin  $i$  (m/s)

$c, k$  - Weibull scale (m/s) and shape factors respectively

$P_i$  - with turbine average electrical power in a given wind speed bin from its power curve (kW)

$N_i$  - total number of wind speed bins

$N_h$  - total number of hours in the year

## 4.5 Results

### 4.5.1 Data quality assessment

From the recorded SCADA data, both the annual turbine availability and 10-minute data availability from 2007 to 2015 are given in Table 4.3.

**Table. 4.3.** Annual wind turbine availability and 10-minute data availability

Year	Turbine availability (%)	10-minute logged raw data availability (%)
2007	97.7	84.6
2008	99.4	98.7
2009	99.9	89.8
2010	-	33.4
2011	97.3	67.7
2012	98.8	94.6
2013	98.75	97.4
2014	99.6	94.6
2015	99.4	95.8

In some years, the lower availability of 10-minute logged data is due to faults in an external communication network that sends the 10-minute SCADA data to a remote computer. The turbine monthly total data values from which turbine availability is assessed is stored in the turbine controller itself independently of the external communications network. The turbine availability for monthly total energy values is above 90% for 8 years. For higher time resolution data analysis based on the 10-minute data, both wind turbine and time-series data availabilities greater than 90% are for the 5 years listed in Table 4.4. Using equation Eq. (4.1), known times when the turbine is not operational ( $T_n$ ) and times when the turbine is in services mode ( $T_e$ ) are filtered from the data. The equation is rearranged, Eq. (4.13), to suit the available data so that only data that corresponds to normal operation of the turbine is carried forward for analysis.

$$O = \frac{T_t - (T_n + T_e) - T_u}{T_t - (T_n + T_e)} \quad (4.13)$$

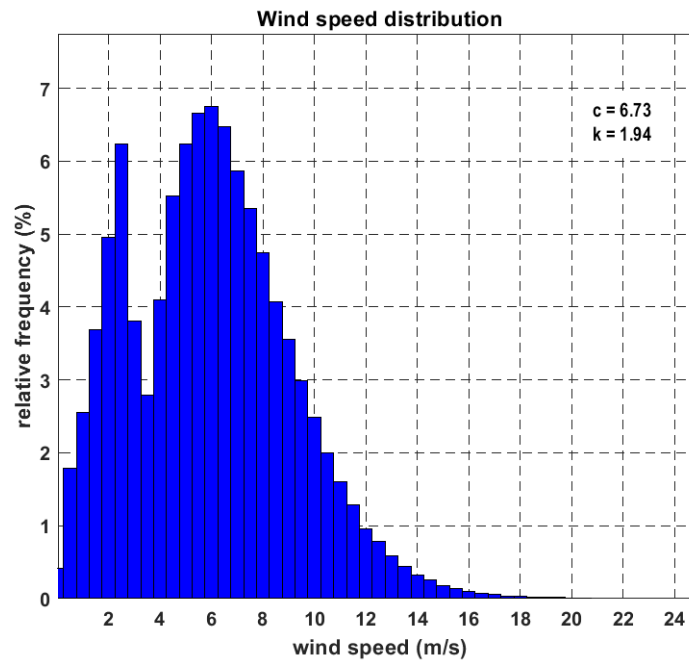
**Table. 4.4.** Yearly operational time fractions (O)

Year	$T_t$ (hrs)	$T_n + T_e$ (hrs)	$T_u$ (hrs)	O (%)
2008	8774	110	124	98.6
2012	8774	294	486	94.3
2013	8760	327	223	97.4
2014	8760	162	471	94.5
2015	8760	309	362	95.7

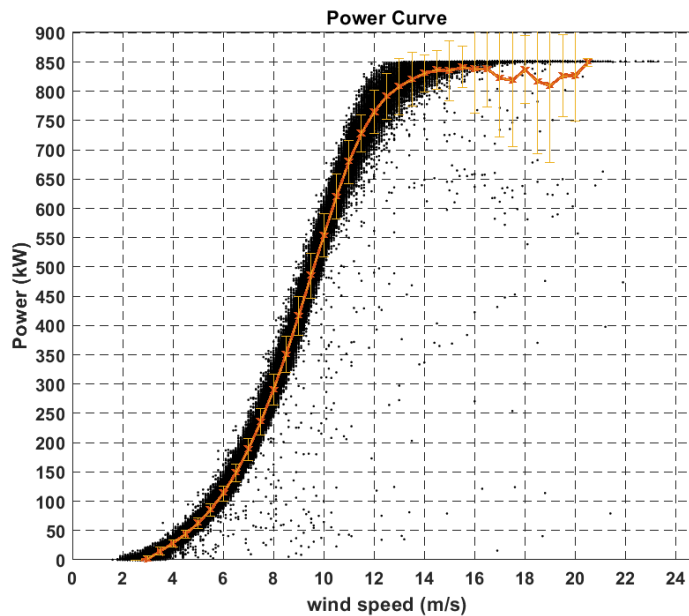
#### 4.5.2 Wind and power data analysis

The wind speed distribution based on the 10-minute average logged data for the 5-year period is shown in Fig. 4.9(a). The impact on the ultrasonic wind sensor located behind the turbine rotor becomes apparent. At the cut-in wind speed of  $\sim 3$  m/s when the turbines starts to generate electricity, the rotor begins to extract significant power from the wind resulting in a wind speed drop behind the rotor and a higher population of data points at wind speeds just below the cut-in wind. In other words, due to the impact of the rotor on the wind flow measured by wind sensor the wind speed distribution is not exactly representative of the distribution upwind of the rotor.





(a) Wind speed distribution

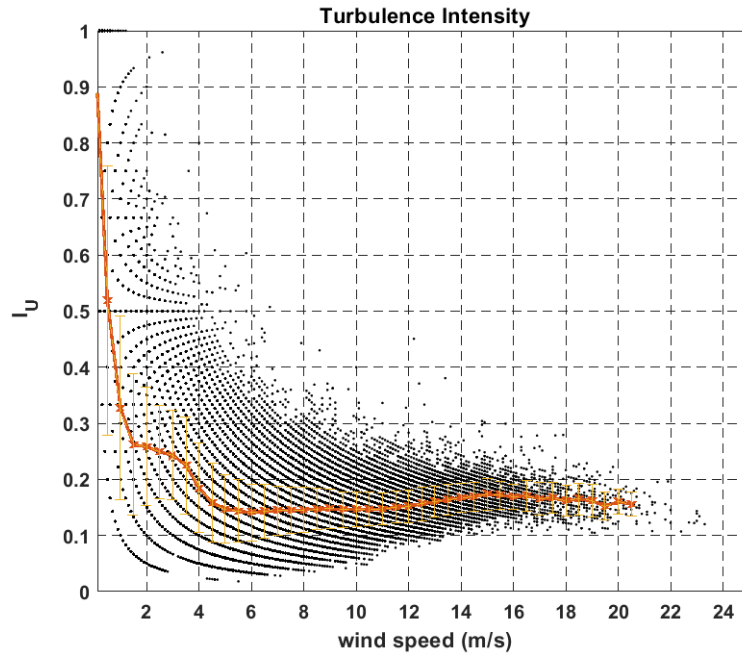


(b) Power curve - scatter plot and binned values

Fig. 4.9. 5-year wind speed distribution and power curve.

A scatter plot and corresponding binned power curve is shown in Fig. 4.9(b). The power vs wind speed exhibits some degree of scatter with some of the power points far away from the binned average. The scatter can be attributed to a number of factors such as the response of the turbine system to wind gusts, instantaneous yaw error and turbulence. In a peri-urban environment with local obstacles wind turbulence can be higher compared to flat field sites. A plot of turbulence intensity is given

in Fig. 4.10. In the current revision of the international wind turbine design standard (IEC 61400-1, 2019), the assessment of design loads use turbulence intensity values from 0.12 to 0.18, depending on turbine design class. The 15 m/s mean wind speed bin is used in the IEC NTM and 0.18 is specified as the highest turbulence intensity. In this case, the mean turbulence intensity value in the 15 m/s bin the falls within 1 standard deviation 0.18, indicating that the turbulence intensity limit of this IEC standard is reached or exceeded on regular basis at this site. However, from the wind speed distribution plot of Fig. 4.9(a), wind speeds of 15 m/s at the site are experienced a relatively small proportion of the time. Correspondingly, the coefficient of performance,  $C_p$ , shown in Fig. 4.10 shows some degree of scatter influenced by the aerodynamic response of the rotor blades and active blade pitching system to the wind inflow conditions. Also, the transitions between the various fixed and variable speed control modes, outlined previously, as well as generator circuit switching between star and delta configurations can introduce systematic discrepancies between the nacelle measured wind speed and measure electrical power output. However, the amount of data is relatively small as the maximum 90<sup>th</sup> percentile value is 0.47 which is inline with maximum electrical  $C_p$  that could be achieved from a modern wind turbine (Contreras Montoya et al., 2021). Only 63 data points the exceed the theoretical the Betz limit representing less than 0.03% of the data points.



(a) Turbulence intensity scatter plot and mean binned values

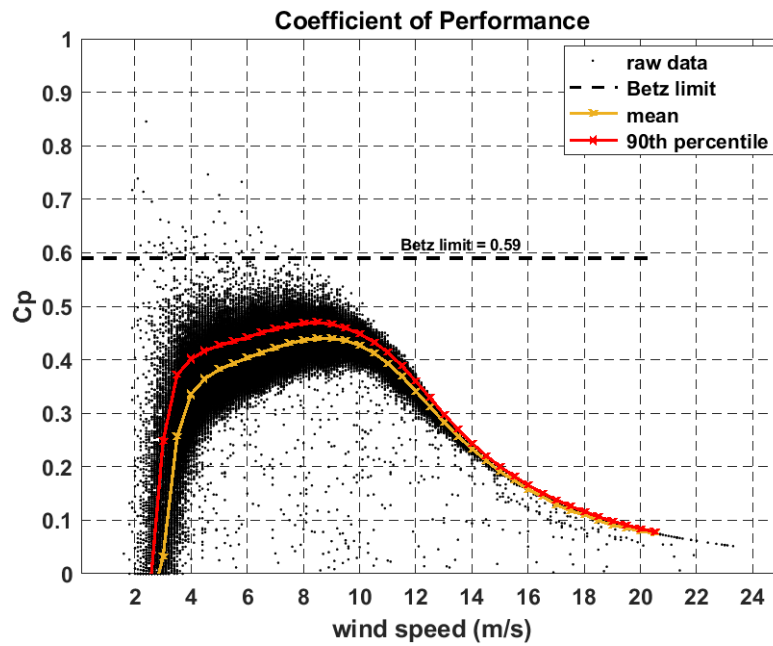
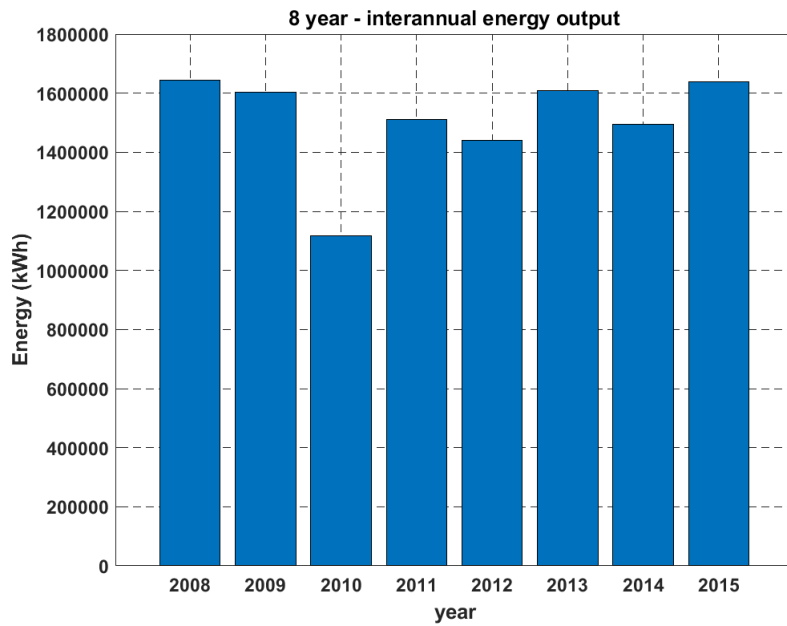
(b)  $C_p$  scatter plot, mean and 90<sup>th</sup> percentile binned values

Fig. 4.10. 5-year wind turbulence intensity and coefficient of performance.

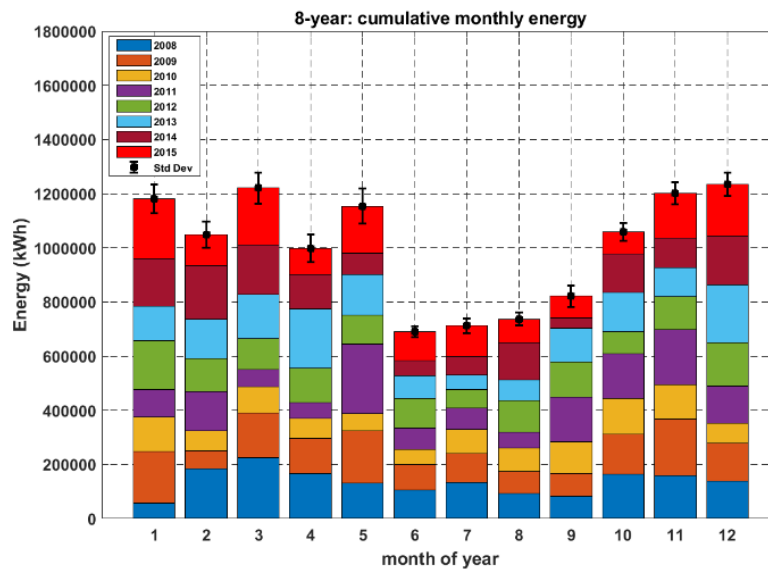
### 4.5.3 Inter-annual and seasonal energy analysis

Fig. 4.11 shows the measured annual electrical energy production in each year from 2008 to 2015 inclusive. The measured annual electrical energy production shows relatively similar values with an 8-year cumulative value of 12057349 kWh, mean value of 1507168 kWh with a standard deviation of 173878 kWh, representing a variation

of  $\pm \sim 12\%$  inter-annual variation about the mean over the period. 2010 was an exceptionally poor wind year in Ireland, due to blocking high pressure systems that occurred in winter and spring months of that year (Leahy and Foley, 2012). This is reflected in lower electrical energy production for this year. This relative outlier has a big influence on the 8-year inter-annual variation. If 2010 is not included, then the average annual electrical energy is 1562800 kWh with a standard deviation of 79887 kWh, representing an inter-annual variation of  $\sim 6\%$ . However, outlier years should be considered over the timeframe of the full lifetime of a wind turbine, therefore an inter-annual variation in the Irish climate of  $\sim 10\%$  in electrical energy is suggested for single turbines of this scale, in behind the meter applications. The cumulative monthly electrical energy production over the 8-year period is shown in the stacked bar graph of Fig. 4.11. The winter months are clearly the more productive months, as expected. They range from 1235000 kWh in December to 56% of this, i.e., 690300 kWh in June. This shows that, on a seasonal basis, in behind-the-meter application that a site with demand that is higher in the autumn, winter and spring months would benefit more from onsite consumption of the electrical energy produced. This is interesting in the Irish context as it shows potential complementarity with onsite solar as part of a hybrid behind-the-meter system, especially if site energy demand is relatively constant over the year.



(a) Inter-annual energy



(b) Mean monthly annual values

Fig. 4.11. 8-year Inter-annual and seasonal energy performance.

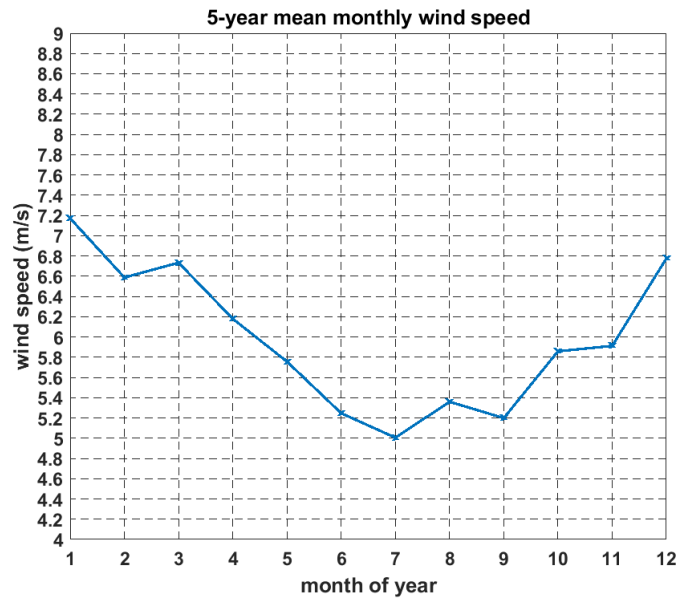
The mean monthly values and variations over the 8-year period are given in Table 4.5. The variation on the monthly mean values, as expected, are higher than the inter-annual variations ranging from 25% in June to 44% in May. The months of April and May show the largest variations. This can be attributed to mesoscale coastal influences at the site where local, thermally generated, sea breezes in the transition period from winter to summer occur. The seasonal distribution of winds will be shown in more detail in the upcoming sections.

**Table. 4.5.** 8-year mean monthly energy output values

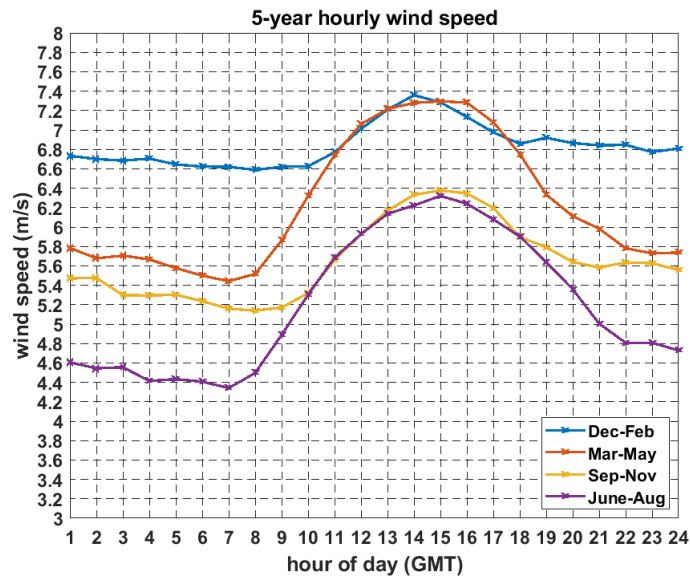
Month	Mean Energy (kWh)	Std Dev (kWh)	Variation (%)
Jan	147559	53348	36
Feb	131113	47757	36
March	152591	56486	37
April	124703	51115	41
May	144218	64130	44
June	86282	21480	25
July	89022	27355	31
Aug	92066	24384	26
Sep	102681	39197	38
Oct	132371	33567	25
Nov	150172	40616	27
Dec	154391	42910	28

#### 4.5.4 Seasonal and diurnal wind analysis

Analysis of the higher resolution 10-minute data over a 5-year period within the 2008 to 2015 timeframe shown in Table 4.4, gives the mean monthly and hourly wind speeds. The mean monthly wind speeds in Fig. 4.12(a) show that the highest range of the mean wind speed, between 5.0 m/s and 7.2 m/s, occurs between summer and winter respectively. Diurnal variation occurs to some extent in all seasons, Fig. 4.12(b), but is most apparent in the spring, summer and autumn months. This can be attributed to the turbulence mixing of upper level higher speed winds with winds at lower levels, caused by thermally driven daytime convective eddy circulation on warmer days. In addition, as mentioned in Chapter 3, thermally driven onshore sea breezes also can enhance the daytime winds, particularly in the spring season. Wind speeds are particularly enhanced in the afternoon between  $\sim 12.00$  and 16.00 when the land surface, due to its heat capacity, is at its warmest following absorption of solar energy over the day from sunrise.



(a) Mean monthly wind speeds



(b) Mean hourly wind speeds

**Fig. 4.12.** 5-year hub-height mean monthly and mean hourly wind speeds.

The resulting breakdown of the cumulative electrical energy, on hourly and seasonal basis, is shown on the stacked bar chart in Fig. 4.13. In line with the wind speed variation, the diurnal electrical energy enhancement occurs in the spring summer and autumn in the early to mid-afternoon. In the summer months, the electrical energy enhancement is from 11.00 to 17.00 which can be attributed to large convective eddies from surface heating and onshore breezes. From an onsite energy demand perspective, an afternoon demand requirement from spring to autumn, could benefit

from behind the meter wind, for example, a summer cooling load. On a diurnal basis in the summer months, behind the meter wind would not be as complementary with solar energy, unlike the monthly seasonal complementary outlined previously. Alternatively, onsite storage could be used to shift energy from the day to night if there is sufficient night time load. However, if night time electricity market prices are lower, the economics of shifting energy from day to night would need to be assessed in further detail.

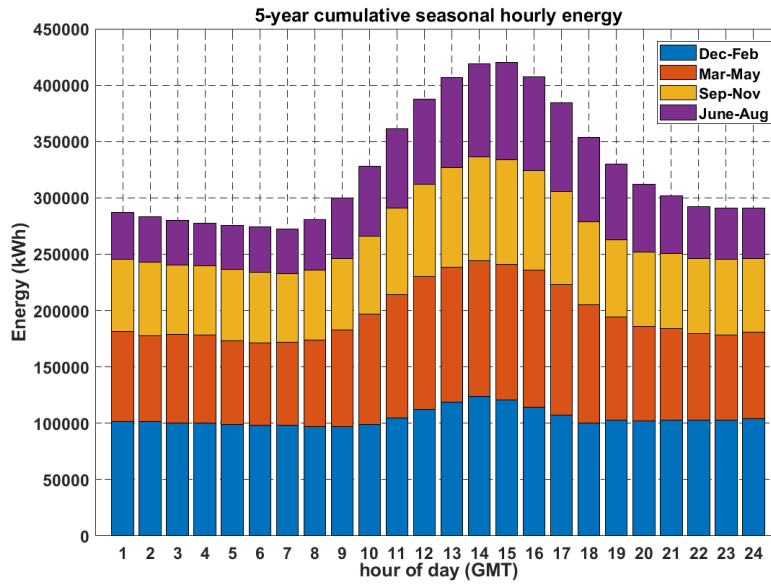


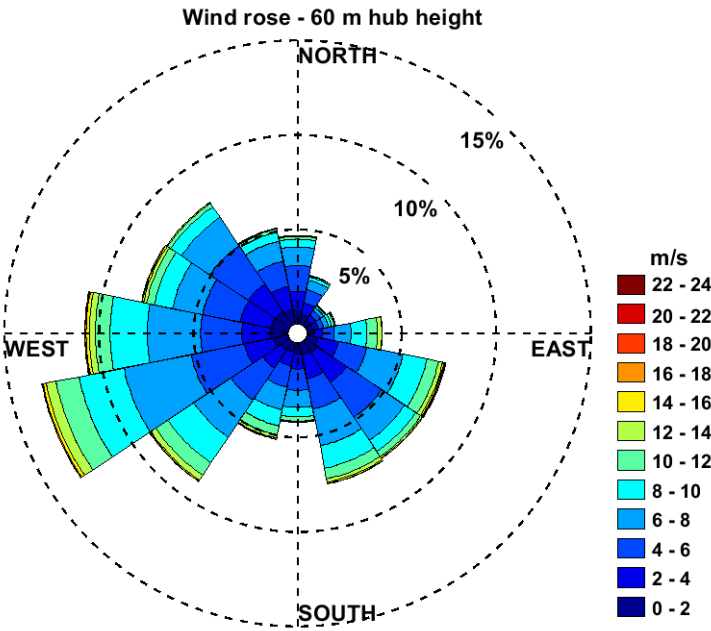
Fig. 4.13. 5-year cumulative hourly energy output.

#### 4.5.5 Directional wind analysis

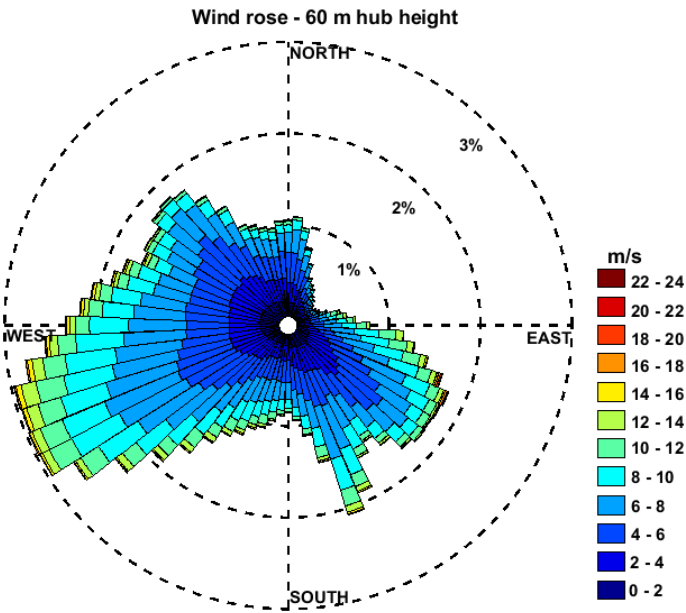
The 5-year 16- and 72-sector wind roses from SCADA data are shown in Fig. 4.14(a). It can be seen that the prevailing winds are from the southwest (SW) and southeast (SE) sectors. There are also significant winds in the northwest (NW) sectors. There are lighter winds from the northeast (NE). The high wind sectors of the SW and low wind sector of the NE sectors can be generally explained by general prevailing wind direction in the climate of Ireland (Dwyer, 2012). However, the 72-sector wind rose shows some interesting characteristics. The wind from the south southwest (SSW) to the south southeast (SSE) are greatly reduced, while in the SE sectors there are distinct individual sectors with higher and lower winds. Referring back to Fig. 4.8, a many of the significant low-rise industrial building appear in the SSW and SE sectors. The SE sector also contains a tall narrow 47 m building. In addition, as



the site is also by the coast, there may be seasonal changes in wind directions with enhanced onshore sea breezes from east.



(a) 16-sector, 5-year wind rose



(b) 72-sector, 5-year wind rose

Fig. 4.14. 5-year wind roses.

To investigate the seasonal changes in wind direction, the seasonal wind roses of the 5-year period are shown in Fig. 4.15.

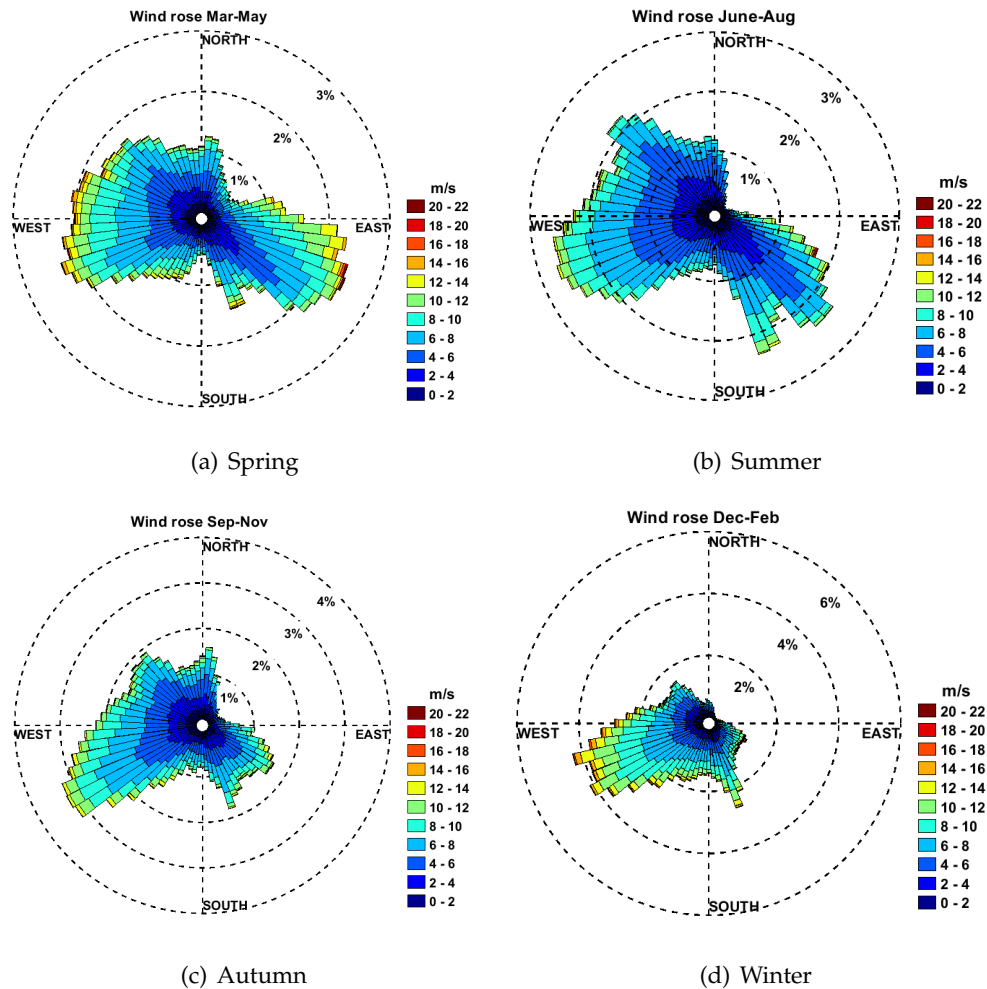
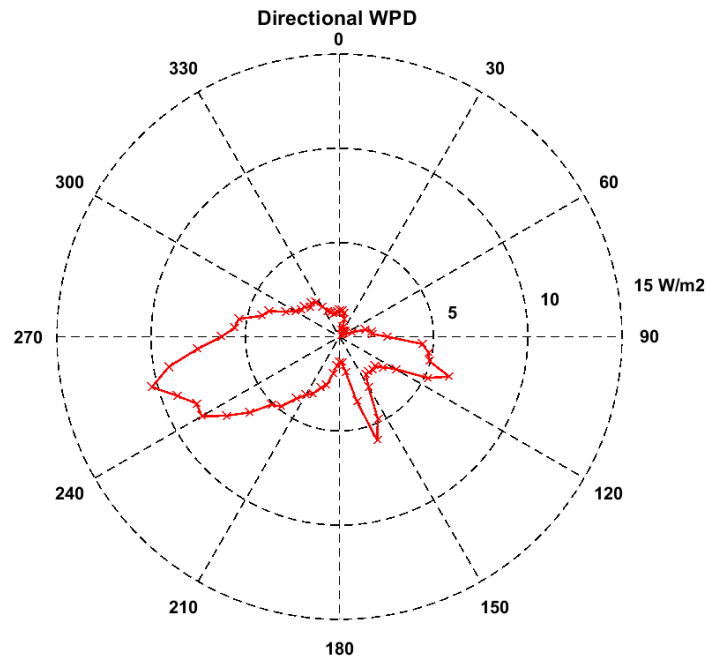


Fig. 4.15. 72-sector seasonal wind roses.

There are particularly prevalent winds in the ESE and SE sectors in the spring season, highlighting the influence of the land-sea interface that creates the thermally driven sea breezes. This is more prominent when the sea temperatures are still low from cooling over the winter season, but the increasing solar isolation heats the land surface faster, due to differences in heat capacities of the land and sea. As the sea warms up into the summer months the easterly winds are more to the southeast. The SE components reduce in the autumn season when solar isolation reduces but the sea temperature remain high from summer warming, therefore the land-sea thermally driven winds are reduced. There is a high SSE wind speed component is present in all seasons, including the winter season, suggesting that not all wind in the SE

sectors are the result of thermally driven onshore winds from the sea. Wind from the west (W) and NW occur more often in spring and summer. In addition, there is the reverse in the direction of diurnal daytime onshore sea breeze, from the east, to offshore land breezes from the west at night when the land cools. These night time land breezes would be of lower strength as the temperature difference between the land and sea would not be as high as in the daytime. Also, vertical convective turbulent eddies in the ABL direction would reduce at night, effectively reducing or stopping turbulent mixing between the upper and lower level winds. The NE sectors have very low wind speeds in all seasons. This can be explained by these sectors not being prevailing wind direction. The hills to the north east of the site may also have a blocking effect on low speed winds. The winter months are dominated by WSW winds. There is a specific standout south SSE sector with high wind speeds in the winter season. It is unlikely that SSE winds in this case is caused by thermally driven sea breezes based on the diurnal wind profiles of Fig. 4.12. It is also notable that there are low winds in the S, SSW and in some SSE sectors across all seasons. This implies that seasonal influences alone on the prevailing don't fully explain shape of the shape of the 5-year 72-sector wind rose. To examine this further in the context of wind energy at the site. The 5-year directional WPD is plotted in Fig. 4.16.



**Fig. 4.16.** 72-sector directional wind power density, (Site average -  $244.5 \text{ W/m}^2$  ).

The site average wind power density over 5-year time frame is  $244.5 \text{ W/m}^2$ . The directional breakdown shows that higher wind power densities appear in the WSW sectors. Distinct reductions are observed in the S to SW sectors, NE sectors and the SE sectors. The particularly sharp changes in the *WPD* in the SE, S and SSW sectors suggest that local building obstacles that occupy those sectors are having an influence. As expected, there is very little wind in the N and NE sectors confirming that the hills  $\sim 8 \text{ km}$  to the northeast have a blocking effect on the weaker non-prevailing wind from these sectors. The next step is to investigate the directional behaviour of the wind turbine power curves and the directional turbulence intensity.

#### 4.5.6 Directional power curve and turbulence analysis

Firstly, Fig. 4.17 compares the site-specific power curve with the manufacturer's power curve. It can be observed that the site power curve at wind speeds below  $10 \text{ m/s}$  is lower than the manufacturer's power curve. Between  $10 \text{ m/s}$  and  $14 \text{ m/s}$  there is a good match between the manufacturer's and site power curve.

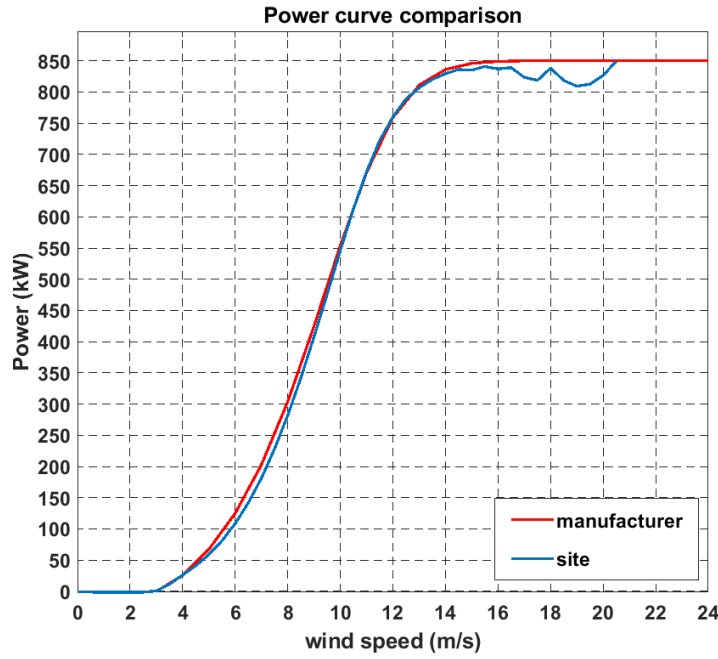
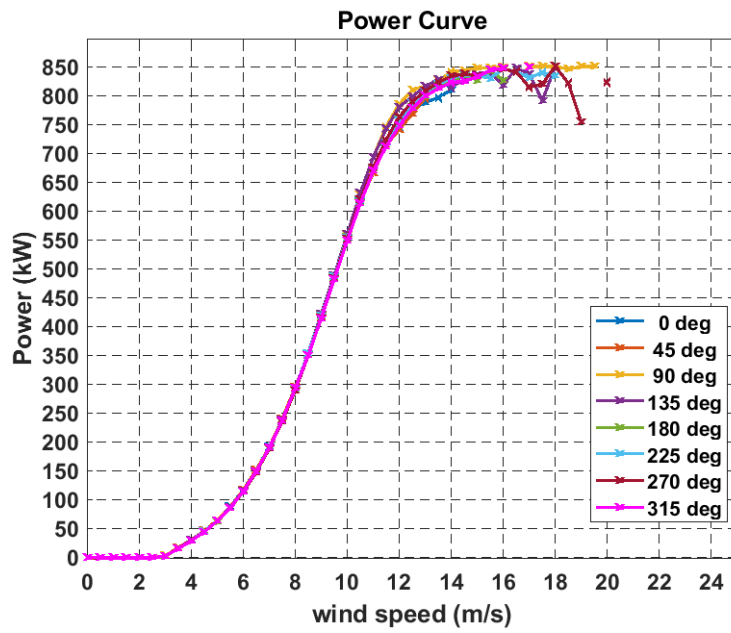


Fig. 4.17. Site and manufacture's power curve.

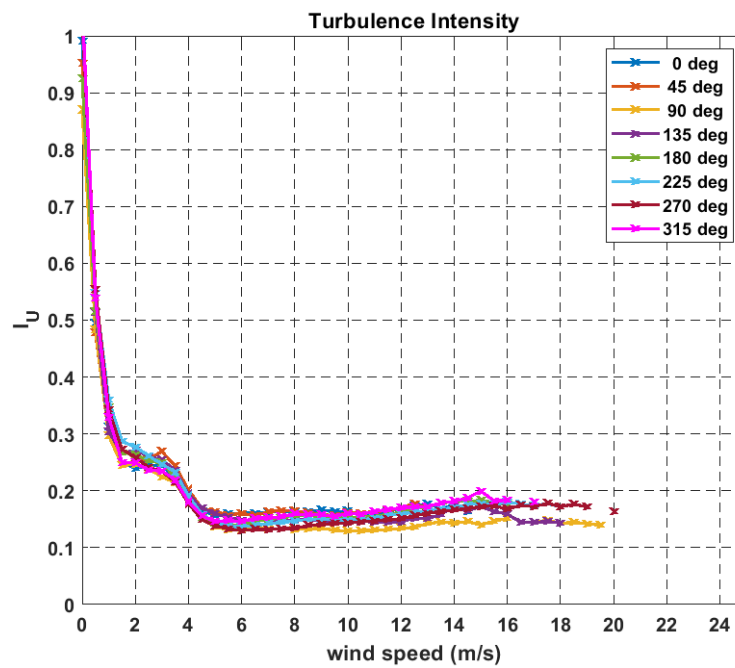
A nacelle transfer function (NTF), that accounts for the difference between the hub-height wind speed upwind of the rotor and at the nacelle anemometer location, is built into the wind turbine SCADA system by the manufacture. The NTF is determined by the manufacturer at an independent accredited wind test site. The details of NTF are not accessible to the end-user in this case. However, some studies in the large-scale wind industry show that wind turbine power output is dependent on a wide range of ambient wind conditions that 10-minute SCADA data may not fully capture such as atmospheric stability effects, high frequency turbulence and complex flow vortices introduced by the increased active blade pitching near rated power (Antoniou, Pedersen, and Enevoldsen, 2009; St. Martin et al., 2017). This means that the site-specific power curve of a given wind turbine may seldom exactly match the manufacture's supplied power curve that was produced at an accredited test site, therefore the site specific directional power curves are examined here.

Fig. 4.18(a) shows the power curves from the SCADA data analysis, applying the methods of Eqs. (4.6) and (4.7), for 8 directional sectors. The power curves appear to deviate the most above wind speeds of about 10 m/s. This could be explained by the turbine control mode changing from variable speed to fixed speed and variable blade pitch operation at these wind speeds. Wind speeds above  $\sim 16$  m/s have a

low frequency of occurrence, Fig. 4.9, therefore scatter in the data may introduce deviations above this wind speed. The best power curve above 10 m/s occurs for wind coming from the east (i.e.,  $90^\circ$ ) looking towards the coast in a direction where there are few local building obstacles. Lower power curves are for directions from  $180^\circ$  and  $225^\circ$  where low-rise industrial building obstacles are situated. Other directions, such as  $315^\circ$ , lower power performance between 10 m/s and 12 m/s is observed, increasing again at higher wind speeds. An analysis of turbulence intensity with direction, shown in Fig. 4.18(b), indicates that directions with lower turbulence intensity, such as  $90^\circ$ , corresponds to direction of higher power performance above wind speeds of 10 m/s. The sectors with higher turbulence intensity coincided with the sectors that contain building obstacles. Interestingly, at lower wind speeds less than 8 m/s the power curves in the higher turbulence sectors are marginally better than those in the lower turbulence sectors. This indicates that the wind turbine can extract more power from higher turbulent wind flows at lower wind speeds due to the rotor being better able to respond to the wind speed variations at lower wind speeds. The directional electrical energy characteristics are examined next.



(a) Directional power curves



(b) Directional turbulence intensity curves

Fig. 4.18. Directional power and turbulence intensity curves.

#### 4.5.7 EER and site feature analysis

The new concept of an *EER* illustrates the directions of greatest electrical energy yield for an operating turbine in real-world conditions. To gain further insights into the local site features on the energy performance an *EER* in 72 sectors defined by Eqs. (4.10) and (4.11) is created which shows the directions where the useful electrical energy comes from. A plot of the *EER* is shown in Fig. 4.19. Its shape has distinctive directional features showing the directional sectors where the electrical energy performance of the wind turbine is high and low. Reduced energy output directional sectors are observed in the S, SSW, SE, N and NE sectors while higher energy appears in W, SSE and NSE sectors. The *EER* shows subtle but important differences to the wind rose, Fig. 4.14, and the power density rose, Fig. 4.16, by illustrating the highest electrical energy yielding sectors for this turbine at this site, which is of most interest to the end-user.

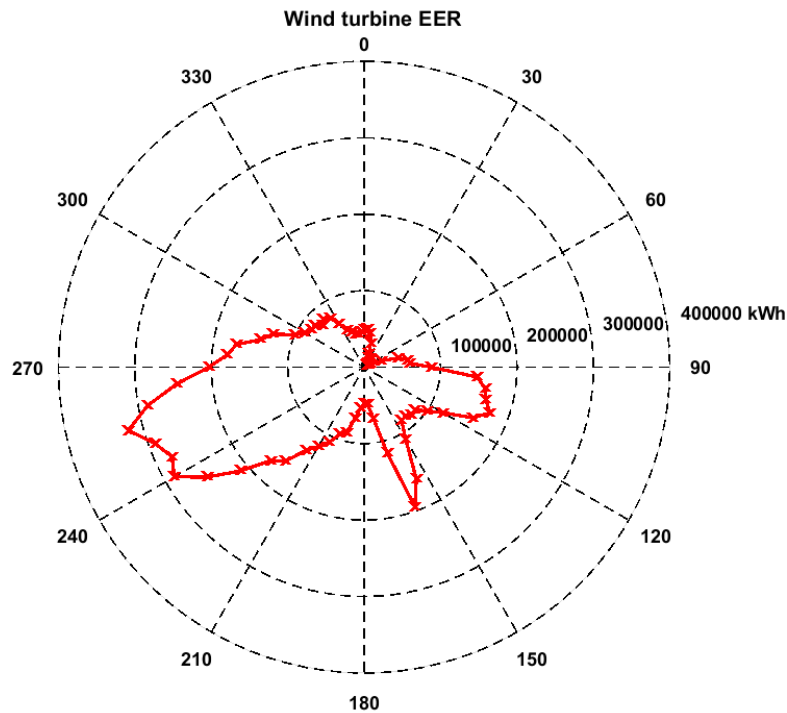
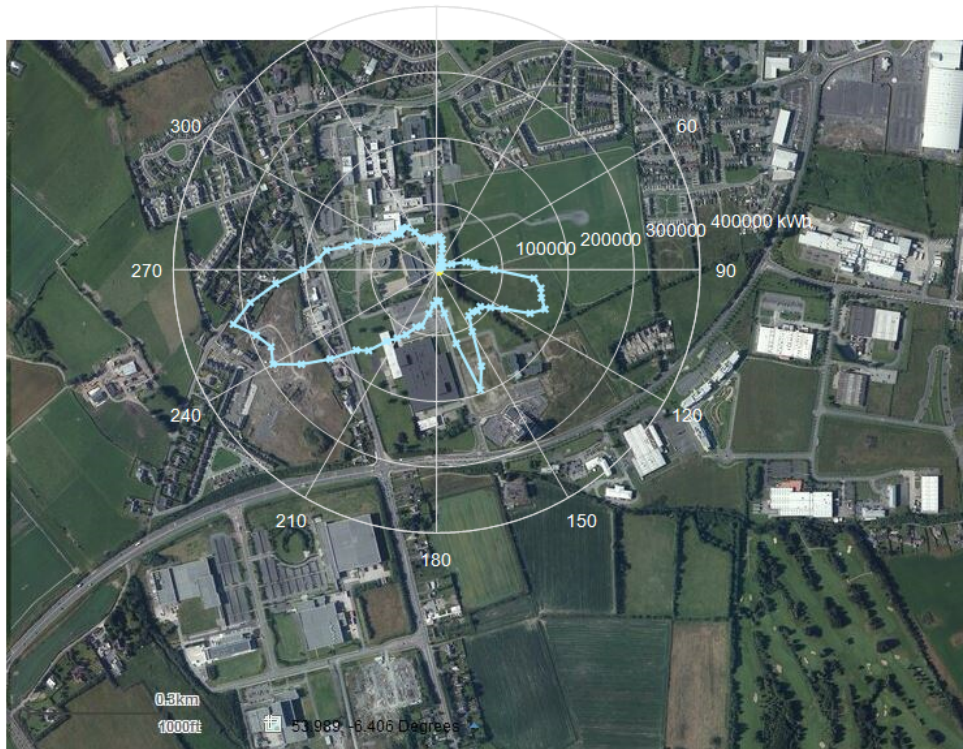


Fig. 4.19. Wind turbine *EER* in 5° sectors.

An overlay of the *EER* on the local map of Fig. 4.20 reveals how local obstacles may be influencing the directional energy performance of the wind turbine. From approximately 170° to 210° there is a much reduced energy output while higher



energy performing sectors occur from  $150^{\circ}$  to  $170^{\circ}$  and  $85^{\circ}$  to  $120^{\circ}$ . The highest energy performing sector is from  $220^{\circ}$  to  $280^{\circ}$ . Very little energy output comes from north east sectors  $0^{\circ}$  to  $90^{\circ}$ .



**Fig. 4.20.** Wind turbine *EER* overlaid at wind turbine location on local site plan.

On closer examination of the overlaid *EER* with the local obstacles described in Fig. 4.20 and Table 4.2, views from the 60 m hub height of the wind turbine, give the following observations. Fig. 4.21 shows the view from the wind turbine in the direction from  $170^{\circ}$  to  $210^{\circ}$  across obstacle Nos. 1 and 5 where there is a much reduced electrical energy output.



**Fig. 4.21.** Wind turbine hub height view looking  $170^\circ$  to  $210^\circ$  (Obstacles: No.1 in foreground, No. 5 in background).

As the wind turbine has a hub height of 60 m and the majority of these buildings are 7 m to 12 m in height (i.e., no more than 20% of the hub height) with a distance of 150 m to 1100 m from the turbine location, they should not be having as great an influence as they appear to be having, according to current IEA siting rules and obstacles models described in the Chapters 2 and 3. Narrower high energy performance sectors from  $150^\circ$  to  $170^\circ$  are observed and the corresponding view from the turbine hub height, Fig. 4.22, shows an opening (including a road) between the 47 m high hotel (obstacle No. 2 in Table 4.2) 335 m away and obstacle No. 1. This may point to channelling or steering effects of wind flow between the tall narrow hotel and the low broad building(s) of obstacle No. 1 and with possible influence from obstacles No. 5 to the far right.



**Fig. 4.22.** Wind turbine hub height view looking  $150^\circ$  to  $170^\circ$  (Obstacles: No. 2 tall hotel to left, No. 1 to right).

Energy reduction is again seen in the  $110^\circ$  to  $150^\circ$  directional sectors due to the tall hotel and additional buildings further to the south east. This view of these additional buildings to the south east is shown in Fig. 4.23 (obstacle No. 2) and Fig. 4.24 (obstacles Nos. 4 and 10) which have heights from 8 m to 13 m and are 520 m to 670 m from the turbine location.



**Fig. 4.23.** Wind turbine hub height view looking  $130^\circ$  to  $150^\circ$  (Obstacle: No.2).

Higher energy appears in  $95^\circ$  to  $120^\circ$  sectors which appear to fall between obstacles Nos. 4 and 11 which are 770 m to 1030 m away from turbine. Between these obstacles is a lower building 7 m in height and a road that runs to the coast. This view, Fig. 4.24, shows the fetch to the east coast with a gap between building obstacles Nos. 10 and 11 that less impede onshore winds on to the site. This is also a direction from which the turbulence intensity is lower and the turbine power curve is better at higher wind speeds. It again appears to indicate the energy reducing impact of low rise building on the turbine energy output and the influence of gaps between building that may be enhancing energy performance.



**Fig. 4.24.** Wind turbine hub height view looking  $95^\circ$  to  $130^\circ$  (Obstacles: Nos.4, 10 and 11).

Energy performance in the N and north NE sectors appear to be drastically reduced with no obvious shaping of the *EER* by local obstacles. There is more open space out to 450 m to the east and northeast of the wind turbine site (area 9 in Table 4.2). When viewed from the turbine hub height as shown in Fig. 4.25, the hills (area A in Table 4.1) with elevations of approximately 650 m at a distance of 8 km away, point to the sheltering impact of the hills on a regional or mesoscale that are being experienced by the wind turbine at its lower elevation.





**Fig. 4.25.** Wind turbine hub height view looking  $30^\circ$  to  $90^\circ$  (Site A: Hills of 650 m elevation  $\sim 8$  km away).

An overlay of the *EER* on the regional plan of Fig. 4.7 is shown in Fig. 4.26. It becomes apparent that the hills to the north east from  $0^\circ$  to  $90^\circ$ , regions A and B in Table 4.1 shape the electrical energy rose in these directions due to blocking effect on low speed non-prevailing winds. The higher energy performing ESE and SSE from the sea primarily influenced by the local building obstacles as describe previously. In fact, in directions from  $90^\circ$  to  $330^\circ$  there are no significant onshore topographical features in the region suggesting that the electrical energy rose is being significantly shaped in these directions by local building obstacles.

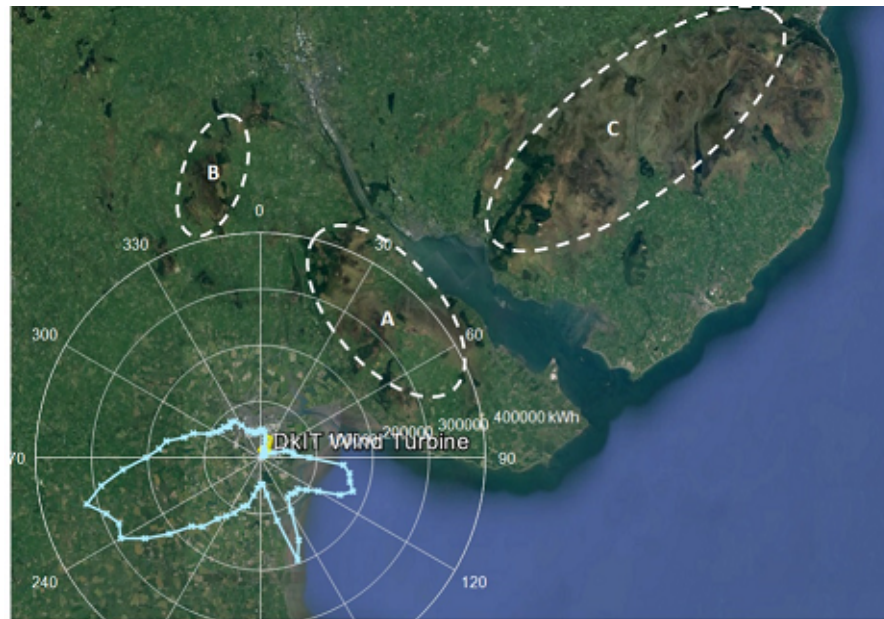


**Fig. 4.26.** Wind turbine electrical energy rose overlaid on regional site plan.

Fig. 4.27 shows the town of Dundalk to the north of the wind turbine site. The hills (Feature B in Table 4.1) in background are approximately 13 km to 18 km away. Most of the town consists of house and commercial building less than 10 m in height that come close to the turbine location. Energy remains much reduced broadly across the NW to NE sectors as the results of non-prevailing winds, mesoscale impacts of hills and the local higher surface roughness impact of town.



**Fig. 4.27.** Wind turbine hub height view looking  $330^{\circ}$  to  $30^{\circ}$  (Features A and B Hills of 650 m elevation  $\sim 13$  km -18 km away).

Finally, the view of the predominantly higher the energy sectors from  $220^{\circ}$  to  $290^{\circ}$  is shown in Fig. 4.28. These sectors have a good wind fetch with open fields beyond  $\sim 500$  m upwind including an upwind motorway that runs in line the oncoming wind flow. An upwind row of dwelling houses (obstacles No. 7) 487 m to 728 m away has a height of  $\sim 7$  m. This appears to have a small shaping impact on the electrical energy rose. Small energy spikes in the *EER* on either side of the row of houses suggest that winds are channelling either side of and reducing over the houses.



**Fig. 4.28.** Wind turbine hub height view looking  $220^{\circ}$  to  $290^{\circ}$  (Obstacle: No. 7).

#### 4.5.8 Impact of gearbox aging and replacement on wind turbine performance

The power curves for 2008, 2014, 12 months in 2017-18 and 2019 are compared in Fig. 4.29.

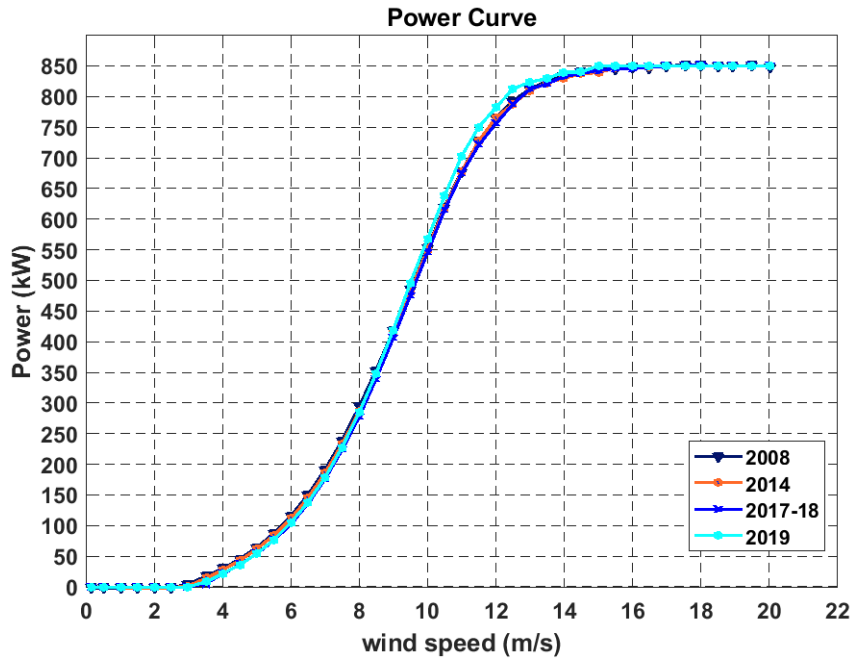
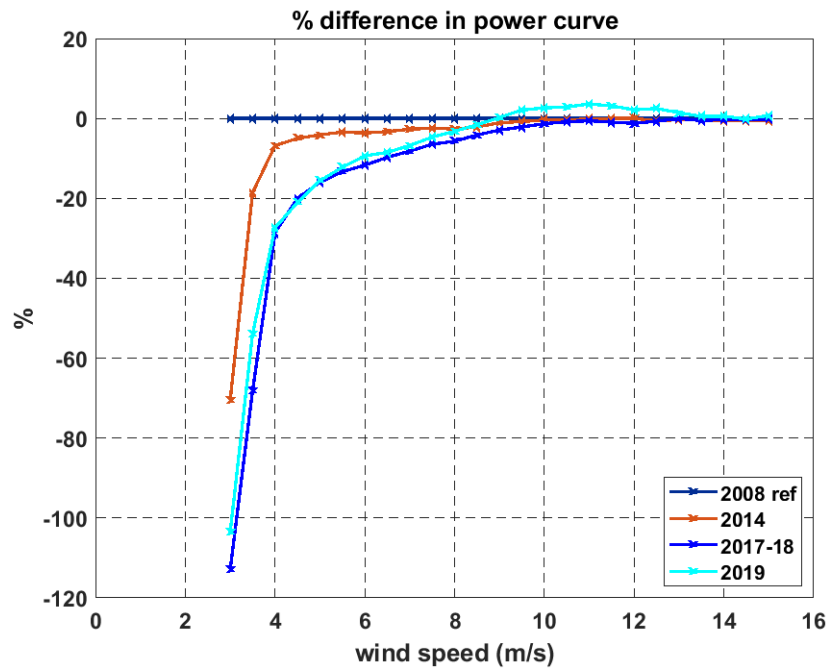


Fig. 4.29. Power curves — 2008, 2014, 2017–2018 and 2019.

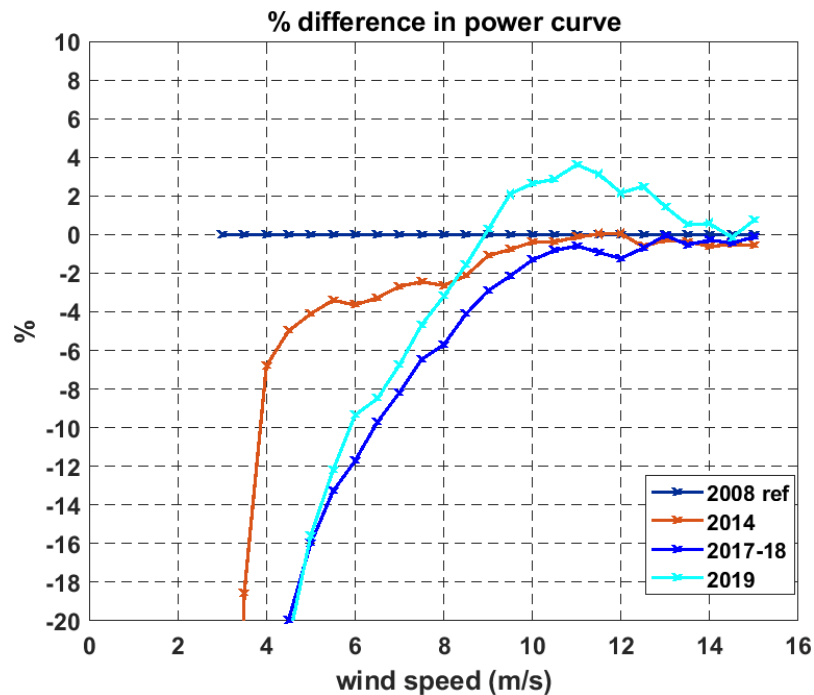
Fig. 4.30 shows the bin-wise percentages differences with respect to the reference year of 2008 with further nightlights the degradation in power between cut-in wind speed and 10 m/s, with biggest reductions below 8 m/s. The 2019 power curve, post gearbox replacement, is different to the power curves of the years prior to the gearbox replacement. It is increased above  $\sim 8$  m/s but less so at lower wind speeds. Table 4.6 shows the % difference in the mean power bins of the power curves with respect to the 2008 power curve along with the bin-wise K-S statistical test of these. The K-S tests show that the null hypotheses is rejected for power data in the wind speed bins from 3.5 m/s to 10.5 m/s, indicating that they are significantly different i.e. years 2014 and 2017-18 have different empirical distributions compared with 2008. This supports the suggestion that the power curve degradation is real in these ranges. Interestingly, for 2019 with the new gearbox the power curve increases most above 8 m/s and surpasses the 2008 power curve above  $\sim 9.5$  m/s. It also supported



by the K-S test rejection of the null hypotheses from 3.5 m/s to 13.5 m/s. This suggest that other factors, such as the influence of aging on other components including the blades, pitching system, yaw system, generator and control anemometer are contributors to turbine power degradation.



(a) Broad overview of power curve differences



(b) A focused view over the most energy productive wind speeds

Fig. 4.30. Relative bin-wise % differences in power curves.

**Table. 4.6.** Power curve bin differences and K-S statistic tests,  $\alpha = 0.05$ 

<b>bin ws (m/s)</b>	<b>2008 vs 2014</b>			<b>2008 vs 2017-18</b>			<b>2008 vs 2019</b>		
	$\Delta P$ (%)	$p$	$k_s$	$\Delta P$ (%)	$p$	$k_s$	$\Delta P$ (%)	$p$	$k_s$
2.50	14.79	0.43	0.28	-20.66	0.47	0.32	-40.61	0.18	0.90
3.00	-70.58	0.41	0.10	-112.93	0.01	0.21	-103.63	0.04	0.26
3.50	-18.57	0.00	0.16	-68.20	0.00	0.41	-53.92	0.00	0.47
4.00	-6.79	0.00	0.17	-28.62	0.00	0.51	-27.34	0.00	0.60
4.50	-4.99	0.00	0.13	-19.95	0.00	0.51	-21.05	0.00	0.58
5.00	-4.10	0.00	0.14	-16.00	0.00	0.48	-15.58	0.00	0.56
5.50	-3.40	0.00	0.13	-13.30	0.00	0.45	-12.21	0.00	0.47
6.00	-3.65	0.00	0.12	-11.72	0.00	0.40	-9.35	0.00	0.43
6.50	-3.28	0.00	0.14	-9.72	0.00	0.36	-8.50	0.00	0.35
7.00	-2.69	0.00	0.13	-8.19	0.00	0.33	-6.76	0.00	0.35
7.50	-2.44	0.00	0.12	-6.46	0.00	0.28	-4.68	0.00	0.31
8.00	-2.64	0.00	0.13	-5.71	0.00	0.23	-3.21	0.00	0.22
8.50	-2.14	0.00	0.13	-4.13	0.00	0.19	-1.58	0.00	0.21
9.00	-1.10	0.00	0.11	-2.91	0.00	0.10	0.25	0.00	0.13
9.50	-0.78	0.00	0.08	-2.15	0.00	0.08	2.10	0.02	0.06
10.00	-0.40	0.02	0.05	-1.31	0.67	0.03	2.64	0.02	0.07
10.50	-0.39	0.07	0.05	-0.83	0.06	0.05	2.87	0.00	0.12
11.00	-0.14	0.04	0.06	-0.59	0.01	0.07	3.62	0.00	0.17
11.50	0.02	0.85	0.03	-0.93	0.00	0.10	3.13	0.00	0.28
12.00	0.04	0.33	0.05	-1.24	0.16	0.07	2.16	0.00	0.27
12.50	-0.63	0.81	0.04	-0.70	0.24	0.08	2.49	0.00	0.27
13.00	-0.29	0.00	0.13	-0.04	0.37	0.08	1.43	0.00	0.26
13.50	-0.36	0.33	0.08	-0.54	0.60	0.08	0.52	0.00	0.28
14.00	-0.62	0.01	0.15	-0.29	0.01	0.17	0.56	0.11	0.16
14.50	-0.51	0.01	0.17	-0.44	0.15	0.13	-0.15	0.05	0.22
15.00	-0.55	0.00	0.25	-0.13	0.43	0.13	0.73	0.29	0.21

A comparative impact on *AEP* is carried out by using these power curves with a number of wind years whose wind speed distributions are plotted in Fig. 4.31. The corresponding wind resource characteristics for each wind year considered are given in Table 4.7.

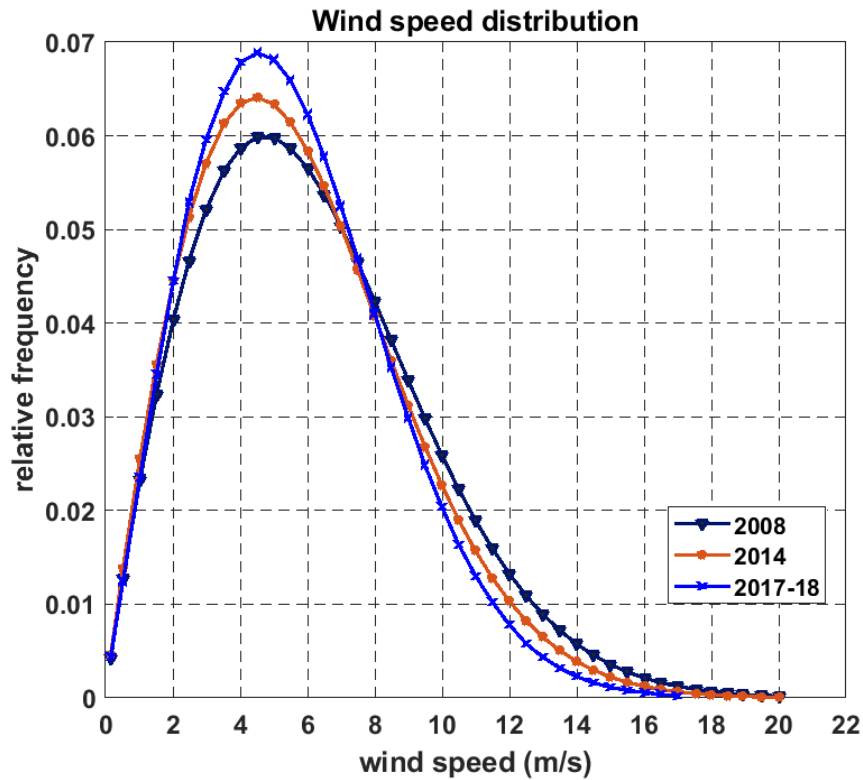


Fig. 4.31. Annual wind speed distributions for 2008, 2014 and 12 months in 2017-18.

Table. 4.7. Wind resource parameters

Year	$U_{ave}$ (m/s)	Weibull c (m/s)	Weibull k	Density (W/m <sup>2</sup> )
2008	6.2	6.95	1.91	280.5
2014	5.8	6.54	1.93	227.2
2017–2018	5.6	6.32	2.04	196.6

The *AEP* comparison for each power curve in each of the wind years in Table 4.8 shows, in all cases, a noticeable change in *AEP* degradation using 2014 and 2017–2018

power curves compared to the 2008 power curve. The *AEP* degradation is consistently reduced when using the 2019 power curve, which corresponds to the gearbox replacement. This shows that the gearbox replacement in 2019 improves performance, as would be expected; however, it did not fully return the wind turbine to the 2008 level of performance. For example, taking the 2008 wind year, the overall 4.3% in *AEP* degradation using the 2017–2018 power curve is reduced to 3.0% using the 2019 power curve, i.e., approximately a 30% contribution to the total *AEP* degradation from the gearbox alone. Interestingly, this improvement of 30% occurs for the higher wind speed year of 2008 with a lower improvement for the lower wind speed year of 2017–2018, equating to approximately 22%. This suggests that other factors, such as the ageing of other components outlined previously may be having an influence and that the influence of the gearbox is less significant at lower wind class sites such as in this case.

**Table. 4.8.** Energy parameters

Wind year	Power curve	<i>AEP</i> (kWh)	$\Delta AEP$ (kWh)	$\Delta AEP$ (%)
2008	2008	1837900		
	2014	1810700	-27200	-1.48
	2017-18	1759600	-78300	-4.26
	2019	1782200	-55700	-3.03
2014	2008	1598300		
	2014	1571500	-26800	-1.68
	2017-18	1520200	-78100	-4.89
	2019	1539900	-58400	-3.65
2018-19 (12 months)	2008	1434500		
	2014	1407300	-27200	-1.90
	2017-18	1354400	-80100	-5.58
	2019	1372000	-62500	-4.36

A comparison of the *AEP* distribution differences with wind speed for each power

curve and the 2008 wind year, shown in Fig. 4.32, reveals that degradation has occurred, particularly at wind speeds below rated power, where this turbine is operating a large proportion of the time. Also, much of the improvement, due to the gearbox replacement (2019 power curve) occurs, at wind speeds above 6 m/s. This is consistent with the greater improvement observed in the higher wind year of 2008 Table 4.8. Therefore, similar wind turbines located at wind farms sites with better wind resources can expect to see a better improvement in energy performance with new gearbox replacements compared to turbines at less windy locations.

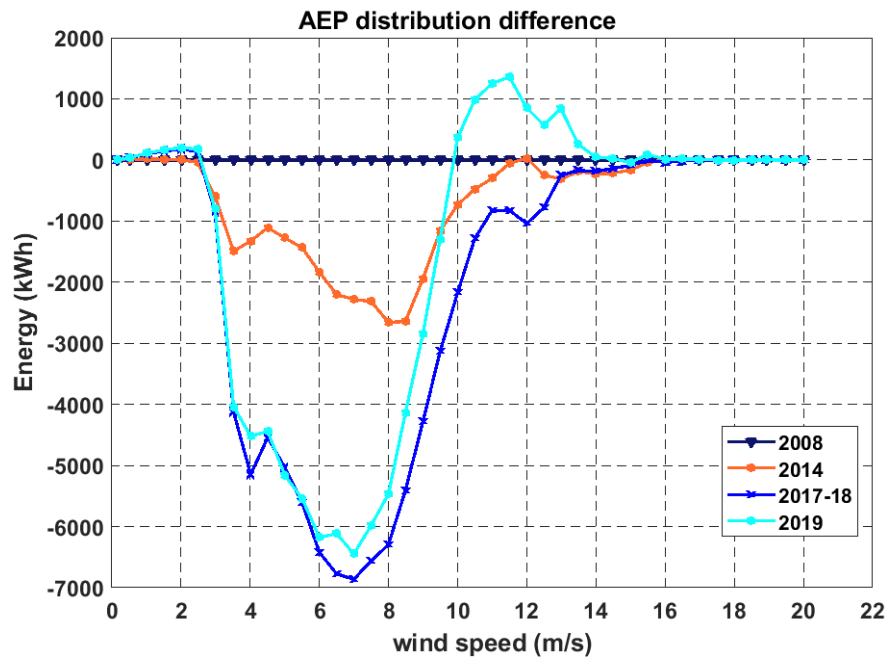


Fig. 4.32. AEP variations compared to 2008 reference year.

## 4.6 Discussion

### 4.6.1 Obstacle impacts

The results show that the power and energy performance of a wind turbine is dependent on both the local site feature impact on wind flow and the behavioural response of the wind turbine system itself to different wind flow conditions. The approach of using a 72-sector *EER* overlaid on local and regional plans reveals more clearly how the energy performance can be significantly impacted by local and regional features. It shows that building obstacles approximately 20% of the turbine hub height and

up to 1.5 km away can have a significant energy blocking effect, e.g., 12 m high industrial buildings, while a smaller impact is observed for building between 10% and 20% of hub height. This implies that simple reported rules of thumb reported in the literature of flow around obstacles and IEA guidance, that state that obstacle up to 2 obstacle heights and up to 20 obstacle heights away from the obstacle, do not fully conform with the finding here. Similarly, findings from a fence experiment by (Peña et al., 2016), with dimensions of 30 m wide 3 m high and 0.04 m thick, that showed influences on wind flow at 1.46 fence heights an up to a maximum 11 fence heights downwind, do not match well with the findings here either. This is possibly due the fence being a thin (i.e., 2D like) body in the direction of wind flow, i.e., unlike a large 3D obstacles like a building.

Wider building obstacles that appeared in directional sectors, viewed from the wind turbine, appeared to have the bigger energy reducing impact on the wind turbine output. This indicates that low broad building obstacles can have a significantly bigger energy reducing impact compared to taller narrower buildings. This may be due to low broad buildings forming wider localised internal boundary layers thereby increasing wind shear and/or steering of the wind flow in other directions, while wind flow may move around taller narrower buildings, giving a smaller sectoral width of energy reduction. This tends to agree with the flow characteristics around the rectangular bodies with various aspect (height to width) ratios reported by (Gu and Lim, 2012) who found that transverse width has a more substantial impact of the surface pressure around bluff bodies compared to the longitudinal length. Channelling of flow in gaps between building and along roads running parallel to the oncoming wind direction from the SSE of the site is observed to enhance energy performance but the turbulence intensity is higher. This may be due to gusting as a result of pressure differences around buildings that form in the channel and the dissipation of vortices in the flow downwind of the channel in the direction of the wind turbine. Mesoscale effects appear to be primarily blocking effects by hills 8 km to 15 km to the northeast of the site, that have an elevation of  $\sim 650$  m, where weaker winds come from. The key outcomes from this study is that broad obstacles with a height of 20% of turbine tower height or greater up to 1.5 km away in prevailing wind direction(s) can have a negative impact on energy performance. Therefore, local obstacles within at least a 1.5 km radius should be considered. If obstacles

greater than 20% of proposed tower height occupy more than 30% of the field of view in prevailing wind directions, the study suggests increasing the tower height or to reconsider the viability of the project location. The study suggests that large energy users considering a large scale behind the meter project stages should, in the initial feasibility stages, consider regional topography within a 20 km radius of the proposed turbine location as there is potential for wind blocking, speed up or steering depending on general prevailing wind direction of the region.

#### 4.6.2 Gearbox replacement energy impact

Replacing the gearbox shows best improvement in energy output above wind speeds of 6 m/s suggesting that the gearbox aging has a smaller influence at lower wind class sites. Allowing the gearbox to run to failure may be economically justified at sites like this, showing that the gearbox has been quite robust and not the dominant factor in performance degradation. The findings add to the broader debate on whether direct-drive gearless wind turbine technology are a significantly better option compared with gear based technology. This may have broader implications for the ever increasing number of older wind turbines and wind farms around the world are nearing the end of operational life in the context of turbine re-powering options. Further research (outside the scope of this thesis) in these techniques, using operational data from a broader range of sites and turbine technologies to improve decision making processes in the operation and re-powering of wind farms, would be of great benefit to the industry.

### 4.7 Conclusions and next steps

It has been shown, based on the analysis of measured multi-annual 10-minute SCADA data, that the energy performance of large scale wind turbine deployed in a peri-urban environment depends on number of local site and regional factors along with the behaviour of the turbine system itself. A novel approach of using an *EER* overlaid on local and regional plans appear to indicate that peri-urban building layouts of up to at least 1.5 km from a proposed wind turbine's location should be considered for building obstacles with heights of more than 20% of hub height. If obstacles greater than 20% of proposed wind turbine hub height occupy more than 30% of the

field of view in prevailing wind direction the study suggests increasing the tower height or to reconsider the viability of the project location. Regional terrain within a 20 km radius of the turbine location should be considered potential for wind blocking, speed up or steering depending on general prevailing wind direction of the region. The replacement of the gearbox after 13 years of operation with a brand new gearbox shows a recovery of  $\sim 3\%$  in *AEP* compared to operation in year 3 of its lifetime. The recovered energy mostly occurs above wind speeds of 6 m/s. It has also been shown that the wind turbines operate in wind turbulence conditions that may regularly reach or exceed the specifications of current NTMs of IEC wind turbine design standards.

In general the study shows that both the power and energy performance of large wind turbines in complex peri-urban areas. Further research is needed to gain a better understanding of wind inflow characteristics at peri-urban sites along with the behaviour of medium to large scale wind systems in these environments. This should involve the improvement and choice of flow models for site-specific analysis and field validation against wind measurements and with power and electrical energy performance data sets of operating turbines. The use of remote wind sensing devices such as LiDARs would enable direct measurements and assessments of obstacles on wind flow at a practicable level. This would help improve existing model validation of wind flow characteristics and wind turbine performance and help enable the standardisation of wind resource and energy assessment approaches in peri-urban environments. To address some of these issues, the next chapter (Chapter 5) will investigate further the mesoscale wind characteristic in the region of the wind turbine site using the remodelled Irish wind atlas and compare its meso to microscale *AEP* prediction of the wind turbine against the *EER* to further investigate directional shape of the *EER*. Preliminary directional wind shear profile from onsite LiDAR wind measurements will also be assessed. Chapter 6 will focus on microscale modelling aspects and Chapter 7 will assess a morphological approach and suggest improvements to IEC NTM models.



## Chapter 5

# Assessment of mesoscale to microscale influences on wind turbine performance from the Irish wind atlas and onsite LiDAR wind measurements

### 5.1 Objectives

Chapter 4 showed that a wind turbine *EER*, from long-term measured SCADA data at the site, had distinct directional characteristics that appeared to be influenced by both local building obstacles and regional topography. The objectives of this chapter are to compare the wind resource and *AEP* predicted by the Irish remodelled mesoscale wind atlas to the measured wind resource and *EER*. The energy impact of mesoscale and microscale features around wind turbine site are further examined in the context of how they each contribute to the shape of the wind turbine *EER*. This is done by assessing the wind resource at multiple locations in the region at a scale of 10s of km from the wind turbine site, local locations on a 1 km scale about the turbine site and at the turbine site itself. This consists of wind rose and *WPD* comparisons. The spatial resolution of the Irish wind atlas is 1 km for its generated time series wind data. In the wind industry, assessment of the wind resource in 12 directional sectors is common practice (Al-Addous et al., 2020). However, due to the more complex nature of the wind resource in peri-urban environments combined with the data available to this research, 16 sectors are used throughout the research to increase the directional resolution in the presence of local site obstacles. Mesoscale influences are initially assessed at 150 m above ground level (a.g.l.) in 16 directional sectors, where local obstacles are assumed to have less of an influence. At the local locations around the wind turbine site, wind roses are compared at a heights of 60 m, i.e., the same height wind turbine hub height. In addition, the directional differences

between the predicted *AEP* and the *EER* are compared to examine the site specific microscale obstacle impacts on the turbine's energy performance. Onsite directional wind shear profiles from 10 m to 300 m using measurements a CW ZX Doppler LiDAR are investigated to give further insights into the directional differences between the energy predictions using the wind atlas and the measured *EER*. A brief comparison of the hub-height wind speed as measured by the nacelle anemometer and LiDAR is also made. Further detailed studies with the LiDAR are carried out in Chapters 6 and 7. The results will be used to help inform the microscale modelling in the next chapter, Chapter 6.

This chapter begins by giving a more detailed description of the Irish Wind Atlas developed by the UK met office, based on its UM NWP model initially described in Chapters 2 and 3. The technical operation of the CW ZX LiDAR used in this research is described, including the end-to-end operation from laser beam transmission to the determination of wind speed. Secondly, the methodology used in applying the Irish wind atlas at the selected regional and local locations about the site is described along with the directional wind speed directional wind speed distributions and the *AEP* predicted by the wind atlas at the turbine location. Thirdly, the results section shows the wind characteristics at all assessed locations to help distinguish the mesoscale and microscale influences on the wind resource at the wind turbine location. The discrepancies between the predictions in directional wind speeds distributions and *AEP* by the wind atlas with the wind speed distributions and *EER* from the measured wind turbine SCADA are assessed. Directional wind shear from on year the onsite LiDAR measurements at multiple heights are plotted to give further insights the observed discrepancies. A comparison is also made of the LiDAR measured wind speed at the 60 m hub height with the wind turbine's nacelle anemometer. Finally, the implication for using the mesoscale wind atlas are discussed in the context of application at peri-urban sites in Ireland and the significance of building obstacles.

## 5.2 Overview of the remodelled Irish Wind Atlas

The remodelled Irish wind atlas was published by SEAI in 2015 (Standen and Wilson, 2015). The UK Met Office, using the UM NWP model, was commissioned to develop it following a tender award. The UM model was initialised from 10 years of the ECMWF ERA-Interim global reanalysis data from 2001 to 2011 and a number of key outputs were produced. These included a 10-year average gridded 100 m data sets of: mean wind speed and the mean frequency of wind direction in 12 sectoral bins, each with a 30° width, mean wind speed for each month and mean wind speed for each hour of day. A 1 km resolution dataset of Weibull parameters in twelve sectoral bins over the 10-year period and a representative year of time series data consisting of wind speed and wind direction in hourly time steps with a 1 km spatial resolution. In developing the Irish wind atlas, the UM model was run as a nested configuration to initialise the global model with a 60 km horizontal resolution and 50 vertical levels. This set up was run in 48 hours periods and a 6-hour spin-up was allowed for the global model to adjust from the ERA-Interim reanalysis. This then provided the initial and spatial boundary conditions for a 12 km model of Western Europe with 38 vertical levels. A further 3-hour spin-up period was allowed before starting simulations of three 4 km domains with 70 vertical levels in 48 hour periods. One of three domains was centred over Ireland and UK. The 4 km models were run with a 100-second time step, but only hourly data was retained in the data set to give hourly wind speed components with a 4 km resolution at each level. The spacing between each level was not the same, i.e., finer resolution is in the boundary layer and progressively decreases with height above this. This data set formed the basis for the Irish wind atlas. Six of the 70 levels were below 150 m at heights of 2.5 m, 13.33 m, 33.33 m, 60 m, 93.33 m and 133.33 m. The 4 km wind components of the 70 levels were downscaled to a 1 km microscale grid using horizontal bi-linear interpolation. This 1 km data was time processed to produce monthly fields that was further downscaled onto a 100 m grid. Data at 8 end-user (SEAI) specified heights, namely; 20 m, 30 m, 40 m, 50 m, 75 m, 100 m, 125 m and 150 m; were produced from the six original downscaled vertical levels that occurred below 150 m, assuming logarithmic wind shear profiles and neutral atmospheric for all onshore locations in the Republic of Ireland and up to 20 km offshore.

Some of the methods used in the UK Met Office Virtual Met Mast<sup>TM</sup> (VMM) tool that creates long term wind climates specifically for wind energy were used in the downscaling process from 4 km to 1 km to correct for the effects of complex orography (Davies et al., 2005; Standen et al., 2017). Wind speeds were adjusted for significance orographic influence below a reference height,  $z_{ref}$  to consider speedup effects and orographic drag. The orographic information used in the production of the wind atlas was obtained from the digital terrain elevation dataset (DTED) from The National Imagery and Mapping Agency (NIMA), as it had the highest resolution at the time. The earth's surface properties were deduced from the Corine land database from which surface roughness values were derived (Silva et al., 2007). An orographic drag scheme was used to represent the effects of turbulent form drag exerted on synoptic scale flow in the boundary layer by orography (Howard and Clark, 2007). The drag force which would be exerted on the flow by the unresolved hills is estimated and added to the surface stress to define an effective roughness length. The effective roughness represents the turbulent form drag exerted on the flow in the ABL by orography, based on the assumption that wind profiles over complex terrain resemble those over flat terrain, but with a substantially higher roughness length. To account for unrealistically low wind speeds near the surface in complex orography, a correction below reference height,  $z_{ref}$ , defined as the height below which the orographic roughness parametrisation significantly affects the wind profile.  $z_{ref}$  is directly related to the mean peak-to-trough amplitude,  $H/2$  and silhouette area  $A$  per unit area  $S$ , of the sub-grid orography. The silhouette area is the area of an orthogonal projection of the orography onto a horizontal plane. This is characterised by the local orographic wave number  $k_w$ , Eq. (5.2) and a tuneable parameter  $a$  as follows:

$$z_{ref} = ak_w^{-1} \quad (5.1)$$

Where:

$$k_w = \begin{cases} \frac{\pi \frac{A}{S}}{\frac{H}{2}} & \text{for } (\frac{H}{2}) \geq (\frac{H}{2})_{min} \\ \frac{\pi \frac{A}{S}}{\frac{H}{2}} & \text{for } (\frac{H}{2}) < (\frac{H}{2})_{min} \end{cases} \quad (5.2)$$

$\frac{A}{S}$  - silhouette area per unit horizontal area

$(\frac{H}{2})$  - the mean peak-to-trough amplitude (m)

$(\frac{H}{2})_{min}$  - minimum value of  $\frac{H}{2}$ , set to 1 m

$$\frac{1}{\Delta x_{min}} \leq \frac{(A/2)}{(H/2)} \leq \frac{1}{\Delta x_{max}} \quad (5.3)$$

$\Delta x_{min}$  and  $\Delta x_{max}$  are set to 500 m and 4 km respectively.

$$a = \begin{cases} -\ln \alpha + \ln(k_w \frac{H}{2}) & \text{for } \ln(k_w \frac{H}{2}) > \beta \\ -\ln \alpha + \beta & \text{for } \ln(k_w \frac{H}{2}) \leq \beta \end{cases} \quad (5.4)$$

$\alpha$  and  $\beta$  are tuneable parameters with values set at 0.12 and -4 respectively, based on UK observations. Orographic complexity is classified by  $A/S$  values shown in Table 5.1.

**Table. 5.1.** Orography complexity classification used in Irish Wind Atlas (Standen and Wilson, 2015)

Classification	$A/S$
Low	$< 0.0075$
Medium	$\leq 0.0075 < 0.02$
High	$0.02 \leq$

The roughness corrected wind speed  $U_{rc}(z)$  accounting for complex orography down to the 1 km grid is given by Eq. (5.5).

$$U_{rc}(z) = U(z_{ref}) \frac{\ln\left(\frac{z-d}{z_0}\right)}{\ln\left(\frac{z_{ref}-d}{z_0}\right)} \quad (5.5)$$

$z_0$  and  $d$  are surface roughness length and displacement height, respectively.

Height correction was applied using this speed up model on the 1 km grid. This process involved using a 100 m resolution orographic map and an orographic wind flow model to height-correct wind speeds due to the effect of the difference between the model orographic heights and actual heights. The orographic wind flow used was a simplified form of the linear solution for turbulent flow over hills in which a reference height is estimated as the inverse horizontal wave number of the sub-grid orography (Howard and Clark, 2007; Standen et al., 2017). A 6.4 km x 6.4 km square centered on each 1 km point was considered. The orography was tapered

away from each central 1 km grid point. The orographic Fourier components in 4 directions ( $60^\circ$ ,  $150^\circ$ ,  $240^\circ$  and  $330^\circ$ ) from each 1 km grid point was used with the orographic wind flow model to give wind speed-up scaling factors at each 1 km and 100 m grid point elevation in the four directions. The scaling factors were applied to wind speeds at the 1 km grid points to produce local wind speed-ups and decreases for each of the four wind directions. This gave height corrected wind speed at the 1 km grid points. These adjustments were used to extract hourly time series speed and direction files on the 1 km grid at the 8 end user heights. The best representative single year of the 2001 to 2011 reanalysed period consisting of hourly time series data of wind speed and wind direction at the 1 km spatial resolution was found to be 2006.

To produce the continuous (static) mean wind maps on a 100 m grid, correction for unresolved sub-grid (i.e., less than 1 km), the speed-up factors at each elevation point on grid 100 m grid were used on a rotated pole grid (i.e., a rotated north pole so that lines of longitude could be parallel) in the downscaling process. For each 100 m point, the four nearest 1 km grid points were considered. The mean wind speeds of each of the four 1 km corner points were multiplied by the speed-up ratios for the given point on the 100 m grid for each of the four wind directions. These were then multiplied by the frequency of each of the four wind directional bins. The four wind speeds corresponding to each corner were then weighted depending on the distance of the 1 km grid point from the given 100 m grid point. The resulting sixteen weighted wind speeds were then summed to produce the final corrected wind speed for the given 100 m grid point. The final continuous map of mean wind speeds and the frequency in each of 12 directional sector bins was produced using this method. Validation of the wind atlas processing procedure was done using from a number of Irish synoptic weather stations, wind farm met masts and some small-scale wind installation met masts in different parts of the country.

### 5.3 Continuous Wave (CW) ZX (ZephIR) LiDAR

Following the LiDAR overview given in Chapter 3, a ZX (ZephIR) CW Doppler LiDAR is used in this research, as shown in Fig. 5.1.



**Fig. 5.1.** ZX (ZephIR) LiDAR onsite.

A rotating prism wedge moves the focused beam creating a circular scan about a vertical centre line, i.e., forming a conical scan as viewed from the transmitter. The cone half-angle is  $30^\circ$ . The beam is focused at the given distance along the line of sight (LOS) of the angled beam corresponding to a vertical height of interest a.g.l. For an ideal beam, the spatial sensitivity along the length of beam direction is Gaussian, Eq. (5.6), making it inversely proportional to the beam cross sectional area (Slinger and Harris, 2012). The focus point of the beam where this area (the beam waste) is smallest, the sensitivity rises to a maximum and decays symmetrically at either side. The contribution of the back-scattered beam at a given point is weighted by the square of the beam's intensity (Harris, Constant, and Ward, 2001). Therefore, the Doppler shifted back-scatter signals from aerosols illuminated in the minimum waist of the transmitted beam have the greatest contribution.

$$\Gamma = \frac{2\lambda R^2}{\pi r^2} \quad (5.6)$$

Where:

$\lambda$  - wavelength of laser beam  $\sim 1.55 \times 10^{-6} \text{ m}$

$R$  - distance from the transmitter lens to the focus point

$r$  - the beam cross sectional radius at the transmitter lens, which is calculated as the distance from the beam centre which the intensity has dropped to  $1/e^2$  of its value at the beam centre

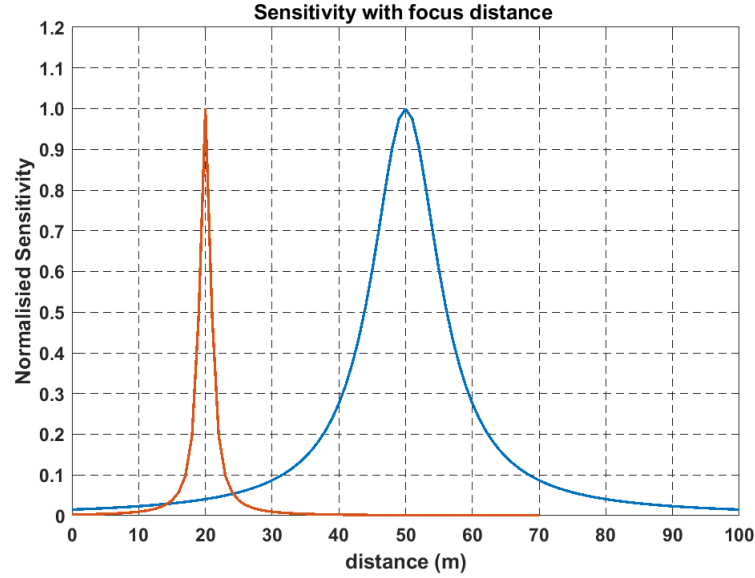


Fig. 5.2. An example of sensitivity focus distance of 20 m and 50 m.

For a real beam the axial weighting function along the beam length can be well approximated by a Lorentzian function, Eq. (5.7), (Peña et al., 2015).

$$F = \frac{\left(\frac{\Gamma}{\pi}\right)}{\Delta^2 + \Gamma^2} \quad (5.7)$$

Where:  $\Delta$  - is the distance along the beam from the focus point

A transverse sensitivity across the beam also exists but is considered negligible, as the beam is very narrow at the focus point.

### 5.3.1 Process of determining wind velocity

At a given height, a circular scan of the transmitted infrared laser beam samples 50 points that each give a Doppler shifted return point, Fig. 5.3(a). As the scanning beam moves from upwind to downwind, a sinusoidal function describes the variation in frequency of the Doppler shifted signal, corresponding to the probe line of



sight velocity  $V_{LOS}$  at each sample point. The points visually form a “figure of eight” in the LiDAR software viewer, illustrated in Fig. 5.3(b).

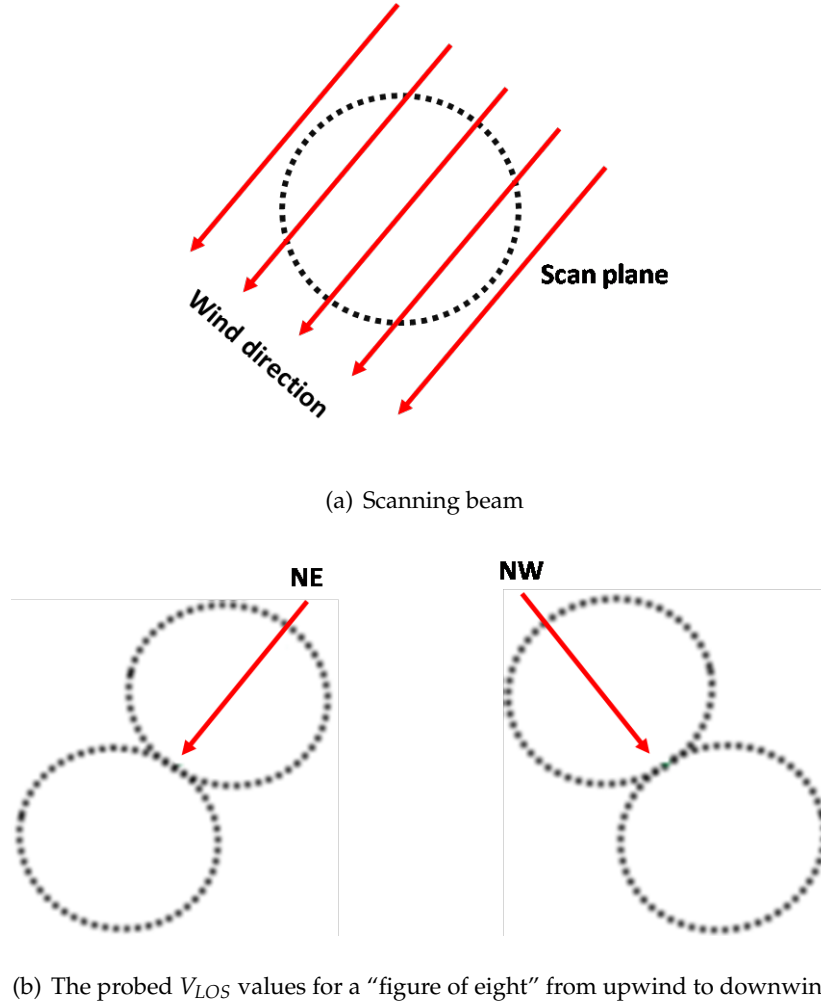


**Fig. 5.3.** Illustration of scanning beam.

The wavelength of the transmitted beam is  $1.55 \mu\text{m}$ . The back-scattered beam is received back through the transmission optics (i.e., transceiver). The detected back scattered beam is mixed with the local oscillator transmitted beam resulting in a beat or Doppler frequency which is the frequency difference between the two beams. The electric field of the local oscillator  $e_{LO}(t)$  and the received back scattered  $e_S(t)$  can be described by Eqs. (5.8) and (5.9).

$$e_{LO}(t) = E_{LO} \cos(\omega_{LO}t) \quad (5.8)$$

$$e_S(t) = E_S \cos(\omega_S t) \quad (5.9)$$

The intensity  $i(t)$  of the fluctuating beam is described by Eqs. (5.10) and (5.11).

$$i_B(t) \propto [E_{LO} \cos(\omega_{LO}t) + E_S \cos(\omega_S t)]^2 \quad (5.10)$$

$$i_B(t) \propto [E_{LO}^2 + E_S^2] + 2E_{LO}E_S \cos(\omega_S - \omega_{LO})t \quad (5.11)$$

The Doppler shifted return signal with a frequency of  $\sim 2 \times 10^{14}$  Hz is down-mixed to the MHz range. The constant term is filtered out leaving the fluctuating term due to the Doppler shift that varies at the beat frequency, Eqs. (5.12) and (5.13).

$$\delta f = \frac{\omega_S - \omega_{LO}}{2\pi} \quad (5.12)$$

$$\delta f = \frac{2V_{LOS}f}{c} = \frac{2V_{LOS}}{\lambda} \quad (5.13)$$

In order to extract the Doppler frequency a Fourier analysis is done on the photodetector output electrical signal, Fig. 5.4.

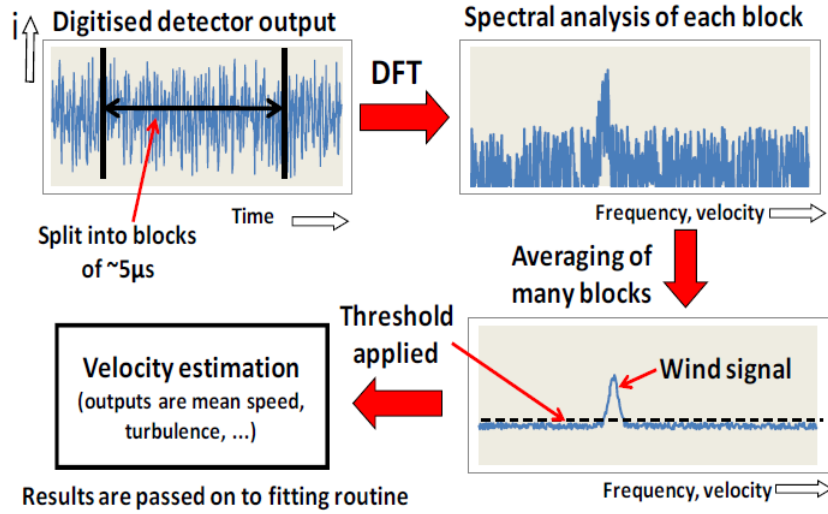


Fig. 5.4. Overview schematic of processing of back-scattered detected signal (Peña et al., 2015).

The detected back-scattered signal is first passed through an analog low pass filter with a cut off frequency of 50 MHz and then through an analog to digital converter (ADC) with a sampling rate of 100 MHz (to eliminate aliasing) for a maximum Doppler frequency detection of 50 MHz ( $V_{LOS} \sim 38.8$  m/s). A 512 point digital

Fourier transform (DFT) is performed to give 256 point output spectrum with a resolution of  $\sim 200$  kHz corresponding to a resolution in the  $V_{LOS}$  of 0.15m/s. A single DFT takes  $5 \mu s$  to execute. Due to the limitations of probe length of the focused transmitted beam and various sources of electrical noise in the photo detection, the voltage spectrum is squared to give a power spectrum. Four thousand DFTs of the Doppler signal for each measuring point on the circular scan at a given height is carried out so that a well defined average power spectrum emerges from which  $V_{LOS}$  can be determined, Eq. (5.14).

$$V_{LOS} = \frac{\delta f \lambda}{2} \quad (5.14)$$

This process takes  $\sim 20$  ms. When complete the transmitted beam moves to the next point on the circular scan at the same height and subsequently for a total of 150 points around the three circular scans at the given height. When all 150  $V_{LOS}$  point values are obtained they are fed into a least squares fitting routine, Eqs. (5.14) and (5.17).

$$V_{LOS} = a \cos \phi - b + c \quad (5.15)$$

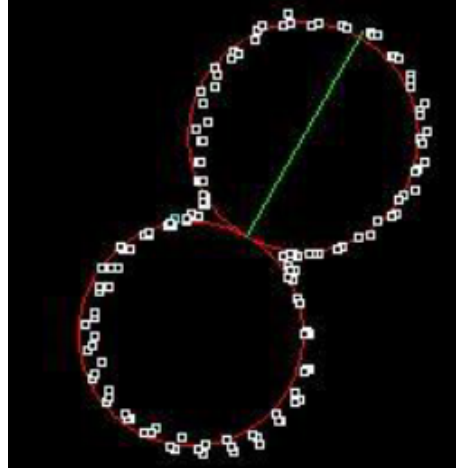
$a$ ,  $b$  and  $c$  are floating variables determined by best fit and  $\phi$  is the azimuth angle. The three dimensional wind velocity is then determined, for a cone angle of  $\theta$ .

$$V_H = \frac{a}{\sin \theta} \quad (5.16)$$

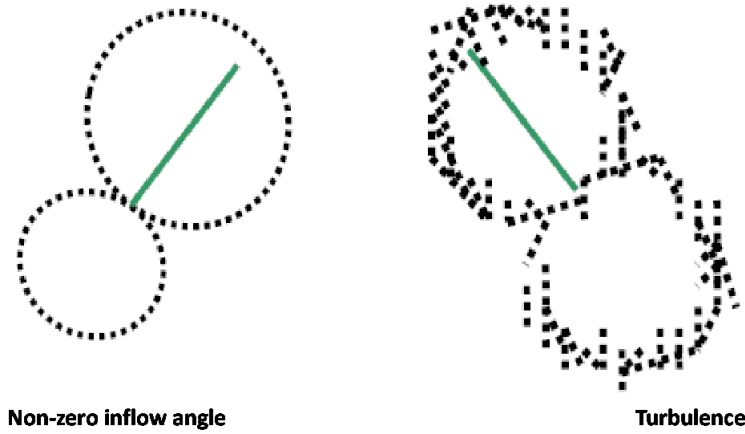
$$w = \frac{-c}{\cos \theta} \quad (5.17)$$

The process of determining end user wind speed direction values at a given height takes a total of  $\sim 1.6$  seconds. The values are then averaged to give 10-minute mean values. When viewing the LiDAR operation live on its user-interface software, the sample points in the circular scans at a given height display “figure of eight” as the scan moves from upwind to downwind positions. The shape of the “figure of eight” visually indicates how homogeneous the wind flow is at the given time, Fig. 5.5(a). In reality, “perfect figures of eight” are not observed, Fig. 5.5(b). For non-zero inflow angles, in complex terrain, or for the LiDAR being not being level and asymmetric

“eight” is observed, For turbulent flow, scatter is observed in the data points of the “figure of eight”.



(a) Scanning beam



(b) The probed  $V_{LOS}$  values for a “figure of eight” from upwind to downwind

**Fig. 5.5.** Illustration of scanning beam.

LiDAR factory acceptance tests carried out by the original equipment manufacturer (OEM), ZX LiDARS, involve checking velocity, direction and signal back-scatter ratio against a calibrated moving belt at speeds up to 5 m/s and subsequent verification against an IEC compliant meteorological mast with calibrated cup anemometry. Wind speed is calibrated within 0.5% and wind direction is within  $3^\circ$  of the references. There are some practical implications associated with detecting the Doppler beat frequency to determine  $V_{LOS}$ . These include the finite nature of the focused beam (or probe length) weighted by the Lorentzian function, Eq. (5.7), at a given height. As the measuring height increases the probe length increases and multiple beat frequencies may be detected at a given measuring height, particularly in high

wind shear. The photodetector used to measure the intensity of the beat frequency has its own limitations in terms of electrical noise, e.g., semiconductor dark noise, photon shot noise and laser relative intensity noise (RIN). Therefore, the requirements for the photodetector are high quantum efficiency, sufficient bandwidth to cope with the maximum Doppler frequencies and for the shot noise contribution to significantly exceed that of dark noise.

### 5.3.2 Error handling in LiDAR system

Errors that may arise in the back scattered signal such as the from the beam being intercepted by solid obstacles not moving at wind aerosol speed (e.g. birds or static structures) will stand out in the 150 samples per scan and can be filtered out in the fitting algorithm. The influence of the downward motion of precipitation on the vertical wind detection can be also be detected as outliers in combination with from the system's rain sensor data. These type of errors reduce the number of valid samples in scan, but in most cases it is a small fraction of the 150 samples which still enables a good determination of wind speed from the least squares fitting algorithms (Branlard et al., 2013). Laboratory tests have shown that even when half of the sample data in a scan is removed that accurate measurements can still be obtained (Slinger and Harris, 2012).

Clouds can give Doppler signal returns that have a narrow spectral bandwidth that can be mitigated. As the sensitivity of CW LiDAR has a beam focus dependency, clouds that are not at the height of interest may have less of an influence as the cloud Doppler return spectrum is independent of beam focus range. Cloud return spectra can be determined by routinely emitting a collimated beam scan to 800 m to determine the cloud return spectrum in different directions. These can be tested for and eliminated from the signal spectra at the measurement height of interest. In cases of low thick cloud and dense surface fog lower than the measurement height of interest the transmitted beam may not penetrate the cloud, resulting in no measurement being possible at the height of interest. However, these conditions tend to occur at low wind speeds, those of which are below wind turbine cut-in wind speeds would be of less interest, yet need to be filtered out. In general, when large errors are encountered in the fitting algorithms process "null" data is time stamped and recorded.

## 5.4 Methods

### 5.4.1 Mesoscale assessment

Regional and local locations about the wind turbine are selected based on the prevailing wind directions that were observed from the SCADA data analysis in Chapter 4. These are outlined in Fig. 5.6. To assess the mesoscale influences, the points M1, OS1 and OS2 mark locations both on and offshore as well the wind turbine location WT where the representative one-year (2006) of hourly time-series data sets from the wind atlas are used to assess the coastal and regional orographic influences on wind resource at 150 m a.g.l. The coordinates and distances of these points from the wind turbine location are given in Table 5.2. The key equations used in the mesoscale assessment is for directional *WPD* for each wind speed bin  $i$  and directional sector  $j$ , defined in Chapter 3, are Eqs. (5.18) to (5.20). The angular sector width chosen is  $22.5^\circ$ , giving  $j$  a total of 16 directional bins. Annual wind roses and directional *WPD* plots in the 16 directional sectors are produced for each location.

$$WPD_{i,j} = \frac{1}{2N_j} \sum_{n_i=1}^{n_i=N_{i,j}} \rho_{i,j} U_{i,j}^3 \quad (5.18)$$

Where:  $\rho_{i,j}$  - density of air  $kg/m^3$

$$WPD_j = WPD_{i,j} \frac{N_{i,j}}{N_{tot}} \quad (5.19)$$

$$WPD_{tot} = \sum_{j=1}^{N_j} WPD_j \quad (5.20)$$

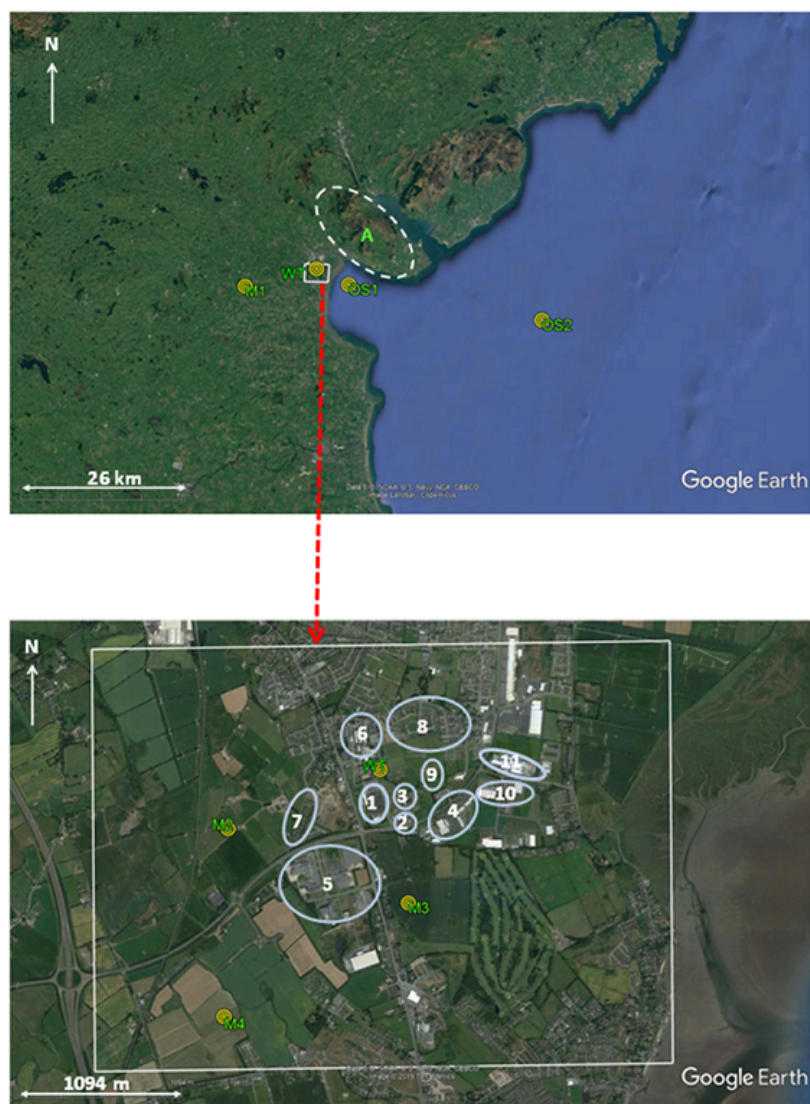


Fig. 5.6. Selected regional (top) and local (bottom) locations for wind atlas analysis.

**Table. 5.2.** Site locations for wind atlas mesoscale and microscale analysis

Site	Coordinates	Elevation a.s.l. (m)	LOS distance to WT (km)
WT	53.98354°N , 6.39139°W	13	-
OS1	53.96197°N, 6.30843°W	0	5.8
OS2	53.92015°N, 5.81943°W	0	38
M1	53.95300° N, 6.56900°W	60	12.2
M2	53.97983°N, 6.40743°W	12	1.13
M3	53.97523°N, 6.38839°W	20	0.90
M4	53.96826° N, 6.40759°W	23	2

#### 5.4.2 Microscale assessment method

The variety of local obstacle features comprising of buildings of various types and densities surrounding the wind turbine site, that were outlined in Chapter 4, are shown in the lower part of Fig. 5.6. The points M2, M3 and M4 chosen, mark point locations in the local area to assess the wind resource outside the influence of local obstacles in the prevailing wind directions. As well as at the wind turbine location, WT, assessments are done these local locations at a height of 60 m a.g.l., corresponding to the hub height of the wind turbine. Hourly time series of wind speed and direction data, over the representative year, are firstly generated from the wind atlas at available heights of 50 m and 75 m. These are then scaled to 60 m wind turbine hub height using on the log law, Eqs. (5.21) and (5.22) assuming neutral atmospheric stability, as was used in the wind atlas itself to generate the 8 end user heights below



150 m, described previously. Wind roses and *WPD* plots from the wind atlas data at all four local site locations are compared to assess the variation of the wind resource across the site.

$$u(z) = \frac{u_*}{\kappa} \ln \left( \frac{z-d}{z_0} \right) \quad (5.21)$$

Where:

$d$  - displacement height of the wind flow (m)

$z$  - height above the ground (m)

$z_0$  - surface roughness length (m)  $u(z)$  - horizontal wind speed at height  $z$  (m/s)

$u_*$  - surface friction velocity (m/s)

$\kappa$  - Von Karman constant (0.4)

At location WT, the displacement height of 3 m is chosen based on values applicable to semi-urban fabric and industrial areas, as was used in the production of Irish wind atlas (Best et al., 2008).

$$z_0 = \exp \left( \frac{u_1(z_1) \ln(z_2) - u_2(z_2) \ln(z_1)}{u_1(z_1) - u_2(z_2)} \right) \quad (5.22)$$

A normalised year of wind turbine SCADA data based measurements between 2008 and 2015 is used to obtain the site annual Weibull parameters and *EER*. This to minimise the effects of inter-annual variation when comparing to the wind atlas predictions. At the WT location, directional wind speed distributions with direction are computed from the wind atlas time series data. The predicted directional *AEP* of the wind turbine is assessed using the fitted directional Weibull scale and shape parameters to the wind data and the wind turbine power curve. The scale factor  $c$  and shape factor  $k$  factor are determined from fitting a Weibull distribution, Eq. (5.23), to the wind speed data distribution using the method of moments from MATLAB® *fitdist* function. The Weibull parameters of the directional wind speed distributions from the wind atlas data are compared to the Weibull parameters from the SCADA measured wind data. The wind atlas predicted directional *AEP*, defined in Chapter 3, for a given directional sector bin  $j$  is based on the fitted Weibull shape and scale factors of the wind speed distribution for the given direction and the wind turbine power curve, Eq. (5.24). The wind atlas directional *AEP* predictions are compared

with the wind turbine *EER*.

$$p(u) = \left(\frac{k}{c}\right) \left(\frac{U}{c}\right)^{k-1} e^{-\left(\frac{u}{c}\right)^k} \quad (5.23)$$

Where:

$p(U)$  = probability density function

$U$  = mean wind speed (m/s)

$c$  = scale factor (m/s)

$k$  = shape factor (dimensionless)

$$AEP(j) = \sum_1^{N(j)_i} \left\{ e^{-\left[\left(\frac{U(j)_{i-1}}{c(j)}\right)^{k(j)}\right]} - e^{-\left[\left(\frac{U(j)_i}{c(j)}\right)^{k(j)}\right]} \right\} \cdot P_{w_i} \left( \frac{U(j)_{i-1} + U(j)_i}{2} \right) N_h(j) \quad (5.24)$$

### 5.4.3 LiDAR data measurement

To help understand differences between *AEP* predictions based on the wind atlas and the wind turbine *EER*, a LiDAR measurement campaign over a 12-month period from March 2018 to March 2019 was carried out at the wind turbine site. For practical reasons, in this case, the LiDAR is positioned approximately 60 m north-west from the base of the wind turbine. This chosen location was influenced by factors concerning device security and power supply availability. Ten-minute averaged wind speed and direction measurements at 11 heights are taken, namely 10 m, 20 m, 34 m, 38 m, 60 m, 72 m, 86 m, 120 m, 200 m, 250 m and 300 m. The measurement heights are chosen, based on the literature, to capture wind flow at various heights of interest to this chapter and upcoming chapters in this thesis. Specifically, the heights of 10 m, 20 m and 30 m are selected to capture wind flow from the approximate average height of the building to 2 and 3 times the heights of the buildings. The heights of 34 m, 60 m, 86 m and 120 m represent the minimum blade tip height, hub height, maximum blade tip height and twice the hub height respectively. Measurements at 200 m, 250 m and 300 m are upper level measurements to capture mesoscale influences, assumed above the local peri-urban microscale influences, as discussed in the

literature review. The measurement height of 38 m is a fixed additional measurement height made by the LiDAR regardless of the other user-selected measurement heights. Plots of the average horizontal wind speed against height in 16 directional sectors are produced to give directional wind speed profiles with height. These vertical directional wind speed profiles are examined in relation to obstacles in each directional sector as viewed from the wind turbine, specifically directions where the *AEP* predicted from wind atlas and the *EER* have large discrepancies. A short regression analysis is made between one year of the LiDAR wind speeds measured at 60 m is made with the wind turbine nacelle anemometer for the same 1-year measurement period is made. This consists of a linear regression and a coefficient of determination,  $R^2$ . This is done for eight directional sectors of  $45^\circ$  widths. It is expected that turbulence introduced by the rotor and nacelle body gives a lower coefficient of determination compared to met mast and LiDAR comparisons at flat field sites of  $\sim 0.99$  (Pitter, Slinger, and Michael, 2015; Goit, Shimada, and Kogaki, 2019). Further use of LiDAR measurements will be made in Chapters 6 and 7.

## 5.5 Results

### 5.5.1 Mesoscale

The wind roses at 150 m a.g.l. for locations OS1, OS2, M2 and the wind turbine site WT are shown in Fig. 5.7.

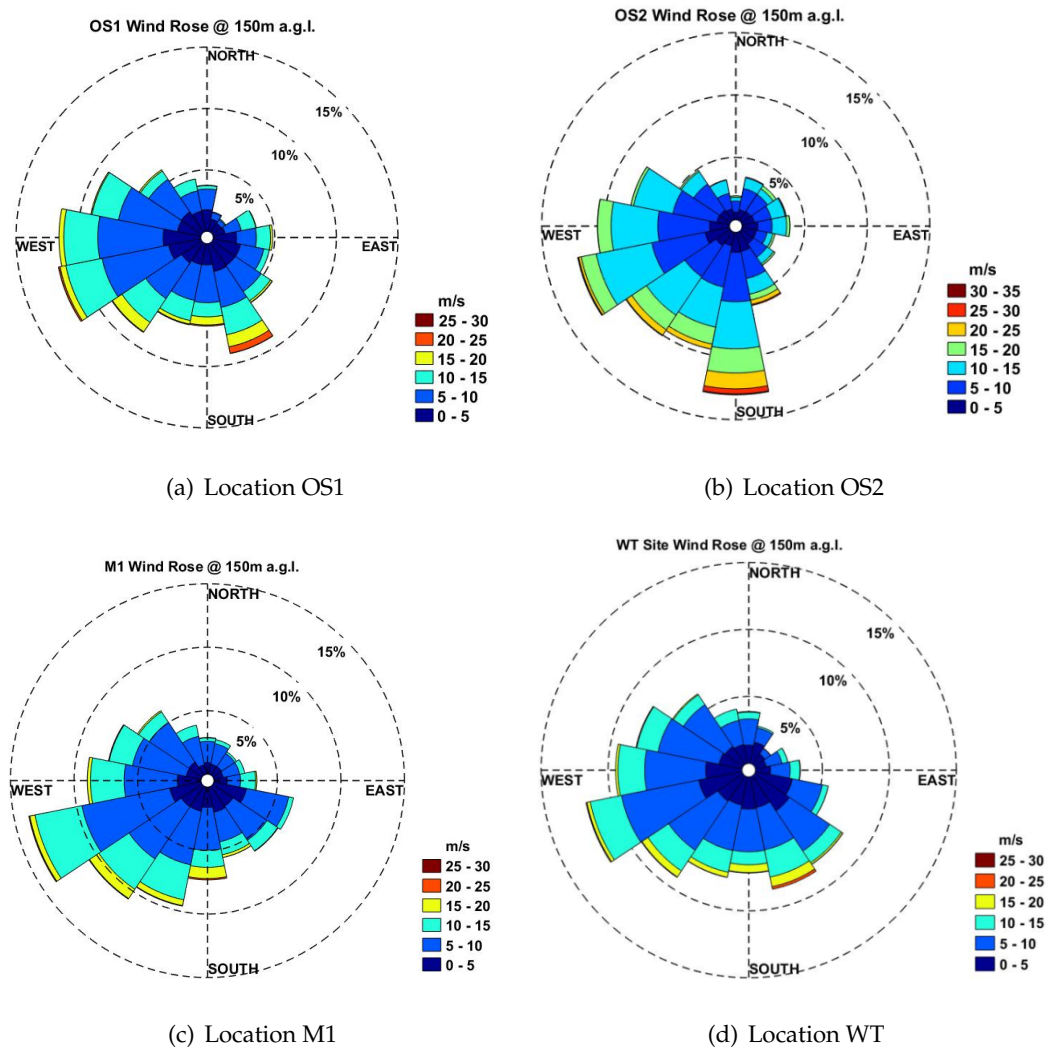


**Fig. 5.7.** Wind roses at 150 m a.g.l. for selected regional locations and at wind turbine site.

In all cases, a significant proportion of the winds comes from west and west south west, as expected. Referring to measurement locations in Fig. 5.6 (top), the offshore location OS2 that is 38 km to the east of the site shows very significant winds from the south. The offshore location OS1 in Dundalk Bay, approximately 5.8 km from the wind turbine site, shows significant south easterly winds. This appears to indicate that southerly offshore winds are being steered through Dundalk Bay by the hills A

to the north of the bay and land to south of wind turbine location. The south easterly winds appear significantly reduced at location M1, approximately 12 km inland, where the southwest winds dominate, i.e., the Irish Sea has a much reduced influence on winds at this location. The seasonal analysis of the wind turbine SCADA measured winds in Chapter 4 showed a high frequency of wind from the southeast in the spring and summer season, however, a strong south southeast wind sector was observed in all seasons. This suggests that at a mesoscale level, all winds from the southeast are not only thermally driven, but also synoptically driven. For example, normally south westerly winds from the Atlantic Ocean incident on the south coast of Ireland are being steered northwards up the Irish Sea between Ireland and Britain, thus increasing the wind potential along the east coast of Ireland. This is also indicated in another study on the nearshore wind and wave potential for Ireland, (Gallagher et al., 2016). From an energy perspective, overlaid plots of directional *WPD* in Fig. 5.8 show a direct comparison of the directional changes and reductions in the wind energy available at the mesoscale level.

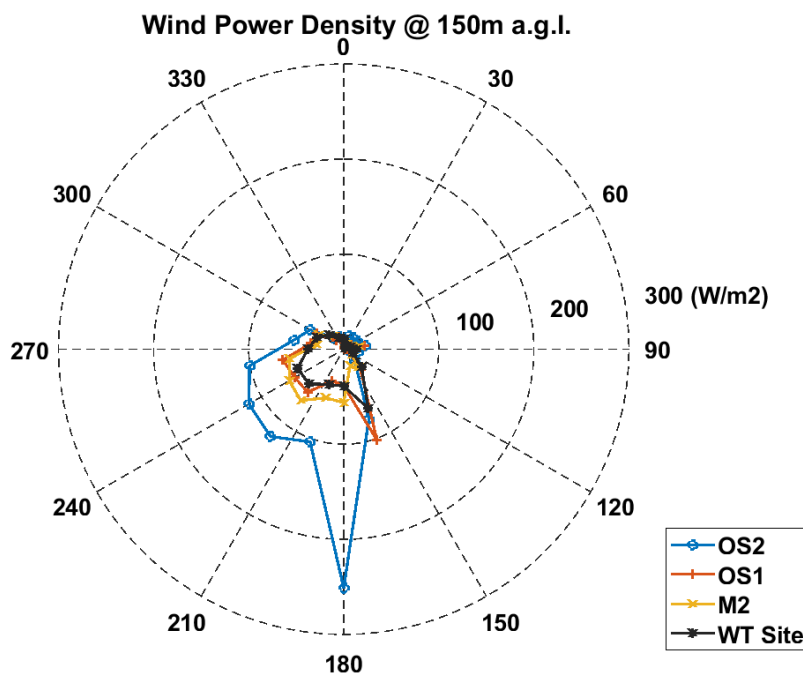


Fig. 5.8. *WPD* comparison at 150 m a.g.l. between the four sites.

The significant reduction in the *WPD* and its changing directional distribution can be seen moving from offshore location OS2 to OS1, with further reduction moving at

the wind turbine site WT. This further illustrates the impact that Dundalk Bay and the hills to the north of the bay may be having on the wind resource. In all cases, little energy comes from the northeast sectors, as these are not the prevailing wind directions. Locations up to more than 10 km in the lee of hills (Vosper, 2004; Sheridan and Vosper, 2006) can, in some cases, experience various wind effects such as speed up, blocking or steering (changes in wind direction) depending on the shape of the hills and the prevailing wind directions. Wind speed up in the lee of hills can occur when winds are strong enough on the windward side to move air up and over hills where it cools, and its speed is enhanced on the leeward side due to the gravitational acceleration of the cooler (denser) air. If winds on the windward side are not strong enough then blocking can occur or the airflow can be steered around the hill(s) depending on the shape of the hills and topography. In Ireland, as the general prevailing wind is SW to W (Dwyer, 2012), the hills to the NE are likely to be having a blocking affect on the weaker winds from the NE and steering effect on northern easterly winds towards the easterly sectors. At the inland location M1, the SE components are significantly reduced, while the SW sectors contain the dominant energy sectors. This shows that the large energy reductions in the broad SSW to SSE sectors in the wind turbine *EER*, shown in Chapter 4, are partially due to a mesoscale low energy transition region between the prevailing SW winds and the coastal influenced SE winds from Dundalk bay. Therefore, the reductions in the *EER* are not wholly attributable to the local buildings in those directional sectors.

### 5.5.2 Microscale

The wind roses and directional *WPD* predicted by the wind atlas at the wind turbine hub height of 60 m a.g.l. are shown in Figs. 5.9 and 5.10 respectively for the microscale comparisons at the local locations, M2, M3, M4, and the wind turbine site WT.

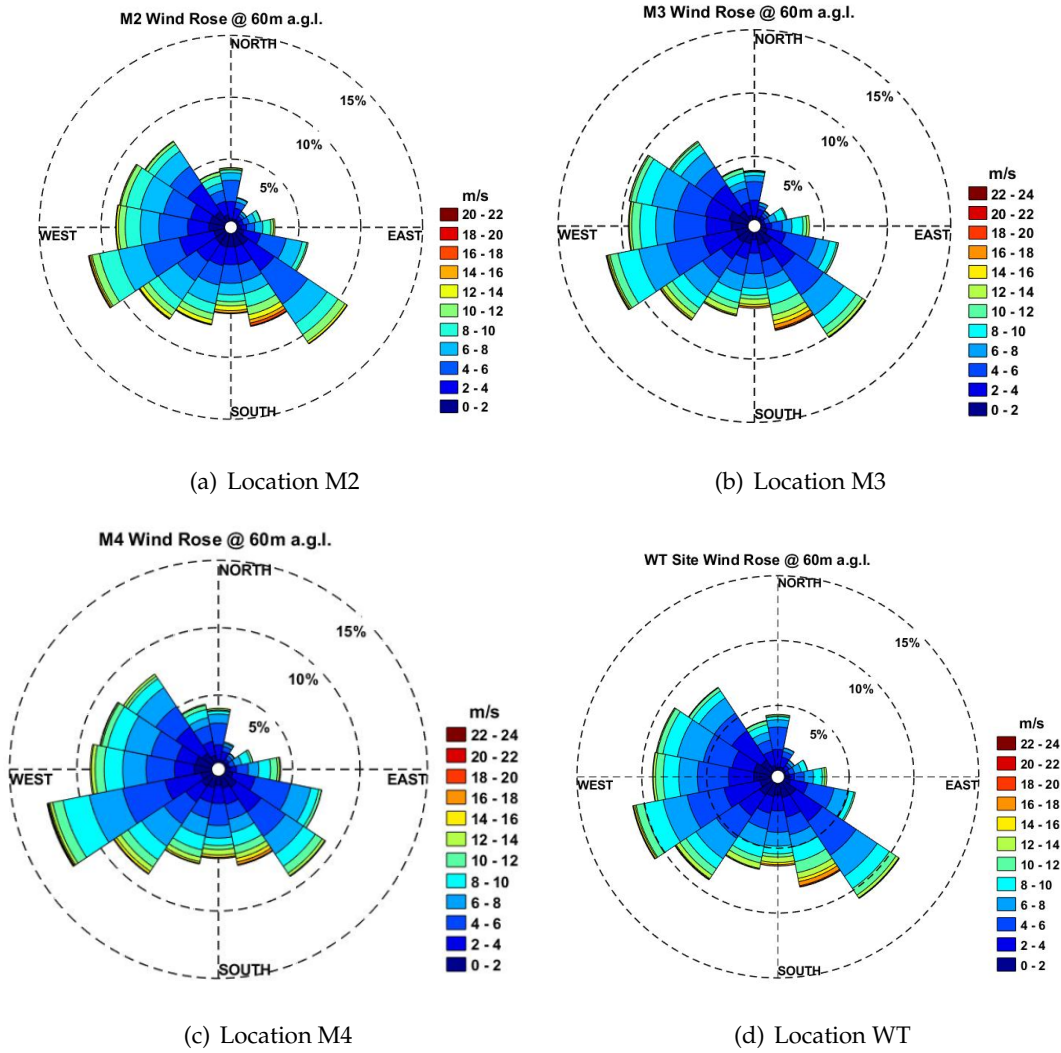


**Fig. 5.9.** Wind roses at 60 m a.g.l. for selected local locations and at wind turbine site, predicted by the wind atlas.

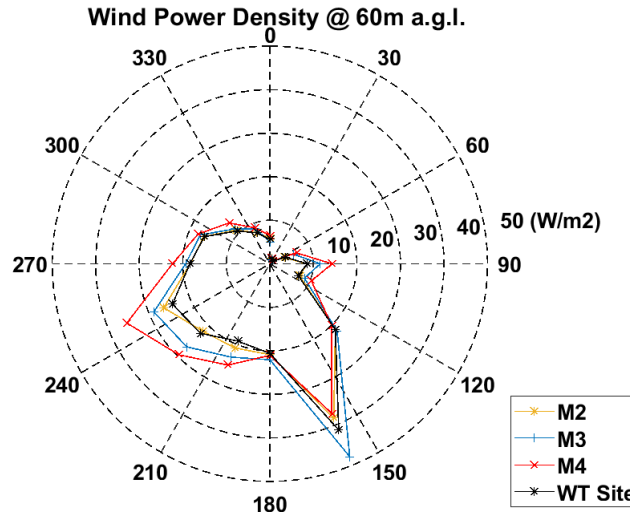


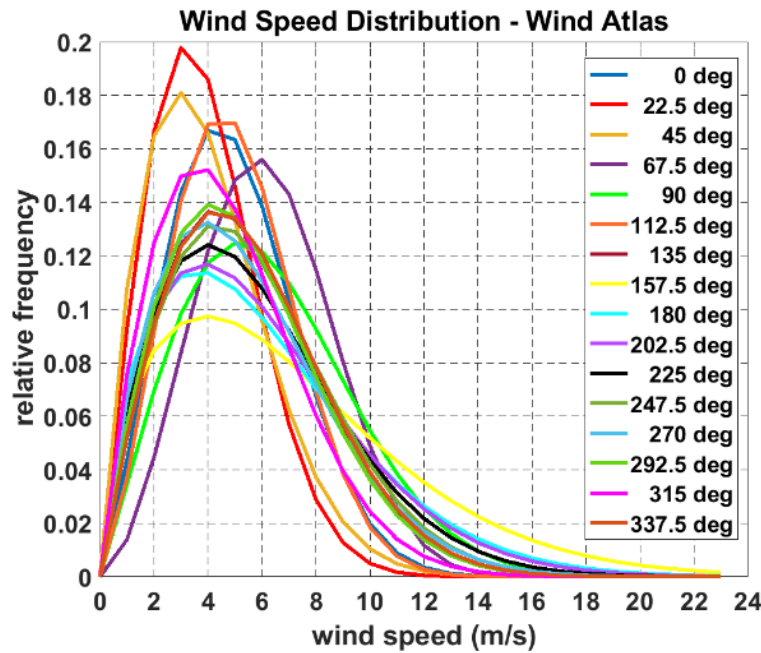
Fig. 5.10. *WPD at 60 m a.g.l. for selected local locations and at wind turbine site, predicted by the wind atlas.*

Referring to the plan view of these local locations, Fig. 5.6, (bottom), location M4 has the highest energy available in the WSW sector while the lowest energy available is in the SSE sector. Location M3 has the highest energy available in the SSE sector. Comparing all four locations, the wind turbine site itself appears to have the lowest energy available in all directions apart from the SSE sector where it has the second lowest energy available. From Table 5.2, M3 and M4 are at slightly higher elevations by  $\sim 8$  to 10 m compared to M2 and WT. Compared to WT, M3 has better exposure to the coast and M4 has more exposure to the southwest. This can explain the better *WPD* values in the southwest at M4 and in the SE sectors. M4 is further inland and therefore has the lowest *WPD* in the SE sectors. In the S sector the reduction in *WPD* at all location further suggests that it not wholly due to local buildings. Interestingly, M2, located just west of WT, but outside the influence of buildings to the west only shows small differences in *WPD* compared to WT. Also in the SE sectors, there are no significant differences in *WPD* between M2, M4 and WT. As the wind atlas time series data is on a 1 km scale variations, it is primarily mesoscale, local topographic and land cover roughness that are the principal influencing factors, while local building influences may not be well captured. To assess this further, the predicted directional wind Weibull parameters and *AEP* at the wind turbine site by the wind atlas and the actual SCADA measured wind parameters and wind turbine *EER* are compared in the next section.

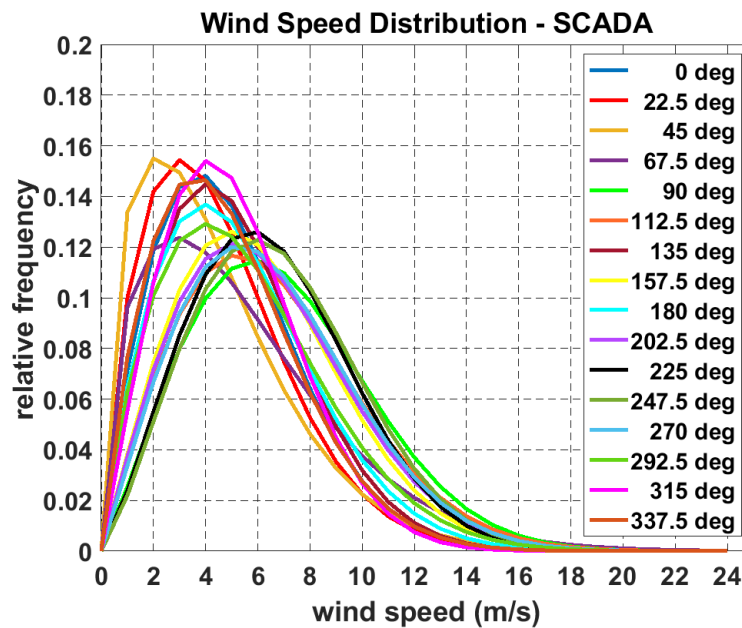


### 5.5.3 Wind Atlas and SCADA directional wind and energy comparisons

The predicted wind turbine *AEP* from the wind atlas is estimated using the Weibull shape and scale parameters of the directional wind speed distributions with the wind turbine power curve as was discussed in Section 5.4.2. The predicted and measured directional wind speed distributions are shown in Fig. 5.11 with the specific Weibull parameter values shown in Table 5.3.



(a) Wind atlas prediction)



(b) SCADA measured

Fig. 5.11. Directional wind distributions predicted by the wind atlas and measured by the wind turbine SCADA system.

**Table. 5.3.** Directional wind speed distribution parameter values

Sector (°)	Wind Atlas				SCADA data			
	c	k	hours	Rel'	c	k	hours	Rel'
	Freq.(%)				Freq.(%)			
22.5	5.60	2.29	378	4.32	5.56	1.89	383.83	4.69
45	4.40	2.06	157	1.79	5.08	1.71	215.60	2.63
67.5	4.51	1.84	92	1.05	4.77	1.47	107.53	1.31
90	6.93	2.72	162	1.85	6.01	1.49	127.10	1.55
112.5	7.07	2.09	287	3.28	7.85	2.15	325.87	3.98
135	5.65	2.40	491	5.61	7.36	2.01	612.93	7.48
157.5	6.18	1.96	945	10.79	5.84	1.96	611.30	7.46
180	7.72	1.55	716	8.17	6.91	2.05	623.73	7.61
202.5	6.67	1.60	559	6.38	5.98	1.86	344.63	4.21
225	6.63	1.67	594	6.78	7.12	2.03	426.77	5.21
247.5	6.43	1.77	794	9.06	7.42	2.27	730.87	8.92
270	6.35	1.92	957	10.92	7.65	2.28	1088.27	13.28
292.5	6.08	1.80	803	9.17	7.28	2.07	880.47	10.75
315	6.04	1.94	796	9.09	6.26	1.81	648.30	7.91
337.5	5.38	1.89	684	7.81	5.69	2.07	641.27	7.83
360	6.21	1.98	345	3.94	5.50	1.84	424.20	5.18

The differences between the predicted directional wind parameter values as well as the hours from the Wind Atlas and values derived from the measured SCADA are shown in Table 5.4. Discrepancies are observed in all directional sectors, however, the high energy sectors with the biggest discrepancies, based on the hours in a given sector are highlighted. These are 135°, 157.5°, 202.5°, 225° and 315°, which are directions that contain many of the local building obstacles.

**Table. 5.4.** Difference in wind atlas predicted & measured

Sector( $^{\circ}$ )	$\Delta c$	$\Delta k$	$\Delta \text{hours}$
22.5	0.04	0.40	-5.83
45	-0.68	0.35	-58.6
67.5	-0.26	0.37	-15.53
90	0.92	1.23	34.9
112.5	-0.78	-0.06	-38.87
<b>135</b>	<b>-1.7</b>	<b>0.39</b>	<b>-121.93</b>
<b>157.5</b>	0.34	0	333.7
180	0.81	-0.50	92.27
<b>202.5</b>	<b>0.69</b>	<b>-0.26</b>	<b>214.37</b>
<b>225</b>	<b>-0.49</b>	<b>-0.36</b>	<b>167.23</b>
247.5	-0.99	-0.50	63.13
<b>270</b>	<b>-1.30</b>	<b>-0.36</b>	<b>-131.27</b>
292.5	-1.20	-0.27	-77.47
<b>315</b>	<b>-0.22</b>	<b>0.13</b>	<b>147.7</b>
337.5	-0.31	-0.18	42.73
360	0.71	0.14	-79.2

Combining the sectoral wind Weibull parameters and wind turbine power curve of Fig. 5.12 gives predictions of the directional *AEP* for comparison with the *EER*. Table 5.5 compares the directional values of the predicted *AEP* from wind atlas data and measured wind turbine *EER*, while Fig. 5.13 shows the overlay comparison on the site plan view.

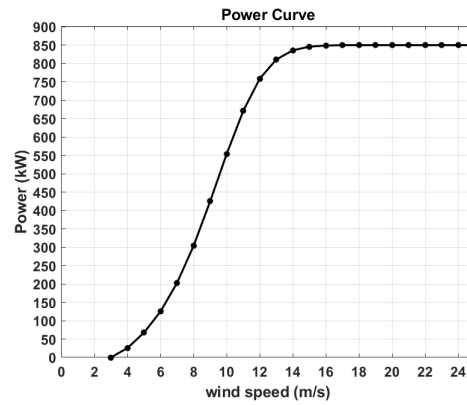
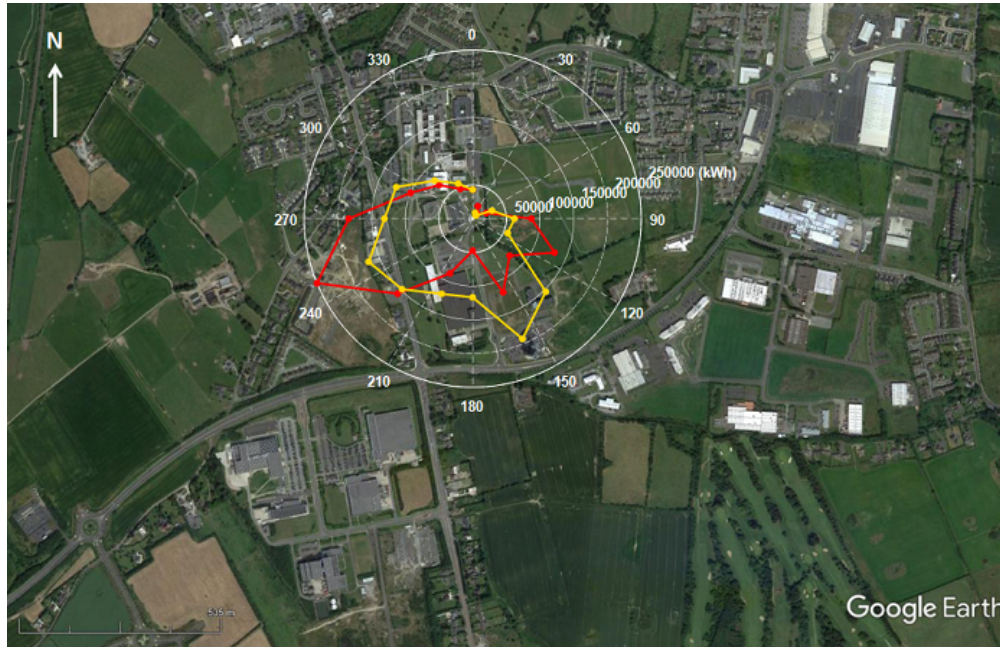


Fig. 5.12. Wind turbine power curve.

Table 5.5. Predicted and measured energy values

Sector <sup>(0)</sup>	Predicted	Measured	$\Delta$ (Predicted-Measured)	$\Delta$ (%)
	<i>AEP</i>	<i>EER</i>		
	(kWh)	(kWh)		
22.5	9322	20198	-10876	-117
45	6610	10184	-3573	-54
67.5	31076	22043	9034	29
90	61991	87057	-25066	-40
112.5	56093	131525	-75432	-134
135	153248	77431	75818	49
157.5	192854	118144	74711	39
180	116737	47354	69382	59
202.5	120609	87705	32904	27
225	148020	157395	-9375	-6
247.5	167082	249880	-82798	-50
270	130878	183866	-52988	-40
292.5	122745	99865	22880	19
315	79825	70549	9276	12
337.5	56406	47790	8616	15
360	43143	43104	39	0
<b>Total</b>	<b>1496639</b>	<b>1454087</b>	<b>42551</b>	<b>3</b>

Notably, the measured *EER* shows significantly higher energy values from the W to SW sectors, while lower values appear the S to SE sectors. Higher values are seen in the E and ESE sectors. The NW to E sectors have energy less discrepancies.



**Fig. 5.13.** Overlaid plots of the predicted wind turbine *AEP* (yellow) and the measured *EER* (red) on plan view.

The directional percentage differences where the measured *EER* exceeds the predicted energy vary from 6% to 134% with the highest percentage exceedances in the ESE ( $112.5^\circ$ ) and NNE ( $22.5^\circ$ ). However, the highest absolute differences in energy exceedance occur in the WSW ( $247.5^\circ$ ) and ESE ( $112.5^\circ$ ) sectors. The directional percentage differences where the measured energy is less than the predicted energy vary from 12% to 59%. The highest absolute differences in energy deficit occur from the SSE ( $135^\circ$ ) to SSW ( $202.5^\circ$ ) sectors inclusive. Therefore, the larger absolute energy discrepancies occur in the sectors with the more significant local building obstacles.

Fig. 5.14 shows pictures of some of the main local obstacles, outlined in Fig. 5.6 and previously described in Chapter 4, as viewed from the turbine at hub height. The directions with largest absolute energy deficits occur in the sectors that contain buildings 1, 2 and 5. The neighbouring sector to the SSW ( $247.5^\circ$ ), with the less dense obstacles 7, has the highest absolute energy exceedance. It suggests that in the SW

sector the low and broad buildings 1 and 5, that are approximately 20% of the turbine height and up to 1.1 km away, are having a significant reducing influence on the energy performance of the wind turbine in the SW sector. However, the energy exceedance in the WSW sector also suggests that building obstacles 1 and 5 may be steering energy into the WSW sector. In the SE sector, the high energy exceedance difference at  $(112.5^\circ)$ , combined with a high energy deficit in the SE sector, suggests the influence of the tall and narrow building 2 and lower buildings 4 are both reducing or steering energy to the east. Interestingly, the measured *EER* appears to show two energy peaks in directions to either side of buildings 2 and 4. This suggests some wind channelling effects along the road between buildings 1 and 2 along with some wind steering to the east of building 4. The E and NE sectors are not in prevailing wind directions and are more difficult to assess due to the regional hill and coastal influences, as was described in the mesoscale results. The NW sectors show small deficits in energy differences that may be due to the more uniform surface roughness of the town to the north of the site being underestimated by the wind atlas.

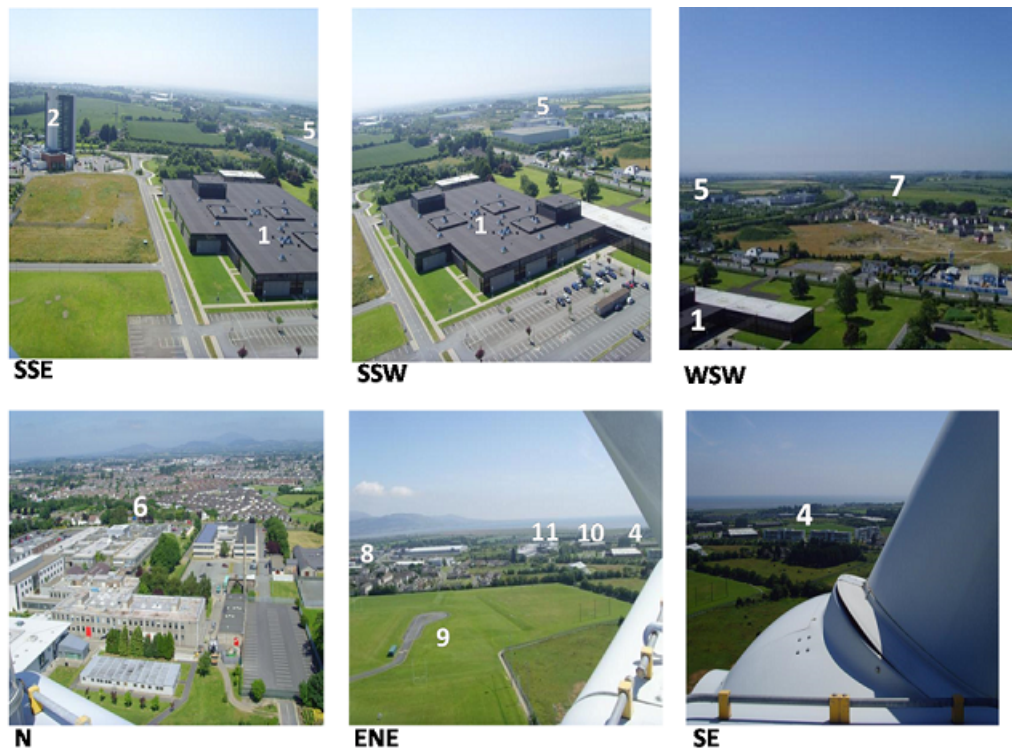


**Fig. 5.14.** Views from wind turbine nacelle at hub height showing some of the local obstacles.



Interestingly, the total annual electrical energy values in each case are very similar with only a 3% difference between the total and predicted. However, the difference in the directional distribution suggests that energy is being steered or enhanced in some directions and reduced in others. This implies that energy losses in some directions are being compensated by energy gains in other directions, i.e., locally, some building obstacles may be redirecting the wind energy resource about the wind turbine site, without having an excessive energy reducing impact. These effects are not well captured by the Irish wind atlas.

#### 5.5.4 Predicted AEP comparison of WT site with other local locations

The total *AEP* estimates from the wind atlas at the other local assessed locations, that were outlined in Fig. 5.6 are shown in Table 5.6.

**Table. 5.6.** *AEP* comparison at other local locations

Location	Predicted <i>AEP</i> (kWh)	$\Delta$ (%)
WT	1496600	-
M2	1477200	-1
M3	1600100	+7
M4	1678800	+12

In line with the results shown Fig. 5.10, the wind turbine location WT appears to be a poorer performing site compared to M3 and M4. Location M3, which is to the south of the buildings, performs up to 8% better than M2 which is to the west of the buildings. This shows that a good wind fetch to the east coast can be significant in the coastal regions despite the general prevailing winds coming from the southwest. Location M2 in Fig. 5.10 has the poorest *WPD* in the southeast sector. This could be explained by the influence of the buildings to the east of M2. Although M4 has the highest *AEP*, the influence of the coast is less, as it is further inland, but has it has a better fetch to the west due to it being at a slightly more elevated location. However, a turbine located at M4 would not be a practical possibility for the DkIT site. Interestingly, the results suggest that location M3 would be preferred over M2,

which highlights the influence of the proximity to Dundalk Bay on the local wind environment.

### 5.5.5 Preliminary onsite LiDAR directional wind shear profiles

Directional wind shear profiles from the 11 measurement heights for 16 directions at the wind turbine site WT are shown in Fig. 5.15. The points at each height represent the mean wind horizontal wind speed over the time period, March 2018 to March 2019.

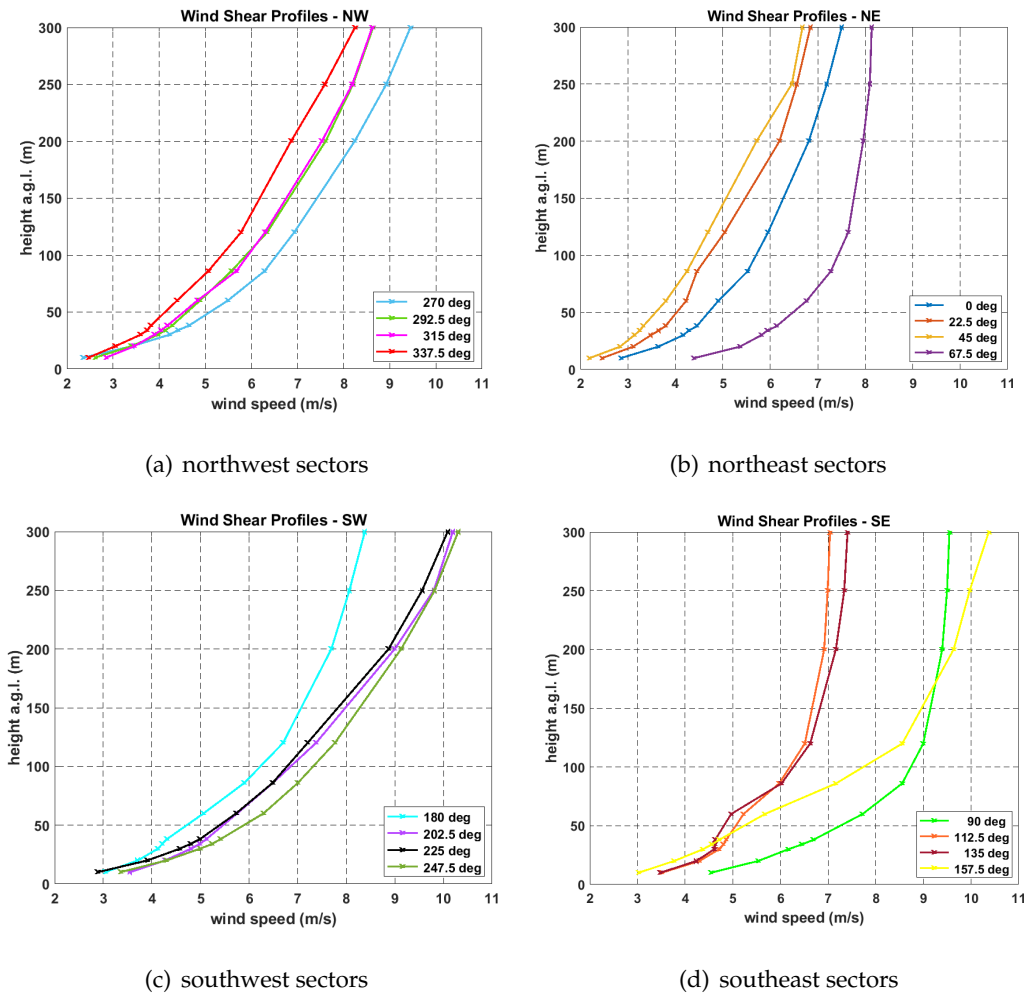


**Fig. 5.15.** Directional wind shear profiles from LiDAR measurements at wind turbine site.

Clearly, the wind shear is not the same for all wind directions. Firstly looking at the higher energy sectors of the SW and SE, the wind speeds in the more open sector of  $247.5^\circ$  are highest at the turbine hub height of 60 m and up to  $\sim 200$  m. At  $202.5^\circ$ , the hub-height wind speed is lower, but exceeds the  $247.5^\circ$  wind speed above  $\sim 250$  m and equals it at  $\sim 30$  m and below. The wind speeds at  $225^\circ$  are similar to  $202.5^\circ$



at the wind turbine hub height, but is less both above and below this and becomes  $\sim$  equal to the wind speed at  $247.5^\circ$  above  $\sim 200$  m. The  $180^\circ$  sector has lower wind speeds away shown from the mesoscale results, but show a defined change in wind shear at  $\sim 30$  m giving lower wind speeds below this height. As low broad building obstacles exist in this sector, it suggests that wind flow is complex and points to the existence of local internal boundary or sub layers, i.e., RSL and ISL that vary with height. The higher wind speeds of  $247.5^\circ$  as indicates potential of winds being shifted into this sector from the neighbouring the SW sectors that have more obstacles. This is in line with the *EER* and suggests that winds are being steered by buildings 1 and 5 towards the  $247.5^\circ$  sector, between buildings 1 and 6, with reduced winds in the  $202.5^\circ$  and  $225^\circ$  sectors. In the southeast, the wind shear profiles in the SE sectors show reduced shear above  $\sim 100$  m a.g.l. at  $112.5^\circ$  and  $135^\circ$  indicating the more open fetch to the sea, but become complicated at heights below 100 m. These sectors contain building obstacles 2, 3 and 4 coinciding with reduced energy output in the *EER*. The profiles at  $135^\circ$  are in the wind turbine rotor wake, evident from the complex wind shear profile from 34 m to 86 m in this sector. At  $157.5^\circ$  the wind speeds increase again. This is a high wind sector but has high wind shear from below  $\sim 120$  m. In this sector, building 2, i.e., a tall 47 m hotel, indicates wind and energy reduction impacts with possible channelling between building obstacles 1 and 2. This is in line with the energy peak observed in the *EER* in Fig. 5.13 in the direction along the road between buildings 1 and 2. In the NW sectors, the W ( $270^\circ$ ) is the most energy dominant. At  $315^\circ$ , the wind shear below 100 m becomes more complicated. This may be caused by the effects from local low rise campus buildings to the NW and densely packed low rise residential buildings and town in the NW to N sectors, obstacle area 6 in Fig. 5.14. This agrees with the small energy deficits observed in the *EER* in this direction. The NE to E sectors have sparse local obstacles, but have the mesoscale features of the hills to the N and the land sea interface with Dundalk Bay. Wind shear profiles centred on  $22.5^\circ$  and  $45^\circ$  are lowest, and wind speeds are relatively low up to 300 m, indicating non-prevailing winds and blocking by the hills to the northeast. Wind speed and shear increases from the N sector centred at  $0^\circ$ , which may indicate some channelling of winds between building areas 6 and 8 matching the small increase in the *EER* from the north. In addition, as the NE sectors are non-prevailing wind sectors, there are a reduced number of data points giving

more scatter. At  $67.5^\circ$ , there is a significant increase in wind speed and wind shear up to 100 m that may indicate the onset steering of wind from the east by the hills to the northeast. Also atmospheric instability introduced by land-sea thermal effects in spring and summer months can reduce wind shear at lower heights. This is more evident at  $90^\circ$  where the wind shear is high at low heights but reduces faster from a low height compared to other directions. The data in the easterly sectors contain wind measurement from a rare high-wind spring storm event in March 2018, that increase the mean winds in the easterly sectors of  $67.5^\circ$  and  $90^\circ$ .

### 5.5.6 Nacelle anemometer and LiDAR measured wind speeds

The mean wind speed at the 60 m hub height, measured by the LiDAR, over the 1-year period is 5.60 m/s. This is in good agreement with the recorded a mean wind speed by the wind turbine SCADA system of 5.61 m/s. Fig. 5.16 compares the hub-height raw wind speed from the nacelle anemometer to the 60 m LiDAR wind speed measurements at wind speeds of most interest i.e., above the the wind turbine cut-in wind speed. The correlation coefficient or slope of the linear regression shows a close to but slightly higher value than 1. This is expected as the nacelle anemometer is behind behind the rotor where wind speeds are reduced. The turbulence introduced by the rotor and nacelle body gives a lower coefficient of determination,  $R^2$ , of  $\sim 0.9$  compared to  $\sim 0.99$  in the case of LiDAR to met comparisons at flat field sites (Pitter, Slinger, and Michael, 2015; Goit, Shimada, and Kogaki, 2019). Some directional variations is also show as summarised in Table 5.7. The values are for  $45^\circ$  wide sectors centered on the directions given. The the  $90^\circ$  sector, with the least surface complexity, i.e., facing the the coast show the better  $R^2$  values. Notably, the direction of  $135^\circ$  gives the poorest  $R^2$ . This can be explained by the positioning of the LiDAR to the northwest of the turbine and therefore, is in the wake flow of the turbine rotor for this sector, as was shown in the wind shear profiles. Plots of all the sectors are given in Appendix B, as illustrated this further. More details of the LiDAR location and position are given in the next chapter where microscale models will be used to be predict the wind turbine *EER* using LiDAR measurements above and below the influence of the wind turbine rotor.

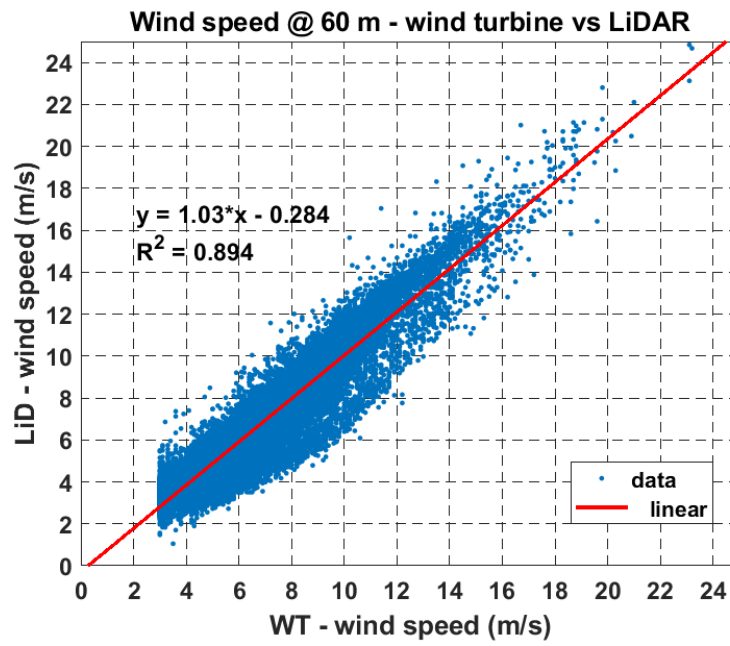


Fig. 5.16. Nacelle anemometer vs LiDAR measured wind speeds at the 60 m hub-height.

Table. 5.7. Linear regression between nacelle anemometer and LiDAR wind speeds

$y=ax+b, R^2$			
Sector( $^{\circ}$ )	a	b	$R^2$
all	1.03	-0.28	0.89
0 (360)	0.96	0.18	0.95
45	1	0.03	0.89
90	1.1	0.31	0.94
135	0.99	-0.39	0.83
180	1.08	0.6	0.89
225	1.07	-0.36	0.93
270	1.03	-0.22	0.92
315	1	-0.01	0.89

## 5.6 Discussion

It has been shown that both the mesoscale and microscale scale factors influence the energy performance of a wind turbine, at a given site, in a distributed wind project development. At the mesoscale level, the geographical size and location of Ireland, Irish Sea and the west coast of Britain appears to have steering influences on the prevailing south westerly winds northwards up the Irish Sea, i.e., increasing the predicted southerly wind speeds at offshore and onshore locations near to the east coast. The wind atlas assessment shows a significant southerly component in the offshore winds approximately 30 km offshore east of the wind turbine site. Closer to the shore at Dundalk, this southerly wind component appears to back to the southeast creating significant south easterly winds through Dundalk Bay towards the wind turbine site, which enhances wind energy from this direction. These south easterly winds become significantly reduced at approximately 10 km inland from the coast indicating that distributed wind projects closer to the coast will have enhanced energy potential and project viability. Contrary to this, the hills to the north of Dundalk Bay appear to have an energy reducing impact on any winds from the northeast, although this is not general prevailing wind direction.

Encouragingly, a comparison of the total *AEP* for the site from the wind atlas data is within 3% of the measured total value of wind turbine *EER*. This indicates how beneficial the open source Irish wind atlas is for pre-feasibility studies and the progress that is being made in mesoscale wind atlas development. However, analysis of the *EER* from the wind turbine SCADA data shows notable directional differences in comparison with the directional breakdown of *AEP* predicted from the wind atlas data. An overlay of wind turbine *EER* and the predicted directional *AEP* on a local plan view highlight directional differences that can be related to the influence of local features such as building obstacles. These influences can reduce and/or redistribute the energy with direction. Buildings can have multiple influences on wind flow at a given location such as wind speed up, channelling, steering and blocking depending on the building sizes and spatial layout (Hassanli et al., 2019; Toparlar et al., 2017). Like in Chapter 4, it is observed in this study that a 12 m high broad building cluster, at a distance of 550 m to 1100 m from the turbine location, has a bigger influence on the turbine energy output compared to a 47 m

high narrow building at a distance of 335 m to 420 m. The horizontal cross-sectional width, as viewed from the turbine, is 635 m and 70 m for the broad building cluster and taller narrow building respectively. This is supported by onsite LiDAR measured directional vertical wind shear profiles.

The results indicate that obstacles of at least 20% of the wind turbine hub height and within at least 20 times the turbine hub height can influence the wind turbine energy performance. Energy reductions due to obstacles can be compensated for through wind steering or channelling depending on their physical geometries and spatial layout. The downscaling process from mesoscale to microscale in the Irish wind atlas to a 1 km resolution does not fully capture these local microscale influences. Therefore, accurate wind turbine micro-siting of medium-to-large-scale wind turbine within peri-urban areas will be critical to optimise project viability by minimising local energy reduction and taking advantage of local energy gains due to obstacles. The finding also indicate that well-judged placement of a met-mast and heights of measurements in peri-urban environments would be very important combined with micro siting tools to male accurate *AEP*.

For distributed wind energy to become more cost-effective in peri-urban environments that involve single or a small number of wind turbines, further research in cost-effective wind resource and energy prediction tools will be required in order to improve wind turbine micro-siting accuracy. This will require additional measurements, testing and validation of both linear and CFD models for micro-siting medium and large scale wind turbines in urbanised environments. However, this in turn will create further challenges in trading off cost effective measurement and modelling complexity against the size of given distributed wind turbine(s) project.

## 5.7 Conclusions and next steps

The study compares the annual energy prediction using a mesoscale modelled wind atlas with real wind turbine performance in a peri-urban area and results in agreement within 3% in this case. Mesoscale influences of regional hills in wind blocking and steering of offshore winds towards the coastal wind turbine site appear to be well represented. Proximity, within 10 km, to the east coast also gives an enhanced wind resource. The results also show that at the microscale level more complex

directional sensitivities in the directional energy from measurements are not fully captured by the predictions using the wind atlas. These sensitivities are dependent on the spatial layout of obstacles around the site and can include numerous effects such as wind speed up, channelling, steering and blocking depending on obstacle features. Buildings with heights as low as 20% of the turbine hub height within 1 km of the wind turbine location have an influence. It is observed that wind turbine energy output enhancement in some directions compensates for energy losses in other directions. The directional sector percentage gains in the measured energy compared to predicted energy varied from 6% to 134%, while the percentage losses varied from 12% to 59%. However, the largest discrepancies in absolute energy terms occur in directional wind sectors occupied by local building obstacles. This is further highlighted by onsite LiDAR wind shear measurements that show variations in wind shear profile with direction, with more complicated wind shear profiles in prevailing directional wind sectors occupied by building obstacles. A comparison of nacelle anemometer wind speeds and LiDAR measurements at hub height shows a consistent linear correlation coefficient between the raw nacelle anemometer and LiDAR wind speed measurements, however, due to the scatter in the data from rotor wake effects, the  $R^2$  was  $\sim 0.90$  compared with met mast studies at flat field sites of  $\sim 0.99$ .

In general, this chapter highlights that accurate wind turbine micro-siting of medium-to-large-scale wind turbine within peri-urban areas will be critical to optimise project viability and the growth of a distributed wind industry into the future. This will require careful use of wind atlas tools, the use of microscale flow models and careful selection of onsite wind measurement heights, especially if met masts are being used. The trade off of cost effective measurement and modelling complexity against the size of given distributed wind turbine(s) project, particularly in a peri-urban environment, remains an area of further investigation.

The next chapter will evaluate four microscale wind modelling approaches, driven by onsite LiDAR measurements, in predicting the wind turbine *EER*. The aim is to assess how best to apply commonly used linear and CFD microscale approaches in the treatment of building obstacles and the wind measurements heights from which the models scale best to given the best directional *AEP* prediction compared to the real-world wind turbine *EER*. LiDAR wind shear profiles in prevailing wind sectors of interest will be compared theoretical logarithmic wind shear profiles to test

---

for the existence of local internal boundary layers, in particular RSL and ISL height variations.





## Chapter 6

# A comparison of four microscale wind flow models, coupled with onsite LiDAR wind measurements, in predicting the wind turbine EER

### 6.1 Objectives

Chapter 5 showed that the remodelled mesoscale based Irish wind atlas did not fully predict the wind turbine *EER* in prevailing wind directional sectors containing building obstacles and that an initial examination of LiDAR measured directional wind shear profiles showed some complicated characteristics. It was concluded that careful application of microscale models would be required as well as well-planned setups of wind measurement campaigns.

The objective of the chapter is to compare four data driven micro-scale modelling approaches, one linear and three RANS CFD, in the prediction of the directional annual energy output with the wind turbine *EER* in this peri-urban environment. One year of wind turbine 10-minute SCADA data is used to produce the *EER* over the same modelled 1-year period. Two industry standard microscale modelling tools, namely WAsP and WindSim are used to run the models. The four modelling approaches each treat building obstacles in a different manner. In the linear case, WAsP-IBZ uses an empirical shelter model, referred to in the literature review, that describes wind speed reduction in the wake of an obstacle (Mortensen, 2016). In the CFD cases, WAsP CFD treats obstacles as roughness elements, while in WindSim, obstacles can be treated as either roughness elements or as blocking elements in the computation mesh. The four approaches are used to predict *EERs* at the wind turbine hub-height, from downscaling or upscaling 1-year of onsite LiDAR wind measurements at multiple heights above and below the wind turbine hub-height.

Wind measurements from a local offsite met mast, outside peri-urban environment, are used to determine the background surface roughness. The hub-height *EER* predicted by each model is compared to the actual *EER* from the wind turbine SCADA data. Wind roses and *WPD* at the LiDAR measurement heights are used to assess power and directional changes in the wind resource from 200 m down to a height of 10 m. Directions with the biggest discrepancies between all four model and measurements are examined in relation to the local obstacles. It is assumed, from the literature review, that winds at heights of 200 m are above the influence of local building obstacles. Measured directional wind shear profiles are compared to theoretical logarithmic profiles. The implications for the use of the models in peri-urban settings are discussed and suggestions provided to help assist the successful deployment of future single medium to large scale wind turbines in peri-urban wind environments.

The chapter begins with a site overview and descriptions of data measurement setup and data logged. Secondly, an overview of the model theory and model setups for the both the linear and CFD cases are given. Thirdly, comparisons of predicted *EERs* by the models and the actual wind turbine *EER* from the SCADA are made and examined in relation to directional wind shear profiles, *WPD* profiles and local site features. Finally, the implications of the findings for distributed wind deployment in peri-urban areas are discussed along with conclusions and suggested next steps.

## 6.2 Methods

### 6.2.1 Site overview and measurement setup

Fig. 6.1 highlights the regions in the local built environment around the wind turbine location that are of most interest, based on the findings in the previous chapters. Within approximately 1.1 km radius of the wind turbine there exists a number industrial buildings. The majority of the buildings, circled in white, range in height from 7 m to 13 m and of low spatial density. Circled in yellow is the standout narrow 47 m high building and a 25 m building circled in red. To the north of the site, the town consists of more dense residential and commercial areas with building heights of  $\sim 6$  m to 7 m.



**Fig. 6.1.** Local buildings (Circled: yellow 47 m, red 25 m, white 6–13 m), wind turbine (WT), LiDAR (LiD), Met mast (M).

As was discussed in Chapter 5, a ZX LiDAR is ground mounted, at location (LiD) in Fig. 6.1, approximately 60 m from the wind turbine location (WT). Ten-minute averaged wind speed and direction measurements at 11 heights are taken, namely 10 m, 20 m, 34 m, 38 m, 60 m, 72 m, 86 m, 120 m, 200 m, 250 m and 300 m. As buildings from southeast through to the west of the turbine are of most interest, a temporary 34 m high met mast, specifically for this research, is located in a rural location (M) approximately 1140 m west of the turbine site. Location M is on private farmland that is outside of the influence buildings in the prevailing westerly wind sectors. The wind turbine and measurement equipment are shown in Fig. 6.2 and data acquisition details are outlined in Table 6.1.

The met mast is equipped with boom mounted NRG 40C anemometers, NRG 200P wind vanes and NRG T60 shielded temperature sensors. The height of the mast is limited by permitting constraints and the mast guy-wire footprint allowed by the landowner. The calibration of direction with voltage for the wind vanes are done in-house by the OEM, NRG Systems. Direction-voltage slope and offset values are provided for data logger setup. In a similar way, the NRG T60 temperature sensors are calibrated with voltage by the OEM using instrumentation and standards that are traceable to the National Institute for Standards and Technology (NIST) of the

USA. The cup anemometer calibrations are certified to IEC standards by an accredited external test laboratory for the OEM. These give relationships of wind speed with frequency, including offsets. Each instrument has its own unique IEC compliant calibration report, but the maximum deviation in wind speed is less than 0.06 m/s for the anemometers, less than a  $1^\circ$  difference in direction for the wind vanes and an uncertainty of  $0.05^\circ\text{C}$  for the temperature sensors. The calibration information is used in the set-up of a Second Wind Nomad2 data logger that logs all met mast data.



(a) Wind turbine (WT)



(b) ZX LiDAR (LiD)



(c) 34 m Met mast (M)

**Fig. 6.2.** Measuring instruments.

**Table. 6.1.** Data acquisition details

Instrument	Location (UTM, 29 U)	Data parameter	Heights a.g.l. (m)	Meas' period	Logging interval
Wind Turbine SCADA	671042 m E 5984840 m N	-wind speed, -wind speed standard deviation, -wind direction, -nacelle direction, -power, -power standard deviation	60	Feb- 2018 to Feb- 2019	10-min'
LiDAR	671003 m E 5984890 m N	-horizontal wind, -vertical wind speed, -wind speed standard deviation, -wind direction, -TI	10, 20, 30, 34, 38, 60, 86, 120, 200, 250, 300	Feb- 2018 to Feb- 2019	10-min'
Met Mast	670006 m E 5984390 m N	-wind speed, -wind speed standard deviation, -wind direction -temperature	10, 30 8,28 2,32	Aug- 2019 to Mar- 2020	1-min' 1-min'

One year of 10-minute time series data from the wind turbine SCADA is used to produce the wind turbine *EER* and the directional energy distributions with wind speed. In this study, wind roses and directional *WPD* at six heights are produced from LiDAR measurements over the same 1-year period as the SCADA data measurements. The six measurement heights are 10 m, 20 m, 30 m, 86 m, 120 m and 200 m. These are used to create annual wind climates as input required by both WASP

and WindSim tools. The highest LiDAR measurement height value of 200 m was chosen based on the maximum height for which the WAsP tool can accept data measurements for its wind climate analysis, and also assumed to be above the influence of the local buildings. The upscaling and downscaling capability of the models to predict the wind turbine *EER* at the 60 m hub height are compared to the measured *EER* from the SCADA data. Directional wind shear is also determined from measurements at nine heights, by including the additional heights of 34 m, 38 m and 60 m, chosen to capture the effects of the buildings at different heights and to assess potential sources of discrepancies in the model predictions with respect to local buildings. In this chapter, the met mast wind measurements at 10 m and 30 m are used to determine the background surface roughness that is used in surface roughness maps required by the modelling tools. More details of the met mast is given in the Chapter 7 where its data will be used to assess offsite wind characteristics in more detail in relation to morphological characteristics around the wind turbine site.

### **6.2.2 Linear flow model approaches**

The linear WAsP-IBZ is diagnostic tool widely used in the wind industry that calculates wind statistics by parameterising the influence of orography, roughness and obstacles (Troen and Lundtang Petersen, 1989). It uses a high-resolution zooming polar computation grid with a digital elevation map (DEM) to calculate the potential flow perturbation profile at the central point of the computation domain. The zooming grid resolution is highest in the centre (i.e., at the point of interest) and gradually decreases towards the edges. It consists of 72 five degree sectors, each divided in to 100 radial segments. It can accept arbitrarily chosen contour lines as input. Therefore, resolution limitation is set by the accuracy and density of the contour data of the DEM and the grid is adjusted to cover the extent of the DEM. For example, the grid radial distance resolution near the centre is approximately 2 m for a total domain of 10 km and approximately 10 m for a domain of 50 km. It is recommended that a DEM should extend at least several times the horizontal scale of significant terrain features from a wind turbine and/or wind measurement site. This means the DEM can be up to 20 km x 20 km, depending on the site terrain features. WAsP requires measurements from a nearby reference measurement mast, preferably within 50 km of the wind turbine or wind farm location, and predicts the



*AEP* of a wind turbine or wind farm. This general approach requires assessment of the terrain features of both the met mast site and the wind turbine site. At least one year of met mast data is up-scaled, to create a terrain independent generalised wind climate for the region. This is done by accounting for the effects of local obstacles, surface roughness and orography at the reference mast location, Fig. 6.3(a). It is assumed the generalised wind climate at the wind turbine location is the same as at the reference met mast location. Alternatively, the wind climatology may be derived from mesoscale modelling at the wind turbine site itself. It is then downscaled at the wind turbine location to the proposed hub height, accounting for orography, surface roughness and obstacles around the wind turbine location. It uses wind turbine power curve(s) to predict the *AEP* of a wind turbine or wind farm. In general, accurate predictions using the WAsP-IBZ flow model may be obtained provided that the met station and wind turbine site experience the same overall general wind climate i.e., mesoscale effects are the same. In addition, atmospheric neutral stability is assumed in prevailing wind directions and surrounding terrain is assumed to have slopes low enough such that wind flows remain attached (Mortensen, 2016). The zooming grid of the IBZ model is constrained to 1 million points, which may be a limitation in more complex terrain. Flow over steep terrain, where flow separation may occur, cannot be captured and therefore is another limitation of the WAsP-IBZ model. A ruggedness index or RIX number is defined as the percentage fraction of the terrain that is steeper than some critical slope  $\theta_c$ , taken to be 0.3 ( $17^\circ$ ). The three determining parameters are radius  $R$  usually taken as 3.5 km, the critical slope  $\theta_c$  of 0.3 ( $17^\circ$ ) and the number of radii  $N$  (Zhang, 2015). The overall RIX value for the site is the mean of the radius-wise RIX values. Attached flows are assumed when the overall RIX close to zero. If  $RIX > 0$ , it is indicative that somewhere in the surrounding area the slopes are greater than 0.3 ( $17^\circ$ ), meaning the onset of flow separation. In the case of a wind farm project in complex terrain that has more than one onsite met mast, RIX numbers are assessed for each met mast location to give the difference in RIX between them i.e.  $\Delta RIX$ . Where  $\Delta RIX$  is greater than 5%, a regression analysis of the cross prediction error in wind speed from one mast to the other against  $\Delta RIX$  enables an empirical correction factor that is applied to the biased wind speed predictions in order to obtain the true wind speed at wind turbine hub height locations

across a site. In this study, the natural terrain slopes are not beyond  $\theta_c$  in any direction up to 3 km and beyond. Therefore, a RIX number assessment is not deemed necessary in this case.

A novelty in this study is that onsite LiDAR measurements at multiple levels in a peri-urban environment are also at the site of the large-scale wind turbine itself and used to create the onsite annual wind climate directly for coupling to the models, Fig. 6.3(b). As described in Chapter 3, traditional method of microscale analysis involves using data measurements from a nearby weather station met mast, preferably within 50 km of the turbine site and scaling this data using microscale models to the wind turbine site of interest. This involves accounting for surface roughness, obstacles, surface roughness and orography in the models at both the met mast and wind turbine sites. In this case, the measurements are taken directly at multiple heights at the turbine site thereby eliminating any potential errors in the modelling process of scaling the wind speed from the met mast site to the wind turbine site. The novelty in having LiDAR measurements taken directly at this site enable the comparison of different models in accounting for local obstacles specifically from scaling the wind data from one height to the wind turbine hub height and comparing the model predictions directly with wind measurements and wind turbine EER.



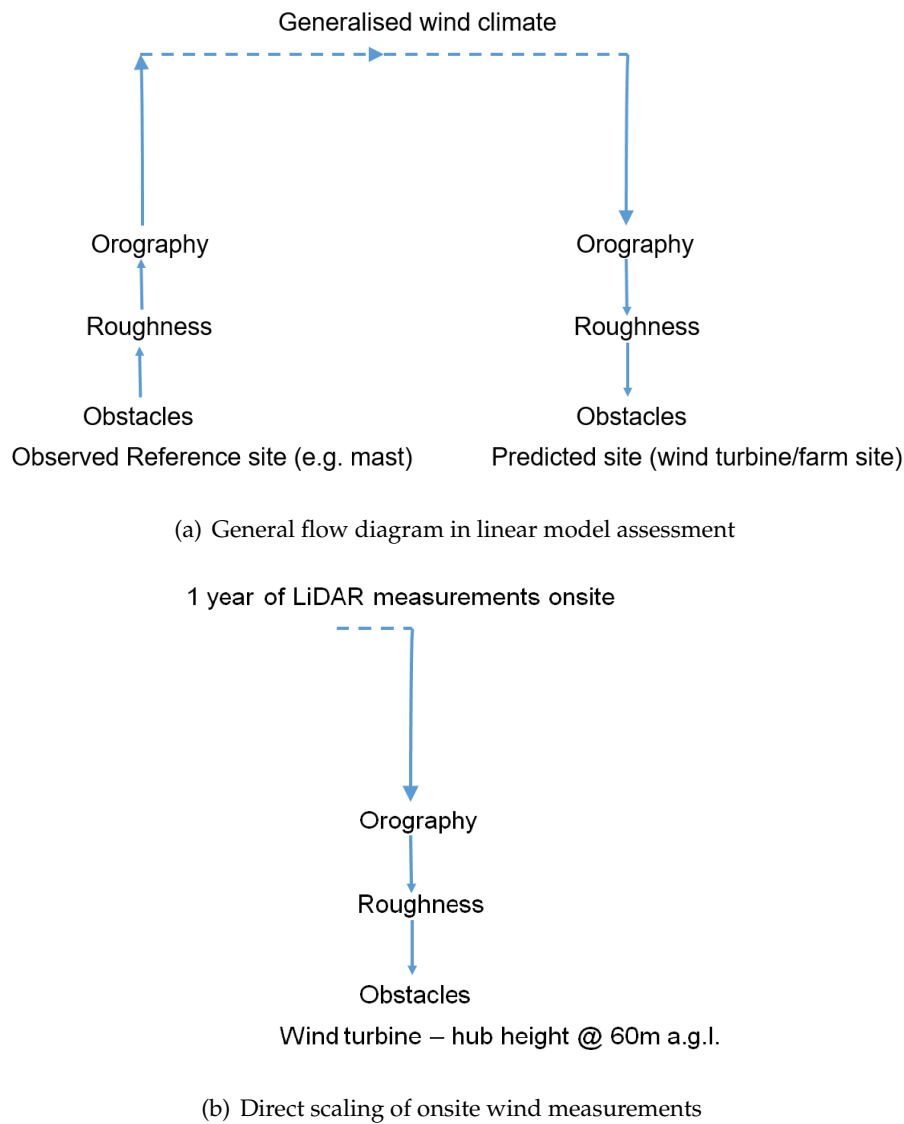


Fig. 6.3. Linear flow models.

WAsP\_IBZ uses the linear 'BZ-model' to calculate the wind velocity perturbations in the ABL induced by orographic features. It is based on models related to the Jackson and Hunt theory that involves linearising the Naiver-Stokes equations, describing two-dimensional turbulent flow over low hills (Zhang, 2015), outlined in the literature review. Ground surface features such as vegetation and obstacles have a slowing effect on wind speed close to the ground and can increase turbulence in the flow. Surfaces roughness for various types of surfaces are categorised by a roughness length  $z_0$ , (Manwell, McGowan, and Rogers, 2009). These are summarised in Table 6.2. Roughness classifications defined in WAsP are also shown.

**Table. 6.2.** Surface roughness values for various terrain types, (Standen and Wilson, 2015; Mortensen, 2016).

Physical $z_0$ (m)	Terrain surface characteristics	Roughness Class	$z_0$ specified in WAsP (m)
1.5		4 (1.5 m)	1.5
>1	tall forest		>1
1.00	city		1.00
0.80	forest		0.80
0.50	suburbs		0.50
0.40		3 (0.40 m)	0.40
0.30	shelter belts		0.30
0.20	many trees and/or bushes		0.20
0.10	farmland with closed appearance	2 (0.10 m)	0.10
0.05	farmland with open appearance		0.05
0.03	farmland with very few buildings/trees	1 (0.03 m)	0.03
0.02	airport areas with buildings and trees		0.02
0.01	airport runway areas		0.01
0.008	mown grass		0.008
0.005	bare soil (smooth)		0.005
0.001	snow surfaces (smooth)		0.003
0.0003	sand surfaces (smooth)		0.003
0.0002	(used for water surfaces in the Atlas)	0 (0.0002 m)	0.0
0.0001	water areas (lakes, fjords, open sea)		0.0

Surface obstacles in close proximity to the site of interest can have wake effects that can additionally perturb wind flow downwind on the obstacle. For a given obstacle, if the turbine hub-height is less than three times the height of an obstacle and is less than fifty obstacle heights away from the obstacle, then the obstacle is modelled by the WAsP shelter model, otherwise it is treated as a surface roughness element. The WAsP shelter model is based on a refined version a simple two dimensional obstacle of infinite length, derived from wind tunnel measurements by Perera (Troen and Lundtang Petersen, 1989; Peña et al., 2016). A zone of flow separation is considered to exist within a region defined by a straight line drawn from the top of the obstacle to the ground from 2 obstacle heights upwind of the obstacle to 5 obstacle heights downwind of the obstacle. The fractional reduction in wind speed, downwind of the obstacle is described by Eqs. (6.1) to (6.3).

$$\frac{\Delta U_z}{U_h} = 9.75 \left( \frac{H}{h} \right)^{0.14} \frac{x}{h} (1 - P) \eta e^{(-0.67\eta^{1.5})} \quad (6.1)$$

$$\eta = \frac{H}{h} \left( K \frac{x}{h} \right)^{\frac{-1}{n+2}} \quad (6.2)$$

$$K = \frac{2\kappa^2}{\ln \frac{h}{z_0}} \quad (6.3)$$

Where:

$\Delta U_z$  – wind speed reduction at height  $z$  (m/s)

$U_h$  – free wind speed at obstacle height (m/s)

$U_z$  – wind speed at height of interest (m) (e.g., turbine hub height)

$P$  – porosity of obstacle (ratio of open area total area)

$h$  – obstacle height (m)

$x$  – distance downstream of obstacle (m)

$H$  – height of interest (m) (e.g., wind turbine hub height)

$z_0$  – surface roughness

$n$  – velocity profile exponent of  $\frac{1}{7}$

This formula has limitations in that it assumes normal non-skewed incident wind flow at the obstacle. Multiple obstacles are treated by considering the obstacle furthest away first and calculating the individual sheltering by all subsequent downstream obstacles towards the site of interest. If the zones of separation of very close obstacles overlap then the relative sheltering is reduced by the fraction of the overlap.

### 6.2.3 WAsP-IBZ setup

WAsP version 11 is used in this study. The WAsP tool has a mapping editor that allows topographic maps of various formats to be digitised for elevation and surface roughness. Shuttle Radar Topography Mission (SRTM) derived elevation data for many regions or zones of the earth's surface can be obtained online from NASA's Earth Resources Observation and Science (EROS) Center<sup>1</sup>. SRTM data is measured using radar interferometry techniques from space shuttle Endeavour with a 25 m<sup>2</sup> resolution. Over 80% of the earth's landmass is covered. Grid point elevations at a resolution of 1 arc-second or  $\sim 30$  meters and a vertical resolution of  $\sim 5$  m to 10 m are available, depending on location and terrain complexity (Farr et al., 2007; EROS, 2017). The elevation data is projected onto a map co-ordinate system of the earth's surface to give the elevation data in spatial latitude-longitude and vertical reference frames. As the earth is not a perfect sphere, a reference system or "datum" is used as an approximation of the earth's surface from which positional measurements are made. A horizontal datum provides a reference frame for latitude and longitude coordinates on the Earth surface. It requires an ellipsoid model of the earth's surface and an anchor point from which latitude and longitude co-ordinates can be determined. The ellipsoid model is a best approximation of a more complex geoid model that has an irregular shape, based on the non-constant gravitational force of the earth that defines sea level. The elevation of a position can be determined using a vertical datum reference, from the geoid model, with respect to the ellipsoid model. A number of horizontal and vertical datums are available. The world geodetic system 1984 (WGS84) is one such widely used system that has an ellipsoid model, horizontal datum and vertical datum, and coordinate system (Kumar, 1988). The coordinate system comprises of the horizontal datum, reference meridian (e.g., Greenwich) and

<sup>1</sup>EROS: <https://www.usgs.gov/centers/eros>

uses angular units to express locations in geographic latitude and longitude degrees. The earth gravitational model (EGM)96 from 1996 is the geoid and vertical datum reference of WGS84. To project the geodetic coordinates and heights onto a two dimensional plane i.e, a map, a transformation of the co-ordinates must be carried out. Numerous transformation are possible depending on the application and accuracy required. However, for the purposes of WAsP topographic map generation, the Universal Transverse Mercator (UTM) coordinate system projection is used. Using a complex number of algebraic and trigonometric functions, the UTM divides the world into 60 zones north to south that are each 6 longitude degrees wide. UTM zones are numbered consecutively beginning with first zone at the most western point of Alaska and progresses eastwards. In each zone, the coordinates are northings and eastings are measured in meters. In the northern hemisphere, the northing values begins at zero meters at the equator and increase in the northerly direction. The central meridian of each zone is set at five hundred thousand meters relative to eastern edge of the zone. This is to avoid negative numbers.

In this study, a 20 km x 20 km terrain DEM, centred on the wind turbine location, is produced from SRTM data. This is projected to the WGS84 reference system and transformed to UTM co-ordinates for Zone 29. Elevation contours are set to a resolution of 2.5 m. A quality checking feature of the WAsP map editing tool allows elevation contour lines to be checked for continuity and values consistency. Any errors are flagged and can be corrected. The resulting DEM is shown in Fig. 6.4. The hills to the northeast are clearly visible while the remaining topography is low lying, particularly to the south and west of the site with Dundalk Bay to the east. Therefore, the terrain in the prevailing wind directions could be considered non-complex. The scaled overlaid background satellite image in the centre outlines Dundalk town and the area of most interest. The map is digitised in the area of interest to include background surface roughness of surrounding, rural, urban and coastal areas area. The default value for the number roughness changes is 10 in each of twelve directional sectors, though up to 10 changes of roughness in each of up to 36 sectors can be made. Two digitised maps are created, one that represents background roughness elements with buildings characterised by a linear obstacle shelter model and one where buildings are treated as roughness elements. Areas and elements of given roughness values are created by tracing closed lines around the areas of interest.

Roughness values at both sides of roughness lines are set according to the surface type, outlined in Table 6.4. At with elevation contours, the quality checking feature allows testing for open roughness lines or lines with inconsistent values of roughness on either side of a line. The background rural surface roughness, determined from measurements at the met mast at location M, is 0.2 m (shown later). This is consistent with published values for agricultural land with shelterbelts in Table 6.2.

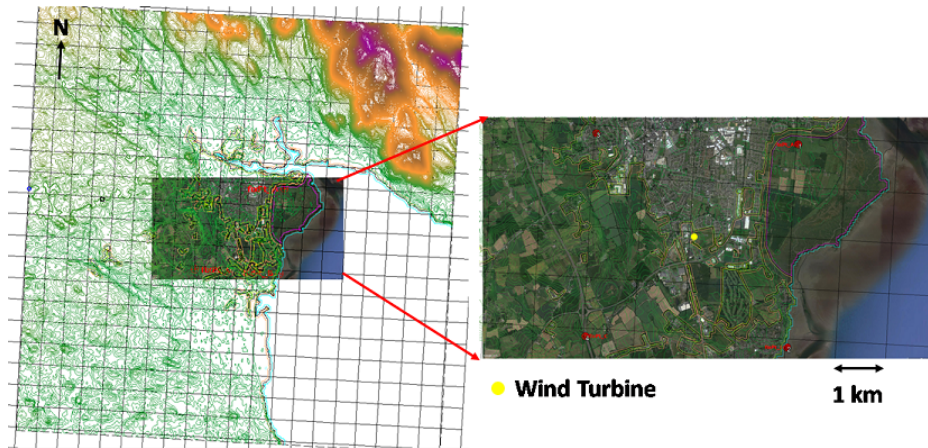


**Fig. 6.4.** Digital elevation map 20 km x 20 km region and local area map digitized for surface roughness.

Local site-specific coordinates are used for specifying obstacles relative to the wind turbine location to create a specific obstacle file in the tool. The position of an obstacle is specified by two angles (measured from North in a clockwise direction) and two distances. A maximum of 50 obstacles are allowed by the tool to modelled at given site, Fig. 6.5.



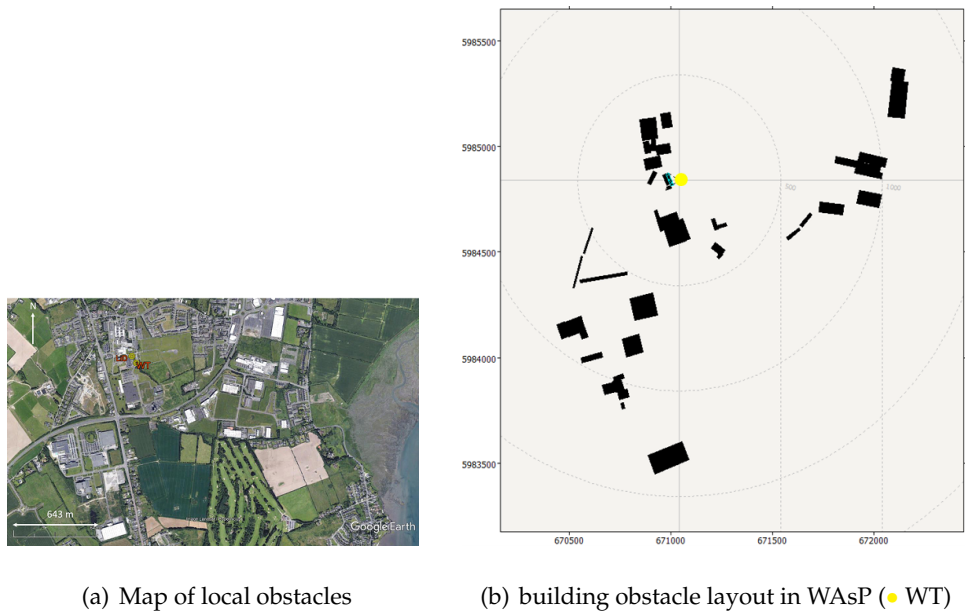


**Fig. 6.5.** Defining buildings as obstacles as in WAsP.

The second digitised map represents obstacles as roughness elements as shown in Fig. 6.6.

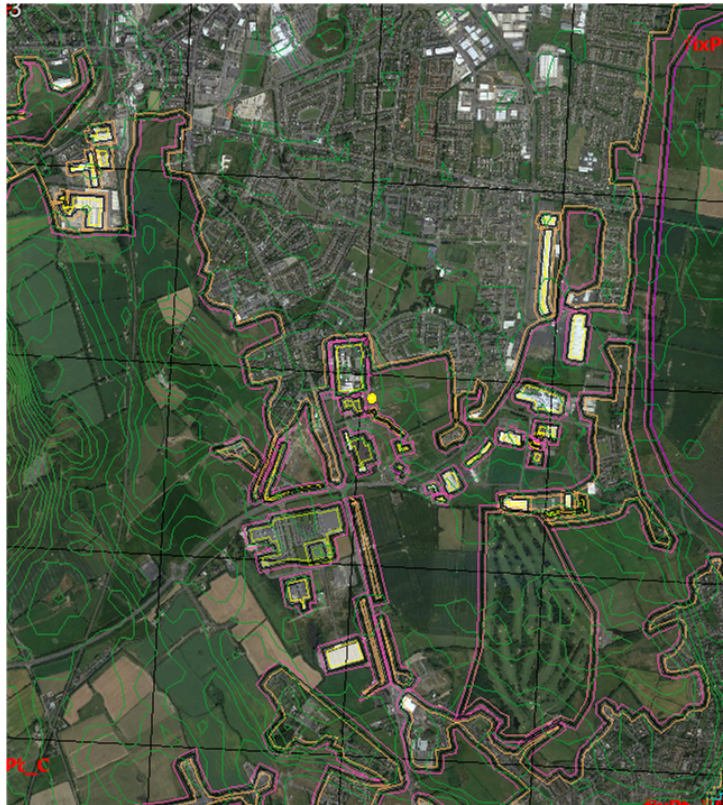


**Fig. 6.6.** Defining buildings as roughness elements in WAsP (● WT).

The WAsP climatology tool takes measured time series wind speed and direction data and creates wind climatology files that describe the statistical wind speed and direction information at the location of the wind measurements. In this study, onsite climatology files are generated at a number of heights, above and below the turbine hub-height, using one year of LiDAR measured time series wind speed and direction data at the different heights. These wind climates are extrapolated to the turbine hub using the various physical model described previously. The directional annual mean energy production of the wind turbine is obtained by providing WAsP with the power curve of the wind turbine. As the natural topography around the site is not complex, both the linear WAsP-IBZ and WAsP-CFD are used to assess their upscaling and downscaling ability to predict the wind turbine *EER*, in the presence of building obstacles, in comparison with the actual *EER* from the SCADA data. A computer processor consisting of an Intel®Core<sup>TM</sup> i7-8650U CPU @ 1.90GHz, 2112 Mhz, 4 Core(s), 8 Logical Processor(s) took less than 15 seconds to a simulation for a single height over all the 16 directional sectors.

#### 6.2.4 CFD flow model approaches

Numerical CFD models, commonly used in the wind industry, are based on the RANS standard  $k - \epsilon$  model model, as was outlined in Chapter 3. The key equations for conservation of mass and momentum respectively are summarised in Eqs. (6.4) and (6.5).

$$\frac{\partial U_i}{\partial x_i} = 0 \quad (6.4)$$

$$U_i \frac{\partial U_i}{\partial x_i} = -\frac{1}{\rho} \frac{\partial P}{\partial x_i} + \frac{\partial}{\partial x_j} \left( v \left( \frac{\partial U_i}{\partial x_j} + \frac{\partial U_j}{\partial x_i} \right) - \overline{u'_i u'_j} \right) \quad (6.5)$$

Where:

$U_i$  - time averaged mean wind speed (m/s)

$P$  - mean pressure (N/m<sup>2</sup>)

$\rho$  - air density (kg/m<sup>3</sup>)

$v$  - kinematic viscosity (m<sup>2</sup>/s)

$u'_i u'_j$  - Reynolds stresses (m<sup>2</sup>/s<sup>2</sup>)



Closure of the momentum equation is achieved using the Boussinesq linear isotropic eddy-viscosity hypothesis, Eq. (6.6).

$$\overline{u'_i u'_j} = -v_T \left( \frac{\partial U_i}{\partial x_j} + \frac{\partial U_j}{\partial x_i} \right) + \frac{2}{3} k \delta_{i,j} \quad (6.6)$$

Where:

$k$  = turbulence kinetic energy ( $\text{m}^2/\text{s}^2$ )

$\delta_{i,j}$  = Kronecker Delta function

$v_T$  = kinematic eddy viscosity ( $\text{m}^2/\text{s}$ )

The standard  $k - \varepsilon$  model uses two model transport equations that describes turbulence kinetic energy production  $k$ , Eq. (6.7), and turbulence dissipation rate  $\varepsilon$  Eq. (6.8).

$$\frac{\partial}{\partial x_i} (U_i k) = \frac{\partial}{\partial x_i} \left( \frac{v_T}{\sigma_k} \frac{\partial k}{\partial x_i} \right) + P_k - \varepsilon \quad (6.7)$$

$$\frac{\partial}{\partial x_i} (U_i \varepsilon) = \frac{\partial}{\partial x_i} \left( \frac{v_T}{\sigma_\varepsilon} \frac{\partial \varepsilon}{\partial x_i} \right) + c_{\varepsilon 1} \frac{\varepsilon}{k} P_k - c_{\varepsilon 2} \frac{\varepsilon^2}{k} \quad (6.8)$$

Where:

$c_{\varepsilon 1}, c_{\varepsilon 2}$  — are constants

$\sigma_k, \sigma_\varepsilon$  - Prandtl number that connect the diffusivities of  $k$  and  $\varepsilon$  to the eddy viscosity

$P_k$ , the production of  $k$ , which is the product of the kinematic eddy viscosity and the modulus mean rate of strain tensor, Eq. (6.9).

$$P_k = v_T \left( \frac{\partial U_i}{\partial x_j} + \frac{\partial U_j}{\partial x_i} \right) \frac{\partial U_i}{\partial x_j} \quad (6.9)$$

The relationship between production of  $k$  and the kinematic eddy viscosity is given by Eq. (6.10).

$$v_T = c_\mu \frac{k^2}{\varepsilon} \quad (6.10)$$

Where:  $c_\mu$  - constant

The coupled algebraic equations are iteratively solved for each time step by an algorithm or solver until dimensionless residuals, monitor points and domain imbalances satisfy specified criteria, i.e., convergence is achieved. The process is continued until a steady state is reached.

### 6.2.5 WAsP CFD setup

The digital elevation map as in the linear mode case is used. However, all building obstacles are represented as roughness elements. Low-rise the low-rise building are a roughness value of 1.0 m, consistent with industrial zones. The single tall 47 m building is given a value of 3.0 m, consistent with high-rise urban zones (Standen and Wilson, 2015). WAsP CFD uses the EllipSys3D code as its core solver, which is multi-block finite volume discretisation of the incompressible RANS equations (Cavar et al., 2016). Convective terms are discretised using the third order quadratic upstream interpolation for convective kinematics (QUICK) scheme (Leonard, 1979). A zooming 3D polar grid (or mesh) with a 15 km radius and 36 directional sectors calculates velocity perturbations and turnings at all grid points. The grid is sized to be computationally independent and its resolution is highest close to the centre of the site of interest, where the highest numerical accuracy is required, and gets progressively lower towards the edge of the model domain. The vertical computation domain extends to 14 km, approximating the top of the ABL. Fig. 6.7 shows terrain height contours of the inner 8 km x 8 km of the domain. Results are given for a 2 km by 2 km central region, denoted by the white square, and at heights from 5 m to 300 m a.g.l. The details computational grid are given in Table 6.3. Convergence is achieved when all residual values are below 0.00005. The number of iterations over the 36 directional sectors required for convergence ranged from 1504 to 1694 per sector. The WAsP CFD calculations are computed on a high-performance computer cluster “Cerebrum” operated by EMD international A/S. The processing time in this case took 31 CPU hours, but were completed in 15 minutes

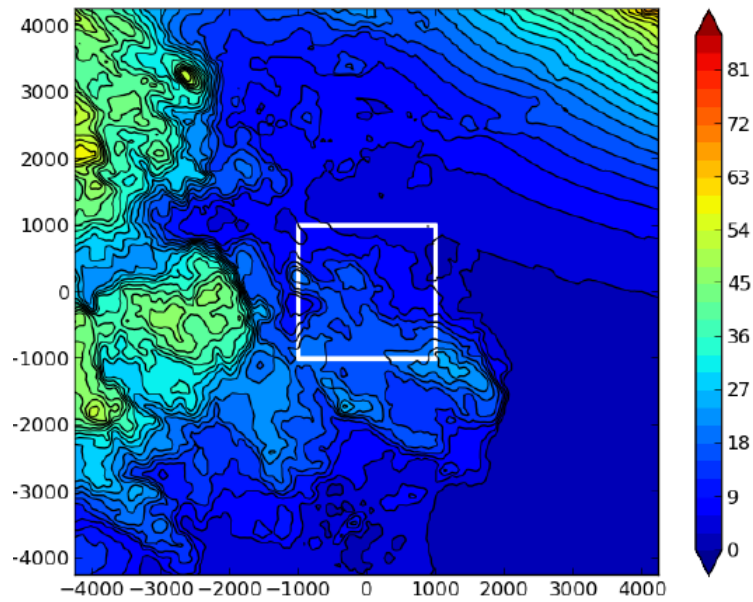


**Fig. 6.7.** 8 km x 8 km digital elevation map showing inner 2 km x 2 km WAsP CFD tile.

**Table. 6.3.** WAsP-CFD Grid Setup – Obstacles as roughness elements

Mesh details		CFD parameters	
No. grid points	7 million	$c_\mu$	0.052
Domain height (m)	14000	$\sigma_k$	1.0
Domain diameter (m)	34000	$\sigma_\epsilon$	1.3
Mean horizontal resolution (m)	20.7	$c_{\epsilon 1}$	1.38
Mean vertical resolution (m)	5	$c_{\epsilon 2}$	1.92
		$\kappa$	0.4

### 6.2.6 WindSim model setup

WindSim version 10 is used. WindSim is a CFD based wind resource assessment tool that solves the RANS equations using the finite volume method with the PHOENICS CFD model as its core solver, (Dhunny, Lollchund, and Rughooputh, 2016). Like WAsP, WindSim also used a modular approach to wind turbine micro-siting, Fig. 6.8. The modules include terrain description, wind field computation, climatology data, wind turbine description and placement, site wind resource and energy prediction.

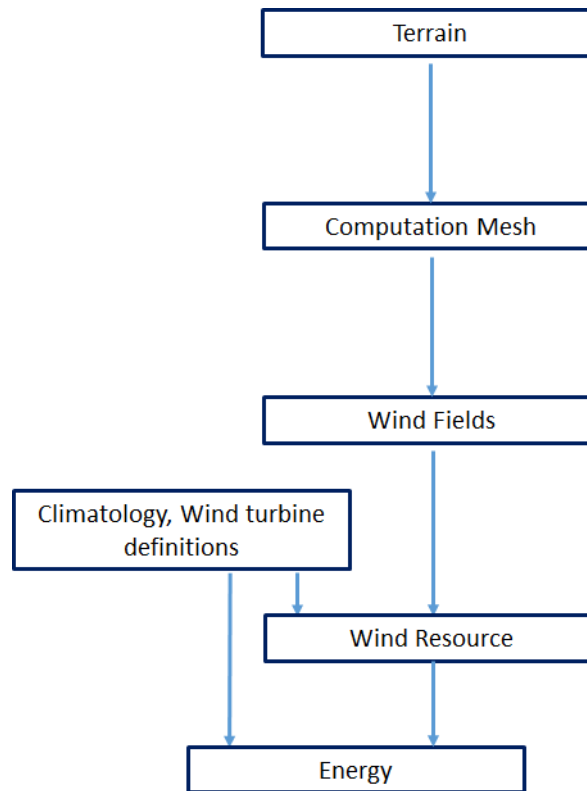


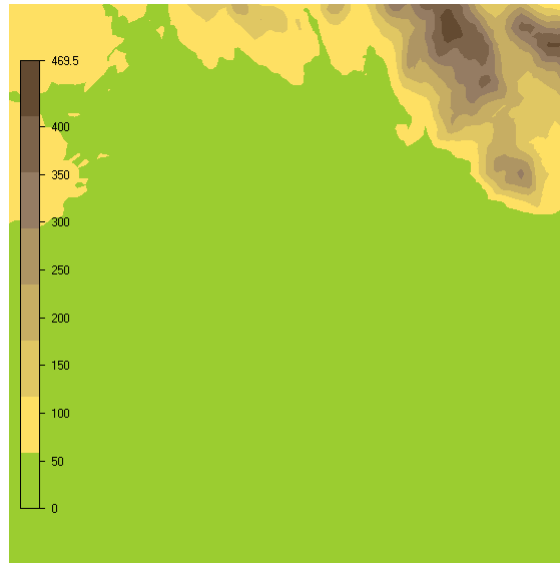
**Fig. 6.8.** Overview of the WindSim tool modular approach to wind turbine micrositing.

The digitised DEMs generated in the WASP map editor, Fig. 6.4, that contain terrain elevation and surface roughness data are used. DEMs in WindSim are in .gws (geo-workspace) format. Buildings can be represented as roughness elements or as volume blocking elements in the computation grid. Both approaches are implemented in this study. Running the terrain module creates a 3D rectangular (Cartesian) grid that can be refined automatically or manually to specific regions of interest. The computation grid is in .bws (blind-write-subcode) format. The user can specify the maximum number of cells as a constraint and using this, the tool automatically creates a grid structure and resolution, depending on height and roughness information from the digitised DEM. In the vertical direction, the grid typically extends to the top of the ABL or to a sufficient height so that elevated terrain does not occupy more than 10% of the vertical cross sectional area of the computational domain. The number of grid nodes are denser closer to the ground. The flow conditions at the domain boundaries are assumed to be fully developed, taking into account the boundary surface roughness conditions. The flow equations using a multi-block formulation and can handle highly non-orthogonal grids, (Semin,

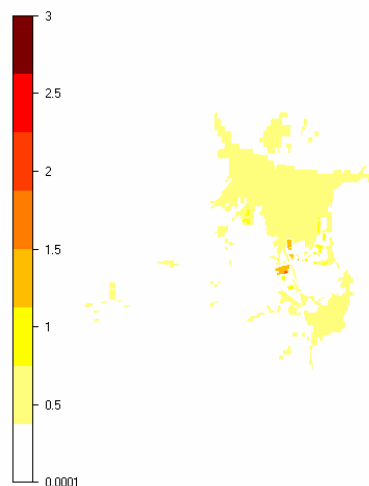
Spalding, and Zhubrin, 1996). A refinement area can be specified in an area of interest that allows finer grid resolution through a denser distribution of grid nodes e.g., in the surrounds of the wind turbine site. By default, the centre of refinement area is placed at the centre of the computational domain. The cell distribution is uniform within the refinement area and then increases in size towards the borders of the computation domain. Alternatively, a user constructed refinement area can be created. This allows the introduction of solid blocking elements, such as buildings, in the computation grid as opposed to representing them as roughness elements. In this case, a domain size of 20 km x 20 km is considered here, as in the WAsP case Fig. 6.9. A DEM that includes buildings as roughness elements and a separate DEM that does not are used. In the later case, the generated grid is refined to include the buildings as mesh blocking elements.

The wind flow variables are generated by solving RANS equations using the standard  $k - \epsilon$  turbulence model applied to the computational grid. The RANS equations are discretised and integrated with a finite-volume method. The flow variables that are solved are pressure, velocity components, TKE and turbulence dissipation rate. The boundary at the top of the computational grid (i.e., representing the top of boundary layer) is set to 500 m with a velocity of 10 m/s and fixed pressure. The initial conditions are used to make an initial guess of the wind field variables. The flow variables are calculated using an iterative procedure until a converged solution is reached. Convergence monitoring is based on spot-checking one of the variables in the iterative procedure to the point where the value becomes stable within a specified tolerance or residual value. Wind speed is the monitored variable in this case and has residual value set at 0.005 m/s. In order to speed up data production of the wind field, the 3-D wind speed and turbulence flow variables are stored from the ground and up to a user specified height of interest. In this case 300 m is chosen as maximum height of interest. Wind resource measurements and wind turbine descriptions are specified in the objects module. The wind resource is described by the same wind climatology files generated in the WAsP analysis from the LiDAR data. The wind climatology for each of the six LiDAR measurement heights are used. The wind turbine is describe by location, power curve, thrust curve, hub-height and rotor diameter. The wind fields computed in the wind fields module database are coupled with the wind climatology information to estimate wind resource maps at

the height and locations of interest, i.e., wind turbine hub-height and location. The gross energy production is the energy production of a wind turbine or wind farm calculated by predicted free stream wind speed distribution at hub height of a turbine location and the wind turbine power curve. Similarly, as in the WAsP analysis, the predictions of the wind turbine *EER* from upscaling or downscaling from the various LiDAR measurement are compared with the actual *EER*.



(a) digital elevation map 20 km x 20 km region

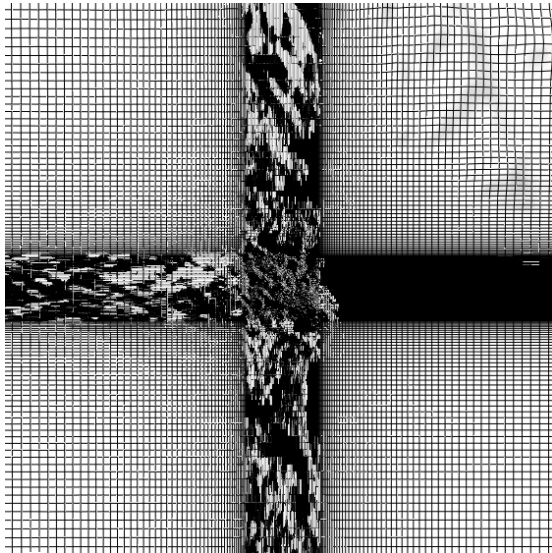


(b) surface roughness map

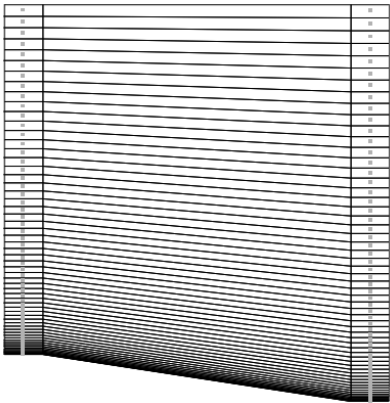
---

**Fig. 6.9.** WindSim digital elevation and surface roughness maps.

An overview schematic of the computational grid, Fig. 6.10, shows the central re-fined horizontal area and vertical distributions with the numerical details given in Table 6.4. The refined horizontal area contains the region of interest and gradually stretches to the outer limits of the grid independent computational domain. In the vertical direction, the grid is refined near the ground and gradually stretches with height to the top of the computational domain. The set height of the computational domain of 3500 m results from a computational requirement that the fraction of open area between the ground and the upper boundary should be larger than 0.95 to avoid flow blocking effects by the terrain. In this case, part of the hills to the northeast that have elevations up to  $\sim 470$  m are in the computational domain. The vertical grid shown in Fig. 6.10(b) displays the distribution of the nodes in the vertical direction, relative to the ground, at the position with maximum elevation on the left to minimum elevation on the right. Simulations are executed for 16 directional sectors and take 85 to 91 iterations per sector to achieve convergence in this study. A computer processor consisting of an Intel®Core™ i7-8650U CPU @ 1.90GHz, 2112 Mhz, 4 Core(s), 8 Logical Processor(s) took approximately 2 hours to carry out the CFD calculations over all 16 directional sectors.



(a) mesh horizontal distribution



(b) mesh vertical distribution (shown from highest to lowest elevation)

**Fig. 6.10.** WindSim CFD grid set up for buildings as roughness elements.

**Table. 6.4.** WindSim Grid Setup – Obstacles as roughness elements

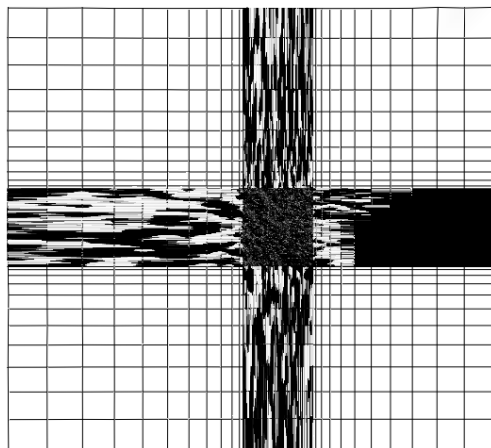
Mesh details		CFD parameters	
No. grid points	5 million	$c_\mu$	0.09
Domain height (m)	3500	$\sigma_k$	1.0
Domain horizontal (km)	20 x 20	$\sigma_\epsilon$	1.314
Refinement area $x - y$ (m)	2584 x 2315		
Horizontal grids spacing $x$ (m)	13.0 - 337.8	$c_{\epsilon 1}$	1.38
Horizontal grids spacing $y$ (m)	13.0 - 347.6		
Vertical grid spacing (m) (First 30 nodes of 60)	2.1 - 64	$c_{\epsilon 2}$	1.92
		$\kappa$	0.4

In the case of buildings represented as blocking elements in the computational grid, the UTM co-ordinates of the building corners and heights of the buildings determine how the grid is refined in the central area. The grid resolution is higher than in the previous case due to the proximity of some buildings to each other and to capture the different building heights. To help reduce the computation requirement, the overall horizontal computational domain is  $\sim 12 \text{ km} \times 10 \text{ km}$  with a refined area of interest of approximately  $2 \text{ km} \times 2 \text{ km}$ , Fig. 6.11. This means the hills to the northeast are less of a feature, resulting in the height of the computational domain being reduced, Fig. 6.12(b). This reduction can be justified in that the northeast is not a prevailing wind direction as discussed in previous chapters. The details of the computational grid are given in Table 6.5. A limitation of this approach, with this tool, is that obstacles can only be defined as orthogonal blocking elements. Simulations are executed for 16 directional sectors that take between 159 to 795 iterations to achieve convergence. A computer processor consisting of an Intel®Core™ i7-8650U CPU @ 1.90GHz, 2112 Mhz, 4 Core(s), 8 Logical Processor(s) took approximately 14 days to complete the CFD calculations over all 16 directional sectors. Although this would be an unrealistic modelling time frame for commercial projects, it was done here from a research perspective and limitations in financial budget available for high speed computing access time.

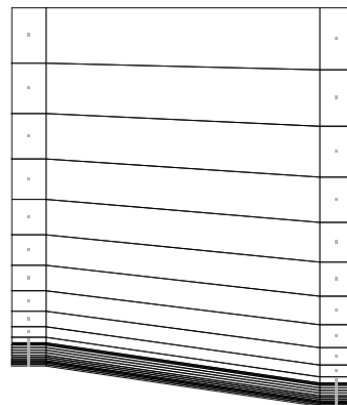




**Fig. 6.11.** Digital elevation map  $\sim 12 \text{ km} \times 10 \text{ km}$  with buildings as mesh blocking elements over  $\sim 2 \text{ km} \times 2 \text{ km}$



(a) mesh horizontal distribution



(b) mesh vertical distribution (shown from highest to lowest elevation)

**Fig. 6.12.** WindSim CFD grid set up for buildings as mesh blocking elements.

**Table. 6.5.** WindSim Grid Setup – Obstacles as mesh blocking elements

Mesh details		CFD parameters	
No. grid points	13.5 million	$c_\mu$	0.09
Domain height (m)	814	$\sigma_k$	1.0
Domain horizontal (km)	12 x 11	$\sigma_\epsilon$	1.314
Refinement area $x - y$ (m)	1683 x 1709		
Horizontal grids spacing $x$ (m)	2.5 – 959.5	$c_{\epsilon 1}$	1.38
Horizontal grids spacing $y$ (m)	2.5 – 747.9		
Vertical grid spacing (m) (24 nodes)	1.8 – 82.4	$c_{\epsilon 2}$	1.92
		$\kappa$	0.4

### 6.2.7 Wind assessment and EER

The measured wind turbine directional energy for the 1-period is presented as a 16 directional sector *EER*, derived from the from wind turbine SCADA data. Wind roses and directional *WPD* at multiple heights at the wind turbine site are determined from LiDAR measurements at location (LiD), Fig. 6.1. The *WPD* at the highest two heights of 120 m and 200 m are used to assess the wind resource, assumed to be above the influence of the local building obstacles within a 2 km radius. This distance stretches up to or beyond the rural to urban interface in the directions of most interest. These and compared with the *WPD* at lower heights down to 10 m to examine reductions and directional changes in *WPD* that may be introduced by the local building obstacle. Log law profiles are compared to LiDAR measured wind shear profiles in each of the 16 directional sectors. The surface roughness,  $z_0$ , values are determined from wind speed measurements.  $z_0$  determined from measurement at 120 m and 200 m is used to to downscale the wind shear profile to 10 m, while  $z_0$  determined from measurement at 20 m and 30 m is used to upscale to 200 m. Both the scaled and measured wind shear profiles are compared in selected directions where the biggest discrepancies between the model predicted *EERs* with the measured wind turbine *EER* occur.

## 6.3 Results

LiDAR measured wind roses, in 16 sectors, at six heights from 10 m to 200 m, for the 1-year period are shown in Fig. 6.13. Wind roses at 200 m and 120 m show the dominant wind directions to the southwest and southeast. From Chapter 5, the high distribution of south easterly winds can be attributed to the proximity of the site to the east coast, in particular, mesoscale effects of Dundalk Bay. While the WSW sector at  $247.5^\circ$  is a dominant wind sector at all heights, there are some notable changes in the wind directional distribution below 86 m. In particular, relatively higher reductions in wind speed occur in the  $157.5^\circ$ ,  $202.5^\circ$  and  $225^\circ$  sectors. Lower wind speeds in sector  $180^\circ$  occur at all heights, which confirms that this is a mesoscale transition region from the southwest prevailing winds to the coastal winds from the southeast. From an energy perspective, the directional *WPD* comparison at each level illustrate these directional changes in available energy at each level, Fig. 6.14. The *WPD* in the  $157.5^\circ$  sector reduces rapidly, with decreasing height, from 120 m to the lower levels and to some extent in the  $202.5^\circ$  and  $225^\circ$  sectors. These reductions coincide with the tall 47 m building to the southeast and the low-rise broad buildings to the southwest of the site respectively, outlined in Fig. 6.1. At heights of 20 m and 10 m the *WPD* directional distributions are notably altered, indicating significant influence from nearby buildings. The  $90^\circ$  sector contains high winds from a rare spring storm event, over 4 days that occurred in March 2018. This is reflected in high *WPD* values but lower times of occurrence in the wind roses for this sector. The north to northeast sectors are non-prevailing wind sectors and therefore are not considered in further detail. Therefore, buildings in sectors from the southeast through to the northwest of the turbine location are of most interest in this study.

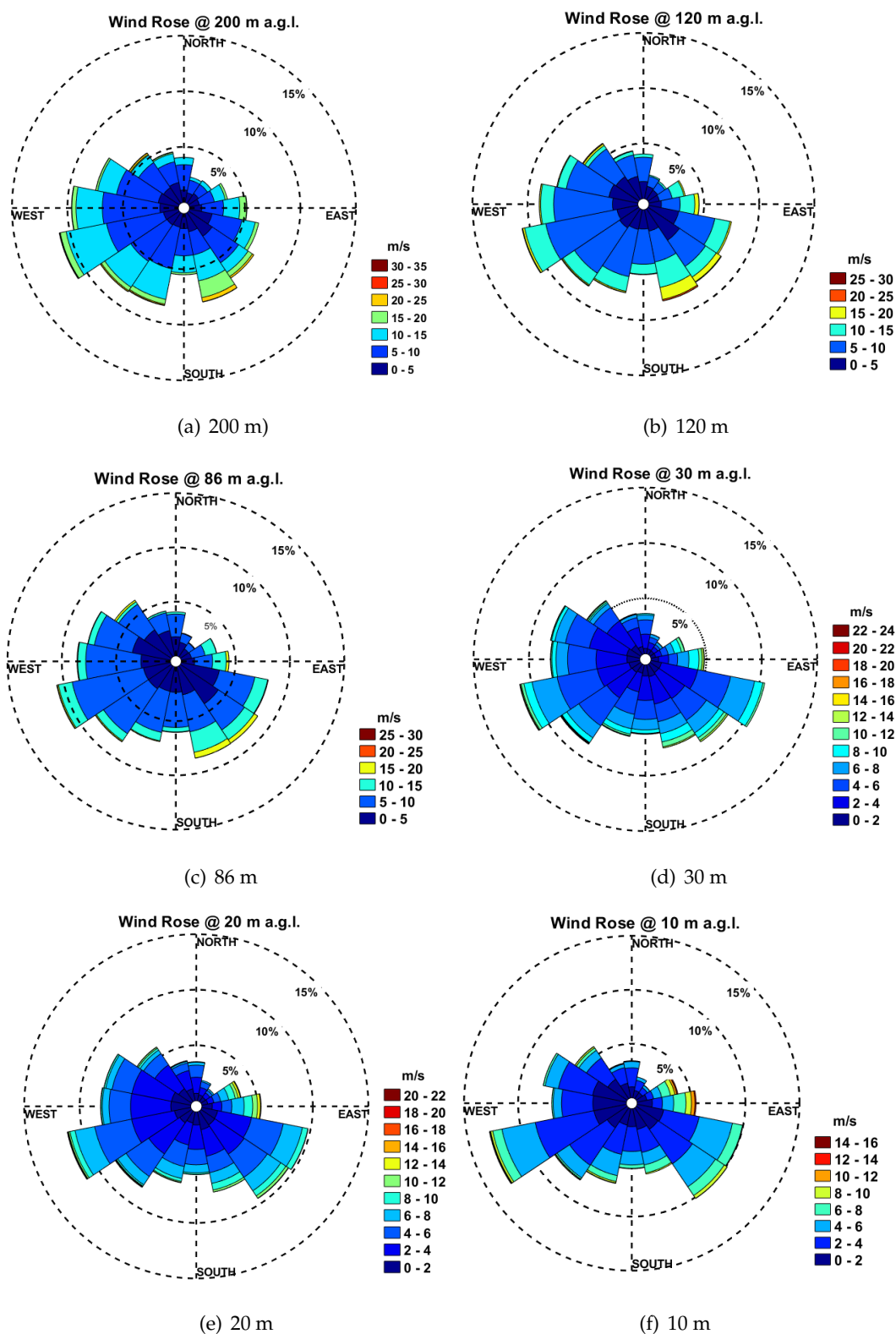


**Fig. 6.13.** Annual wind roses at multiple levels from LiDAR measurements.

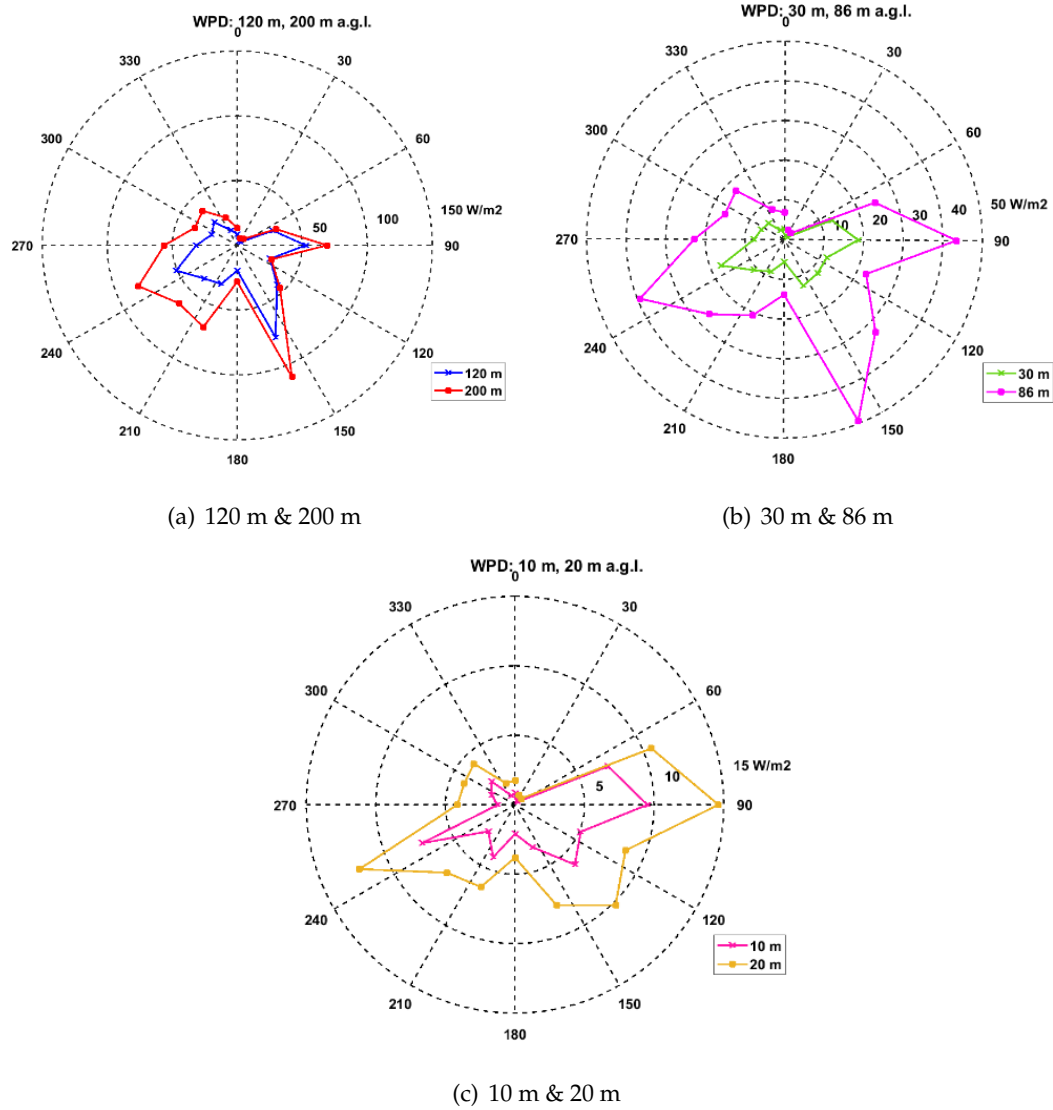


**Fig. 6.14.** Annual *WPD* at multiple levels from LiDAR measurements.

Table 6.6 shows the directional *WPD* values of the plots in Fig. 6.14 and also the percentage of each value with respect to its correspond value at 200 m. The highlighted sectors show the higher energy sectors at 200 m that also have the higher energy reductions at the lower heights, corresponding to buildings in the south-easterly to westerly sectors.

**Table. 6.6.** Directional WPD ( $W/m^2$ ) and (%) values w.r.t. to 200 m

Sector ( $^{\circ}$ )	10 m	20 m	30 m	86 m	120 m	200 m
0	1.02 (6.3%)	2.15 (13.3%)	3.25 (20.0%)	8.33 (51.3%)	10.41 (64.1%)	16.24
22.5	0.44 (6.5%)	0.93 (13.7%)	1.32 (19.4%)	3.24 (47.5%)	4.05 (59.4%)	6.82
45	0.36 (4.9%)	0.76 (10.3%)	1.07 (14.5%)	2.82 (38.2%)	4.26 (57.7%)	7.37
67.5	8.93 (22.6%)	13.09 (33.1%)	15.95 (40.4%)	30.43 (77.0%)	36.51 (92.4%)	39.52
90	11.73 (13.9%)	18.04 (21.4%)	22.98 (27.3%)	53.64 (63.7%)	64.74 (76.9%)	84.16
112.5	6.24 (18.2%)	10.50 (30.6%)	14.24 (41.4%)	27.50 (80.0%)	33.42 (97.3%)	34.36
135	7.46 (13.1%)	12.52 (22.0%)	14.62 (25.7%)	40.22 (70.6%)	53.37 (93.7%)	56.96
157.5	<b>4.07</b> <b>(3.0%)</b>	<b>9.63</b> <b>(7.1%)</b>	<b>15.46</b> <b>(11.4%)</b>	<b>60.74</b> <b>(44.9%)</b>	<b>94.53</b> <b>(69.8%)</b>	<b>135.37</b>
180	2.56 (7.5%)	4.66 (13.7%)	6.90 (20.3%)	16.96 (49.8%)	23.65 (69.4%)	34.06
202.5	<b>5.03</b> <b>(6.1%)</b>	<b>7.89</b> <b>(9.5%)</b>	<b>10.77</b> <b>(13.0%)</b>	<b>25.40</b> <b>(30.6%)</b>	<b>39.39</b> <b>(47.5%)</b>	<b>82.88</b>
225	<b>3.33</b> <b>(4.4%)</b>	<b>8.51</b> <b>(11.3%)</b>	<b>13.45</b> <b>(17.9%)</b>	<b>32.79</b> <b>(43.5%)</b>	<b>43.99</b> <b>(58.5%)</b>	<b>75.17</b>
247.5	8.89 (8.9%)	14.91 (14.9%)	21.35 (21.4%)	48.50 (48.5%)	62.47 (62.5%)	99.91
270	<b>1.51</b> <b>(2.2%)</b>	<b>5.06</b> <b>(7.5%)</b>	<b>9.42</b> <b>(14.0%)</b>	<b>27.91</b> <b>(41.4%)</b>	<b>38.53</b> <b>(57.1%)</b>	<b>67.49</b>
292.5	2.20 (5.2%)	4.80 (11.4%)	7.76 (18.4%)	19.90 (47.2%)	25.89 (61.4%)	42.16
315	<b>2.90</b> <b>(6.4%)</b>	<b>5.08</b> <b>(11.2%)</b>	<b>6.97</b> <b>(15.3%)</b>	<b>21.28</b> <b>(46.8%)</b>	<b>30.71</b> <b>(67.6%)</b>	<b>45.44</b>
337.5	0.88 (3.1%)	2.01 (7.1%)	3.19 (11.3%)	10.00 (35.4%)	15.23 (53.9%)	28.27

### 6.3.1 Wind turbine measured energy and model predictions

The background surface roughness at the met mast location (M) in the rural area is determined from log law and gives a value of 0.2 m. A fitted log law plot is shown in Fig. 6.15. This is the background surface roughness value used in the models.

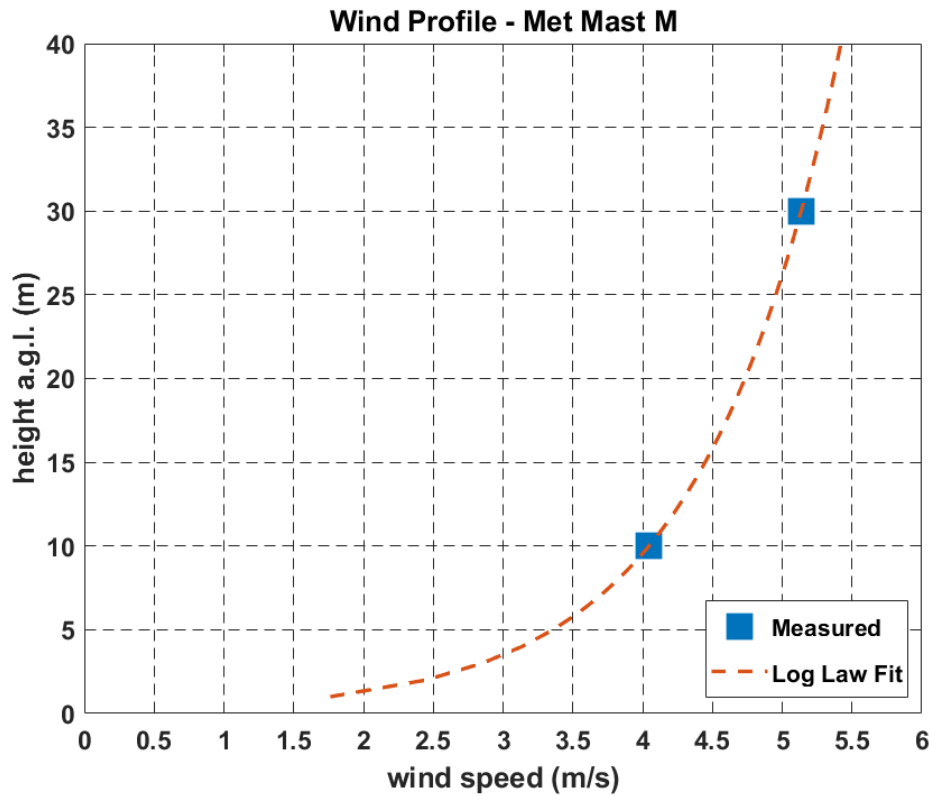


Fig. 6.15. Log law fit to two measurements of 10 m and 30 m at met mast located at M.

Table 6.7 compares the measured mean hub-height wind speed with the predicted hub-height mean wind speed by each of the four modelling approaches considered that are each driven by LiDAR data from other heights. WAsP-CFD, treating buildings as roughness elements, gives the best prediction over a wider range of heights, particularly when upscaling from below the 60 m hub height. The linear WAsP-IBZ model gives best result when downscaling from 86 m. WindSim gives best results, treating buildings as blocking mesh elements when upscaling from 20 m and 30 m below hub height. Upscaling from 10 m in the linear WAsP-IBZ case, gives a significant over prediction of hub-height wind speed. This may be explained by the measurements at 10 m being influenced by complex recirculation in the wake of nearby buildings to the southwest, which are less than  $\sim 5$  obstacle heights away. In

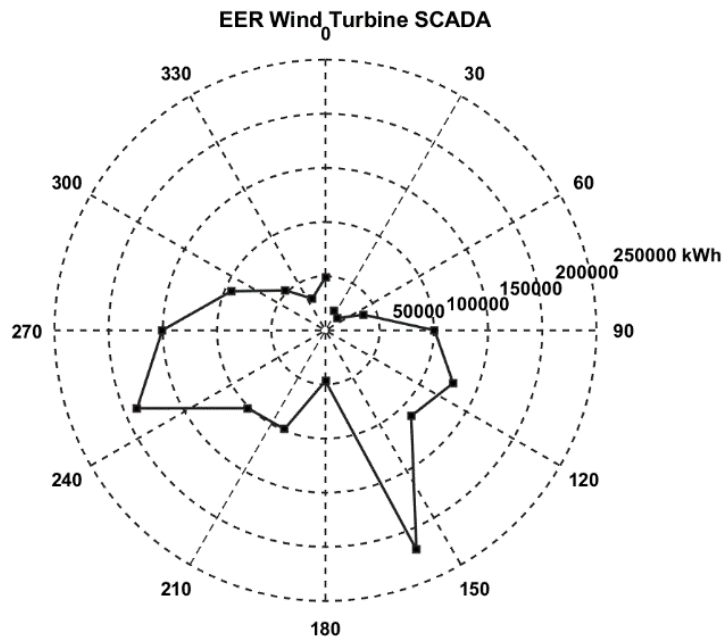
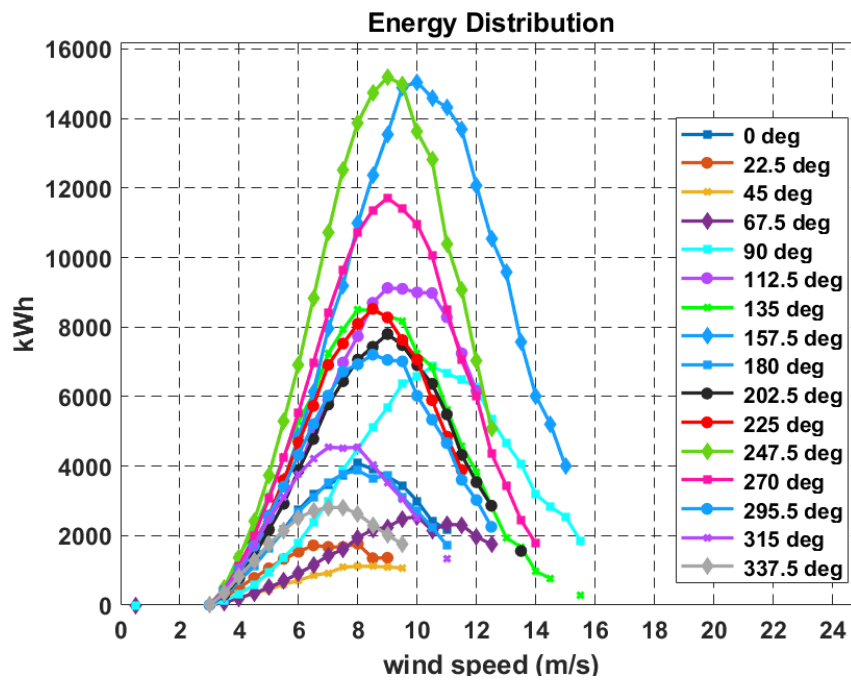
this case, over estimations of the wind speed deficit by the linear shelter model, as noted in the literature, may result in wind speed over estimates when scaled up to heights above the influence of the building.

**Table. 6.7.** Annual mean wind speed predictions and (%) differences to the measured hub height annual mean wind speed of 5.6 m/s

Scaling Height (m)	WAsP-IBZ (Obstacle Model)	WAsP-CFD RANS (Roughness)	WindSim-CFD RANS (Roughness)	WindSim-CFD RANS (Blocking mesh)
200	6.00 (7.1%)	6.03 (7.7%)	6.65 (18.8%)	6.96 (24.3%)
120	5.78 (3.2%)	5.86 (4.6%)	6.22 (11.1%)	6.38 (13.9%)
86	<b>5.68 (1.4%)</b>	<b>5.74 (2.5%)</b>	5.93 (5.9%)	6.00 (7.1%)
30	5.80 (3.6%)	<b>5.66 (1.1%)</b>	<b>5.46 (-2.5%)</b>	<b>5.51 (-1.6%)</b>
20	6.26 (11.8%)	<b>5.64 (0.7%)</b>	5.35 (-4.5%)	<b>5.57 (-0.5%)</b>
10	9.09 (62.3%)	<b>5.63 (0.5%)</b>	5.29 (-5.5%)	6.14 (9.6%)

As the electrical energy output is of most importance to wind turbine end-users, the total measured electrical energy output from the wind turbine for the 1-year period is 1447786 kWh. The *EER*, Fig. 6.16(a), shows that dominant directions are the SW and SE sectors, as expected. However, consecutive energy peaks are present in neighbouring sectors from  $90^\circ$  to  $270^\circ$ . Lower energy values occur in sectors at  $135^\circ$ ,  $180^\circ$  and  $202.5^\circ$  compared with higher energy values in sectors  $112.5^\circ$ ,  $157.5^\circ$  and  $247.5^\circ$ . Comparing the energy distribution with wind speed, Fig. 6.16(b), relatively higher proportions of energy occur at higher wind speeds in the east and south easterly sectors, due to higher wind speeds from the coast. In the SW sectors, it is interesting to note that more energy in the  $202.5^\circ$  sector occurs at higher wind speeds compared to sector  $225^\circ$ . The  $202.5^\circ$  sector is occupied by more low-rise obstacles compared to sector  $225^\circ$ . This suggests that the low-rise building obstacles with heights of 9 m to 25 m, may have more of an influence on lower wind speeds, below  $\sim 9$  m/s, at the turbine hub-height.



(a) Wind turbine *EER*

(b) Directional energy distribution with wind speed

Fig. 6.16. *EER* and directional energy distribution with wind speed.

The predicted hub-height *EERs* for each of the model approaches from six different heights, initialised with 1 year of LiDAR measurements in each case, are compared in Table 6.8. The percentage difference in the predictions with the actual measured output value of 1447786 kWh are also shown.

**Table. 6.8.** *AEP* predictions and (%) differences compared with wind turbine *EER*

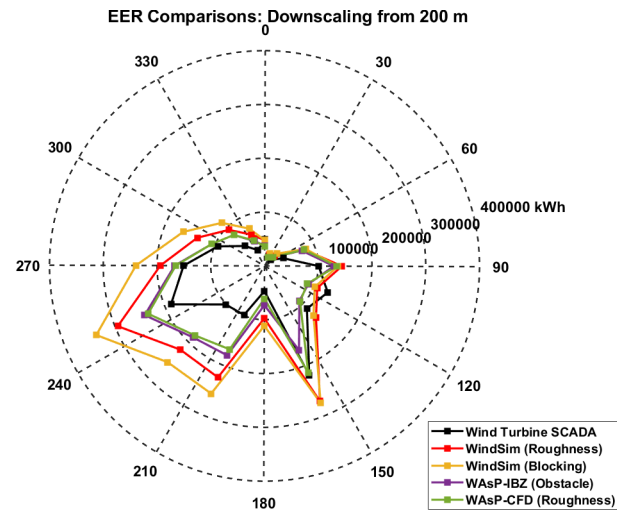
Scaling Height (m)	WAsP-IBZ (Obstacle Model)	WAsP-CFD RANS (Roughness)	WindSim- CFD RANS (Roughness)	WindSim- CFD RANS (Blocking mesh)
200	171800 (+18.7%)	1733000 (+19.7%)	2159500 (+49.2%)	2382000 (+64.5%)
120	159300 (+10.0%)	1636000 (+13.0%)	1855700 (+28.2%)	1963500 (+35.6%)
86	155000 (+7.1%)	1588000 (+9.7%)	1666700 (+15.1%)	1719800 (+18.7%)
30	156800 (+8.3%)	<b>1482000</b> <b>(+2.4%)</b>	<b>1395100</b> <b>(-3.6%)</b>	<b>1427000</b> <b>(-1.4%)</b>
20	186100 (+28.5%)	<b>1454000</b> <b>(+0.4%)</b>	1358100 (-6.2%)	<b>1489900</b> <b>(+2.9%)</b>
10	2904000 (+201.0%)	<b>1442000</b> <b>(-0.4%)</b>	1354000 (-6.5%)	1871200 (+29.2%)

Comparing the results of Table 6.7 and Table 6.8 show how discrepancies in the hub-height mean annual wind speed predictions between the models and the measurements of greater than  $\sim 2\%$  can result in large *AEP* discrepancies, which has a bigger impact on end-users. The linear obstacle model shows that it has a lower percentage difference in *EER* prediction, when downscaling from above hub height, compared to the other three CFD approaches assessed in this study. This indicates that linear model performs better when scaling measured wind data from above the influence of buildings on the flow. On the contrary, the *EER* prediction for each of the CFD approaches scaled up from 20 m and 30 m give the best results when buildings are treated as roughness elements or as mesh blocking elements. The largest differences appear, in the case of upscaling, from 10 m for the linear obstacle model and the CFD blocking mesh, which may be explained by complex building wake effects at this height not being well captured in these cases. These results suggest that onsite measurements taken at approximately three times the height of the local building

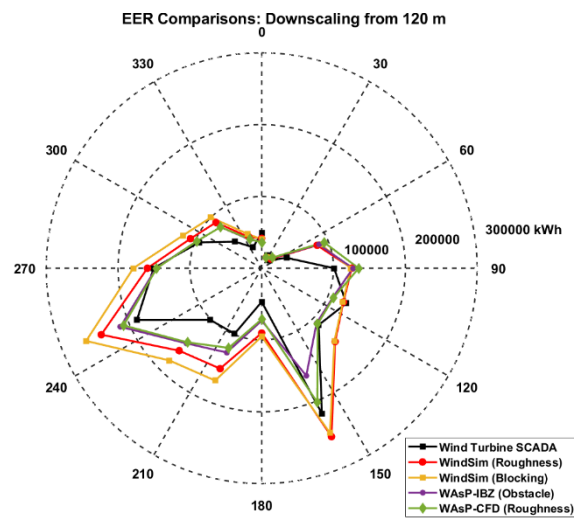
heights (7 m to 13 m) give better results consistently across all the CFD model approaches. Therefore, upscaling any measurements from heights similar to building heights or at heights well above the site, e.g., downscaling mesoscale wind atlas data, should be done with caution. It also highlights the need for well-designed on-site measurement campaigns, especially if met mast heights are a constraint. From a directional perspective, comparisons in the predicted *EERs* with the measured wind turbine *EER* show directional discrepancies, Figs. 6.17 and 6.18, The following observations are made:

- (a) In the prevailing southwest sectors of  $202.5^\circ$ ,  $225^\circ$  and  $247.5^\circ$ , the upscaling cases of 20 m and 30 m give the closest predictions. For the  $202.5^\circ$  and  $225^\circ$  sectors that contain low-rise buildings, the three CFD models perform well, but the linear WAsP-IBZ model performs the poorest. Upscaling from 10 m gives poor results, but WAsP-CFD gives the better result in this case. In the downscaling cases, the four models over predict the energy significantly in these sectors, though WAsP-CFD and linear WAsP-IBZ perform better than the WindSim models. Therefore, this suggests to get best results, measurements should be made 2 to 3 times the height of low rise broad building. These occur within  $\sim 1$  km from the rural to urban interface to turbine location in this sector.
- (b) In the northwest sectors the four model perform well downscaling from 86 m. WAsP-CFD and WAsP-IBZ perform best when downscaling from 120 m and 200 m. Both WindSim models over predict the most from 200 m. The four models, upscaling from 20 m and 30 m notably under predict energy at  $270^\circ$ , but perform well in the other northwest sectors, with WAsP-IBZ being slightly poorer. This indicates that some energy may be getting steered from the southwest to the more open westerly sectors that is not fully captured by the measurements at 30 m and below. The remaining northwest sectors are occupied by larger areas of suburban residential buildings with  $\sim 7$  m heights. Distances from the wind turbine location to the rural to urban interface are greater than 2 km in this case. This suggests that flow is fully adjusted to the local surface roughness conditions and better computed by the models.

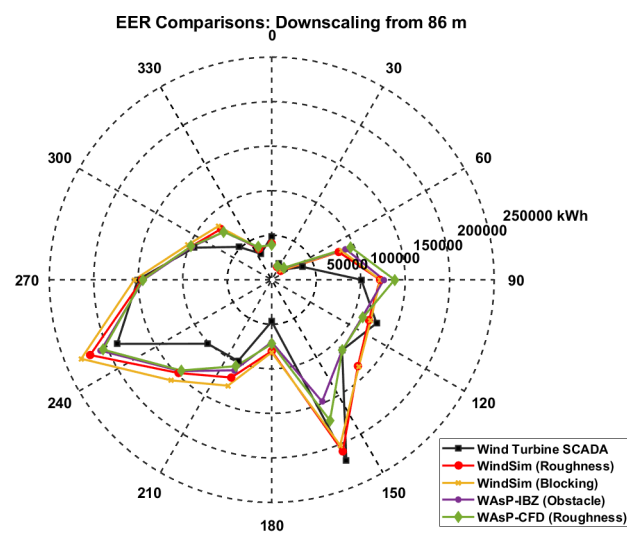
- (c) The northeast sectors are non-prevailing wind directions and are sheltered by hills  $\sim 7$  km to the northeast. However, there are energy over predictions by the models at  $67.5^\circ$  and  $90^\circ$ . Although these sectors have less obstacle influences, they contain winds speeds of the, previously mentioned, winter storm event of March 2018. During this period, the wind turbine was in shut down, i.e., no electrical energy was produced. Also, the effects of the land/sea interface in these directions can have an impact on atmospheric stability that alter wind shear profiles in a different way than obstacles. The northeast sectors are not considered in detail in this study.
- (d) In the southeast sectors, the significant energy sector at  $157.5^\circ$  is best predicted by the WAsP-CFD downscaling from 200 m and 120 m. The WindSim models perform best at  $157.5^\circ$  when downscaled from 86 m. In the upscaling cases, none of the four models well predict the energy in the  $157.5^\circ$  sector. This can be explained by the wake effect of 47 m high building that is  $\sim 330$  m from the turbine or 7 obstacle heights away and  $\sim 80\%$  of the turbine hub height. This can also explain why downscaling from more than twice the height of this obstacle gives better predictions.



(a) 200 m

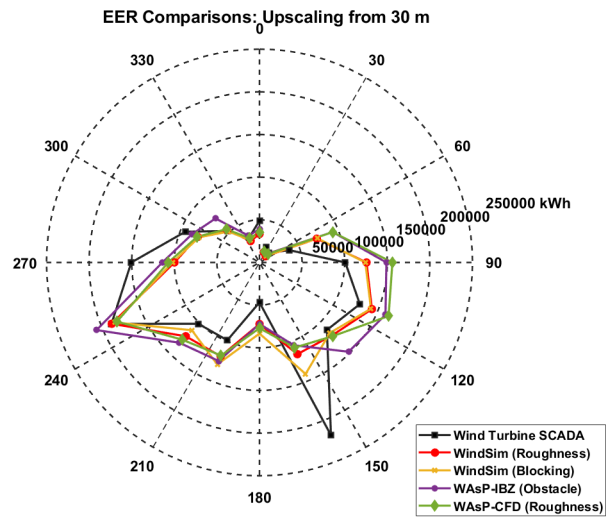


(b) 120 m

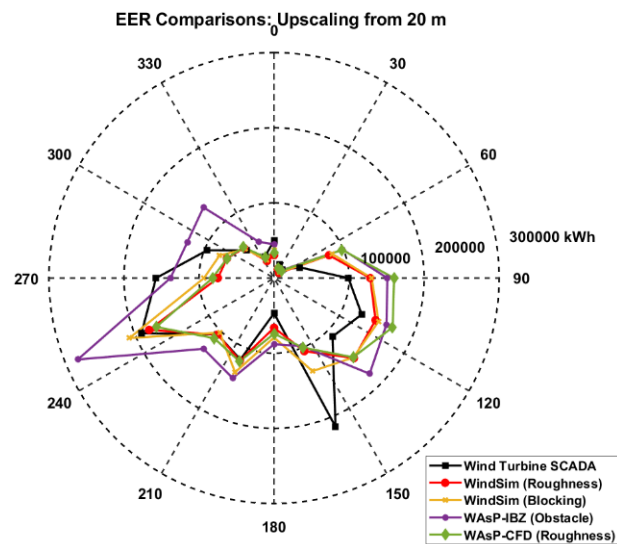


(c) 86 m

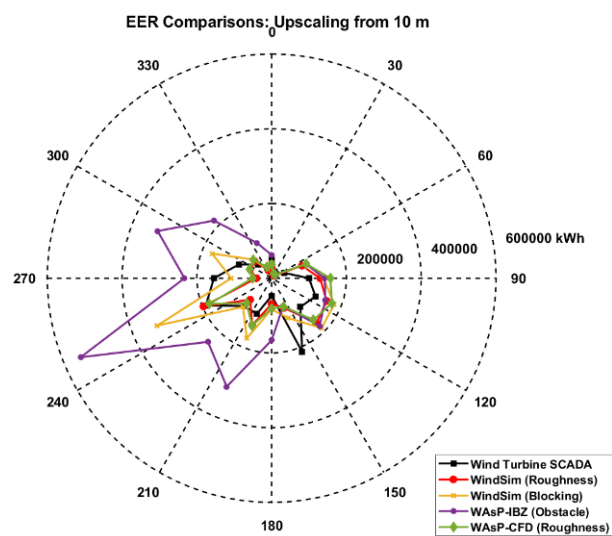
Fig. 6.17. Comparisons of model predicted *EERs* from multiple heights with the measured wind turbine *EER* (Downscaling).



(a) 30 m



(b) 20 m



(c) 10 m

Fig. 6.18. Comparisons of model predicted *EERs* from multiple heights with the measured wind turbine *EER* (Upscaling).

The four worst case directional predictions by the four models at the turbine hub height in Figs. 6.17 and 6.18 are given in Tables 6.9 and 6.10. They are shown primarily to occur in the directional sectors occupied by buildings. It shows that for the downscaling cases,  $225^\circ$  is the most common occurring direction with poorest prediction across the four models. This is followed by  $67.5^\circ$ ,  $247.5^\circ$  and  $202.5^\circ$ . The WindSim models over predicts the most in the SW sectors, coinciding with buildings to the southwest of the site. This suggests that in the southwest sectors the local RSL may be growing across the buildings from 500 m to 1 km away from the turbine location that is not fully captured in the downscaling processes. Downscaling from 86 m gives the better predictions, indicating a better capture of the RSL in the southwest sectors. For the upscaling cases,  $157.5^\circ$  has the highest under predictions across all models. The linear WAsP-IBZ performs poorest. This may be attributed to the wake effect of the tall 47 m building in this sector. This followed by  $67.5^\circ$ ,  $270^\circ$  and  $90^\circ$ . The under predictions at  $270^\circ$  energy may be due to energy steering into this more open sector, as explained previously. At  $67.5^\circ$  and  $90^\circ$ , atmospheric instability effects, not captured, may be introducing added discrepancies in the predictions.

**Table. 6.9.** Four worst case directional % discrepancies in predicted EERs at 60 m from each downscaling height

Scaling Height (m)	SCADA (kWh)	WAsP-IBZ (Obstacle Model) ( $\Delta\%$ )	WAsP-CFD RANS (Roughness) ( $\Delta\%$ )	WindSim-CFD RANS (Roughness) ( $\Delta\%$ )	WindSim-CFD RANS (Blocking mesh) ( $\Delta\%$ )
<b>200 m</b>					
67.5	36768	-	115	-	-
157.5	212791	-21	-	28	29
202.5	102687	75	64	119	150
225	105057	79	74	110	142
247.5	190646	26	23	55	77
<b>120 m</b>					
67.5	36768	134	156	127	139
90	99585	-	36	-	-
157.5	212791	-24	-	-	-
180	47277	-	50	-	-
202.5	117309	-	-	41	57
225	105057	41	39	55	73
247.5	190646	-	-	27	39
315	52119	55	-	-	-
<b>86 m</b>					
67.5	36768	145	161	122	131
90	99585	27	39	-	-
157.5	212791	-30	-20	-	-
180	47277	-	-	69	72
225	105057	38	37	41	52
247.5	190646	-	-	16	22



**Table. 6.10.** Four worst case directional% discrepancies in predicted EERs at 60 m from each upscaling height

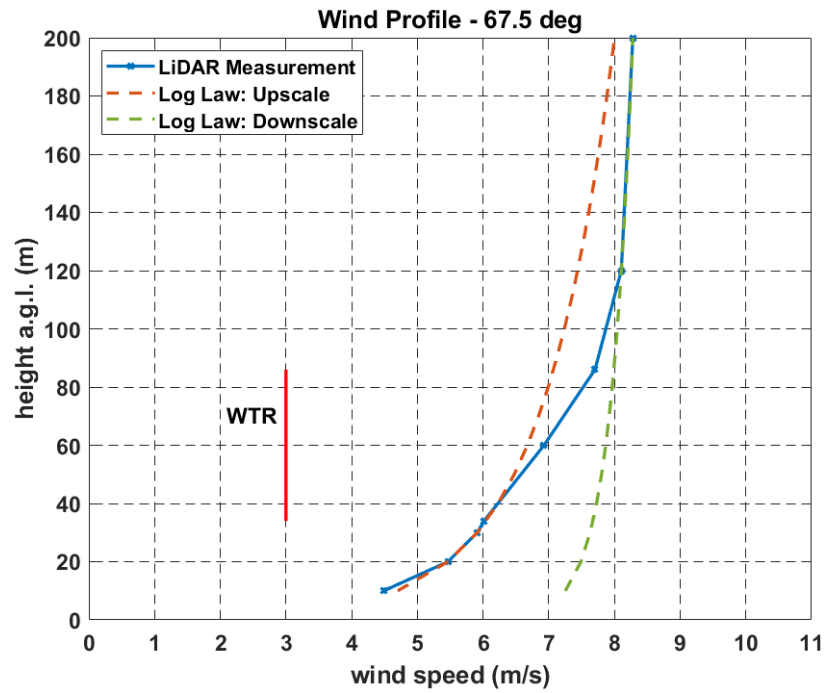
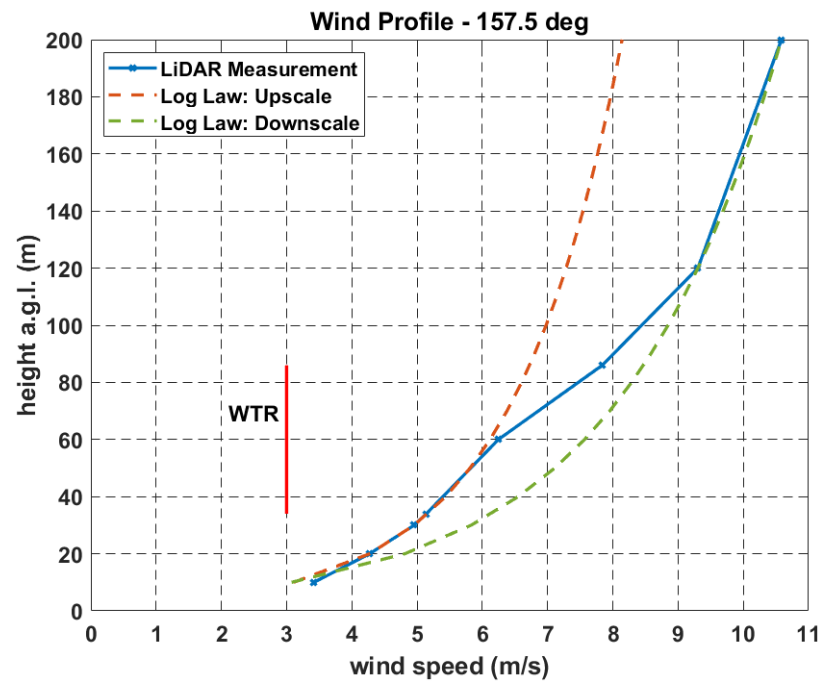
Scaling Height (m)	SCADA (kWh)	WAsP-IBZ (Obstacle Model) ( $\Delta\%$ )	WAsP-CFD RANS (Roughness) ( $\Delta\%$ )	WindSim- CFD RANS (Roughness) ( $\Delta\%$ )	WindSim- CFD RANS (Blocking mesh) ( $\Delta\%$ )
<b>30 m</b>					
67.5	36768	153	153	97	101
90	99585	50	57	27	-
157.5	212791	-51	-49	-46	-34
180	47277	-	-	-	76
270	154374	-26	-33	-31	-34
<b>20 m</b>					
67.5	36768	169	167	116	128
90	99585	-	61	-	-
135	108614	66	0	39	38
157.5	212791	-54	-53	-51	-37
247.5	190646	48	-	-	-
270	154374	-	-47	-52	-40
<b>10m</b>					
67.5	36768	-	172	138	-
90	99585	-	58	-	-
135	108614	-	-	56	74
157.5	212791	-62	-61	-60	-46
202.5	102687	206	-	-	137
247.5	190646	190	-	-	-
270	154374	-	-67	-74	-
292.5	95389	-	-	-	81
315	52119	318	-	-	-

### 6.3.2 Wind shear profiles

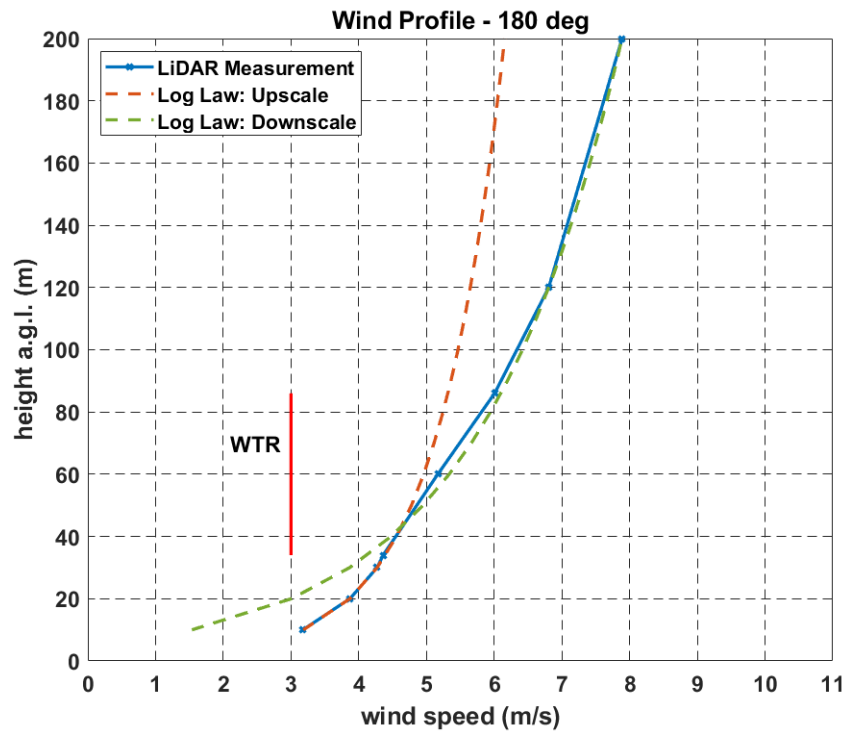
Log law profiles fitted to the LiDAR measured wind shear profiles for common occurring directions, in Tables 6.9 and 6.10, are shown in Figs. 6.19 to 6.22. The fitted wind shear profiles diverge from each other at different heights and by varying amounts depending on direction. These divergences suggest changes in the logarithmic flow regimes, which may be explained by variations in the RSL height. In the south and westerly directions, greater divergence occurs in sectors  $180^\circ$ ,  $202.5^\circ$ ,  $225^\circ$  and  $315^\circ$  that have low-rise buildings. At  $180^\circ$  the wind shear profile height crossover at  $\sim 50$  m. In this direction a large single large 7 m high that is 170 m long and 100 m wide exists  $\sim 150$  m south of the turbine. A similar wind shear profile is observed at  $315^\circ$ . In this case there are densely packed buildings 100 m away, with heights of  $\sim 9$  m covering an area of 220 m long and 80 m wide, with some 7 m high residential areas beyond these. Larger wind shear divergences occur for the  $202.5^\circ$ ,  $225^\circ$  sectors with wind shear crossover heights at  $\sim 80$  m. These sectors have buildings from 550 m away from the turbine and occupy an area  $\sim 600$  m long and 480 m wide with heights of  $\sim 11$  m, including a single 25 m height building that is 75 m long and 80 m wide,  $\sim 1000$  m away. Smallest wind shear divergences occurs in the more open sectors of  $247.5^\circ$  and  $270^\circ$  that have fewest obstacles. The profile at  $270^\circ$  is matched best with the up-scaled profile up to 200 m, implying that winds from this direction is in steady state with local roughness conditions, as it is shortest distance to the rural background, with few buildings. In the easterly sectors of  $67.5^\circ$  and  $157.5^\circ$  the fitted profiles do not crossover. The largest divergence occurs in the high wind energy sector of  $157.5^\circ$ , which has the 47 m tall obstacle 330 m away. In addition, the easterly sectors may be influenced unstable atmospheric conditions of winds from Dundalk bay.

When the wind turbine rotor (WTR) disc is considered, the modelled wind shear profile transitions occur within the rotor disc in some directional sectors. The wind shear across the rotor disc in sectors  $202.5^\circ$ ,  $225^\circ$ ,  $247.5^\circ$  and  $270^\circ$  are more in equilibrium with the up-scaled profiles, but divergence occurs towards the top of the rotor disc for the  $202.5^\circ$ ,  $225^\circ$  and  $247.5^\circ$  sectors. The *EER* predictions in these sectors are closest to the measured *EER* for the up-scaled CFD cases, apart from sector  $270^\circ$ . In contrast, the largest discrepancies in the *EER* predictions for the downscaled cases occur in these directions. This suggests that the winds measured at 20 m and 30 m

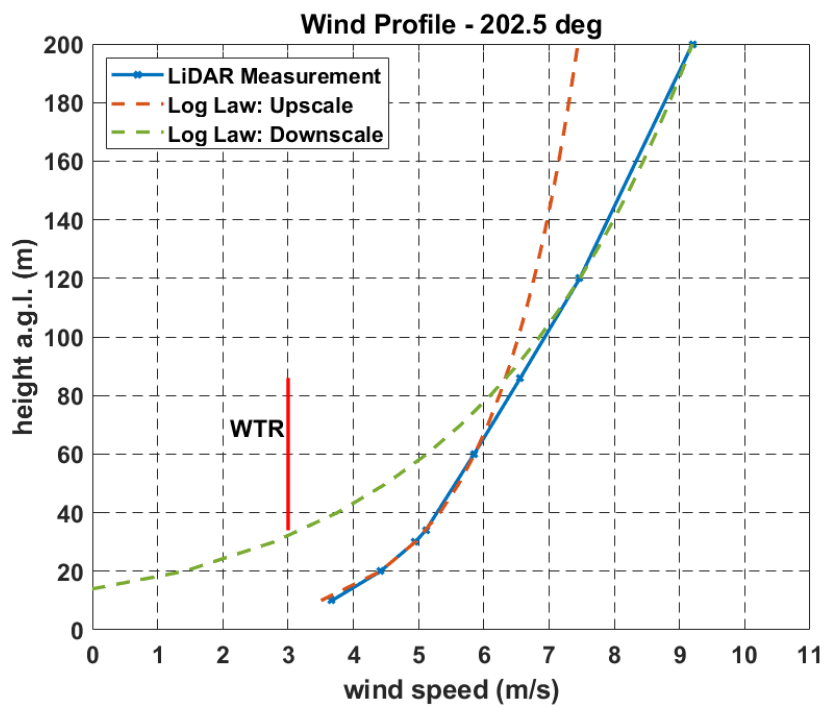
used for upscaling are more adjusted to the local flow influences of buildings beyond 500 m away. The under prediction of wind speed at lower heights from downscaling and the under prediction of wind speed at upper heights from upscaling in the cases of sectors  $202.5^\circ$ ,  $225^\circ$  and  $247.5^\circ$  suggest that obstacles have less an impact on higher wind speeds. In other words, there is a higher proportion of data points with high wind speed values, at lower heights, in the sectors with obstacles. Therefore, wind flow at lower wind speeds in these sectors are steered by the obstacles from these sectors into the neighbouring more open sector of  $270^\circ$ , thereby compensating for some of the perceived energy losses. This may be one reason why the four model under predict the wind turbine *EER* in the  $270^\circ$  sector in the upscaling cases, but predict it better when downscaling from 86 m. In the  $180^\circ$  and  $315^\circ$  sectors, the downscaled profiles matches the LiDAR profiles down to the lowest heights, resulting in a split between the up-scaled downscaled profiles within the rotor disc area. Upscaling from 30 m and downscaling from 86 m give similar *EER* predictions. This suggests that flow in these sectors has not fully adjusted at hub-height to the local surface influences, as the principal building are less than 500 m away from the wind turbine in these two sectors. In the easterly sectors, the high-energy sector at  $157.5^\circ$  show high wind speeds above 120 m and reduces at a faster rate below this to 86 m. Winds measured at 30 m and below, show much reduced wind speeds. The up-scaled *EER* predictions are poorest in this sector owing to wakes or sheltering effects of the 47 m height building, 330 m away, indicates that using wind measurement below the heights building obstacles, less than 10 obstacles height away, lead to poor predictions at heights above the buildings as expected.

(a)  $65.5^\circ$ (b)  $157.5^\circ$ 

**Fig. 6.19.** Fitted log law profiles to LiDAR measured wind shear profiles (WTR - wind turbine rotor).

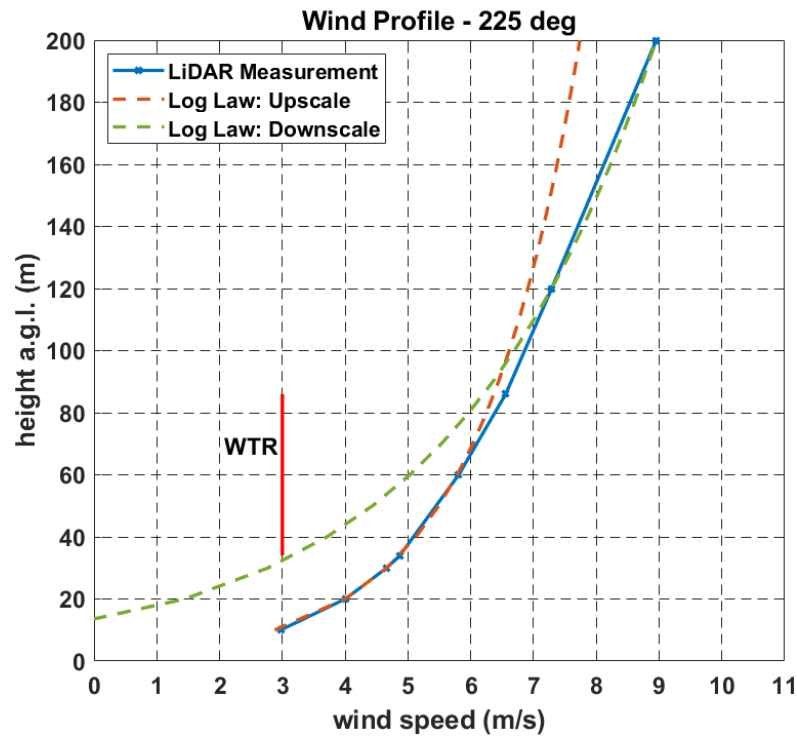


(a) 180°

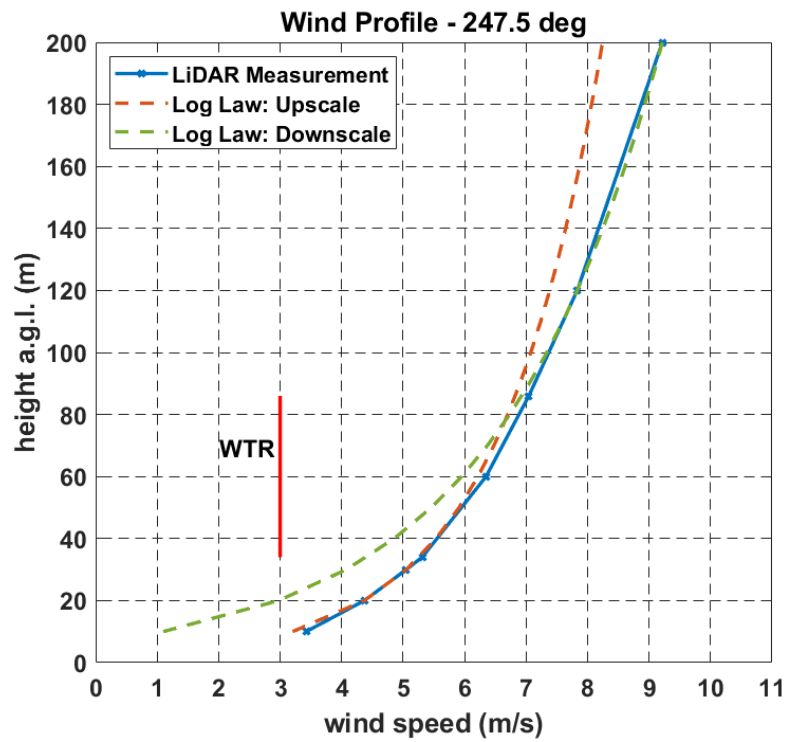


(b) 202.5°

Fig. 6.20. Fitted log law profiles to LiDAR measured wind shear profiles (WTR - wind turbine rotor).

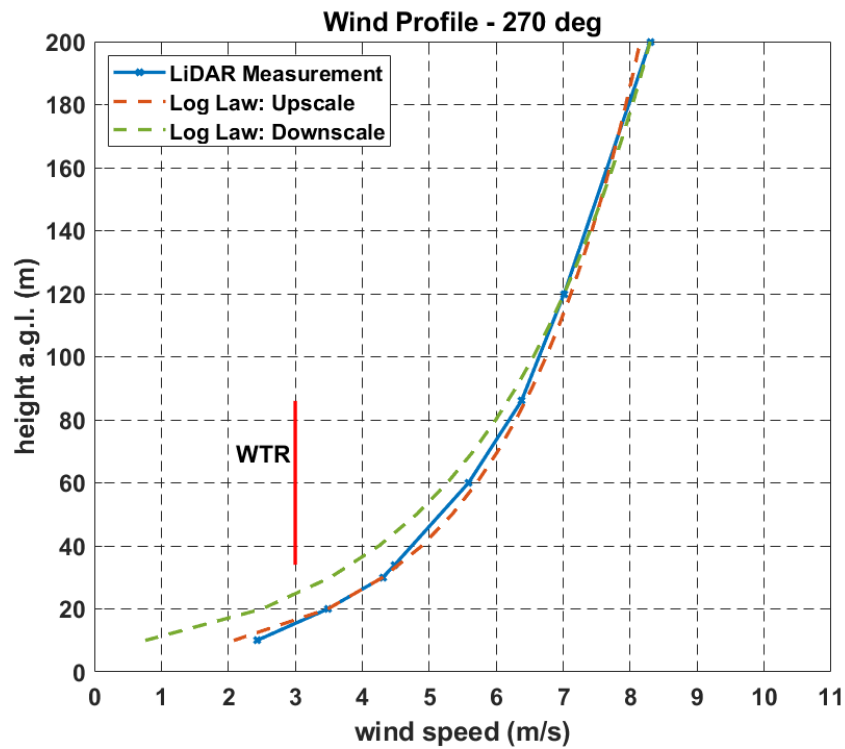


(a) 225°

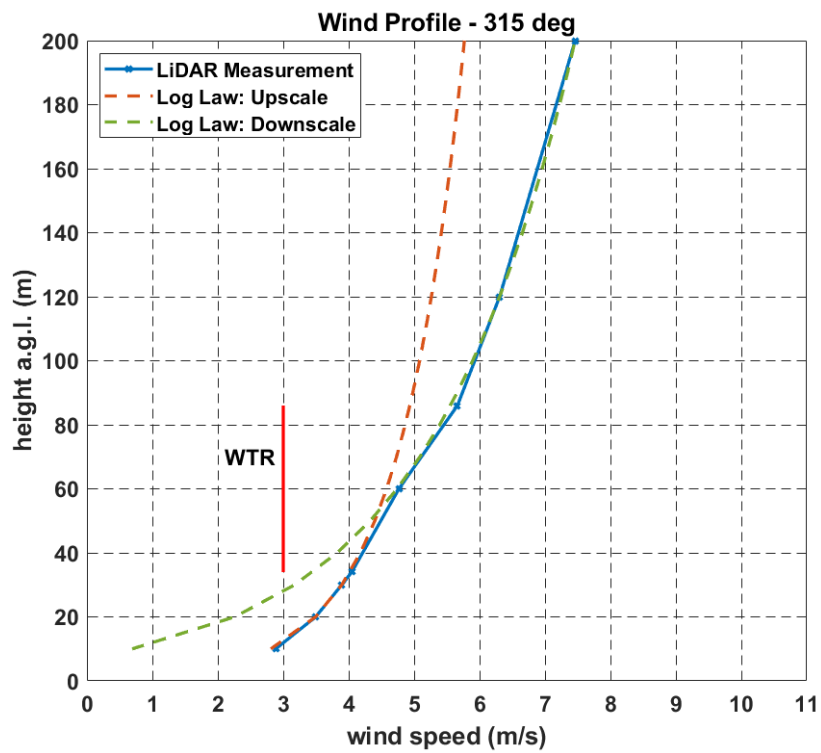


(b) 247.5°

Fig. 6.21. Fitted log law profiles to LiDAR measured wind shear profiles (WTR - wind turbine rotor).



(a) 270°

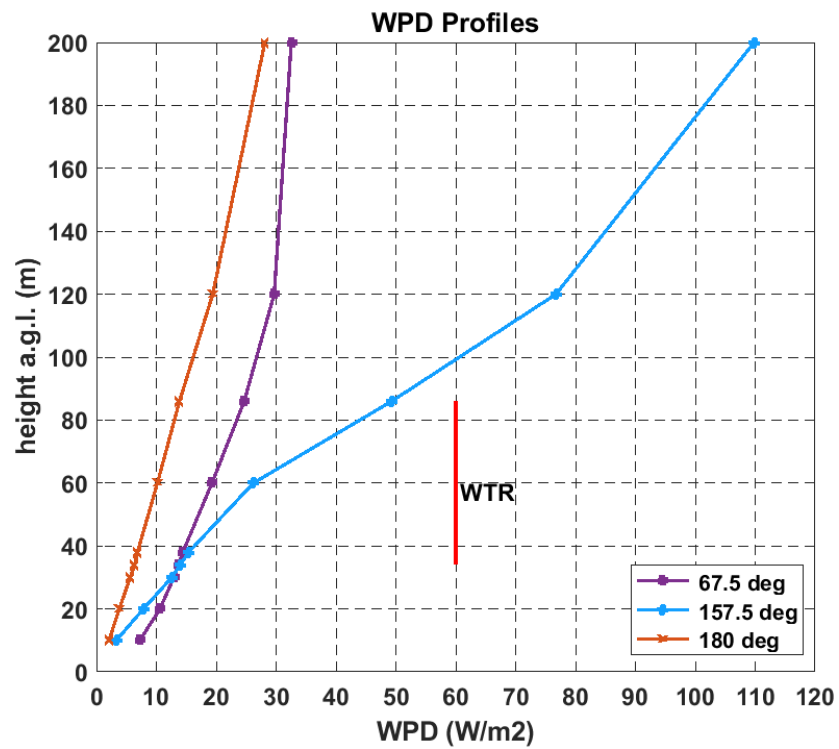


(b) 315°

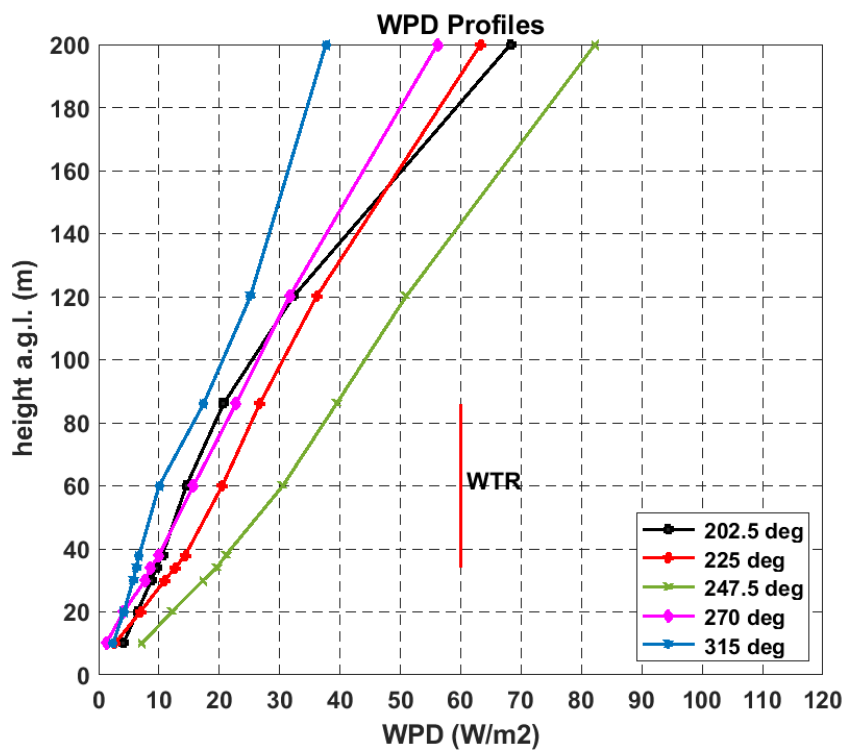
Fig. 6.22. Fitted log law profiles to LiDAR measured wind shear profiles (WTR - wind turbine rotor).

The vertical *WPD* profiles account for the time proportion of wind in each sector, Fig. 6.23. In the westerly sectors, the rate of increase of *WPD* with height in sector  $202.5^\circ$  reduces while it increases in the neighbouring  $225^\circ$  and  $247.5^\circ$  sectors. Above 120 m, the *WPD* in  $202.5^\circ$  exceeds the *WPD* in sector  $225^\circ$ . This further suggests that energy may be shifting from sector  $202.5^\circ$ , that has obstacles 550 m to 1100 m away, to its more open neighbouring sectors. This is also independently reflected in the electrical energy distribution from the wind turbine SCADA data, Fig. 6.16, where energy in sector  $202.5^\circ$  occurs at higher wind speeds compared to sectors  $225^\circ$ ,  $245.5^\circ$  and  $270^\circ$ . However, this requires more investigation. The reduction in *WPD* in sector  $157.5^\circ$ , particularly across the rotor disc, in the wake of the 47 m building is evident.





(a) easterly sectors



(b) westerly sectors

Fig. 6.23. Directional WPD profiles.

## 6.4 Discussion

The energy performance of a Vestas V52 wind turbine, in a peri-urban environment, has been shown to be influenced by low-rise broad buildings as well as narrow high-rise buildings. Four commonly used microscale models, based on linear and RANS CFD approaches show discrepancies in *EER* predictions compared to the real-world *EER* of the operational wind turbine. Similar to studies outlined in literature, there is no clear standout best modelling approach covering all directions from all scaling heights. The WindSim mesh blocking approach gives a slightly a better result than the WindSim roughness approach. In contract, WAsP-CFD roughness with the polar grid, simulated in  $10^\circ$  wide sectors, performs slightly better than the rectangular grid used in both WindSim models for simulations in  $22.5^\circ$  degree wide sectors. WindSim models tend to perform better in upscaling cases, while the WAsP models perform better in the downscaling cases. However, it is observed that the height chosen for wind measurements is of high importance for how the models perform. This can be explained by the modified wind shear profiles due to internal boundary layers that vary in heights from 30 m to 120 m, depending on obstacle heights and distance from wind turbine location. Largest discrepancies occurred when downscaling from 200 m and when upscaling from a 10 m height, i.e., less than twice the height of the low-rise buildings. The linear model performs the poorest, particularly when upscaling from 10 m.

The findings suggest a number of implications for distributed wind, especially in the deployment of medium and large-scale wind turbines in peri-urban industrial zones. Firstly, obstacles down to 20% of the turbine hub-height and at distances up to 50 obstacle heights away can create an internal RSL whose boundary with the ISL is within the rotor disc area. Similarly, obstacles from 50 to 100 obstacle heights away from the turbine location may create an RSL that will cover the rotor disc area. This is in line with internal boundary layer formation from the urban-rural interface outlined in the literature. Therefore, the desire to have the rotor entirely in the ISL may lead to impractical turbine tower heights for medium and large-scale wind turbines. For best model predictions, it would be desirable to have wind measurements and the minimum height of the lowest point of the rotor swept area to

be at least 3 times the height of broad low-rise buildings, to avoid any CL complex flow effects and reduce errors in upscaling modelling processes. Secondly, for tall buildings with heights of 80% of the turbine height and less than 10 obstacles heights away from the turbine location, mesh blocking and roughness approaches may give better results when downscaling from twice the building height. Upscaling from below building heights may lead to poor model predictions at turbine hub heights above the building heights. Thirdly, the linear WAsP-IBZ model performs the poorest in all cases, but is particularly erroneous when upscaling from heights similar to the building heights, as its shelter model does not capture complex flow. It is therefore not recommended to use linear shelter models in peri-urban area or areas that have numerous building obstacles, particularly in prevailing wind directions. Finally, it is observed that building obstacles in directional sectors that have neighbouring open sectors to the rural environment may have a steering effect on incoming winds, so that energy losses in the more blocked sector may be recovered in the neighbouring open sector. Therefore, the total annual energy out may be less impacted by obstacles with open neighbouring areas.

Future research could involve examining alternative approaches to flow modelling, such as simple low-cost empirical rules developed from morphological methods. In addition, wind turbines whose rotors operate across multiple local internal boundary layers, in peri-urban wind environments, may experience extra fatigue loads and have different aerodynamic noise characteristics, requiring further research. LiDAR technology can play an important future role in the distributed wind industry to address some these questions.

## 6.5 Conclusions and next steps

This study compared the performance of four commonly used wind flow models, including linear and CFD RANS, in predicting the energy performance of an operating Vestas V52 wind turbine in peri-urban environment using onsite LiDAR measurements. Variations in the evaluated models, from 1.4% to 64% between the model predicted *EERs* and the measured wind turbine *EER* were observed and shown to be directional dependent. Over all, the linear shelter model performed the poorest. Low-rise buildings below  $\sim 1/3$  of wind hub-height appeared to be best represented

as roughness elements in the CFD RANS models rather than as mesh blocking elements. The model predictions were highly dependent on the height at wind measurements, supplied to the models, were taken. For low-rise buildings, with heights up to 20% of turbine hub height, the evaluated models were most accurate using wind measurements from 2 to 3 times the height of the buildings. In the case of a tall narrow building,  $\sim 80\%$  of the turbine height, the models were more accurate using wind measurements from twice the height of the obstacle. Over all, the linear shelter model performed the poorest. Measured directional wind shear profiles showed the possible existence of internal boundary layers in height from 30 m to 120 m influenced by obstacles from 50 to 100 obstacle heights away from the turbine location, within  $\sim 1$  km of the urban-rural interface. Directional sectors with obstacles appeared to steer energy at lower wind speeds in open neighbouring sectors, reducing overall energy losses. Onsite measurements, not only at hub height, but also at multiple heights of the rotor disc are recommended to capture these effects. Further peri-urban wind energy research is suggested in the evaluation of other modelling approaches, impacts of turbulence, shear and atmospheric stability as well as alternative low cost assessment methods, such as morphological approaches.

In Chapter 7, an investigation of a morphological scheme describing local building patterns as viewed from both the turbine (WT) and offsite met mast (M) locations is carried out. *EERs* at both locations will be compared to examine possible correlations with the morphological properties of the local peri-urban environment. In addition, comparison of turbulence intensity and gust factors from the met mast measurements and onsite LiDAR measurements will be made the context of current IEC wind turbine design standards. Suggestions for modifications of the parameters for peri-urban environments will be given. Directional wind shear and turbulence across the rotor disc will be examined to assess which of them is more dominant in the rotor equivalent wind speed (REWS). REWS will also be examined to see if it is more appropriate for this size of rotor in this environment, as opposed to hub-height wind speed only. A preliminary assessment atmospheric stability influences will also be made.

## Chapter 7

# Measured wind and morphological characteristics of the peri-urban environment and their impact on wind turbine performance

### 7.1 Objectives

Chapter 6 showed the variations of four evaluated microscale wind flow models, from 1.4% to 64% between the model predicted *EERs* and the measured wind turbine *EER*. The discrepancies were directional dependant, with highest deviations in prevailing wind directions that contained obstacles. Low-rise buildings below  $\sim 1/3$  of wind hub-height appeared to be best represented as roughness elements in the CFD RANS models rather than as mesh blocking elements. The model predictions were highly dependent on the height at wind measurements, supplied to the models, were made. Measured directional wind shear profiles showed the possible existence of internal boundary layers in height from 30 m to 120 m influenced by obstacles up to 100 obstacle heights away from the turbine location, within  $\sim 1$  km of the urban-rural interface. Energy at lower wind speeds appeared to be steered from directional sectors with obstacles into more open neighbouring sectors, thereby reducing overall energy losses. Overall, the linear shelter WAsP model performed the poorest and is not recommended for peri-urban environments.

This chapter investigates an alternative approach to assessing obstacles based on simplified morphological descriptions of the peri-urban environment and to assess possible trends with wind turbine energy performance. The principal aim is to enhance simplified wind turbine siting guidelines in vicinity of obstacles, outlined in the literature review. The study also further examines directional wind shear profiles across the rotor disc, turbulence and gust factors at multiple heights in the context

of current IEC wind turbine design standards. Suggestions are made to improve existing IEC design standards specifically for medium to large-scale wind turbines that are deployed peri-urban environments. A combination of multi-annual turbine SCADA data, 1 year of wind measurements from an onsite LiDAR and wind measurements from an offsite rural met mast, located  $\sim 1140$  m away, are analysed. The directional turbine energy performance, wind turbulence, wind shear and gust factors are assessed in relation to the morphological properties of building obstacles in 16 directional sectors around both the wind turbine and met mast locations. The validity of current normal turbulence models (NTM), specified by IEC standards, for both small and large-scale wind turbines are tested for validity against the analysed data. To test the assumption of neutral atmospheric stability over measurement period, an assessment of the indicative atmospheric stability is made, based on the Richardson number ( $R_i$ ), for different directions from wind speed, wind direction and temperature measurements at the local offsite met mast.

The study begins with a site description and assessment of local building obstacles, using morphological methods, at both the wind turbine and met mast locations. Secondly, the long-term directional energy output, power curves, power curve standard deviations and turbulence intensity at the wind turbine site are assessed from 7 years of time-series turbine SCADA data. Wind measurements at 10 m and 30 m at the offsite rural met mast and turbine SCADA data, over a concurrent 7-month period, are used to compare the impact of the building obstacles on energy and turbulence between both locations. Thirdly, continuing on from Chapter 6, one year of LiDAR wind measurements at the wind turbine location, measured at 10 heights from 10 m to 300 m, are used to examine directional *WPD* at multiple heights, wind shear across the rotor disc, rotor equivalent wind speed (*REWS*), gust factors, and horizontal and vertical turbulence intensity. Temperature and wind data are used to assess atmospheric stability. Finally, the implications for large-scale wind turbine micro-siting in peri-urban environments and future IEC design standard revisions are discussed. New peri-urban micro-siting recommendations for best energy capture and revisions to IEC standard NTMs are suggested.

## 7.2 Methods

### 7.2.1 Measurement setup

Fig. 7.1 gives a reminder of the local built environment around the wind turbine location for the purposes of this study. The LiDAR is ground mounted at location (LiD), approximately 60 m from the wind turbine location (WT). The 11 user-selected heights from 10 m to 300 m were discussed in Chapter 5 are 10 m, 20 m, 30 m, 34 m, 38 m, 60 m, 86 m, 120 m, 200 m, 250 m and 300 m. As buildings from southeast through to the west of the turbine are of most interest, a 34 m met mast (M) is located in a rural location approximately 1140 m west southwest of the wind turbine location. This location is chosen to capture prevailing south-westerly winds that are less influenced by building obstacles, compared to location WT.

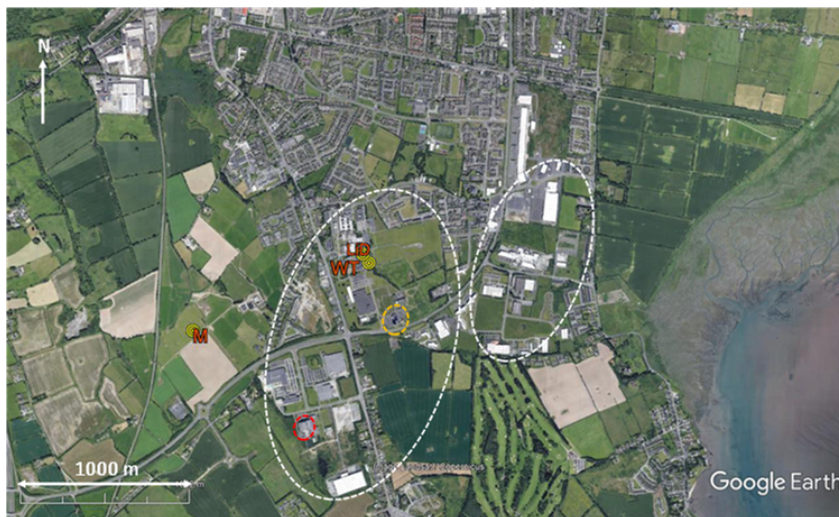


**Fig. 7.1.** Local buildings (Circled: yellow 47 m, red 25 m, white 6–13 m), wind turbine (WT), LiDAR (LiD), Met mast (M).

Fig. 7.2 shows the met mast set up in more detail. The met mast is a lattice tower with a total height of 34 m. In addition to measuring wind speed at the two height of 10 m and 30 m, wind direction is measured at 8 m and 28 m. At each wind speed measurement height, wind speed is measured by two NRG anemometers mounted on booms on both sides of the mast to enable the filtering out of mast tower influences on the wind flow. The booms are mounted perpendicular to the prevailing south westerly direction on the mast. This is in accordance with IEC standards for mounting wind sensor booms on lattice masts to minimise influence on measured

wind flow, (IEC 61400-12, [2019](#)). The wind vanes are placed at 8 m and 28 m to avoid wind flow influences on the anemometers. In addition, to assess the atmospheric stability, temperature measurements are made at heights of 2 m and at 32 m. Two T60 NRG shielded temperature sensors are used for the temperature measurements. The heights of the temperature sensors are chosen to obtain vertical temperature gradients that are as accurate as possible within the mast height constraints, while avoiding localised ground distorting influences on temperature, e.g., from the mast foundation etc. Also, the avoidance of the wind flow interference by the temperature sensors on the anemometer and wind vane measurements was a factor in the temperature sensor placements. All met mast data is logged by a Second Wind Nomad data logger in 1-minute averages.

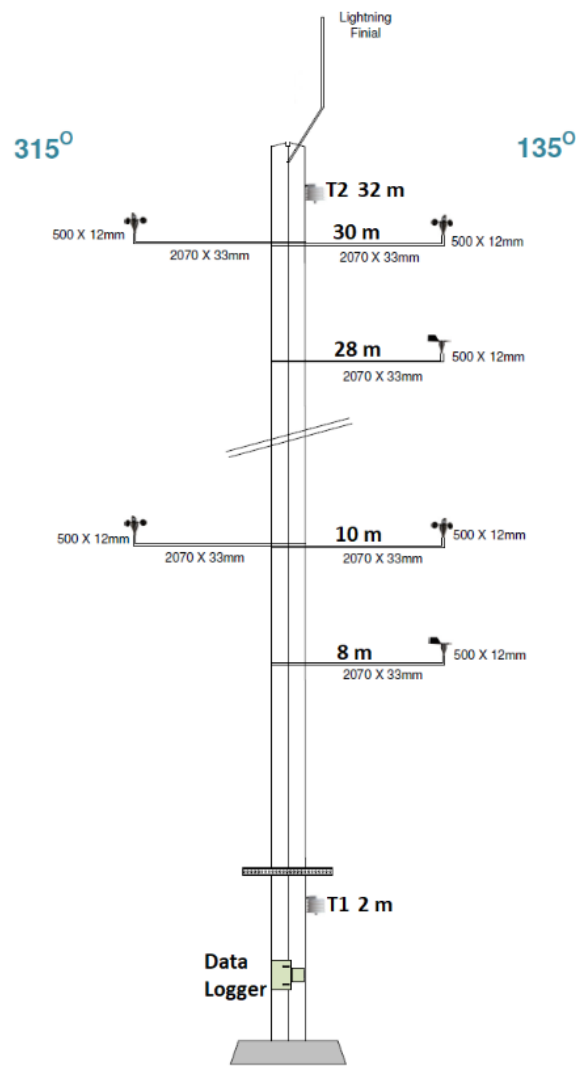




(a) Installation (M)



(b) Data logger



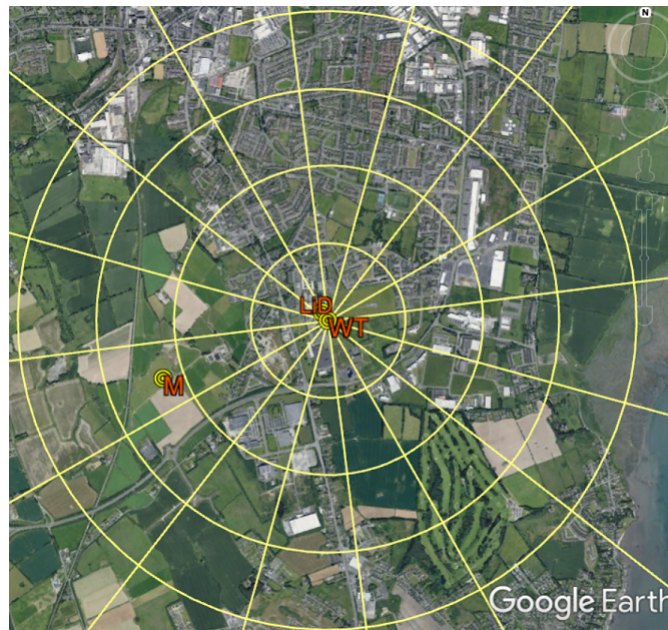
(c) Measuring instrument schematic

Fig. 7.2. Met mast installation setup.

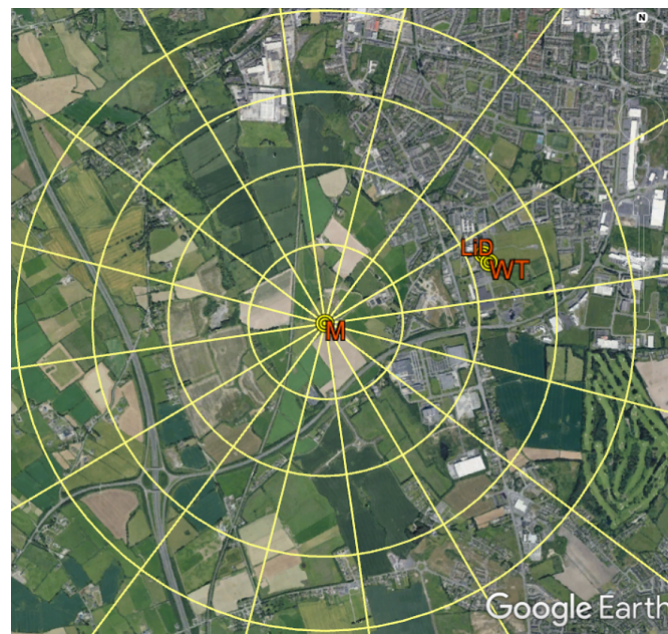
The met mast installation was a temporary installed structure that was planned for a 1-year measurement period from March 2018 to 2019, coinciding with the LiDAR measurement period. However, installation delays were encountered due to local planning permitting processes, insurance considerations and forming access agreements to the private land at location M in Fig. 7.1. This led to the mast being not being installed until August 2019. Unfortunately, restrictions of the COVID 19 pandemic forced an earlier than anticipated end to the measurements in early March 2020, due to restriction of movement. This meant that met mast data was logged from August 2019 to March 2020. Therefore, in this study, the common time period for measurements at locations M and WT for *EER* comparison purposes is limited to a 7-month time period.

### 7.2.2 Morphological assessment of obstacle characteristics

As shown in Fig. 7.1, within approximately 1.1 km radius of the wind turbine there exists a number of industrial buildings. The majority of the buildings, circled in white, range in height from 7 m to 13 m. Circled in yellow is a narrow 47 m high building and a 25 m building circled in red. To the north of the site, the town consists of residential and commercial buildings that are  $\sim 6$  m to 7 m in height. Due to the large number of individual buildings in the area, it becomes impractical or even impossible to assess the influence of every individual building or obstacle, apart from particular standout obstacles. Therefore, a morphological approach is used to describe the building patterns as viewed from both the wind turbine and met mast locations, shown in Fig. 7.3. All area and the building height information is obtained from the 3D Buildings feature of Google Earth Pro.



(a) Sectoral and segments divisions at WT



(b) Sectoral and segments divisions at M

**Fig. 7.3.** 16 sector divisions in 500 m segments in a 2 km radius as viewed from locations WT and M.

For both the WT and M locations, 16 directional sectors are divided into four segments (regions of interest) of 500 m distances in the radial direction, extending out to 2 km. It is apparent that the sectors and segments to the south and west viewed from location M have far fewer building obstacles compared to location WT. In the case of location WT, the 2 km extremity stretches beyond the physical urban-rural

interface in the southwest prevailing wind directions. It also covers a distance of approximately 40 times the highest obstacle (47 m), which is well in excess of current siting recommendations of 20 times the highest obstacle and exceeds IEC criteria for obstacle assessments used at accredited wind turbine test sites (IEA Wind, 2018; IEC 61400-12, 2019).

The principal morphological parameters applied in 500 m segments of each sector are defined as follows, (He et al., 2019): The average obstacle height weighted by obstacle plan area,  $\bar{h}_{AW}$ , is defined by Eq. (7.1).

$$\bar{h}_{AW} = \frac{\sum_{i=1}^N A_i h_i}{\sum_{i=1}^N A_i} \quad (7.1)$$

Where:

$h_i$  – height of an individual obstacle  $i$  (m)

$A_i$  – plan area occupied by an individual obstacle  $m^2$

$N$  – total number of obstacles

The obstacle plan area fraction  $\lambda_p$  is defined as the ratio of the total plan area occupied by all obstacles to the total surface area in region of interest, Eq. (7.2).

$$\lambda_p = \frac{A_p}{A_T} \quad (7.2)$$

Where:

$A_p$  – total plan area of the buildings and obstacles

$A_T$  – total plan area of region of interest

The frontal area density  $\lambda_f$  is a measure of the frontal area per unit horizontal area per unit height, Eq. (7.3). Only the portions of the frontal area of obstacles that are in view in a given direction are considered, i.e., any portions of the frontal area of obstacles masked by other obstacles are not included.

$$\lambda_f(z, \theta) = \frac{A(\theta)_{proj(\Delta z)}}{A_T \Delta z} \quad (7.3)$$

Where:

$A(\theta)_{proj(\Delta z)}$  is the area of building surfaces normal to a given wind direction  $\theta$  and height increment  $\Delta z$

### 7.2.3 Energy assessment

The long-term, 7 year, directional energy output in kWh, in 16 directional sectors, from wind turbine SCADA data is determined using an *EER*, described in Chapter 4. Directional power curves and directional power curved standard deviations are plotted from the long-term time-series data to give a more clearer picture of the variations in the power performance with direction, particularly in directions with obstacles. Short term wind roses and *EERs* at both the WT and M locations over the same 7-month measurement period (August 2019 to March 2020) are compared in the southwest direction where low rise building are prevalent as viewed from the WT location but not from location M. The met mast wind speeds at 10 m and 30 m at location M are first projected to 60 m using the power law, Eqs. (7.4) and (7.5).

$$\alpha = \frac{\log \frac{U_1}{U_2}}{\log \frac{z_1}{z_2}} \quad (7.4)$$

Where:

$U_1$  - wind speed at 10 m (m/s)

$U_2$  - wind speed at 30 m (m/s)

$z_1 = 10$  m

$z_2 = 30$  m

$$U_{60m} = U_{30m} \left( \frac{60}{30} \right)^\alpha \quad (7.5)$$

The *EER* at location M can is then estimated from the wind turbine power curve and 60 m wind speed distribution us the equations for directional *AEP* from Chapter 6, but for the 7-month period. From Chapter 6, the multi-level LiDAR directional *WPD* at multiple heights at the wind turbine site are given at location LiD. The *WPD* at higher heights of 120 m and 200 m are used to assess the wind resource, assumed to be above the influence of the local building obstacles within the 2 km radius. These are compared with *WPD* at lower heights down to 34 m i.e. bottom of rotor disc) to examine reductions and directional changes in the directional *WPD* that may be introduced by the local building obstacles.

## 7.2.4 Turbulence and gust factors

Turbulence and gusts create dynamic fatigue and extreme static loads than can manifest themselves in turbine wear and possible failures. Equations for horizontal turbulence intensity  $I_U$  and vertical turbulence intensity  $I_W$  are described by Eqs. (7.6) to (7.9).

$$I_U(t, T) = \frac{\sigma_u(t, T)}{\bar{U}(T)} \quad (7.6)$$

The standard deviation  $\sigma_u(t, T)$  is given by root mean square of the variance, Eq. (7.7)

$$\sigma_U = \sqrt{u'^2(t, T)} \quad (7.7)$$

$$I_W(t, T) = \frac{\sigma_w(t, T)}{\bar{U}(T)} \quad (7.8)$$

$$\sigma_W = \sqrt{w'^2(t, T)} \quad (7.9)$$

Where:

$\bar{U}(T)$  - average horizontal wind speed in given time averaging period  $T$

$u'(t, T)$  - longitudinal fluctuation in wind speed

$w'(t, T)$  - vertical fluctuation in wind speed

The prescribed NTMs in the IEC 61400 design standards are equations that give a longitudinal wind speed standard deviation relationship to horizontal wind speed, scaled by a reference turbulence intensity at 15 m/s and other constant scaling factors. NTMs are given for both small scale and large scale wind turbines. In the case of large-scale wind turbines that conform to (IEC 61400-1, 2019), a characteristic value of  $\sigma_U$  is given by Eq. (7.10).

$$\sigma_U = I_{ref} (0.75U_{hub} + b) \quad (7.10)$$

Where:

$U_{hub}$  - wind turbine hub height wind speed (m/s)

$I_{ref}$  - reference turbulence intensity (specified as a fraction),  $b$  - constant of 5.6 m/s

$I_{ref}$  can have a range of values depending on the turbulence conditions a turbine is designed to operate in. An  $I_{ref}$  value of 0.18 represents the highest turbulence condition specified in the IEC standard in the 15 m/s wind speed bin. It is referred to as an A+ turbulence classification. For small wind turbines, conforming to (IEC 61400-2, 2013), the characteristic value of  $\sigma_U$  is given by Eq. (7.11).

$$\sigma_U = I_{ref} \frac{(15 + aV_{hub})}{(a + 1)} \quad (7.11)$$

Where:  $a$  - constant slope value of 2

The mean binned directional  $I_U$  at location M and WT from the met mast data and the turbine SCADA data respectively are compared to plots of IEC NTM turbulence intensity predictions for small-scale wind and A+ predictions for large-scale wind turbines. In addition, the 90<sup>th</sup> percentile values of  $I_U$  at the 11 LiDAR measurement heights at location LiD to assess how high above the buildings  $I_U$  falls within the NTM predictions. Modified values for  $I_{ref}$  and constant parameters are suggested for heights where  $I_U$  exceeds current NTM predictions in this peri-urban environment. Gust factor is defined as the ratio of maximum 3-second gust  $\hat{u}(t, T)$  to the mean wind speed over a specified time period, Eq. (7.12), (Lombardo, 2021).

$$G_U(t, T) = \frac{\hat{u}(t, T)}{U(T)} \quad (7.12)$$

In the case of the IEC small wind turbine design standard,  $G_U$  is specified as 1.4. Gust factors are used in extreme wind calculation with 1-year and 50-year recurrence periods, (IEC 61400-2, 2013). In a similar way to  $I_U$ , the mean binned and 90<sup>th</sup> percentile values for  $G_U$  are assessed and compared at the M and LiD locations. These are also examined in relation to the building obstacles between both locations. The wind turbine SCADA data does not have sufficient information to assess  $G_U$ . It should be noted that the maximum wind speed  $\hat{u}(t, T)$  in a 10-minute period measured by the LiDAR are those captured in the 16 second time window it takes to measure at all 11 heights, i.e.,  $\sim 1.5$  second sample rate at each height. Therefore,  $G_U$  values should just be taken as indicative here.



### 7.2.5 Wind shear and REWS

At locations with high wind shear or wind turbines with large rotors, the wind speed at hub height alone may not adequately represent the wind flow incident on the rotor. *REWS* attempts to account for variation in wind speed across the rotor disc wind. (Wagner et al., 2014) developed a method to calculate the *REWS* for large wind turbine rotors, from wind speed measurements at multiple heights across a rotor, for wind turbine with large rotors (e.g., rotor diameters above 90 m) in rural locations. The *REWS* is determined from Eq. (7.13). Although the rotor of diameter of 52 m is relatively small in this case, in Chapter 5, wind shear profiles were shown to vary with direction and deviate from the log law, suggesting that the hub height wind speed may not adequately represent the wind flow incident on the rotor. In this study, directional *REWS* is estimated from the LiDAR measurements across the rotor and compared to the hub height wind speed. The measured directional wind shear across the rotor disc is compared to the power law, Eq. (7.4), predicted wind shear profiles across the lower and upper halves of the rotor disc using wind measurements at the lower blade tip height of 34 m, hub height of 60 m and maximum blade tip height of 86 m. The predicted shear profiles are extended down to 10 m and up to 120 m, a range of interest to distributed wind systems, to examine any deviations from the power law profiles from the measured profiles. Plots of the directional wind shear exponent  $\alpha$  for both the lower and upper parts of the rotor disc are compared to test for any abrupt changes that might indicate building wake affects or internal boundary transitions across the rotor disc height range.

$$U_{REWS} = \left( \sum_{i=1}^n U_i^3 \frac{A_i}{A} \right)^{1/3} \quad (7.13)$$

Where:

$U_i$  – horizontal wind speed measured at a given height within the rotor swept area

$A_i = g(z_{(i+1)}) - g(z_i)$  - the area of the rotor segment between two heights  $z_i$  and  $z_{(i+1)}$

$$g(z) = (z - H) \sqrt{(R^2 - (z - H)^2)} + R^2 \tan^{-1} \left( \frac{z - H}{\sqrt{(R^2 - (z - H)^2)}} \right) \quad (7.14)$$

$R$  - rotor diameter (m)

$H$  - hub height (m)

$z$  - height of a point that is half way between two wind measurement points



Fig. 7.4 shows a schematic of the rotor showing wind measurement at heights of 34 m, 60 m and 86 m and division into three segments at heights of 47 m and 73 m.

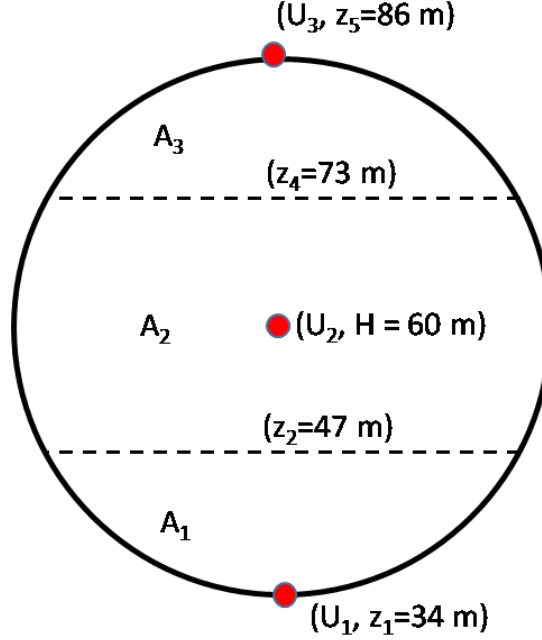


Fig. 7.4. Rotor segments and wind measurement heights used to calculate REWS.

Turbulence also contains energy that can potentially extracted depending on turbine rotor design. In terms of wind speed, the turbulent equivalent wind speed in general terms can be described by Eq. (7.15), (Wharton and Lundquist, 2012).

$$U_{h-I_U}(T) = \sqrt[3]{U_h(T) \left(1 + 3I_{U_h}^2\right)} \quad (7.15)$$

$U_{hub-I_U}(T)$  at hub height is the specific case of  $U_{h-I_U}(T)$  when  $h$  is 2, i.e., the 60 m height and the REWS including turbulence is determined from Eq. (7.16).

$$U_{REWS-I_U} = \left( \sum_{h=1}^{n_h} U_{h-I_U}^3(T) \frac{A_h}{A} \right)^{1/3} \quad (7.16)$$

A comparison of directional hub height wind speed  $U_{hub}$ , rotor equivalent wind speed  $U_{REWS}$ , hub height wind speed including turbulence  $U_{hub-I_U}(T)$ , and rotor equivalent wind speed including turbulence  $U_{REWS-I_U}(T)$  are compared. This is to assess if wind shear or turbulence has a bigger impact on wind speed deviation across the rotor from the hub-height wind speed.

### 7.2.6 Atmospheric Stability

It is assumed that general atmospheric conditions are near neutral most of the time, however, to test this assumption an indication of the background environmental atmospheric stability for each wind direction in the region is made using temperature measurements at the met mast location. It is based on the Richardson number  $R_i$  described by equation Eq. (7.17). As the met mast is located outside of the peri-urban zone it can give a better indication of the general background atmospheric stability where temperature measurements are less influenced by the local buildings.

$$R_i = \frac{\frac{g}{\theta} \frac{\partial \bar{\theta}}{\partial z}}{\left( \frac{\partial \bar{u}}{\partial z} \right)^2} \quad (7.17)$$

Where:

$\bar{\theta}_v$  – virtual potential temperature (K) (it accounts for the effects of pressure and humidity

From Chapter 3, this can be approximated, Eq. (7.18), to a usable form for less costly measurement setups of temperatures and horizontal wind speeds, measured at two heights, on a met mast (Kelley, 2017). The measurement can be logged in 10-minute mean values.

$$R_i = \frac{g(T_2 - T_1)(z_2 - z_1)}{0.5((T_2 + T_1)(U_2 - U_1)^2)} \quad (7.18)$$

Where:

$z_1, z_2$  - two measurement heights (m)

$T_1, T_2$  - mean absolute temperature measurements at the two heights (K)

$U_1, U_2$  - horizontal mean wind speeds at the two heights (m/s)

A range of stability classes are defined as shown in Table 7.1, (Newman and Klein, 2014). Distributions of  $R_i$  over the 7-month measurement period are given, including distribution for day and night time hours taken as between 07:00 to 19:00 and 19:00 to 7:00 respectively. These average daily time periods are chosen based on the overall measurement period at the met mast being mostly dominated by autumn, through winter to spring months. Binned distributions of  $R_i$  with wind speed for directions of most interest are used to show the wind speeds at which atmospheric

stability deviates most from neutral stability on average. They are also used to help indicate if atmospheric stability may be having a significant impact on wind shear in the directions of interest. However, as the 7-month measurement period has no simultaneous time overlap with the one-year LiDAR measurement as well the non-availability of 3D high frequency wind speed measurements at the met mast location, the atmospheric stability assessment should only be taken as indicative.

**Table. 7.1.** Stability classes, (Newman and Klein, [2014](#))

Stability class	$R_i$ Range	Classification
STC1	$R_i < -0.2$	highly unstable
STC2	$-0.2 \leq R_i < -0.1$	unstable
STC3	$-0.1 \leq R_i < 0.1$	neutral
STC4	$0.1 \leq R_i < 0.25$	stable
STC5	$R_i \geq 0.25$	highly stable

## 7.3 Results

### 7.3.1 Obstacle morphological characteristics

For both M and WT locations, Fig. 7.5 shows obstacle area-weighted average height  $\bar{h}_{AW}$  in the four 500 m segments for each of the 16 directional sectors. As expected, the morphological characteristics of the local obstacles are different when viewed from locations M and WT. However, the north and northeast sectors have similar values of  $\bar{h}_{AW}$ , due to the spatial expanse of Dundalk town that consists of buildings of broadly uniform height and density. Differences in  $\bar{h}_{AW}$  occur in the remaining sectors from the southeast to the northwest, highlighting the differences between the rural and peri-urban locations in these directions. Specifically, at  $157.5^\circ$  for the WT location, the 47 m hotel primarily influences the value of  $\bar{h}_{AW}$  in the 0 m - 500 m segment. In contrast, no obstacles are present for location M at  $157.5^\circ$ , in the 0 m - 500 m segment, while the hotel appears in the  $90^\circ$  sector, in the 500 m - 1000 m segment, that has a lower  $\bar{h}_{AW}$  value. The  $202.5^\circ$  sector location WT has a number of low-rise building from 11 m to 25 m in the 500 m to 1500 m segments resulting in the highest instance of  $\bar{h}_{AW}$ . This coincides with some of the lowest values in the corresponding segments for location M. In all westerly and north westerly sectors, obstacles exist to some degree in all four segments for location WT. This is not the case for location M, where obstacles don't appear in any 0 m to 500 m segment and in some cases only appear in the furthest segment of 1500 m to 2000 m, for example at  $315^\circ$ . The maximum obstacle height values  $h_m$  highlight the individual standout obstacles, such as the 47 m hotel and 25 m high buildings. It shows how they are closer to, and occupy more sectors at the WT location.

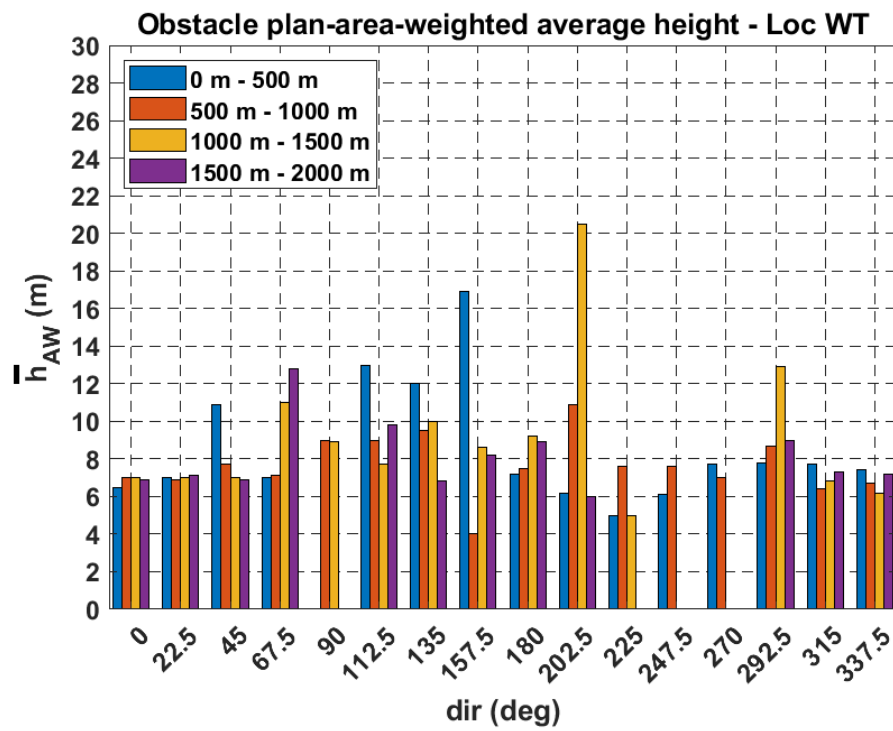
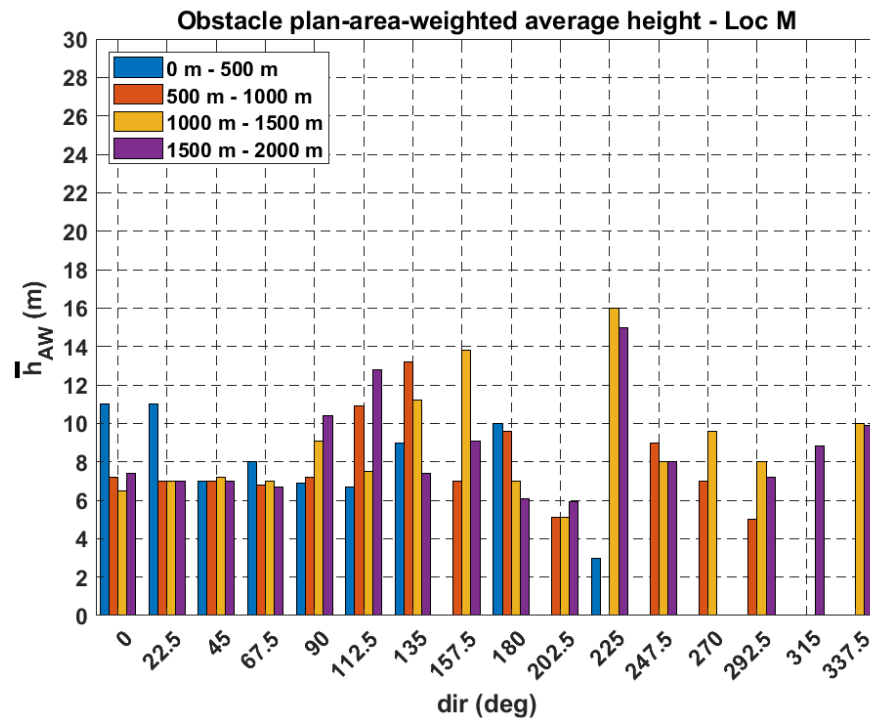


Fig. 7.5. Obstacle area-weighted heights viewed from M at WT.

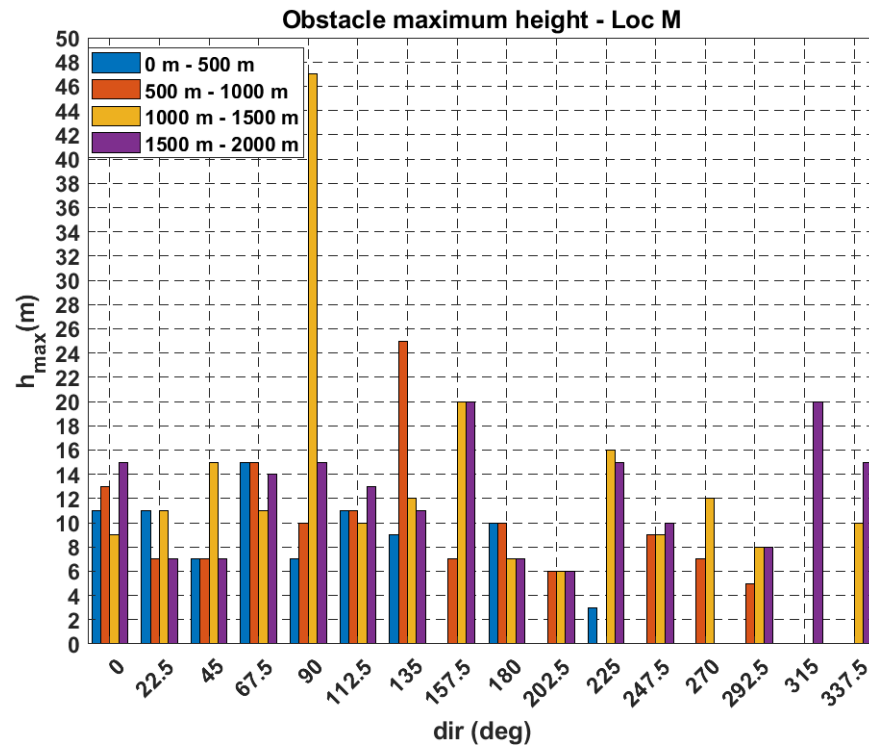
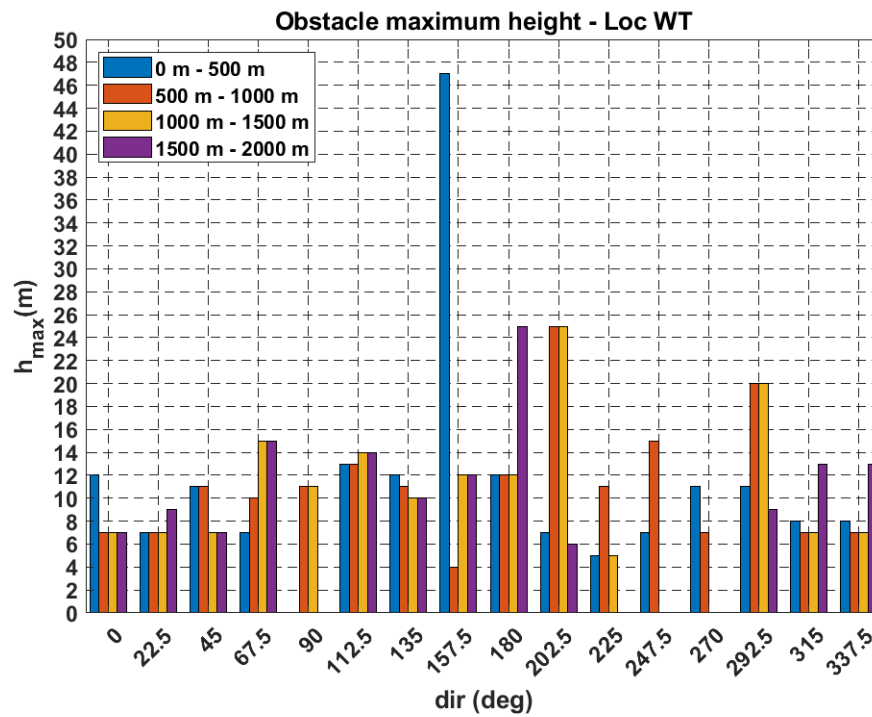
(a)  $h_m$  (M)(b)  $h_m$  (WT)

Fig. 7.6. Obstacle maximum heights viewed from M at WT.

A comparison of the obstacle plan area fractions  $\lambda_P$  is shown in Fig. 7.7. Dundalk town to the northeast shows values for  $\lambda_P$  of 60% to 70%, which is characteristic of urban areas (He et al., 2019). The town also features in the northwest sectors for WT. For location M, the  $\lambda_P$  values in sectors from the southeast to the west show that obstacle plan areas occupy less than 10% in all segments, whereas for WT,  $\lambda_P$  in certain segments from  $135^\circ$  to  $225^\circ$  is over 20% and as high as 60%. It should be noted that segments that appear to have no values for  $\lambda_P$ , while having positive values for  $\bar{h}_{AW}$ , indicate obstacles that have very small plan areas compared to the segment area. The obstacle frontal area density  $\lambda_F$ , by definition, places emphases on obstacle width, Eq. (7.3). Values are small as the visible frontal areas, at ground level, per unit height are small compared to total segment plan areas, Fig. 7.8. However, the relative trends are clear in that low broad obstacles close to the locations of interest show the higher values. As expected, values of  $\lambda_F$  from the southeast to northwest for location M are lower where fewer obstacles exist. For location WT, the local campus buildings within 500 m result in the higher values of  $\lambda_P$  in sectors from  $180^\circ$  to  $315^\circ$ .

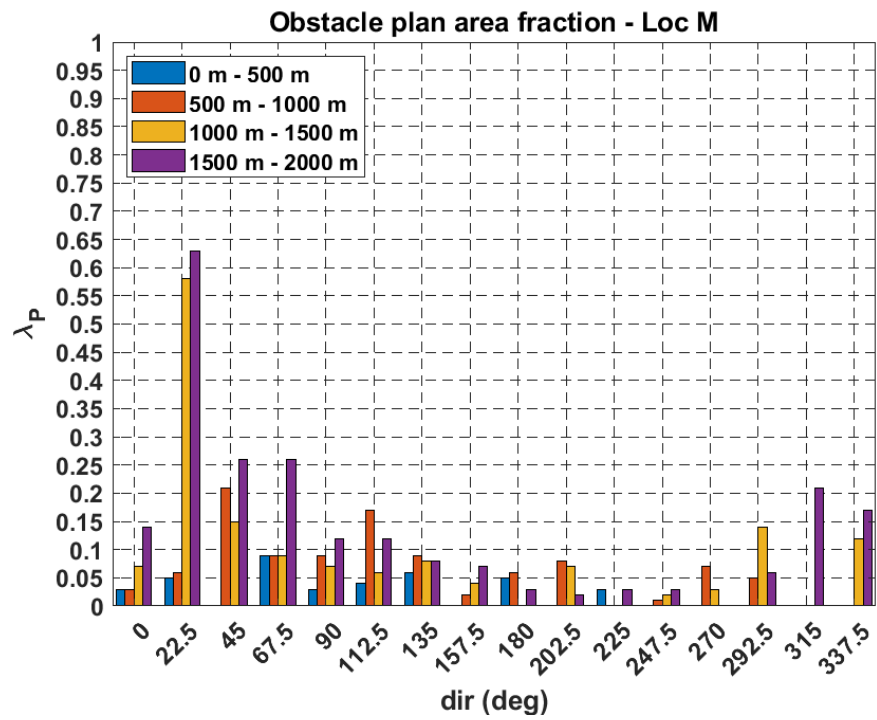
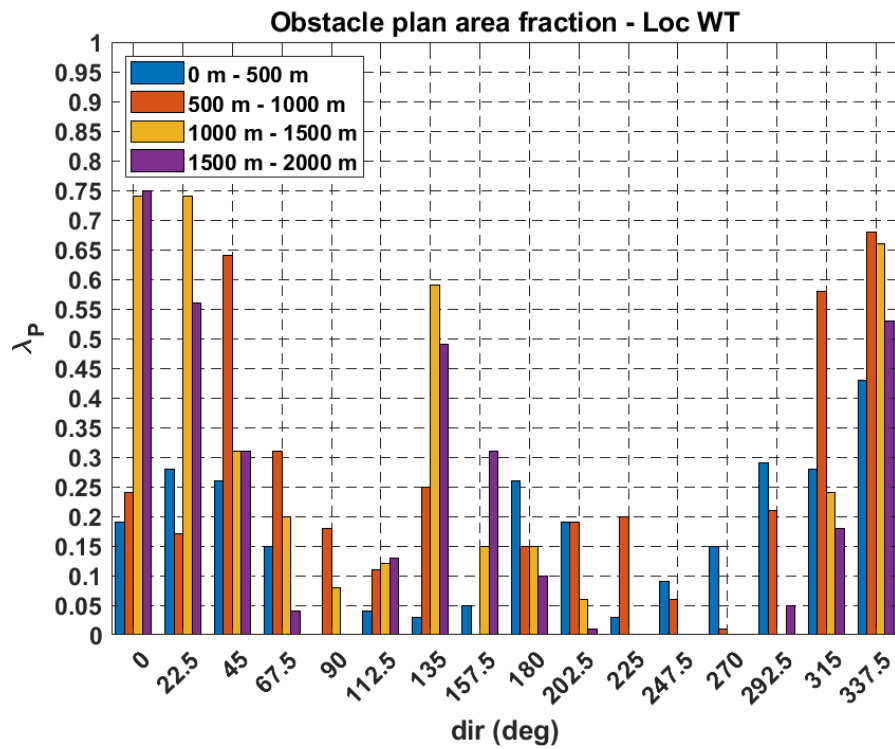
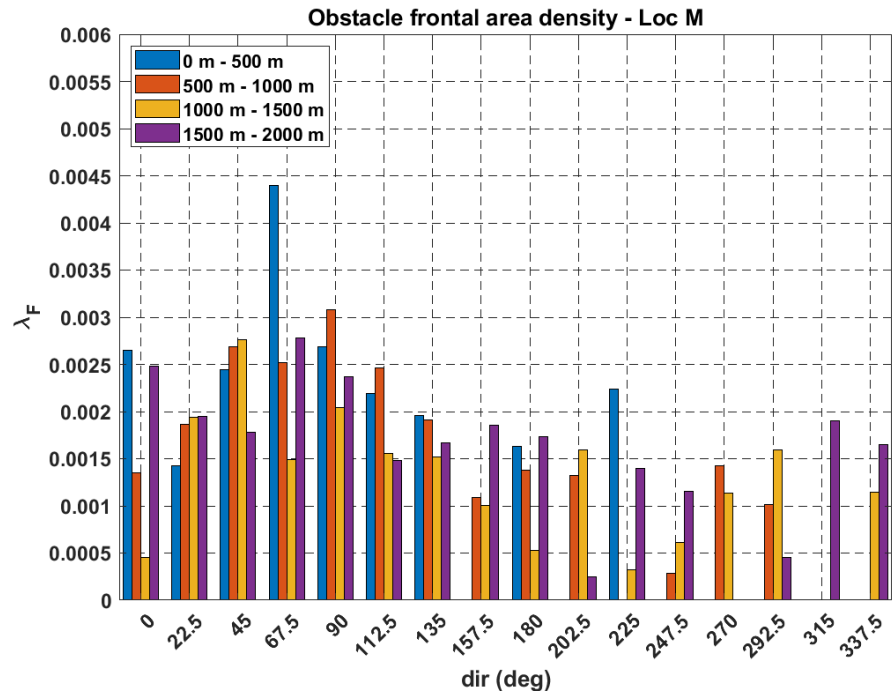
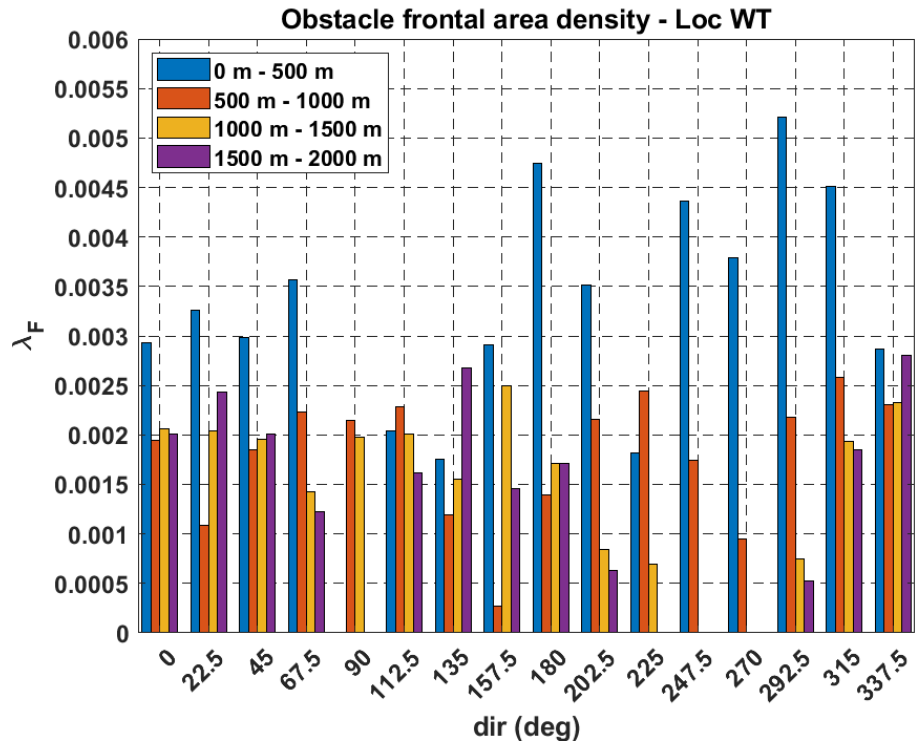
(a)  $\lambda_p$  (M)(b)  $\lambda_p$  (WT)

Fig. 7.7. Obstacle plan area fractions viewed from M and WT.





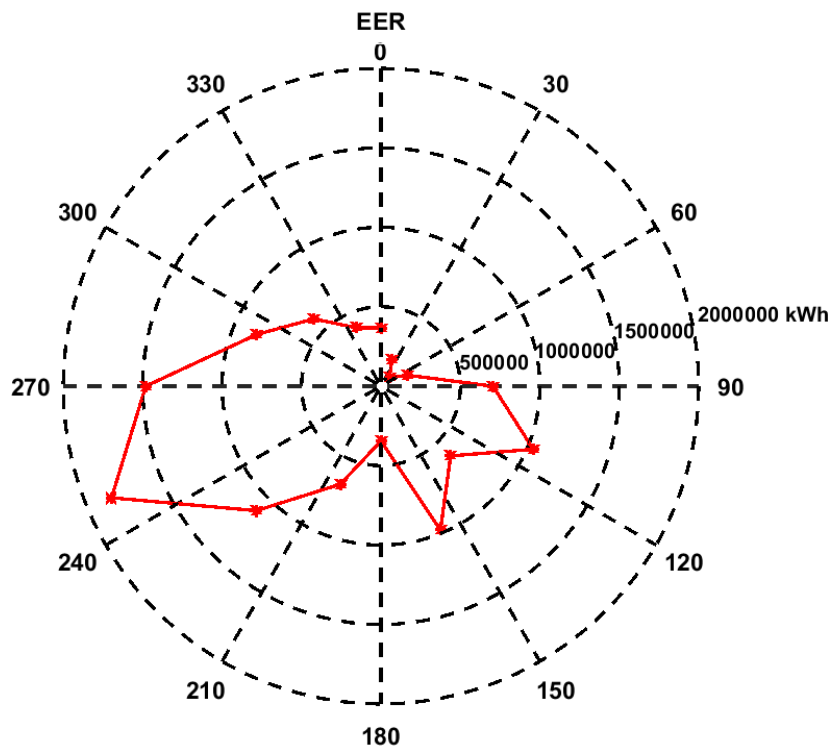
(a)  $\lambda_F$  (M)



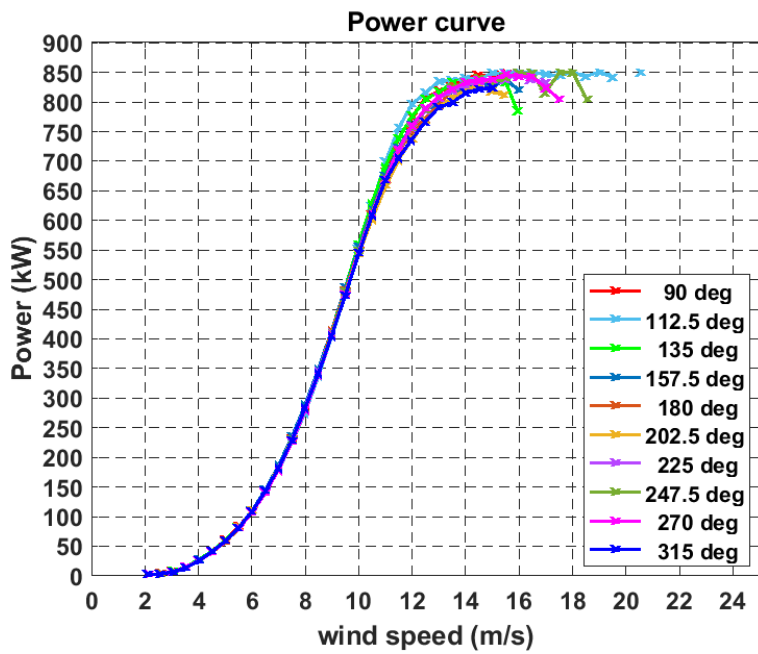
(b)  $\lambda_F$  (WT)

Fig. 7.8. Obstacle frontal area densities viewed from M and WT.

As discussed in previous chapters, the long term *EER* over 7 years, Fig. 7.9, shows that southwest and southeast directions are the most electrically productive sectors. Consecutive energy peaks and troughs are observed in some neighbouring sectors from  $90^\circ$  to  $270^\circ$ . Lower energy values occur in sectors at  $135^\circ$ ,  $180^\circ$  and  $202.5^\circ$  compared with higher energy values in sectors  $112.5^\circ$ ,  $157.5^\circ$  and  $247.5^\circ$ . Selected directions that capture the best and worst case binned power curves show that at winds above 10 m/s, the best power curves occur at  $90^\circ$  and  $112.5^\circ$ , while poorer power curves appear at  $157.5^\circ$ ,  $202.5^\circ$ ,  $225.5^\circ$ , and  $315^\circ$ . However, plots of the directional power standard deviation and turbulence intensity, in Fig. 7.10, clearly illustrate the directional nature of both power performance and turbulence intensity.

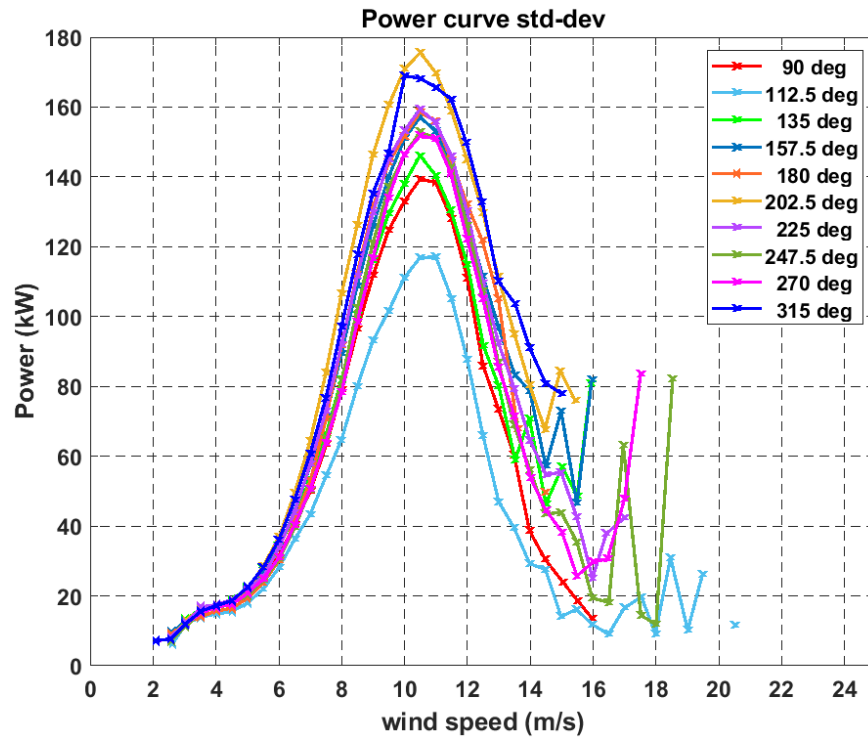


(a) 7-year EER

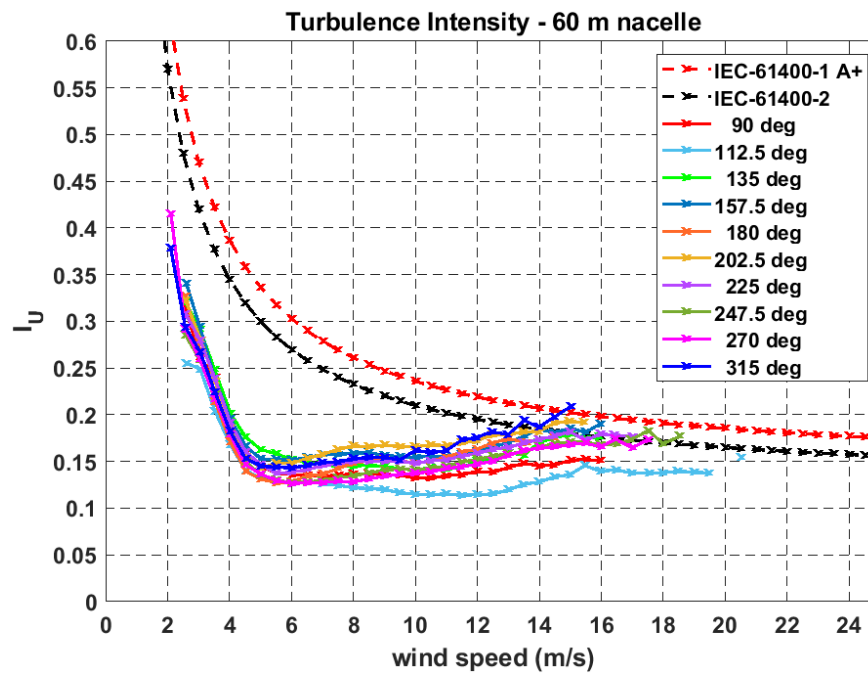


(b) 7-year selected power curves

Fig. 7.9. 7-year EER and selected directional power curves.



(a) directional power curve standard deviation



(b) turbulence intensity

Fig. 7.10. 7-year directional power curve standard deviation and turbulence intensity.

The highest variation power curves occurs in sectors 202.5° and 315° followed by 157.5°, 225° and 180°. In these directions, the turbulence intensity values exceed the A+ levels values of IEC NTM design values at wind speeds of 15 m/s for large scale

winds and the NTM for small scale wind turbines. The lowest variations in power curve occur at  $90^\circ$  and  $112.5^\circ$  and turbulence intensity values fall within both IEC NTM models. Tables 7.2 and 7.3 qualitatively summarises the relative energy and turbulence in these sectors with respect to the obstacle morphological characteristics within each of their four segments for the WT location.

**Table. 7.2.** Sectoral description of energy, turbulence and morphological parameters (easterly to southerly sectors)

Sector ( $^\circ$ )	Description	0 - 500 m	500 - 1000 m	1000 - 1500 m	1500 - 2000 m
90	Low turbulence, better power curve		$h_{AW} = 9 \text{ m},$ $h_{max} = 11 \text{ m},$ $\lambda_P \sim 17\%,$ $\lambda_F = 0.0021,$	$h_{AW} = 9 \text{ m},$ $h_{max} = 11 \text{ m},$ $\lambda_P \sim 7\%,$ $\lambda_F = 0.0020,$	
112	Low turbulence, best case power curve, increased energy output	$h_{AW} = 13 \text{ m},$ $h_{max} = 13 \text{ m},$ $\lambda_P \sim 4\%,$ $\lambda_F = 0.0020,$	$h_{AW} = 9 \text{ m},$ $h_{max} = 14 \text{ m},$ $\lambda_P \sim 11\%,$ $\lambda_F = 0.0023,$	$h_{AW} = 8 \text{ m},$ $h_{max} = 14 \text{ m},$ $\lambda_P \sim 12\%,$ $\lambda_F = 0.0020,$	$h_{AW} = 10 \text{ m},$ $h_{max} = 14 \text{ m},$ $\lambda_P \sim 13\%,$ $\lambda_F = 0.0016,$
135	Turbulence and power curve mid-range between best and worst case, reduced energy output	$h_{AW} = 13 \text{ m},$ $h_{max} = 12 \text{ m},$ $\lambda_P \sim 3\%,$ $\lambda_F = 0.0017,$	$h_{AW} = 9 \text{ m},$ $h_{max} = 11 \text{ m},$ $\lambda_P \sim 25\%,$ $\lambda_F = 0.0012,$	$h_{AW} = 8 \text{ m},$ $h_{max} = 10 \text{ m},$ $\lambda_P \sim 59\%,$ $\lambda_F = 0.0016,$	$h_{AW} = 10 \text{ m},$ $h_{max} = 10 \text{ m},$ $\lambda_P \sim 49\%,$ $\lambda_F = 0.0026,$
157	High turbulence, poorer power curve, increased energy output	$h_{AW} = 17 \text{ m},$ $h_{max} = 47 \text{ m},$ $\lambda_P \sim 5\%,$ $\lambda_F = 0.0029,$		$h_{AW} = 8.5 \text{ m},$ $h_{max} = 12 \text{ m},$ $\lambda_P \sim 15\%,$ $\lambda_F = 0.0025,$	$h_{AW} = 8 \text{ m},$ $h_{max} = 12 \text{ m},$ $\lambda_P \sim 31\%,$ $\lambda_F = 0.0015,$
180	Turbulence and power curve mid-range between best and worst case, low energy output	$h_{AW} = 7 \text{ m},$ $h_{max} = 12 \text{ m},$ $\lambda_P \sim 26\%,$ $\lambda_F = 0.0047,$	$h_{AW} = 7.5 \text{ m},$ $h_{max} = 12 \text{ m},$ $\lambda_P \sim 15\%,$ $\lambda_F = 0.0014,$	$h_{AW} = 9 \text{ m},$ $h_{max} = 12 \text{ m},$ $\lambda_P \sim 15\%,$ $\lambda_F = 0.0017,$	$h_{AW} = 8.5 \text{ m},$ $h_{max} = 25 \text{ m},$ $\lambda_P \sim 10\%,$ $\lambda_F = 0.0017,$

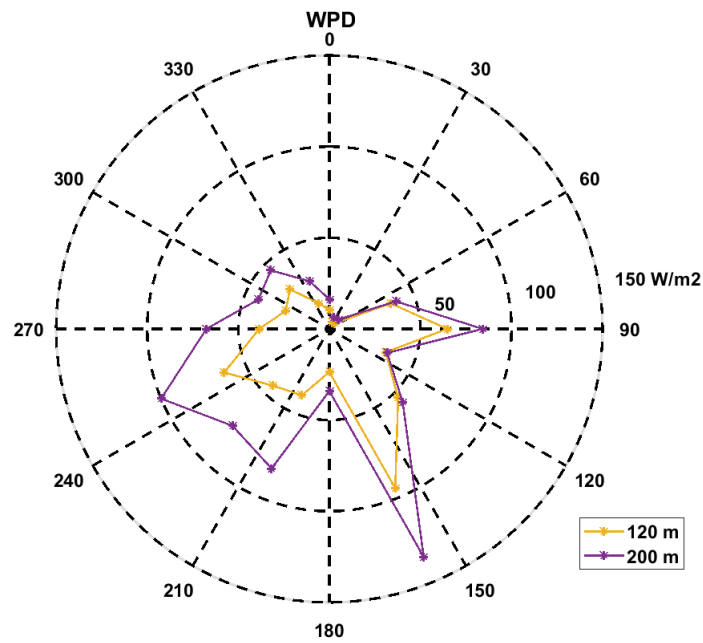
**Table. 7.3.** Sectoral description of energy, turbulence and morphological parameters (westerly to northerly sectors)

Sector (°)	Description	0 - 500 m	500 - 1000 m	1000 - 1500 m	1500 - 2000 m
202.5	High turbulence, highest variation in directional power curves, low energy output	$h_{AW} = 6 \text{ m},$ $h_{max} = 7 \text{ m},$ $\lambda_P \sim 19\%,$ $\lambda_F = 0.0035,$	$h_{AW} = 11 \text{ m},$ $h_{max} = 25 \text{ m},$ $\lambda_P \sim 19\%,$ $\lambda_F = 0.0022,$	$h_{AW} = 20.5 \text{ m},$ $h_{max} = 25 \text{ m},$ $\lambda_P \sim 6\%,$ $\lambda_F = 0.0007$	$h_{AW} = 6 \text{ m},$ $h_{max} = 6 \text{ m},$ $\lambda_P \sim 1\%,$ $\lambda_F = 0.0006,$
225	Turbulence and power curve mid-range between best and worst case, decreased energy output	$h_{AW} = 6 \text{ m},$ $h_{max} = 5 \text{ m},$ $\lambda_P \sim 2\%,$ $\lambda_F = 0.0017,$	$h_{AW} = 11 \text{ m},$ $h_{max} = 7.5 \text{ m},$ $\lambda_P \sim 20\%,$ $\lambda_F = 0.0024,$		
247.5	Turbulence and power curve mid-range between best and worst case, highest energy output	$h_{AW} = 6 \text{ m},$ $h_{max} = 7 \text{ m},$ $\lambda_P \sim 9\%,$ $\lambda_F = 0.0043,$	$h_{AW} = 7.5 \text{ m},$ $h_{max} = 15 \text{ m},$ $\lambda_P \sim 6\%,$ $\lambda_F = 0.0017,$		
270	Turbulence and power curve mid-range between best and worst case, high energy output	$h_{AW} = 7 \text{ m},$ $h_{max} = 13 \text{ m},$ $\lambda_P \sim 15\%,$ $\lambda_F = 0.0037,$	$h_{AW} = 7.5 \text{ m},$ $h_{max} = 7 \text{ m},$ $\lambda_P \sim 1\%,$ $\lambda_F = 0.0014,$		
315	Highest turbulence, poor power curve, decreased energy output	$h_{AW} = 7.5 \text{ m},$ $h_{max} = 8 \text{ m},$ $\lambda_P \sim 25\%,$ $\lambda_F = 0.0045,$	$h_{AW} = 6 \text{ m},$ $h_{max} = 7 \text{ m},$ $\lambda_P \sim 57\%,$ $\lambda_F = 0.0026,$	$h_{AW} = 6.5 \text{ m},$ $h_{max} = 7 \text{ m},$ $\lambda_P \sim 24\%,$ $\lambda_F = 0.0019,$	$h_{AW} = 7 \text{ m},$ $h_{max} = 13 \text{ m},$ $\lambda_P \sim 17\%,$ $\lambda_F = 0.0018,$

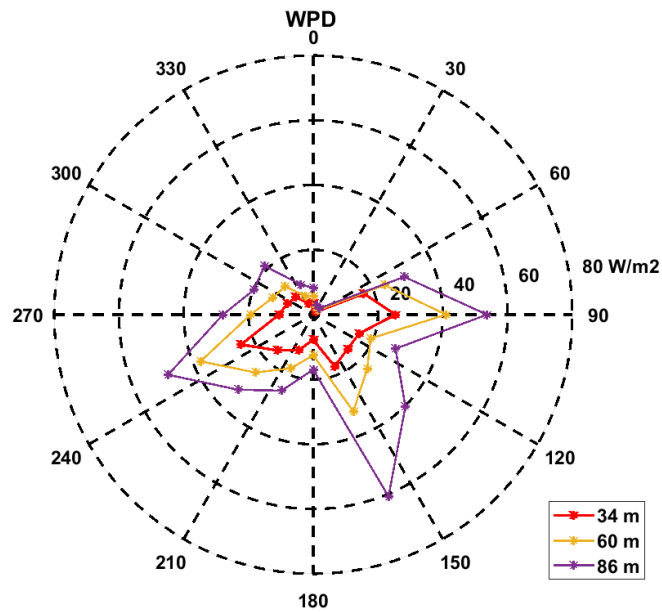
The high turbulence and low energy of sectors of  $315^\circ$ ,  $202.5^\circ$ ,  $225^\circ$  and  $180^\circ$  have  $\lambda_P$  values of  $\sim 20\%$  or higher in a least one of the first two segments up to 1000 m with  $\bar{h}_{AW}$  ranging from 6 m and 11 m. Sector  $202.5^\circ$  has a standout obstacle in its sector with a segment  $h_{max}$  of 25 m. The lowest turbulence sector  $112.5^\circ$  has few obstacles in all segments denoted by lower  $\lambda_P$  values of 4% to 13% and  $\bar{h}_{AW}$  values

ranging from 8 m and 13 m. The  $135^\circ$  sector, with reduced energy, has higher values of  $\lambda_P$  from 25% to 59%. The turbulence is lower than the worst case  $315^\circ$  which may be due to the higher  $\lambda_P$  values occurring further away in the third and fourth segments. Sector  $157.5^\circ$  has values of  $\lambda_P$  from 15% to 31% occurring only in the third and fourth segments. However, it has higher turbulence than for sector  $135^\circ$ , indicating the impact of the standout obstacle of the 47 m (max) high hotel in the first 0 m to 500 m segment. The higher energy sectors at  $247.5^\circ$  and  $270^\circ$  have low  $\lambda_P$  values from 0% to 9%, but do not have the lowest turbulence. As the wind turbine rotor is well above the normal frontal view of the buildings, there are no obvious trends in the values of  $\lambda_F$  with energy or turbulence. These initial findings suggest that  $\lambda_P$  values above 20% in 16 sector divisions, combined with  $\bar{h}_{AW}$  values down to 10% of wind turbine hub-height, within 1 km have an impact on turbulence and energy output. Standout obstacles of above  $\sim 1/3$  of hub-height also have an impact regardless of  $\lambda_P$  value. However, they do not fully explain the higher turbulence in the  $247.5^\circ$  and  $157.5^\circ$  sectors that have low  $\lambda_P$  values.

From Chapter 6, directional *WPD* plots based on one year of LiDAR measurements, at location LiD, from 34 m to 200 m are shown in Fig. 7.11. The *WPD* at the 200 m height shows winds from the Irish Sea specifically dominates the  $157.5^\circ$  sector, indicating a mesoscale influence from the coast. It reduces rapidly with decreasing heights below 120 m compared to its neighbouring sectors. This indicates high wind shear coinciding with the 47 m hotel, i.e., wake effects of this single obstacle in a sector that otherwise has low  $\lambda_P$  values. This can also explain the higher turbulence in this sector. Low values of *WPD* appear at all levels in the  $180^\circ$  sector. This shows that that local buildings are not wholly responsible for reduced energy in this sector, but rather, it is a low energy transition region between the higher southeast winds from the sea and the prevailing south-westerly winds. The *WPD* in the southwest sectors from  $202.5^\circ$  to  $247.5^\circ$  sectors show the prevailing high energy sectors at 200 m. However, the energy in sectors  $202.5^\circ$  and  $225^\circ$  sectors is more reduced from 86 m and below, coinciding with the buildings in these sectors that have  $\lambda_P$  values in the first two sectors of  $\sim 20\%$ . In addition, a stand out 25 m obstacle occurs in the  $202.5^\circ$  sector. These sectors are examined further with respect to the met mast measurements at location M.



(a) 120 m &amp; 200 m



(b) 34 m, 60 m, &amp; 86 m

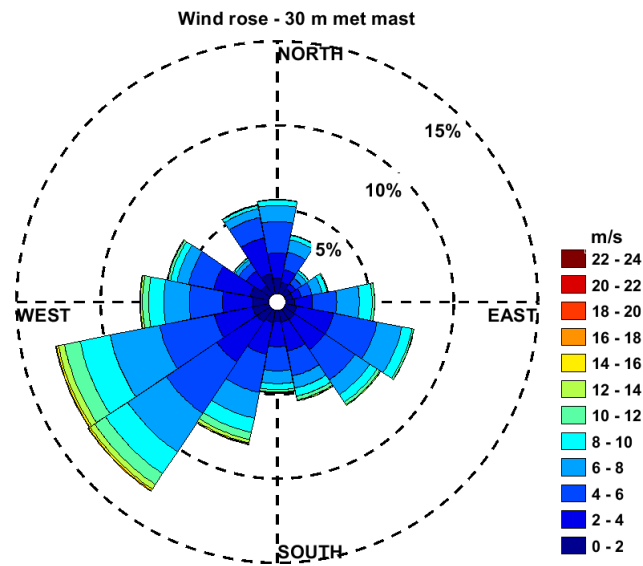
Fig. 7.11. Directional WPD at six heights.

### 7.3.2 Energy comparison between mast and wind turbine locations

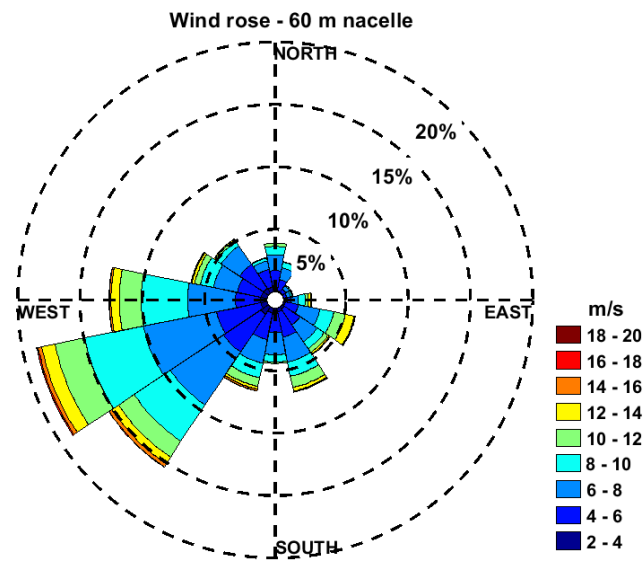
An energy comparison is made between location and M and WT over the same 7-month period from August 2019 to March 2020. Firstly, wind roses at a 30 m height at the met mast and at the 60 m turbine hub-height, Fig. 7.12, show that winds come mostly from the southwest during the assessment period. Sector by sector statistical comparison of the Weibull parameters are shown in Table 7.4. In the case of WT,



the relative frequency of wind data point occurrences in the  $202.5^\circ$  and  $225^\circ$  sectors are lower in comparison to sector  $247.5^\circ$ . At M, the wind occurrences in the  $225^\circ$  and  $247.5^\circ$  sectors are closer in value. There is also a higher frequency of wind data point occurrences in sector  $202.5^\circ$  and lower occurrences in sector  $270^\circ$  compared to WT. This suggests that the buildings to the southwest of WT are having an influence on wind flow. Two sample K-S statistical tests for  $\alpha = 0.05$ , Table 7.4, suggest that many of the sector are significantly different from each other i.e. data values are unlikely from the same data distributions. However, they also suggest that  $180^\circ$  and  $202.5^\circ$  sectors are not significantly different statistically. It is noted that in these two sectors that the Weibull scale factors are higher (i.e. higher wind speeds) at location M such that its wind speed distributions can fully envelope the lower wind speed distributions at location WT. In the  $222.5^\circ$  to  $292^\circ$  sectors the opposite is the case with the location WT having higher scale factors. This suggests the steering of wind flow into the more westerly sectors as location M. The northerly sectors viewed from M have fewer obstacles, Fig. 7.7, and have higher wind occurrences compared to WT. The southeast occurrences are also different at M, that also has a different obstacle morphology, but in both cases winds are too low during the assessment period to have a significant energy impact.



(a) 30 m wind rose at location M



(b) 60 m wind rose at location WT

Fig. 7.12. 7-month wind roses at M and WT.

**Table. 7.4.** Met mast and SCADA data and K-S statistic tests,  $\alpha = 0.05$ 

	Met Mast			SCADA data			K-S test	
Sector (°)	c	k	Rel' Freq.(%)	c	k	Rel' Freq.(%)	p	k <sub>s</sub>
0.0	6.62	2.91	4.93	6.28	2.19	4.19	0.14	0.04
22.5	6.55	2.96	2.59	6.16	2.39	2.77	0.21	0.05
45.0	5.24	2.56	0.98	4.94	1.72	1.12	0.00	0.15
67.5	5.75	2.47	1.72	6.01	1.67	1.02	0.00	0.18
90.0	6.75	2.66	3.16	7.30	2.00	2.27	0.00	0.13
112.5	6.69	2.63	5.39	8.34	2.19	5.41	0.00	0.25
135.0	6.51	2.22	6.08	6.61	2.01	4.79	0.00	0.12
157.5	6.98	2.37	6.75	7.43	2.20	6.52	0.00	0.14
180.0	6.68	2.63	5.60	6.33	2.40	4.81	0.11	0.04
202.5	7.73	2.29	10.73	7.34	2.11	7.18	0.62	0.01
225.0	7.78	2.65	19.08	7.92	2.54	14.48	0.00	0.07
247.5	8.35	2.64	18.03	8.48	2.59	17.65	0.00	0.05
270.0	7.59	2.65	9.52	8.09	2.40	12.07	0.00	0.16
292.5	6.63	2.48	2.71	6.29	1.83	6.98	0.03	0.06
315.0	6.77	2.98	0.13	5.24	1.86	5.31	0.96	0.03
337.5	6.07	3.04	2.61	4.98	2.06	3.42	0.99	0.00

The hourly mean differences between the 10-minute time series wind speed and direction data of the met mast logger are compared with the wind turbine SCADA data Fig. 7.13 over the total directional range  $180^\circ$  to  $360^\circ$  of most interest. A positive directional shift is observed from  $\sim 0^\circ$  to almost  $20^\circ$  at the WT location i.e. a westerly shift. In general the wind speeds are less at location WT, but a correlation appears to exist between wind direction difference and wind speed difference between both locations. As the wind difference reduces the directional shift increases, indicating a recovery of wind speeds in a neighbouring directional sector from a more blocked sector. The cyclical diurnal nature wind speeds, highlighted in Chapter 4, can also be observed showing that more unstable (windier) atmospheric conditions in the afternoon is when wind steering may be more prominent, giving

lower wind speed differences. However, these results should be taken as preliminary as comparing independent time series (time stamped) data directly between in the met mast logger and wind turbine SCADA can be subject independent clock drift and therefore would require further investigation.

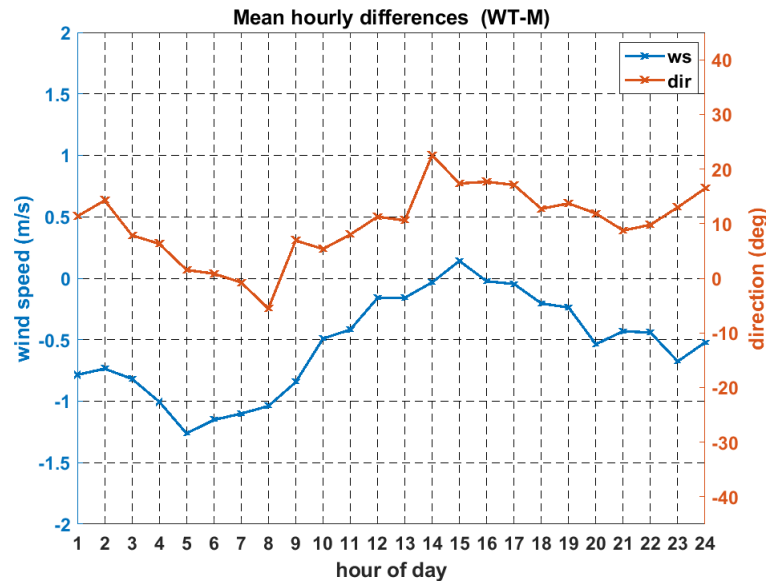
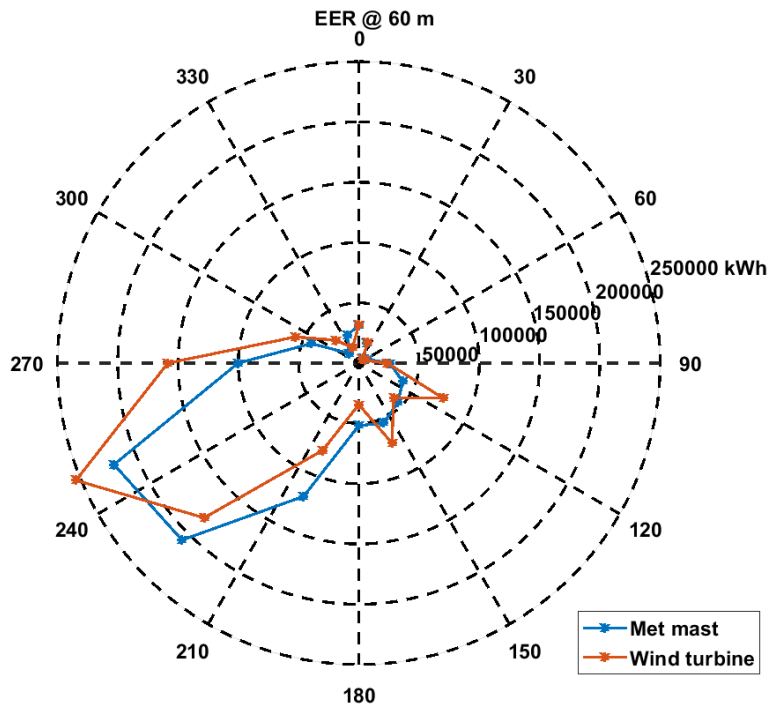
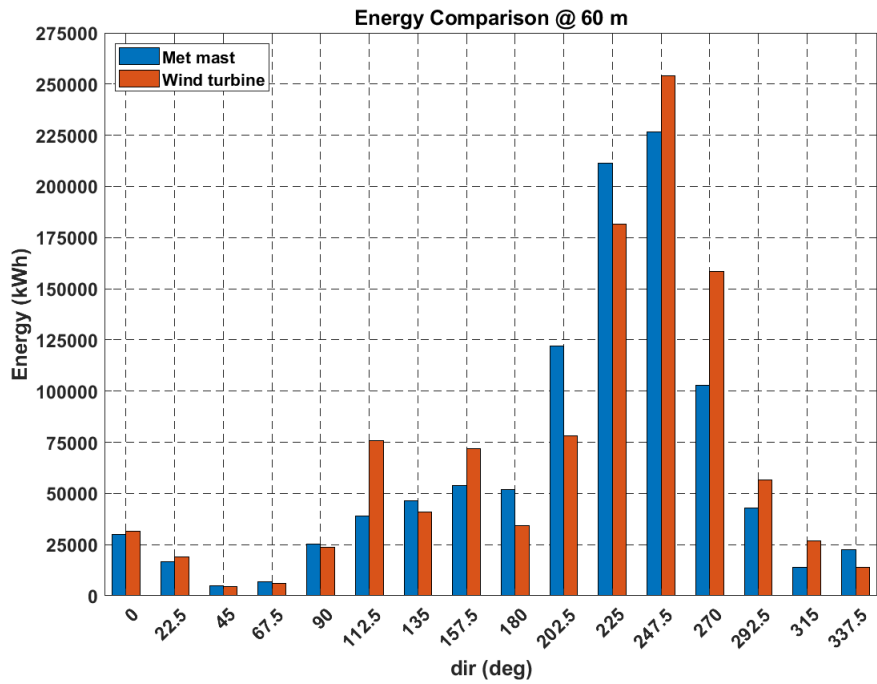


Fig. 7.13. Mean hourly differences in wind speed and direction from south to north between the WT and met M.

The impact on energy is illustrated using an *EER* overlay at hub height at locations M and WT location is shown Fig. 7.14. Here, the met mast data at M projected to 60 m using the power law Eq. (7.5) with measured data at 10 m and 30 m and combined with turbine power curve to produce the 60 m *EER* at M. A directional shift in energy towards the west appears at the turbine location WT.



(a) 60 m, 7-month *EER* comparison



(b) 60 m, directional energy comparison

**Fig. 7.14.** 7-month *EER* and directional energy comparisons between locations M & WT.

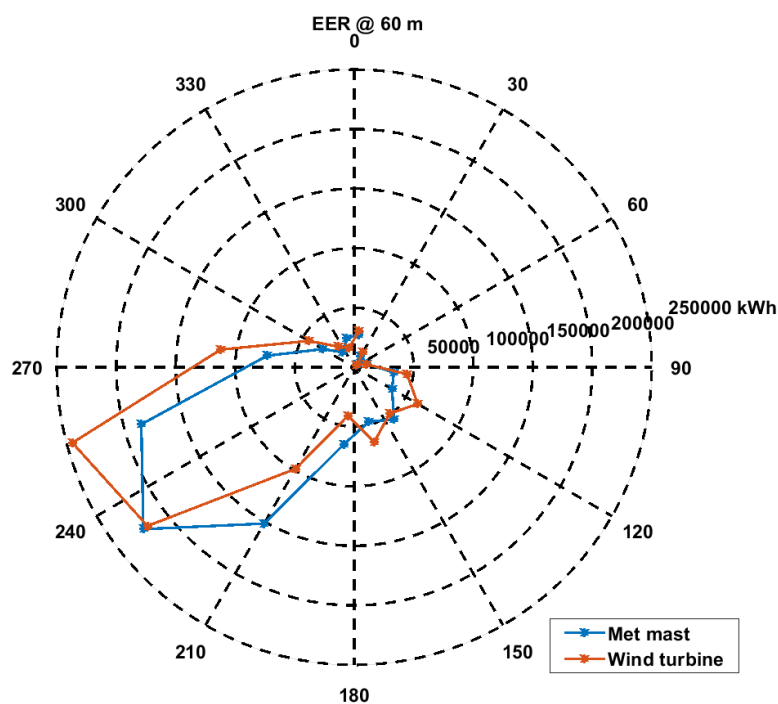
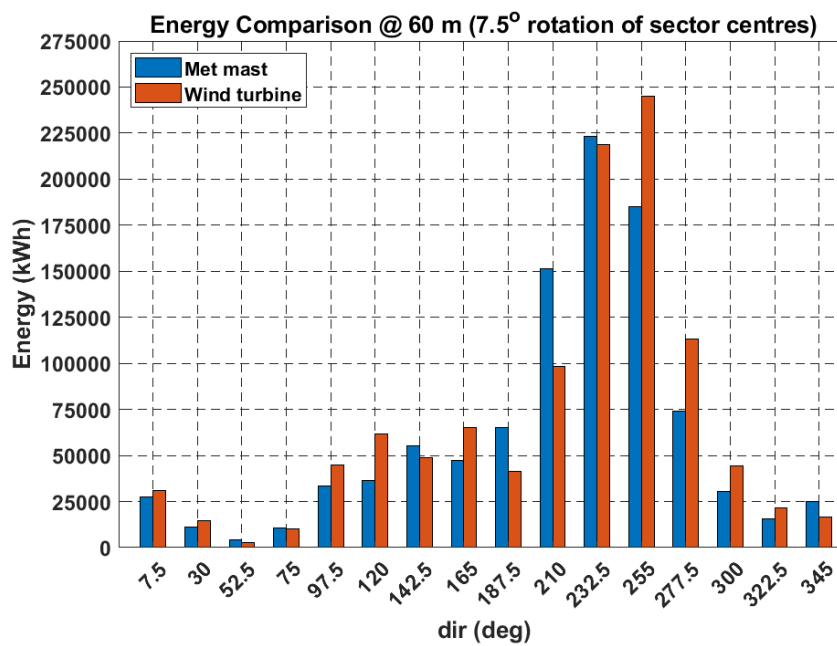
**Table. 7.5.** 7-month directional energy comparison

Sector (°)	Met Mast M (kWh)	Wind turbine WT (kWh)	Difference (WT-M) (kWh)
0	30076	31518	1442
22.5	16648	18829	2181
45	4810	4408	-402
67.5	6951	5905	-1045
90	25377	23620	-1758
112.5	39161	75638	36477
135	46522	41026	-5497
157.5	54051	71707	17656
180	52086	34375	-17711
202.5	122136	78334	-43803
225	211169	181382	-29787
247.5	226658	253963	27305
270	102653	158392	55738
292.5	42896	56784	13888
315	13868	26825	12956
337.5	22507	13767	-8740
<b>Total</b>	<b>1017571</b>	<b>1076473</b>	<b>58902</b>

The directional energy values in Table 7.5 show that the biggest energy reductions at location WT are in the 202.5° and 225° sectors. However, these appear to be compensated by energy enhancements in the 247.5° and 270° sectors. This suggests the low-rise buildings in the 202.5° and 225° sectors,  $\lambda_P$  above 20% in first two segments, are having a steering influence of the winds into the more open 247.5° and 270° sectors whose  $\lambda_P$  values are below 20%. Low occurrences of wind and energy appear in the east to south sectors at both locations over the test period. However, the energy is distributed more evenly over these sectors in the case of M that has low  $\lambda_P$  values, well below 20%. The WT location has a better fetch to coast but small energy enhancements occur in sectors 112.5° and 157.5° with reductions in sectors 135° and 180°, which have  $\lambda_P$  above 20% in their first two segments. These findings

suggest that if a sector is occupied by obstacles ( $\lambda_P > 20\%$ ) and has neighbouring open sectors with fewer obstacles, then it is possible for energy to be shifted into the open sector(s) without a significant overall loss in energy. However, this may have implications for enhancing turbulence and wind gusts.

To assess these findings further, the data is analysed with the directional sector centres shifted by  $7.5^\circ$ ,  $15^\circ$  and a full sector width of  $22.5^\circ$  respectively. Fig. 7.21(a) and Table 7.6 show the results for the  $7.5^\circ$ . A similar trend is observed in that the  $210^\circ$  sector at location M has more energy at compared to location WT, becoming almost equal, though still slightly higher, at  $232.5^\circ$  and then enhanced in the more westerly sector of  $255^\circ$  at location WT. For the directional sector centre of rotation of  $15^\circ$  the enhancement of energy at location begins at  $240^\circ$  becoming more enhanced at  $262.5^\circ$ , Fig. 7.21(b) and Table 7.7. These results from the shift support the initial observations that buildings in the southwest sectors are having a steering impact on the southerly winds, shifting them in a westerly direction on to the wind turbine site. From the three sets of analysis, the direction at which the energy deficit turns to energy enhancement occurs between  $232.5^\circ$  and  $240^\circ$ . which coincides with near where the low rise buildings end their northerly side i.e. view from WT opens to the west. Rotating the directional sector centres by  $22.5^\circ$ , Fig. 7.17 and Table 7.8, is a rotation by a full directional sector and repeats results of the original analysis of Fig. 7.14 and Table 7.5, as would be expected and thereby further confirming that the buildings are having an energy steering impact.

(a) 60 m, 7-month *EER* comparison

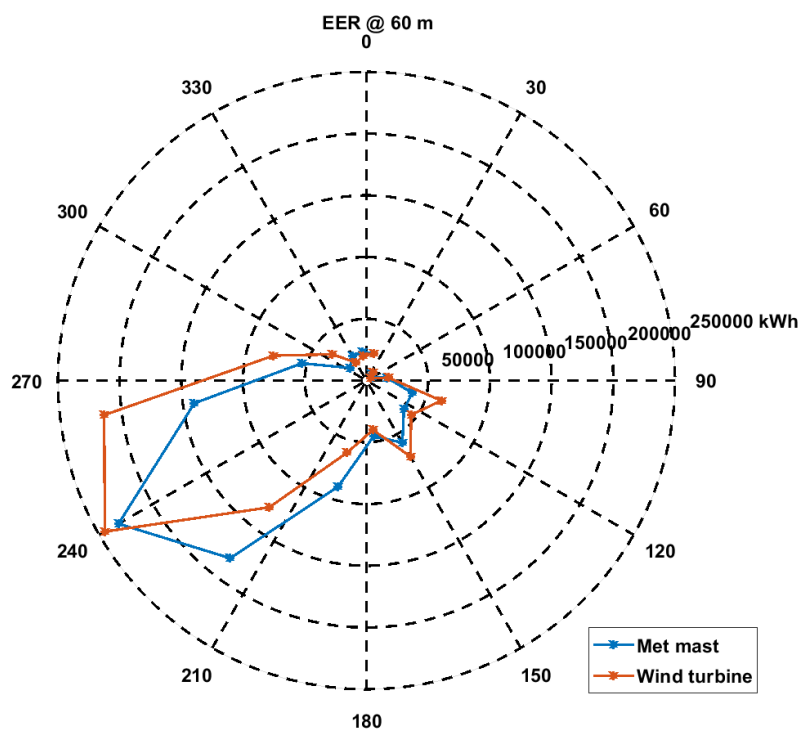
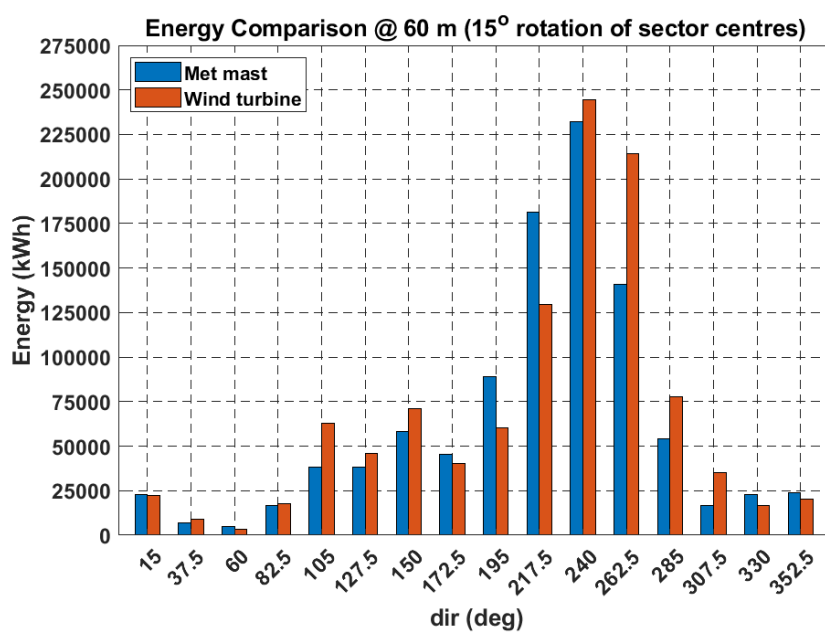
(b) 60 m, directional energy comparison

Fig. 7.15. 7-month *EER* and directional energy comparisons between locations M & WT for a bin centre clockwise rotation of 7.5°.



**Table. 7.6.** 7-month directional energy comparison

Sector ( $^{\circ}$ )	Met Mast M (kWh)	Wind turbine WT (kWh)	Difference (WT-M) (kWh)
7.5	28280	30799	2518
30	11154	14381	3227
52.5	4389	2531	-1858
75	10890	10048	-842
97.5	34324	44705	10381
120	37316	61653	24337
142.5	56338	48960	-7377
165	48268	64984	16716
187.5	66525	41138	-25387
210	154743	98465	-56277
232.5	228022	218939	-9083
255	189092	245140	56049
277.5	75406	113216	37810
300	31116	44195	13080
322.5	16149	21750	5600
345	25559	16751	-8808
<b>Total</b>	<b>1017571</b>	<b>1077656</b>	<b>60085</b>

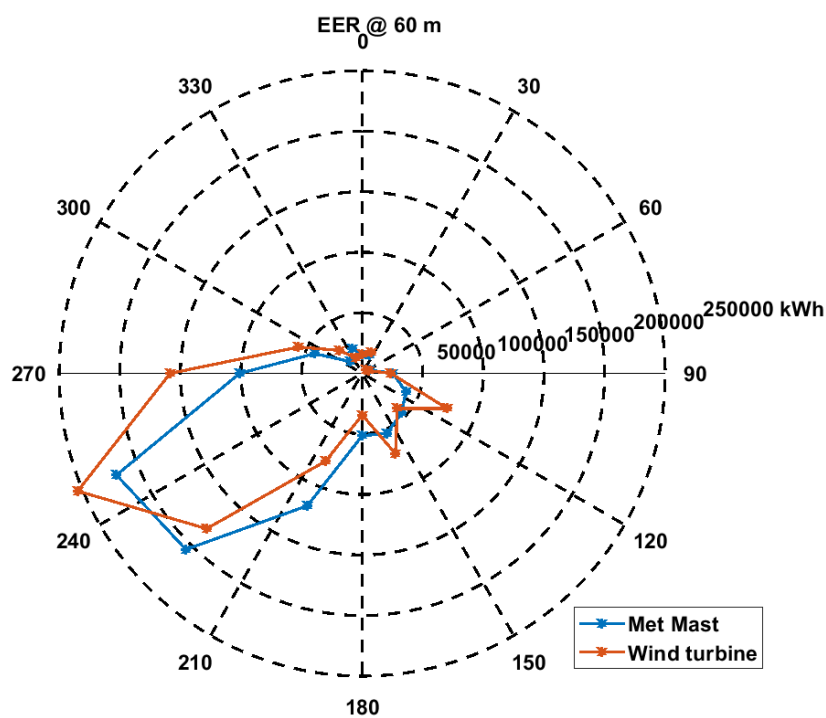
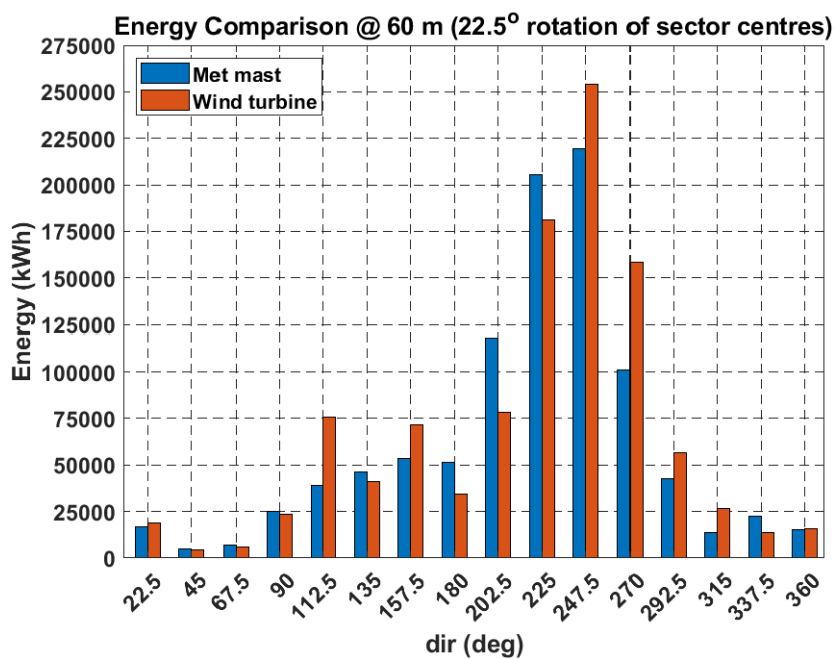
(a) 60 m, 7-month *EER* comparison

(b) 60 m, directional energy comparison

Fig. 7.16. 7-month *EER* and directional energy comparisons between locations M & WT for a bin centre clockwise rotation of 15°.

**Table. 7.7.** 7-month directional energy comparison

Sector ( $^{\circ}$ )	Met Mast M (kWh)	Wind turbine WT (kWh)	Difference (WT-M) (kWh)
15	23116	22355	-760
37.5	7145	8748	1603
60	5182	3585	-1597
82.5	17010	17955	945
105	39248	62772	23523
127.5	39050	45705	6656
150	59402	70969	11566
172.5	46306	40291	-6015
195	90862	60415	-30447
217.5	185133	129410	-55723
240	236828	244628	7800
262.5	143555	214375	70820
285	55165	77929	22764
307.5	17053	34890	17837
330	23165	16725	-6440
352.5	24112	20238	-3875
<b>Total</b>	<b>1012332</b>	<b>1070990</b>	<b>58658</b>

(a) 60 m, 7-month *EER* comparison

(b) 60 m, directional energy comparison

**Fig. 7.17.** 7-month *EER* and directional energy comparisons between locations M & WT for a bin centre clockwise rotation of 22.5°.

**Table. 7.8.** 7-month directional energy comparison

Sector ( $^{\circ}$ )	Met Mast M (kWh)	Wind turbine WT (kWh)	Difference (WT-M) (kWh)
22.5	17157	18829	1672
45	4939	4408	-531
67.5	7169	5905	-1264
90	26164	23620	-2545
112.5	40407	75638	35230
135	47731	41026	-6706
157.5	55428	71707	16280
180	53421	34375	-19046
202.5	122616	78334	-44283
225	213109	181382	-31726
247.5	227275	253963	26688
270	104664	158392	53727
292.5	44058	56784	12726
315	14270	26825	12554
337.5	23168	13767	-9401
360	15993	15637	-355
<b>Total</b>	<b>1017571</b>	<b>1060592</b>	<b>43021</b>

### 7.3.3 Turbulence intensity and gust factor comparison between mast and wind turbine locations

A comparison of the measured directional turbulence intensity at location M, at a 30 m height, with the WT location at hub-height is shown in Fig. 7.18. Clearly, the turbulence intensity at M is below IEC NTM levels and shows less directional variation when compared to location WT. The sectors with the higher turbulence at M are in the easterly sectors and lower in the south-westerly sectors. This can be explained by the buildings to the east. As was observed in the long-term data analysis previously, the high turbulence at location WT occurs in the 202.5°, 225°, 247.5° and 315° sectors and approaches the limits of IEC NTM models. The turbulence intensity in the 90° and 112.5° sectors at location WT have the lowest values as they have

the fewest obstacles in these sectors. Similar trends are seen in the directional gust factors, Fig. 7.19, with values approaching 1.4 in the higher turbulence sectors. This suggests that energy shifted from the sectors with obstacles to neighbouring open sectors is accompanied by increases in turbulence intensity and gust factors.

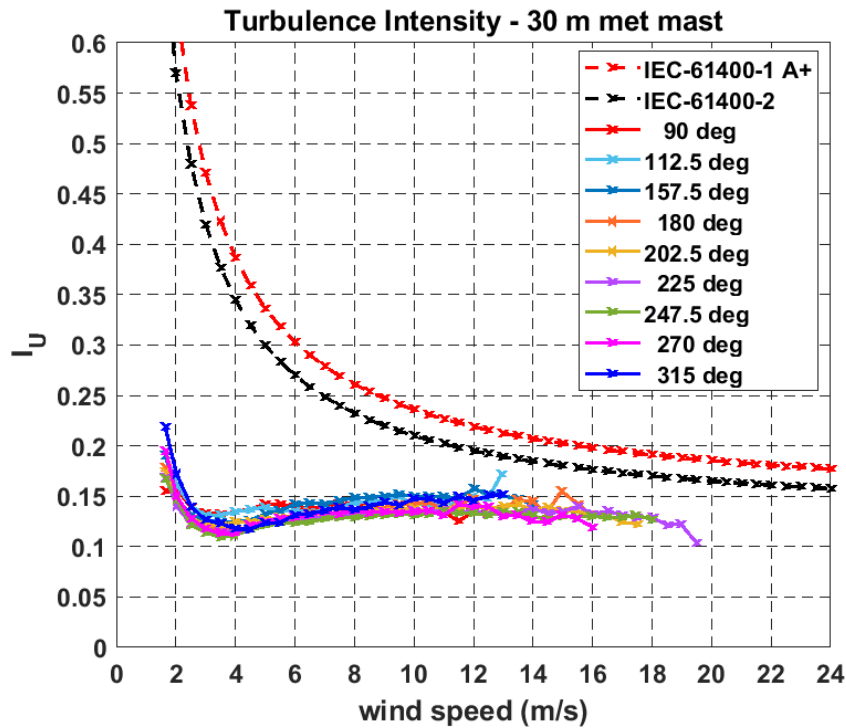
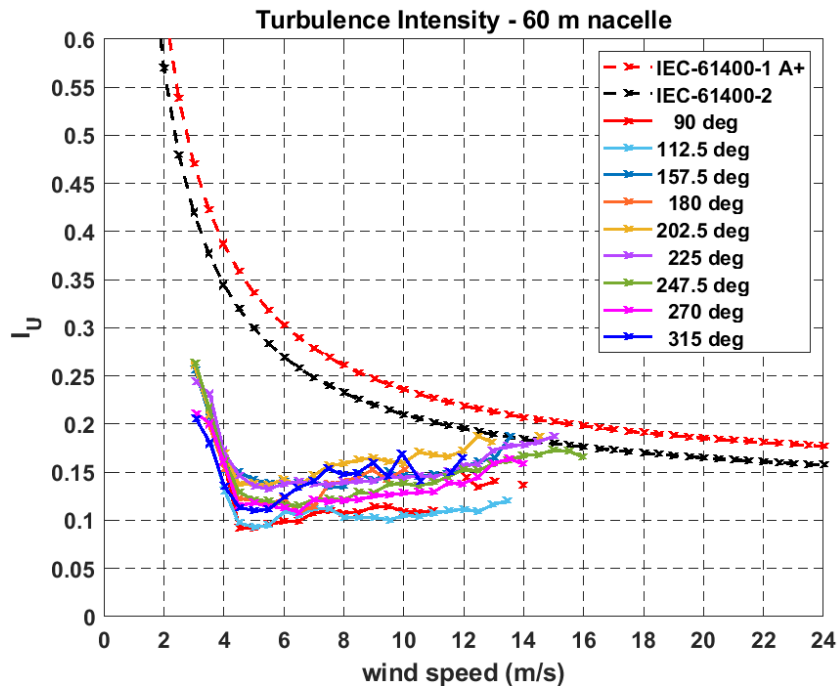
(a) directional  $I_U$  at M(b) directional  $I_U$  at WT

Fig. 7.18. Directional turbulence intensity at M and WT.

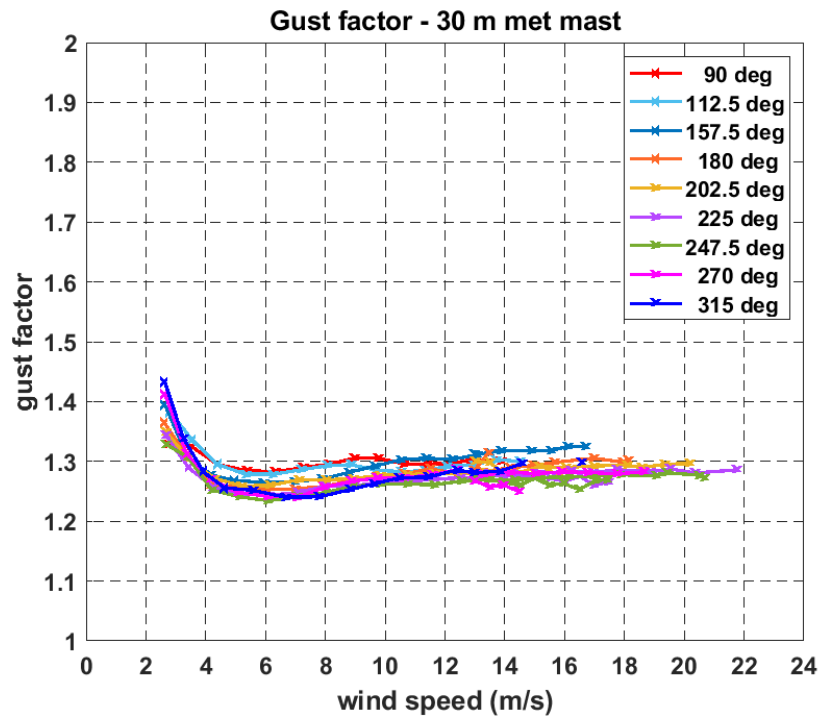
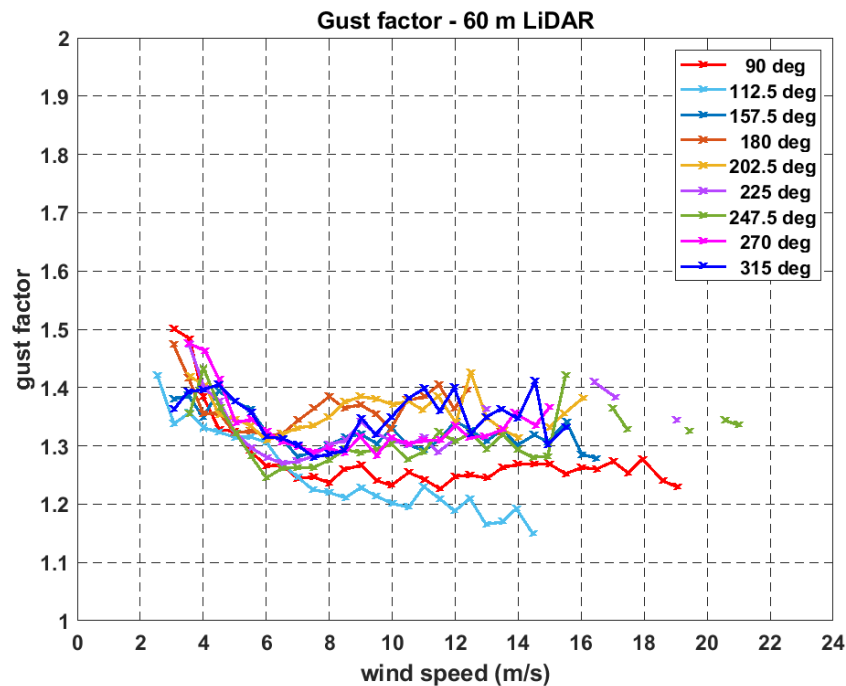
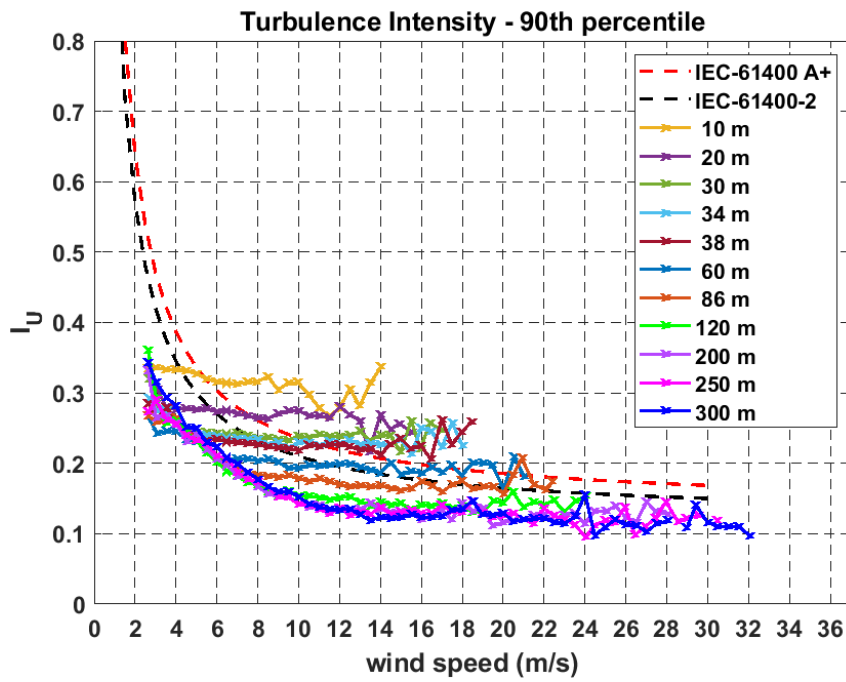
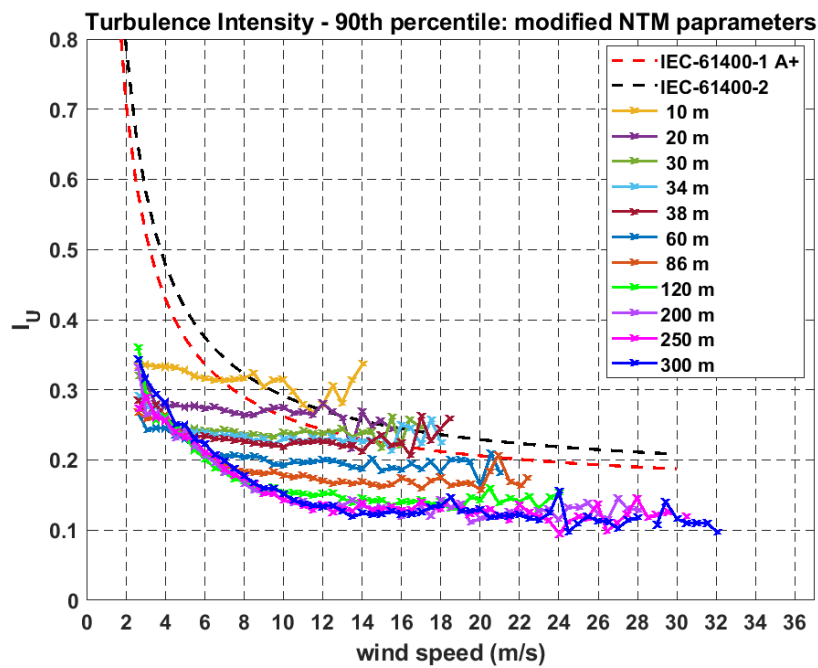
(a) directional  $G_U$  at M(b) directional  $G_U$  at WT

Fig. 7.19. Directional gust factors at M and WT.

As turbulence intensity and gust factors are statistical and important parameters for extreme load calculations in the design of wind turbines, the mean binned values do not fully capture their potential ranges. For information of interest to IEC wind turbine standard development regarding peri-urban environments, the 90<sup>th</sup> percentile

of omnidirectional turbulence intensity at different heights are shown in Fig. 7.20. The plots show that below 60 m the IEC design standard values at 15 m/s are exceeded and need to be at 86 m to meet current IEC recommendations. Typically, medium and large scale wind turbines have hub heights above 30 m and small scale turbines heights up to 30 m. Suggested modifications to the IEC NTMs are for low-rise peri-urban are also plotted. The modification to Eq. (7.10) is  $I_{ref} = 0.2$  and to Eq. (7.11),  $I_{ref} = 0.25$ . These suggestions are for hub-heights from 2 to 6 times the value of  $\bar{h}_{AW}$ , i.e.,  $\sim 20$  m to 60 m here. Below this height range the turbulence intensity appears excessive, while above it the existing NTM models appear to be valid. However, further research is required in this area.

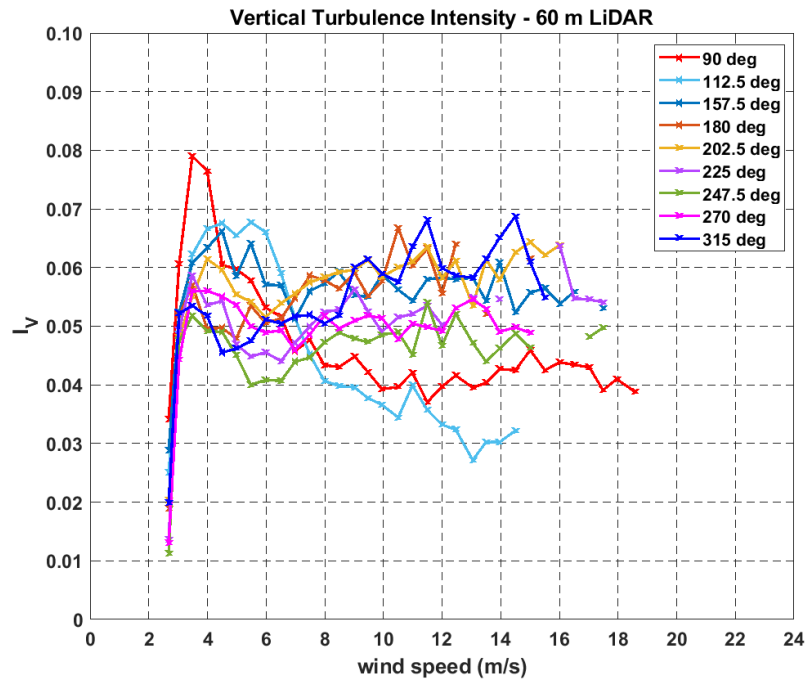
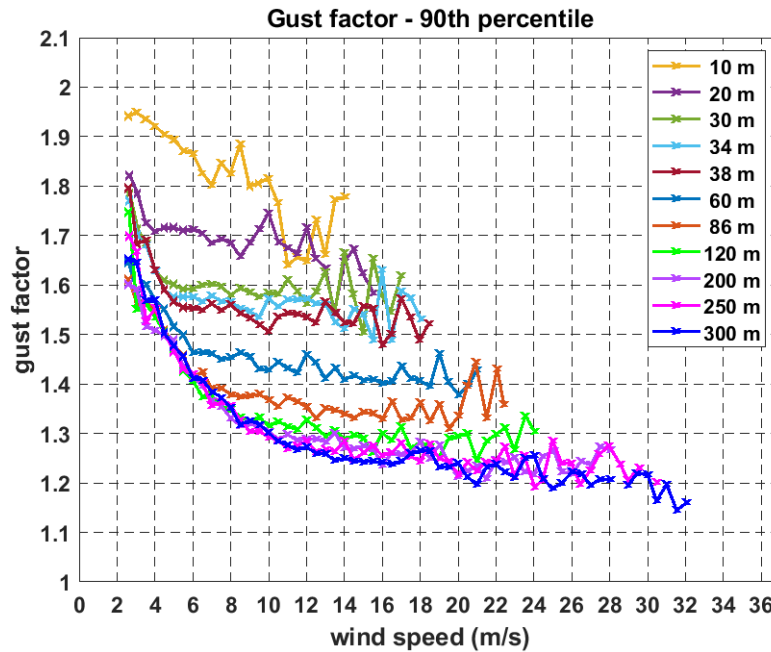


(a) 90<sup>th</sup> percentile turbulence intensity

(b) suggested modification to IEC NTMs

**Fig. 7.20.** 90<sup>th</sup> percentile turbulence intensity at various heights and suggested modification to IEC NTMs.

Vertical turbulence intensity is not currently considered in IEC standards. The mean binned directional vertical turbulence at 60 m for the LiDAR location shows a high range. It is observed to be approximately one third of horizontal turbulence intensity Fig. 7.21(a) The directional trends are similar to the horizontal turbulence intensity. The 90<sup>th</sup> percentile gust factors are at 1.4 at 60 m and below, Fig. 7.21(b).

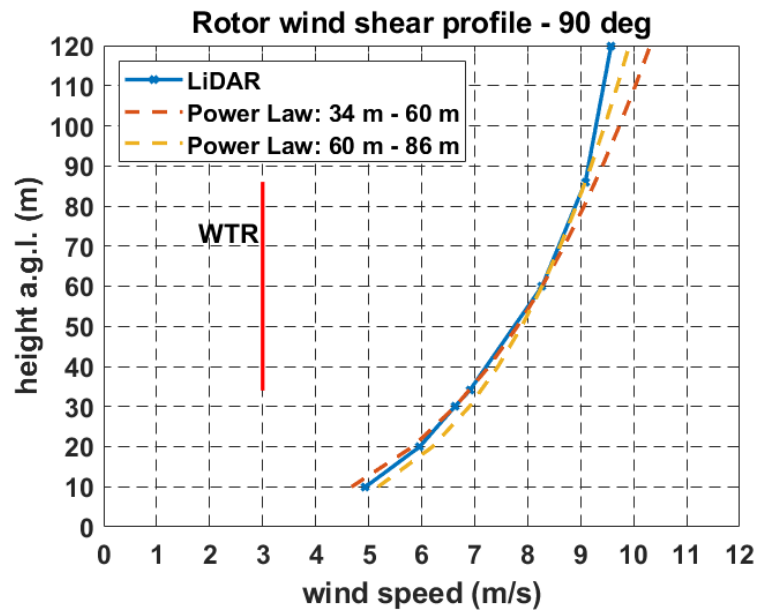
(a) Directional  $I_W$  at 60 m(b) omnidirectional 90<sup>th</sup> percentile gust factors

**Fig. 7.21.** Directional vertical turbulence intensity at 60 m and omnidirectional 90<sup>th</sup> percentile gust factors.

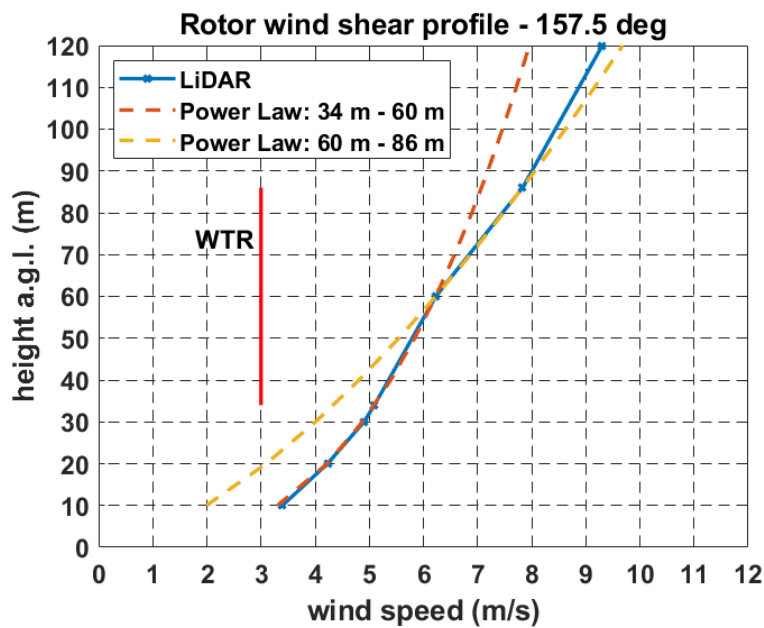
These findings suggest that even though there may not be significant losses in energy due to energy being shifted from one sector to another, increases in turbulence intensity and gust factors may have implications for turbine wear and operational life. In particular at 60 m and below, IEC NTM predictions are exceeded and gust factors are high in this peri-urban environment.

### 7.3.4 Wind shear across the rotor and REWS

LiDAR measured wind shear profile across the rotor disc in the sectors of interest are given in Fig. 7.22. Directional power law profiles are fitted to both the bottom and top halves of rotor disc using one year of measured LiDAR measured data 34 m to 60 m and 60 m to 86 m. The fitted profiles are extended down to 10 m and up to 120 m alongside the measured LiDAR profiles.

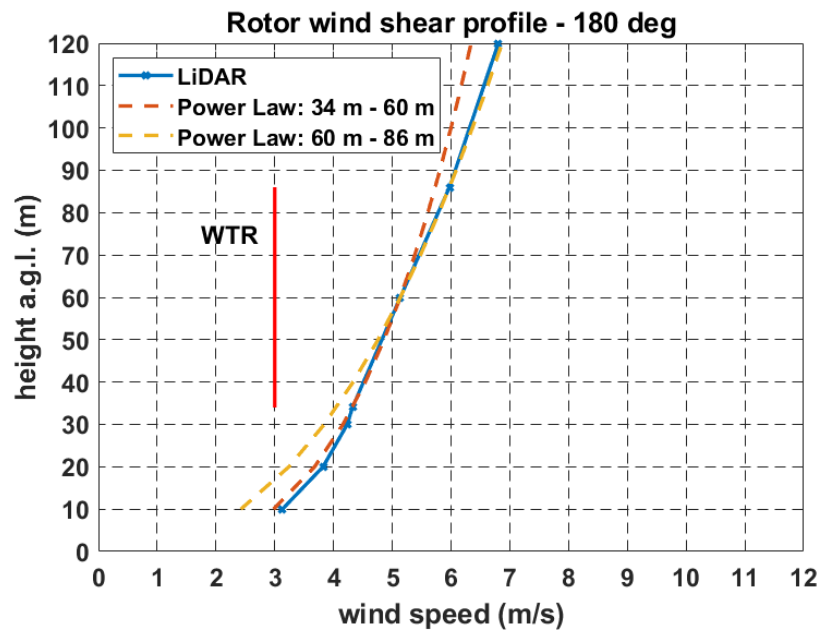


(a) 90°

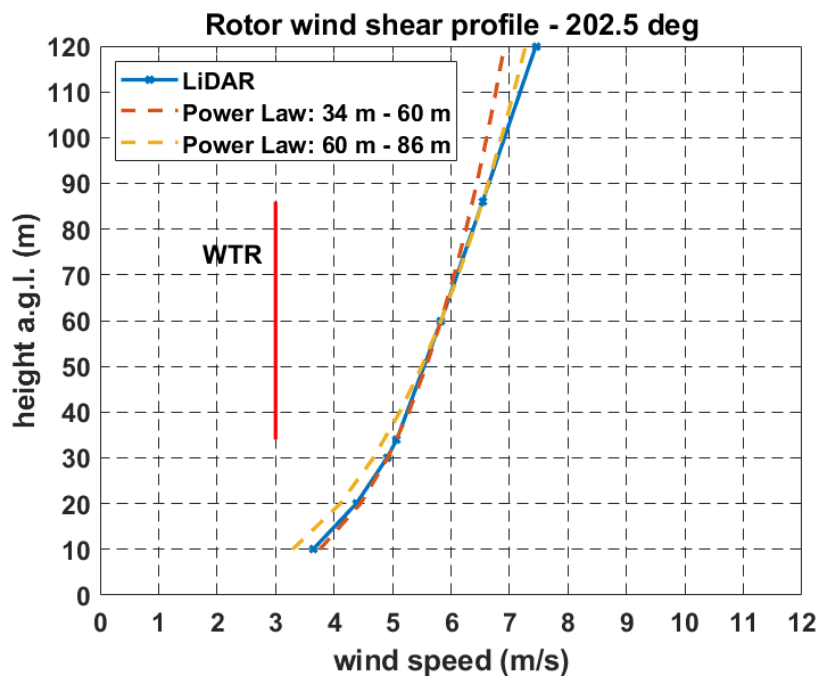


(b) 157.5°

Fig. 7.22. Fitted power law profiles to LiDAR measured directional wind profiles across the rotor disc WTR (90°, 157.5°).



(a) 180°



(b) 202.5°

**Fig. 7.23.** Fitted power law profiles to LiDAR measured directional wind profiles across the rotor disc WTR (180°, 202.5°).

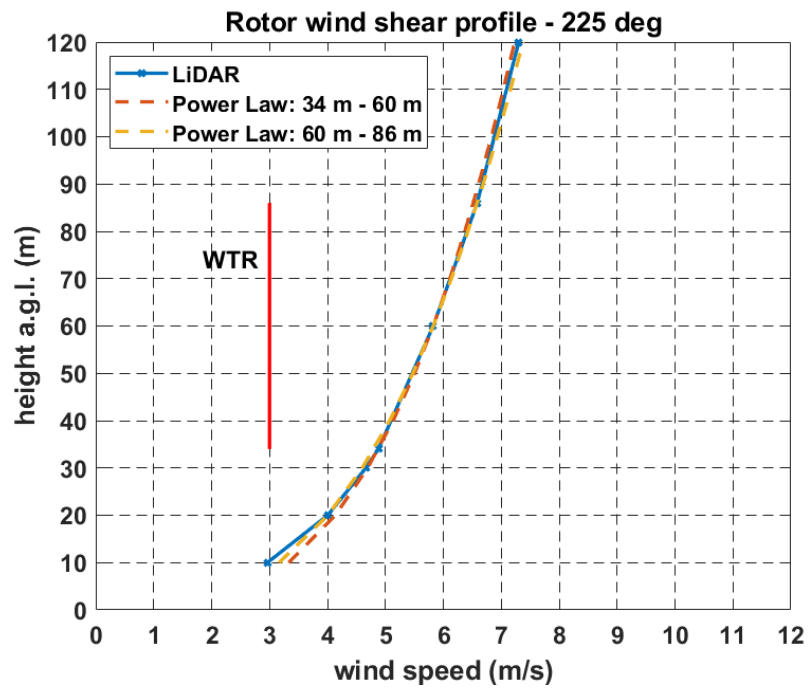
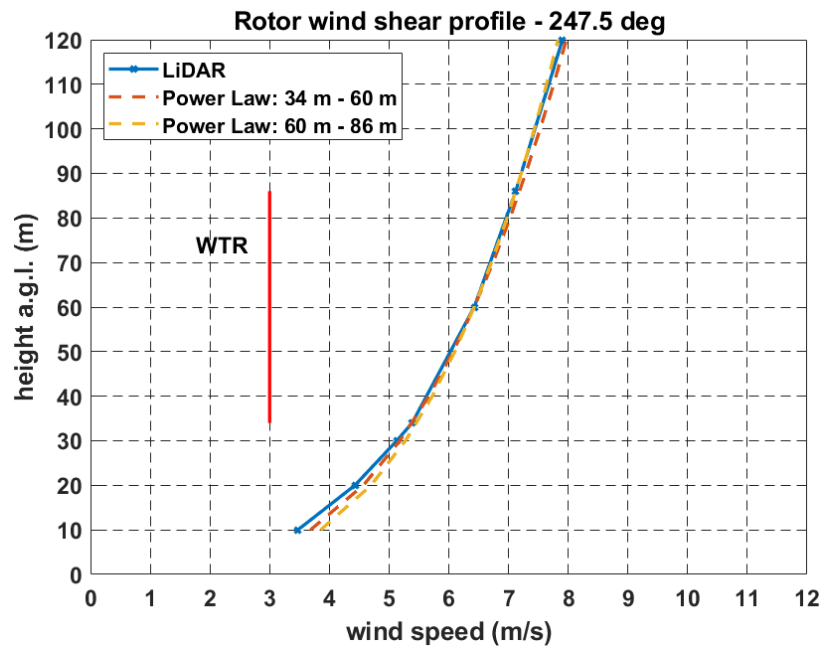
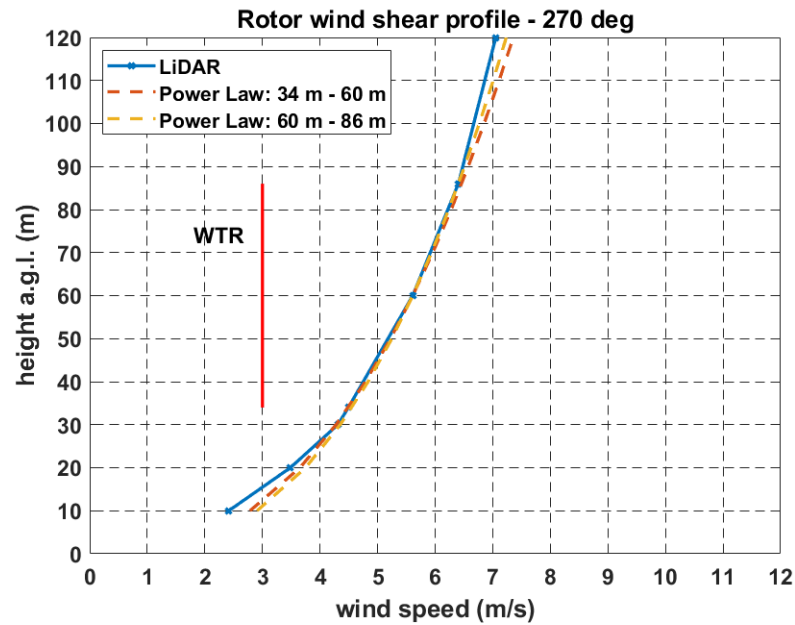
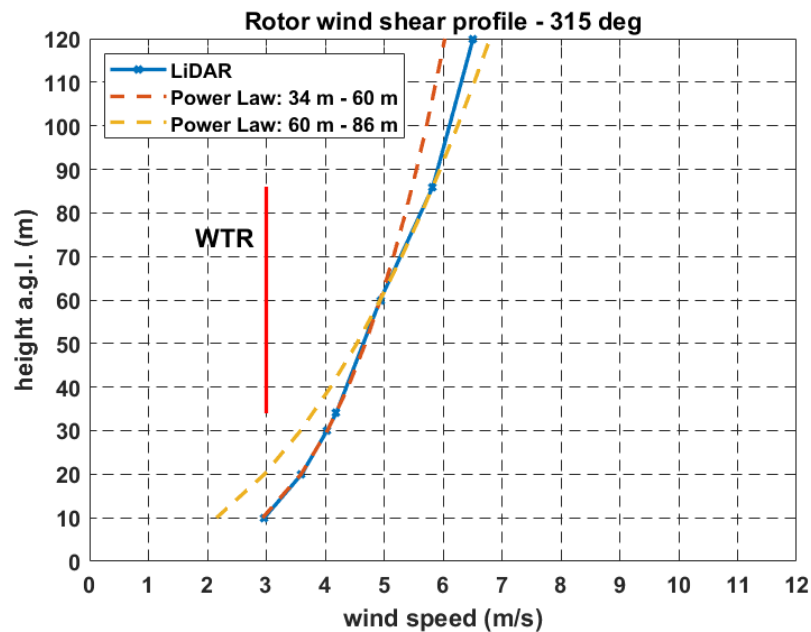
(a)  $225^\circ$ (b)  $247.5^\circ$ 

Fig. 7.24. Fitted power law profiles to LiDAR measured directional wind profiles across the rotor disc WTR ( $225^\circ$ ,  $247.5^\circ$ ).



(a) 270°



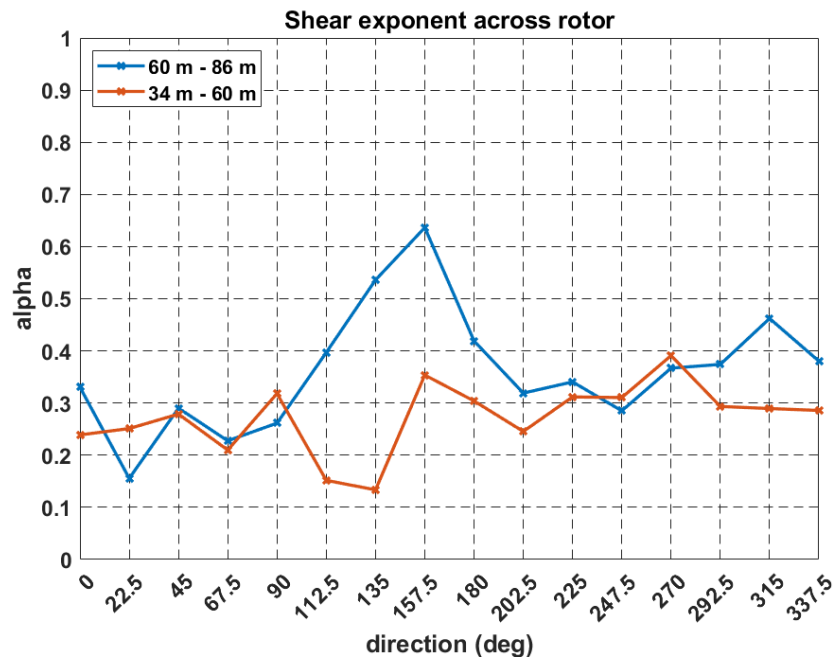
(b) 315°

Fig. 7.25. Fitted power law profiles to LiDAR measured directional wind profiles across the rotor disc WTR (270°, 315°).

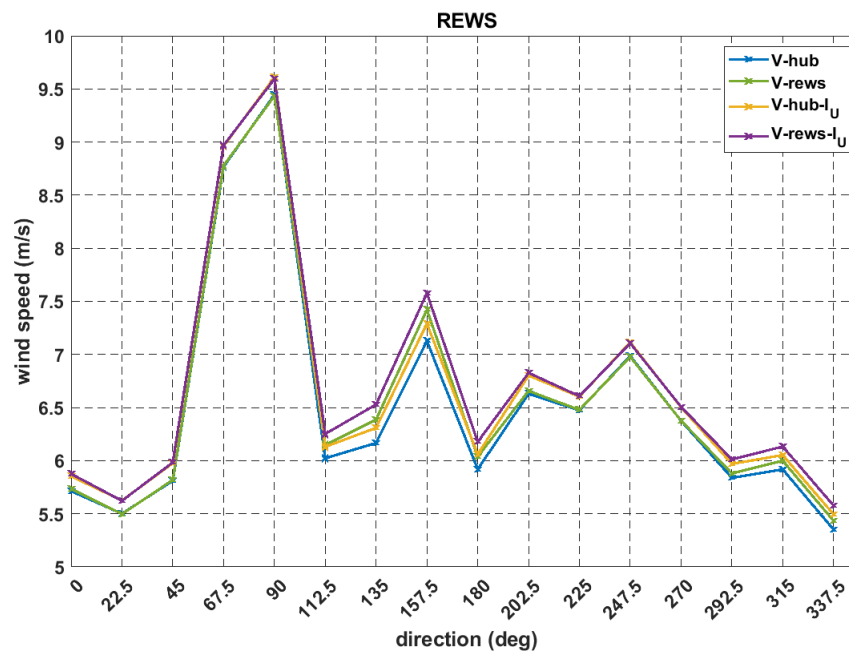
The best fits across the rotor occur for sectors 225°, 247.5° and 270° suggesting the wind flow is in steady state as described by the power law. The extended power law profiles deviate the least from measurements. In the case of 180°, 202.5° and 315° deviations occur within the rotor disc. Upscaling of winds from the bottom half of the rotor under predict winds in the top half of rotor and above, while downscaling winds from the top half of the rotor under predict winds in the bottom half of the

rotor and lower down. This suggests winds measured at lower levels below hub height, in these sectors have a higher proportion of data points with higher wind values. In other words, the building obstacles have a lower impact on incoming winds of higher wind speed. This may explain why the neighbouring open sectors of  $225^\circ$  and  $247.5^\circ$  has slightly over predicted winds due to the steering wind of lower wind speeds into these sectors. The deviations are most evident in sector  $315^\circ$ , that has  $\lambda_p$  values from 24% to 57% with  $\bar{h}_{AW}$  of 6 m to 7 m. These deviations suggest that sectors  $\lambda_p$  values above 20% impacts wind flow at the rotor disc level. These results show that it would be unrealistic to increase the hub height to the extent to have the rotor fully above the influence of the low-rise buildings. The worst-case deviation occurs in the high energy sector of  $157.5^\circ$ , which lies in the wake of the tall narrow 47 m building. In the case of the  $90^\circ$  sector, which has a low surface roughness and few obstacles, the shear of the measured profile reduces faster above the rotor. This may be explained by atmospheric instability in this sector, due to coastal influence, particularly in the spring and summer seasons when onshore sea breezes are more common. It is also seen to a lesser extent in sector  $157.5^\circ$ .

Fig. 7.26(a) shows the difference in shear exponent between the bottom and top halves of the rotor, evident from  $157.5^\circ$  to  $225^\circ$  and from  $292.5^\circ$  to  $0^\circ$  ( $360^\circ$ ), which coincide with buildings. The larger variation in sector  $315^\circ$  coincides with the higher  $\lambda_p$  values. The deviation between  $112.5^\circ$  to  $135^\circ$  occurs as the LiDAR measurements are in the rotor wake. The directional REWS considering shear and turbulence both separately and combined are compared with the hub height wind speed in Fig. 7.26(b). Turbulence appears to have more of an influence, effectively an additional wind speed of up to 0.25 m/s. In the case of  $157.5^\circ$  which has the high shear, there is an equal influence with turbulence giving a combined influence of 0.5 m/s. Therefore, unlike for larger wind turbines in rural environments where wind shear across the rotor is considered important, wind turbulence appears to be more important for medium and large wind turbines in peri-urban environments.



(a) Directional wind shear exponent across the rotor



(b) REWS comparison with shear and turbulence

Fig. 7.26. Directional wind shear exponent across the rotor and REWS comparison with shear and turbulence.

### 7.3.5 Atmospheric Stability

At the met mast location M, the distributions of  $R_i$  from August 2019 to March 2020 is shown in Fig. 7.27. The neutral stability class range, STC 3, is highlighted. It shows that the most common occurring is the neutral stability class, but unstable and stable values are present. As expected the night time periods have more stable points,



Fig. 7.27, when there is little or no solar insolation. Table 7.9 gives a breakdown of the data points in all the stability classes. STC 3 accounts for over 52% of the data point followed by the stable class ST4 of almost 23% of the total data points. A small number of data points occur in the unstable classes. These occur in the day hours. However, as the measurement period does not include summer months, the solar insolation is lower and fewer occurrences of wind come from the east and southeast, as was indicated by the wind rose in Fig. 7.12(a).

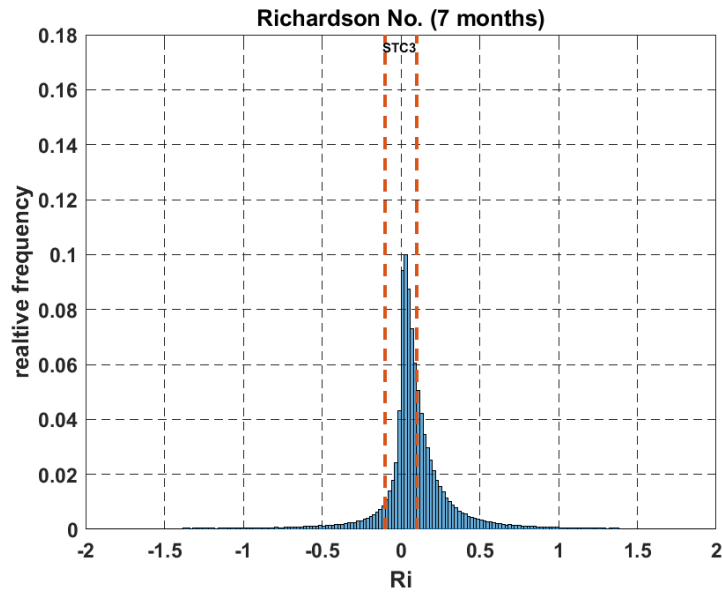
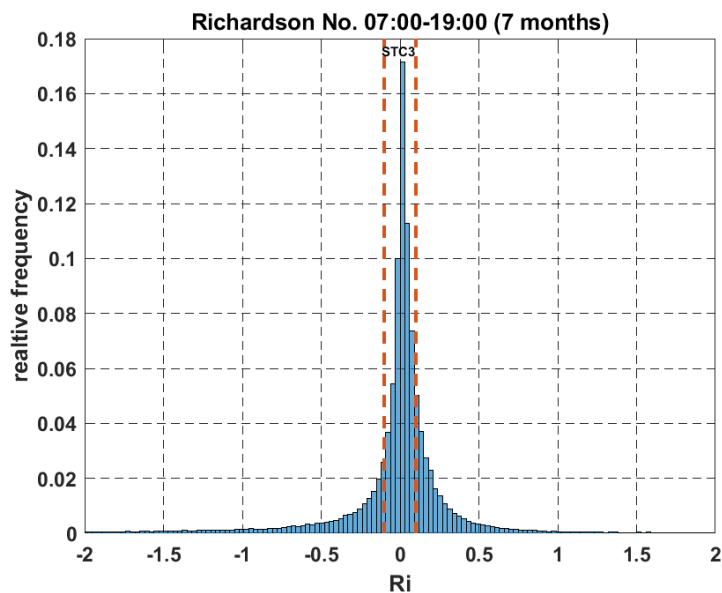
(a)  $R_i$  overall(b)  $R_i$  day

Fig. 7.27.  $R_i$ . distribution characteristics (overall) and day time hours.

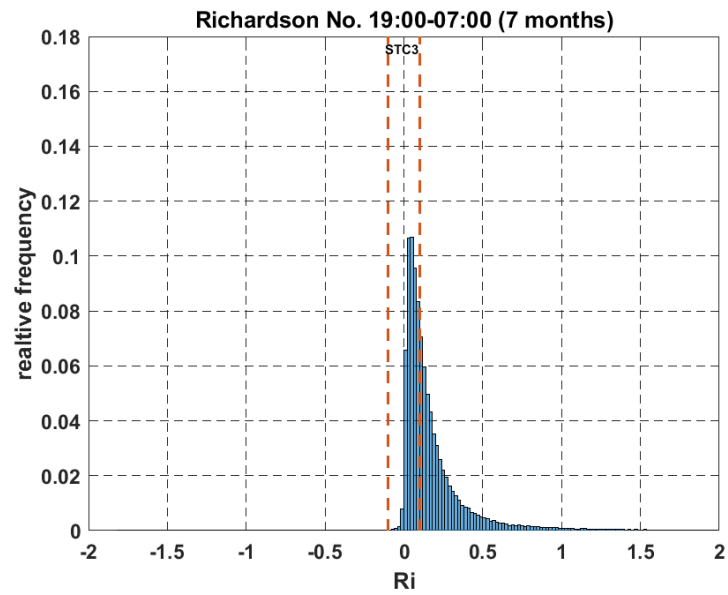
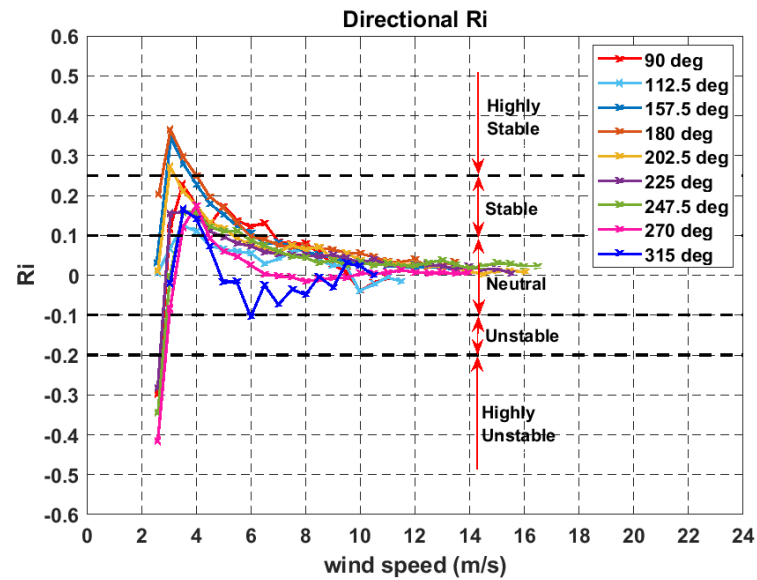
(a)  $R_i$  night(b)  $R_i$  directional distribution with wind speed

Fig. 7.28.  $R_i$ . distribution characteristics night time and mean directional characteristics (overall).

**Table. 7.9.** Stability class distributions

<b>Stability Class</b>	<b>Count</b>	<b>%</b>	<b>Day Count</b>	<b>Day %</b>	<b>Night Count</b>	<b>Night %</b>
STC 1	13712	6.81	13625	6.77	87	0.04
STC 2	6381	3.17	6302	3.13	79	0.04
STC 3	105749	52.51	60637	30.11	45112	22.40
STC 4	46182	22.93	14781	7.34	31401	15.59
STC 5	29379	14.59	9790	4.86	19589	9.73
<b>Total</b>	<b>201403</b>	<b>100</b>	<b>105135</b>	<b>52.20</b>	<b>96268</b>	<b>47.80</b>

As atmospheric stability is wind speed dependent, the directional binned distributions of  $R_i$  with wind speed is shown in Fig. 7.28(b). They are given in the directions of most interest from shown previously. At wind speeds above  $\sim 6$  m/s the neutral stability class is common for all of the direction of interest. From 6 m/s down to  $\sim 4$  m/s wind become more stable which is likely to be the result of when these lower wind speeds occur on colder nights from Table 7.9, i.e., when air temperatures where the temperature at the lower 2 m height becomes lower than the temperature at the 30 m height. The instances of unstable data occur below  $\sim 3$  m/s. From Table 6.4 these are likely to represent sunny days of very low wind speeds where the temperature at the lower 2 m height becomes higher than the temperature at the 30 m height. Interestingly, the higher energy sectors of  $202.5^\circ$ ,  $225^\circ$  and  $247.5^\circ$  over the 7-month period have similar  $R_i$  distributions. For the purposes of wind speeds above the wind turbine cut-in wind speed of 3 m/s it appears reasonable to assume near neutrality in these sectors. Sectors  $270^\circ$  and  $315^\circ$  remain more neutral. Sectors  $90^\circ$  and  $157.5^\circ$  from the east and southeast are similar and more stable at lower wind speeds, which can be explained by winter height pressure systems giving synoptic scale easterly winds that are colder and more stable. The more unstable thermal mesoscale winds from the east and south east in the summer months, described in Chapters 3 and 4 are not captured by this limited 7-month data set. Therefore, it may be reasonable to conclude that in the case of southwest sectors with the low rise buildings, wind shear profile differences are influenced more by the building than atmospheric stability. Similarly the complex wind shear profile observed at  $157.5^\circ$  is

likely to be more highly influenced by the 47 m high narrow hotel building than by atmospheric stability.

## 7.4 Discussion

As in previous chapters, the study further shows that low-rise buildings with heights greater than 20% of hub height can influence wind turbine performance. These influences are complex depending on the layout the buildings, areas occupied and distance from wind turbine location. Large openings between buildings, in prevailing wind directions, can allow wind flow to be shifted in direction and the energy to be recovered. In the context of medium and large-scale wind turbines deployment in peri-urban environments, morphological methods that describe building obstacles can be a valuable low cost site pre-screening tool to help determine the best locations to site single medium and large scale wind turbines. Where the rural to urban transition occurs within  $\sim 1\text{-}2$  km of a turbine location, a 16-sector division of the surrounding area of the turbine location shows that in a given sector, obstacles with an area weighted average height of 20% of the turbine hub height and plan area fractions higher than 20% have an energy reducing affect. However, if a neighbouring sector is relatively open, to the rural environment, with plan area fraction of less than 10%, the energy is shown to be recovered by the steering of winds around the blocked sector to the more open sector. This supports findings in Chapters 4 and 5 that suggested building obstacles in peri-urban environments have a steering effects on wind energy that are not fully captured by some widely used models in the distributed wind industry. Specifically, considering 16 directional sectors, low-rise buildings within 500 m of the wind turbine location appear to cause the crossover of the RSL and ISL within the rotor swept area between 34 m and 86 m for cases where both the area weighted average building height is above 20% of the turbine hub height and the building plan area fractions are higher than 20%. Beyond 500 m the wind turbine rotor appeared to be fully immersed in the altered RSL.

Wind turbulence and gust factors increase significantly compared to the rural location M upwind of the obstacle influences in the prevailing southwest sectors. The 90<sup>th</sup> percentile values of turbulence intensity at the wind turbine location exceed the limits of current NTM in current IEC standards, below heights of 86 m in

this case. This suggests a need to revise current IEC standards for medium and large wind turbines deployed in peri-urban environments. With reference to the IEC NTM for large wind turbines described by Eq. (7.10), suggested modifications of “ $I_{ref}$ ” to “0.2” would better account for turbulence, in this case, for turbines with a hub height of 30 m up to 6 times the value of  $\bar{h}_{AW}$ . At heights above this, the existing NTM for large scale wind turbines appear valid. For small wind turbines on the shorter towers, NTM described by Eq. (7.11), suggested modifications of “ $I_{ref}$ ” to “0.25” would account for turbulence intensity down to 20 m, i.e., approximately twice the height of the majority of surrounding buildings. Vertical turbulence intensity is shown to be  $\sim 20\%$  of horizontal turbulence intensity at the 60 m hub height and would be expected to increase at heights below this. Gust factors exceed those currently used in IEC design standards, i.e., a value of 1.4 below 60 m, which are more of a concern for small wind turbines. The power law best fits measured wind shear profiles across the 52 m rotor diameter in open sectors with obstacle plan area fractions below 10%. Its deviation increases with increasing plan area fractions above 20%. For standout obstacles, the biggest deviation occurs in a sector that contains a 47 m obstacle 330 m away from the wind turbine. It is observed that building obstacles have a lower impact on incoming winds of higher wind speed and may be steering winds of lower wind speed around obstacles. This is relevant for peri-urban sites that may have lower annual wind speeds in general, particularly at low elevation locations. *REWS*, accounting for both wind shear and turbulence, exceeds hub-height wind speed from 0.25 m/s to 0.5 m/s. It is shown to be dominated by turbulence in all sectors apart from the sector in the wake of the 47 m obstacle. However, it may not be a critical parameter to assess for wind turbines with rotors of this size or below.

A preliminary assessment of atmosphere stability showed that assuming neutral or near neutral stability was not unreasonable at wind speeds above the turbine cut-in wind speed and therefore building obstacles are a significant influence on wind shear. However, in lower wind speed situations such as in the cases of smaller wind turbines with shorter towers, larger deviations from neutral atmospheric conditions may become significant and requires further investigation. The learnings from this study can be of benefit for low cost pre-feasibility assessments for medium and large-scale turbine deployed in peri-urban environments. It shows that existing obstacle rules, based only on obstacle height and distance may not be sufficient for

peri-urban environments. A limitation of the study is that one turbine site with one particular type of active pitch regulated wind turbine has been studied. This study has an advantage in that different obstacle densities in different directions enable an assessment of various type of obstacle morphologies, but it should be emphasised that sites deeper into urban areas, beyond 2 km from the rural-urban interface, would require further research. A further limitation is that different turbine types may behave differently, particularly passive stall regulated wind turbines compared to active pitch machines. However, passive stall regulation is more a feature of small wind technologies (below 50 kW) i.e. below the needs of commercial scale industrial sites. The general application of the finding will be outlined in the framework for deploying medium and large scale wind turbines (above 50 kW) in peri-urban environments. Finally, the study again shows the usefulness of LiDAR technology in assessing the wind resource in peri-urban environments, in terms of ease of deployment and three dimensional wind measurements at multiple levels applicable to both large and small-scale tower mounted wind turbines.

## 7.5 Conclusions and next steps

This study shows the need for careful consideration in the micro-siting of turbines with respect to surrounding building in peri-urban environments. A 16-sector morphological approach shows that for average plan-area-weighted obstacle heights of 20% of the wind turbine hub-height, with obstacle plan area fractions of above 20% and within  $\sim 1$ -2 km of a wind turbine location can have energy reducing impacts. The energy can be recovered in cases where a sector with high obstacle plan area fraction has a neighbouring sector with obstacle plan area fractions below 10% by energy. This is due to steering of winds from one sector to another, especially at lower wind speeds. Maximum obstacle heights should be considered to determine any individual standout obstacles that are above  $1/3$  of the wind turbine, particularly within 500 m of the wind turbine. These should be avoided in prevailing wind directions. It may not be practical to increase wind turbine hub height to a height to avoid the influence of buildings, therefore, the rotor may always be in complex flow to some extent. It is also suggested that IEC wind turbine standards be revised in relation to normal turbulence models for peri-urban environments, as they have

been shown to be exceeded in this case, at heights below  $\sim 6$  times the plan-area-weighted obstacle heights. The 90<sup>th</sup> percentile values of turbulence intensity have been shown to be exceeded at heights below 6 times the average plan-area-weighted obstacle height. Modification of " $I_{ref}$ " to "0.2" for large-scale wind turbines and "0.25" for small-scale wind turbine are suggested for peri-urban environments. It is expected that LiDAR technology will become a more prevalent and necessary tool in the distributed wind industry in the future as its cost reduces.

The next chapter collates the learnings from this and the previous three study chapters and discusses the findings of this in broader context of distributed wind that was discussed in the literature review. The findings will be used to develop a framework for deploying medium and large distributed wind turbine from measurement and modelling perspectives to improve micro-siting procedures for medium and large scale wind turbines in peri-urban environments. The challenges encountered in this research will also be discussed and suggestions for future research will be given.





## Chapter 8

# Discussion and development of a site pre-screening framework for distributed wind in peri-urban environments

### 8.1 General discussion of findings

This research has shown that the distributed wind industry for projects, particularly below 1 MW in size, is a sector of the wind industry that is still in development and faces numerous challenges in becoming a mainstream market. The literature review, in Chapter 2, described how in recent years, the wind industry has heavily focused on the development of offshore wind that has been largely investor driven with the support of governments in various jurisdictions. This has led to more mature turbine technologies above 1 MW in size. The distributed wind industry, whilst in existence at relatively minor scales over decades, has been developing at a sluggish pace. This has primarily been due to lack of investment in technology development, lack of robust design standards, intermittent government supports, high upfront costs, poor deployment choices and over expectation of real-world performance, that ultimately has led to lack end-user confidence in the technology. In urban wind energy, it was found that much of the research to date has focused on small scale wind, particularly building integrated wind systems. There has been little or no commercial success of these systems to date due to the complex wind regimes around buildings and the unsuitability of the current small-scale wind technologies to operate in these wind regimes. New climate and greenhouse gas reduction directives and policies across the world promoting community and individual consumer

engagement with local electricity generation in the coming years and decades, highlighted the current pressing need for the distributed wind industry to further develop into a mature mainstream industry. This is also becoming more relevant as centralised electricity systems evolve to distributed grid systems with localised renewable electricity generation. Behind-the-meter wind deployment can play a major part in enabling energy consumers to offset their own energy needs while participating in evolving electricity markets. The integration with other behind-the-meter technologies such as storage and demand side management can create mutual benefits in helping these technologies to develop at a faster pace. It was also found that there is substantial potential for distributed wind off grid applications, both in bespoke applications and in remote communities where access to centralised electricity grids remains limited for large portions of the world's population. In the area of distributed wind resource assessment and wind turbine micro-siting. Chapter 3 outlined the broad and complex nature of the wind resource on a range of inter-dependent temporal and spatial scales from global to mesoscale to microscale and the many current efforts improving wind resource assessment in the wind industry as a whole. Numerous studies have compared model predictions with wind measurements for a variety of models and locations across the world. Many of these studies have compared prediction of wind velocities and turbulence against field measurements at prospective wind sites from urban small scale to large rural based utility scales. They all have shown mixed results with wide variations depending on measurement setup, site terrain complexity, model complexity and importantly, how models are setup and implemented. In many cases, few of the prospective sites studied had operating wind turbines in situ, so the corresponding power and energy performance impacts on real-world wind turbine operation could not be assessed. In other cases where wind turbine data was recorded, it consisted of low resolution cumulative monthly or annual energy totals. It has been reported that distributed wind industry has lacked representative high-resolution time-series real-world data to assess how current wind resource assessment models, micro-siting techniques and design standards represent these systems. Acquiring such data would need robust high-resolution measurements and knowledge of a wind turbine's operational status and/or behaviour. This lack of data has also been a limiting factor in progressing IEC design standards development with regard to turbulence models and extreme

wind loading assessment driven by gusts. This is even more the case for medium and large-scale wind turbine deployed in peri-urban environments for which, up to now, little or no detail studies or real-word data operation data have been published. The wind regimes in these environments are further complicated by building obstacles and higher surface roughness. Solid obstacles such as buildings have been treated as isolated bodies in large-scale wind farm studies, but traditionally have not been a significant feature in such wind resource assessments. Therefore, they have not been given as much attention compared to complex natural terrain. Urban boundary layer studies in small wind deployment have shown how multiple local internal boundary layers can form below height ranges from 200 m to 500 m, but only the lowermost canopy and roughness sublayers are of interest to small-scale wind, but this remains a very challenging area. As few studies in deployment of medium and large scale wind turbines in peri-urban environments, a research gap in this area was identified in terms of energy performance, micro-siting and wind turbine design standards.

The availability of long-term high-resolution real data from an operating Vestas V52 wind turbine in a peri-urban environment and site wind measurements enabled a heuristic evaluation of its energy performance to be the focus of this research. Therefore, contributions of this research has been strongly based on unique high-resolution data sets from the wind turbine SCADA system along with newly generated high resolution wind data from the deployment of an onsite LiDAR and an offsite met mast specific to the project to give data-driven additional insights to improve wind energy deployment in peri-urban wind environments. The four main study chapters 4 to 7 have examined a range of factors that influence the real world energy performance of a Vestas V52 wind turbine in a peri-urban wind environment. These included assessments of how well some wind flow models and aspects of IEC design standards, that are currently widely used in the wind industry, represent such an environment. A temporal analysis of the SCADA data at the wind turbine site on multiannual, seasonal and diurnal time frames, in Chapter 4, showed that inter-annual variation over an 8-year period was of the order of 12% and from 25% to 44% for inter-annual monthly comparisons. The larger variations occurring in April and May as the only months that surpass 40%. This can be attributed to the coastal location of the site where a seasonal analysis showed that strong onshore

winds from Dundalk bay occur in the spring and summer months. In the winter months the dominant winds were from the west and southwest, however, there were south southeast neighbouring  $5^\circ$  directional sectors with a combined width of  $\sim 15^\circ$  that had high wind speeds. These were synoptic scale winds driven northwards up the Irish sea. Diurnal energy variations were observed with higher energy occurring in the afternoon hours, particularly in the summer months. Although not the focus of this research, the seasonal and diurnal observations highlight the importance of comprehensive end-user energy demand analysis for distributed wind systems deployed in behind-the-meter applications so that systems can be sized correctly and/or integrated with other appropriate onsite generation and storage technologies. This in turn requires accurate understanding of the wind resource and electrical energy generation as well as site factors that impact on these, which this research focused on. The development of the novel *EER* from high resolution SCADA has shown to give an effective breakdown of the directional real-world energy output. The value of recording long term high time-resolution wind direction data enables an *EER* to be overlaid on local and regional plans to show how the energy performance can be significantly impacted by local and regional features. This can serve to create a robust benchmarking method to assess the impact of both local and regional site features on energy performance. In this research the *EER* showed that building obstacles approximately 20% of the turbine hub height and up to 1-2 km away can have a significant impact on energy. The width of building obstacles as viewed from the turbine location appeared to have energy reduction impacts indicating that low broad building obstacles can have a bigger energy reducing impact compared to taller narrower buildings. This can be explained by low broad buildings forming wider localised internal boundary layers thereby increasing wind shear and/or steering of the wind flow in other directions, while wind flow may move around taller narrower buildings. It tends to agree with the flow characteristics around the rectangular bodies with various aspect (height to width) ratios reported by (Gu and Lim, 2012) who found that the transverse width has a substantial impact of the surface pressure around bluff bodies. Channelling of flow in gaps between building and along roads running parallel to the oncoming wind direction was observed to enhance energy performance, but the turbulence intensity is higher. This can be explained by wind gusting as a result of pressure differences

around buildings that form the channel and the dissipation of vortices in the flow downwind of the channel in the direction of the wind turbine. Therefore, micro-siting rules based on studies of isolated obstacles, outlined in Chapter 3 by (Peterka, Meroney, and Kothari, 1985; Millward-Hopkins, 2013) and simple rules of thumb as reported in IEA guidance regarding single obstacles do not well represent peri-urban zones in the context of medium or large scale wind turbine deployment. The same could be said for the fence experiment by (Peña et al., 2016), the fence being a thin (i.e., 2D like) body in the direction of wind flow. An extra short study on replacing the gearbox after 13 years of operation with a new one showed that loss in *AEP* associated with gearbox aging was  $\sim 3\%$ . The best improvement in energy output, following gearbox replacement occurred at wind speeds above 6 m/s suggesting that the gearbox aging has a smaller influence at lower wind class sites. Therefore, allowing the gearbox to run to failure may be economically justified at sites like this, showing that the gearbox has been quite robust and not a dominant factor in performance degradation. The findings add to the broader debate on whether direct-drive gearless wind turbine technology a significantly better option compared with gear based technology. This may have broader implications for the ever increasing number of older wind turbines and wind farms around the world are nearing the end of operational life in the context of turbine re-powering options. Further research in these techniques, using operational data from a broader range of sites and turbine technologies to improve decision making processes in the operation and re-powering of wind farms, would be of benefit to the industry. It was shown in Chapter 5 that the remodelled Irish wind atlas can be very useful in determining the mesoscale influence of the region on the energy performance of a wind turbine in a distributed wind project development. In particular in this case, the influence of Dundalk and the hills  $\sim 7.5$  km to the northeast in steering southerly winds into the southeast to the wind turbine site through Dundalk Bay. It explained why there are high wind south easterly sectors in the winter season due to geographical size and location of Ireland, where the Irish Sea and the west coast of Britain appears to have steering influences on synoptic scale prevailing south south westerly winds from the Atlantic ocean northwards. It highlighted the impacts of geographical shape of a land mass on the wind resource, such as the increased south easterly wind speeds at offshore and onshore locations near to the east coast. These south easterly winds significantly reduce at

approximately 10 km inland from the coast. Therefore, distributed wind projects closer to the coast can have enhanced energy potential and project viability not only due to thermally driven seasonal winds but also due to the geographical features of the coastline with respect to prevailing winds at the synoptic scale. Contrary to this, the hills to the north east have an energy reducing impact on any winds from the northeast as is not general prevailing wind direction. No wind enhancement was observed from gravity mountain waves that can occur in stable atmospheres. Interestingly, a comparison of the total *AEP* for the site from the wind atlas data was within 3% of the measured wind turbine *EER*. This indicates how beneficial the open source Irish wind atlas is for pre-feasibility studies and the progress that has been made in mesoscale modelled wind atlas development. However, analysis of the *EER* from the wind turbine SCADA data shows notable directional differences at the microscale level in comparison with the directional breakdown of *AEP* predicted from the wind atlas data. An overlay of wind turbine *EER* and the predicted directional *AEP* on a local plan view highlighted directional differences that could be aligned to local building obstacles. These influences can reduce and/or redistribute the energy with direction. It supported the findings in Chapter 4 the multiple influences on wind flow by building obstacles at a given location, such as wind speed up, channelling, steering and blocking depending on the building sizes and spatial layout, also suggested by (Toparlar et al., 2017; Hassanli et al., 2019). It was observed that a 12 m high broad building cluster, at a distance of 550 m to 1100 m from the turbine location, appeared to have a bigger influence on the turbine energy output compared to a 47 m high narrow building at a distance of 335 m to 420 m away. The horizontal cross-sectional width, as viewed from the turbine, was 635 m and 70 m for the broad building cluster and taller narrow building respectively. The results support the idea that that low broad buildings have high impact on energy and indicate that obstacles of at least 20% of the wind turbine hub height and within at least 20 times the turbine hub height can influence the wind turbine energy performance. Preliminary onsite LiDAR measured directional vertical wind shear profiles were more complex in the directions with obstacles. Energy reductions due to obstacles were also shown to be somewhat compensated for through wind steering or channelling depending on their physical geometries and spatial layout and the overall energy reduction was relatively low. However, the assessment showed that the

downscaling process from mesoscale to microscale in the Irish wind atlas to a 1 km resolution did not fully capture these local microscale influences. Therefore, additional microscale modelling is a requirement for accurate wind turbine micro-siting of medium-to-large-scale wind turbine within peri-urban environments. In particular, minimising local energy reduction and taking advantage of local energy gains due to obstacles is critical to optimise project viability in peri-urban environments. In Chapter 6, a comparison of four commonly used microscale models, based on linear and RANS CFD approaches, was carried out in predicting the real-world *EER* of the wind turbine over 1 year of operation. This were driven by 1-year of onsite LiDAR wind measurements at multiple heights. Similar to studies outlined in literature, there was no clear standout best modelling approach covering all directions from all scaling heights and was dependent on the modelling approach, model setup and the onsite wind data acquisition setup. Model predictions for hub-height wind speed varied from within 0.5% to 24.3% for CFD RANS models and 1.4% to 62.3% for the linear WASP approach. However, from an energy perspective, the variation in the prediction of *AEP* ranged from 0.4% to 64% for the CFD RANS models and at 8% to  $\sim 200\%$  for the linear model. Notably in all cases, the predictions were highly dependent on the height at which wind measurements used to drive the models were taken. It was observed that measurements taken at  $\sim 3$  times the heights of low-rise broad buildings gave the best results when upscaling to the turbine hub height. Upscaling from heights below or similar to low-rise building heights led to poor prediction due to wake and complex CL layer influences. This is of most relevance to the deployment of medium and large-scale wind turbines deployed in low-rise peri-urban environments. For tall buildings with heights of 80% of the turbine height and less than 10 obstacles heights away from the turbine location, mesh blocking and roughness approaches gave better results when downscaling from  $\sim$  twice the building height. Downscaling from 200 m gave the poorest results in all cases. This suggests that the scaling approach used by UK met office in upscaling rural based to 200 m, assumed to be above the UBL, and downscaling to the desired hub-height in an urban environment may not be the best approach. In relation to the setup of the models, the WASP-CFD roughness with the polar grid combined with simulations in  $10^\circ$  wide sectors performed slightly better than the rectangular grid used in both WindSim mesh blocking and roughness models for simulations in  $22.5^\circ$

degree wide sectors. The linear WASP-IBZ model performed the poorest and is not recommended for peri-urban environments. Therefore, is not recommended to use linear shelter models in peri-urban areas or areas that have numerous building obstacles, particularly in prevailing wind directions. This also confirmed that current IEA simple rules of thumb guidelines have limited suitability for micro-siting wind turbines in peri-urban environments. It was suggested that obstacles down to 20% of the turbine hub-height and at distances up to 50 obstacle heights away can create an internal RSL whose boundary with the ISL is within the rotor disc area. Similarly, obstacles from 50 to 100 obstacle heights away from the turbine location may create a RSL that will cover rotor disc area. This is in line with internal boundary layer formation from the urban rural interface outlined in the literature (Millward-Hopkins et al., 2013b; Millward-Hopkins et al., 2013a). This implies that the desire to have the rotor entirely in the ISL may lead to impractical turbine tower heights for medium and large-scale wind turbines and that both the RSL and ISL may commonly split the rotor swept area. Therefore, for best model predictions, it would be desirable to have wind measurements and the minimum point of the rotor swept area to be at least 3 times the height of broad low-rise buildings within 50 obstacle heights to reduce errors in upscaling model processes. An added complication is that building obstacles appear to have a directional energy shift into neighbouring open sectors due to a steering effect on incoming winds, depending on their layout. As was also indicated in Chapter 5, energy losses in the more blocked sector may be recovered in the neighbouring open sector. Therefore, the total annual energy out may be less impacted by obstacles with open neighbouring areas. These directional effects are more difficult to capture without more complex CFD models such as LES, but these may be cost prohibitive for distributed wind projects. Despite these complexities, the impact of buildings on the total annual energy performance on the wind turbine can be predicted using CFD RANS models with a high degree of accuracy so long as on-site measurement heights for model input data are well chosen.

Morphological descriptions of building obstacles were investigated in Chapter 7 to develop the basis of a low cost site pre-screening method to help determine good locations for single medium and large scale wind turbines in peri-urban environments. The method can be used to help maximise energy capture in the absence of costly flow modelling or to help with optimising the use of flow models. It could



also be used to assist with improving met mast placement. The method considered an area within a 2 km radius of the wind turbine, divided into 16 sectors with each sector divided into four 500 m segments. This stretched beyond the rural to urban interface as many of the buildings of interest was within 1 km of the wind turbine location. Each 500 m segment in a given sector was morphologically analysed in terms of area-weighted average building height, building plan area fraction and building frontal area fraction. It was shown that segments with an area-weighted average building height of 20% of the turbine hub height and plan area fractions higher than 20% appeared to have an energy reducing affect. However, it also showed that when a neighbouring sector is relatively open, to the rural environment, with a building plan area fraction of less than 10%, energy was recovered by the steering of winds around the blocked sector in to the more open sector. A short term met mast wind measurement campaign and morphological analysis at a location to the west of the turbine location, outside of the influence of buildings, showed directly that the energy was shifting from the more blocked sectors into neighbouring open sectors. This supports findings in Chapters 4 and 5 that suggested building obstacles in peri-urban environments have a steering effects on wind energy that are not fully captured by some widely used models in the distributed wind industry. It was also observed that building obstacles have a lower impact on incoming winds of higher wind speeds above  $\sim 7$  m/s implying that it is the steering of winds with lower wind speeds around obstacles that occurs more. This is relevant for peri-urban sites that may have lower annual wind speeds which may occur at locations with low elevations in general. An examination of wind shear across the rotor disc itself showed that low-rise buildings within 500 m of the turbine alter the RSL to ISL boundary to fall within the rotor swept area between heights of 34 m and 86 m. This occurred in segments with plan-area-weighted average building heights above 20% of the turbine hub height and building plan area fractions higher than 20%. Therefore, from the literature (Grimmond and Oke, 1999), areas with surfaces roughness's of 0.5 m to 1.5 m with building plan area fractions of 20% are significant in this case. Beyond 500 m the wind turbine rotor appeared to be fully immersed in the altered RSL. The power and log laws gave best fits with measured wind shear across the 52 m rotor diameter in directions with open sectors having building plan area fractions below 10%. Their deviations increased with increasing plan area fractions above 20%. For

standout obstacles, the biggest deviation occurred in a sector containing a 47 m obstacle  $\sim 330$  m away from the wind turbine. The *REWS*, accounting for both wind shear and turbulence, exceeded hub-height wind speed from 0.25 m/s to 0.5 m/s. It was shown to be dominated by turbulence in all sectors apart from the sector in the wake of the 47 m obstacle. However, it may not be a critical parameter to assess for rotors of this size. A preliminary assessment of atmosphere stability showed that assuming neutral or near neutral stabilities was not unreasonable at wind speeds above the turbine cut-in wind speed, suggesting that the building obstacles dominated the influence on wind shear. At higher wind speeds, above  $\sim 6$  m/s, in all directions the flow converged to neutral flow conditions. At lower wind speed sites, such as in the cases of smaller wind turbines with shorter towers larger, deviations from neutral atmospheric conditions may have a significant impact on wind shear and should not be ignored when scaling measurement to other heights. Comparing wind turbulence and gust factors from measurements at the peri-urban wind turbine and rural met mast sites, they both increased significantly at the wind turbine site. The 90<sup>th</sup> percentile of turbulence intensity at the wind turbine location exceeded limits of current NTM in current IEC standards below heights of 86 m, in this case. This suggests a need to revise current IEC standards for medium and large wind turbines deployed in peri-urban environments. With reference to the IEC NTM for large wind turbines (IEC 61400-1, 2019), modifications of  $I_{ref}$  from "0.18" to "0.2" would better account for turbulence, in this case, for turbines with hub heights from 30 m up to 6 times the value of the area-weighted mean heights of the buildings. At heights above this, the existing NTM for large scale wind turbines appear to be valid. For small wind turbines on the shorter towers using the NTM of the small wind turbine standard (IEC 61400-2, 2013), suggested modifications of  $I_{ref}$  from "0.18" to "0.25" would account for turbulence intensity down to a height of 20 m, i.e., approximately twice the height of the majority of surrounding buildings. Vertical turbulence intensity was shown to be  $\sim 20\%$  of horizontal turbulence intensity at the 60 m hub height and increases at heights below this as expected. Gust factors were shown to exceed the currently used in IEC design standards value of 1.4 below 60 m, with values of 1.6 at 30 m heights and can exceed 1.8 at below 30 m, which is more of a concern for small wind turbines. However, improving IEC NTM and gust factors require further investigation for peri-urban environments.

## 8.2 A peri-urban site pre-screening framework

Open source wind atlas models based on mesoscale models can be useful in determining the general prevailing wind directions that can be used with morphological assessment procedures and microscale models to determine the most energetic wind directions.

Based on the finding is this thesis, the following framework for pre-screen a prospective peri-urban sites in the Irish and UK climate within 2 km of the rural to urban transition is suggested in Fig. 8.1 with more details given below.

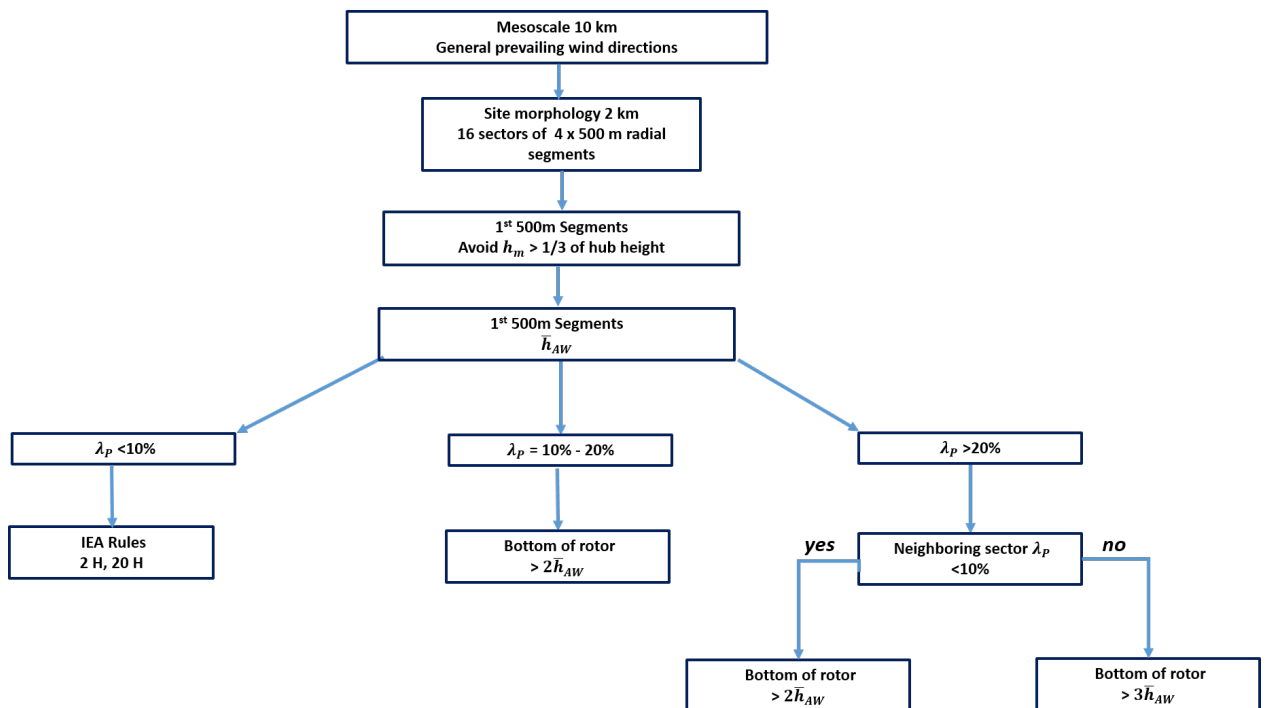


Fig. 8.1. Outline flow diagram to site pre-screening to set the minimum height of bottom of rotor disc considering buildings in the first 500 m segments.

The use Fig. 8.1 can be explained as follows:

1. Use a mesoscale model to establish the prevailing wind direction at the site and at other locations within 10 km, particularly if the site is coastal or in complex natural terrain.
2. Select an initial preferred onsite turbine location and select an area within 2 km radius and divide it into 16 sectors.
3. Divide each sector into 4 segments of 500 m in the radial direction.
4. Determine plan area fractions and area-weighted height of the buildings for each segment in each sector as well as the maximum obstacle heights in each segment.
5. Segregate the sectors by building plan area fraction into: less than 10%, between 10% and 20% and greater than 20%.
6. In the prevailing wind direction (s) established from the mesoscale model, avoid standout obstacles with a maximum height of more than  $1/3$  of the proposed wind turbine hub height within a 500 m distance of the preferred wind turbine location, or increase hub height to achieve this.
7. In prevailing wind sectors that have building plan area fractions of 20% and above in the first 500 m segment, the lowest point on the rotor swept area should be set at 3 times the area-weighted height of the buildings for that segment.
8. If a neighbouring sector has a building plan area fraction of less than 10% in all segments out to the rural environment, then the energy impact of the more blocked sector is reduced and the lowest point on the rotor swept area can be reduced to 2 times the area-weighted height of the buildings of the more blocked segment.
9. In prevailing wind sectors that have building plan area fractions of between 10% and 20% in the first 500 m segment, then the lower tip of rotor should be no less than 2 times the area-weighted height of the buildings for that segment.
10. Segments with building plan area fractions of less than 10% have minor influences so long as current IEA rules (IEA Wind, 2018) are met, i.e., the lower tip

height of the rotor is 2 times the height for any obstacle of within 20 times the obstacle height of the wind turbine location.

11. Beyond 500 m and on to a rural-urban interface up to 2 km away segments with building plan area fractions greater than 20% and area-weighted heights above 20% lower tip of the rotor disc may modify internal boundary layers. If neighbouring segments don't have plan area fractions less than 10% then then the influence may not be realistically avoided by increasing hub or rotor heights. Therefore, modifying the lateral spatial location of the wind turbine to avoid these in prevailing winds, where possible, should be investigated while maintaining the recommendations for the first 500 m segments.

This framework should be taken as a general guidance decision making tool to assist with wind turbine placement and hub height selection. From this research, this framework is generally applicable to wind turbines with rotor spans that are intended to occupy heights in the range above 30 m and below 100 m above ground level in low-rise peri-urban environments, within 2 km of the rural-urban interface. As a minimum, current IEA rules (IEA Wind, 2018) should be followed, however, if the guidance outlined here can be applied to sectors with prevailing wind directions that have obstacle plan area fractions above 10%, then up to a 10% gain in annual energy output can be expected.

For medium and large-scale projects that have significant capital costs, accurate *AEP* assessments become more critical. If the previous recommendations can be met then onsite measurements and microscale modelling can be pursued. A project that cannot easily meet the suggested specifications is advised to carry out more in-depth measurement and/or modelling investigations depending on the specifics of the given site.

- (a) If the height or the number of heights that wind measurements are limited then it is recommended that wind measurement are made and not below 3 times the highest mean area-weighted height of the buildings in the first 500 m segments of the prevailing wind sectors.
- (b) Where possible, CFD RANS microscale modelling is recommended, treating building as roughness elements with a polar computational mesh of with 10 degree sectors with at 10 km computation domain with less than 10% area

blocking in the vertical direction if the full atmospheric boundary layer height is not included.

- (c) The use of linear flow models are not recommended, particularly in peri-urban areas where building plan area fractions exceed 10% in prevailing wind directions.

As discussed in Chapter 7, a limitation of the study is that one turbine site with one particular type of active pitch regulated wind turbine has been studied. This study has an advantage in that different obstacle densities in different directions enable the assessment of various type of obstacle morphologies, but it should be emphasised that sites deeper into urban areas, beyond 2 km from the rural-urban interface, would require further research. A further limitation is that different turbine types may behave differently, particularly passive stall regulated wind turbines compared to active pitch machines. However, passive stall regulation is more a feature of small wind technologies (below 50 kW) i.e. below the needs of commercial scale industrial sites.

### **8.3 Wind turbine design standard considerations**

Current IEC NTMs and gust factors appear to not adequately represent the wind turbulence and gust factors in peri-urban environments up to 6 times the mean area-weighted building heights heights. This presents new needs for robust wind turbine designs and NTM standards for peri-urban environments for operation longevity over a 20-year period. Manufactures and end users should clarify wind turbine design classes for a given peri-urban site. This further shows the need for onsite measurements.

### **8.4 Peri-urban wind measurement implementation experiences**

The study has shown the benefits of LiDAR technology at peri-urban locations where met masts may be more challenging to deploy due to spatial restrictions, other onsite activities and planning/permitting rules. Installing the temporary 34 m met mast at the offsite rural location took longer than anticipated. The permitting process, insurance, site access agreements took  $\sim 18$  months to complete before the mast could be

installed. Installation of the mast itself took two days. Installing a mast on the Dundalk IT campus proved not to be feasible because of spatial constraints, other onsite activities and security. Therefore, the LiDAR device was invaluable for carrying out onsite wind measurements that did not require permitting, had insignificant space requirements and could be easily secured inside a small fenced off compound. A disadvantage of the LiDAR device is the power supply requirements, which had a continuous power demand of  $\sim 80$  W in this case. Therefore an AC mains supply is preferable and may be more likely available at peri-urban sites. However, in a remote situation, this is a daily energy requirement of  $\sim 2$  kWh. In standard 12 V deep cycle battery terms, this would equate to approximately a 250 Ah to 300 Ah requirement per day considering battery and inverter losses, i.e.,  $3 \times 12$  V 100 Ah batteries, each with a mass of  $\sim 30$  kg. Therefore, long-term wind measurements with LiDARs in the absence of AC mains power will require careful (costly) power supply considerations. In contrast, the 34 m met mast sensors and data logger with power requirements at the mW level can easily be supplied for 1 year with the capacity of a single 12 V, 100 Ah battery.





## Chapter 9

### Summary conclusions and future research needs

This research overall has shown some of the challenges and complexities associated with accurately determining the energy performance of a large-scale Vestas V52 wind turbine in a peri-urban environment. A site pre-screening framework consisting of measurement and modelling recommendations has been given that can improve the annual energy prediction of real-world turbine energy performance in peri-urban environments. The research was informed by long term wind turbine SCADA data, onsite LiDAR and offsite met mast measurements, along with a mesoscale wind atlas model and four microscale wind flow modelling approaches using the WAsP and WindSim modelling tools. A novel electrical energy rose derived from wind turbine SCADA provided a real-world benchmark to compare model predictions against. It was observed that energy can be over predicted or under predicted by models in some directions, but overall, wind steering can occur from directional sectors more blocked by obstacles to less blocked sectors, thereby reducing the impact on total energy output. This steering tends to occur more at lower wind speeds below  $\sim 6$  to  $8$  m/s, which may be more typical of peri-urban sites. LiDAR measured directional wind shear profiles indicated the roughness and inertial sublayers may split the rotor swept area or totally submerge the rotor in the roughness sublayer, depending on the building plan area fractions and plan-area-weighted heights. Using higher towers to avoid this may be unrealistic. Linear flow models are not recommended in peri-urban environments or should be used with extreme caution. At lower wind speed sites below  $6$  m/s, such as in the cases of smaller wind turbines with shorter towers, larger deviations from neutral atmospheric conditions may have a significant impact on wind shear and should not be ignored when scaling measurements taken one height to other heights. The research suggests that the developed framework can give up to a 10% increase annual

energy output compared to using current IEA micro-siting recommendations. IEC normal turbulence models have been shown not to adequately represent turbulence intensity, and gust factors used for extreme wind predictions are lower than was measured at this site. Recommendations for modification to improving IEC normal turbulence models have been suggested, specifically increasing the turbulence intensity design reference value from 15% to 25% for peri-urban environments. The relative ease of deploying LiDAR technology will make this technology an invaluable tool for wind measurements in peri-urban areas where met masts are difficult and time consuming to install. It was also found during the research from an ageing study of the gearbox, that replacement after 13 years of operation with a brand new gearbox gave an improvement in annual energy output of 3%. It suggested that allowing this component to run to failure was the most viable option in this case.

Future research in distributed wind includes the optimum deployment of medium and large-scale wind turbines in peri-urban environments. For distributed wind energy to become more cost-effective in peri-urban environments that involve single or a small number of wind turbines, continued research in cost-effective wind resource and energy prediction tools will be required in order to improve wind turbine micro-siting accuracy. Further testing and improving a wider range of modelling approaches and performing sensitivity analyses of power and energy output for a comprehensive range of measured wind parameters. These wind parameters should include, 3D wind speed, wind direction, wind shear, wind veer, inflow angle, turbulence, density and atmospheric stability. The site and climate specific nature of the wind resource means that different modelling approaches may perform differently when applied across different site situations. Therefore specific site model and measurement classifications across a wind range of peri-urban zones should be developed for different project/wind turbine sizes so that the appropriate assessment approach(s) can be taken for a given classification. This should include a framework for evaluating uncertainties in the end-to-end processes of energy prediction, from measurements through flow model types, setups and implementations such that the trade-off between cost effective measurement and modelling complexity against the size of given distributed wind project can be effectively made. This future research would require building up high-resolution long term time-series wind and power data banks in peri-urban environments, which are lacking at present. The behaviour

of different wind turbine technologies in relation to power deviations from published power curves, particularly for stall regulated small and medium scale wind turbine should also be examined further in real-world situations. Further investigation is also suggested of wind turbulence and gusts for peri-urban environments. This can include improving the NTM for both small wind and large scale wind turbines and developing a peri-urban wind turbine design class. This would require high frequency (e.g., 20 Hz) 3D wind speed data to assess the power density spectra of the turbulence and the occurrences of extreme local wind gusts induced by building obstacles. In addition, wind turbines whose rotors operate across multiple local internal boundary layers, in peri-urban wind environments, may experience extra fatigue loads and have different aerodynamic noise characteristics, requiring further research. Given the variations in energy output on multiple time scales, from inter-annual to diurnal shown in this study, such data banks would also be very useful for other areas of distributed wind research and development. These areas could include aging and O&M optimisation studies as well as optimising integration with other technologies operating behind the meter, such as solar PV, energy storage and demand side management as well as contributing to grid flexibility. Artificial intelligence and data analytics could also play a significant role across all areas of future deployed distributed wind.

In closing, the experience of the research carried out in this thesis at just one peri-urban site shows that it would be very challenging for one organisation alone to address the above future research needs in terms of resources, time and cost. Therefore, to help the development and deployment distributed wind systems in general, both national and international research collaborations should be fostered. Initial efforts in international collaboration are being formed on an ad-hoc small scale such as through the efforts of IEA Wind Task 41, as demonstrated during this PhD. However, funding bodies and policy makers should be made more aware of the potential holistic benefits of distributed wind so that such collaborations could be supported and become more impactful on a long-term basis. This would accelerate the development of distributed wind, including medium and large-scale behind the meter wind deployed in peri-urban environments, to become a robust and mainstream renewable energy technology.



## Bibliography

- Abdelilah, Yasmina et al. (2020). *Renewables 2020, Analysis and forecast to 2025*. Tech. rep. International Energy Agency. URL: [www.iea.org/reports/renewables-2020](http://www.iea.org/reports/renewables-2020). [accessed: 01.12.2020].
- Abdulrahim Saeed, Saeed (2017). "The Feasibility of Utilizing Wind Energy in Commercial Buildings with Special Reference to the Kingdom of Bahrain". In: *E3S Web of Conferences* 23, pp. 1–13. ISSN: 22671242. DOI: [10.1051/e3sconf/20172309001](https://doi.org/10.1051/e3sconf/20172309001).
- Aho, J et al. (2012). "A tutorial of wind turbine control for supporting grid frequency through active power control". In: *2012 American Control Conference (ACC)*, pp. 3120–3131. ISBN: 2378-5861 VO -. DOI: [10.1109/ACC.2012.6315180](https://doi.org/10.1109/ACC.2012.6315180).
- Ahrens, Donald C and Robert Henson (2017). *Essentials of Meteorology : An Invitation to the Atmosphere*. 8th. CA, United States: Cengage Learning, Inc, p. 508. ISBN: 1305628454.
- Al-Addous, Mohammad et al. (2020). "The Significance of Wind Turbines Layout Optimization on the Predicted Farm Energy Yield". In: *Atmosphere* 11.1. ISSN: 2073-4433. DOI: [10.3390/atmos11010117](https://doi.org/10.3390/atmos11010117). URL: <https://www.mdpi.com/2073-4433/11/1/117>.
- Allen, D J et al. (2017). "A boundary layer scaling technique for estimating near-surface wind energy using numerical weather prediction and wind map data". In: *Applied Energy* 208, pp. 1246–1257. ISSN: 0306-2619. DOI: [10.1016/j.apenergy.2017.09.029](https://doi.org/10.1016/j.apenergy.2017.09.029).
- Ambrizzi, Tércio et al. (2019). "The state of the art and fundamental aspects of regional climate modeling in South America". In: *Annals of the New York Academy of Sciences* 1436.1, pp. 98–120. ISSN: 0077-8923. DOI: [10.1111/nyas.13932](https://doi.org/10.1111/nyas.13932).
- Antoniou, Ioannis, Søren Markilde Pedersen, and Peder Bay Enevoldsen (2009). "Wind Shear and Uncertainties in Power Curve Measurement and Wind Resources". In: *Wind Engineering* 33.5, pp. 449–468. DOI: [10.1260/030952409790291208](https://doi.org/10.1260/030952409790291208). eprint: <https://doi.org/10.1260/030952409790291208>. URL: <https://doi.org/10.1260/030952409790291208>.

- Apata, O. and D.T.O. Oyedokun (2020). "An overview of control techniques for wind turbine systems". In: *Scientific African* 10, e00566. ISSN: 2468-2276. DOI: [/10.1016/j.sciaf.2020.e00566](https://doi.org/10.1016/j.sciaf.2020.e00566).
- Arsenault, Marc-Olivier (2017). *Kolmogorov–Smirnov test, A needed tool in your data science toolbox*. URL: <https://towardsdatascience.com/kolmogorov-smirnov-test-84c92fb4158d>. [accessed: 19.10.2022].
- Arthur, Robert S. et al. (2020). "Multi-scale simulation of wind farm performance during a frontal passage". In: *Atmosphere* 11.3, pp. 1–17. ISSN: 20734433. DOI: [10.3390/atmos11030245](https://doi.org/10.3390/atmos11030245).
- Ayala, M. et al. (2017). "Wind Power Resource Assessment in Complex Terrain: Vil-lonaco Case-study Using Computational Fluid Dynamics Analysis". In: *Energy Procedia* 107, pp. 41–48. ISSN: 1876-6102. DOI: [10.1016/J.EGYPRO.2016.12.127](https://doi.org/10.1016/J.EGYPRO.2016.12.127).
- Azad, Abul Kalam, Mohammad Golam Rasul, and Talal Yusaf (2014). "Statistical diagnosis of the best weibull methods for wind power assessment for agricultural applications". In: *Energies*. ISSN: 19961073. DOI: [10.3390/en7053056](https://doi.org/10.3390/en7053056).
- Badger, Jake et al. (2014). "Wind-Climate Estimation Based on Mesoscale and Microscale Modeling: Statistical–Dynamical Downscaling for Wind Energy Applications". In: *Journal of Applied Meteorology and Climatology* 53.8, pp. 1901–1919. DOI: [10.1175/JAMC-D-13-0147.1](https://doi.org/10.1175/JAMC-D-13-0147.1).
- Bailey, Bruce H and Scott L McDonald (1997). *Wind Resource Assessment Handbook, Fundamentals for Conducting a Successful Monitoring Program*. Tech. rep. TAT-5-15283-01. AWS Scientific, Inc & National Renewable Laboratory (NREL), USA.
- Balogun, Ahmed A et al. (2010). "In-Street Wind Direction Variability in the Vicinity of a Busy Intersection in Central London". In: *Boundary-Layer Meteorology* 136.3, pp. 489–513. ISSN: 1573-1472. DOI: [10.1007/s10546-010-9515-y](https://doi.org/10.1007/s10546-010-9515-y).
- Banta, Robert M. et al. (2018). "Evaluating and improving NWP forecast models for the future: How the Needs of Offshore Wind Energy Can Point the Way". In: *Bulletin of the American Meteorological Society* 99.6, pp. 1155–1176. ISSN: 00030007. DOI: [10.1175/BAMS-D-16-0310.1](https://doi.org/10.1175/BAMS-D-16-0310.1).
- Bardal, Lars Morten, Lars Roar Sætran, and Erik Wangsness (2015). "Performance test of a 3MW wind turbine - Effects of shear and turbulence". In: *Energy Procedia*. DOI: [10.1016/j.egypro.2015.11.410](https://doi.org/10.1016/j.egypro.2015.11.410).

- Barlow, Janet F (2014). "Progress in observing and modelling the urban boundary layer". In: *Urban Climate* 10, pp. 216–240. ISSN: 2212-0955. DOI: [10.1016/j.uclim.2014.03.011](https://doi.org/10.1016/j.uclim.2014.03.011).
- Beaucage, Philippe, Michael C. Brower, and Jeremy Tensen (2014). "Evaluation of four numerical wind flow models for wind resource mapping". In: *Wind Energy* 17.2, pp. 197–208. ISSN: 10954244. DOI: [10.1002/we.1568](https://doi.org/10.1002/we.1568).
- Bechmann, A et al. (2011). "The Bolund Experiment, Part II: Blind Comparison of Microscale Flow Models". In: *Boundary-Layer Meteorology* 141.2, p. 245. ISSN: 1573-1472. DOI: [10.1007/s10546-011-9637-x](https://doi.org/10.1007/s10546-011-9637-x).
- Belcher, S E, N Jerram, and J C R Hunt (2003). "Adjustment of a turbulent boundary layer to a canopy of roughness elements". In: *Journal of Fluid Mechanics* 488, pp. 369–398. ISSN: 0022-1120. DOI: [DOI:10.1017/S0022112003005019](https://doi.org/10.1017/S0022112003005019).
- Best, Martin et al. (2008). *Small-scale wind energy Technical Report, Urban Wind Energy Research Project*. Tech. rep. Carbon Trust, UK & UK Met Office), USA, pp. 1–191. URL: [www.carbontrust.com/resources/small-scale-wind-energy](http://www.carbontrust.com/resources/small-scale-wind-energy). [accessed: 09.15.2017].
- Bloomberg (2020). *State of the Global Mini-grids Market Report 2020*. URL: [www.minigrids.org/market-report-2020/](http://www.minigrids.org/market-report-2020/). [accessed: 09.02.2021].
- Böhm, Margi et al. (2013). "Turbulence Structure Within and Above a Canopy of Bluff Elements". In: *Boundary-Layer Meteorology* 146.3, pp. 393–419. ISSN: 1573-1472. DOI: [10.1007/s10546-012-9770-1](https://doi.org/10.1007/s10546-012-9770-1).
- Bollmeyer, C et al. (2015). "Towards a high-resolution regional reanalysis for the European CORDEX domain". In: *Quarterly Journal of the Royal Meteorological Society* 141.686, pp. 1–15. ISSN: 0035-9009. DOI: [10.1002/qj.2486](https://doi.org/10.1002/qj.2486).
- Bottema, Marcel and Patrice G Mestayer (1998). "Urban roughness mapping – validation techniques and some first results". In: *Journal of Wind Engineering and Industrial Aerodynamics* 74-76, pp. 163–173. ISSN: 0167-6105. DOI: [10.1016/S0167-6105\(98\)00014-2](https://doi.org/10.1016/S0167-6105(98)00014-2).
- Bou-Zeid, Elie, Charles Meneveau, and Marc B Parlange (2004). "Large-eddy simulation of neutral atmospheric boundary layer flow over heterogeneous surfaces: Blending height and effective surface roughness". In: *Water Resources Research* 40.2. ISSN: 0043-1397. DOI: [10.1029/2003WR002475](https://doi.org/10.1029/2003WR002475).

- Bou-Zeid, Elie, Marc B Parlange, and Charles Meneveau (2007). "On the Parameterization of Surface Roughness at Regional Scales". English. In: *Journal of the Atmospheric Sciences* 64.1, pp. 216–227. DOI: [10.1175/JAS3826.1](https://doi.org/10.1175/JAS3826.1).
- Branlard, E. et al. (2013). "Retrieving wind statistics from average spectrum of continuous-wave lidar". In: *Atmospheric Measurement Techniques* 6.7, pp. 1673–1683. ISSN: 1867-8548. DOI: [10.5194/amt-6-1673-2013](https://doi.org/10.5194/amt-6-1673-2013).
- Britter, R. E. and S. R. Hanna (2003). "Flow and Dispersion in Urban Areas". In: *Annual Review of Fluid Mechanics* 35.1, pp. 469–496. ISSN: 0066-4189. DOI: [10.1146/annurev.fluid.35.101101.161147](https://doi.org/10.1146/annurev.fluid.35.101101.161147).
- Bromwich, D H et al. (2018). "The Arctic System Reanalysis, Version 2". English. In: *Bulletin of the American Meteorological Society* 99.4, pp. 805–828. DOI: [10.1175/BAMS-D-16-0215.1](https://doi.org/10.1175/BAMS-D-16-0215.1).
- Büttner, György et al. (2021). *CORINE Land Cover, User Manual*. Tech. rep. Copenhagen, Denmark: Copernicus Land Monitoring Service (CLMS), European Environment Agency (EEA), p. 129. URL: [www.land.copernicus.eu/](http://www.land.copernicus.eu/). [accessed: 07.06.2021].
- Cariou, Jean-Pierre (2015). *Remote Sensing for Wind Energy, Summer School*. Tech. rep. E-Report-No. 0084(EN). DTU Wind Energy.
- Castro, Ian P. (2017). "Are Urban-Canopy Velocity Profiles Exponential?" In: *Boundary-Layer Meteorology* 164.3, pp. 337–351. ISSN: 15731472. DOI: [10.1007/s10546-017-0258-x](https://doi.org/10.1007/s10546-017-0258-x).
- Cavar, Dalibor et al. (2016). "Comparison of OpenFOAM and EllipSys3D for neutral atmospheric flow over complex terrain". In: *Wind Energy Science* 1.1, pp. 55–70. ISSN: 23667451. DOI: [10.5194/wes-1-55-2016](https://doi.org/10.5194/wes-1-55-2016).
- Cheng, H et al. (2007). "Flow over cube arrays of different packing densities". In: *Journal of Wind Engineering and Industrial Aerodynamics* 95.8, pp. 715–740. ISSN: 0167-6105. DOI: [10.1016/j.jweia.2007.01.004](https://doi.org/10.1016/j.jweia.2007.01.004).
- Cheng, Hong and Ian P Castro (2002). "Near Wall Flow over Urban-like Roughness". In: *Boundary-Layer Meteorology* 104.2, pp. 229–259. ISSN: 1573-1472. DOI: [10.1023/A:1016060103448](https://doi.org/10.1023/A:1016060103448). URL: <https://doi.org/10.1023/A:1016060103448>.



- Cheng, Y. et al. (2003). "A comparison of large Eddy simulations with a standard  $k-\epsilon$  Reynolds-averaged Navier-Stokes model for the prediction of a fully developed turbulent flow over a matrix of cubes". In: *Journal of Wind Engineering and Industrial Aerodynamics*. ISSN: 01676105. DOI: [10.1016/j.jweia.2003.08.001](https://doi.org/10.1016/j.jweia.2003.08.001).
- Clifton, Andrew, Dennis Elliott, and Michael Courtney (2013). *Expert Group Study on Recommended Practices 15. Ground-Based Vertically-Profiling Remote Sensing for Wind Resource Assessment*. Tech. rep. International Energy Agency. URL: [www.iea-wind.org/task32/t32-publications/](http://www.iea-wind.org/task32/t32-publications/). [accessed: 23.10.2018].
- Coceal, O. and S. E. Belcher (2004). "A canopy model of mean winds through urban areas". In: *Quarterly Journal of the Royal Meteorological Society*. ISSN: 00359009. DOI: [10.1256/qj.03.40](https://doi.org/10.1256/qj.03.40).
- Coceal, O and S E Belcher (2005). "Mean Winds Through an Inhomogeneous Urban Canopy". In: *Boundary-Layer Meteorology* 115.1, pp. 47–68. ISSN: 1573-1472. DOI: [10.1007/s10546-004-1591-4](https://doi.org/10.1007/s10546-004-1591-4).
- Contreras Montoya, Leidy Tatiana et al. (2021). "4 - Renewable energy systems". In: *Hybrid Renewable Energy Systems and Microgrids*. Ed. by Ersan Kabalci. Academic Press, pp. 103–177. ISBN: 978-0-12-821724-5. DOI: [10.1016/B978-0-12-821724-5.00013-1](https://doi.org/10.1016/B978-0-12-821724-5.00013-1).
- Cooney, Ciaran et al. (2017). "Performance characterisation of a commercial-scale wind turbine operating in an urban environment, using real data". In: *Energy for Sustainable Development* 36.Supplement C, pp. 44 –54. ISSN: 0973-0826. DOI: [doi.org/10.1016/j.esd.2016.11.001](https://doi.org/10.1016/j.esd.2016.11.001).
- Counihan, J, J C R Hunt, and P S Jackson (1974). "Wakes behind two-dimensional surface obstacles in turbulent boundary layers". In: *Journal of Fluid Mechanics* 64.3, pp. 529–564. ISSN: 0022-1120. DOI: [10.1017/S0022112074002539](https://doi.org/10.1017/S0022112074002539).
- Crago, Richard D, Winnie Okello, and Michael F Jasinski (2012). "Equations for the Drag Force and Aerodynamic Roughness Length of Urban Areas with Random Building Heights". In: *Boundary-Layer Meteorology* 145.3, pp. 423–437. ISSN: 1573-1472. DOI: [10.1007/s10546-012-9747-0](https://doi.org/10.1007/s10546-012-9747-0).
- Dadioti, Rallou and Simon Rees (2017). "Performance of Detached Eddy Simulation applied to Analysis of a University Campus Wind Environment". In: *Energy Procedia* 134.Supplement C, pp. 366–375. ISSN: 1876-6102. DOI: [10.1016/j.egypro.2017.09.551](https://doi.org/10.1016/j.egypro.2017.09.551).

- Davies, T et al. (2005). "A new dynamical core for the Met Office's global and regional modelling of the atmosphere". In: *Quarterly Journal of the Royal Meteorological Society* 131.608, pp. 1759–1782. ISSN: 0035-9009. DOI: [10.1256/qj.04.101](https://doi.org/10.1256/qj.04.101).
- DCCAE (2019a). *Climate Action Plan 2019: to Tackle Climate Breakdown*. Tech. rep. Irish Department of the Environment, Climate and Communications. URL: [www.gov.ie/en/publication/ccb2e0-the-climate-action-plan-2019/](http://www.gov.ie/en/publication/ccb2e0-the-climate-action-plan-2019/). [accessed: 05.02.2020].
- (2019b). *Ireland's Transition to a Low Carbon Energy Future 2015-2030*. Tech. rep. Irish Department of Communications, Climate Action and Environment. URL: [www.gov.ie/en/publication/550df-the-white-paper-irelands-transition-to-a-low-carbon-energy-future-2015-2030/](http://www.gov.ie/en/publication/550df-the-white-paper-irelands-transition-to-a-low-carbon-energy-future-2015-2030/). [accessed: 09.05.2019].
- DECC (2021). *Climate Action Plan 2021: Securing Our Future*. Tech. rep. Irish Department of Communications, Climate Action and Environment. URL: [www.gov.ie/en/publication/6223e-climate-action-plan-2021/](http://www.gov.ie/en/publication/6223e-climate-action-plan-2021/). [accessed: 22.11.2021].
- DECC(UK) (2009). *Numerical Objective Analysis Boundary Layer*. URL: [https://wind-power-program.com/UK\\_wind\\_speed\\_database.htm](https://wind-power-program.com/UK_wind_speed_database.htm). [accessed: 17.05.2022].
- Desmond, Cian J., Simon J. Watson, and Philip E. Hancock (2017). "Modelling the wind energy resources in complex terrain and atmospheres. Numerical simulation and wind tunnel investigation of non-neutral forest canopy flows". In: *Journal of Wind Engineering and Industrial Aerodynamics*. ISSN: 01676105. DOI: [10.1016/j.jweia.2017.03.014](https://doi.org/10.1016/j.jweia.2017.03.014).
- Dhunny, A. Z., M. R. Lollchund, and S. D.D.V. Rughooputh (2016). "Numerical analysis of wind flow patterns over complex hilly terrains: Comparison between two commonly used CFD software". In: *International Journal of Global Energy Issues* 39.3-4, pp. 181–203. ISSN: 09547118. DOI: [10.1504/IJGEI.2016.076339](https://doi.org/10.1504/IJGEI.2016.076339).
- DOE (2007). *Small Wind Electric Systems, A U.S. Consumer's Guide*. Tech. rep. DOE/GO-102007-2465. U.S. Department of Energy.
- Dörenkämper, M et al. (2020). "The Making of the New European Wind Atlas – Part 2: Production and evaluation". In: *Geoscientific Model Development* 13.10, pp. 5079–5102. DOI: [10.5194/gmd-13-5079-2020](https://doi.org/10.5194/gmd-13-5079-2020).
- Draxl, Caroline et al. (2015). "The Wind Integration National Dataset (WIND) Toolkit". In: *Applied Energy* 151, pp. 355–366. ISSN: 0306-2619. DOI: [10.1016/j.apenergy.2015.03.121](https://doi.org/10.1016/j.apenergy.2015.03.121).

- Drew, D R, J F Barlow, and T T Cockerill (2013). "Estimating the potential yield of small wind turbines in urban areas: A case study for Greater London, UK". In: *Journal of Wind Engineering and Industrial Aerodynamics* 115.Supplement C, pp. 104–111. ISSN: 0167-6105. DOI: <https://doi.org/10.1016/j.jweia.2013.01.007>.
- Drew, D R et al. (2015). "The importance of accurate wind resource assessment for evaluating the economic viability of small wind turbines". In: *Renewable Energy* 77.Supplement C, pp. 493–500. ISSN: 0960-1481. DOI: [10.1016/j.renene.2014.12.032](https://doi.org/10.1016/j.renene.2014.12.032).
- Duijm, Nijs Jan (1999). "Estimates of Roughness Parameters for Arrays of Obstacles". In: *Boundary-Layer Meteorology* 91.1, pp. 1–22. ISSN: 1573-1472. DOI: [10.1023/A:1001794831176](https://doi.org/10.1023/A:1001794831176).
- DWEA (2015). *Distributed wind vision 2015-2030*. Tech. rep. Distributed Wind Energy Association, USA.
- Dwyer, N (2012). *Status of Ireland's Climate*. Tech. rep. Environmental Protection Agency, Ireland.
- Elia, A et al. (2020). "Wind turbine cost reduction: A detailed bottom-up analysis of innovation drivers". In: *Energy Policy* 147, p. 111912. ISSN: 0301-4215. DOI: <https://doi.org/10.1016/j.enpol.2020.111912>.
- Elshurafa, Amro M. et al. (2018). "Estimating the learning curve of solar PV balance-of-system for over 20 countries: Implications and policy recommendations". In: *Journal of Cleaner Production* 196, pp. 122–134. ISSN: 0959-6526. DOI: [10.1016/J.JCLEPRO.2018.06.016](https://doi.org/10.1016/J.JCLEPRO.2018.06.016).
- Emeis, Stefan (2013). *Wind Energy Meteorology, Atmospheric Physics for Wind Power Generation*. Springer, Berlin. ISBN: 978-3-642-30523-8. DOI: [10.1007/978-3-642-30523-8](https://doi.org/10.1007/978-3-642-30523-8).
- Emejeamara, F. C. and A. S. Tomlin (2020). "A method for estimating the potential power available to building mounted wind turbines within turbulent urban air flows". In: *Renewable Energy* 153, pp. 787–800. ISSN: 18790682. DOI: [10.1016/j.renene.2020.01.123](https://doi.org/10.1016/j.renene.2020.01.123).
- Emejeamara, F.C., A.S. Tomlin, and J.T. Millward-Hopkins (2015). "Urban wind: Characterisation of useful gust and energy capture". In: *Renewable Energy* 81, pp. 162–172. ISSN: 0960-1481. DOI: [10.1016/J.RENENE.2015.03.028](https://doi.org/10.1016/J.RENENE.2015.03.028).

- Encraft (2009). *The Warwick Wind Trials Project*. Tech. rep. URL: [www.warwickwindtrials.org.uk](http://www.warwickwindtrials.org.uk). [accessed: 08.06.2015].
- EROS (2017). *Shuttle Radar Topography Mission (SRTM) 1 Arc-Second Global*. DOI: 10.5066/F7PR7TFT. URL: [https://www.usgs.gov/centers/eros/science/usgs-eros-archive-digital-elevation-shuttle-radar-topography-mission-srtm-1-arc?qt-science\\_center\\_objects=0#qt-science\\_center\\_objects](https://www.usgs.gov/centers/eros/science/usgs-eros-archive-digital-elevation-shuttle-radar-topography-mission-srtm-1-arc?qt-science_center_objects=0#qt-science_center_objects). [accessed: 19.10.2022].
- ESMAP (2019). *Mini Grids for Half a Billion People: Market Outlook and Handbook for Decision Makers. Executive Summary. Energy Sector Management Assistance Program (ESMAP)*. Tech. rep. 014/19. Washington, DC: World Bank. URL: [www.hdl.handle.net/10986/31926](http://www.hdl.handle.net/10986/31926). [accessed: 01.12.2019].
- Evans, Samuel P. et al. (2017). "The suitability of the IEC 61400-2 wind model for small wind turbines operating in the built environment". In: *Renewable Energy and Environmental Sustainability* 2, p. 31. ISSN: 2493-9439. DOI: 10.1051/rees/2017022.
- Farr, Tom G et al. (2007). "The Shuttle Radar Topography Mission". In: *Reviews of Geophysics* 45.2. ISSN: 8755-1209. DOI: 10.1029/2005RG000183.
- Fields, Jason, Heidi Tinnesand, and Ian Baring-Gould (2016). *Distributed Wind Resource Assessment: State of the Industry*. Tech. rep. NREL/TP-5000-66419. Golden, USA: National Renewable Energy Laboratory (NREL).
- Fields, Jason et al. (2016). *Deployment of Wind Turbines in the Built Environment: Risks, Lessons, and Recommended Practices*. Tech. rep. NREL/TP-5000-65622. Golden, USA: National Renewable Energy Laboratory (NREL).
- Forsyth, Trudy et al. (2015). *Quality Infrastructure for RETs - Small Wind Turbines (for policy makers)*. Tech. rep. December, p. 56. URL: [www.irena.org/publications](http://www.irena.org/publications). [accessed: 05.11,2019].
- Forsyth, Trudy et al. (2017). *The Distributed Wind Cost Taxonomy*. Tech. rep. NREL/TP-5000-67992. Golden CO, USA: National Renewable Energy Laboratory. URL: [www.nrel.gov/publications](http://www.nrel.gov/publications). [accessed: 05.11,2019].
- Foster, Nikolas et al. (2020). "The "perfect storm" for distributed wind markets". In: *Renewable Energy*. ISSN: 18790682. DOI: 10.1016/j.renene.2019.05.058.

- Franke, Jorg et al. (2011). "The COST 732 Best Practice Guideline for CFD simulation of flows in the urban environment: a summary". In: *International Journal of Environment and Pollution* 44.1-4, pp. 419–427. DOI: [10.1504/IJEP.2011.038443](https://doi.org/10.1504/IJEP.2011.038443).
- Gallagher, Sarah et al. (2016). "The nearshore wind and wave energy potential of Ireland: A high resolution assessment of availability and accessibility". In: *Renewable Energy* 88, pp. 494–516. ISSN: 0960-1481. DOI: [10.1016/J.RENENE.2015.11.010](https://doi.org/10.1016/J.RENENE.2015.11.010).
- Gannon, Jim (2018). *Energy in Ireland*. Tech. rep. Sustainable Energy Authority of Ireland. URL: [www.seai.ie/publications/Energy-in-Ireland-2018.pdf](http://www.seai.ie/publications/Energy-in-Ireland-2018.pdf). [accessed: 02.03.2019].
- Gasset, Nicolas, Mathieu Landry, and Yves Gagnon (2012). "A Comparison of Wind Flow Models for Wind Resource Assessment in Wind Energy Applications". In: *Energies* 5.11, pp. 4288–4322. ISSN: 1996-1073. DOI: [10.3390/en5114288](https://doi.org/10.3390/en5114288).
- Ghani, Rizwan et al. (2019). "Wind energy at remote islands in arctic region—A case study of Solovetsky islands". In: *Journal of Renewable and Sustainable Energy* 11.5, p. 53304. DOI: [10.1063/1.5110756](https://doi.org/10.1063/1.5110756).
- Giebel, Gregor and George Kariniotakis (2017). "3 - Wind power forecasting—a review of the state of the art". In: *Woodhead Publishing Series in Energy*. Ed. by George B T Renewable Energy Forecasting Kariniotakis. Woodhead Publishing, pp. 59–109. ISBN: 978-0-08-100504-0. DOI: [10.1016/B978-0-08-100504-0.00003-2](https://doi.org/10.1016/B978-0-08-100504-0.00003-2).
- Goit, Jay Prakash, Susumu Shimada, and Tetsuya Kogaki (2019). "Can LiDARs Replace Meteorological Masts in Wind Energy?" In: *Energies* 12.19. ISSN: 1996-1073. DOI: [10.3390/en12193680](https://doi.org/10.3390/en12193680).
- Gorroño-Albizu, Leire, Karl Sperling, and Søren Djørup (2019). "The past, present and uncertain future of community energy in Denmark: Critically reviewing and conceptualising citizen ownership". In: *Energy Research & Social Science* 57, p. 101231. ISSN: 2214-6296. DOI: [10.1016/j.erss.2019.101231](https://doi.org/10.1016/j.erss.2019.101231).
- Greco, Steven et al. (2020). *Polar Winds: Airborne Doppler Wind Lidar Missions in the Arctic for Atmospheric Observations and Numerical Model Comparisons*. DOI: [10.3390/atmos1111141](https://doi.org/10.3390/atmos1111141).

- Greenwood, D M et al. (2017). "Frequency response services designed for energy storage". In: *Applied Energy* 203, pp. 115 –127. ISSN: 0306-2619. DOI: [10.1016/j.apenergy.2017.06.046](https://doi.org/10.1016/j.apenergy.2017.06.046).
- Grieser, Benno, Yasin Sunak, and Reinhard Madlener (2015). "Economics of small wind turbines in urban settings: An empirical investigation for Germany". In: *Renewable Energy* 78.Supplement C, pp. 334 –350. ISSN: 0960-1481. DOI: [10.1016/j.renene.2015.01.008](https://doi.org/10.1016/j.renene.2015.01.008).
- Griffin, Seanie (2017). *Global Gridded Meteorological Datasets*. Tech. rep. Dublin: Energy Systems Integration Partnership Programme, University College Dublin. URL: <https://metclim.ucd.ie/2017/09/gridded-meteorological-datasets/>. [accessed: 05.03.2018].
- Grimmond, C S B and T R Oke (1999). "Aerodynamic Properties of Urban Areas Derived from Analysis of Surface Form". English. In: *Journal of Applied Meteorology* 38.9, pp. 1262–1292. DOI: [10.1175/1520-0450\(1999\)038<1262:APOUAD>2.0.CO;2](https://doi.org/10.1175/1520-0450(1999)038<1262:APOUAD>2.0.CO;2).
- Gu, Dan and Hee-Chang Lim (2012). "Wind flow around rectangular obstacles and the effects of aspect ratio". In: *The Seventh International Colloquium on Bluff Body Aerodynamics and Applications (BBAA7)*. Shanghai, China: International Association for Wind Engineering.
- Gualtieri, Giovanni (2019). "A comprehensive review on wind resource extrapolation models applied in wind energy". In: *Renewable and Sustainable Energy Reviews* 102, pp. 215–233. ISSN: 18790690. DOI: [10.1016/j.rser.2018.12.015](https://doi.org/10.1016/j.rser.2018.12.015).
- Gylling, Niels et al. (2015). "Comparison of Resource and Energy Yield Assessment Procedures 2011-2015: What have we learned and what needs to be done?" In: *Proceedings of the EWEA Annual Event and Exhibition*. Paris, France.
- Hall, S et al. (2020). *Business Models for Prosumers in Europe. PROSEU - Prosumers for the Energy Union: Mainstreaming active participation of citizens in the energy transition*. (Deliverable N°D4.1). URL: [www.proseu.eu](http://www.proseu.eu). [accessed: 01.12.2020].
- Hanrahan, Brian Leif et al. (2014). "A powerful visualization technique for electricity supply and demand at industrial sites with combined heat and power and wind generation". In: *Renewable and Sustainable Energy Reviews* 31.Supplement C, pp. 860–869. DOI: [10.1016/j.rser.2013.12.016](https://doi.org/10.1016/j.rser.2013.12.016).

- Harris, Michael, Graham Constant, and Carol Ward (2001). "Continuous-wave bistatic laser Doppler wind sensor". In: *Applied Optics* 40.9, pp. 1501–1506. DOI: [10.1364/AO.40.001501](https://doi.org/10.1364/AO.40.001501).
- Hassanli, Sina et al. (2019). "Application of through-building openings for wind energy harvesting in built environment". In: *Journal of Wind Engineering and Industrial Aerodynamics* 184, pp. 445–455. ISSN: 0167-6105. DOI: [10.1016/J.JWEIA.2018.11.030](https://doi.org/10.1016/J.JWEIA.2018.11.030).
- He, Xiaodong et al. (2019). "High-resolution dataset of urban canopy parameters for Beijing and its application to the integrated WRF/Urban modelling system". In: *Journal of Cleaner Production* 208, pp. 373–383. ISSN: 09596526. DOI: [10.1016/j.jclepro.2018.10.086](https://doi.org/10.1016/j.jclepro.2018.10.086).
- Heath, Malcolm A., John D. Walshe, and Simon J. Watson (2007). "Estimating the potential yield of small building-mounted wind turbines". In: *Wind Energy*. ISSN: 10954244. DOI: [10.1002/we.222](https://doi.org/10.1002/we.222).
- Herrmann-Priesnitz, Benjamín, Williams R. Calderón-Muñoz, and Richard Leboeuf (2015). "Effects of urban configuration on the wind energy distribution over a building". In: *Journal of Renewable and Sustainable Energy*. ISSN: 19417012. DOI: [10.1063/1.4921369](https://doi.org/10.1063/1.4921369).
- Higgins, Paraic and Aoife Foley (2014). "The evolution of offshore wind power in the United Kingdom". In: *Renewable and Sustainable Energy Reviews* 37, pp. 599–612. ISSN: 1364-0321. DOI: [10.1016/j.rser.2014.05.058](https://doi.org/10.1016/j.rser.2014.05.058).
- Hildreth, Laura and Arne Kildegaard (2009). "Avoided demand charges and behind-the-meter wind: insights from an application at the University of Minnesota". In: *Wind Energy* 12.4, pp. 363–374. ISSN: 1099-1824. DOI: [10.1002/we.298](https://doi.org/10.1002/we.298).
- Holton, R. James and J. Hakim Gregory (2012). *An Introduction to Dynamic Meteorology*. San Diego, United States: Elsevier Science Publishing Co Inc. ISBN: 9780123848666.
- Howard, Tom and Peter Clark (2007). "Correction and downscaling of NWP wind speed forecasts". In: *Meteorological Applications* 14.2, pp. 105–116. ISSN: 1469-8080. DOI: [10.1002/met.12](https://doi.org/10.1002/met.12).
- IEA (2020). *World Energy Outlook 2020*. Tech. rep. International Energy Agency. URL: [www.iea.org/reports/world-energy-outlook-2020](http://www.iea.org/reports/world-energy-outlook-2020). [accessed: 01.12.2020].



- IEA Wind (2018). *Micro-Siting Small Wind Turbines for Highly Turbulent Sites*. Tech. rep. IEA Wind TCP RP19. International Energy Agency. URL: [www.iea-wind.org/iea-publications/](http://www.iea-wind.org/iea-publications/). [accessed: 13.02.2019].
- IEC 61400-1 (2019). *IEC Wind energy generation systems - IEC 61400-1: Design requirements*. Tech. rep. International Electrotechnical Commission.
- IEC 61400-12 (2019). *IEC Wind energy generation systems - 61400-12-1 Power performance measurements of electricity producing wind turbines*. Tech. rep. September 2019. International Electrotechnical Commission.
- IEC 61400-2 (2013). *IEC Wind energy generation systems - IEC 61400-2, Small Wind Turbines*. Tech. rep. International Electrotechnical Commission.
- IRENA (2020a). *Renewable Power Generation Costs in 2019*. Tech. rep. International Renewable Energy Agency, p. 160. URL: <https://www.irena.org/publications/2020/Jun/Renewable-Power-Costs-in-2019>. [accessed: 18.11.2020].
- (2020b). *Stimulating investment in community energy, Broadening the ownership of renewables*. Tech. rep. Abu Dhabi: International Renewable Energy Agency, p. 44. URL: [www.irena.org/publications/2020/Dec/Stimulating-investment-in-community-energy-Broadening-the-ownership-of-renewables](http://www.irena.org/publications/2020/Dec/Stimulating-investment-in-community-energy-Broadening-the-ownership-of-renewables). [accessed: 18.01.2021].
- Ishugah, T F et al. (2014). “Advances in wind energy resource exploitation in urban environment: A review”. In: *Renewable and Sustainable Energy Reviews* 37.Supplement C, pp. 613–626. ISSN: 1364-0321. DOI: [10.1016/j.rser.2014.05.053](https://doi.org/10.1016/j.rser.2014.05.053).
- Jackson, P S and J C R Hunt (1975). “Turbulent wind flow over a low hill”. In: *Quarterly Journal of the Royal Meteorological Society* 101.430, pp. 929–955. ISSN: 0035-9009. DOI: [10.1002/qj.49710143015](https://doi.org/10.1002/qj.49710143015).
- Jung, Christopher and Dirk Schindler (2020a). “Integration of small-scale surface properties in a new high resolution global wind speed model”. In: *Energy Conversion and Management* 210.January, p. 112733. ISSN: 01968904. DOI: [10.1016/j.enconman.2020.112733](https://doi.org/10.1016/j.enconman.2020.112733).
- (2020b). “The annual cycle and intra-annual variability of the global wind power distribution estimated by the system of wind speed distributions”. In: *Sustainable Energy Technologies and Assessments* 42.September, p. 100852. ISSN: 22131388. DOI: [10.1016/j.seta.2020.100852](https://doi.org/10.1016/j.seta.2020.100852).



- Kalverla, Peter et al. (2018). "Evaluation of three mainstream numerical weather prediction models with observations from meteorological mast IJmuiden at the North Sea". In: *Wind Energy*. ISSN: 10991824. DOI: [10.1002/we.2267](https://doi.org/10.1002/we.2267).
- Kastner-Klein, Petra and Mathias W Rotach (2004). "Mean Flow and Turbulence Characteristics in an Urban Roughness Sublayer". In: *Boundary-Layer Meteorology* 111.1, pp. 55–84. ISSN: 1573-1472. DOI: [10.1023/B:BOUN.0000010994.32240.b1](https://doi.org/10.1023/B:BOUN.0000010994.32240.b1).
- KC, Anup, Jonathan Whale, and Tania Urmee (2019). "Urban wind conditions and small wind turbines in the built environment: A review". In: *Renewable Energy* 131, pp. 268–283. ISSN: 0960-1481. DOI: [10.1016/j.renene.2018.07.050](https://doi.org/10.1016/j.renene.2018.07.050).
- Keller, Jan D and Sabrina Wahl (2021). "Representation of Climate in Reanalyses: An Intercomparison for Europe and North America". English. In: *Journal of Climate* 34.5, pp. 1667–1684. DOI: [10.1175/JCLI-D-20-0609.1](https://doi.org/10.1175/JCLI-D-20-0609.1).
- Kelley, Neil. D (2017). "Wind Potential and Turbulence Characteristics Assessment for Complex Sites". In: *Austrian Small Wind Conference*. University of Applied Sciences. Vienna.
- Kent, Christoph W et al. (2017). "Evaluation of Urban Local-Scale Aerodynamic Parameters: Implications for the Vertical Profile of Wind Speed and for Source Areas". In: *Boundary-Layer Meteorology* 164.2, pp. 183–213. ISSN: 1573-1472. DOI: [10.1007/s10546-017-0248-z](https://doi.org/10.1007/s10546-017-0248-z).
- Kim, Hyun-Goo, Jin-Young Kim, and Yong-Heack Kang (2018). "Comparative Evaluation of the Third-Generation Reanalysis Data for Wind Resource Assessment of the Southwestern Offshore in South Korea". In: *Atmosphere* 9.2. ISSN: 2073-4433. DOI: [10.3390/atmos9020073](https://doi.org/10.3390/atmos9020073).
- Knievel, Jason (2006). "Numerical Weather Prediction (NWP) and the WRF Model". In: *ATEC Forecasters' Conference*. Boulder: National Centre for Atmospheric Research.
- Komusanac, Ivan et al. (2021). *Wind energy in Europe, 2020 Statistics and the outlook for 2021-2025*. Tech. rep. Wind Europe. URL: [www.windeurope.org/intelligence-platform/product/wind-energy-in-europe-in-2020-trends-and-statistics/](https://www.windeurope.org/intelligence-platform/product/wind-energy-in-europe-in-2020-trends-and-statistics/). [accessed: 26.02.2021].

- Kulovesi, Kati and Sebastian Oberthür (2020). "Assessing the EU's 2030 Climate and Energy Policy Framework: Incremental change toward radical transformation?" In: *Review of European, Comparative & International Environmental Law* 29.2, pp. 151–166. ISSN: 2050-0386. DOI: [10.1111/reel.12358](https://doi.org/10.1111/reel.12358).
- Kumar, Muneendra (1988). "World geodetic system 1984: A modern and accurate global reference frame". In: *Marine Geodesy* 12.2, pp. 117–126. ISSN: 0149-0419. DOI: [10.1080/15210608809379580](https://doi.org/10.1080/15210608809379580).
- Kurita, Susumu and Manabu Kanda (2009). "Characteristics of Boundary Layer over a Sequence of Small Localized Urban Canopies with Various Heights Obtained by Wind-Tunnel Experiment". In: *Journal of the Meteorological Society of Japan* 87.4, pp. 705–719. DOI: [10.2151/jmsj.87.705](https://doi.org/10.2151/jmsj.87.705).
- Landberg, Lars et al. (2003). "Wind Resource Estimation—An Overview". In: *Wind Energy* 6.3, pp. 261–271. ISSN: 1095-4244. DOI: [10.1002/we.94](https://doi.org/10.1002/we.94).
- Lantz, Eric et al. (2016). *Assessing the Future of Distributed Wind: Opportunities for Behind-the-Meter Projects*. Tech. rep. NREL/TP-6A20-67337. National Renewable Energy Laboratory (NREL). DOI: [10.2172/1333625](https://doi.org/10.2172/1333625).
- Leahy, P G and A M Foley (2012). "Wind generation output during cold weather-driven electricity demand peaks in Ireland". In: *Energy* 39.1, pp. 48–53. ISSN: 0360-5442. DOI: [10.1016/j.energy.2011.07.013](https://doi.org/10.1016/j.energy.2011.07.013).
- Lee, Joyce and Feng Zhao (2020). *GWEC Global Wind Report*. Brussels: Global Wind Energy Council. URL: [www.gwec.net/market-intelligence/resources/](http://www.gwec.net/market-intelligence/resources/). [accessed: 01.12.2020].
- (2021). *Global Wind Energy Report*. Tech. rep. Brussels: Global Wind Energy Council. URL: <https://www.gwec.net/market-intelligence/resources/>. [accessed: 18.05.2021].
- Leonard, B P (1979). "A stable and accurate convective modelling procedure based on quadratic upstream interpolation". In: *Computer Methods in Applied Mechanics and Engineering* 19.1, pp. 59–98. ISSN: 0045-7825. DOI: [doi.org/10.1016/0045-7825\(79\)90034-3](https://doi.org/10.1016/0045-7825(79)90034-3).
- Lettau, H (1969). "Note on Aerodynamic Roughness-Parameter Estimation on the Basis of Roughness-Element Description". In: *Journal of Applied Meteorology* (1962-1982) 8.5, pp. 828–832. ISSN: 00218952, 2163534X. URL: [www.jstor.org/stable/26174682](http://www.jstor.org/stable/26174682). [accessed: 11.08.17].

- Liu, W Y, J G Han, and X N Lu (2014). "Experiment and performance analysis of the Northwind 100 wind turbine in CASE". In: *Energy and Buildings* 68, pp. 471–475. ISSN: 0378-7788. DOI: <https://doi.org/10.1016/j.enbuild.2013.09.033>. URL: <https://www.sciencedirect.com/science/article/pii/S0378778813006154>.
- Liu, Zhengliang et al. (2019). *A Review of Progress and Applications of Pulsed Doppler Wind LiDARs*. DOI: [10.3390/rs11212522](https://doi.org/10.3390/rs11212522).
- Lombardo, Franklin T (2021). "History of the peak three-second gust". In: *Journal of Wind Engineering and Industrial Aerodynamics* 208, p. 104447. ISSN: 0167-6105. DOI: <https://doi.org/10.1016/j.jweia.2020.104447>. URL: <https://www.sciencedirect.com/science/article/pii/S0167610520303573>.
- Lopes, A Silva, J M L M Palma, and U Piomelli (2015). "On the Determination of Effective Aerodynamic Roughness of Surfaces with Vegetation Patches". In: *Boundary-Layer Meteorology* 156.1, pp. 113–130. ISSN: 1573-1472. DOI: [10.1007/s10546-015-0022-z](https://doi.org/10.1007/s10546-015-0022-z). URL: <https://doi.org/10.1007/s10546-015-0022-z>.
- Luo, Xing et al. (2015). "Overview of current development in electrical energy storage technologies and the application potential in power system operation". In: *Applied Energy* 137, pp. 511–536. ISSN: 0306-2619. DOI: <https://doi.org/10.1016/j.apenergy.2014.09.081>. URL: <http://www.sciencedirect.com/science/article/pii/S0306261914010290>.
- Ma, Zheng et al. (2018). "Solutions for Remote Island Microgrids : Discussion and analysis of Indonesia's remote island energy system". In: *International Conference on Innovative Smart Grid Technologies, ISGT Asia 2018*. Singapore: IEEE, pp. 493–498. DOI: [10.1109/ISGT-Asia.2018.8467954](https://doi.org/10.1109/ISGT-Asia.2018.8467954).
- MacArtain, Paul, Raymond Byrne, and Neil J Hewitt (2018). "Increased Benefit Of ZnBr Flow Battery With 33kWp PV System And Smart Tariff Structure". In: *Energy Procedia* 155, pp. 514–523. ISSN: 1876-6102. DOI: [10.1016/J.EGYPRO.2018.11.029](https://doi.org/10.1016/J.EGYPRO.2018.11.029). URL: <https://www.sciencedirect.com/science/article/pii/S1876610218309755>.
- Macdonald, R. W. (2000). "Modelling the mean velocity profile in the urban canopy layer". In: *Boundary-Layer Meteorology* 97.1, pp. 25–45. ISSN: 00068314. DOI: [10.1023/A:1002785830512](https://doi.org/10.1023/A:1002785830512).
- Macdonald, R W, R F Griffiths, and D J Hall (1998). "An improved method for the estimation of surface roughness of obstacle arrays". In: *Atmospheric Environment*

- 32.11, pp. 1857–1864. ISSN: 1352-2310. DOI: [https://doi.org/10.1016/S1352-2310\(97\)00403-2](https://doi.org/10.1016/S1352-2310(97)00403-2). URL: <http://www.sciencedirect.com/science/article/pii/S1352231097004032>.
- Mann, J. et al. (2017). “Complex terrain experiments in the New European Wind Atlas”. In: *Philosophical Transactions of the Royal Society A: Mathematical, Physical and Engineering Sciences*. ISSN: 1364503X. DOI: [10.1098/rsta.2016.0101](https://doi.org/10.1098/rsta.2016.0101).
- Manwell, James F., Jon G. McGowan, and Anthony L. Rogers (2009). *Wind Energy Explained: Theory, Design and Application*. 2nd. Wiley. ISBN: 978-0-470-01500-1.
- Mazzi, Nicoló and Pierre Pinson (2017). “10 - Wind power in electricity markets and the value of forecasting”. In: *Woodhead Publishing Series in Energy*. Ed. by George B T Renewable Energy Forecasting Kariniotakis. Woodhead Publishing, pp. 259–278. ISBN: 978-0-08-100504-0. DOI: [10.1016/B978-0-08-100504-0.00010-X](https://doi.org/10.1016/B978-0-08-100504-0.00010-X).
- Mertens, Sander (2006). *Wind Energy in the Built Environment Concentrator Effects of Buildings*. Multi-Science. ISBN: 0906522 35 8.
- Mesinger, Fedor et al. (2006). “North American Regional Reanalysis”. English. In: *Bulletin of the American Meteorological Society* 87.3, pp. 343–360. DOI: [10.1175/BAMS-87-3-343](https://doi.org/10.1175/BAMS-87-3-343).
- Micallef, Daniel and Gerard Van Bussel (2018). “A review of urban wind energy research: Aerodynamics and other challenges”. In: *Energies* 11.9, pp. 1–27. ISSN: 19961073. DOI: [10.3390/en11092204](https://doi.org/10.3390/en11092204).
- Milciuvienė, Saule et al. (2019). “The role of renewable energy prosumers in implementing energy justice theory”. In: *Sustainability (Switzerland)* 11.19. ISSN: 20711050. DOI: [10.3390/su11195286](https://doi.org/10.3390/su11195286).
- Millward-Hopkins, J. T. et al. (2011). “Estimating Aerodynamic Parameters of Urban-Like Surfaces with Heterogeneous Building Heights”. In: *Boundary-Layer Meteorology* 141.3, pp. 443–465. ISSN: 00068314. DOI: [10.1007/s10546-011-9640-2](https://doi.org/10.1007/s10546-011-9640-2).
- Millward-Hopkins, J. T. et al. (2013a). “Aerodynamic Parameters of a UK City Derived from Morphological Data”. In: *Boundary-Layer Meteorology* 146.3, pp. 447–468. ISSN: 00068314. DOI: [10.1007/s10546-012-9761-2](https://doi.org/10.1007/s10546-012-9761-2).
- Millward-Hopkins, J T et al. (2013b). “Assessing the potential of urban wind energy in a major UK city using an analytical model”. In: *Renewable Energy* 60. Supplement C, pp. 701–710. ISSN: 0960-1481. DOI: [10.1016/j.renene.2013.06.020](https://doi.org/10.1016/j.renene.2013.06.020).

- Millward-Hopkins, J. T. et al. (2013c). "Mapping the wind resource over UK cities". In: *Renewable Energy* 55, pp. 202–211. ISSN: 09601481. DOI: [10.1016/j.renene.2012.12.039](https://doi.org/10.1016/j.renene.2012.12.039).
- Millward-Hopkins, Joel (2013). "Predicting the Wind Resource Available to Roof-Mounted Wind Turbines in Urban Areas". PhD thesis. University of Leeds, p. 197.
- Mortensen, N. G. (2016). *Wind resource assessment using the WAsP software (DTU Wind Energy E; No. 0135)*. Tech. rep. Technical University of Denmark (DTU).
- Mortensen, N.G. and E.L. Petersen (1998). "Influence of topographical input data on the accuracy of wind flow modelling in complex terrain". In: *European wind energy conference*. Dublin: EWEA, pp. 317–320.
- N. Sørensen, Niels et al. (2018). "Aerodynamic effects of compressibility for wind turbines at high tip speeds". In: *Journal of Physics: Conference Series* 1037, p. 22003. ISSN: 1742-6588. DOI: [10.1088/1742-6596/1037/2/022003](https://doi.org/10.1088/1742-6596/1037/2/022003).
- Nakayama, Y and R.F Boucher (2000). *Introduction to Fluid Mechanics*. Ed. by Matthew Flynn and Liz Gooster. Yokendo Co. Ltd, p. 322. ISBN: 0 340 67649 3.
- Nazir, Muhammad S et al. (2020). *Wind Generation Forecasting Methods and Proliferation of Artificial Neural Network: A Review of Five Years Research Trend*. DOI: [10.3390/su12093778](https://doi.org/10.3390/su12093778).
- Neuhoff, Karsten, Sophia Wolter, and Sebastian Schwenen (2016). "Power markets with Renewables: New perspectives for the European Target Model". In: *The Energy Journal* 37. ISSN: 1944-9089. DOI: [10.5547/01956574.37.2.kneu](https://doi.org/10.5547/01956574.37.2.kneu).
- Newman, Jennifer F and Petra M Klein (2014). *The Impacts of Atmospheric Stability on the Accuracy of Wind Speed Extrapolation Methods*. DOI: [10.3390/resources3010081](https://doi.org/10.3390/resources3010081).
- Nieuwpoort, A.M.H., J.H.M. Gooden, and J.L. de Prins (2010). *Wind criteria due to obstacles at and around airports*. Tech. rep. Amsterdam: National Aerospace Laboratory NLR and DGTI, pp200. DOI: [NLR-TP-2010-312](https://doi.org/10.1016/j.nlr-tp-2010-312). URL: <http://reports.nlr.nl:8080/xmlui/handle/10921/164>.
- Nock, Destenie and Erin Baker (2017). "Unintended consequences of Northern Ireland's renewable obligation policy". In: *Electricity Journal* 30.7, pp. 47–54. ISSN: 10406190. DOI: [10.1016/j.tej.2017.07.002](https://doi.org/10.1016/j.tej.2017.07.002).
- Olsen, B T et al. (2017). "An intercomparison of mesoscale models at simple sites for wind energy applications". In: *Wind Energ. Sci.* 2.1, pp. 211–228. ISSN: 2366-7451. DOI: [10.5194/wes-2-211-2017](https://doi.org/10.5194/wes-2-211-2017).

- Olsen, Tim and Robert Preus (2015). *Small Wind Site Assessment Guidelines*. Tech. rep. NREL/TP-5000-63696. Golden, USA: National Renewable Energy Laboratory (NREL). DOI: [10.2172/1225476](https://doi.org/10.2172/1225476).
- Orrell, Alice and Ian Baring-Gould (2018). *IEA Wind Task 41: Enabling Wind as a Distributed Energy Resource*. Tech. rep. PNNL-SA-152370. International Energy Agency (IEA), pp. 1–5. URL: [www.iea-wind.org/task41/t41-publications/](http://www.iea-wind.org/task41/t41-publications/). [accessed: 10.06.2019].
- Orrell, Alice et al. (2019). *2018 Distributed Wind Market Report*. Tech. rep. August. Pacific Northwest National Laboratory, p. 52. URL: [www.energy.gov/eere/wind/wind-energy-technologies-office](http://www.energy.gov/eere/wind/wind-energy-technologies-office). [accessed: 10.06.2019].
- Oteri, Frank et al. (2018). *2017 State of Wind Development in the United States by Region*. Tech. rep. NREL/TP-5000-70738. Golden CO, USA: National Renewable Energy Laboratory (NREL), p. 179. URL: <https://www.energy.gov/eere/wind/downloads/2017-state-wind-development-united-states-region>. [accessed: 11.12.2018)].
- Panigrahi, R et al. (2020). “Grid Integration of Small-Scale Photovoltaic Systems in Secondary Distribution Network—A Review”. In: *IEEE Transactions on Industry Applications* 56.3, pp. 3178–3195. ISSN: 1939-9367 VO - 56. DOI: [10.1109/TIA.2020.2979789](https://doi.org/10.1109/TIA.2020.2979789).
- Peña, Alfredo et al. (2015). *Remote Sensing for Wind Energy, Summer School*. Tech. rep. E-Report-No. 0084(EN). Roskilde: DTU Wind Energy.
- Peña, Alfredo et al. (2016). “The fence experiment – full-scale lidar-based shelter observations”. In: *Wind Energ. Sci* 1, pp. 101–114. DOI: [10.5194/wes-1-101-2016](https://doi.org/10.5194/wes-1-101-2016).
- Perera, M.D.A.E.S. (1981). “Shelter behind two-dimensional solid and porous fences”. In: *Journal of Wind Engineering and Industrial Aerodynamics* 8.1, pp. 93–104. ISSN: 0167-6105. DOI: [10.1016/0167-6105\(81\)90010-6](https://doi.org/10.1016/0167-6105(81)90010-6).
- Peterka, J.A., R.N. Meroney, and K.M. Kothari (1985). “Wind flow patterns about buildings”. In: *Journal of Wind Engineering and Industrial Aerodynamics* 21.1, pp. 21–38. ISSN: 0167-6105. DOI: [10.1016/0167-6105\(85\)90031-5](https://doi.org/10.1016/0167-6105(85)90031-5).
- Petersen, Erik Lundtang and Ib Troen (2012). “Wind conditions and resource assessment”. In: *Wiley Interdisciplinary Reviews: Energy and Environment*. ISSN: 20418396. DOI: [10.1002/wene.4](https://doi.org/10.1002/wene.4).

- Pitter, Mark, Chris Slinger, and Harris Michael (2015). *Remote Sensing for Wind Energy, Summer School*. Tech. rep. E-Report-No. 0084(EN). DTU Wind Energy.
- Poudel, R. C., H. Tinnesand, and I. E. Baring-Gould (2020). "An Evaluation of Advanced Tools for Distributed Wind Turbine Performance Estimation". In: *Journal of Physics: Conference Series* 1452.1. ISSN: 17426596. DOI: [10.1088/1742-6596/1452/1/012017](https://doi.org/10.1088/1742-6596/1452/1/012017).
- Raupach, M R (1992). "Drag and drag partition on rough surfaces". In: *Boundary-Layer Meteorology* 60.4, pp. 375–395. ISSN: 1573-1472. DOI: [10.1007/BF00155203](https://doi.org/10.1007/BF00155203).
- RenewableNI (2021). *An economic review of small-scale wind in Northern Ireland*. Tech. rep. RenewableNI. URL: [www.renewableuk.com/resource/resmgr/policy\\_uploads/An\\_Economic\\_Review\\_of\\_Small\\_.pdf](http://www.renewableuk.com/resource/resmgr/policy_uploads/An_Economic_Review_of_Small_.pdf). [accessed: 10.05.2021].
- RenewableUK (2014). *Small and Medium Wind Strategy, The current and future potential of the sub-500kW wind industry in the UK*. Tech. rep. URL: [www.renewableuk.com/resource/resmgr/Docs/small\\_medium\\_wind\\_strategy\\_r.pdf](http://www.renewableuk.com/resource/resmgr/Docs/small_medium_wind_strategy_r.pdf). [accessed: 10.05.2021].
- (2015). *Small and Medium Wind UK Market Report*. Tech. rep. RenewableUK. URL: [www.renewableuk.com/news/304391/Small-and-Medium-Wind-UK-Market-Report-2015.htm](http://www.renewableuk.com/news/304391/Small-and-Medium-Wind-UK-Market-Report-2015.htm). [accessed: 10.05.2021].
- Ringkjøb, Hans-Kristian, Peter M Haugan, and Astrid Nybø (2020). "Transitioning remote Arctic settlements to renewable energy systems – A modelling study of Longyearbyen, Svalbard". In: *Applied Energy* 258, p. 114079. ISSN: 0306-2619. DOI: [10.1016/j.apenergy.2019.114079](https://doi.org/10.1016/j.apenergy.2019.114079).
- Rodrigo, J Sanz et al. (2018). "Comparing Meso-Micro Methodologies for Annual Wind Resource Assessment and Turbine Siting at Cabauw". In: *Journal of Physics: Conference Series*, p. 72030. DOI: [10.1088/1742-6596/1037/7/072030](https://doi.org/10.1088/1742-6596/1037/7/072030).
- Roeth, Jacques (2010). *Wind Resource Assessment Handbook*. Tech. rep. NYSERDA Report 10-30. AWS Truepower/New York State Energy Research and Development Authority.
- Rooney, G G (2001). "Comparison Of Upwind Land Use And Roughness Length Measured In The Urban Boundary Layer". In: *Boundary-Layer Meteorology* 3, pp. 469–485. ISSN: 1573-1472. DOI: [10.1023/A:1019265913011](https://doi.org/10.1023/A:1019265913011).



- Ruth, Conall E. et al. (2019). "Electricity autoproduction, storage and billing: A case study at Dundalk Institute of Technology, Ireland". In: *Sustainable Energy Technologies and Assessments*. ISSN: 22131388. DOI: [10.1016/j.seta.2019.07.008](https://doi.org/10.1016/j.seta.2019.07.008).
- Santhosh, Madasthu, Chintham Venkaiah, and D M Vinod Kumar (2020). "Current advances and approaches in wind speed and wind power forecasting for improved renewable energy integration: A review". In: *Engineering Reports* 2.6, e12178. DOI: [10.1002/eng2.12178](https://doi.org/10.1002/eng2.12178).
- Sanz Rodrigo, Javier et al. (2017). "Mesoscale to microscale wind farm flow modeling and evaluation". In: *Wiley Interdisciplinary Reviews: Energy and Environment* 6.2, e214. ISSN: 2041-8396. DOI: [10.1002/wene.214](https://doi.org/10.1002/wene.214).
- Semin, V, D Spalding, and Sergey Zhubrin (1996). *Some novel algorithms for the simulation of flow around turbine blades*. DOI: [10.13140/2.1.2151.1205](https://doi.org/10.13140/2.1.2151.1205).
- Shapkalijevski, M.M (2017). "Turbulent exchange of energy, momentum, and reactive gases between high vegetation and the atmospheric boundary layer". PhD thesis. Wageningen. DOI: [DOI:10.18174/404603](https://doi.org/10.18174/404603).
- Sheridan, P F and S B Vosper (2006). "A flow regime diagram for forecasting lee waves, rotors and downslope winds". In: *Meteorol. Appl* 13, pp. 179–195. DOI: [10.1017/S1350482706002088](https://doi.org/10.1017/S1350482706002088).
- Shimada, Susumu et al. (2020). *Coastal Wind Measurements Using a Single Scanning LiDAR*. DOI: [10.3390/rs12081347](https://doi.org/10.3390/rs12081347).
- Silva, Julieta et al. (2007). "Roughness length classification of Corine Land Cover classes". In: *Proceedings of EWEC 2007*. Milan, Italy.
- Simiu, Emil and DongHun Yeo (2019). *Wind Effects on Structures*. 4th. Oxford: John-Wiley & Sons, p. 495. ISBN: 9781119375883.
- Simley, Eric et al. (2018). *Optimizing Lidars for Wind Turbine Control Applications—Results from the IEA Wind Task 32 Workshop*. DOI: [10.3390/rs10060863](https://doi.org/10.3390/rs10060863).
- Simões, Teresa and Ana Estanqueiro (2016). "A new methodology for urban wind resource assessment". In: *Renewable Energy* 89, pp. 598–605. ISSN: 0960-1481. DOI: [10.1016/j.renene.2015.12.008](https://doi.org/10.1016/j.renene.2015.12.008).
- Skamarock, William C. et al. (2021). *A Description of the Advanced Research WRF Model Version 4.3*. Tech. rep. NCAR/TN-556+STR. Boulder, Colorado, USA: National Center for Atmospheric Research (NCAR), p. 162. DOI: [10.5065/1dfh-6p97](https://doi.org/10.5065/1dfh-6p97).



- Slinger, Chris and Michael Harris (2012). *Introduction to continuous-wave Doppler lidar*. Tech. rep. Ledbury HR8 1EU, U.K.: ZX LiDARs Ltd.
- Smith, Matt et al. (2014). "Necessity is the Mother of Invention: Nacelle-mounted Lidar for Measurement of Turbine Performance". In: *Energy Procedia*, pp. 13–22. ISSN: 1876-6102. DOI: [10.1016/j.egypro.2014.07.211](https://doi.org/10.1016/j.egypro.2014.07.211).
- Souba, Fletcher and Pam Bloch Mendelson (2018). "Chaninik Wind Group: Lessons learned beyond wind integration for remote Alaska". In: *The Electricity Journal* 31.6, pp. 40–47. ISSN: 1040-6190. DOI: [10.1016/j.tej.2018.06.008](https://doi.org/10.1016/j.tej.2018.06.008).
- St. Martin, C. M. et al. (2017). "Atmospheric turbulence affects wind turbine nacelle transfer functions". In: *Wind Energy Science* 2.1, pp. 295–306. DOI: [10.5194/wes-2-295-2017](https://doi.org/10.5194/wes-2-295-2017). URL: <https://wes.copernicus.org/articles/2/295/2017/>.
- Standen, Jessica and Clive Wilson (2015). *Remodelling the Irish national onshore and offshore wind atlas*. Tech. rep. Technical Report No: 591. UK Met Office. URL: [https://irp-cdn.multiscreensite.com/d6332898/files/uploaded/UKMetOfficeCombinedReport\\_SEAI\\_part1.pdf](https://irp-cdn.multiscreensite.com/d6332898/files/uploaded/UKMetOfficeCombinedReport_SEAI_part1.pdf). [accessed: 01.03.2018].
- Standen, Jessica et al. (2017). "Prediction of local wind climatology from Met Office models: Virtual Met Mast techniques". In: *Wind Energy* 20.3, pp. 411–430. ISSN: 1095-4244. DOI: [10.1002/we.2013](https://doi.org/10.1002/we.2013).
- Stathopoulos, Ted et al. (2018). "Urban wind energy: Some views on potential and challenges". In: *Journal of Wind Engineering and Industrial Aerodynamics* 179, pp. 146–157. ISSN: 0167-6105. DOI: [10.1016/j.jweia.2018.05.018](https://doi.org/10.1016/j.jweia.2018.05.018).
- Staudt, Lawrence (2006). "Development and Cost Benefits of the Campus Wind Turbine at Dundalk Institute of Technology". In: *Renewable Energy in Maritime Climates*. Dublin.
- Stull, Roland B (1988). *An Introduction to Boundary Layer Meteorology*. 1st. Netherlands: Springer. ISBN: 9789027727695.
- Sunderland, Keith and Michael F Conlon (2010). "Estimating the Yield of Micro Wind Turbines in an Urban Environment: A Methodology". In: *Power Engineering Conference (UPEC)*, pp. 1–6. URL: <http://arrow.dit.ie/engscheleart>. [accessed: 01.03.2018].
- Talbot, Charles, Elie Bou-Zeid, and Jim Smith (2012). "Nested Mesoscale Large-Eddy Simulations with WRF: Performance in Real Test Cases". In: *Journal of Hydrometeorology* 13.5, pp. 1421–1441. DOI: [10.1175/JHM-D-11-048.1](https://doi.org/10.1175/JHM-D-11-048.1).

- Tasneem, Zinat et al. (2020). "An analytical review on the evaluation of wind resource and wind turbine for urban application: Prospect and challenges". In: *Developments in the Built Environment* 4, p. 100033. ISSN: 2666-1659. DOI: [10.1016/j.dibe.2020.100033](https://doi.org/10.1016/j.dibe.2020.100033).
- Taylor, Peter A and James R Salmon (1993). "A Model for the Correction of Surface Wind Data for Sheltering by Upwind Obstacles". In: *Journal of Applied Meteorology* (1988-2005) 32.11, pp. 1683–1694. ISSN: 08948763, 15200450. URL: <http://www.jstor.org/stable/44713968>.
- Theeuwes, Natalie E et al. (2019). "Parametrizing Horizontally-Averaged Wind and Temperature Profiles in the Urban Roughness Sublayer". In: *Boundary-Layer Meteorology* 173.3, pp. 321–348. ISSN: 1573-1472. DOI: [10.1007/s10546-019-00472-1](https://doi.org/10.1007/s10546-019-00472-1).
- Tin, Tina et al. (2010). "Energy efficiency and renewable energy under extreme conditions: Case studies from Antarctica". In: *Renewable Energy* 35.8, pp. 1715–1723. ISSN: 0960-1481. DOI: [10.1016/j.renene.2009.10.020](https://doi.org/10.1016/j.renene.2009.10.020).
- Tinnesand, Heidi and Latha Sethuraman (2019). *Distributed Wind Resource Assessment Framework: Functional Requirements and Metrics for Performance and Reliability Modeling*. Tech. rep. NREL/TP-5000-72523. Golden, USA: National Renewable Energy Laboratory (NREL). DOI: [10.2172/1514852](https://doi.org/10.2172/1514852).
- Toja-Silva, Francisco et al. (2015). "Roof region dependent wind potential assessment with different RANS turbulence models ". In: *Journal of Wind Engineering and Industrial Aerodynamics* 142, pp. 258 –271. ISSN: 0167-6105. DOI: [10.1016/j.jweia.2015.04.012](https://doi.org/10.1016/j.jweia.2015.04.012).
- Toja-Silva, Francisco et al. (2018). "A review of computational fluid dynamics (CFD) simulations of the wind flow around buildings for urban wind energy exploitation". In: *Journal of Wind Engineering and Industrial Aerodynamics* 180, pp. 66–87. ISSN: 01676105. DOI: [10.1016/j.jweia.2018.07.010](https://doi.org/10.1016/j.jweia.2018.07.010).
- Topaloglu, Fatih and Hüseyin Pehlivan (2018). "Analysis of Wind Data, Calculation of Energy Yield Potential, and Micrositing Application with WAsP". In: *Advances in Meteorology* 2018. Ed. by Ismail Gultepe, p. 2716868. ISSN: 1687-9309. DOI: [10.1155/2018/2716868](https://doi.org/10.1155/2018/2716868).
- Toparlar, Y. et al. (2017). "A review on the CFD analysis of urban microclimate". In: *Renewable and Sustainable Energy Reviews* 80, pp. 1613–1640. ISSN: 1364-0321. DOI: [10.1016/J.RSER.2017.05.248](https://doi.org/10.1016/J.RSER.2017.05.248).

- Toparlar, Yasin et al. (2019). "CFD simulation of the near-neutral atmospheric boundary layer: New temperature inlet profile consistent with wall functions". In: *Journal of Wind Engineering and Industrial Aerodynamics* 191, pp. 91–102. ISSN: 0167-6105. DOI: [10.1016/j.jweia.2019.05.016](https://doi.org/10.1016/j.jweia.2019.05.016).
- Troen, I and E Lundtang Petersen (1989). *European Wind Atlas*. Roskilde: Risø National Laboratory. ISBN: 87-550-1482-8.
- US DOE (2020). *Distributed Wind Tools Assessing Performance*. Tech. rep. DOE/GO-102020-5255. US Department of Energy. URL: [energy.gov/eere/wind](https://energy.gov/eere/wind). [accessed: 01.12.2020].
- van, G A M et al. (2016). "Long-term research challenges in wind energy – a research agenda by the European Academy of Wind Energy". In: *Wind Energy Science* 1.1, pp. 1–39. DOI: [10.5194/wes-1-1-2016](https://doi.org/10.5194/wes-1-1-2016).
- Vasilopoulos, Konstantinos, Ioannis E. Sarris, and Panagiotis Tsoutsanis (2019). "Assessment of air flow distribution and hazardous release dispersion around a single obstacle using Reynolds-averaged Navier-Stokes equations". In: *Heliyon* 5.4, e01482. ISSN: 24058440. DOI: [10.1016/j.heliyon.2019.e01482](https://doi.org/10.1016/j.heliyon.2019.e01482).
- Veers, Paul et al. (2019). "Grand challenges in the science of wind energy". In: *Science* 366.6464, eaau2027. DOI: [10.1126/science.aau2027](https://doi.org/10.1126/science.aau2027).
- Vilar, Alberto Álvarez, George Xydis, and Evanthia A Nanaki (2020). "Small Wind: A Review of Challenges and Opportunities BT - Sustaining Resources for Tomorrow". In: ed. by Jacqueline A Stagner and David S.-K. Ting. Cham: Springer International Publishing, pp. 185–204. ISBN: 978-3-030-27676-8. DOI: [10.1007/978-3-030-27676-8\\_10](https://doi.org/10.1007/978-3-030-27676-8_10).
- Vosper, S.B. (2004). "Inversion effects on mountain lee waves". In: *Quarterly Journal of the Royal Meteorological Society*. ISSN: 00359009. DOI: [10.1256/qj.03.63](https://doi.org/10.1256/qj.03.63).
- Wagner, R. et al. (2011). "Accounting for the speed shear in wind turbine power performance measurement". In: *Wind Energy* 14.8, pp. 993–1004. ISSN: 10954244. DOI: [10.1002/we.509](https://doi.org/10.1002/we.509).
- Wagner, R. et al. (2014). "Rotor equivalent wind speed for power curve measurement-comparative exercise for IEA Wind Annex 32". In: *Journal of Physics: Conference Series* 524.1. ISSN: 17426596. DOI: [10.1088/1742-6596/524/1/012108](https://doi.org/10.1088/1742-6596/524/1/012108).

- Wallace, Emily (2015). *Complex wind shear*. Tech. rep. UK Met Office. URL: [www.windenergynetwork.co.uk/wp-content/uploads/2015/09/Met-Office-White-Paper-Windshear.pdf](http://www.windenergynetwork.co.uk/wp-content/uploads/2015/09/Met-Office-White-Paper-Windshear.pdf). [accessed: 10.07.2018].
- Wang, B. et al. (2017). "Estimation of wind energy of a building with canopy roof". In: *Sustainable Cities and Society*. ISSN: 22106707. DOI: [10.1016/j.scs.2017.08.026](https://doi.org/10.1016/j.scs.2017.08.026).
- Weekes, Shemaiah Matthias and Alison S Tomlin (2014). "Low-cost wind resource assessment for small-scale turbine installations using site pre-screening and short-term wind measurements". In: *IET Renewable Power Generation* 8, pp. 349–358. ISSN: 1752-1416. DOI: [10.1049/iet-rpg.2013.0152](https://doi.org/10.1049/iet-rpg.2013.0152).
- Wegley, H L et al. (1980). "Siting handbook for small wind energy conversion systems". In: p. 105. DOI: [10.2172/5490541](https://doi.org/10.2172/5490541).
- WEI (2022). *Facts & Stats*. URL: <https://windenergyireland.com/about-wind/the-basics/facts-stats/>. [accessed: 19.10.2022].
- Weis, Timothy M and Adrian Ilinca (2010). "Assessing the potential for a wind power incentive for remote villages in Canada". In: *Energy Policy* 38.10, pp. 5504–5511. ISSN: 0301-4215. DOI: <https://doi.org/10.1016/j.enpol.2010.04.039>.
- Wharton, S and Jk Lundquist (2010). *Atmospheric stability impacts on power curves of tall wind turbines—an analysis of a west coast north american wind farm*. Tech. rep. LLNL-TR-424425. Lawrence Livermore National Laboratory. DOI: [10.2172/973337](https://doi.org/10.2172/973337).
- Wharton, Sonia and Julie K. Lundquist (2012). "Atmospheric stability affects wind turbine power collection". In: *Environmental Research Letters* 7.1. ISSN: 17489326. DOI: [10.1088/1748-9326/7/1/014005](https://doi.org/10.1088/1748-9326/7/1/014005).
- Whitmarsh, Martin (2018). *Offshore Wind Industry Prospectus*. Tech. rep. United Kingdom: CATAPULT, Offshore Renewable Energy. URL: <https://ore.catapult.org.uk>. [accessed: 01.03.2019].
- Wiser, Ryan and Mark Bolinger (2018). *2017 Wind Technologies Market Report*. Tech. rep. Oak Ridge National Laboratory: U.S. Department of Energy. URL: [www.energy.gov/eere/wind/2017-wind-market-reports](http://www.energy.gov/eere/wind/2017-wind-market-reports). [accessed: 01.03.2019].
- Wyngaard, John C (1990). "Scalar fluxes in the planetary boundary layer — Theory, modeling, and measurement". In: *Boundary-Layer Meteorology* 50.1, pp. 49–75. ISSN: 1573-1472. DOI: [10.1007/BF00120518](https://doi.org/10.1007/BF00120518).

- Wyngaard, John C. (2004). "Toward numerical modeling in the "Terra Incognita"". In: *Journal of the Atmospheric Sciences* 61.14, pp. 1816–1826. ISSN: 00224928. DOI: [10.1175/1520-0469\(2004\)061<1816:TNMITT>2.0.CO;2](https://doi.org/10.1175/1520-0469(2004)061<1816:TNMITT>2.0.CO;2).
- Zajic, D et al. (2011). "Flow and Turbulence in an Urban Canyon". English. In: *Journal of Applied Meteorology and Climatology* 50.1, pp. 203–223. DOI: [10.1175/2010JAMC2525.1](https://doi.org/10.1175/2010JAMC2525.1).
- Zhang, Matthew Huaiquan (2015). *Wind Resource Assessment and Micro-siting*. 1st ed. Singapore: Wiley. ISBN: 978-1-118-90010-9. DOI: [10.1002/9781118900116](https://doi.org/10.1002/9781118900116).



## Appendix A

### Supplementary wind resource and modelling information

#### A.1 Overview of the atmosphere

##### A.1.1 Global circulation

The origin of wind on the earth is the result of unequal heating by the sun of the earth's surface. Higher solar energy input in the lower latitudes compared to the higher latitudes result in thermally driven global wind circulation patterns that moves warmer air from equatorial regions towards the poles, Fig. A.1. The earth's rotation and curvature gives rise to the Coriolis force that causes wind flow from the equator towards the poles to move eastwards and wind flow from the poles towards the equator to move westwards. The Coriolis force results in the formation of three principal global flow circulation cells, namely Hadley, Ferrel and Polar cells. These are associated with well-known, latitude dependent, surface winds such as mid latitude westerlies and trade winds (Ahrens and Henson, 2017).

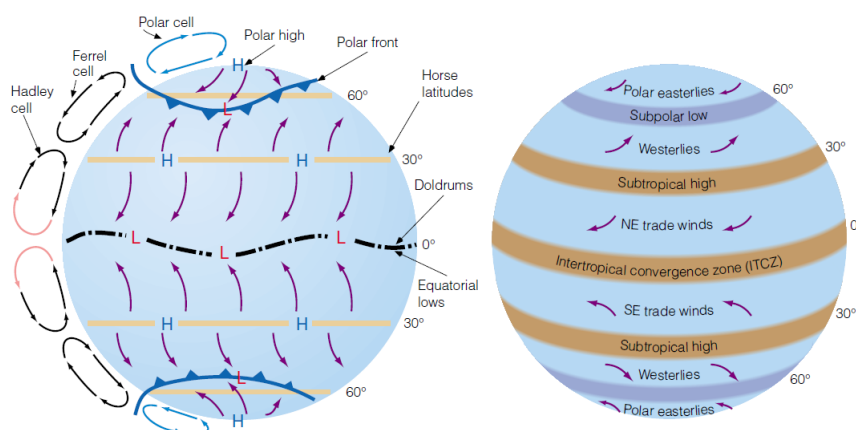


Fig. A.1. Principal global wind circulation patterns (Ahrens and Henson, 2017).

The lower part of the earth's atmosphere where weather systems form is known as the troposphere. It contains  $\sim 80\%$  of the total mass of the atmosphere and varies in depth (height) from 6 km at the poles to 18 km at the equator with an average of  $\sim 10$  km in the mid latitudes. The atmospheric boundary layer (ABL), also known as the planetary boundary layer (PBL), is that part of the troposphere that is influenced by the earth's surface. The depth (height) of the ABL extends to  $\sim 2$  km. Interaction of the ABL with the earth's surface can modify global circulation patterns due to frictional stresses, orographic drag, ocean and coastal influences, heat energy and moisture exchange. This can create a wide variety of wind climates and wind conditions at numerous spatial and temporal scales, from thousands of km to sub-metre and inter-annual to sub-second respectively. The laws of conservation of mass, momentum and energy can fundamentally describe airflow in the ABL. As air is a viscous fluid, the conservations of mass and momentum can be described by the Navier Stokes differential equations of fluid flow, Eqs. (A.1) to (A.5) (Emeis, 2013).

$$\nabla \cdot (\rho \vec{v}) + \frac{\partial \rho}{\partial t} = 0 \quad (\text{A.1})$$

$$\nabla \cdot \vec{v} = 0 \quad (\text{A.2})$$

Where:

$\vec{v}$  - three dimensional wind velocity vector (m/s)  $\left[ \nabla = \left( \frac{\partial}{\partial x} + \frac{\partial}{\partial y} + \frac{\partial}{\partial z} \right) \right]$

$\rho$  - air density ( $\text{kg/m}^3$ )

$$\frac{\partial u}{\partial t} + \vec{v} \nabla u + \frac{1}{\rho} \frac{\partial p}{\partial x} - f v + f^* w \mp v \frac{|\vec{v}|}{r} + F_x = 0 \quad (\text{A.3})$$

$$\frac{\partial v}{\partial t} + \vec{v} \nabla v + \frac{1}{\rho} \frac{\partial p}{\partial y} + f u \pm u \frac{|\vec{v}|}{r} + F_y = 0 \quad (\text{A.4})$$

$$\frac{\partial w}{\partial t} + \vec{v} \nabla w + \frac{1}{\rho} \frac{\partial p}{\partial z} - g - f u - f^* u + F_z = 0 \quad (\text{A.5})$$

**I      II      III      IV      V      VI      VII**

Where:

$u$  - x component of the velocity vector (m/s)

$v$  - y component of the velocity vector (m/s)



$w$  -  $z$  component of the velocity vector (m/s)

$g$  - acceleration due to gravity (m/s<sup>2</sup>)

$f$  - horizontal Coriolis parameter  $2\Omega\sin(\Phi)$  (where  $\Omega$  is the angular rotation of the earth =  $7.3 \times 10^{-5}$ /s and  $\Phi$  is latitude in degrees)

$f^*$  - vertical Coriolis parameter  $2\Omega\cos(\Phi)$  (considered not be significant in wind energy)

$r$  - radius of curvature (of a pressure system) (m)

$F_{(x,y,z)}$  - three components of frictional and/or dissipative forces (N)

The terms of the moment equation I, II, III, IV, V, VI and VII are described below for reference in later sections.

**I** - an inertial term that describes the temporal variation of the wind components.

**II** - expresses the influence of local inertial interactions between the three wind velocity components on the wind flow vector (such as from advection).

**III** - pressure forces (e.g., between high and low pressure systems and hydrostatic pressure).

**IV** – gravitational force that acts only in the negative  $z$  direction.

**V** - Coriolis force due to the Earth's rotation.

**VI** - centrifugal force of curved motion around pressure systems (the upper sign applies to flows around low pressure systems, the lower sign to flows around high pressure systems).

**VII** - frictional forces due to the turbulent viscosity (Reynolds stresses) of air and surface friction.

Each term can have a greater or smaller significance depending on the spatial and temporal scale of the atmospheric flow in question.

Air pressure is a measure of the air mass above a given location that is dependent on temperature. In the absence of strong vertical accelerations, pressure decreases with height described by the hydrostatic equation, Eq. (A.6).

$$\frac{\partial p}{\partial z} = -g\rho = -g\frac{p}{RT} \quad (\text{A.6})$$

Where:

$R$  - universal gas constant (JK<sup>-1</sup>mol<sup>-1</sup>)

$T$  – absolute temperature (K)

The pressure gradient forces (III) are the principal driving forces in atmospheric flow. At large spatial scales (i.e., synoptic scales of  $\sim 1000$  km), when unequal heating occurs across the earth's surface, rising air in warm air masses creates lower surface air pressures. However, the rate of reduction in pressure with height is lower in warmer air masses compared to the cooler air masses. This gives rise to horizontal pressure gradients aloft which produces winds that blow from the high pressure area to the lower pressure area aloft to reduce the pressure gradients. This further reduces the pressure on the surface of the warmer air mass and surface air flows (wind) from the cold air mass that has higher surface pressure. All the other terms in the momentum equations just redistribute or dissipate the momentum created by the pressure gradient forces, i.e., the pressure gradients are the only driving forces. Above the ABL in the free stream wind, frictional forces (VII) are not significant. The Coriolis force (V), an "apparent" force, balances the pressure gradient forces (III) giving geostrophic winds that flow parallel to pressure isobars, Eqs. (A.7) and (A.8).

$$-\rho f u_g = \frac{\partial p}{\partial y} \quad (\text{A.7})$$

$$\rho f v_g = \frac{\partial p}{\partial x} \quad (\text{A.8})$$

Where:

$u_g$  and  $v_g$  are geostrophic wind components towards east and north respectively

In some instances the centrifugal forces (VI), also apparent forces, around pressure systems of high curvature must also be considered. As the tendency for flow is from high to low pressure, the centrifugal forces of high pressure systems create winds that add to the geostrophic winds, while the opposite is the case for low pressure systems. The resulting gradient winds are described by Eqs. (A.9) and (A.10) (Holton and Gregory, 2012).

$$-\rho f u = \frac{\partial p}{\partial y} \pm \rho u \frac{|\vec{v}|}{r} \quad (\text{A.9})$$

$$\rho f v = \frac{\partial p}{\partial x} \mp \rho v \frac{|\vec{v}|}{r} \quad (\text{A.10})$$

Below the free stream wind, i.e., in the ABL, drag forces (VII) due to surface roughness become increasingly significant the closer to the earth's surface. These have a deceleration effect the wind flow as the pressure gradient and frictional forces at the earth's surface come into balance. This causes a directional change in the wind flow from the geostrophic wind direction, that is parallel to pressure isobars, towards the direction of the pressure gradient forces (III) across the isobars. The interaction of flow with larger surface physical features such as mountain ranges, flat continental plains and coastal regions can alter large scale circulation patterns, creating smaller scale flow pattern on horizontal spatial scales from 10s to 1000s km, giving rise to regional or mesoscale wind climates. At the microscale level from single km down to sub-metre wind flow is further influence local terrain, surface roughness features, obstacles etc. Drag forces (VII) dominate at this scale and flow is normal to pressure isobars, i.e., in the direction of the pressure gradient.

### A.1.2 Vertical profile of the ABL

The ABL over flat terrain is divided into three basic sub layers, Fig. A.2.

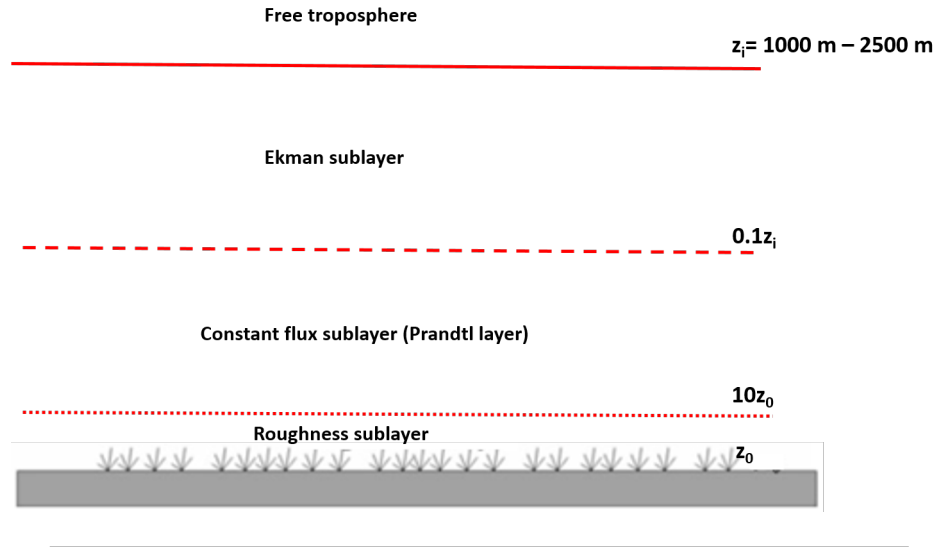


**Fig. A.2.** Basic structure of the ABL (not to scale) - adapted from (Emeis, 2013).

At flat field locations, the RSL is just millimetres to a few centimetres high and is of little relevance to wind energy. The constant flux sub-layer (also known as surface boundary layer (SBL) or the Prandtl layer) is defined meteorologically as the region of the atmosphere where turbulent vertical fluxes of heat, momentum and moisture deviate less than 10% from surface values. It covers  $\sim$  the first 10% of the total ABL depth. In this layer, wind flow is heavily influenced by the roughness of the earth's surface due to frictional forces giving rise to a variation of wind speed with height. Ground surface features such as vegetation and obstacles have a slowing effect on wind speed close to the ground and can increase turbulence in the flow. Wind shear represents the variation in the horizontal component of wind speed with height as a result of frictional influence (turbulent shear stress) of the earth's surface and the state of thermal stability of the ABL. The SBL extends up to  $\sim 200 \text{ m}$  and is where most onshore commercially operating wind turbines are situated today, i.e., rotor tip heights  $\sim 100 \text{ m}$  to  $200 \text{ m}$ . The Ekman layer is the third and uppermost layer that occupies approximately 90% of the ABL. In the Ekman layer the variation of wind speed with height decreases and gradually changes direction (wind veer) as the Coriolis force has an increasing influence on wind flow with increasing height. At the top of the Ekman layer, wind flow returns to geostrophic flow, entering the

free troposphere (or free atmosphere) where surface effects don't impact on wind flow and the Coriolis force and pressure forces dominate. As wind turbines become larger, their rotors may partially extend into the Ekman layer where the influence of the Coriolis effect needs to be considered, particularly with respect to the wind veer within the rotor swept area. However, this would be more of more concern for future large offshore wind turbines and not deemed to be a significant issue for distributed wind systems that are likely to remain operating in the Prandtl layer.

The wind speed at the surface reduces to zero at or near the surface at a height known aerodynamic roughness length  $z_0$  which is defined by the no-slip condition for viscous fluid flow, Fig. A.3 (Nakayama and Boucher, 2000).  $z_0$  is an aerodynamic parameter that gives a measure of the height above a surface at which wind speed reduces to zero. It is a function of surface physical properties only and does not change with wind speed or atmospheric stability (see later) (Stull, 1988). Surface roughness lengths are used to categorise the roughness of various surface types (Manwell, McGowan, and Rogers, 2009).  $u'$  and  $w'_s$  represent turbulent the fluctuating wind speed about the mean wind speed in the horizontal direction and the vertical direction (at surface) respectively.

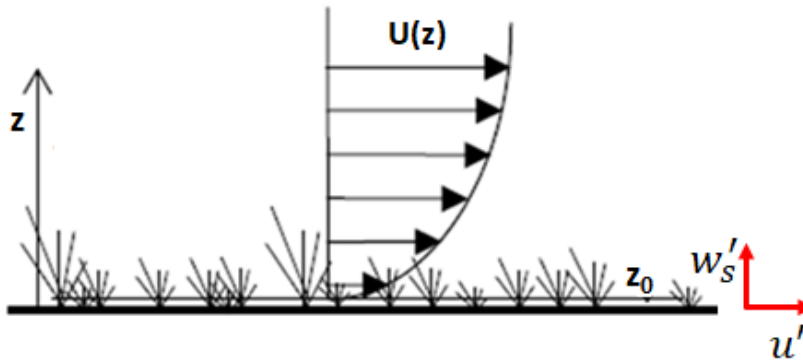


**Fig. A.3.** Surface roughness height, wind speed fluctuations and mean wind speed profile (not to scale) - adapted from (Mertens, 2006).

For a number of roughness elements distributed over a given area the average horizontal area available to each element can be accounted for by a relationship for surface roughness, Eq. (A.11) (Lettau, 1969; Mertens, 2006).

$$z_0 = 0.5 \frac{hS}{A_H} \quad (\text{A.11})$$

Where:

$h$  - height of roughness element (m)

$S$  - cross section area facing the wind ( $m^2$ )

$A_H$  - the average horizontal area available to each element ( $m^2$ )

It is suggested that this equation gives reasonable results when  $A_H$  is much larger than  $S$  and overestimates  $z_0$  when  $A_H$  is in the order of  $S$ . This is because when roughness elements are close together flow can be displaced over them, referred to as the displacement height (described below). The equation also assumes that the porosity of the roughness elements themselves are zero, i.e., fully solid. For porous elements, the values of  $z_0$  must be reduced by the fraction of porosity in cross-sectional area  $S$ . The European Wind Atlas characterises four broad types of surface roughness classifications with corresponding tables of surface roughness values and terrain surface characteristics (Troen and Lundtang Petersen, 1989). The classifications include water surfaces, flat open country with few wind breaks, open areas with many wind breaks and forested and urban areas. The classifications were based on empirical descriptions, which characterises a roughness element by its height and cross sectional area facing the wind (Lettau, 1969).

When wind flow interacts with the earth's surface the frictional forces (VII) usually dominate and are in equilibrium with the pressure gradient force. Momentum transfer from the flow to a surface by mechanical turbulence creates a shear stress described by Reynolds stress, Eqs. (A.12) to (A.16). It represents (VII) in the momentum equations.

$$\tau_{x,z} = -\bar{\rho} \overline{u'w'_s} \quad (\text{A.12})$$

$$\tau_{y,z} = -\bar{\rho} \overline{v'w'_s} \quad (\text{A.13})$$

$$|\tau_{Reynolds}| = \sqrt{\tau_{x,z}^2 + \tau_{y,z}^2} \quad (\text{A.14})$$

The Reynolds stress, normalised by density, can be expressed as a friction velocity  $u_*$  that describes the shear in the wind flow, Eqs. (A.15) and (A.16).

$$u_*^2 = \sqrt{(\overline{u'w'_s})^2 + (\overline{v'w'_s})^2} \quad (\text{A.15})$$

$$u_* = \left( (\overline{u'w'_s})^2 + (\overline{v'w'_s})^2 \right)^{\frac{1}{4}} \quad (\text{A.16})$$

Reynolds stress can also be expressed in terms of viscosity and vertical wind shear. Assuming that the principal horizontal wind flow vector is along the x-direction so that the wind speed is  $u$  then the relationship between the vertical wind shear and friction velocity can be expressed, Eqs. (A.17) and (A.18).

$$|\tau_{Reynolds}| = \mu \frac{\partial u}{\partial z} \quad (\text{A.17})$$

$$\frac{|\tau_{Reynolds}|}{\bar{\rho}} = \frac{\mu}{\bar{\rho}} \frac{\partial u}{\partial z} = u_* \quad (\text{A.18})$$

Gradient transport theory (K-theory) relates vertical turbulent fluxes of vector and scalar quantities in the atmospheric surface layer to the corresponding mean gradients using turbulent exchange coefficients (Shapkalijevski, 2017). As the Prandtl layer in a constant flux layer, a constant of proportionality  $K_M$  describes the vertical turbulent exchange coefficient for momentum, Eq. (A.19). It has the physical dimensions of viscosity. A turbulence mixing of scale length  $l$  represent the average length scale of the turbulent eddies, Fig. A.4. It is restricted by earth's surface (wall) and is therefore proportional to the height above the ground, Eq. (A.20). The constant of proportionality between the turbulence mixing of scale length and height is the Von Karman constant  $\kappa$  that has a value of  $\sim 0.4$ . This can be used with  $K_M$  to derive a relationship between the vertical wind shear profile and friction velocity at a given height  $z$ , Eqs. (A.20) to (A.24).

$$K_M \frac{\partial u}{\partial z} = u_*^2 \quad (\text{A.19})$$

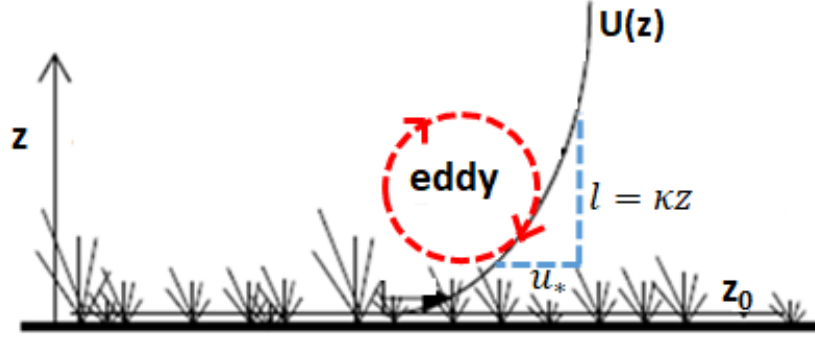


Fig. A.4. Turbulence scale length and friction velocity (not to scale).

$$l = \kappa z \quad (\text{A.20})$$

$$\frac{\partial u}{\partial z} = \frac{u_*}{l} \quad (\text{A.21})$$

$$K_M = \kappa u_* z \quad (\text{A.22})$$

$$\kappa u_* z \frac{\partial u}{\partial z} = u_*^2 \quad (\text{A.23})$$

$$\frac{\partial u}{\partial z} = \frac{u_*}{\kappa z} \quad (\text{A.24})$$

Integrating Eq. (A.24) from  $z_0$  (where the wind speed is zero) to get the horizontal wind speed at any height  $z$  is given by Eq. (A.25).

$$u(z) = \frac{u_*}{\kappa} \ln \frac{z}{z_0} \quad (\text{A.25})$$

This is the logarithmic vertical profile of horizontal wind speed with height in the Prandtl layer that describes wind shear. In areas of very high surface roughness, e.g., a forest, city or a densely packed area of obstacles a vertical displacement  $d$  of surface can lead to a vertical displacement in whole wind flow regime so that log law used these circumstances is given by Eq. (A.26).

$$u(z) = \frac{u_*}{\kappa} \ln \left( \frac{z - d}{z_0} \right) \quad (\text{A.26})$$



At a given location, if wind speed measurements  $U_1(z_1)$  and  $U_2(z_2)$  are made at two heights of  $z_1$  and  $z_2$  respectively, then  $z_0$  at that location can be determined from Eq. (A.27). The wind speed  $U(z)$  at any other height of interest can then be determined from Eq. (A.28).

$$z_0 = \exp \left( \frac{u_1(z_1) \ln(z_2) - u_2(z_2) \ln(z_1)}{u_1(z_1) - u_2(z_2)} \right) \quad (\text{A.27})$$

$$u(z) = u(z_{ref}) \left( \frac{\ln \left( \frac{z-d}{z_0} \right)}{\ln \left( \frac{z-z_{ref}}{z_0} \right)} \right) \quad (\text{A.28})$$

Where:

$z_{ref}$  – reference measurement height (m)

$u(z_{ref})$  – wind speed measurement at height  $z_{ref}$  (m/s)

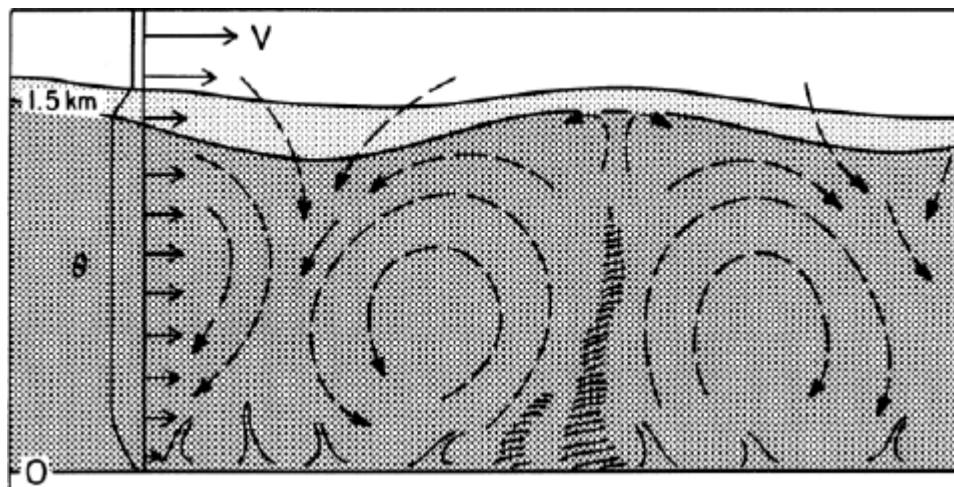
### A.1.3 Thermal stability in the ABL

The height and wind speed profile with height of the ABL is further complicated by the impact of thermal energy exchange between the earth's surface the ABL on turbulence. This can vary substantially on a diurnal basis depending on heat flux exchange (as result of solar irradiation) between the earth's surface at any given time and space. The heat flux exchange can either be positive or negative depending on complex physical processes that are taking place at any given time, which is dependent on the electromagnetic properties of the earth's surface (e.g., absorptivity, reflectivity, and emissivity) at a given location. Heat flux is considered positive if it is directed from the atmosphere towards the ground (i.e., cooling the atmosphere) and negative if it is directed towards or heating the atmosphere. These give rise to three states of stability in the ABL (Wyngaard, 1990), which are:

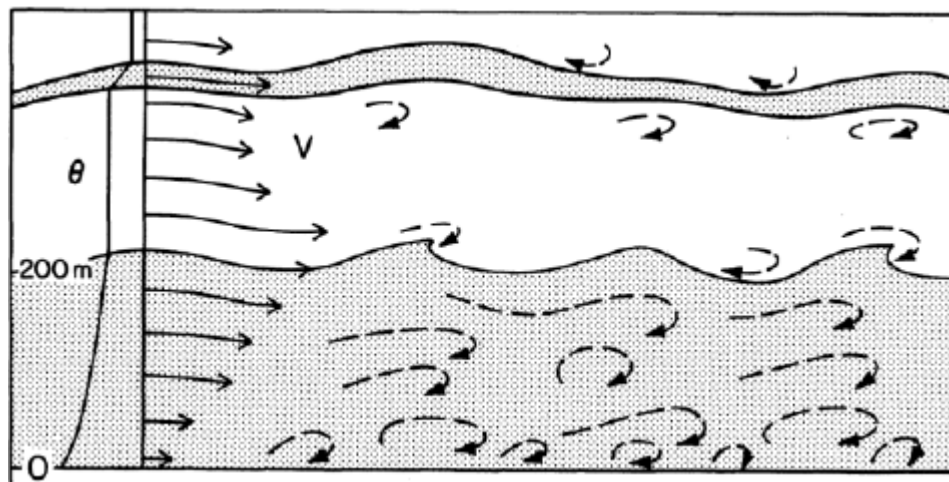
- *Unstable* - heat exchange is from the earth's surface to the atmosphere that usually occurs at time of high solar irradiance. This gives rise to warmer air of lower density on the bottom and cooler denser above and results in a convective boundary layer in which wind shear is reduced by turbulence mixing from vertical convective eddies, but turbulence is increased, Fig. A.5(a).
- *Stable* - net heat exchange from the atmosphere to the earth's surface, i.e., the atmosphere is cooled from below, usually occurs at night. This give rise to a

stable atmosphere where more dense cooler air is at the bottom under warmer air higher up. This suppresses convective eddies and thermally generated turbulence. High wind shear is feature of a stable atmosphere that can generate turbulence (mechanically) in horizontal wind flow, Fig. A.5(b).

- *Neutral* - there no net heat exchange between the earth's surface and atmosphere, which usually occurs during periods of reduced solar irradiance, e.g., cloudy days or diffuse radiation. Neutral like conditions are more common at higher wind speeds.



(a) Unstable convective ABL



(b) Stable ABL

Fig. A.5. Schematic overviews of unstable and stable ABL (Wyn-gaard, 1990).

In the context of wind energy, stability impacts on both wind shear and turbulence can give rise to added cyclical forces on wind turbine blades as they move round the rotor disc area. This has implications for the overall mechanical and structural

design of a wind turbine system (including foundations, tower, nacelle and rotor). It also has implications for power performance as the wind turbine rotor disc is subjected to varying wind speed across the rotor disc.

Stability can be accounted for in the log law using a stability correction factor  $\psi$ , Eq. (A.29).

$$u(z) = \frac{u_*}{\kappa} \left( \ln \left( \frac{z-d}{z_0} \right) - \psi \left( \frac{z}{L} \right) \right) \quad (\text{A.29})$$

$L$  is a length scale, known as the Obukuv length. It can be interpreted as the height above which turbulence production from buoyancy factors begins to dominate over production from mechanical wind shear, (Stull, 1988), and can be calculated from, Eq. (A.30).

$$L = \frac{-\bar{\theta}_v u_*^3}{\kappa g \left( \overline{w' \theta'_v} \right)_s} \quad (\text{A.30})$$

Where:

$\bar{\theta}_v$  - virtual potential temperature (K) (it accounts for the effects of pressure and humidity

$\overline{w' \theta'_v}$  - virtual potential heat flux (Km/s) (It includes both sensible and latent heat flux)

It should be noted that the virtual potential temperature used in this context is a per unit (kinematic) representation of heat energy, i.e., normalised to density and specific heat.

A positive  $L$  is a stable atmosphere,  $L = 0$  is neutral and a negative  $L$  is unstable. Based on meteorological field experiments, the following  $\psi$  relations have been formulated for the different stability conditions (Stull, 1988; Emeis, 2013). The unstable form of  $\psi$  is given by Eq. (A.31)

$$\psi \left( \frac{z}{L} \right) = 2 \ln \left( \frac{1+x}{2} \right) + \ln \left( \frac{1+x^2}{2} \right) - 2 \tan^{-1}(x) + \frac{\pi}{2} \quad (\text{A.31})$$

Where:

$$x = \left( 1 - \frac{16z}{L} \right)^{\frac{1}{4}}$$

The stable form is given by Eq. (A.32).

$$\psi\left(\frac{z}{L}\right) = \begin{cases} -\frac{az}{L} & \text{for } 0 < \frac{z}{L} \leq 0.5 \\ -\frac{az}{L} + B\left(\frac{az}{L} - \frac{C}{D}\right)e^{-\left(\frac{BC}{D}\right)} - \frac{BC}{D} & \text{for } 0.5 < \frac{z}{L} \leq 7 \end{cases} \quad (\text{A.32})$$

Where:

$a = 5$ ,  $A = 1$ ,  $B = 2/3$ ,  $C = 5$  and  $D = 0.35$

A practical implication in the determination of  $L$  using Eq. (A.30) requires the use of three dimensional ultrasonic anemometry with sample rates of at least 10 Hz in order to determine  $\overline{w'\theta'_v}$  and  $u_*$  as well as temperature sensors for  $\overline{\theta'_v}$ . An alternative method to determine atmospheric stability based on the Richardson number is described by Eq. (A.33).

$$R_i = \frac{\frac{g}{\theta} \frac{\partial \overline{\theta}}{\partial z}}{\left(\frac{\partial \overline{u}}{\partial z}\right)^2} \quad (\text{A.33})$$

This can be approximated, Eq. (A.34), to a usable form for less costly measurement setups of temperatures and horizontal wind speeds, measured at two heights, on a met mast (Kelley, 2017). The measurement can be logged in 10-minute mean values.

$$R_i = \frac{g(T_2 - T_1)(z_2 - z_1)}{0.5((T_2 + T_1)(U_2 - U_1)^2)} \quad (\text{A.34})$$

Where:

$z_1, z_2$  - two measurement heights (m)

$T_1, T_2$  - mean absolute temperature measurements at the two heights (K)

$U_1, U_2$  - horizontal mean wind speeds at the two heights (m/s)

In general,  $R_i < 0 \Rightarrow$  unstable;  $R_i = 0 \Rightarrow$  neutral;  $R_i > 0 \Rightarrow$  stable.

## A.2 Modelling the atmosphere for wind energy

As air motion in atmosphere occurs on a wide range of spatial and temporal scales, it is computationally not possible at present to simulate wind flow at all scales simultaneously at high resolutions in a single modelling process. Therefore, modelling of the ABL for wind energy is divided into different categories of scale to solve the dynamic equations (Sanz Rodrigo et al., 2017). At each scale, the appropriate terms

of Eqs. (A.3) to (A.5) are used and some may be simplified or ignored depending on their significance, Fig. A.6.

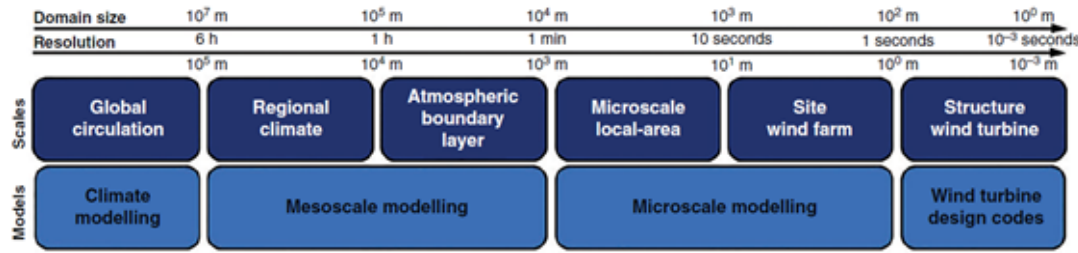


Fig. A.6. Categories of modelling scales applicable to wind energy - adapted from (Sanz Rodrigo et al., 2017).

### A.2.1 Global circulation models

Atmospheric global climate models (GCM) simulate large scale atmospheric motions and thermodynamic processes. They assimilate weather data observation from numerous surface observations stations around the globe and use numeric weather prediction models (NWP) to simulate the state of the atmosphere in three to six hour timeframes in a process termed “analysis”. They solve the sets of partial differential equations Eqs. (A.1) to (A.5) outlined in the previous section, along with equations of state (relating to density, pressure and temperature) and other process equations that describe the dynamic and thermodynamic processes in the earth’s atmosphere. The equations are discretised appropriate to the domain of interest, therefore not all scales of motions and processes are represented (Knierel, 2006).

In GCMs, computational grid spatial resolutions are in the order of hundreds of km (Ambrizzi et al., 2019). In recent decades, the increasing availability of remote satellite weather and earth observation data has enabled GCMs to simulate more detailed and accurate short-term global weather forecasts. In addition, historical surface data observations over a long term time period, e.g., years or decades, combined with the increasing volume of remote observation can be used by the NWP models to perform hind casts or reanalyses to generate long-term historical “reanalysis” data sets, which have now an increasing significance in wind resource assessment (Kim, Kim, and Kang, 2018). These reanalysed data sets include of a variety of meteorological parameters, including wind speed and direction at multiple heights in the atmosphere. These have temporal scales in the order of hours with spatial scales of about

100 km, but in some cases down to one hour time resolution and 50 km spatial resolution. The choice of the horizontal and vertical grid structure and domain impacts the equation set and model performance. These include the ECMWF Modern-Era Retrospective analysis for Research and Applications, (MERRA-2), NCEP/NCAR Reanalysis and the JRA-25 reanalysis (Griffin, 2017). Current spatial scales implemented in GCM models, due to computational constraints, don't capture the effects of mesoscale features associated with associated with regional orography, such as mountains and coastal areas, i.e., spatial scales down the order of 10s of km. Therefore, limited area models (LAM) or regional climate models (RCM), also referred to as mesoscale models, are used to simulate the climate and weather forecasts at higher spatial and temporal resolutions (Ambrizzi et al., 2019).

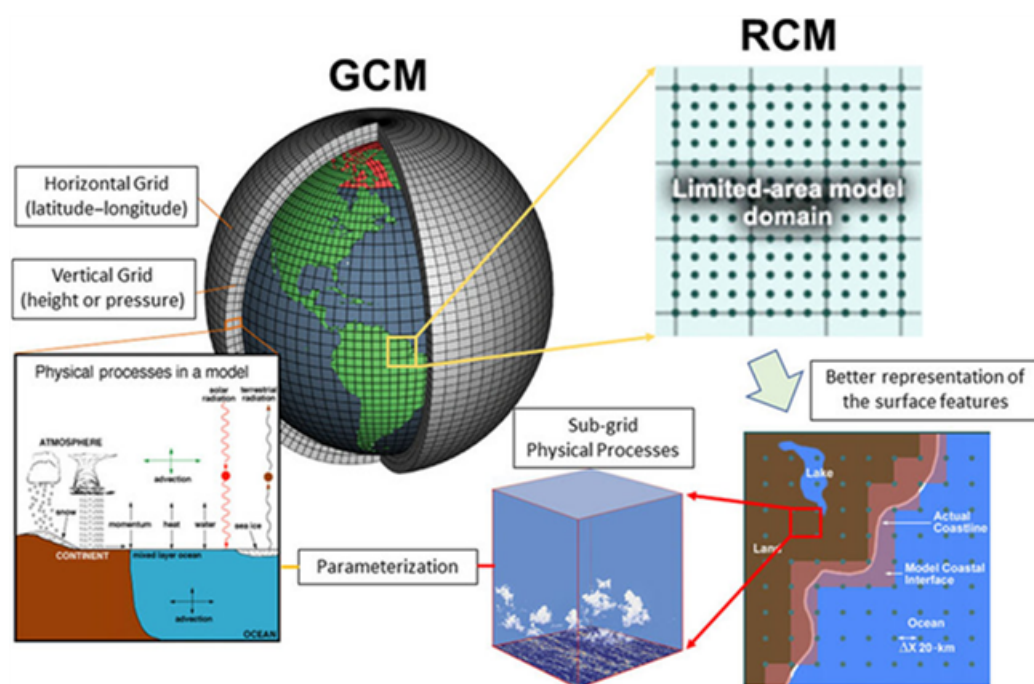


Fig. A.7. Downscaling from GCMs to RCMs (Ambrizzi et al., 2019).



These regional or mesoscale models attempt to capture orographic features such as hills, valleys, and escarpments that can affect wind flow by channelling winds caused by deflection forces near a single feature. Such features include, single mountains, gaps between hills, narrow valleys and over a water body between two landmasses. Channelling usually results in an increase in wind speed however, wind speed and directional changes depending on the size of the physical feature and scales of the winds involved. A number of thermally influenced flows, such as diurnal katabatic flows and gravity accelerated downslope winds in the lee of hills that can occur when strong thermally stable winds are forced over hills. Similarly, at locations near to large water bodies, such as coastal areas or near the shorelines of large lakes, the high heat capacity of water leads to uneven heating of the land and water surfaces that can result in thermally driven circulation of winds between the landmass and water body giving rise to land and sea breezes.

### A.2.2 Mesoscale models

Mesoscale models operate on a similar basis to GCMs but use the output of GCMs at the lateral boundaries of their computational grids. Mesoscale models downscale to spatial resolutions to a few km. They are used to provide short term forecast from hours to a few days ahead. They also use long term reanalysis data from GCMs to model regional wind climates and create regional wind atlases. In some cases, there are also high-resolution regional reanalysis datasets available for different regions of the world. Some examples of these are the North American Regional Reanalysis (NARR); European Consortium for Small-scale Modeling (COSMO)-REA6, Copernicus European Regional ReAnalysis (CERRA); Australian Bureau of Meteorology Atmospheric High-Resolution Regional Reanalysis (BARRA) for Australia; and ASRv2 in the Arctic region (Mesinger et al., 2006; Bollmeyer et al., 2015; Bromwich et al., 2018; Keller and Wahl, 2021). The basis of many NWP models applied at the mesoscale level are non-hydrostatic and fully compressible, which mean that vertical momentum equations Eq. (A.5) are solved and considers situations of air compression or density changes (Gasset, Landry, and Gagnon, 2012; Skamarock et al., 2021). However, in relation to wind flow in the ABL, air is considered incompressible as air flow is below speeds of 100 m/s (N. Sørensen et al., 2018; Toparlar et al., 2019). The principal focus of NWP model development to date has been in meteorological

weather forecasting for a variety of sectors, such as public safety, agriculture, aviation, marine transport, pollution dispersion etc. The application of NWP models in wind energy is a relative recent area of growth. NWP models for short-term wind and power forecasting for operating wind farms, utility grid control and electricity market pricing is an ongoing area of development and improvement (Giebel and Kariniotakis, 2017; Mazzi and Pinson, 2017; Nazir et al., 2020; Santhosh, Venkaiah, and Vinod Kumar, 2020). However, it is recognised that greater research collaboration between the meteorological/climate and renewable energy communities is needed to deliver robust technological renewable energy solutions, sooner rather than later. Although, less developed to date, the use of NWP models in wind energy resource assessment and life time energy prediction of prospective wind projects is a growing area of interest (Giebel and Kariniotakis, 2017; Mazzi and Pinson, 2017; Nazir et al., 2020; Sanz Rodrigo et al., 2017). Specifically, the generation of wind climates and wind atlases that can produce sufficiently accurate wind information at any location as a means to provide the initialisation of microscale models at wind farm and wind turbine sites, thereby reducing the need for long-term wind onsite measurements. Currently in wind resource assessment, the mesoscale model approaches used can be divided into three classes (Emeis, 2013; Zhang, 2015). Mass consistent (MC) flow models which generate a divergence-free flow over orography from measurements are the simplest class. They solve the conservation of mass equation Eqs. (A.1) and (A.2) but not the dynamic momentum equations Eqs. (A.3) to (A.5). MC models require a larger number of wind observations. The next level of complexity are hydrostatic flow models that solve equations Eqs. (A.1) to (A.4) for horizontal flow but do not account for vertical accelerations. Eq. (A.5) is substituted by the hydrostatic equation, Eq. (A.6). Hydrostatic models work best for spatial scales larger than  $\sim 10$  km. For smaller scales, full non-hydrostatic model that solve Eqs. (A.1) to (A.5) have to be used. Downscaling from mesoscale to sub-grid microscales of less than 1 km to determine local surface wind can be done separately using statistical or microscale modelling approaches or a combination of both (this will be described later). Statistical approaches, in general, combine long-term outputs from mesoscale models, or in some cases reanalysis data, with short-term (e.g., 1-year) onsite measurements to reconstruct long term high-resolution wind data sets.



Another approach is mesoscale-microscale dynamic coupling where mesoscale forcing is progressively modelled to higher-resolutions towards the microscale domain of interest. A number of sub-grid scale processes are represented, including convection, boundary layer turbulence, radiation, cloud, microphysics and orographic drag. The UK Met Office Virtual Met Mast that is based on the UM mesoscale model is an example of this approach (Standen et al., 2017). Mesoscale models can use ancillary files that represent physical characteristics of the surface, such as orography, vegetation and soil types from digital terrain maps (DTM) and land cover types from satellite observation databases, such as the CORINE Land Cover database (Büttner et al., 2021).

As well as surface roughness properties, large variations in elevation associated with hill and mountainous areas can introduce orographic drag. Orography refers to the elevation characteristics of the terrain. Depending on orographic complexity, the application of the wind speed profile laws in complex hilly and mountainous terrain is not always straight forward. One of the challenges with mesoscale models is a biased under estimations of wind speeds and accuracy of wind direction estimations due to unresolved complex and mountainous terrain effects (Standen et al., 2017). The shape, spatial scale and elevation variation can create a variety of mechanically influenced wind flows, such as speed up over crests of hills, gap and valley channelled flows between hills, flow blockage and flow steering. Orographic influences can span across the mesoscale to microscale ranges. Many linear downscaling flow models that assess orography and based on, or on some variation, of the Jackson-Hunt model that describes two dimensional wind flows over two dimensional low hills (Jackson and Hunt, 1975). In the Jackson-Hunt model, flow streamlines over hills are forced up and displaced by height variation of the terrain in the lower layer, Fig. A.8(a). Flow is divided into an inner layer where the perturbation shear stress and turbulence are significant and an inviscid outer layer where the perturbation diminishes and eventually vanishes with height.

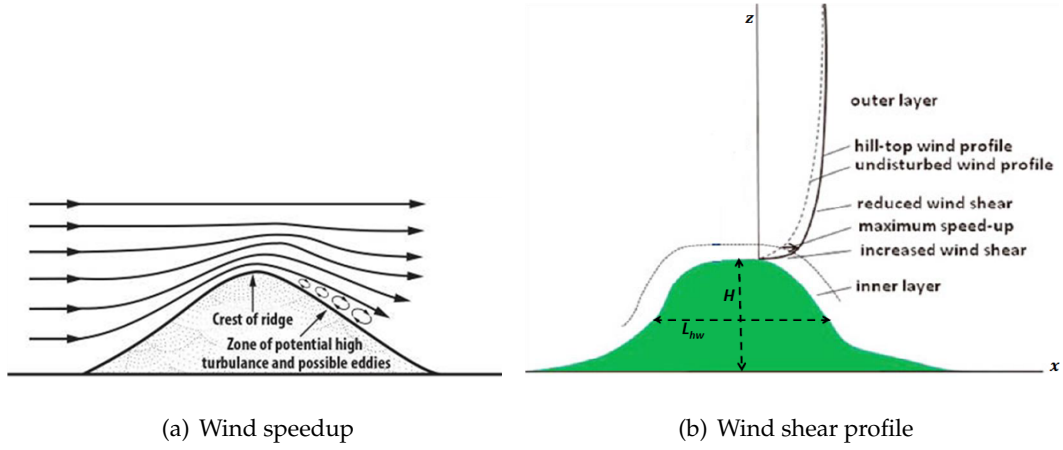


**Fig. A.8.** Schematic of flow over the crest of a hill - adapted from (Emeis, 2013; Zhang, 2015).

The generated pressure perturbation in the outer layer, forces flow back to the lower level. In the outer layer, the pressure gradient force and advection of momentum are balanced with vanishing turbulent momentum transfer. For a simple symmetric hill, a basic description of the vertical perturbed wind speed profile over the hilltop,  $u_{out}$ , in the outer layer can be described by Eq. (A.35) which has a dependency on both vertical height  $z$  and horizontal distance  $x$  (Emeis, 2013).

$$u_{out}(x, z) = u_{\infty} + u_{\infty}(L_{hw}) \frac{H}{L_{hw}} \sigma_f \left( \frac{x}{L_{hw}}, \frac{z}{L_{hw}} \right) \quad (\text{A.35})$$

Where:

$H$  is the maximum height of the hill above local reference (e.g., base of hill)

$L_{hw}$  is the width of the hill at  $\frac{H}{2}$

$\sigma_f$  is form function for a height variation  $h(x)$  in the cross-section

If  $h_x$  the variation of the hill height with horizontal distance  $x$  can be described by an inverse polynomial Eq. (A.36), then the form function  $\sigma_f$  can be described by Eq. (A.37).

$$h \left( \frac{x}{L_{hw}} \right) = \frac{1}{1 + \left( \frac{x}{L_{hw}} \right)^2} \quad (\text{A.36})$$

$$\sigma_f \left( \frac{x}{L_{hw}}, \frac{z}{L_{hw}} \right) = \frac{\left( 1 + \left( \frac{z}{L_{hw}} \right)^2 \right)^2 - \left( \frac{x}{L_{hw}} \right)^2}{\left( \left( 1 + \left( \frac{z}{L_{hw}} \right)^2 \right)^2 + \left( \frac{x}{L_{hw}} \right)^2 \right)^2} \quad (\text{A.37})$$

The height of the inner layer,  $l_i$ , layer is can be described by Eq. (A.38).

$$l_i \ln \left( \frac{l_i}{z_0} \right) = 2\kappa^2 L_{hw} \quad (\text{A.38})$$

At heights much smaller than  $l_i$ , turbulence transfer forms a balance between the surface stress and wind shear to give a logarithmic profile of the velocity perturbation. At heights close to  $l_i$  maximum flow perturbation occurs. The vertical wind speed profile in the inner layer across the hill or ridge by Eq. (A.39).

$$u(x, z < l_i) = u_\infty + u_\infty(z) \frac{\ln \frac{L_{hw}}{z_0}}{\ln \frac{l_i}{z_0}} \frac{H}{L_{hw}} \sigma_f \left( \frac{x}{L_{hw}}, \frac{z}{L_{hw}} \right) + \delta u(x, z < l_i) \quad (\text{A.39})$$

The additional influence of surface pressure gradient on wind speed is  $\delta u$ , Eq. (A.40).

$$\delta u(x, z < l_i) = \frac{1}{\kappa} \delta u_* \left( \frac{x}{L_{hw}} \right) \ln \frac{z}{z_0} \quad (\text{A.40})$$

The impact on the frictional velocity is described by Eq. (A.41)

$$\delta u_* \left( \frac{x}{L_{hw}} \right) = u_{*\infty} \frac{\ln \frac{L_{hw}}{z_0}}{\ln \frac{l_i}{z_0}} \frac{H}{L_{hw}} \Delta \sigma_f \left( \frac{x}{L_{hw}} \right) \quad (\text{A.41})$$

The incremental change in the form functions and incremental distances  $\Delta x$  that are small compared to  $L_{hw}$  is given by Eq. (A.42).

$$\begin{aligned} \Delta \sigma_f \left( \frac{x}{L_{hw}} \right) &= \frac{1}{2\Delta x} \left( \sigma_f \left( \frac{x}{L_{hw}} + \Delta x, \frac{z}{L_{hw}} = 0 \right) \right) \\ &\quad - \frac{1}{2\Delta x} \left( \sigma_f \left( \frac{x}{L_{hw}} - \Delta x, \frac{z}{L_{hw}} = 0 \right) \right) \end{aligned} \quad (\text{A.42})$$

The overall vertical wind speed profile over both the inner and outer layers can then be described by Eq. (A.43).

$$\begin{aligned} u(x, z) &= u_\infty(z) + u_\infty(L_{hw}) \frac{H}{L_{hw}} \sigma_f \left( \frac{x}{L_{hw}}, \frac{z}{L_{hw}} \right) P_0(z) \\ &\quad + \frac{1}{\kappa} \delta u_* \left( \frac{x}{L_{hw}} \right) \ln \frac{l_i}{z_0} P_\delta(z) \end{aligned} \quad (\text{A.43})$$

$P_0(z)$  and  $P_\delta(z)$  are pressure factors given by Eq. (A.44) and Eq. (A.45) respectively.

$$P_0(z) = 1 + \frac{\ln \frac{z}{z_0}}{\ln \frac{l_i}{z_0}} \exp \left( -\frac{z - z_0}{l_i} \right) \quad (\text{A.44})$$

$$P_\delta(z) = \frac{\ln \frac{z}{z_0}}{\ln \frac{l_i}{z_0}} \exp \left( -2 \left( \frac{\ln \frac{z}{z_0}}{\ln \frac{l_i}{z_0}} \right)^2 \right) \quad (\text{A.45})$$

Another approach is analysing the terrain shape causing the flow perturbation in terms of Fourier components and the equation are solved in Fourier space. Fourier transforms are used to independently calculate of velocity perturbations for each wavenumber vector. Inversion of the Fourier transforms gives the solutions for velocity perturbations in real space. A limitation of the approach is that it cannot account for flow separation effect and thus limits usage to terrain slopes of less than  $\sim 17^\circ$ . It has limitations in that the ratio of the height of the hill to its width must be small. The UK Met Office UM, in mesoscale to microscale downscaling, employs orographic roughness parametrisation below reference height  $z_{ref}$ , Fig. A.9, that is characterised by a local orographic wave number  $k_w$  and a tuneable parameter  $a$ , Eq. (A.46), (Howard and Clark, 2007).

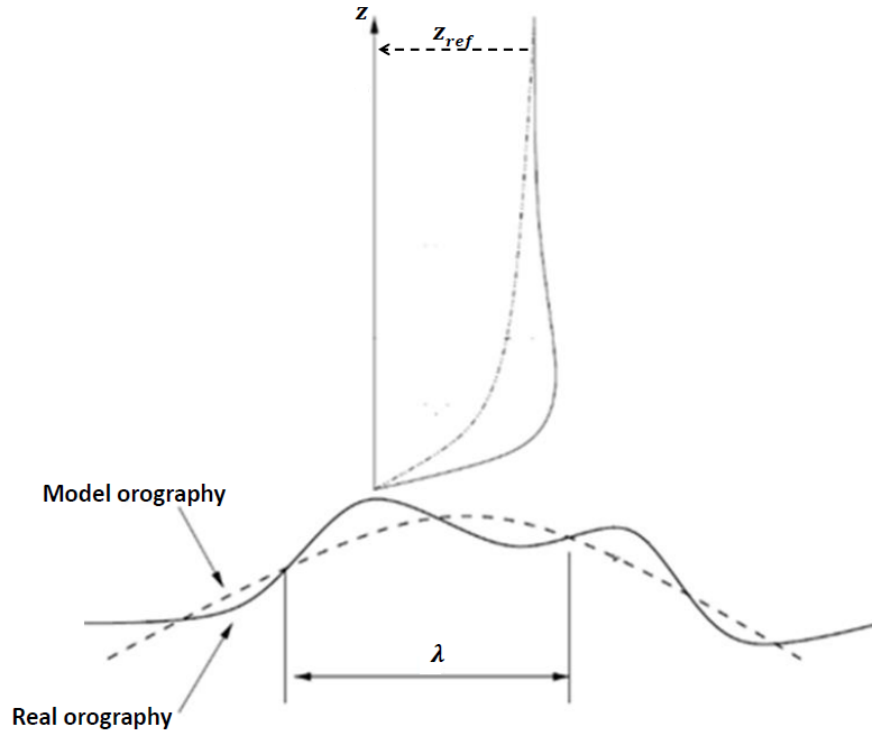


**Fig. A.9.** A simplified schematic of flow over a hill approximated by a wave number - adapted from (Howard and Clark, 2007).

$$z_{ref} = ak_w^{-1} \quad (\text{A.46})$$

Where:

$$k_w = \begin{cases} \frac{\pi \frac{A}{S}}{\frac{H}{2}} & \text{for } (\frac{H}{2}) \geq (\frac{H}{2})_{min} \\ \frac{\pi \frac{A}{S}}{\frac{H}{2}} & \text{for } (\frac{H}{2}) < (\frac{H}{2})_{min} \end{cases} \quad (\text{A.47})$$

$\frac{A}{S}$  - silhouette area per unit horizontal area

$(\frac{H}{2})$  - the mean peak-to-trough amplitude (m)

$(\frac{H}{2})_{min}$  is the minimum value of:

$$\frac{1}{\Delta x_{min}} \leq \frac{(A/2)}{(H/2)} \leq \frac{1}{\Delta x_{max}} \quad (\text{A.48})$$

$$a = \begin{cases} -\ln \alpha + \ln(k_w \frac{H}{2}) & \text{for } \ln(k_w \frac{H}{2}) > \beta \\ -\ln \alpha + \beta & \text{for } \ln(k_w \frac{H}{2}) \leq \beta \end{cases} \quad (\text{A.49})$$

$\alpha$  and  $\beta$  are tuneable parameters with values set at 0.12 and -4 respectively, based

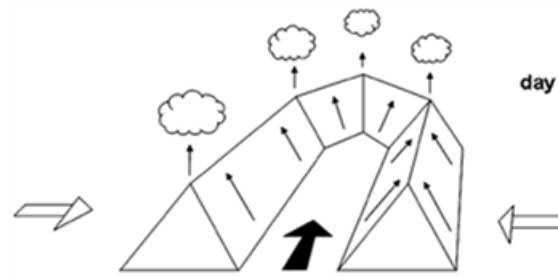
on UK observations on the scale of interest. The resulting roughness corrected wind speed below  $z_{ref}$  is  $U_{rc}(z)$  for complex orography down to a 1 km horizontal scale is Eq. (A.50)

$$U_{rc}(z) = U(z_{ref}) \frac{\ln\left(\frac{z-d}{z_0}\right)}{\ln\left(\frac{z_{ref}-d}{z_0}\right)} \quad (\text{A.50})$$

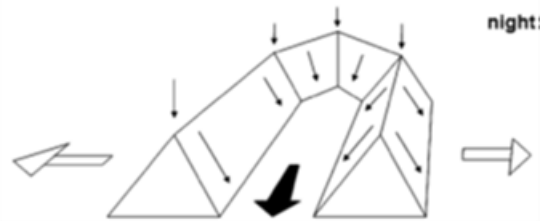
More details of the UK Met Office UM model will be given in Chapter 5 in describing the mesoscale remodelled Irish wind atlas, on which it is based. In this research, assessment of the mesoscale wind features in the region of the wind turbine site is made with the wind atlas and an evaluation of its energy prediction of the wind turbine compared to the actual wind turbine EER. This will help inform the separate mesoscale influences with the microscale influences, particularly buildings, in shaping the measured *EER* of the wind turbine assessed in Chapter 4.

### A.2.3 Thermal influences

Thermal influences on wind climates can vary on seasonal and diurnal scales depending on location, broadly determined by atmospheric stability. In mountain/valley areas, heated rising air during the day can give relatively gently upslope winds from valley floors, known as anabatic winds, Fig. A.10. At night, faster radiative cooling of the elevated mountain surface cool the local air that results in cool denser air flow back down the valley slopes, known as katabatic winds. Depending on the valley shapes and the amount of diurnal heating and cooling, the colder air may pool at the valley floor or may drain out into external planes, referred to as mountain or drainage winds. Valley winds may return from the plains to the valley during the day if sufficient heating reoccurs (Stull, 1988).



(a) Warmer ascending anabatic flow



(b) Cooler descending katabatic flow

**Fig. A.10.** Schematic of mountain/valley flow - adapted from (Stull, 1988).

In the vicinity of large water bodies, such as the sea, during the day the land heats faster and air rises and reduces local air pressure at the surface. This results in wind flow from the sea to give a sea breeze. The sea breezes may be strongest in the afternoon when land is warmest and vertical turbulence circulation is strongest. The circulation reverses at night to give a land breeze from the land to the sea, but is not as strong, as the land can cool down faster. The strength of these winds may have seasonal peaks due to seasonal time lags in heating the water body, e.g., in early summer when water is still cold from the winter season, while solar irradiation is getting more intense and heating the land more quickly.

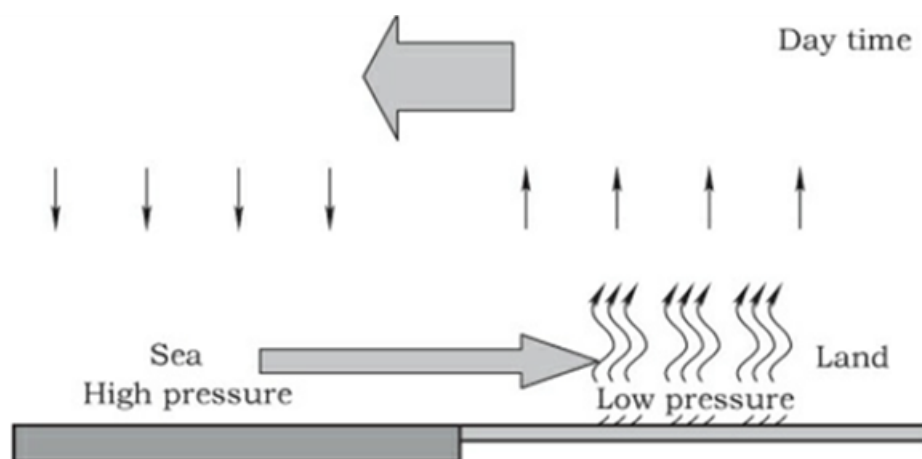


**Fig. A.11.** Schematic sea breeze formation (Emeis, 2013).

NWP models at all scales are still far from perfect and have number of limitations, such as errors introduced in the discretisation process of the governing equations Eqs. (A.1) to (A.5), goodness of knowledge of initial conditions, boundary conditions and unresolved sub-grid processes that need to be parametrised. Another inherent limitation of current mesoscale modelling techniques for wind atlas generation is that the physical models of the atmosphere use don't fully account for the dynamical chaos of the atmospheric system (Sanz Rodrigo et al., 2017). It is intended that the next generation of mesoscale models for wind resource assessment will use probabilistic approaches based on ensemble predictions to help account for uncertainty of the physical models and imperfect observations of the atmosphere. However, these may still be limited by not being able to fully account for all sources of error (Dörenkämper et al., 2020). This will require further research to improve the physical models along with higher resolution downscaling and calibration based on the past records of the ensemble errors.

#### A.2.4 Microscale models

Microscale models are used to assess local influences at a location of interest at smaller spatial scales in the order of 100s m to 10 s of km to optimise the siting of wind turbines for energy production. Microscale models consider influences of local orography and surface roughness at higher resolutions than mesoscale models as well as obstacles. Frictional forces (VII) in equations Eqs. (A.3) to (A.5) dominate at this scale and flow characteristics in the Prandtl layer is of most interest,



particularly for distributed wind. Microscale models can consist of analytical or numerical flow models. They can be initialised from the outputs of mesoscale models, but can also be driven by local wind measurements, if available in sufficient quality and quantity, i.e., good quality measurement setup with records of a least one year of high-resolution wind measurements (e.g., 10-minute average data or higher resolutions). Both linear and CFD microscale modelling approaches are widely used in the wind industry. They have varying degrees of complexity, accuracy and cost depending on the site complexity and size a of wind project.

### A.2.5 Linear flow model approaches

The Wind Atlas Application Program (WAsP) is a relatively common microscale modelling method used in the wind industry. Linear WAsP-IBZ is a diagnostic tool which calculates wind statistics by parametrising the influence of orography, roughness and obstacles (Topaloğlu and Pehlivan, 2018). It was used in the development of the first European Wind Atlas (Troen and Lundtang Petersen, 1989). The general approach to linear flow models is outlined in Fig. A.12. It requires measurements from a nearby measurement mast, preferably within 50 km of the wind turbine or wind farm location, and extrapolates it to the turbine hub height at the site of interest. At least one year of wind data from the reference masts at some reference measurement height is recommended (Landberg et al., 2003; Petersen and Troen, 2012).

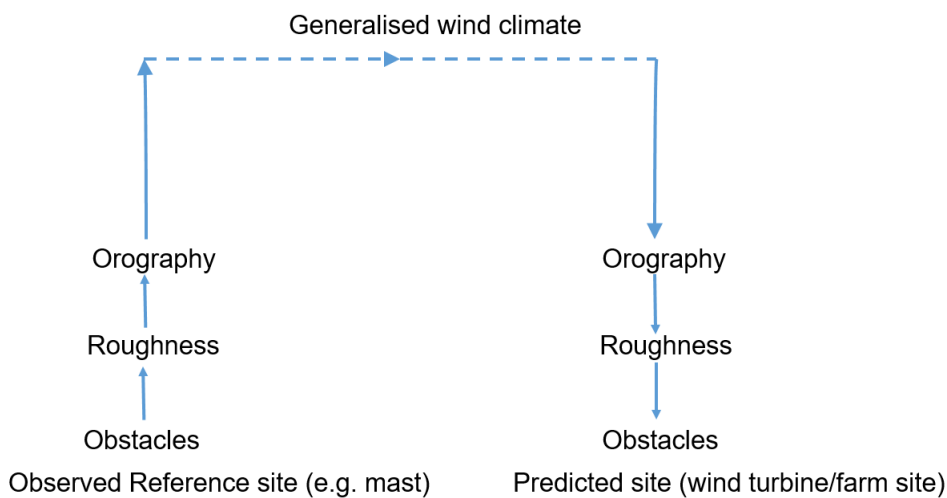


Fig. A.12. General flow diagram in linear model assessment.

Assessments are carried out on local obstacles, surface roughness and orography at the reference mast location. Their impacts on wind speed and direction are accounted for in upscaling the met mast data to create a terrain independent generalised wind climate for the region. The generalised wind climate is describe by statistically binned wind speeds and directional sectors. It is assumed the generalised wind climate at the wind turbine location is the same as that at the reference met mast location. It is then downscaled at the wind turbine location to hub height accounting for local surfaces roughness, obstacles, orography and any neighbouring wind turbines. Wind turbine power curves are then combined with the modelled hub-height wind statistics data to predict and optimise wind turbine or wind farm *AEP*.

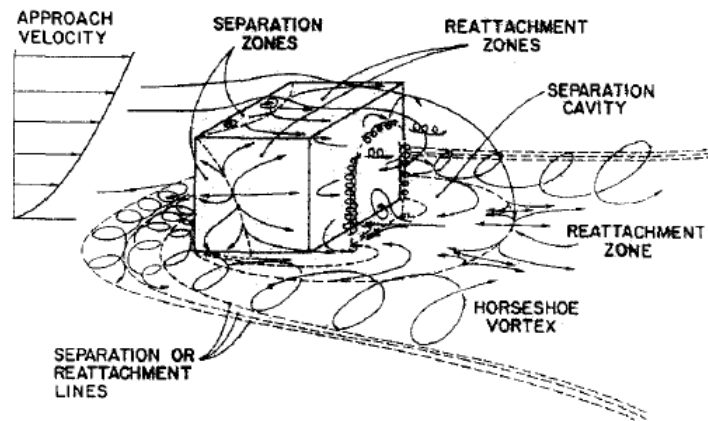
### A.2.6 Orography

In the microscale modelling context, orography is modelled by linearization of the Naiver-Stokes equations, describing two-dimensional turbulent flow over low hills. The linear 'BZ-model' of (Troen and Lundtang Petersen, 1989), which is a wavenumber scaling technique based on Jackson-Hunt model referred to previously, is integrated (IBZ) into WAsP. It calculates the wind velocity perturbations in the boundary layer induced by orographic features. It uses a zooming mesh of high-resolution terrain height contour lines (20 m) close ( $\sim 1$  to 2 km radius from the centre of site location) to the site of interest with a lower resolution further away up to 5 km from the site. It works best in terrain with slopes less than  $17^\circ$  and assumes steady state attached flow and neutral atmosphere stability. To improve the model in more complex terrain, (Mortensen and Petersen, 1998) applied a statistical correction based on a terrains ruggedness index (RIX). The RIX value at given site is defined as the fractional extent of the surrounding terrain that is steeper than a certain critical slope and is a coarse measure of the extent of flow separation and bias of the model induced by terrain slopes. This technique uses a polar coordinate system, each radial line originating from the location of interest is divided into line segments by terrain height contour lines. The RIX value of the radius in question is the sum of the line segments representing slopes greater than a critical slope value divided by the entire radius. The overall RIX value for the site is the mean of the radius-wise RIX values. Attached flows are assumed when the overall RIX is close to zero. If  $RIX >$

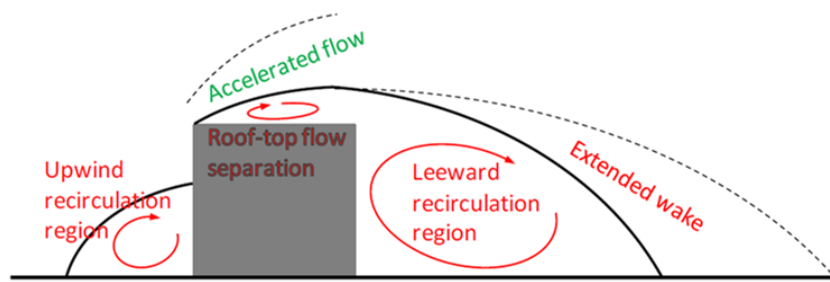
0, it is indicative that somewhere in the surrounding area the slopes are greater than 0.3 ( $17^\circ$ ) meaning the onset of flow separation. Accuracy can be improved by using at least two mast measuring locations on a site and establishing relationships using RIX differences ( $\Delta RIX$ ) between the measured (met mast) location and the wind turbine/farm site of interest. A regression analysis of WAsP-IBZ cross prediction error in wind speed from one mast to the other against  $\Delta RIX$  enables an empirical correction factor that is applied to the biased wind speed predictions in order to obtain the true wind speed at wind turbine hub height locations across a site. However, implementing multiple met masts increases costs.

### A.2.7 Obstacles

Surface obstacles in close proximity to the site of interest can have wake effects that can additionally perturb wind flow downwind of the obstacle. Fig. A.13 show the complex wind flow around standalone three-dimensional cuboid structures that can consist of flow detachment, separation cavities and recirculation zones in the wake, flow reattachment and vortex shedding (Peterka, Meroney, and Kothari, 1985; Millward-Hopkins, 2013; Micallef and Van Bussel, 2018). As outlined in the literature review, complex recirculation zones that define the near wake can extend up to 2 to 6 times the obstacle height downwind of an obstacle, while the far wake may extend to up to 18 times the obstacle height. (Nieuwpoort, Gooden, and Prins, 2010; Vasilopoulos, Sarris, and Tsoutsanis, 2019).



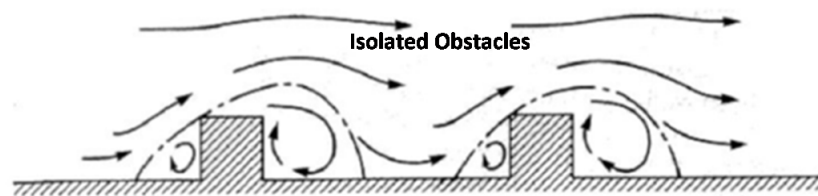
(a) Schematic of 3D flow



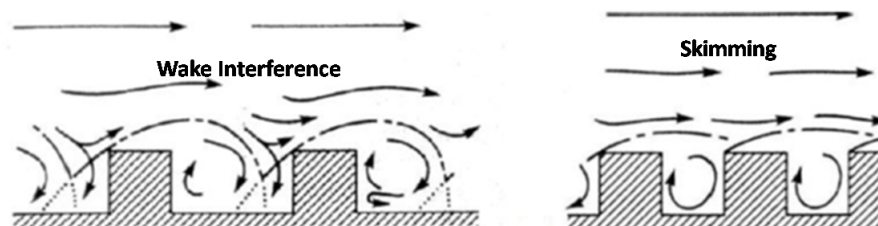
(b) Zones of flow in vertical plane

**Fig. A.13.** Flow around bluff obstacles (Peterka, Meroney, and Kothari, 1985; Millward-Hopkins, 2013).

(Macdonald, Griffiths, and Hall, 1998) state that it is incorrect to apply the log law lower than twice the height of an obstacle. Some of the basic wind flow regimes are shown in Fig. A.14 for different building densities (Grimmond and Oke, 1999).



(a) Isolated obstacles sufficiently spaced with no wake interference in the flow



(b) Closer spaced obstacles with wake interference to skimmed flow for high density

**Fig. A.14.** Flow around multiple obstacles - adapted from (Grimmond and Oke, 1999).

The wakes of sufficiently spaced obstacles have little interference with each other. At closer proximities, wake interference can occur, while increasing spatial density leads to skimmed flow that results in uplift or displacement of the flow (Zajic et al., 2011). In WAsP-IBZ, for a given obstacle, if the turbine hub-height is less than 3 times the height of an obstacle and is less than 50 obstacle heights away from the obstacle then the obstacle is modelled by the WAsP-IBZ shelter model, otherwise it is treated as a surface roughness element. The WAsP-IBZ shelter model is based on a refined version a simple two dimensional obstacle of infinite length, derived from wind tunnel measurements by (Perera, 1981), Fig. A.15. The fractional reduction in wind speed, downwind of the obstacle is described by Eqs. (A.51) to (A.53), (Troen and Lundtang Petersen, 1989; Peña et al., 2016).

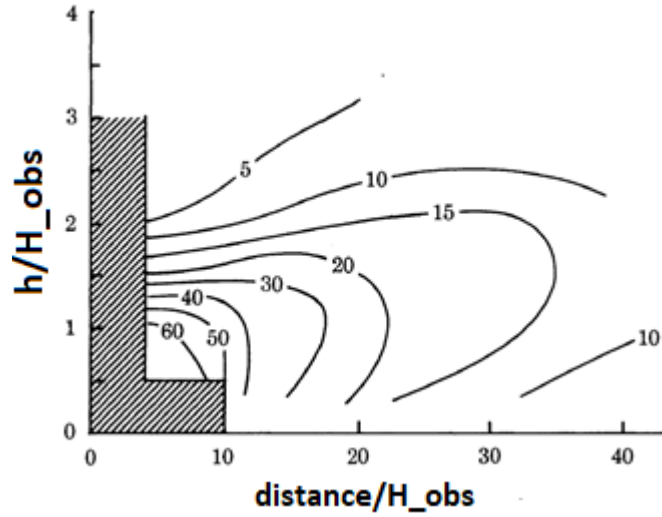


Fig. A.15. Percentage wind speed reduction in the wake of a two dimensional obstacle - adapted from (Perera, 1981).

$$\frac{\Delta U_z}{U_h} = 9.75 \left( \frac{H}{h} \right)^{0.14} \frac{x}{h} (1 - P) \eta e^{(-0.67\eta^{1.5})} \quad (\text{A.51})$$

$$\eta = \frac{H}{h} \left( K \frac{x}{h} \right)^{\frac{-1}{n+2}} \quad (\text{A.52})$$

$$K = \frac{2\kappa^2}{\ln \frac{h}{z_0}} \quad (\text{A.53})$$

Where:

$\Delta U_z$  – wind speed reduction at height  $z$  (m/s)

$U_h$  – free wind speed at obstacle height (m/s)

$U_z$  – wind speed at height of interest (m) (e.g., turbine hub height)

$P$  – porosity of obstacle (ratio of open area total area)

$h$  – obstacle height (m)

$x$  – distance downstream of obstacle (m)

$H$  – height of interest (m) (e.g., wind turbine hub height)

$z_0$  – surface roughness

$n$  – velocity profile exponent of  $\frac{1}{7}$

In the WASP-IBZ shelter model, a zone of flow separation is considered to exist within a region defined by a straight line drawn from the top of the obstacle to the ground from 2 obstacle heights upwind of the obstacle to 5 obstacle heights downwind of the obstacle. The formula has limitations as it assumes normal non-skewed incident wind flow at the obstacle. Multiple obstacles are treated by considering the obstacle furthest away first and calculating the individual sheltering by all subsequent downstream obstacles towards the site of interest. If the zones of separation of very close obstacles overlap, then the relative sheltering is reduced by the fraction of the overlap.

### A.2.8 CFD flow approaches

Numerical CFD models, commonly used in the wind industry are based on Reynolds averaged Navier Stokes (RANS) equations. In RANS CFD modelling wind speed is considered as fluctuations superimposed on time-averaged values, Fig. A.16. This is represented by Eq. (A.54).

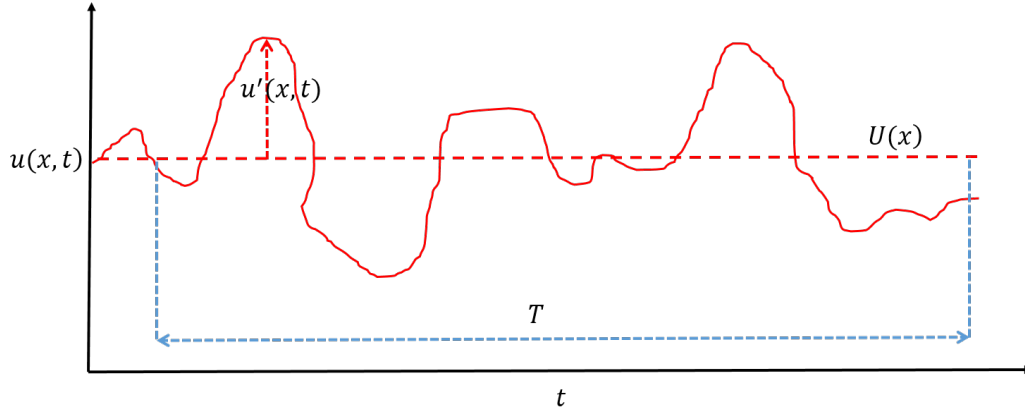


**Fig. A.16.** Time averaging of wind speed of a period  $T$ .

$$u(x, t) = U(x) + u'(x, t) \quad (\text{A.54})$$

Where:

$U(x)$  – time averaged mean wind speed (m/s)

$u'(x, t)$  – wind speed fluctuation about the mean (m/s)

This representation of wind speed is applied to the Navier Stokes equations Eqs. (A.1) to (A.5) to give the RANS representation that consists of the continuity Eq. (A.55), momentum Eq. (A.56) and turbulence models equations, Eqs. (A.57) to (A.61), for incompressible fluids without body forces (Cheng et al., 2003).

$$\frac{\partial U_i}{\partial x_i} = 0 \quad (\text{A.55})$$

$$U_i \frac{\partial U_i}{\partial x_i} = -\frac{1}{\rho} \frac{\partial P}{\partial x_i} + \frac{\partial}{\partial x_j} \left( v \left( \frac{\partial U_i}{\partial x_j} + \frac{\partial U_j}{\partial x_i} \right) - \overline{u'_i u'_j} \right) \quad (\text{A.56})$$

Where:

$U_i$  – time averaged mean wind speed (m/s)

$P$  – mean pressure (N/m<sup>2</sup>)

$\rho$  – air density (kg/m<sup>3</sup>)

$v$  – kinematic viscosity (m<sup>2</sup>/s)

$u'_i u'_j$  – Reynolds stresses (m<sup>2</sup>/s<sup>2</sup>)

To enable closure of the momentum equation, the Boussinesq linear isotropic eddy-viscosity hypotheses that gives a linear relationship between the Reynolds stresses and the mean velocity gradients is used, Eq. (A.57), (Toja-Silva et al., 2018). It assumes that variations in density does not effect the flow field (inertial term I in Eqs. (A.3) to (A.5)), apart from giving rise to buoyancy forces (term IV in Eq. (A.5)).

$$\overline{u'_i u'_j} = -v_T \left( \frac{\partial U_i}{\partial x_j} + \frac{\partial U_j}{\partial x_i} \right) + \frac{2}{3} k \delta_{i,j} \quad (\text{A.57})$$

Where:

$k$  - turbulence kinetic energy ( $\text{m}^2/\text{s}^2$ )

$\delta_{i,j}$  - Kronecker Delta function

$v_T$  - kinematic eddy viscosity ( $\text{m}^2/\text{s}$ )

To solve Eq. (A.57) a statistical turbulence model is required. In this case, the standard  $k - \varepsilon$  turbulence model is used. The  $k - \varepsilon$  model uses two model transport equations that describes turbulence kinetic energy production  $k$  Eq. (A.58) and turbulence dissipation rate  $\varepsilon$  Eq. (A.59) .

$$\frac{\partial}{\partial x_i} (U_i k) = \frac{\partial}{\partial x_i} \left( \frac{v_T}{\sigma_k} \frac{\partial k}{\partial x_i} \right) + P_k - \varepsilon \quad (\text{A.58})$$

$$\frac{\partial}{\partial x_i} (U_i \varepsilon) = \frac{\partial}{\partial x_i} \left( \frac{v_T}{\sigma_\varepsilon} \frac{\partial \varepsilon}{\partial x_i} \right) + c_{\varepsilon 1} \frac{\varepsilon}{k} P_k - c_{\varepsilon 2} \frac{\varepsilon^2}{k} \quad (\text{A.59})$$

Where:

$c_{\varepsilon 1}, c_{\varepsilon 2}$  - constants

$\sigma_k, \sigma_\varepsilon$  - Prandtl number that connect the diffusivities of  $k$  and  $\varepsilon$  to the eddy viscosity

$P_k$  - the production of  $k$ , which is the product of the kinematic eddy viscosity and the modulus mean rate of strain tensor, Eq. (A.60).



$$P_k = v_T \left( \frac{\partial U_i}{\partial x_j} + \frac{\partial U_j}{\partial x_i} \right) \frac{\partial U_i}{\partial x_j} \quad (\text{A.60})$$

$$v_T = c_\mu \frac{k^2}{\varepsilon} \quad (\text{A.61})$$

Where:

$c_\mu$  - a constant

### A.3 Some wind flow model comparison studies in the field

Various studies comparing these modelling approaches in complex rural terrain show mixed results in accuracy of wind resource predictions, depending on site physical features and atmospheric conditions. A blind comparison was made of various microscale flow models, implemented by 57 participants, to model wind speed-up and turbulence across the Bolund escarpment in the Roskilde Fjord in Denmark, with dimensions 120 m wide, 150 m long and 12 m high (Bechmann et al., 2011). The microscale flow models included CFD LES, RANS and linearised models. Eight masts with measurements at an array of 10 heights from 2 m to 15 m arranged to cover two directional transects were used to compare model predictions. The reported mean speed-up error of the RANS two-equation models was 13.6%, with a best case of 10.2%. Despite its computational superiority, the LES results were poorer, due to difficulties in applying the specified boundary conditions. Many assumptions of the linear models were violated because of recirculation in the flow. (Gasset, Landry, and Gagnon, 2012) carried out a study on Prince Edward Island in Canada to assess the accuracy of various coupled mesoscale-microscale wind flow modelling methodologies for wind energy applications. The Canadian mesoscale compressible community model (MC2), with a 5 km resolution, was combined and two linear microscale models, namely MsMicro and WAsP-IBZ. The MC2 and WAsP-IBZ modelling approach gave best agreement in mean wind speed predictions with the measurements across the 10 sites, ranging from -3.89% to 11.92%.

(Beaucage, Brower, and Tensen, 2014) evaluated four numerical models against high-quality observations to predict the variation in mean wind speed across sites with a wide range of terrain complexities. The models included linear WAsP-IBZ, Meteodyn CFD RANS, a coupled mesoscale numerical weather prediction model (NWP) downscaled by a mass-consistent model, and a coupled NWP and LES model. The coupled NWP-MC model and NWP-LES model gave the best predictions of observed mean wind speeds with a  $\sim 5.5\%$  difference, while the linear and CFD RANS models were within 8.0% and 9.4% respectively. It was found that NWP coupled models provide the lowest error compared with measurements indicating that thermal stability, temperature and moisture gradients developed in dynamic mesoscale simulations are very important in understanding atmospheric wind flow even over domains of a relatively small size. (Ayala et al., 2017) studied a 16.5 MW wind farm in complex terrain in the Ecuadorian Andes to compare actual power predictions using linear WAsP-IBZ model and Meteodyn CFD RANS. The CFD RANS approach underestimated the total *AEP* by 7%, WAsP-IBZ underestimated it by 8%. It was noted that, in addition to higher computation demand, CFD RANS modelling required more expertise than simpler linear model and, in general, a CFD approach may not always justify the extra expense. (Poudel, Tinnesand, and Baring-Gould, 2020) compared a number of models aimed at the distributed wind industry in the USA at two sites that contained met mast measurements. The models included the MC model, Openwind; a simplified Navier-Stokes equation model, Continuum; and a CFD RANS based tool WindNinja that uses the OpenFOAM solver. The models were initialised by external input data to the models from the US Wind Integration National Database (WIND) toolkit (Draxl et al., 2015). It was found that mean wind speeds were overestimated from 16% to 28%, compared to met mast measurements, across the two separate sites. However, it was also reported that external input data to the models from the US WIND toolkit contributed to this overestimation. A large blind comparative wind resource assessment study on two Scottish wind farms, involving many industrial and academic organisations, was co-ordinated by Wind Europe (Gylling et al., 2015). Many different models were used, but on average it was difficult to determine whether either linear models or CFD approaches was better. Long-term extrapolation procedures, though seemingly simple and well described, produced widely different results for the same input data. The broad conclusion

was that well defined and validated procedures are needed in order to obtain more reliable results and the choice and configuration of flow model should be based on reliable validation data.

In Chapter 6, the WAsP linear model and three CFD RANS approaches, supplied with onsite LiDAR wind measurements, will be applied in the peri-urban environment and their energy predictions compared to the actual wind turbine energy performance.

## A.4 Urban wind energy

### A.4.1 Urban vertical wind profiles

A number of empirical power laws have been proposed to describe wind shear profiles in urban environments. (Mertens, 2006) describes an IBL formation for a significant step change in roughness (e.g., from flat rural terrain to an urban area), Fig. A.17.

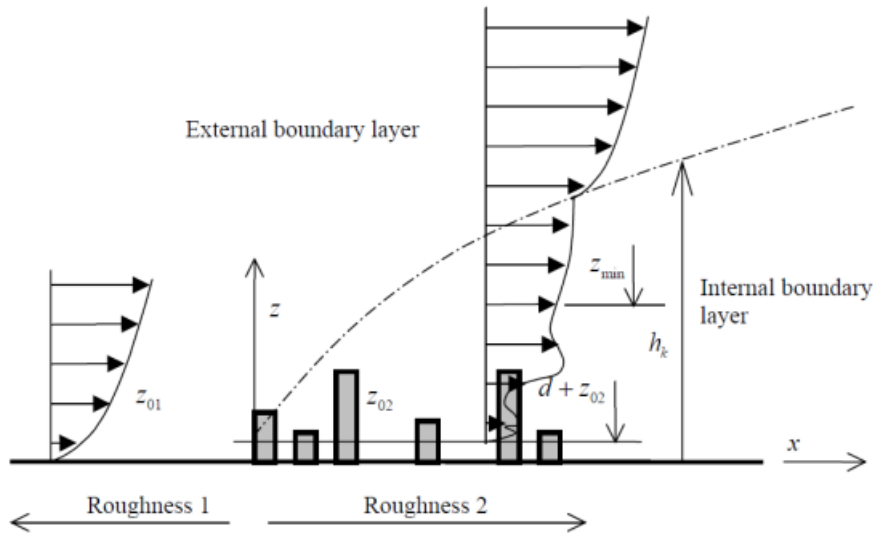


Fig. A.17. Simple schematic of IBL growth following a change in surface roughness (Mertens, 2006).

Once such empirical law suggests the growth of the IBL  $h_k(x)$  with distance  $x$  downwind from a roughness change can be described by Eq. (A.62), (Mertens, 2006; Drew, Barlow, and Cockerill, 2013).

$$h_k(x) = 0.28z_{0,max} \left( \frac{x}{z_{0,max}} \right)^{0.8} \quad (\text{A.62})$$

Where:

$z_{0,max}$  the greater of  $z_{01}$  and  $z_{02}$  (m)

The wind shear profile within the IBL is described by Eq. (A.63).

$$U(z) = U_1(z_1) \frac{\ln\left(\frac{h_k}{z_{01}}\right) \ln\left(\frac{z-d}{z_{02}}\right)}{\ln\left(\frac{z_1}{z_{01}}\right) \ln\left(\frac{h_k-d}{z_{02}}\right)} \quad (\text{A.63})$$

(Simiu and Yeo, 2019) state that the log law can be applied within the IBL after a distance of 500 m to 5 km downwind of the roughness change. However, urban environments have complex surface roughness characteristics due to various building sizes, shapes and packing densities (Tasneem et al., 2020). Wind flow over the surface roughness change from a rural to urban environment can result in the growth of a boundary layer that leads to a fully formed UBL. In a study of small scale wind potential in urban areas of the UK by the UK Met Office, commissioned by the UK Carbon Trust, 200 m was used as the reference height for the UBL in its methodology (Best et al., 2008). The wind flow at this reference height is assumed to be above the influence of local surface features (Weekes and Tomlin, 2014; Allen et al., 2017). Fig. A.18 shows a basic schematic of determining wind speed at a given height within the UBL. A blending height above buildings is defined to be where wind flow is considered horizontally homogeneous with an area-averaged surface roughness the broader local region (Grimmond and Oke, 1999; Bou-Zeid, Meneveau, and Parlange, 2004; Lopes, Palma, and Piomelli, 2015). The area is chosen to be 1 km<sup>2</sup> in the UK Met Office methodology. Below the blending height, local buildings are considered to influence the wind speed profiles over spatial distances (fetches) of 250 m.

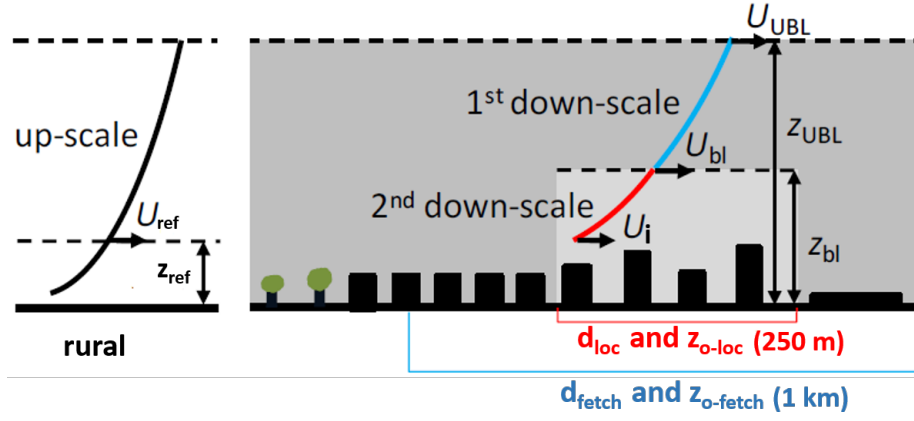


Fig. A.18. Basic schematic of UBL - Adapted from (Best et al., 2008; Millward-Hopkins et al., 2013c).

Wind speed measurements at a reference height outside the urban area are up scaled, using the log law, Eq. (A.64) to a height of 200 m using rural surface roughness value as a reference. The wind speeds are then firstly downscaled to the blending height using Eq. (A.65) using the 1 km<sup>2</sup> surface roughness values, followed by further downscaling to the height of interest, Eq. (A.66), using the local roughness values. In the UK, the rural reference winds are obtained by interpolation of UK Met Office surface observations.

$$U_{UBL}(z) = U_{ref} \frac{\ln \frac{z_{UBL}}{z_0}}{\ln \frac{z_{ref}}{z_0}} \quad (A.64)$$

$$U_{bl}(z) = U_{UBL} \frac{\ln \frac{z_{bl} - d_{fetch}}{z_{0fetch}}}{\ln \frac{z_{UBL} - d_{fetch}}{z_{0fetch}}} \quad (A.65)$$

$$U_i(z) = U_{UBL} \frac{\ln \frac{z_{bl} - d_{loc}}{z_{0loc}}}{\ln \frac{z_{UBL} - d_{fetch}}{z_{0loc}}} \quad (A.66)$$

Where:

$z_0$  - rural surface roughness (m)

$z_{0fetch}$  - rural surface roughness over larger urban fetch of 1 km (m)

$z_{0loc}$  - rural surface roughness over local urban fetch of 250 m (m)

$z_{UBL}$  - height of UBL (m)

$z_{bl}$  - blending height (m)

$d_{fetch}$  - displacement height over larger urban fetch of 1 km (m)

$d_{loc}$  - displacement height over local urban fetch of 250 m (m)

(Britter and Hanna, 2003; Millward-Hopkins, 2013; Barlow, 2014) suggest that a fully formed UBL can vary from 200 m in suburban areas to over 400 m dense in city centre environments, but that three sublayers within the UBL can form, Fig. A.19. In descending order with height, these are the ISL, RSL and CL layers, as was discussed in the literature review.

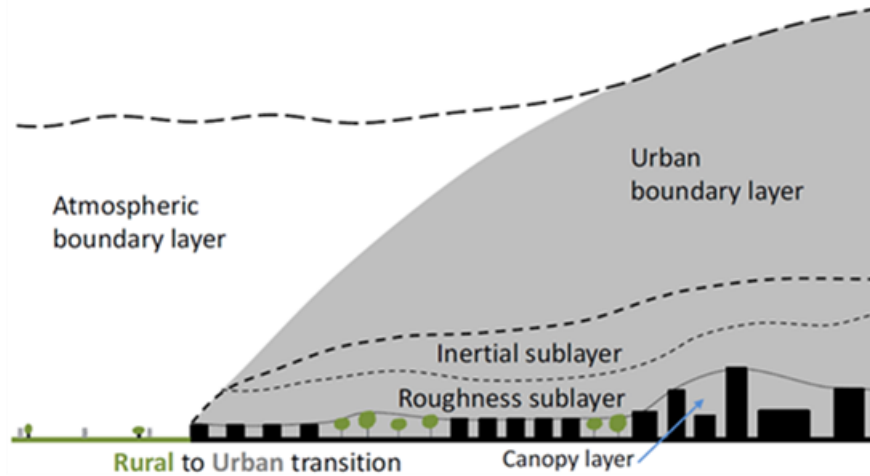
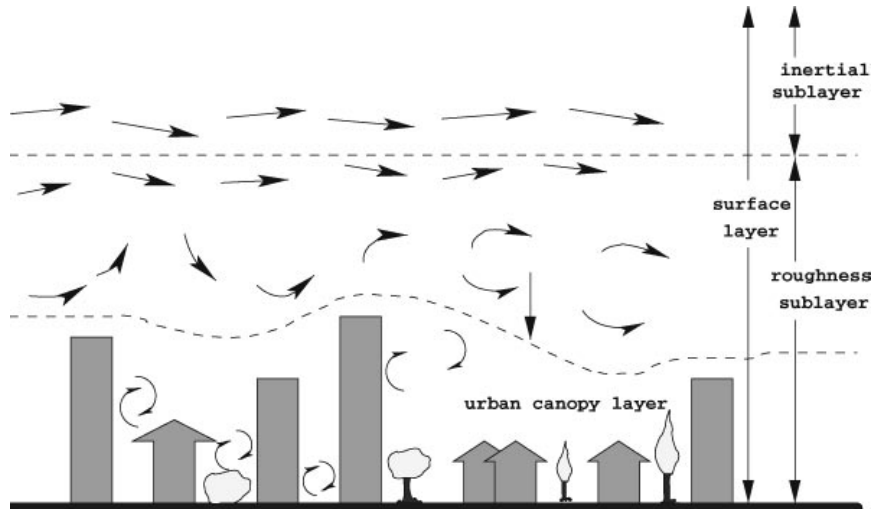


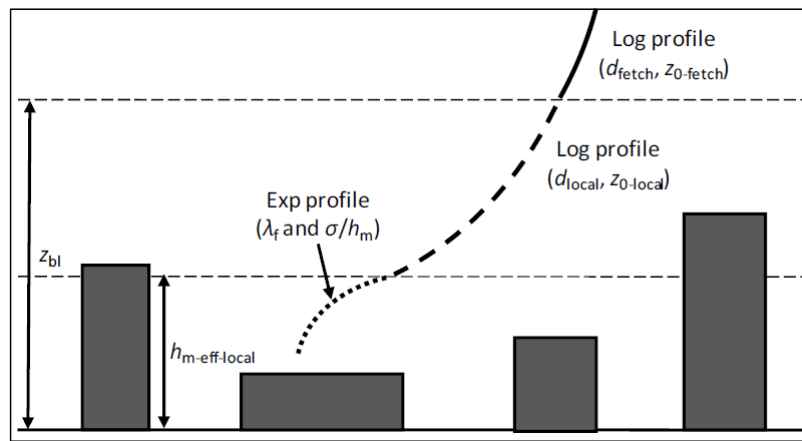
**Fig. A.19.** Schematic of sublayers within the UBL (Millward-Hopkins, 2013).

The ISL is defined by a constant shear stress that gives homogeneous flow. It extends from  $\sim 100$  m to 200 m. This is a reason for UK Met Office approach using 200 m as a reference height for the UBL. Above the ISL wind speeds increase at a lower rate with height, i.e., reduced wind shear. The wind shear profile within the ISL can be described by the log law, assuming neutral stability at higher wind speeds. The profile depends on the broader region,  $\sim 1$  km, of surface roughness and displacement height, Fig. A.20. The RSL has a higher level of spatial variation in the flow as it is more influenced by buildings. The RSL can extend from 2 to 5 times the height of the buildings (Barlow, 2014). The upper extent of the RSL is also referred to as the blending height (Grimmond and Oke, 1999). The average vertical wind speed profile can also be described as logarithmic and depends on the local surface roughness and displacement height. However, the high spatial deviations in wind speed can lead to greater uncertainty in energy predictions from wind turbines in this layer. (Rooney, 2001; Britter and Hanna, 2003; Cheng et al., 2007; Millward-Hopkins et al.,

2013c). Also, a limitation of Eq. (A.63) is that its prediction of the IBL height exceeds the upstream wind ISL with fetches greater than a few km (Best et al., 2008).



(a) Sublayers within UBL (Britter and Hanna, 2003)



(b) Schematic of sublayer wind speed profiles - adapted from (Millward-Hopkins et al., 2013b)

**Fig. A.20.** Schematic of sublayer wind speed profiles.

The lowest layer, the CL, has a height in that is similar to the building heights up to  $\sim 25\%$  of the mean building height above the rooftops (Millward-Hopkins et al., 2013a). It consists of complex flow above, around and in between buildings. The flow complexities can include vortices, channelling and flow recirculation (Balogun et al., 2010; Theeuwes et al., 2019). Wind shear profiles are very difficult to predict in the CL. (Macdonald, 2000; Coceal and Belcher, 2004) suggest that that wind shear profiles can be approximated by exponential functions. When canopy forces are in equilibrium, the stress divergence is equated with the drag force, Eq. (A.67), giving an exponential wind profile for  $u(z)$ , Eq. (A.68).

$$\frac{d}{dz} \left( l_c \frac{du}{dz} \right)^2 = \frac{u^2}{L_c} \quad (\text{A.67})$$

$$u(z) = u(h) e^{a \frac{z-d}{h}} \quad (\text{A.68})$$

$$a = \sqrt[3]{\frac{h^3}{2l_c^2 L_c}} \quad (\text{A.69})$$

Where:

$h$  - plane area weighted building height (m) (see later)

$l_c$  - canopy turbulence mixing length scale (m)

$L_c$  - canopy drag scale length (m)

However, there are very high uncertainties in the profiles. The CL is very challenging for wind energy exploitation.

In real urban zones, to estimate logarithmic wind shear profiles, the aerodynamic parameters of the heterogeneous surfaces still have to be considered. The area considered should contain a sufficient number of buildings for surface homogeneity so that the bulk aerodynamic effects are meaningfully represented by  $z_0$  and  $d_0$ , but must not be overly large so that it does not contain a large mix of surface types, e.g., parks, industrial, residential etc. (Millward-Hopkins, 2013). In many studies, regions or surface roughness patches up to 1 km to 2 km are considered (Barlow, 2014; Allen et al., 2017). This is because up to a certain height (blending height), the influence of roughness patches of these sizes can affect wind flow such that individual IBLs can form for significant surface roughness changes from one patch to another, Fig. A.21.



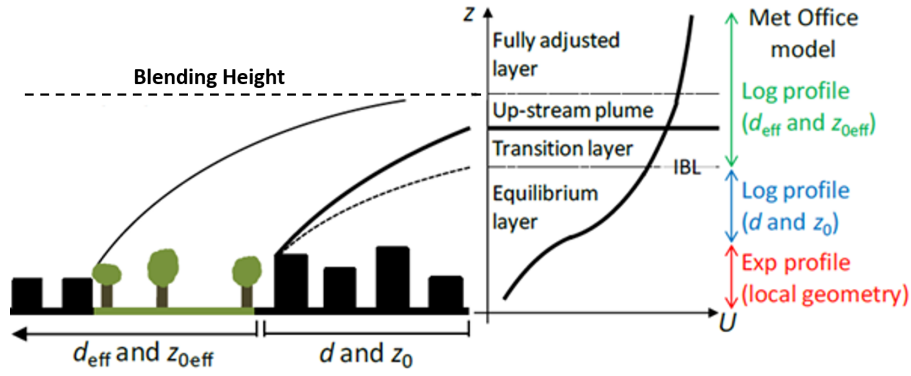


Fig. A.21. Schematic of vertical wind profiles over multiple roughness patches (Adapted from (Millward-Hopkins, 2013)).

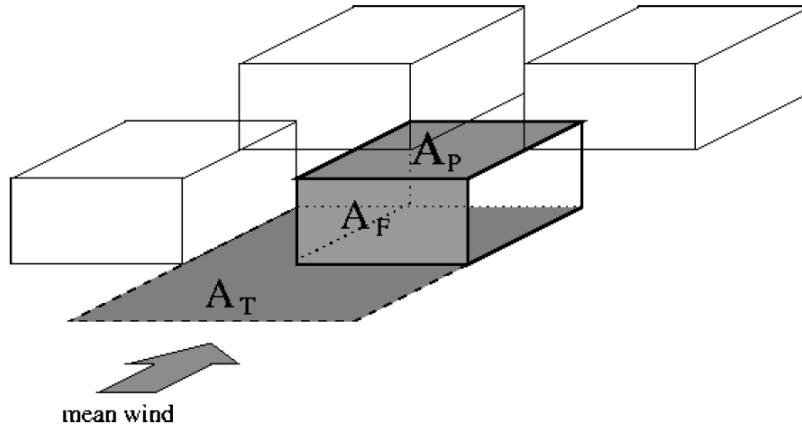
Each new IBL can consist of a transition layer (TL) and an equilibrium layer. The wind profile in the TL is affected by, but not fully adapted to, the new surface while it is fully adapted in the equilibrium layer. The wind profile in the TL is more difficult to assess as it partially depends on varying degrees on both local and upwind surface roughness characteristics, while above the TL and below the blending height, an upstream plume that depends only on the upwind surface may form. If the surface cover in a given patch region remains homogeneous over a sufficiently long fetch then the CL, RSL and ISL layers can develop in the equilibrium layer. The logarithmic profile can be applied to the ISL and RSL from local aerodynamic parameters. An exponential profile can describe CL considering local building geometries. The CL may develop after 3 to 6 rows of buildings, while the RSL may be established over the new surface after 10 rows of buildings (Cheng and Castro, 2002; Coceal and Belcher, 2005; Kurita and Kanda, 2009). The ISL may develop more slowly or may not form at all over urban patch regions.

Above the blending height, where the flow is fully adapted, the wind profile is considered logarithmic. Wind flow is considered to be impacted by the aggregate of the surface roughness patches as a whole. An effective roughness length,  $z_{0eff}$ , is calculated from a blending method of aerodynamic parameters of the individual patches and an effective displacement height,  $d_{eff}$ , can be calculated from an average of the individual patch surface values for  $d$  (Millward-Hopkins, 2013).  $z_{0eff}$  may be determined from balancing the average shear stress above the blending height with the sum of the shear stresses due to each of the individual roughness patches (Bou-Zeid, Meneveau, and Parlange, 2004). This is further developed for more real

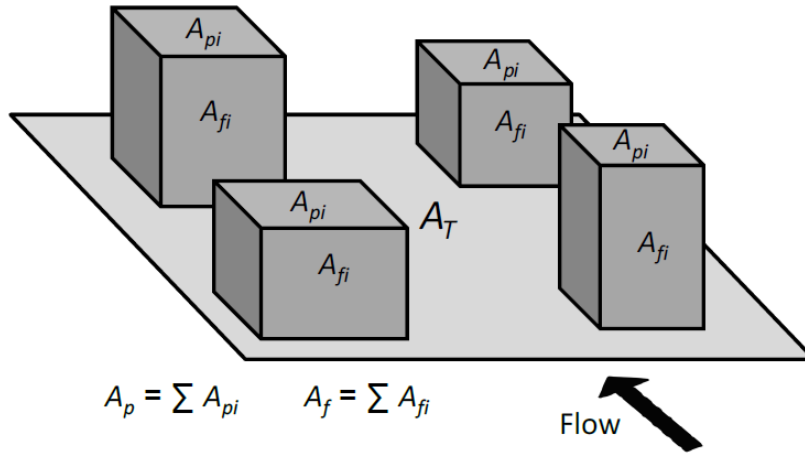
like heterogeneous surfaces using a structure function that estimates the variability of  $z_{\text{eff}}$  (Bou-Zeid, Parlange, and Meneveau, 2007). It is assumed that the wind profile above the blending height is not so sensitive to  $d_{\text{eff}}$ . However, major practical challenges still remain in the determination of accurate roughness parameters and displacement heights in urban wind resource assessment. This is because of the three possible flow regimes from isolated wakes to skimmed flow, previously shown in Fig. A.14, that can exist in the CL depending on building on building heights, plan area, frontal areas and packing density.

#### A.4.2 Morphological approaches to determine surface roughness and displacement height

Morphological approaches consider geometric properties of buildings to determine surface roughness and displacement height in urban areas. (Macdonald, Griffiths, and Hall, 1998) reviewed morphological methods including those suggested in the European Wind Atlas, (Troen and Lundtang Petersen, 1989), and suggested an improved method to estimate surface roughness from obstacles described earlier by Eq. (A.11). It attempts to account for the non-linear increase in surface roughness length at high roughness densities. They account for peaks in the value of  $z_0$  vs building density and drag coefficients of isolated obstacles of different shapes and layouts. It also allows some calibration of the method with experiments to refine values for  $z_0$  and displacement height  $d$ . A number of experimental wind tunnel studies have attempted to relate morphological characteristics of urban environments to surface roughness and displacement heights using idealised arrays of cubes (Raupach, 1992; Bottema and Mestayer, 1998; Macdonald, Griffiths, and Hall, 1998; Duijm, 1999; Kastner-Klein and Rotach, 2004; Crago, Okello, and Jasinski, 2012; Böhm et al., 2013). The morphological parameters used are the *plan area fraction*,  $\lambda_p$ ; *frontal area fraction*,  $\lambda_f$ ; Eqs. (A.70) and (A.71), and the *mean building/obstacle height*,  $h_m$ .



(a) Geometrical properties of a single obstacle



(b) Geometrical properties of multiple obstacle

**Fig. A.22.** Geometrical properties used in morphological definitions (Macdonald, Griffiths, and Hall, 1998; Grimmond and Oke, 1999).

$$\lambda_p = \frac{A_p}{A_T} \quad (\text{A.70})$$

$$\lambda_f = \frac{A_f}{A_T} \quad (\text{A.71})$$

Where:

$A_f$  - building frontal area ( $m^2$ )

$A_p$  - building plan area ( $m^2$ )

$A_T$  - total spatial area occupied by the buildings ( $m^2$ )

Assuming that surface drag is dominated by pressure exerted by buildings and that the ISL can be extended by a logarithmic profile, the ISL shear stress Eq. (A.72) and the surface drag Eq. (A.73) can be balanced to derive expressions for  $z_0$ ,  $h_m$  and  $d$  in terms of  $\lambda_p$  and  $\lambda_f$ , Eqs. (A.74) to (A.80).

$$F_D = \rho u_* A_T \quad (\text{A.72})$$

$$F_D = 0.5\rho U_{hm}^2 C_D A_f \quad (\text{A.73})$$

$$U(h_m) = \frac{u_*}{\kappa} \ln\left(\frac{h_m}{z_0}\right) \quad (\text{A.74})$$

Where:

$h_m$  - mean building height (m)

Equating Eqs. (A.72) and (A.73) leads to gives relations of  $z_0$ ,  $h_m$  and  $d$  with morphological parameters  $\lambda_p$  and  $\lambda_f$ .

$$\rho u_* A_T = 0.5\rho \left(\frac{u_*}{\kappa} \ln\left(\frac{h_m}{z_0}\right)\right)^2 C_D A_f \quad (\text{A.75})$$

$$\frac{z_0}{h_m} = e^{\left[-\left(0.5\frac{C_D}{\kappa^2}\lambda_f\right)^{-0.5}\right]} \quad (\text{A.76})$$

When the displacement height  $d$  is included, equations Eq. (A.76) becomes Eq. (A.80).

$$\rho u_* A_T = 0.5\rho \left(\frac{u_*}{\kappa} \ln\left(\frac{h_m - d}{z_0}\right)\right)^2 C_D A_f \left(1 - \frac{d}{h_m}\right) \quad (\text{A.77})$$

$$\frac{z_0}{h_m} = \left(1 - \frac{d}{h_m}\right) e^{\left[-\left(0.5\frac{C_D}{\kappa^2}\left(1 - \frac{d}{h_m}\right)\lambda_f\right)^{-0.5}\right]} \quad (\text{A.78})$$

$$\frac{z_0}{h_m} = \left(1 - \frac{d}{h_m}\right) e^{\left[-\left(0.5\beta\frac{C_D}{\kappa^2}\left(1 - \frac{d}{h_m}\right)\lambda_f\right)^{-0.5}\right]} \quad (\text{A.79})$$

(Macdonald, Griffiths, and Hall, 1998) give a relation between displacement height  $d$  and  $h_m$ , Eq. (A.80).

$$\frac{d}{h_m} = 1 + A^{-\lambda_p} (\lambda_p - 1) \quad (\text{A.80})$$

Where:

$A$  - constant of 4.43 for staggered arrays of cubes and 3.59 for square arrays.

(Grimmond and Oke, 1999) reviewed various studies that used morphological methods for application in real-world urban environments that use the geometric properties of building from GIS systems, i.e., the plan areas, frontal areas and spacing between buildings to create algorithms that determine  $z_0$  and  $d$ . The studies focused on a number of cities in North America. They concluded that morphological methods have the potential advantage that tall met towers are not required for measurement. However, because their empirical equations are derived from wind tunnel experiments, a challenge of application in real-world urban environments is the heterogeneous nature of building heights leading to a large scatter in the predicted values of  $z_0$  and  $d$ , illustrated by the grey areas shown in Fig. A.23.

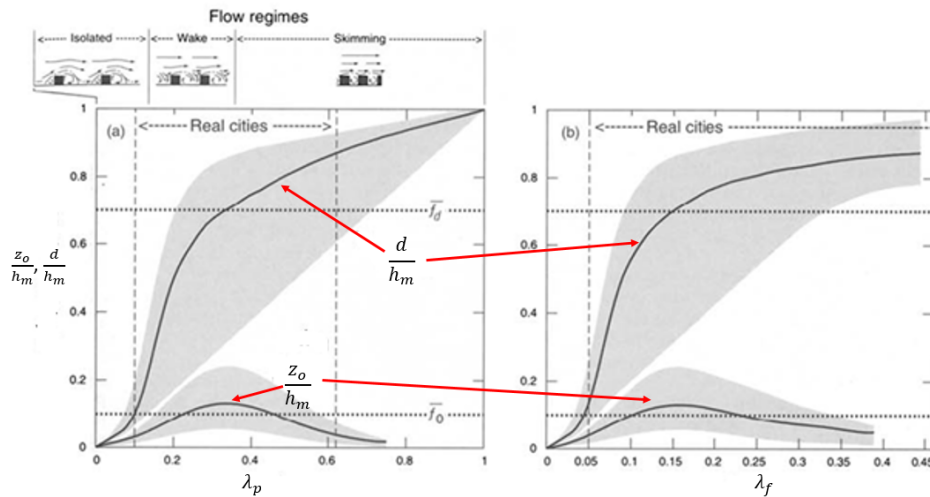


**Fig. A.23.** A representation of the relationship of  $z_0$  and  $d$  to the plan and frontal area density ratios, (Grimmond and Oke, 1999).

It was also found that a number of the studies were carried out with a limited amount of high quality measurement data at the time resulting in poor agreement and therefore could not find a standard to which morphological algorithms could be tested. Another partial reason for poor agreement was due to necessary simplification of geometric description of the surface and the irreducible errors in the analysis of the available wind measurements over the inhomogeneous surfaces. More recent morphological studies that build on this work, in the context of small scale

wind deployment, showed that these approaches could work well down to the effective mean building heights, but that errors increase in environments with more heterogeneous environments. (Millward-Hopkins et al., [2011](#)) showed that large uncertainties in defining building geometries gave up to 30% to 40% in wind speed predictions that can be even more exacerbated in energy predictions. This particularly was the case in the lower RSL near the CL where wind flow is very sensitive to building geometry. Other methods of urban wind resource assessment methods for small scale wind deployment have been proposed where the surface features of an urban environment described in the form of very complex topographic map that can be used as a compatible input to exiting mesoscale and microscale modelling tools (Simões and Estanqueiro, [2016](#)). The method reduces computation time and is more user friendly. However, the methodology presented needs further characterization and calibration with measured data.

## Appendix B

### Nacelle anemometer and LiDAR comparisons

#### B.1 Linear regressions between nacelle anemometer and LiDAR wind speeds

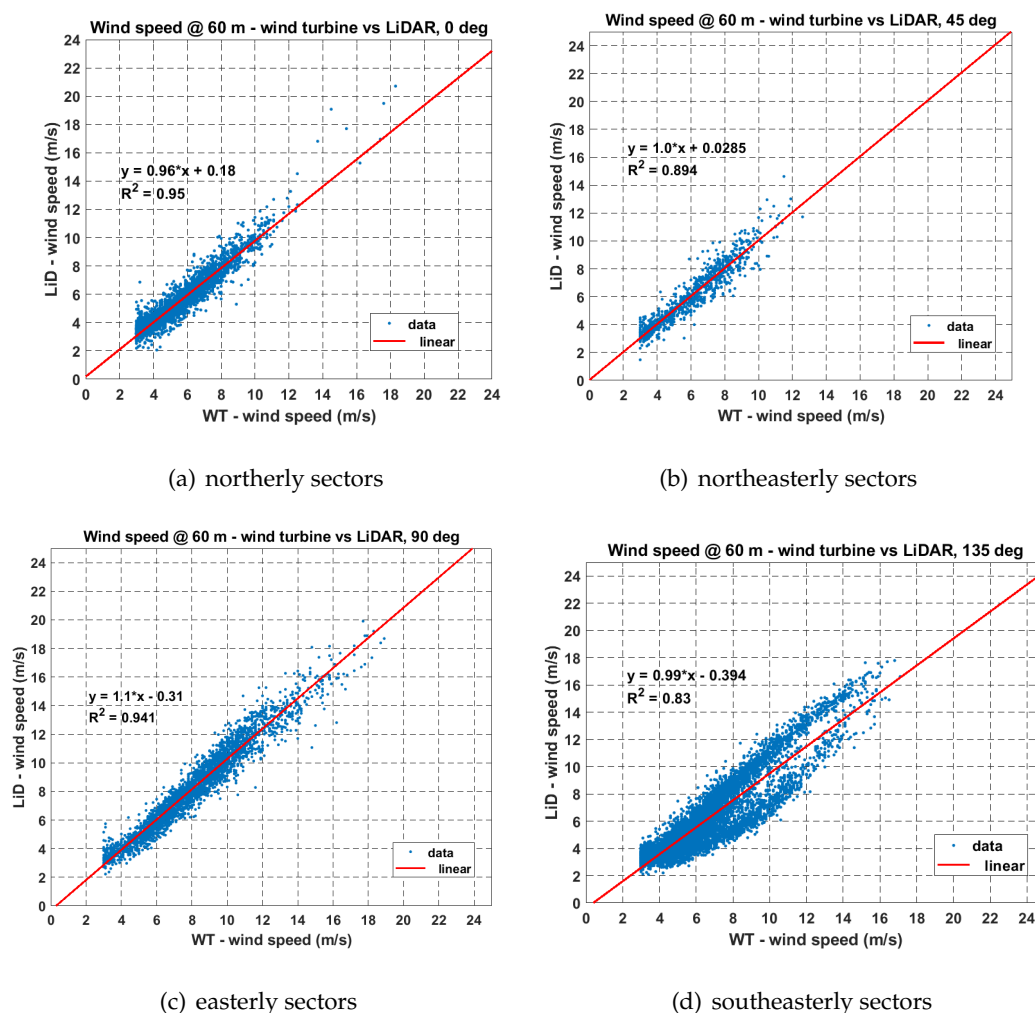
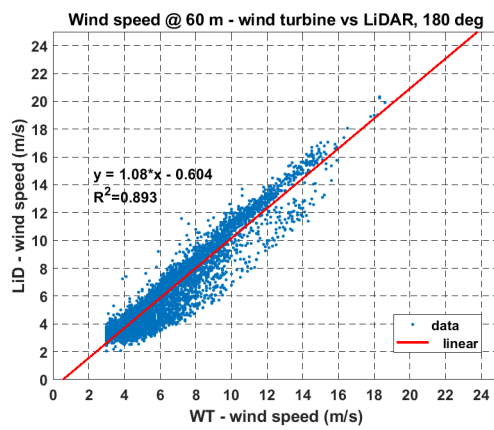
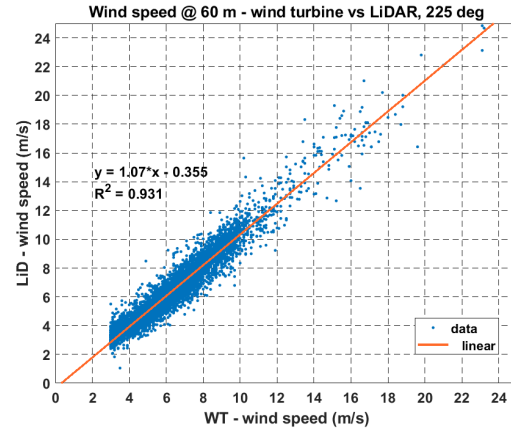


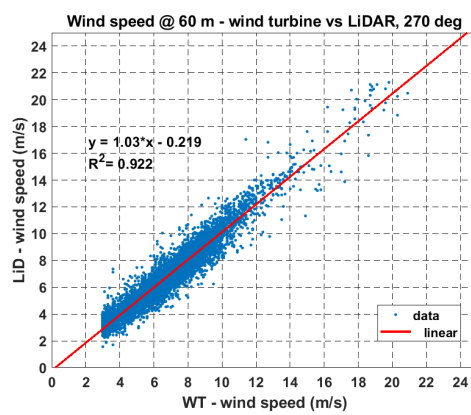
Fig. B.1. Directional linear regressions between nacelle anemometer and LiDAR wind speeds in north to southeast sectors.



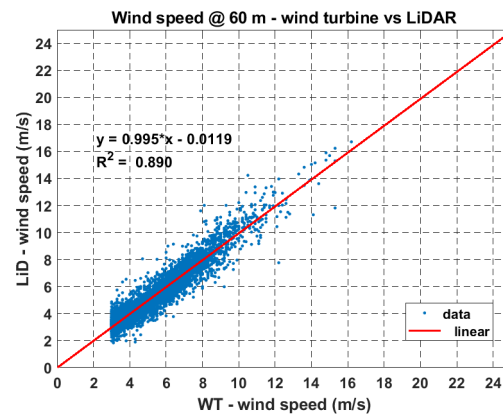
(a) southerly sectors



(b) southwesterly sectors



(c) westerly sectors



(d) northwesterly sectors

**Fig. B.2.** Directional linear regressions between nacelle anemometer and LiDAR wind speeds in south to northwest sectors.